Synthesis, Characterization, and Reactivity of Iron Hydrides in Nitrogen Fixation and Proton Coupled Electron Transfer from C-H bonds

Thesis by

Dirk Jacob Schild

In Partial Fulfillment of the Requirements for the

degree of Doctor of Philosophy

CALIFORNIA INSTITUTE OF TECHNOLOGY

Pasadena, California

2022

(Defended September 27, 2021)

Dirk Jacob Schild

ORCID 0000-0003-0179-6023

ACKNOWLEDGEMENTS

The last 5 years at Caltech have been enjoyable, albeit challenging and frustrating at times. My time here has been incredibly formative as I developed into a better scientist. This growth is thanks to all the people I interacted with along the way. I had the opportunity to work and learn from great people and I would like to acknowledge them. First and foremost, I thank Jonas Peters for his support and mentorship during my graduate studies and as a visiting student. His feedback and approach to research have pushed me to become a better and more rigorous scientist. Jonas has given me the freedom to work on problems that interested me while providing me with advice and guidance when needed. I would also like to thank my committee, Theo Agapie, Tom Miller and Harry Gray for their advice during exams and meetings.

In the Peters lab, I had the opportunity to work with incredibly talented coworkers and I would like to thank them all. Several students and postdocs worked on related projects and guided me during the first months of my time in the group. I would like to thank Marc-Etienne Moret for introducing me to Jonas and starting the iron nitrido project. Trixia Buscagan paved the way for my first N_2-fixation based project, and I thank her for the contributions and interest as I continued the project. Matt Chalkley and Niklas Thompson, both exceptional chemists have thaught me the basics on N_2-fixation as well as EPR and Mössbauer spectroscopy, two techniques of paramount importance to this thesis. Besides working in the same office, I had the pleasure to collaborate in the lab with Marcus Drover on two PCET projects. Marcus kept me focused and assured that the research kept moving forward. Patricia Nance, Pablo Garrido Barros, and Mike Zott, thanks for being great glovebox coworkers! I am also grateful for the many, not always scientific, discussions in

the office with Cooper Citek, Heejun Lee, Nina Gu, and often Christian Johansen. Recently I have been enjoing working with Lucie Nurdin in the office, who will continue the N_2 fixation work. To all the people I have overlapped with during my time in the group, I wish you the best of luck in what will undoubtedly be great futures.

The exceptional staff at Caltech made my research possible, and I would like to thank all of them for their contributions. Larry Henling has spent an incredible amount of time teaching me the different aspects of X-ray crystallography, while Paul Oyala has been incredible in increasing my understanding of EPR spectroscopy.

I would like to thank many friends outside of the lab. Brian Sanders, Wes Kramer, Paul, and Cooper have led us to many victories at T-Boyles. I will miss the fun times with all of you. In addition to trivia, Wes kept me company during endless bike rides. Pat, Axl LeVan, Madeline Meier, Christian Goodnow, Josh Zak, and Anna Scott, thanks for the great times with you as roommates.

Lastly, I would like to thank my family. My parents, brother and sister have always been there during this time. It has been hard being so far away from home, but the regular calls have made it a lot easier. I would also like to thank my grandparents who were ready to fly for the first time in their life to visit me, but then the pandemic happened. I promise I will visit Hardinxveld more often now! Finally, I would like to thank Tanvi. You have been my best friend, and your love and support may have been the most important in completing this work.

ABSTRACT

Mitigating the hydrogen evolution (HER) is an outstanding challenge in small molecule reduction catalysis using protons and electrons. Nitrogen fixation is a fundamental reaction where this selectivity is of great importance. This thesis details mechanistic studies into the nitrogen fixation reaction and factors that contribute to hydrogen evolution. In addition to the mechanistic studies, the development of reagents with weak X-H bonds, with applications in N-H bond formation is presented. Chapter 1 presents a brief overview of catalytic nitrogen fixation, the role of hydride ligands, and the importance of reagents required for the formation of weak N-H bonds. Chapter 2 details the mechanism of photo-enhanced iron mediated N_2 fixation. It is shown that off-path iron complexes bearing hydride ligands play an active role in hydrogen evolution by N_2 fixation catalysts. The data presented lends further insight into the selectivity, activity, and required driving force relevant to iron (and other) N_2RR catalysts. The third chapter describes the synthesis and characterization of a highly reactive iron(III) nitrido complex, a proposed key intermediate in nitrogen fixation mediated by $[(P_3^B)Fe]^+$. The ability to synthesize and characterize such an intermediate provides additional support for a distal catalytic cycle for this catalyst. In Chapters 4 and 5, the reactivity of iron hydrides and their role as precursors towards weak C-H bonds is discussed. These chapters outline a valuable approach for the differentiation of a ring- versus a metal bound H-atom. Chapter 4 provides a structural, thermochemical, and mechanistic foundation for the characterization of ring protonated indene-based ligands with remarkably weak C-H bonds. Chapter 5 extends the characterization of such reactive species and presents ligand induced migration of the hydride to a Cp* ring.

PUBLISHED CONTENT AND CONTRIBUTIONS

1. Schild, D. J.; Peters, J. C. Light Enhanced Fe-Mediated Nitrogen Fixation: Mechanistic Insights Regarding H_2 Elimination, HER, and NH_3 Generation. *ACS Catal.*, **2019**, 9, 4286-4295 DOI: 10.1021/acscatal.9b00523

D.J.S performed the design and execution of experimental work and calculations and participated in the preparation of the manuscript.

2. Drover, M. W.; Schild, D. J.; Oyala, P. H.; Peters, J. C. Snapshots of a Migrating H-Atom: Characterization of a Reactive Iron (III) Indenide Hydride and its Nearly Isoenergetic Ring-Protonated Iron(I) Isomer. *Angew. Chem. Int. Ed.*, **2019**, 58, 15504-15511 DOI: 10.1002/anie.201909050

DJS participated in the design and execution of the chemical reactions, performed DFT calculation, collected and analyzed spectroscopic data, and participated in the preparation of the manuscript.

3. Schild, D. J.; Drover, M. W; Oyala, P.; Peters, J. C. Generating potent C-H PCET donors: Ligand-induced Fe-to-ring proton migration from a Cp^*Fe^{III}-H complex demonstrates a promising strategy. *J. Am. Chem. Soc.*, **2020**, 142, 44, 18963–18970 DOI: 10.1021/jacs.0c09363

DJS participated in the design and execution of the chemical reactions, performed DFT calculation, collected and analyzed spectroscopic data, and participated in the preparation of the manuscript.

TABLE OF CONTENTS

LIST OF FIGURES

LIST OF TABLES

Abbreviations

β_e	The Bohr magneton
δ	Isomer shift or chemical shift
ΔE_q	Quadrupole splitting
12-c-4	12-crown-4
15-c-5	15-crown-5
18-c-6	18-crown-6
^{1}H	Hydrogen-1
^{2}H	Hydrogen-2
^{11}B	Boron-11
^{13}C	Carbon-13
^{15}N	Nitrogen-15
^{31}P	Phosphorus-31
2-MeTHF	2-methyltetrahydrofuran
$[BAr^{F}{}_{4}]^{-}$	Tetrakis(3,5-bis(trifluoromethyl)phenyl)borate
$[OTf]^{-}$	Trifluoromethanesulfonate
$[TBA]^{+}$	Tetrabutylammonium
*n*BuLi	*n*-butyllithium
A	Hyperfine tensor
a_{iso}	Isotropic hyperfine value
BDFE	Bond Dissociation Free Energy
CO	Carbon Monoxide
Cp	Cyclopentadienide
Cp*	Pentamethylcyclopentadienide

CPET	Concerted Proton-electron Transfer
CV	Cyclic Voltammogram
CW	Continuous Wave
DFT	Density Functional Theory
dppe	1,2-bis(diphenylphosphino)ethane
ENDOR	Electron Nuclear Double Resonance
EPR	Electron Paramagnetic Resonance
Et_2O	Diethyl Ether
Fc	Ferrocene (FeCp2)
G	Gauss
HAT	Hydrogen Atom Transfer
HER	Hydrogen Evolving Reaction
HOMO	Highest-Occupied Molecular ORbital
HYSCORE	Hyperfine Sublevel Correlation
Hz	Hertz
K	Kelvin
KC_8	Potassium Graphite
kcal	kilocalorie
*i*Pr	isorpropyl
IR	Infrared
MO	Molecular Orbital
Na/Hg	Sodium–mercury amalgam
N_2RR	Nitrogen reduction reaction

NMR	Nuclear Magnetic Resonance
P_2P^{Ph}	Bis(*o*-diisopropylphosphino-phenyl)-phenylphosphine
P_3^B	Tris(*o*-diisopropylphosphinophenyl)borane
PCET	Proton-coupled Electron Transfer
Q-band	Approximately 34 GHz
SQUID	Super-conducting Quantum Interference Device
T	Tesla
THF	Tetrahydrofuran
TMS	Trimethylsilyl
TiPS	Triisorpopylsilyl
X-band	Approximately 9.4 GHz

Chapter 1 : Introduction

1.1 Opening Remarks

The global nitrogen cycle is a crucial biogeochemical cycle required to sustain most life on Earth.[1] The proton-coupled reduction of molecular nitrogen (N_2) into ammonia (NH_3), a small but crucial part of this cycle, is the focus of this thesis. In the following chapters this process is referred to nitrogen fixation or the nitrogen reduction reaction (N_2RR). Although almost 80% of our atmosphere consists of dinitrogen and nitrogen is a key component in many biomolecules (*e.g.* amino acids, DNA, and RNA), the nitrogen in our atmosphere cannot be directly incorporated into these biomolecules. Dinitrogen must first be fixed into a chemically reactive form such as nitrate or ammonia through nitrogen fixation.[1] The formation of bioavailable nitrogen sources can occur via non-biological natural processes, as in the splitting of N_2 by lightning, or via biological and industrial processes.[1,2]

The biological process of converting N_2 to reduced forms, such as NH_3, in essence nitrogen fixation, is performed by a class of enzymes termed Nitrogenases (Figure 1.1). These enzymes use abundantly available N_2 from air, and protons derived from water to produce ammonia (Figure 1.1). In addition to the biological process, which accounts for almost half of all fixed nitrogen, an industrial counterpart exists: the Haber-Bosch process (Figure 1.1). Nowadays, biological nitrogen fixation and the Haber-Bosch process both account for nearly equivalent amounts of "*fixed*" nitrogen globally.[3–7] Although the Haber-Bosch process is routinely employed today, it boasts some major drawbacks such as the requirement of high pressure and temperature. It is estimated that 3-5% of the world's annual natural gas production is consumed in the Haber Bosch process, which translates into 1-2% of the world's annual energy consumption.[8,9] The increased access to readily

available ammonia in the last century resulted in a fundamental altering of the global carbon and nitrogen cycle, and the consequences of these disruptions will continue to play out for millennia.[10]

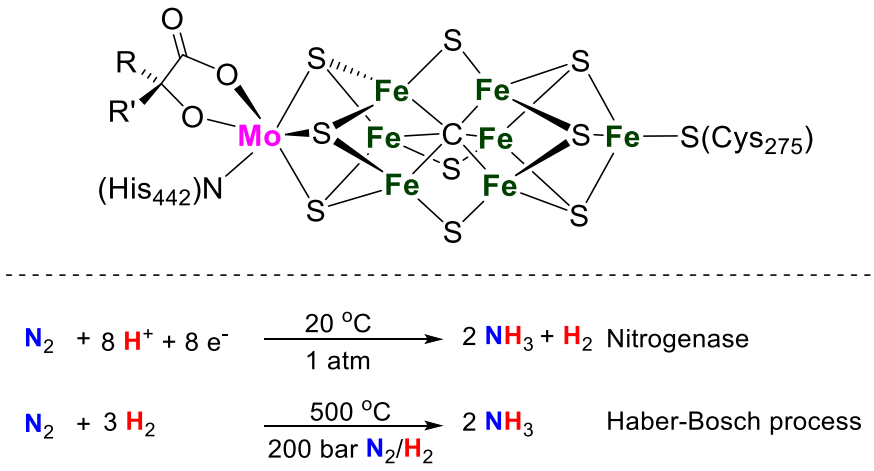

Figure 1.1. (Top) Biological nitrogen fixation is catalyzed by the iron-molybdenum cofactor (FeMoco) in nitrogenase enzymes. (Bottom) Stoichiometry and conditions for the conversion of dinitrogen (N_2) into ammonia (NH_3) by nitrogenase and the Haber-Bosch process (Bottom).

1.2 Synthetic Molecular Catalysts for N_2RR

Studies into the nitrogenase enzyme have revealed three major subtypes: iron-molybdenum nitrogenase, vanadium-iron nitrogenase, and all iron nitrogenase. Despite the advances made in the last decades, such as the characterization of the interstitial atom,[11] an atomically-precise mechanism for N_2 reduction by nitrogenase is far from established. Even basic questions, such as geometry and number of ligating sulfur atoms during catalysis remain unanswered.[12] Since the discovery of the nitrogenase cofactors, biological nitrogen fixation has provided inspiration in the development of synthetic N_2 fixation catalysts.

The binding of N_2 to a synthetic transition metal center was first observed for a Ru ammine complex, synthesized by Allen and Senoff in 1965.[13] Binding of N_2 to a metal center results in charge-transfer from the metal to the N_2 π^* orbitals, polarizing the N_2 ligand, towards functionalization with electrophiles. Chatt and coworkers demonstrated this activation followed by functionalization in 1972, reporting the first well-defined example of protonation of N_2 bound to a transition metal center.[14] Soon after, many more systems where reported, with some capable of complete reduction of N_2 to NH_3 and N_2H_4.[15]

On the basis of stochiometric studies, Chatt and co-workers proposed a mechanism for the catalytic reduction of N_2 by a single-site transition metal catalyst (Figure 1.2).[15] In the distal cycle (sometimes referred to as Chatt cycle), a metal-bound N_2 moiety is sequentially reduced at N_β prior to the key N-N bond cleavage step to produce a terminal metal nitrido (M≡N). On the other hand, a mechanism in which an N_2 moiety is reduced through alternating reduction at N_β and N_α is possible, which is referred to as the alternating mechanism (Figure 1.2).

Several intermediates, such as $FeNNH_2^+$, and $FeNH_2NH_2^+$ which represent intermediates along both pathways have been isolated on the ligand platforms studied in our group.[16–18] Recently, our group reported the characterization of a terminal iron nitride (Fe^{IV}≡N), through stepwise protonation of N_β from $[(P_3^B)Fe(N_2)]^2$, providing direct evidence for the feasibility of the distal pathway for this catalytic system. The synthesis and characterization of the proposed subsequent reduction product, a formal Fe^{III} nitrido, is the focus of **Chapter 3**.

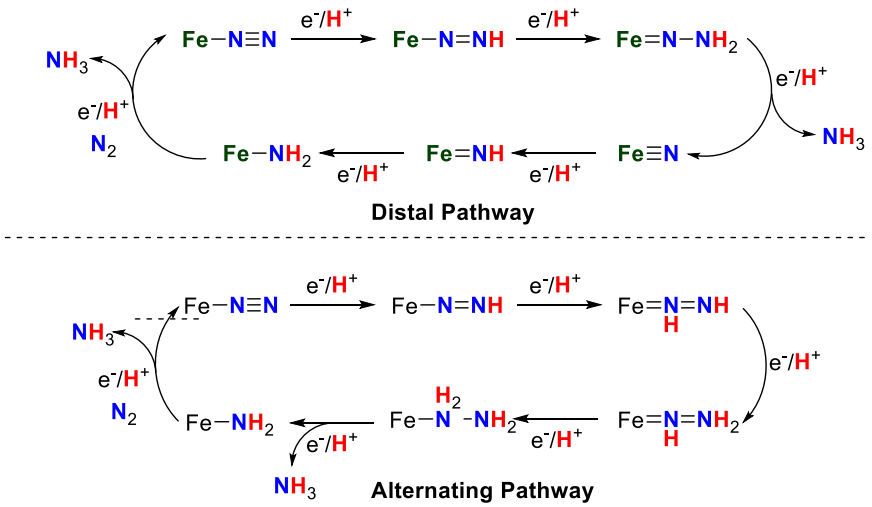

Figure 1.2. A schematic depiction of postulated N_2 binding and reduction at an Fe site by limiting distal (top) and alternating (bottom) mechanisms.

Since the initial characterization of the Ru amine complex, the search for molecular models has yielded hundreds of metal complexes that can bind dinitrogen involving transition metals far beyond those observed in nature. However, only a few systems are capable of catalytic reduction of N_2 to products such as hydrazine (N_2H_4) and[19,20] tris(trimethylsilyl)amine[21–27]. Even fewer examples are known of direct catalytic fixation of N_2 to NH_3.[19,28–43]

Schrock and Yandulov reported the first well-defined molecular system suitable for catalytic nitrogen fixation and observed up to eight equivalents of ammonia per molybdenum center.[34] More recently, Nishibayashi and coworkers obtained higher yields with molybdenum-based systems.[35,36,38,43,44] It was not until 2013 that iron-based fixation of nitrogen by a molecular model system was reported and since then the number of iron systems have been increasing steadily.[20,37,40,42,45]

Although the catalysts studied in our group are not an exact copy of the nitrogenase cofactor, design elements, including the metal identity (Fe), threefold symmetry, and the flexible anchor atom are used (Figure 1.3). Based on the success with $[(P_3^B)Fe(N_2)]^-$, new trisphosphine-based ligands were developed, but these have not yet matched the catalytic activity observed with the P_3^B ligand. Elucidating the principles behind the activity required driving force, and selectivity of these catalysts may inform the design of novel nitrogen fixation catalysts.

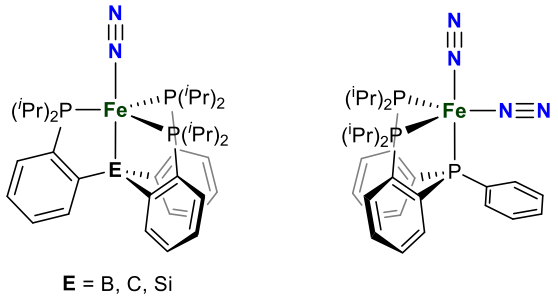

Figure 1.3. Molecular nitrogen fixation catalysts used in this thesis.

1.3 Selectivity in Nitrogen Fixation Catalysis

One of the challenges of small molecule reduction is selectivity, with the focus of recent research being the selectivity for N_2 vs H^+ reduction. H_2 formation can occur directly via a reaction between the acid and reductant, which is strongly dependent on the reductant and acid used or mediated by the nitrogen fixation catalysts. The use of $HBAr^F_4$ and KC_8 provides the most complete comparison between HER catalyzed by the iron systems discussed. All P_3^EFe catalysts are formally N_2RR catalysts, but have drastically different selectivities for N_2RR and HER.[41] Various mechanisms have been proposed through which

HER is catalyzed by the nitrogen fixation catalysts. Early intermediates along the cycle have weak bonds and are thermodynamically set up to evolve H_2 (Figure 1.4). On the other hand, the selectivity for N_2RR over HER is determined by the site of protonation. Protonation at the metal center leads to formation of a transition metal hydride (M-H), which can subsequently release H_2 upon protonation (Figure 1.4).

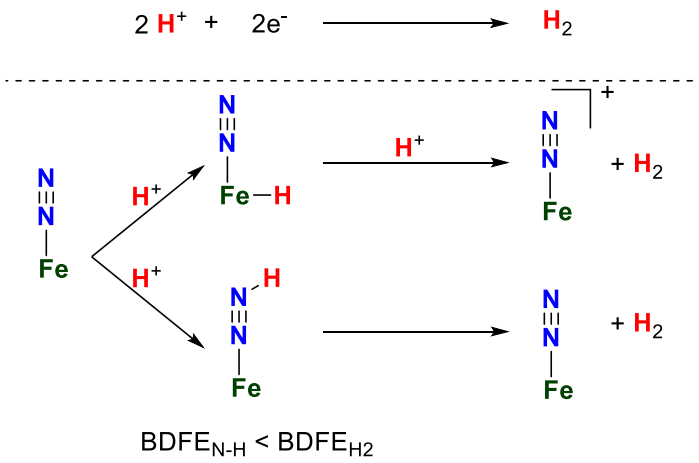

Figure 1.4. Overview of proposed HER mechanism in iron mediated nitrogen fixation. (Top) Direct HER via reaction of acid and reductant in solution. (Bottom) Two of the proposed pathways for HER mediated by the iron-based catalyst.

Currently the factors that govern the activity and selectivity of these catalyst is not understood. **Chapter 2** describes an investigation into some of the factors that govern the driving force, selectivity, and activity of $(P_2P^{Ph})Fe(N_2)_2$, and the role of hydrides in HER is discussed.

1.4 Weak N-H bonds as Determinants of the Driving Force in Nitrogen Fixation

Three limiting mechanisms can be considered for the formation of N-H bonds. Two stepwise pathways, either electron transfer followed by proton transfer and *vice versa*

(Scheme 1.1). Alternatively, a concerted pathway in which a proton and electron are delivered simultaneously is possible. The stepwise pathways have long been considered in N-H bond formation, and recently the proton coupled electron transfer (PCET) has been considered based on our groups observations that acids can protonate commonly used reductants in nitrogen fixation.

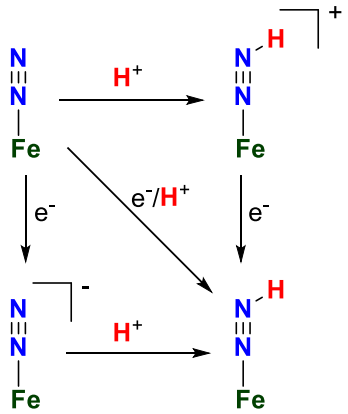

Scheme 1.1. Square scheme relating the stepwise ET-PT and PT-ET pathway to the PCET pathway for the first step of nitrogen fixation.

The proton-coupled reduction of N_2 requires the formation of a series of N-H bonds with varying bond strengths. The various intermediates encountered during the nitrogen fixation cycle (Figure 1.2) have intrinsically different N-H bond strengths, but on average, the N-H bond strengths formed during nitrogen fixation is 54.4 kcal mol^{-1}. The strength of an X-H bond can be determined through determination of the relevant reduction potential and acidity (Eq 1.1).

$$BDFE_{eff} = 1.37pK_a + 23.06E° + C \qquad \textbf{Eq 1.1}$$

Equation 1.1 can be extended beyond a discrete X-H bond to a reductant acid combination, as used in small molecule activation. In such a scenario, E° corresponds to

the reduction potential of the reductant, and the pK_a corresponds to that of the acid used. During nitrogen fixation, formation of an N-H bond is only favorable if $BDFE_{eff}$ of the reductant and acid combination is lower than $BDFE_{N-H}$ ($\Delta G < 0$). For the formation of the weakest N-H bond to be downhill, an acid/reductant combination with a weaker $BDEF_{eff}$ is required. For $(P_3^B)Fe$, the weakest N-H bond formed is below 30 kcal mol^{-1}. In an ideal situation, each N-H bond formed would have the same strength *i.e.,* 54.4 kcal mol^{-1}, as this allows the reaction to proceed with no overpotential.

1.5 Development of Reagents with Weak X-H Bonds

As the BDFE of N-H bonds formed during N_2 fixation is incredibly low (< 30 kcal mol^{-1}), reagents with even weaker $BDFE_{eff}$ bonds are required for a thermodynamically favorable reaction. Such low BDFE's can be achieved by carefully choosing a reductant and acid, with a sufficiently low $BDFE_{eff}$ (Eq 1.1). However, these separate reagents do not necessarily go through a PCET pathway. Well defined complexes with sufficiently weak X-H are basically non-existent, as they rapidly evolve H_2. Reagents with sufficiently weak X-H bonds can be generated through the coordination-induced weakening of an O-H bond, for example by paring SmI_2 with a polar protic solvent. Recently, our group provided evidence for the protonation of Cp^*_2Co via (CW) EPR spectroscopy.[46] The C-H bonds formed upon protonation of the Cp* fragment (BDFE < 29 kcal mol^{-1}) is almost 70 kcal mol^{-1} weaker than a typical C-H bond and such bonds have the potential to be utilized in the formation of weak N-H bonds during the proton-coupled reduction of N_2.

Due to the weak C-H bond and propensity to release H_2 even at temperatures below −100 °C, productive X-H bond formation through PCET could be observed. However, the developed understanding of conditions that leads to these remarkably weak C-H bonds

(Scheme 1.2) can be used as a design principle for other complexes with similar weak C-H bonds. The development of novel reagents with such weak C-H bonds, with applications in N-H bond formation will be the focus of **Chapters 4** and **5**.

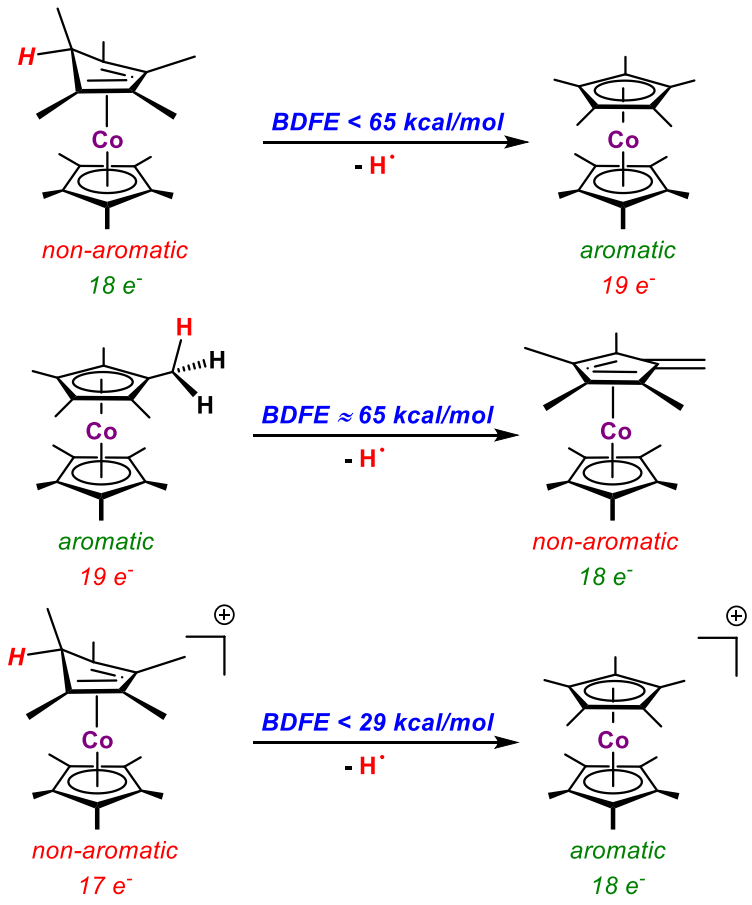

Scheme 1.2. A comparison of the experimental $BDFE_{C–H}$ for a variety of related Cp*Co-species, demonstrating the importance of aromaticity and electron count in predicting the stability of the indicated C–H bond.[46]

1.6 References

(1) Smil, V. *Enriching the Earth*; MIT Press: Cambridge, MA, 2001.

(2) Howard, J. B.; Rees, D. C. How Many Metals Does It Take to Fix N_2? A Mechanistic Overview of Biological Nitrogen Fixation. *Proceedings of the National Academy of Sciences* **2006**, *103* (46), 17088–17093.

(3) Canfield, D. E.; Glazer, A. N.; Falkowski, P. G. REVIEW The Evolution and Future of Earth ' s Nitrogen Cycle. *Science* **2010**, *330*, 192–196.

(4) Gruber, N.; Galloway, J. N. An Earth-System Perspective of the Global Nitrogen Cycle. *Nature* **2008**, *451* (7176), 293–296.

(5) Thamdrup, B. New Pathways and Processes in the Global Nitrogen Cycle. *Annual Review of Ecology, Evolution, and Systematics* **2012**, *43* (1), 407–428.

(6) Patil, B. S.; Hessel, V.; Seefeldt, L. C.; Dean, D. R.; Hoffman, B. M.; Cook, B. J.; Murray, L. J. Nitrogen Fixation. In *Ullmann's Encyclopedia of Industrial Chemistry*; Wiley-VCH Verlag GmbH & Co. KGaA: Weinheim, Germany, 2017; pp 1–21.

(7) Appl, M. Ammonia, 2. Production Processes. In *Ullmann's Encyclopedia of Industrial Chemistry*; Wiley-VCH Verlag GmbH & Co. KGaA: Weinheim, Germany, 2011.

(8) Smil, V. *Enriching the Earth: Fritz Haber, Carl Bosch, and the Transformation of World Food Production. Cambridge, MA: MIT Press*; 2004.

(9) Smith, B. E. Its Inner Secrets. *Science* **2001**, *109* (1987), 64–65.

(10) Erisman, J. W.; Sutton, M. A.; Galloway, J.; Klimont, Z.; Winiwarter, W. How a Century of Ammonia Synthesis Changed the World. *Nat. Geosci.* **2008**, *1* (10), 636–639.

(11) Spatzal, T.; Aksoyoglu, M.; Zhang, L. M.; Andrade, S. L. A.; Schleicher, E.; Weber, S.; Rees, D. C.; Einsle, O. Evidence for Interstitial Carbon in Nitrogenase FeMo Cofactor. *Science* **2011**, *334* (6058), 940–940.

(12) Hoffman, B. M.; Lukoyanov, D.; Yang, Z. Y.; Dean, D. R.; Seefeldt, L. C. Mechanism of Nitrogen Fixation by Nitrogenase: The Next Stage. *Chem. Rev.* **2014**, *114* (8), 4041–4062.

(13) Allen, A. D.; Senoff, C. V. Nitrogenopentammineruthenium(II) Complexes. *Chem. Commun.* **1965**, *24*, 621–622.

(14) Chatt, J.; Heath, G. A.; Richards, R. L. The Reduction of Ligating Dinitrogen to Yield a Ligating N_2H_2 Moiety. *J. Chem. Soc., Chem. Commun.* **1972**, *18*, 1010–1011.

(15) Chatt, J.; Dilworth, J. R.; Richards, R. L. Recent Advances in Chemistry of Nitrogen-Fixation. *Chem. Rev.* **1978**, *78* (6), 589–625.

(16) Moret, M.; Peters, J. C. N 2 Functionalization at Iron Metallaboratranes. *J. Am. Chem. Soc.* **2011**, *4350* (9), 18118–18121.

(17) Moret, M.-E.; Peters, J. C. Terminal Iron Dinitrogen and Iron Imide Complexes Supported by a Tris(Phosphino)Borane Ligand. *Angewandte Chemie International Edition* **2011**, *50* (9), 2063–2067.

(18) Anderson, J. S.; Cutsail, G. E.; Rittle, J.; Connor, B. A.; Gunderson, W. A.; Zhang, L.; Hoffman, B. M.; Peters, J. C. Characterization of an Fe≡N–NH $_2$ Intermediate Relevant to Catalytic N $_2$ Reduction to NH $_3$. *Journal of the American Chemical Society* **2015**, *137* (24), 7803–7809.

(19) Bazhenova, T. A.; Shilov, A. E. Nitrogen Fixation in Solution. *Coordination Chemistry Reviews* **1995**, *144* (C), 69–145.

(20) Hill, P. J.; Doyle, L. R.; Crawford, A. D.; Myers, W. K.; Ashley, A. E. Selective Catalytic Reduction of N2 to N2H4 by a Simple Fe Complex. *Journal of the American Chemical Society* **2016**, *138* (41), 13521–13524.

(21) Shiina, K. Reductive Silylation of Molecular Nitrogen via Fixation to Tris(Trialkylsilyl)Amine. *Journal of the American Chemical Society* **1972**, *94* (26), 9266–9267.

(22) Komori, K.; Oshita, H.; Mizobe, Y.; Hidai, M. Catalytic Conversion of Molecular Nitrogen into Silylamines Using Molybdenum and Tungsten Dinitrogen Complexes. *Journal of the American Chemical Society* **1989**, *111*, 1939–1940.

(23) Ung, G.; Peters, J. C. Low-Temperature N2 Binding to Two-Coordinate L2Fe0 Enables Reductive Trapping of L2FeN2- and NH3 Generation. *Angewandte Chemie - International Edition* **2015**, *54* (2), 532–535.

(24) Imayoshi, R.; Tanaka, H.; Matsuo, Y.; Yuki, M.; Nakajima, K.; Yoshizawa, K.; Nishibayashi, Y. Cobalt-Catalyzed Transformation of Molecular Dinitrogen into Silylamine under Ambient Reaction Conditions. *Chemistry - A European Journal* **2015**, *21* (24), 8905–8909.

(25) Siedschlag, R. B.; Bernales, V.; Vogiatzis, K. D.; Planas, N.; Clouston, L. J.; Bill, E.; Gagliardi, L.; Lu, C. C. Catalytic Silylation of Dinitrogen with a Dicobalt Complex. *Journal of the American Chemical Society* **2015**, *137* (14), 4638–4641.

(26) Liao, Q.; Saffon-Merceron, N.; Mezailles, N. Catalytic Dinitrogen Reduction at the Molybdenum Center Promoted by a Bulky Tetradentate Phosphine Ligand. *Angewandte Chemie - International Edition* **2014**, *53* (51), 14206–14210.

(27) Pellei, M.; Lobbia, G. G.; Santini, C.; Spagna, R.; Camalli, M.; Fedeli, D.; Falcioni, G. Synthesis, Characterization and Antioxidant Activity of New Copper(I) Complexes of Scorpionate and Water Soluble Phosphane Ligands. *Dalton Trans.* **2004**, *17*, 2822–2828.

(28) Fryzuk, M. D.; Johnson, S. A. The Continuing Story of Dinitrogen Activation. *Coordination Chemistry Reviews* **2000**, *200–202*, 379–409.

(29) MacKay, B. a.; Fryzuk, M. D. Dinitrogen Coordination Chemistry: On the Biomimetic Borderlands. *Chemical Reviews* **2004**, *104* (2), 385–401.

(30) Gardiner, M. G.; Stringer, D. N. Dinitrogen and Related Chemistry of the Lanthanides: A Review of the Reductive Capture of Dinitrogen, as Well as Mono- and Di-Aza Containing Ligand Chemistry of Relevance to Known and Postulated Metal Mediated Dinitrogen Derivatives. *Materials* **2010**, *3* (2), 841–862.

(31) Shilov, A. E. Catalytic Reduction of Molecular Nitrogen in Solutions. *Russian Chemical Bulletin* **2003**, *52* (12), 2555–2562.

(32) Pickett, C. J.; Talarmin, J. Electrosynthesis of Ammonia. *Nature* **1985**, *317*, 652–653.

(33) Chatt, J.; Heath, G. A.; Richards, R. L.; Fixation, N. 2074 J.C.S. Dalton. *J. Chem. Soc., Dalton Transactions* **1974**, 2074–2082.

(34) Yandulov, D. V.; Schrock, R. R. Esearch Rticles. *Science* **2003**, *301*, 76–79.

(35) Arashiba, K.; Miyake, Y.; Nishibayashi, Y. A Molybdenum Complex Bearing PNP-Type Pincer Ligands Leads to the Catalytic Reduction of Dinitrogen into Ammonia. *Nature Chemistry* **2011**, *3* (2), 120–125.

(36) Kuriyama, S.; Arashiba, K.; Nakajima, K.; Tanaka, H.; Kamaru, N.; Yoshizawa, K.; Nishibayashi, Y. Catalytic Formation of Ammonia from Molecular Dinitrogen by Use of Dinitrogen-Bridged Dimolybdenum-Dinitrogen Complexes Bearing Pnp-Pincer Ligands: Remarkable Effect of Substituent at Pnp-Pincer Ligand. *Journal of the American Chemical Society* **2014**, *136* (27), 9719–9731.

(37) Anderson, J. S.; Rittle, J.; Peters, J. C. Catalytic Conversion of Nitrogen to Ammonia by an Iron Model Complex. *Nature* **2013**, *501* (7465), 84–87.

(38) Tanaka, H.; Arashiba, K.; Kuriyama, S.; Sasada, A.; Nakajima, K.; Yoshizawa, K.; Nishibayashi, Y. Unique Behaviour of Dinitrogen-Bridged Dimolybdenum Complexes Bearing Pincer Ligand towards Catalytic Formation of Ammonia. *Nature communications* **2014**, *5*, 3737.

(39) Ritleng, V.; Yandulov, D. V.; Weare, W. W.; Schrock, R. R.; Hock, A. S.; Davis, W. M. Molybdenum Triamidoamine Complexes That Contain Hexa-Tert-Butylterphenyl, Hexamethylterphenyl, or p-Bromohexaisopropylterphenyl Substituents. An Examination of Some Catalyst Variations for the Catalytic Reduction of Dinitrogen. *Journal of the American Chemical Society* **2004**, *126* (19), 6150–6163.

(40) Del Castillo, T. J.; Thompson, N. B.; Suess, D. L. M.; Ung, G.; Peters, J. C. Evaluating Molecular Cobalt Complexes for the Conversion of N_2 to NH_3. *Inorganic Chemistry* **2015**, *54* (19), 9256–9262.

(41) Del Castillo, T. J.; Thompson, N. B.; Peters, J. C. A Synthetic Single-Site Fe Nitrogenase: High Turnover, Freeze-Quench 57 Fe Mössbauer Data, and a Hydride Resting State. *Journal of the American Chemical Society* **2016**, *138* (16), 5341–5350.

(42) Creutz, S. E.; Peters, J. C. Catalytic Reduction of N2 to NH3 by an Fe-N 2 Complex Featuring a C-Atom Anchor. *Journal of the American Chemical Society* **2014**, *136* (3), 1105–1115.

(43) Arashiba, K.; Kinoshita, E.; Kuriyama, S.; Eizawa, A.; Nakajima, K.; Tanaka, H.; Yoshizawa, K.; Nishibayashi, Y. Catalytic Reduction of Dinitrogen to Ammonia by Use of Molybdenum-Nitride Complexes Bearing a Tridentate Triphosphine as Catalysts. *Journal of the American Chemical Society* **2015**, *137* (17), 5666–5669.

(44) Ashida, Y.; Arashiba, K.; Nakajima, K.; Nishibayashi, Y. Molybdenum-Catalysed Ammonia Production with Samarium Diiodide and Alcohols or Water. *Nature* **2019**, *568* (7753), 536–540.

(45) Chalkley, M. J.; Del Castillo, T. J.; Matson, B. D.; Roddy, J. P.; Peters, J. C. Catalytic N2-to-NH3Conversion by Fe at Lower Driving Force: A Proposed Role for Metallocene-Mediated PCET. *ACS Central Science*. 2017, pp 217–223.

(46) Chalkley, M. J.; Oyala, P. H.; Peters, J. C. Cp* Noninnocence Leads to a Remarkably Weak C–H Bond via Metallocene Protonation. *J. Am. Chem. Soc.* **2019**, *141* (11), 4721–4729.

Chapter 2 : Light Enhanced Fe-Mediated Nitrogen Fixation: Mechanistic Insights Regarding H_2 Elimination, HER, and NH_3 Generation

Reproduced in part with permission from:

Schild, D. J.; Peters, J. C. Light Enhanced Fe-Mediated Nitrogen Fixation: Mechanistic Insights Regarding H_2 Elimination, HER, and NH_3 Generation *ACS Catal.* 2019, *9, 5, 4286–4295*.

2.1. Introduction

Substantial progress has been made in the development and understanding of molecular catalysts for N_2-to-NH_3 conversion, commonly referred to as the nitrogen reduction reaction (N_2RR).[1,,3] The number of well-defined complexes capable of N_2RR is expanding rapidly, and significant improvements in turnover and efficiency have been made.[4,5] With the growing number of systems available, it becomes increasingly possible to uncover general design principles that will aid in further progress for the field. The selectivity of N_2RR versus the competing hydrogen evolution reaction (HER) is a central selectivity issue in need of model studies.[6] Competing HER not only limits the efficiency of molecular catalyst systems, but also limits nitrogenase enzymes.[7,8] Additionally, and relatedly, a deeper understanding as to why seemingly related synthetic catalysts often require very different reductant and acid combinations to be competent for N_2RR is needed.

HER can occur by the background reaction between the reductant and acid; synthetic N_2RR catalysts depend on limiting the rate of background HER relative to the catalytic N_2RR rate. A catalyzed HER process, presumably accessible and competitive for many N_2RR catalysts, can also limit the efficacy of N_2RR selectivity. Both scenarios can be at play.[4,9]

For a complex that catalyzes both N_2RR and HER, numerous pathways for the latter process are possible. H_2 may evolve via protonation of a metal-bound hydride,[3,9] a commonly proposed pathway for synthetic HER catalysts. Accordingly, the build-up of M–H species has been observed both during and after catalytic N_2RR experiments.[2,9,10] The accumulation of M–H species is generally thought to attenuate N_2RR activity, and hydride precatalysts can give rise to diminished yields for N_2RR.[2,3,9] When hydride precursors serve

as active precatalysts for N_2RR, it is presumed they react with acid and reductant to release H_2, thereby generating a species that is on-path for N_2RR.[3,9] As an example of this, for a tris(phosphine)borane iron catalyst system studied extensively by our lab, $[(P_3^B)Fe(N_2)]^-$ (P = *o*-(P*i*Pr$_2$)$_2$C$_6$H$_4$), a dihydride intermediate was observed as an off-path resting state of the system when KC_8 and $HBAr^F_4(Et_2O)$ (BAr^F_4 = tetrakis-(3,5-bis(trifluoromethyl)phenyl)borate) were employed (Figure 2.1).[9] This dihydride species can be converted to an on path intermediate by reductive protonation.[9] A conceptually similar pathway has been described by Nishibayashi and coworkers for a (PNP)Fe system (Figure 2.1).[3]

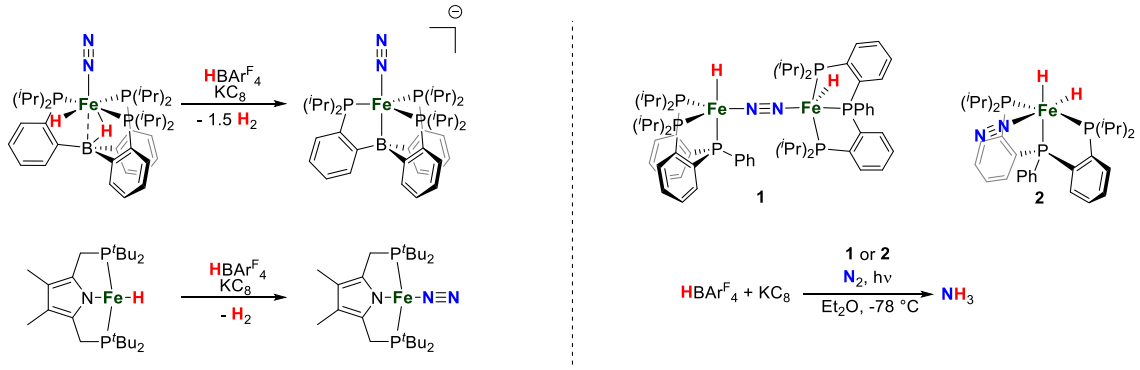

Figure 2.1. (Left) Protonation and reduction of off-path iron hydrides results in the formation of on-path species capable of N_2RR. (Right) Previously reported iron based catalysts and the conditions under which light enhanced nitrogen fixation by mercury lamp irradiation was observed.[1g]

Another possible competing HER pathway present within N_2RR systems that has been considered by our lab involves a bimolecular, N_xH_y ligand-mediated step wherein two Fe(N_xH_y) intermediates that feature weak N–H bonds evolve H_2 (Eqs. 2.1 and 2.2).[6]

$$2\ \text{Fe-NNH} \rightarrow 2\ \text{Fe-N}_2 + \text{H}_2 \qquad \textbf{(Eq. 2.1)}$$

$$2\ \text{Fe-NNH}_2 \rightarrow\ 2\ \text{Fe-NNH} + \text{H}_2 \qquad \textbf{(Eq. 2.2)}$$

Protonation at the metal versus at coordinated N_2 to form a metal hydride should be thermodynamically favored,[6] though the kinetic site of protonation can involve the coordinated N_2 ligand. Even if protonation at N_2 is kinetically favored, this can be followed by intra- or intermolecular H-atom/hydride/proton transfer to form a metal hydride.[11] Initial protonation at a site on the auxiliary ligand can also be kinetically favored.[12] Protonation at the terminal nitrogen (N_β) is desired for selectivity towards nitrogen fixation. For the $P_3{}^BFe$-system, iron is by far the thermodynamically favored site for protonation. However, the steric profile of the complex and the acids used appear to render functionalization at N_β kinetically favorable.[13]

Recently, our group reported two related iron-based complexes bearing hydride ligands, $(P_2P^{Ph})Fe(H)]_2(\mu\text{–}N_2)$ (**1**) and $(P_2P^{Ph})Fe(N_2)(H)_2$ (**2**) (P_2P^{Ph} = bis(*o*-diisopropylphosphino-phenyl)-phenylphosphine), that are modestly active systems for N_2RR (Figure 2.1, right).[2] For complex 2, photo-induced H_2 elimination was proposed to yield a more activated $Fe–N_2$ species that could undergo subsequent reductive protonation steps to generate NH_3. An H_2-elimination step can also be observed for $(P_3B)(\mu\text{-}H)Fe(N_2)(H)$, resulting in the formation of $(P_3B)Fe(N_2)$.[2,14]

Although precatalysts **1** and **2** are significantly less efficient for N_2RR than $[(P_3{}^B)Fe(N_2)]^-$ and certain other metal catalysts, they provide a fascinating model system for in-depth study because they have been shown to display substantial enhancement for N_2RR under irradiation.[2] Furthermore, these catalysts bear hydride ligands but are nonetheless active for N_2RR, affording an opportunity to investigate the role of the hydride ligands in N_2RR and competing HER. Finally, a better understanding of the electronic and

structural factors that influence the required redox potential for N_2RR in this phosphine-iron catalyst system compared to other systems can aid in the development of selective catalysts that operate at a comparatively low net driving force.

2.2 Results and Discussion

2.2.1 Synthesis and structural Analysis

In our prior communication we proposed that the product of H_2 elimination from well-characterized dihydride **2** might be "$(P_2P^{Ph})Fe(N_2)$".[2] Reasoning that this or a related species might be on-path for N_2RR, we targeted an independent synthesis. $(P_2P^{Ph})FeBr_2$ (**3**) provided a logical starting point. Treatment of **3** with 1.05 equiv sodium mercury amalgam resulted in the formation of $(P_2P^{Ph})FeBr$ (**4**) in 65% yield (Scheme 2.1). **4** exhibits C_s symmetry in solution based on its ^1H NMR spectrum and a distorted tetrahedral geometry ($\tau_4 = 0.77$)[15] in the solid state.

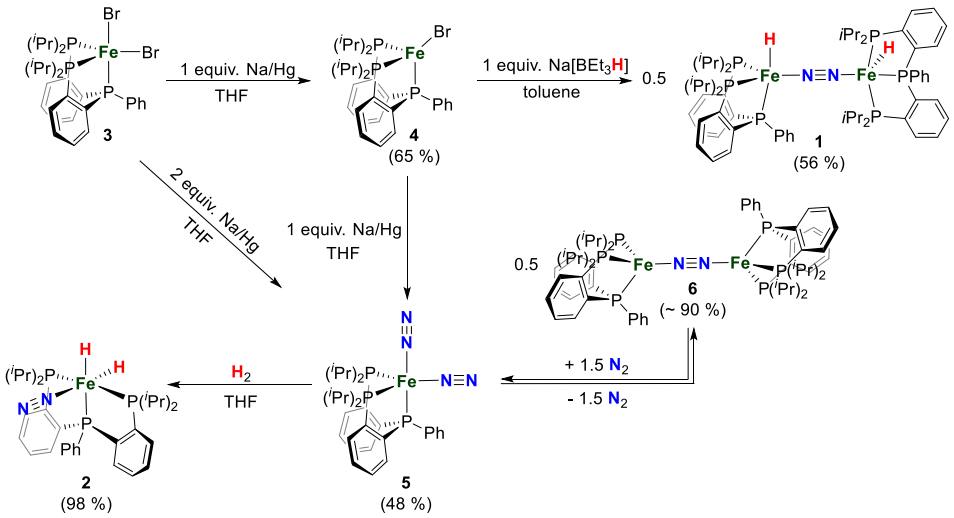

Scheme 2.1. Preparation of dinitrogen adducts of $(P_2P^{Ph})Fe$ from the bromide precursors **3** and **4**.

Bromide **4** is a useful synthon for several complexes of present interest. For example, treatment of **4** with $NaHBEt_3$ in toluene at −78 °C provides a more favorable route to the diiron complex 1 (Scheme 2.1), whose preparation was previously described by $NaHBEt_3$ reduction of **3**. Furthermore, **4** can be reduced with sodium mercury amalgam in either benzene or THF to provide a new, maroon red complex (P_2P^{Ph}) $Fe(N_2)_2$ (**5**). Complex **5** can be alternatively prepared by reduction of **3** with excess sodium mercury amalgam in benzene (Scheme 2.1).

18-electron **5** exhibits two intense bands in its IR spectrum (thin film; ν_{symm} = 2065 cm^{-1}, ν_{asymm} = 2005 cm^{-1}) and its solid-state crystal structure, reveals a distorted trigonal bipyramidal geometry at iron (τ_5 = 0.54)[16] with Fe–P distances ~0.15 Å shorter than in **3**, reflecting its singlet ground state.[2] The structure and stretching frequencies of the five-coordinate N_2 complex 5 is closely related to recently reported ($P^RP^{Cy}_2$)$Fe(N_2)_2$ ($P^RP^{Cy}_2$ = $RP(CH_2CH_2PCy_2)_2$, R = Ph, tBu) complexes.[17] In the latter N_2 complexes, facile N_2 dissociation hampers their isolation. Although **5** is also susceptible to N_2 dissociation (*vide infra*) it can be readily isolated by evaporation of the solvent *in vacuo* followed by extraction with pentane.

2.2.2. N2-Binding Equilibria of 5.

A solution equilibrium exists between **5** and a dinuclear, mono-N_2-bridged complex **6** (Scheme 2.1). This is clearly gleaned from ^1H and ^{31}P NMR spectroscopies. For example, the ^1H NMR signal intensities for **5** decay upon degassing the solution in a J-Young NMR tube and the signals corresponding to **6** grow in. Addition of N_2 regenerates 5. The absence of an N_2 stretch in the IR spectrum of **6**, and the release of 1.5 equiv of N_2 per Fe on

conversion of **5** to **6**, as measured by a Toepler pump experiment, are consistent with our formulation of 6 (Scheme 2.1; Eq. 3):

$$2\ (P_2P^{Ph})Fe(N_2)_2 \rightarrow \{(P_2P^{Ph})Fe\}_2(\mu\text{–}N_2) + 3/2\ N_2 \quad \text{(Eq. 3)}$$

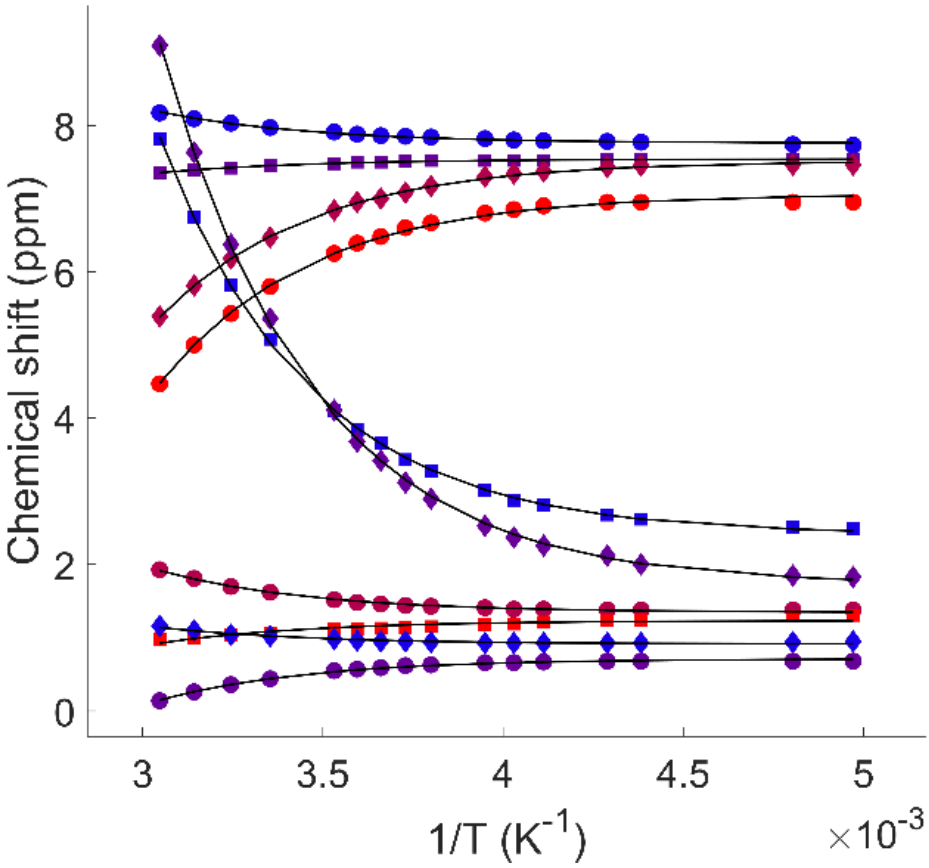

Figure 2.2. The ^{1}H NMR chemical shifts of **6** plotted as a function of 1/T display a deviation from Curie-behavior, due to the population of a low-lying exited state. A fit of the data, indicated with black lines, gives $J = -940 \pm 9.4\ cm^{-1}$.

Monitoring the ^{1}H and ^{31}P chemical shifts of **6** over a 130 °C range under vacuum reveals deviation from Curie-behavior (Figure 2.2). The singlet ground state of 6 likely arises from antiferromagnetic coupling of two $S = 1$ iron nuclei. The dramatic shifts in the NMR spectra are therefore attributed to partial population of triplet and quintet states

separated by 2*J* and 6*J* from the ground state, respectively (as obtained for the Heisenberg-Dirac-VanVleck Hamiltonian in the notation $H_{HDVV} = -2JS_1S_2$). Fitting of the appropriate Boltzmann function to the experimental data yields $J = -940 \pm 9.4$ cm^{-1}.[18] Antiferromagnetic coupling for an N_2–bridged diiron species has been observed previously.[19]

2.2.3 Increased Turnover with Non-Hydride Precatalysts and Identification of Off-Path Species.

Previous N_2RR studies using the (P_2P^{Ph})Fe-system were performed with the hydride complexes **1** and **2** as (pre)catalysts. We wondered whether increased turnover numbers might be realized with $(P_2P^{Ph})Fe(N_2)_2$, **5**, devoid of hydride ligands. Indeed, catalysis under the same conditions with 5 resulted in significantly higher NH_3 yields than those afforded by **1** and **2**. For example, at a loading of 150 equivalents acid and 180 equivalents reductant at −78 °C in Et_2O, in the absence of light, complexes **1** and **2** catalyzed only 3.6 ± 0.6 and 2.6 ± 0.01 equiv NH_3 per iron, respectively, whereas **5** catalyzed the generation of 6 ± 0.5 equiv. Interestingly, a comparable NH_3 yield (5.1 ± 0.02 equiv per iron center) could be realized with 5 using only 1/3 as much reductant and acid (50 equiv $HBAr^F_4(Et_2O)$ and 60 equiv KC_8), which was not the case for either **1** or **2**. A possible explanation for this difference is that HER catalysis from the hydrides, which are present in the highest concentration at the onset of runs with **1** and **2**, outcompetes N_2RR.

Similar NH_3 yields were obtained for the three different precatalysts **1**, **2**, and **5** in catalytic experiments irradiated with a mercury lamp. We presume that dihydride **2** releases H_2 upon irradiation with light to yield **5**, and that this transformation occurs rapidly under turn-over conditions as all (pre)catalysts give similar yields. The consumption of hydride

species via photolysis reduces HER catalyzed by the hydrides, thus increasing overall efficiency for NH_3.

To determine whether catalyzed HER contributes to the low yields of NH_3 obtained with dihydride **2**, hydrogen evolution was measured under catalytically relevant conditions. As shown in **Figure 2.3**, the initial rate of H_2 evolution at −78 °C, is significantly enhanced by the presence of either **2** or **5**. These data suggests both **2** and **5** are comparatively competent catalysts for HER, whereas complex **5** is a more effective (pre)catalyst for N_2RR. Indeed, the fact that most of the acid is consumed within 30 minutes at −78 °C speaks to how rapidly **5** must catalyze NH_3 production for N_2RR to be kinetically competitive.

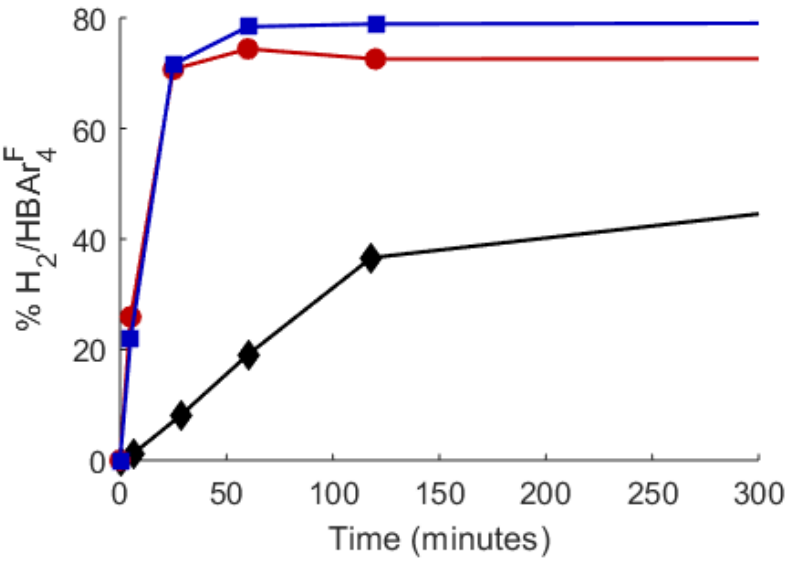

Figure 2.3. Time profiles of the formation of H_2 from $HBAr^F_4$ and KC_8 in Et_2O at −78 °C. Data are presented for the background reaction of these reagents in the absence of catalyst (black diamonds), as well as in the presence of either **2** (red circles) or **5** (blue squares).

Each time course was collected continuously from a single experiment. The final data points, recorded after 16 hours, are omitted from the graph.

Additional evidence for the active role of **2** in HER is obtained from Mossbauer studies of freeze-quenched samples. Freeze-quenching of a catalytic run using ^{57}Fe-labeled **2**, 50 equiv acid, and 60 equiv reductant, shows its disappearance within 5 minutes (Figure 2.4, middle trace). A new broad feature, likely due to the overlap of several species, is observed. Freeze-quenching the reaction after 30 minutes provides a similarly broad signal (Figure 2.4, bottom trace), but one that also contains **2**, with its characteristic small quadrupole splitting (constituting ~ 40% of the total). Experiments using **5** as the precatalyst provide an analogously broad signal after 5 and 30 minutes (See Figure A59-S60). Notably, dihydride **2** is always observed at the end of a catalytic experiment, once the sample has been warmed to room temperature. It is the major species present (typically ~ 90% by Mössbauer spectroscopy). Furthermore, IR and NMR spectra recorded after runs using **5** as the precatalyst show **2** as the only identifiable species upon warming. These data collectively suggest that the catalytic system converts to a Fe–H species (**2**), which is on path for HER (*vide infra*), as the major product.[2] This finding is similar to that of $[(P_3^B)Fe(N_2)]^-$, which also ends tied-up in an off-path hydride-borohydride state (Figure 2.1, left).[9]

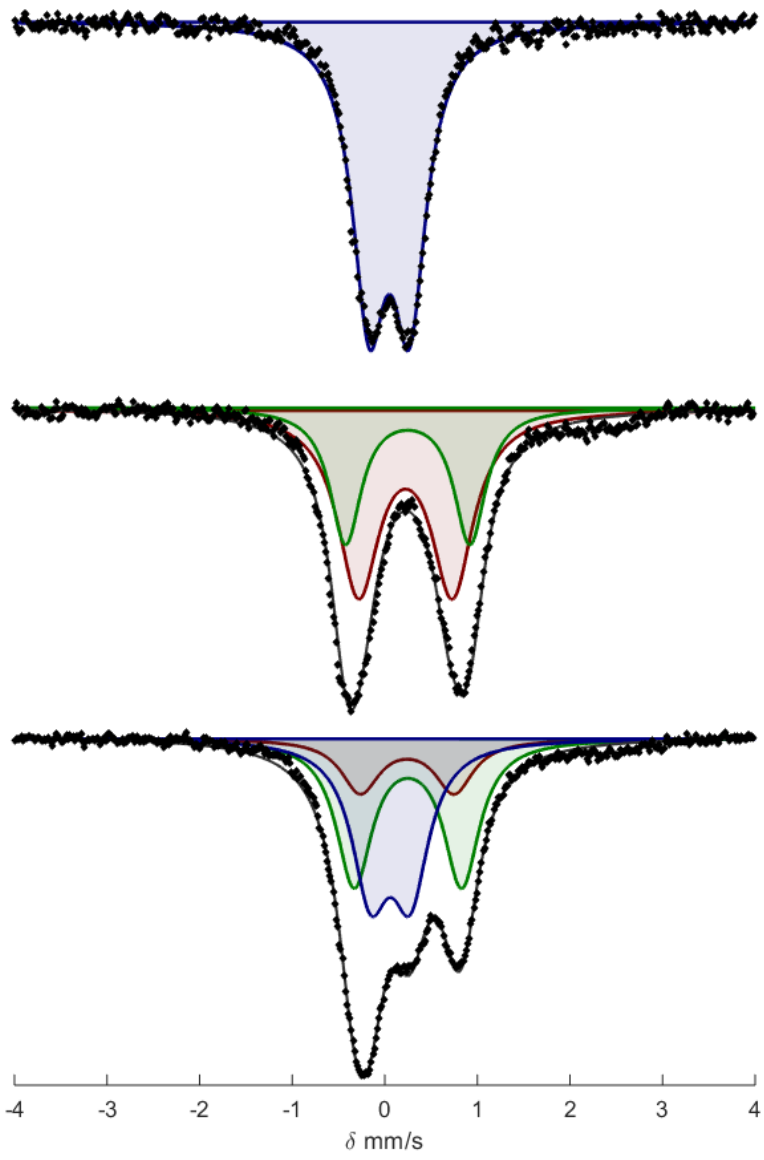

Figure 2.4. Frozen solution Mössbauer spectra collected at 80 K in the presence of a 50 mT parallel magnetic field. Spectra of a catalytic mixture, using **2** (blue) as precatalysts (top), quenched after 5 minutes (middle) and 30 minutes (bottom) of stirring. For parameters of individual components, see Supporting Information.

2.2.4 Oxidative addition and reductive elimination of H_2.

To investigate potential pathways by which hydride species form during catalysis, stoichiometric reactions were performed with dihydride **2**, the bis–N_2 complex **5**, and dinuclear **6**. Addition of H_2 to **5** (or **6**), followed by N_2, resulted in the quantitative formation of **2** (Scheme 2.2). However, addition of H_2 to **5** at −78 °C in a J-Young tube for one hour resulted in the appearance of a trace amount of **2**. Full conversion was only observed upon warming to room temperature. The latter result strongly suggests that the formation of **2** under the catalytic conditions at −78 °C does not occur by a reaction between 5 and H_2.

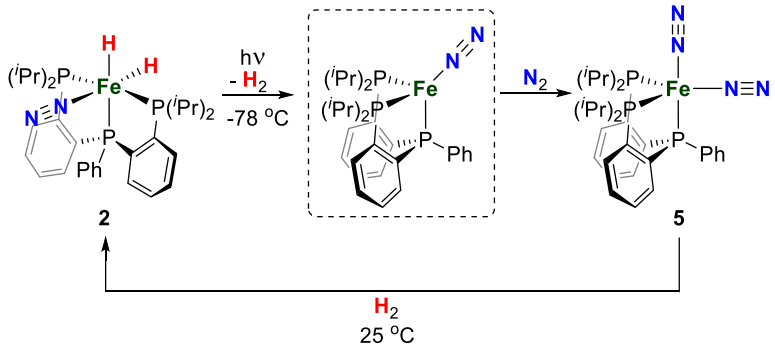

Scheme 2.2. Light induced reductive elimination of H_2 from **2** leads to a transient unobserved four coordinate species, which binds N_2 to form **5**. The H_2 elimination is reversible as **5** reacts back to **2** in the presence of H_2.

Irradiating solutions of **2** with a 100 W mercury lamp at −78 °C or room temperature results in darkening of the solution and the formation of **5** (Scheme 2.2). Complete disappearance of **2** is not observed, suggesting the reaction is reversible. A possible 16-

electron intermediate, such as "(P_2P^{Ph})Fe(N_2)",[2] could not be identified by NMR, IR, or Mössbauer spectroscopy.

H_2 elimination from **2** to **5** leads to a significant decrease in ν(NN) stretching frequencies due to increased backbonding upon H_2 elimination. A similar effect was observed previously for (P_3^B)(μ-H)Fe(N_2)(H).[2] In this context, these systems crudely model a proposed N_2 binding/activation via H_2 elimination at the E_4 state of the iron-molybdenum cofactor (Figure 2.5).[20] Clearly, increased N_2 activation upon H_2 elimination observed for this P_2P^{Ph}Fe-system would be even more pronounced for the unobserved, but perhaps catalytically relevant mono-N_2 adduct "P_2P^{Ph}Fe(N_2)" (*vide infra*).

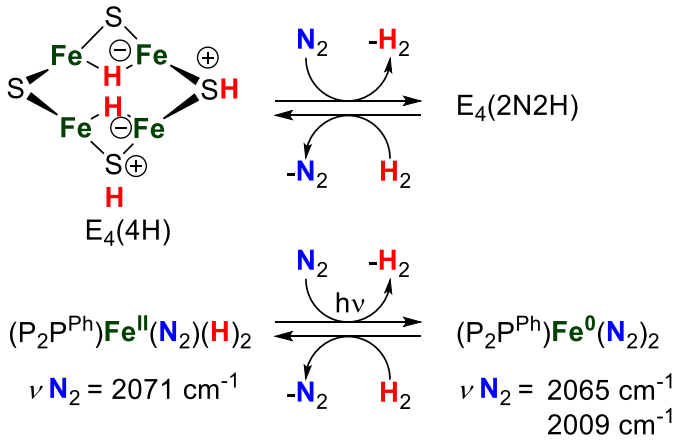

Figure 2.5. (Top) H_2 elimination from the E_4 state resulting in a more electron rich center is proposed from Mo-nitrogenase, and Fe-nitrogenase. Light induced reductive elimination of H_2 from **2** leads to increased back-bonding due to the formal reduction from Fe^{II} to Fe^0 (Bottom).

2.2.5 Stoichiometric reactivity and hydrogen evolution.

To further probe HER catalysis by the present system, $HBAr^F_4$ was added to (P_2P^{Ph})Fe(N_2)$_2$ **5** at −78 °C, causing a color change from maroon to dark yellow upon

warming. The product of protonation at iron was identified as $[(P_2P^{Ph})Fe(N_2)_2(H)][BAr^F{}_4]$ (**7**) (Scheme 2.3), featuring a diagnostic ^1H NMR hydride resonance (−17 ppm) and bands at 2069, 2194 and 2264 cm^{-1}, corresponding to the ν(Fe–H) and ν(NN) IR stretches. Its solid-state structure was also determined. This complex can also be obtained by oxidation of $\{(P_2P^{Ph})Fe(H)\}_2(\mu\text{–}N_2)$ **1** with either $FcBAr^F{}_4$ (Fc = bis(η^5-cyclopentadienyl)iron) or $HBAr^F{}_4$ (Scheme 2.3). Of primary interest, protonation of **2** with $HBAr^F{}_4$ likewise generates **7** with concomitant H_2 release, possibly via an "$[Fe(H_2)(H)]^+$" adduct.[21]

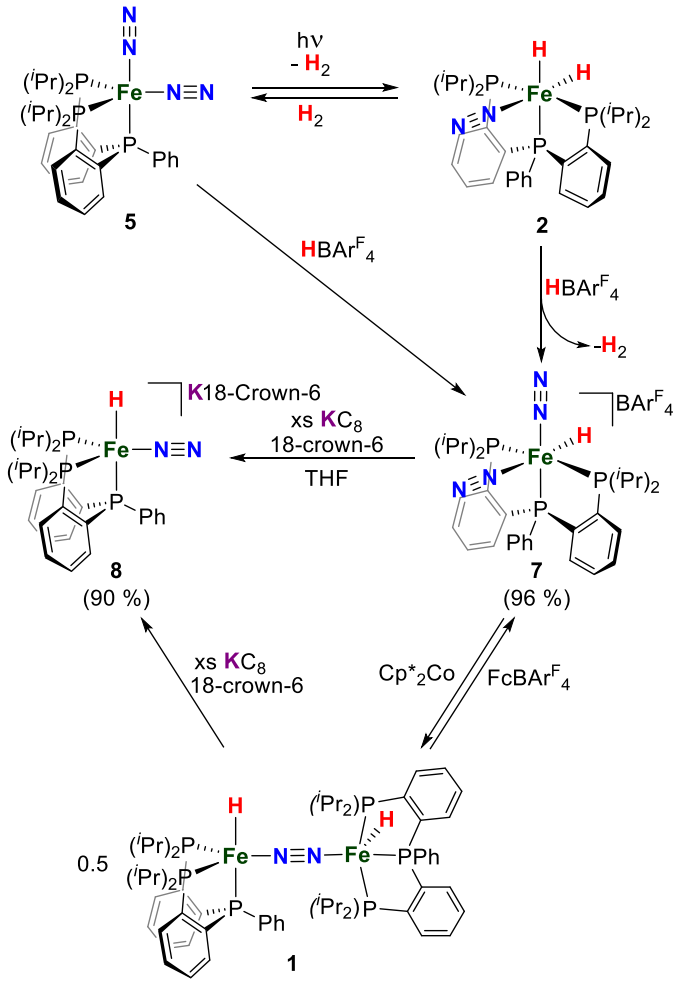

Scheme 2.3. Pathways towards **7** and **8**. Preparative and NMR scale reactions were performed at −78 °C.

Monohydride **7** can be cleanly reduced to dinuclear **1** using either Cp^*_2Co or stoichiometric KC_8. Reduction of **7** with an excess of KC_8 by contrast generates a different diamagnetic species which, following addition of 18-crown-6, could be isolated in pure form as $[P_2P^{Ph}Fe(N_2)(H)][K(18\text{-crown-6})]$ (**8**) (Scheme 2.3). Complex **8** features a diagnostic hydride resonance in its ^1H NMR spectrum (δ = -9.69 ppm, dt), and its solid-state structure displays a short Fe–N (1.774(1) Å) and an elongated N–N (1.139(2) Å) bond. A high degree of activation of N_2 is reflected by its ν(NN) (1924 cm^{-1}).

Stoichiometric mixing of cation **7** and anion **8** resulted in comproportionation to 1 (> 90% yield). Proton transfer (PT) from **7** to **8** might have alternatively resulted in the formation of **2** and **5** (Scheme 2.4), but this was not observed. This may be rationalized by low acidity of the hydride ligand in **7**, which is not deprotonated by NaO*t*Bu. Relatedly, **8** is weakly basic and is not protonated by MeOH at −78 °C. The absence of proton transfer between **7** and **8** makes this an unlikely step for (re)generating **2** and **5** under turnover conditions. Dihydride **2** can, however, be obtained readily by protonation of **8** with $HBAr^F_4$ at low temperature (Scheme 2.4).

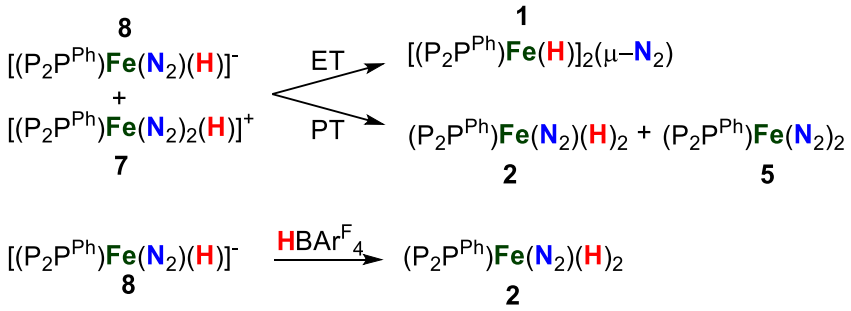

Scheme 2.4. Electron and proton transfer from **7** and **8**

Apparent differences in reactivity of the hydrides with respect to N_2RR can be rationalized by the availability, or lack of, kinetically competent pathways for the hydrides to be converted to on-path Fe–N_2 species at −78 °C. For the P_2P^{Ph} system, no pathway has been identified via which hydrides convert back to on-path Fe–N_2 species. Instead, in stoichiometric reactions, the different hydrides interconvert in an HER cycle (Figure 2.6). However, the observation of NH_3 production during catalytic experiments with **1** or **2** as precatalysts indicates that there must be some pathway to a species active for N_2RR, even if comparatively inefficient.

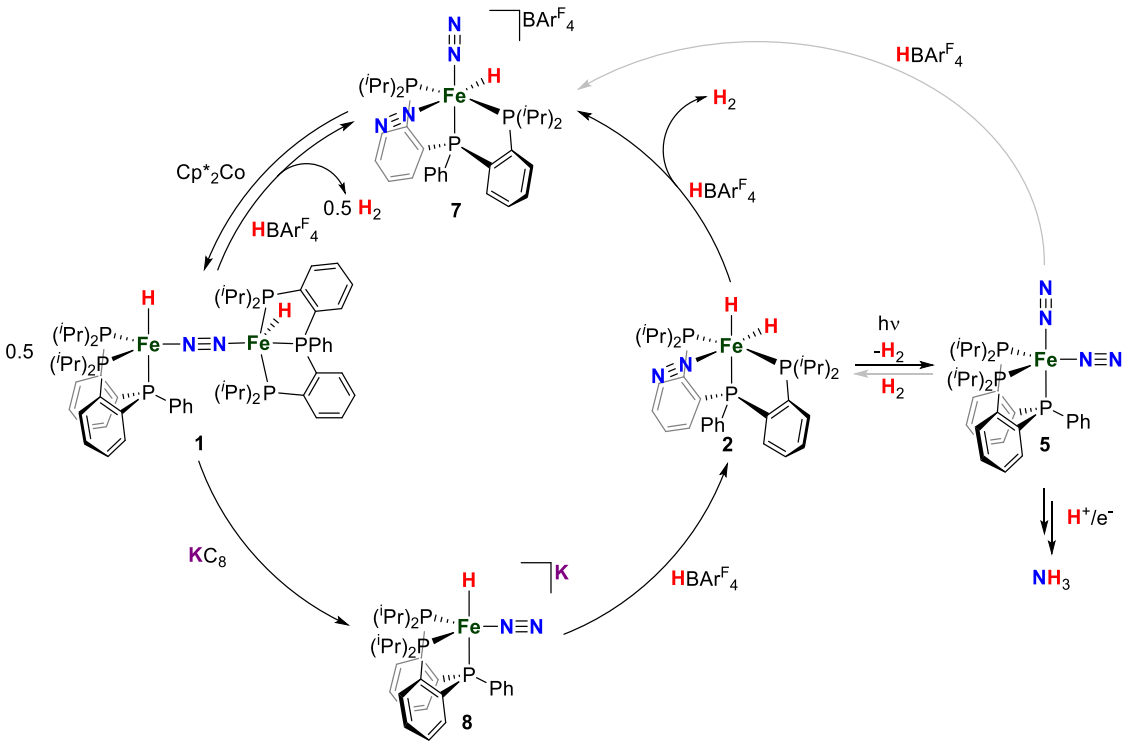

Figure 2.6 Summary of the stoichiometric reactivity observed with $[P_2P^{Ph}Fe(N_2)_x(H)_y]^{+/0/-}$. Grey arrows indicate reactions that do not occur at −78 °C. Black arrows indicate reactions that occur at −78 °C

2.2.6. Reduction of $(P_2P^{Ph})Fe(N_2)_2$.

The fact that there is no reactivity between **5** and $HBAr^F_4$ at −78 °C indicates that the N_2 ligands are not sufficiently activated to be protonated, in accord with comparatively high N_2 stretching frequencies for 5 (2065 and 2009 cm^{-1}). To explore whether further reduction might generate a more reactive and hence on-path species, **5** was stirred with 1 equiv potassium naphthalide followed by the addition of 18-crown-6. This produced the anionic, 4-coordinate S = 1/2 (μ_{eff} = 1.80) complex $[(P_2P^{Ph})Fe(N_2)][K(18\text{-crown-6})]$ (**9**) (Scheme 2.5). **9** features a single and highly activated N_2 ligand (1872 cm^{-1}). Its solid-state crystal structure shows a disordered tetrahedral iron center (τ_4 = 0.75), and CV measurements

show a quasi-reversible $Fe^{0/-}$ redox event centered at −2.5 V vs Fc/Fc^{+} (Figure 2.7). At more negative potential, an irreversible, presumably $Fe^{-2/-1}$ redox event is observed.

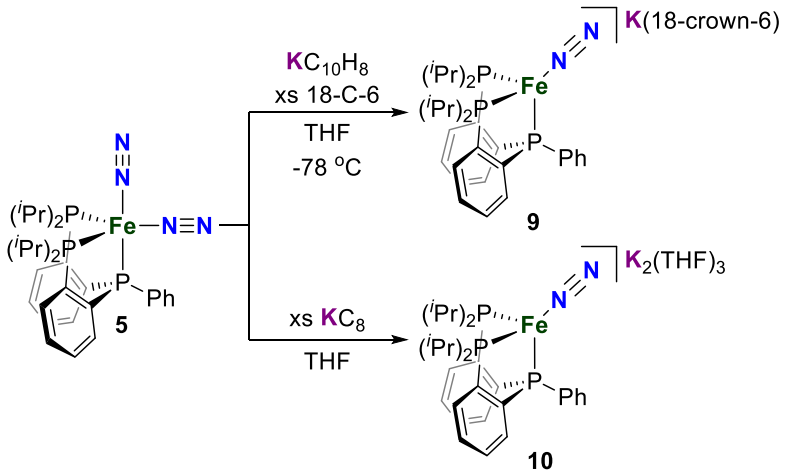

Scheme 2.5. The reduction of **5** results in the formation of **9** or **10** depending on the equivalents of reductant used.

Reduction of **5** with an excess of KC_8 produced a diamagnetic species (^{31}P NMR: δ = 113.13, doublet; 95.15 ppm, triplet) identified as $[(P_2P^{Ph})Fe(N_2)][K_2(THF)_3]$ (**10**) (Scheme 2.5). Complex **10** is an unusual iron species in that it is isoelectronic with $[Fe(CO)_4]^{2-}$ (*vide infra*).[22,23] A ^{15}N-labeled analogue was synthesized by reduction of $(P_2P^{Ph})FeBr_2$ under $^{15}N_2$; its ^{15}N NMR spectrum (2.36 and −26.23 ppm) rules out the possibility of a dinuclear structure $[\{(P_2P^{Ph})Fe\}_2(\mu\text{-}N_2)]K_2$.[24] Consistent with our assignment of dianion **10**, its IR spectrum displays a ν(NN) at 1677 cm^{-1} (1591 cm^{-1} for 10–$^{15}N_2$) that is broadened due to ion-pairing, consistent with a very strongly activated N_2 ligand. Addition of 18-crown-6 resulted in intractable decomposition, suggesting tight ion-pairing is important to its stability.[25]

The structure of **10** in the solid-state (Figure 2.7) presents two distorted tetrahedral iron centers (τ_4 = 0.71) that are related by an inversion center within a dimeric unit. Tight ion pairing is evident from the close proximity of each iron center to the potassium cations (Fe–K = 3.442 and 3.567 Å); each N_2 ligand interacts with three potassium ions. The Fe–N bond is remarkably short (1.728(2) Å), ~ 0.1 Å shorter than the Fe–N bonds in **5**, reflective of very strong backbonding. Relatedly, significant N–N elongation is also observed (1.189(3) Å). The Fe–P bond distances are also highly contracted at 2.1494(6) Å, in line with the very strong covalency expected of a d^{10} tetrahedral iron center. Prior to this study, tetrahedral Fe^{-II} species have been limited to complexes with very strong pi-acceptor ligands, such as CO,[22,23] PF_3,[26] (C_2H_4),[27,28] (COD) (COD = cyclooctadiene),[27] and CNAr.[25,29] Additional species bearing phosphorine[30] and nitrosyl[31] ligands have also been reported, however the assignment of their oxidation state is ambiguous.

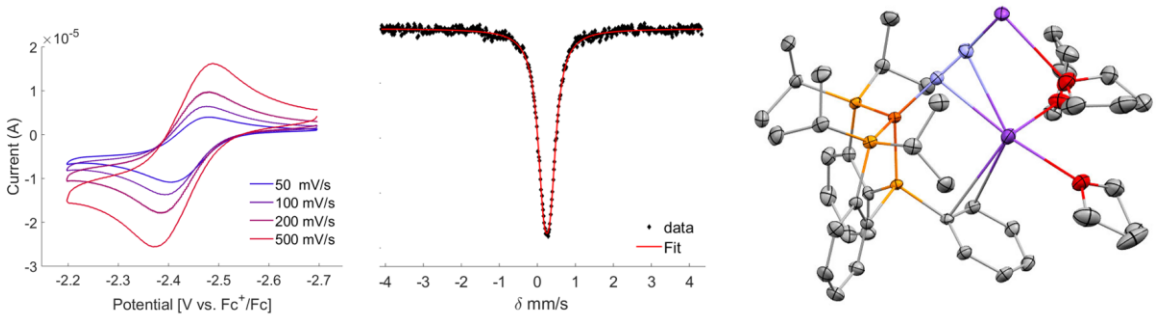

Figure 2.7. (Left) Cyclic voltammetry data of **9** scanning cathodically, (Middle) Mössbauer spectrum of **10**, (Right) Asymmetric unit of the XRD structure of **10**. In the dimeric structure, the iron centers are related by an inversion center. Hydrogen atoms and disorder in one of the *i*-Pr moieties are omitted for clarity.

The Mössbauer spectrum of a perfectly tetrahedral d^{10} iron complex, such as $Na_2[Fe(CO)_4]$, should show a singlet instead of a quadrupole doublet due to the spherical

electric field gradient at the iron nucleus;[22,32] any quadrupole splitting in $Na_2[Fe(CO)_4]$ is barely discernable.[32] Similarly, the Mössbauer spectrum of **10** shows an apparent singlet (Figure 2.7) which can be fit by a small quadrupole splitting (δ = 0.27 mm/s, ΔE_Q = 0.26 mm/s). The very small quadrupole splitting in **10**, which is required to have at least a modest electric field gradient owing to the presence of three unique types of donor ligands, indicates its classification as a d^{10} tetrahedral structure is appropriate, at least to the extent this description is apt for $Na_2[Fe(CO)_4]$ given the significant covalency in both species.

2.2.7 Functionalization of formal Fe^{-I} and Fe^{-II} species.

Current examples of Fe-mediated N_2RR are thought to proceed through Fe–N_2 intermediates with ν(NN) stretching frequencies below 1970 cm^{-1}.[1d,3,33] The N_2 ligand of $[(P_2P^{Ph})Fe(N_2)][K(18\text{-crown-6})]$ (**9**) has a stretching frequency of 1872 cm^{-1} and in this context should be activated enough to be functionalized. Attempts to protonate **9** with stoichiometric $HBAr^F_4$ unfortunately resulted in complex product mixtures. Silylium ions (R_3Si^+) have been used as surrogate electrophiles for protons to model unstable protonated Fe-N_xH_y species.[1c,34-38]Reacting **10**, generated *in situ*, with one equivalent of Me_3SiCl at −78 °C, results in an immediate color change from dark purple to dark orange. After work-up, diamagnetic $[(P_2P^{Ph})Fe(NNSiMe_3)]K$ ([**11**-$NNSiMe_3$]$^-$) was isolated as a dark brown solid in 50% yield (**Scheme 2.6**). As for **10**, a tight ion-pair seems to be important for its stability; addition of 18-crown-6 results in its decomposition. The solid-state structure of [**11**-$NNSiMe_3$]$^-$ reveals a four-coordinate iron center with a distorted tetrahedral geometry (τ_4 = 0.76). The Fe–N bond length of [11-$NNSiMe_3$]$^-$ is even shorter than that in 10 (1.664(7) Å vs. 1.728(2) Å respectively), and the N–N bond length is much longer (1.270(9) Å vs. 1.189(3) Å) in 10.

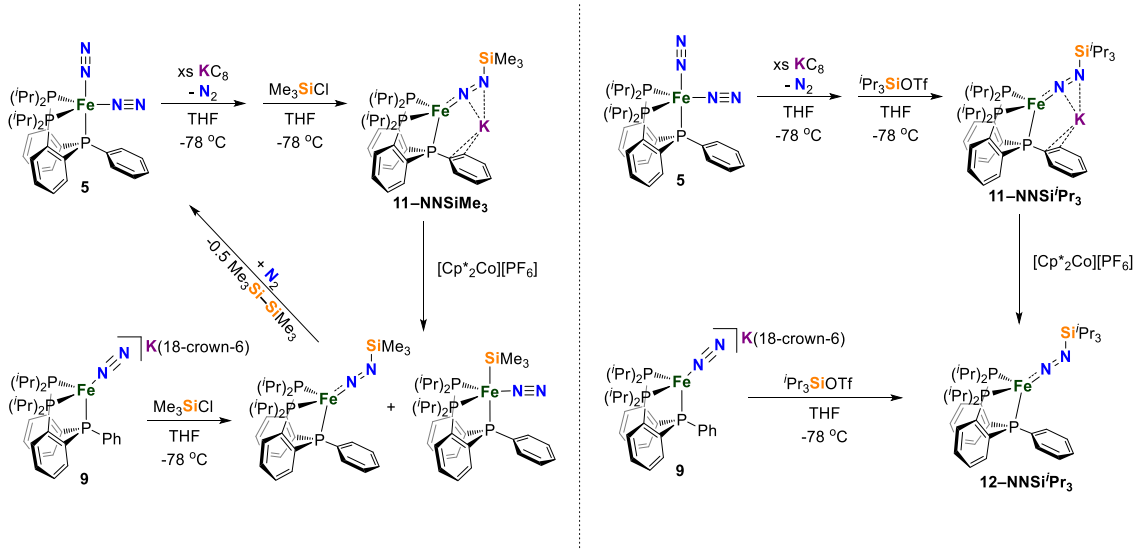

Scheme 2.6. Synthesis of Fe–silyldiazenido complexes [**11**-NNSiMe$_3$]K, [**11**-NNSi^{i}Pr$_3$]K and **12**-NNSi^{i}Pr$_3$.

Attempts to oxidize [**11**-NNSiMe$_3$]$^-$ at −78 °C with cobaltocenium to generate the neutral diazenido species (P_2P^{Ph})Fe-NNSiMe$_3$ resulted in a mixture of species, presumably complicated by the loss of Me$_3$Si·. Based on low temperature EPR data (Figure 2.8), we assign the major product of oxidation to be the iron-silyl complex (P_2P^{Ph})Fe(SiMe$_3$)(N$_2$) (its EPR signature is highly similar to that of (P_2P^{Ph})Fe(N$_2$)(H);[2] see Figure 2.8). There is also a minor component in the EPR trace that can be tentatively assigned as the expected diazenido (P_2P^{Ph})Fe(NNSiMe$_3$). Use of ^{i}Pr$_3$SiOTf instead leads to the analogous [**11**-NNSi^{i}Pr$_3$]$^-$ complex, but in this case its oxidation affords a clean EPR spectrum consistent with the diazenido species **12**-NNSi^{i}Pr$_3$ (Figure 2.8). Addition of ^{i}Pr$_3$SiOTf to [(P_2P^{Ph})Fe(N$_2$)]$^-$ 9 generates the same species as is evident by IR and EPR spectroscopy (Figure 2.8). The IR spectrum of **12**-NNSi^{i}Pr$_3$ displays an intense band corresponding to νNN at 1660 cm^{-1}, characteristic of iron diazenido species.[34,37,39] In contrast with the -

$SiMe_3$ derivative, the -Si^iPr_3 species is stable for days. We suspect that for the less bulky -$SiMe_3$ derivative, kinetically competitive N-to-Fe silyl migration is operative.

We intuit that **9**, or its further reduced state $[(P_2P^{Ph})Fe(N_2)]^{2-}$ **10**, must be reached before nitrogen functionalization occurs via protonation or silylation. The iron centers in **9** and **10** are exposed, and are therefore susceptible to direct protonation at iron, or to facile migration from N-to-Fe. An N-protonated form of **9** (or **10**) can presumably react further under the catalytic conditions to produce NH_3, when both excess acid and reductant are present. Such reactivity must be kinetically competitive with a step that produces an off-path hydride.

The need to access an anionic state of the system (either **9** or **10**) before functionalization at N_2 can occur sets the requirement of a potent reductant for N_2RR in the P_2P^{Ph}Fe-system. The $Fe^{-I/0}$ couple of **9** is −2.47 V vs. Fc/Fc^+, which is ~ 0.30 V more negative than the corresponding $Fe^{-I/0}$ couple for $[(P_3^B)Fe(N_2)]^{0/-}$; N_2RR can be driven rather efficiently with the latter system using Cp^*_2Co paired with anilinium acids, which are ineffective with this precatalyst.[4,5]

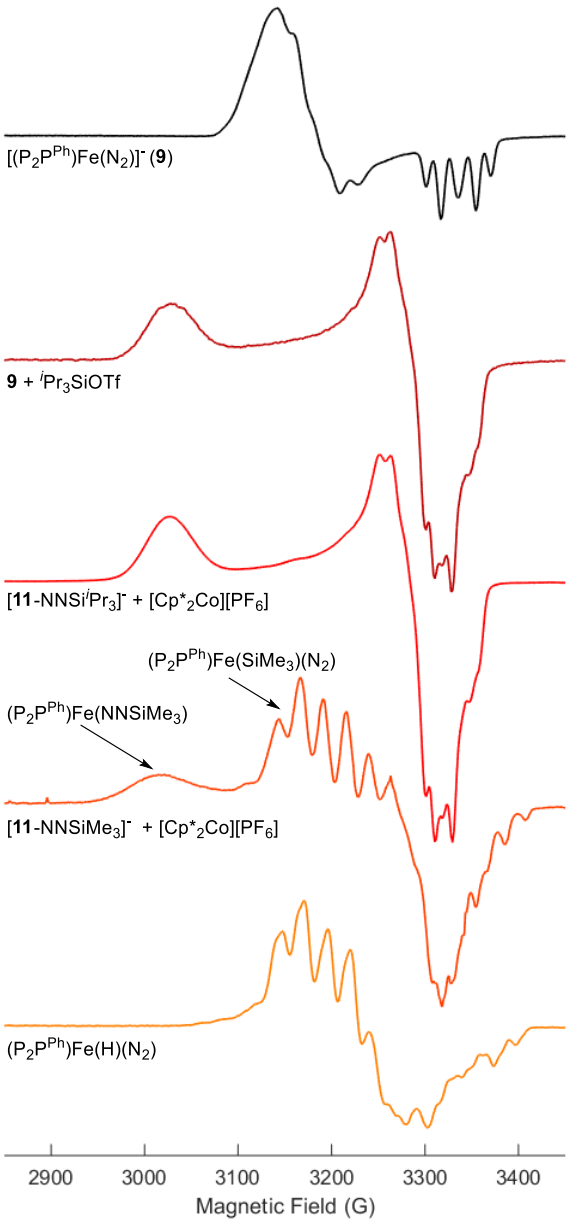

Figure 2.8. Collected EPR data; (Black) Spectrum of [(P_2P^{Ph})Fe(N_2)][18-crown-6)] (**9**). (Maroon) Spectrum observed upon addition of $^{i}Pr_3SiOTf$ to 9, showing conversion to **12**-NNSi^{i}Pr$_3$. (Red) Spectrum of 12-NNSi^{i}Pr$_3$ obtained by oxidation of [**11**-NNSi^{i}Pr$_3$]$^-$ with [Cp*$_2$Co][PF_6]. (Orange) Spectrum of the oxidation of [**11**-NNSiMe$_3$]$^-$ with Cp*$_2$Co][PF_6]

showing the formation of $(P_2P^{Ph})Fe(SiMe_3)(N_2)$ and $(P_2P^{Ph})Fe(NNSiMe_3)$. (Yellow) Spectrum of $(P_2P^{Ph})Fe(H)(N_2)$.[2]

2.3. Conclusions

The present study highlights the detrimental effect of hydride ligands on an iron–catalyzed N_2RR model system whose efficiency is enhanced by irradiation. Stoichiometric reactivity as well as freeze-quench Mossbauer studies reveal that off-path $(P_2P^{Ph})Fe(N_2)_x(H)_y$ species are formed but are not inert resting states. On the contrary, they rapidly produce hydrogen in an HER cycle operating parallel to the desired N_2RR cycle. In the absence of light, these pathways compete with one another but operate along different cycles. Irradiation of $(P_2P^{Ph})Fe(N_2)(H)_2$ (**2**) results in photoinduced H_2 elimination and the formation of $(P_2P^{Ph})Fe(N_2)_2$ (**5**), which is significantly more competent for N_2RR. Thus, photolysis shifts the speciation from favoring an unproductive HER cycle to one where N_2RR becomes kinetically competitive.

A deeper understanding of the required driving force for N_2 functionalization is obtained by stoichiometric reactions with Fe–N_2 species. No protonation reactivity is observed with a strong acid for $(P_2P^{Ph})Fe(N_2)_2$ at −78° C; further reduction is required before functionalization can take place. Protonation experiments with the Fe^{-I} and Fe^{-II} species **9** and **10** provide complex mixtures, but silylation experiments are informative.

The need to access an anionic or a dianionic state of the system before productive functionalization at N_2 occurs sets the low reduction potential required for N_2RR by this $P_2P^{Ph}Fe$-system and explains why comparatively milder reductants such as Cp^*_2Co, which are effective for a related $(P_3^B)Fe$-catalyst system, are ineffective in the present case. Future

catalyst designs for iron systems should focus on anodically shifting the needed redox couple to generate an Fe–N_2 species while maintaining a strongly activated N_2 ligand.

2.4. References

[1] (a) Yandulov, D. V.; Schrock, R. R. Catalytic reduction of dinitrogen to ammonia at a single molybdenum center. *Science* **2003**, *301*, 76–79. (b) Arashiba, K.; Miyake, Y.; Nishibayashi, Y. A molybdenum complex bearing PNP-type pincer ligands leads to the catalytic reduction of dinitrogen into ammonia. *Nat. Chem.* **2011**, *3*, 120–125. (c) Anderson, J. S.; Rittle, J.; Peters, J. C. Catalytic conversion of nitrogen to ammonia by an iron model complex. *Nature* **2013**, *501*, 84–87. (d) Hill, P. J.; Doyle, L. R.; Crawford, A. D.; Myers, W. K.; Ashley, A. E. Selective catalytic reduction of N_2 to N_2H_4 by a simple Fe complex. *J. Am. Chem. Soc.* **2016**, *138*, 13521–13524. (e) Sekiguchi, Y.; Arashiba, K.; Tanaka, H.; Eizawa, A.; Nakajima, K.; Yoshizawa, K.; Nishibayashi, Y. Catalytic reduction of molecular dinitrogen to ammonia and hydrazine using vanadium complexes. *Angew. Chem. Int. Ed.* **2018**, *57*, 9064–9068. (f) Doyle, L. R.; Wooles, A. J.; Jenkins, L. C.; Tuna, F.; McInnes, E. J. L.; Liddle, S. T. Catalytic dinitrogen reduction to ammonia at a triamidoamine-titanium complex. *Angew. Chem. Int. Ed.* **2018**, *57*, 6314–6318.

[2] Buscagan, T. M.; Oyala, P. H.; Peters, J. C. N_2 -to-NH_3 Conversion by a triphos-iron catalyst and enhanced turnover under photolysis. *Angew. Chem. Int. Ed.* **2017**, *56*, 6921-6926.

[3] Sekiguchi, Y.; Kuriyama, S.; Eizawa, A.; Arashiba, K.; Nakajima, K.; Nishibayashi, Y. Synthesis and reactivity of iron–dinitrogen complexes bearing anionic methyl- and phenyl-substituted pyrrole-based PNP-type pincer ligands toward catalytic nitrogen fixation. *Chem. Commun.* **2017**, *53*, 12040–12043.

[4] Chalkley, M. J.; Del Castillo, T. J.; Matson, B. D.; Roddy, J. P.; Peters, J. C. Catalytic N_2-to-NH_3 Ccnversion by Fe at lower driving force: A proposed role for metallocene-mediated PCET. *ACS Cent. Sci.* **2017**, *3*, 217–223.

[5] Chalkley, M. J.; Castillo, T. J. Del; Matson, B. D.; Peters, J. C. Fe-mediated nitrogen fixation with a metallocene mediator: Exploring pK_a effects and demonstrating electrocatalysis. *J. Am. Chem. Soc.* **2018**, *140*, 6122–6129.

[6] Matson, B. D.; Peters, J. C. Fe-mediated HER vs N_2RR: Exploring factors that contribute to selectivity in $P_3^EFe(N_2)$ (E = B, Si, C) catalyst model systems. *ACS Catal.* **2018**, *8*, 1448–1455.

[7] Simpson, F. B.; Burris, R. H. A nitrogen pressure of 50 atmospheres does not prevent evolution of hydrogen by nitrogenase. *Science* **1984**, *224*, 1095–1097.

[8] Schubert, K. R.; Evans, H. J. Hydrogen evolution: A major factor affecting the efficiency of nitrogen fixation in nodulated symbionts. *Proc. Natl. Acad. Sci.* 1976, *73*, 1207–1211.

[9] Del Castillo, T. J.; Thompson, N. B.; Peters, J. C. A synthetic single-site Fe nitrogenase: High turnover, freeze-quench ^{57}Fe Mössbauer data, and a hydride resting state. *J. Am. Chem. Soc.* **2016**, *138*, 5341–5350.

[10] (a) Fajardo, J.; Peters, J. C. Catalytic nitrogen-to-ammonia conversion by osmium and ruthenium complexes. *J. Am. Chem. Soc.* **2017**, *139*, 16105–16108. (b) Kuriyama, S.; Arashiba, K.; Nakajima, K.; Matsuo, Y.; Tanaka, H.; Ishii, K.; Yoshizawa, K.; Nishibayashi, Y. Catalytic transformation of dinitrogen into ammonia and hydrazine by iron-dinitrogen complexes bearing pincer ligand. *Nat. Commun.* **2016**, *7*, 12181. (c) Kuriyama, S.; Arashiba, K.; Tanaka, H.; Matsuo, Y.; Nakajima, K.; Yoshizawa, K.;

Nishibayashi, Y. Direct transformation of molecular dinitrogen into ammonia catalyzed by cobalt dinitrogen complexes bearing anionic PNP pincer ligands. *Angew. Chem. Int. Ed.* **2016**, *55*, 14291–14295. (d) Creutz, S. E.; Peters, J. C. Catalytic reduction of N_2 to NH_3 by an Fe–N_2 complex featuring a C-atom anchor. *J. Am. Chem. Soc.* **2014**, *136*, 1105–1115.

[11] (a) Yandulov, D. V.; Schrock, R. R.; Rheingold, A. L.; Ceccarelli, C.; Davis, W.M. Synthesis and reactions of molybdenum triamidoamine complexes containing hexaisopropylterphenyl substituents. *Inorg. Chem.* **2003**, *42*, 796-813. (b)Yandulov, D. V.; Schrock, R. R. Studies relevant to catalytic reduction of dinitrogen to ammonia by molybdenum triamidoamine complexes. *Inorg. Chem.* **2005**, *44*, 1103-1117.

[12] Kinney, R. A.; McNaughton, R. L.; Chin, J. M.; Schrock, R. R.; Hoffman, B. M. Protonation of the dinitrogen-reduction catalyst [$HIPTN_3N$]Mo^{III} investigated by ENDOR spectroscopy. *Inorg. Chem.* **2011**, *50*, 418-420.

[13] Anderson, J. S.; Cutsail, G. E.; Rittle, J.; Connor, B. A.; Gunderson, W.; Zhang, L.; Hoffman, B. M.; Peters, J. C. Characterization of an Fe≡N–NH_2 intermediate relevant to catalytic N_2 reduction to NH_3. *J. Am. Chem. Soc.* **2015**, *137*, 7803–7809.

[14] Other molecular $Fe(H)_x$ complexes undergo photoinduced reductive H_2 elimination with associated N_2 binding. See: (a) Sacco, A.; Aresta, M. Nitrogen fixation: Hydrido- and hydrido-nitrogen-complexes of Iron(II). *Chem. Commun.* **1968**, 1223–1224. (b) Whittlesey, M. K.; Mawby, R. J.; Osman, R.; Perutz, R. N.; Field, L. D.; Wilkinson, M. P.; George M. W. Transient and matrix photochemistry of $Fe(dmpe)_2H_2$ (dmpe = $Me_2PCH_2CH_2Me_2$): dynamics of C-H and H-H activation *J. Am. Chem. Soc.* **1993**, *115*,

8627–8637. (c) Perutz, R. N.; Procacci, B. Photochemistry of Transition Metal Hydrides, *Chem. Rev.* **2016**, *116*, 8506−8544.

[15] Okuniewski, A.; Rosiak, D.; Chojnacki, J.; Becker, B. Coordination polymers and molecular structures among complexes of mercury(II) halides with selected 1-benzoylthioureas. *Polyhedron* **2015**, *90*, 47–57.

[16]Addison, A. W.; Rao, T. N.; Reedijk, J.; van Rijn, J.; Verschoor, G. C. Synthesis, structure, and spectroscopic properties of copper(II) compounds containing nitrogen-sulphur donor ligands; the crystal and molecular structure of Aqua[l,7-bis(N-methylbenzimidazol-2'-yl)-2,6-dithiaheptane]copper(II) Perchlorate. *J. Chem. Soc., Dalt. Trans.* **1984**, *0*, 1349–1356.

[17] Cavaillé, A.; Joyeux, B.; Saffon-Merceron, N.; Nebra, N.; Fustier-Boutignona, M.; Mézailles, N. Triphos–Fe dinitrogen and dinitrogen–hydride complexes: relevance to catalytic N_2 reductions, *Chem. Commun.* **2018**, *54*, 11953-11956.

[18] Examples of deriving the coupling between metal centers by NMR can be found in a) Pfirrmann, S.; Limberg, C.; Herwig, C.; Knispel, C.; Braun, B.; Bill, E.; Stösser, R. A reduced β-diketiminato-ligated Ni_3H_4 unit catalyzing H/D Exchange. *J. Am. Chem. Soc.* **2010**, *132*, 13684–13691. b) Tepper, A. W. J. W.; Bubacco, L.; Canters, G. W. Paramagnetic properties of the halide-bound derivatives of oxidised tyrosinase investigated by ^{1}H NMR spectroscopy. *Chem. Eur. J.* **2006**, *12*, 7668–7675.

[19]Stoian, S. A.; Vela, J.; Smith, J. M.; Sadique, A. R.; Holland, P. L.; Münck, E.; Bominaar, E. L. Mössbauer and computational study of an N_2-bridged diiron diketiminate complex:

parallel alignment of the iron spins by direct antiferromagnetic exchange with activated dinitrogen. *J. Am. Chem. Soc.* **2006**, *128* (31), 10181–10192.

[20] (a) Hoffman, B. M.; Lukoyanov, D.; Yang, Z. Y.; Dean, D. R.; Seefeldt, L C. Mechanism of nitrogen fixation by nitrogenase: the next stage. *Chem. Rev.* **2014**, *114*, 4041–4062. (b) Lukoyanov, D.; Khadka, N.; Yang, Z. Y.; Dean, D. R.; Seefeldt, L. C.; Hoffman, B. M. Reversible photoinduced reductive elimination of H_2 from the nitrogenase dihydride state, the E_4(4H) janus intermediate. *J. Am. Chem. Soc.* **2016**, *138*, 1320–1327. (c) Lukoyanov, D.; Khadka, N.; Yang, Z.-Y.; Dean, D. R.; Seefeldt, L. C.; Hoffman, B. M. Reductive elimination of H_2 activates nitrogenase to reduce the N≡N triple bond: Characterization of the E_4(4H) Janus Intermediate in wild-type enzyme. *J. Am. Chem. Soc.* **2016**, *138*, 10674–10683. (d) Lukoyanov, D.; Yang, Z. Y.; Khadka, N.; Dean, D. R.; Seefeldt, L. C.; Hoffman, B. M. Identification of a key catalytic intermediate semonstrates that nitrogenase is activated by the reversible exchange of N_2 for H_2. *J. Am. Chem. Soc.* **2015**, *137* (10), 3610–3615. (e) Lukoyanov, D.; Yang, Z.-Y.; Barney, B. M.; Dean, D. R.; Seefeldt, L. C.; Hoffman, B. M. Unification of reaction pathway and kinetic scheme for N_2 reduction catalyzed by nitrogenase. *Proc. Natl. Acad. Sci.* **2012**, *109* (15), 5583–5587.

[21] (a) Baker, M. V.; Field, L. D.; Young, D. J. Formation of molecular hydrogen complexes of iron by the reversible protonation of iron dihydrides with alcohols. *J. Chem. Soc. Chem. Commun.* **1988**, *2*, 546–548. Hills, A.; Hughes, D. L.; Jimenez-Tenorio, M.; Leigh, G. J.; Rowley, A. T. Bis[1,2-bis(dimethylphosphino)ethane]dihydrogenhydridoiron(II) tetraphenylborate as a model for the function of nitrogenases. *J. Chem. Soc. Dalt. Trans.* **1993**, 3041–3049.

[22] Erickson, N. E.; Fairhall, A. W. Mössbauer spectra of iron in $Na_2[Fe(CO)_4]$ and $Na[Fe_3(CO)_{11}H]$ and comments regarding the structure of $Fe_3(CO)_{12}$. *Inorg. Chem.* **1965**, *4*, 1320–1322.

[23] Collman, J. P. Disodium tetracarbonylferrate, a transition metal analog of a Grignard reagent. *Acc. Chem. Res.* **1975**, *8*, 342–347.

[24] Bridged $M–N_2–M$ species should give rise to only one peak in the ^{15}N NMR spectra. See: (a) Doyle, L. R.; Hill, P. J.; Wildgoose, G. G.; Ashley, A. E. Teaching old compounds new tricks: efficient N_2 fixation by simple $Fe(N_2)(diphosphine)_2$ complexes. *Dalton. Trans.* **2016**, *45*, 7550–7554. (b) Hazari, N. Homogeneous iron complexes for the conversion of dinitrogen into ammonia and hydrazine. *Chem. Soc. Rev.* **2010**, *39*, 4044–4056. (c) Eizawa, Field, L. D.; Guest, R. W.; Turner, P. Mixed-valence dinitrogen-bridged Fe(0)/Fe(II) complex. *Inorg. Chem.* **2010**, *49*, 9086–9093. (d) A.; Arashiba, K.; Tanaka, H.; Kuriyama, S.; Matsuo, Y.; Nakajima, K.; Yoshizawa, K.; Nishibayashi, Y. Remarkable catalytic activity of dinitrogen-bridged dimolybdenum complexes bearing NHC-based PCP-pincer ligands toward nitrogen fixation. *Nat. Commun.* **2017**, *8*, 1–12. (e) Kokubo, Y.; Yamamoto, C.; Tsuzuki, K.; Nagai, T.; Katayama, A.; Ohta, T.; Ogura, T.; Wasada-Tsutsui, Y.; Kajita, Y.; Kugimiya, S.; Masuda, H. Dinitrogen fixation by vanadium complexes with a triamidoamine ligand. *Inorg. Chem.* **2018**, *57*, 11884-11894. (f) Lindley, B. M.; van Alten, R. S.; Finger, M.; Schendzielorz, F.; Würtele, C.; Miller, A. J. M.; Siewert, I.; Schneider, S. Mechanism of chemical and electrochemical N_2 splitting by a rhenium pincer complex. *J. Am. Chem. Soc.* **2018**, *140*, 7922–7935.

[25] Other formal d^{10} species also suffer from decomposition upon addition of a crown ether. See: Mokhtarzadeh, C. C.; Margulieux, G. W.; Carpenter, A. E.; Weidemann, N.; Moore, C. E.; Rheingold, A. L.; Figueroa, J. S. Synthesis and protonation of an encumbered iron tetraisocyanide dianion. *Inorg. Chem.* **2015**, *54*, 5579–5587.

[26] Kruck, T.; Prasch, A. Synthese und Struktur der tetrakis(trifluorphosphin)-metalldihydride und -metallate(-II) von Eisen, Ruthenium und Osmium. *Z. Anorg. Allg. Chem*. **1969**, *371*, 1–22.

[27] Jonas, K.; Schieferstein, L.; Krüger, C.; Tsay, Y.-H. Tetrakis(ethylene)irondilithium and Bis(η^4-1,5-cyclooctadiene) irondilithium. *Angew. Chemie Int. Ed.* **1979**, *18*, 550–551.

[28] Martin, R.; Fürstner, A. Reversal of reactivity cross-coupling of alkyl halides with aryl Grignard reagents catalyzed by a low-valent iron complex. *Angew. Chem. Int. Ed.* **2004**, *43*, 3955–3957.

[29] Brennessel, W. W.; Ellis, J. E. $[Fe(CNXyl)_4]_2$-: an isolable and structurally characterized homoleptic isocyanidemetalate dianion. *Angew. Chem. Int. Ed.* **2007**, *46*, 598–600.

[30] Orsay Rosa, P.; Mézailles, N.; Ricard, L.; Mathey, F.; Floch, P. Le; Jean, Y. Dianionic iron and ruthenium(2-) bisphosphinine complexes: a formal d^{10} ruthenium complex with a square planar geometry. *Angew. Chem. Int. Ed.* **2001**, *40*, 1251–1253.

[31] Cullen, W. R.; Crow, J. P.; Herring, F. G.; Sams, J. R.; Tapping, R. L. Mössbauer and electron paramagnetic resonance studies of some iron nitrosyl complexes. *Inorg. Chem.* **1971**, *10*, 1616–1623.

[32] Farmery, K.; Kilner, M.; Greatrex, R.; Greenwood, N. N. Structural studies of the carbonylate and carbonyl hydride anions of iron. *J. Chem. Soc. A*, **1969**, 2339–2345.

[33] (a) Moret, M.-E.; Peters, J. C. Terminal iron dinitrogen and iron imide complexes supported by a tris(phosphino)borane ligand. *Angew. Chem. Int. Ed.* **2011**, *50*, 2063–2067. (b) Mankad, N. P.; Whited, M. T.; Peters, J. C. Terminal Fe^{I}-N_2 and Fe^{II}...H-C interactions supported by tris(phosphino)silyl ligands. *Angew. Chem., Int. Ed*. **2007**, 46, 5768–5771.

[34] Moret, M.; Peters, J. C. N_2 Functionalization at iron metallaboratranes. *J. Am. Chem. Soc.* **2011**, *4350*, 18118–18121.

[35] McWilliams, S. F.; Bill, E.; Lukat-Rodgers, G.; Rodgers, K. R.; Mercado, B. Q.; Holland, P. L. Effects of N_2 binding mode on iron-based functionalization of dinitrogen to form an iron(III) hydrazido complex. *J. Am. Chem. Soc.* **2018**, *140*, 8586–8598.

[36] Piascik, A. D.; Li, R.; Wilkinson, H. J.; Green, J. C.; Ashley, A. E. Fe-catalyzed conversion of N_2 to $N(SiMe_3)_3$ via an Fe-hydrazido resting state. *J. Am. Chem. Soc.* **2018**, 10691-10694.

[37] Piascik, A. D.; Hill, P. J.; Crawford, A. D.; Doyle, L. R.; Green, J. C.; Ashley, A. E. Cationic silyldiazenido complexes of the Fe(diphosphine)$_2$(N_2) platform: structural and electronic models for an elusive first intermediate in N_2 fixation. *Chem. Commun.* **2017**, *53*, 7657–7660.

[38] Alex Rudd, P.; Planas, N.; Bill, E.; Gagliardi, L.; Lu, C. C. Dinitrogen Activation at Iron and Cobalt Metallalumatranes *Eur. J. Inorg. Chem.* **2013**, *2* (22–23), 3898–3906.

[39] (a) Lee, Y.; Mankad, N.P.; Peters, J. C. Triggering N_2 uptake via redox-induced expulsion of coordinated NH_3 and N_2 silylation at trigonal bipyramidal iron, *Nat. Chem.* **2010**, 558–565. (b) Ung, G.; Peters, J. C. Low temperature N_2 binding to 2-coordinate L_2Fe^0 enables reductive trapping of $L_2FeN_2^-$ and NH_3 generation. *Angew. Chem. Int. Ed.* **2015**, 54, 532–535.

Chapter 3 : EPR Detection of a Terminal Formal Iron(III) Nitride Stabilized by a Trisphosphine-Borane Ligand

3.1 Introduction

In recent years, substantial progress has been made in the development of molecular catalysts for N_2-to-NH_3 conversion, with significant improvements in turnover and efficiency.[1,2] With the growing number of systems available, it becomes increasingly possible to probe the mechanism(s) by which the key N-N cleavage step occurs in these functional systems. Two fundamentally different pathways are generally considered for catalysts featuring an end-on N_2 moiety: (1) a Chatt-type mechanism (via an M≡N intermediate) or (2) a late state cleavage pathway (an alternating mechanism via an M-N_2H_4 intermediate).[1,3] Recent work demonstrates that with strong reductants and acids a Chatt-type mechanism is viable for a trisphosphine iron complexes $[(P_3^B)Fe(N_2)]^-$ (P_3^B = tris(o-diisopropylphosphinophenyl)borane) (Scheme 3.1). Reduction of $[(P_3^B)Fe(N_2)]^-$ followed by three subsequent protonation steps yielded $[(P_3^B)Fe(N)]^+$.[4] Given that $[(P_3^B)Fe{\equiv}N]^+$ appears stable to protonation at low temperature, the next step in the catalytic cycle is either reduction to produce the formally Fe(III) nitrido $(P_3^B)Fe{\equiv}N$, or direct N–H bond formation via PCET to produce the terminal imido $[(P_3^B)Fe{=}NH]^+$.

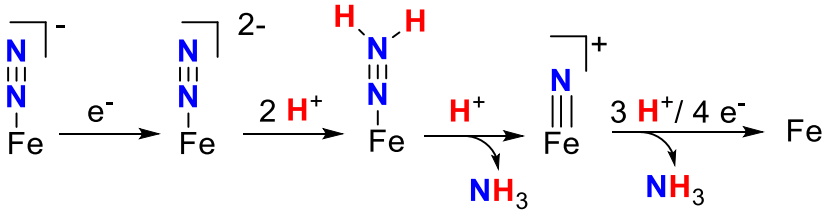

Scheme 3.1. Selected intermediates characterized with the P_3^B ligand manifold along a Chatt-type cycle.

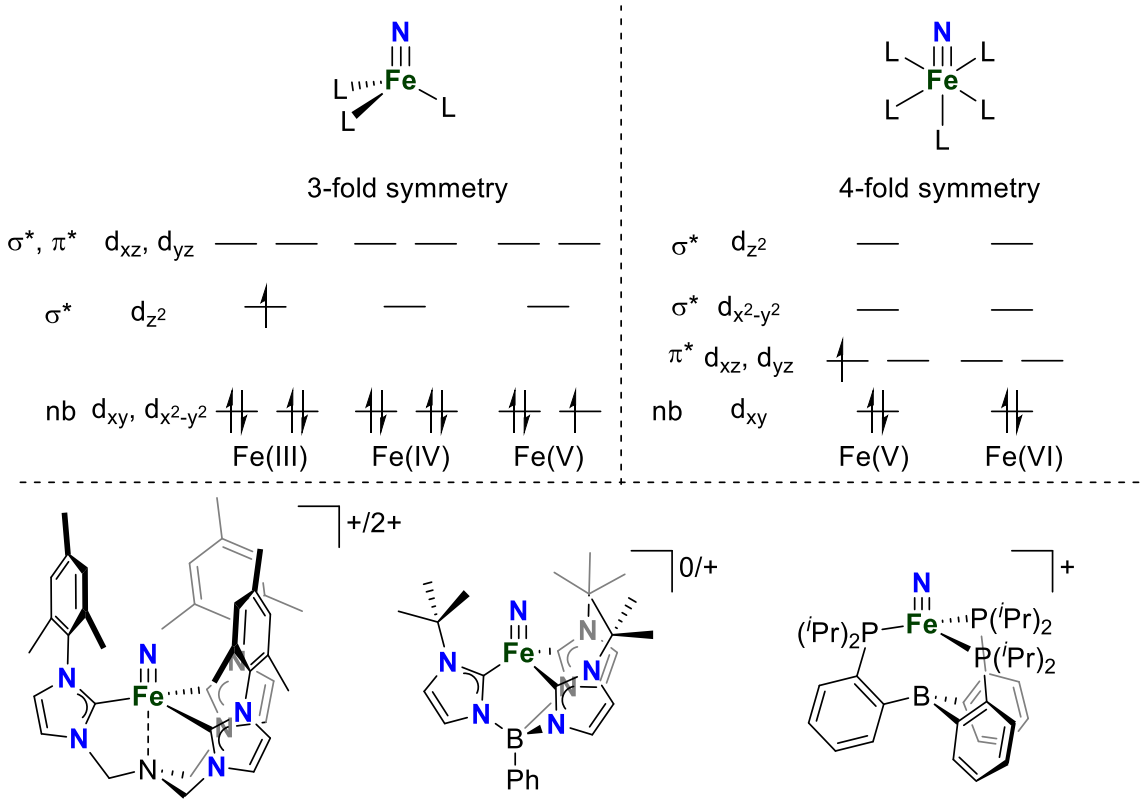

Figure 3.1. (Top) Simplified molecular orbital diagram of nitridoiron compounds in 3 and 4-fold symmetry and representative three-fold symmetric d^3 and d^4 terminal iron nitrido complexes.

The reduction of $[(P_3^B)Fe{\equiv}N]^+$ during nitrogen fixation would result in a d^5 electron count, akin to a highly unstable Co(IV) nitride described by Meyer and coworkers.[5] The stability of compounds featuring Fe≡N triple bonds, is highly dependent on the coordination environment of the metal and the corresponding ligand-field splitting (Figure 3.1).[6] In 4-fold symmetry, an Fe-N bond order of 3 is only achieved in the unusual Fe(VI) state, as the Fe(V) state populates a π-antibonding orbital, reducing the bond order to 2.5. Such Fe(V) and Fe(VI) nitrides have only been observed as thermally unstable compounds generated by low temperature photolysis of suitable azide precursors.[7] In contrast, 3-fold

symmetric complexes have granted access to stable terminal nitridoiron compounds in the Fe(IV)[8] and Fe(V)[9] states. The pseudotetrahedral geometry affords two nonbonding *d* orbitals, alleviating the need to populate a σ-antibonding orbital for d^3 and d^4 electron counts, increasing stability in lower oxidation states (Figure 3.1).

Based on the expected electronic structure, the desired Fe(III) nitride is anticipated to be highly reactive. The Co(IV) nitrodo reported by Meyer and coworkers could only be characterized by EPR spectroscopy at temperatures below 50 K (Scheme 2).[5] At higher temperatures, insertion of the nitrido ligand into the M-C bond was observed. Similarly, a highly reactive Co(IV) nitrido, formed upon photolysis of an azide precursor, was proposed by Chirik and coworkers for which ligand C-H activation was observed (Scheme 3.2). These examples demonstrate that the characterization of d^5 nitrides remains virtually impossible.

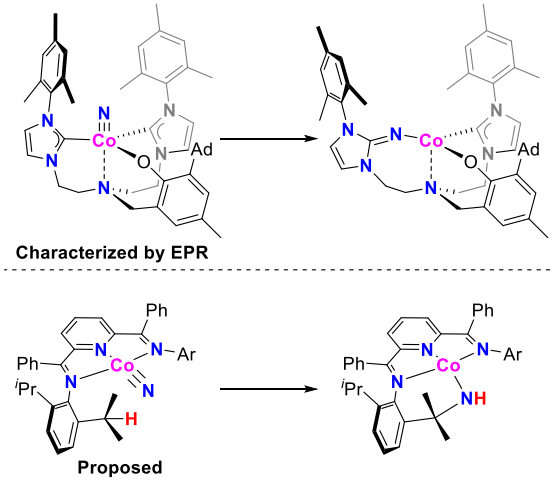

Scheme 3.2. Examples of (proposed) Co^{IV} nitridos and their decomposition products

Here, we report the characterization of a d^5 terminal Fe(III) nitride, formed by photolysis of an iron azide precursor at low temperature. Characterization by EPR, ENDOR, HYSCORE and Mössbauer spectroscopy in combination with DFT supports the

formation of a discrete but highly reactive Fe(III) nitrido stabilized by a redox active borane moiety. The observed *g* values and hyperfine coupling constants eliminate other potential structures formed upon photolysis of the iron azide precursor.

3.2. Results and Discussion

The azide precursor (P_3^B)Fe(N_3) (**2**) was synthesized by salt metathesis of NaN_3 with (P_3^B)FeCl (**1**) (Scheme 3.3). Synthesis of the ^{15}N labeled analogs was achieved using $Na^{15}NNN$, yielding a 1:1 mixture of the α- and γ-^{15}N labeled compounds. Compound **2** exhibits an intense IR absorption at 2069 cm^{-1}, which shifts to 2058 cm^{-1} for the ^{15}N labeled analog, attributed to the azide moiety. Its solid-state structure exhibits crystallographic 3-fold symmetry and a geometry intermediate between trigonal-bipyramidal and pseudotetrahedral (Σ<(P-Fe-P) = 348°).

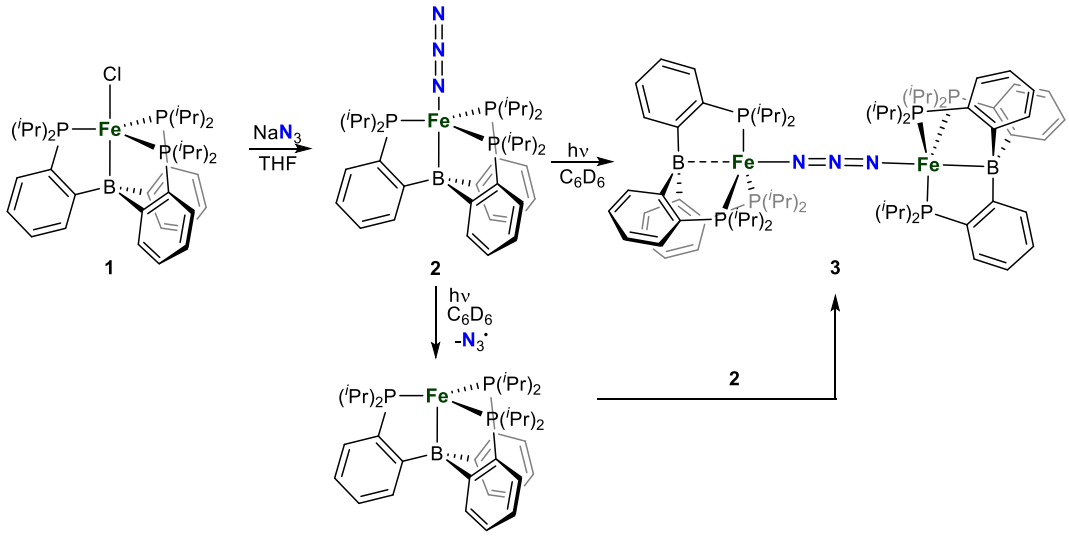

Scheme 3.3. Synthesis of 2 and 3 from the chloride precursor 1

Photolysis of **2** in C_6D_6 solution at room temperature resulted in darkening of the brown solution accompanied by the appearance of new paramagnetic ^1H NMR resonances.

Upon standing, these solutions deposited crystals of $[(P_3^B)Fe]_2(\mu\text{-}1,3\text{-}N_3)$ (**3**). XRD crystallography (See SI), revealed a symmetrical linear Fe–NNN–Fe linkage. Formation of **3** likely proceeds through photoreduction of **2** releasing one equivalent of azide radical N_3• and subsequent reaction with a second equivalent of **2** (Scheme 3.3). Complex **3** could also be independently generated by mixing solutions of **2** and the previously reported complex $(P_3^B)Fe(N_2)$.[10]

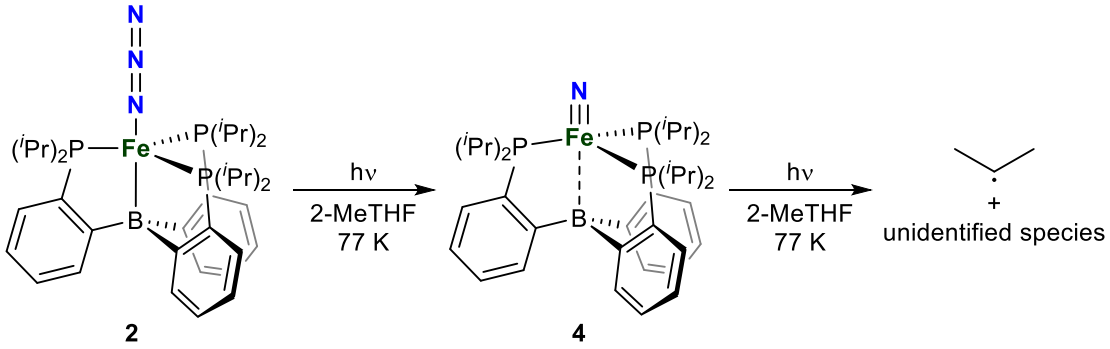

Scheme 3.4. Photolysis of $(P_3^B)Fe(N_3)$ (2)

Changing the photolysis medium from solution to frozen solvent has previously been shown to drastically affect product distributions in related reactions.[7b] Irradiation of a frozen 1 mM solution of **2** in 2-MeTHF with a 40 W 390 nm LED results in the formation of an axial structure-rich doublet signal centered at g = 2.02 (Figure 3.2) assigned to the S = ½ nitridoiron complex $(P_3^B)Fe{\equiv}N$ (**4**) (Scheme 3.4). Identical signals are observed upon irradiation of 1 mM solutions in various glassing solvents such as (d_8)-toluene, *cis*-decalin and methylcyclohexane (See SI). A similar signal, albeit broader and with less resolved hyperfine structure, is observed upon photolysis of frozen pentane solutions or thin films of **2** (See SI). After irradiating samples for 3 minutes, photolysis yields are estimated to be ca. 80 % by spin integration against an external standard (TEMPO). A decrease in signal

intensity is observed upon prolonged photolysis with the complete loss of signals corresponding to **4**, and the concomitant formation of a new signal corresponding to an isopropyl radical in 76 % yield after 30 minutes.[11]

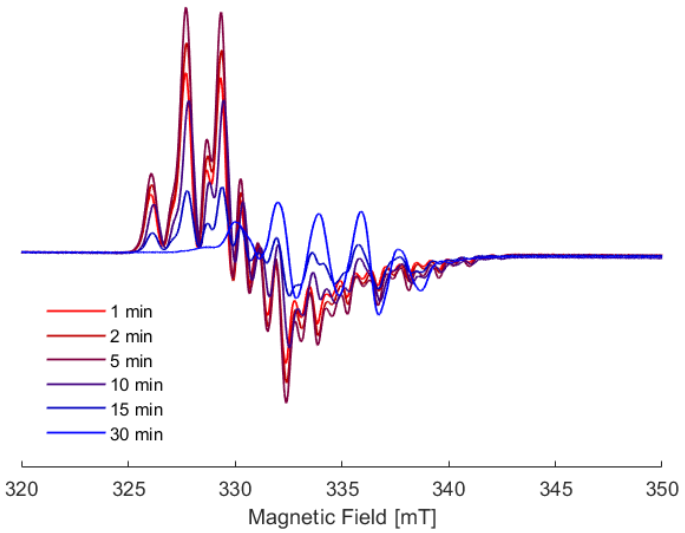

Figure 3.2. Continues wave X-band EPR-monitored photolysis of **2** in a frozen 1 mM 2-MeTHF solution at 77 K.

The low g-anisotropy ($\Delta g = 0.032$) and small deviation of the free electron *g* value (2.002) (Table 3.1) are consistent with a C_3-symmetric iron nitride species having an isolated ^{2}A ground state, where an electron resides in an orbital of d_{z2} parentage (Figure 1).[12] The low *g*-anisotropy of **4** stands in stark contrast with those observed for Fe(V) nitridos ($\Delta g > 0.175$) where the electron resides in nearly degenerate d_{xy} and d_{x2-y2} orbitals (Figure 3.1). The near degeneracy of the orbitals, resulting in significant spin orbit coupling and a considerable increase in Δg.[5,13] The absence of such low-lying excited states in **4**, due to the isolated nature of the A-symmetry orbital, results in a dramatic decrease of Δg. The

low *g*-anisotropy is a characteristic feature of **4** and is not expected for any other photolysis products (*vide infra*).

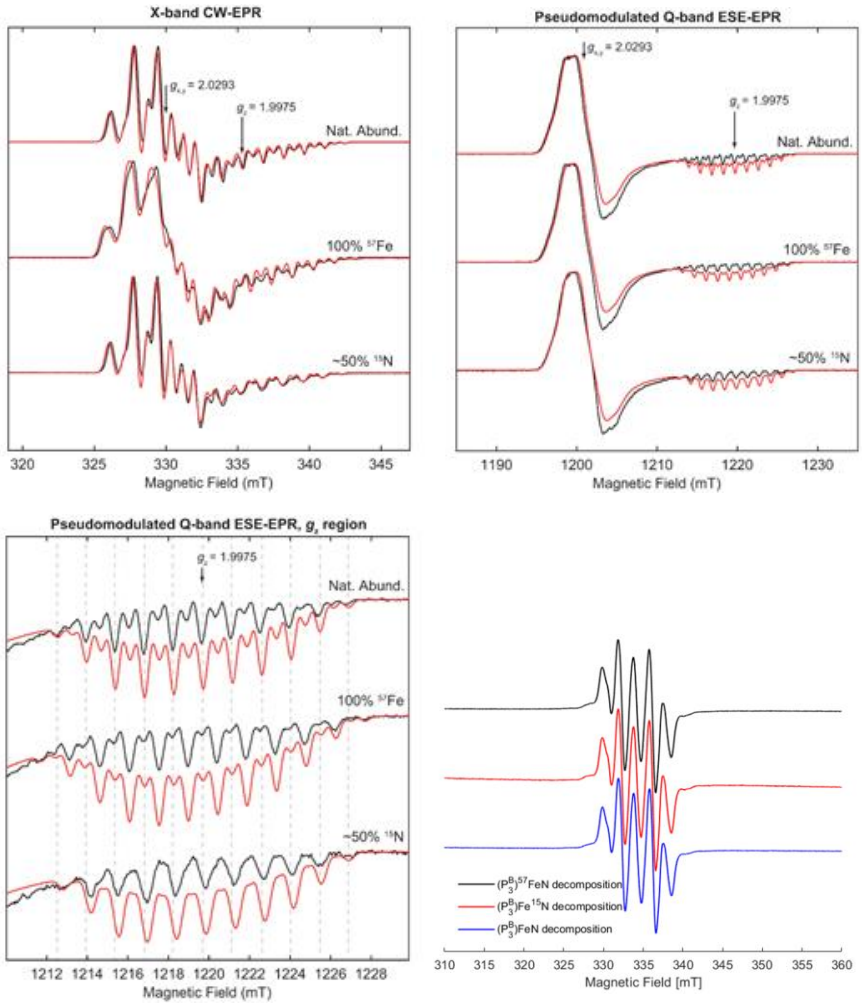

Figure 3.3. CW X-band (a) and psuedomodulated Q-band ESE-EPR (b and c) spectra and corresponding simulations (red) of 4. The dashed dotted lines in (c) are a guide for the eye highlighting the change in hyperfine coupling with different isotopic compositions. (d) EPR spectra after 30 minutes of photolysis with a 40 W 390 nm LED.

The marked difference in the hyperfine patterns, especially at g_z in the X and Q-Band EPR spectra after photolysis of **2-^{57}Fe** and **2-^{15}N** (Figure 3.3), demonstrates that the product contains iron and nitrogen. In contrast, no change is observed in the signal corresponding to liberated isopropyl radical upon isotope substitution (Figure 3.3).

As an additional tool to probe the (electronic) structure of **4**, Davies electron-nuclear double resonance (ENDOR) spectra were acquired at X-band frequencies (ca 9.7 GHz, see SI). This in combination with hyperfine sublevel correlation (HYSCORE) spectroscopy enabled the determination of the distinct ^{11}B, ^{15}N, ^{31}P and ^{57}Fe hyperfine tensors (Table 3.1). The large axial anisotropy for ^{11}B, ^{15}N, and ^{57}Fe and the presence of three identical P nuclei further corroborate the C_3-symmetry present in **4**.

Examples of thoroughly characterized S = ½ nitrides by EPR are limited.[5,14] The observed ^{14}N hyperfine coupling ±[20.3, 20.3, 9.6] is significantly larger than those observed for [PhB(^{t}BuIm)$_3$Fe^{V}≡N]$^+$, which are +[9.11, 6.48, 0.71] respectively. Just as the significant difference in Δg between the nitrides, the difference in hyperfine coupling arises from the different electronic ground states. In [PhB(^{t}BuIm)$_3$Fe^{V}≡N]$^+$ the spin on nitrogen arises through spin-polarization, while in **4** direct delocalization is the origin of the spin on nitrogen (*vide infra*). DFT calculations (TPSS, CP(PPP) on iron and IGLO-III on all others) predict the observed hyperfine coupling constants and nuclear quadrupole moments remarkably well (Table 3.1).

Table 3.1. Experimental g-values, and experimental and theoretical hyperfine in MHz of [(P_3^B)Fe(N) (4). $g_\perp > g_\parallel$, $g_\perp$ corresponds to the xy-plane (g_x and g_y) and $g_\parallel$ to the B-Fe-N axis (g_z). All experimental hyperfine values are in MHz.

	g	*A* (^{14}N)		*A* (^{11}B)		*A* (^{31}P)		*A* (^{57}Fe)	
		EPR	DFT	EPR	DFT	EPR	DFT	EPR	DFT
$g_\parallel$	1.997	20.3	21.2	81.0	79.9	39	-35.5	|46.0	42.7
$g_\perp$	2.029	-4.3	-7.7	21.5	20.3	49 45	-45.8 -39.8	10.0	11.3
Δg	0.032								

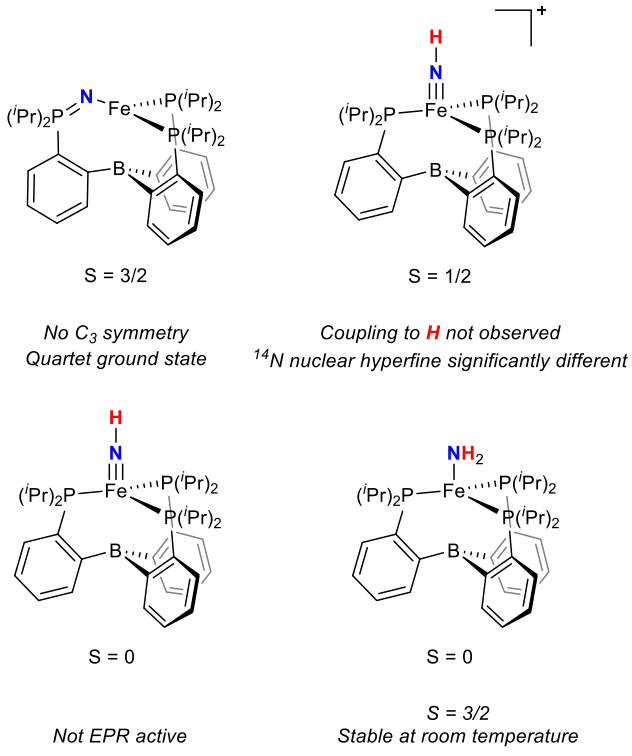

Scheme 3.5. Potential products formed upon photolysis of **2**.

It is improbable that the signal assigned to $(P_3^B)Fe{\equiv}N$ (**4**) corresponds to potential products such as those depicted in Figure 3.4. All data indicates almost perfect C_3 symmetry, where the insertion of the nitride into the Fe-L bond, as observed by Meyer and coworkers, would result in the loss of C_3-symmetry. Similarly, any form of ligand activation would result in a drastic reduction of the symmetry.

Either one or two hydrogen atom abstractions from *e.g.* solvent molecules results in the formation of $(P_3^B)Fe{\equiv}NH$ and $(P_3^B)Fe\text{-}NH_2$, respectively, an EPR silent singlet or previously characterized stable quartet, ruling out these products.

As **4** is expected to be a strong base, one could consider protonation of the nitride. In such a scenario the expected product, $[(P_3^B)Fe{\equiv}NH]^+$ would be a doublet. Based on the observed hyperfine coupling in a terminal amido by Hoffmann, hyperfine coupling to the proton is expected. For the spectrum corresponding to **4**, no change in EPR, ENDOR and HYSCORE spectra is observed upon using deuterated solvents, eliminating the possibility of solvent acting as H^+ source. Furthermore, the electronic structure of $[(P_3^B)Fe{\equiv}NH]^+$ is expected to be comparable to that of $[(P_3^B)Fe{\equiv}NAd]^+$, which has a significantly larger *g* -anisotropy (**4** $\Delta g = 0.032$) as the unpaired electron resides in a nearly degenerate *e*-orbital. The remarkably low *g*-anisotropy of **4**, as well as the absence of observable proton hyperfine coupling, and the ^{14}N quadrupole moment rule out $[(P_3^B)Fe{\equiv}NH]^+$ as product.

Compound **4** decays instantly at −78 °C in fluid as well as frozen solutions. The thermal instability precludes the possibility to manipulate a sample outside of an EPR tube. Furthermore, light-induced decomposition of **4** hampers the ability to perform for example Raman spectroscopy.

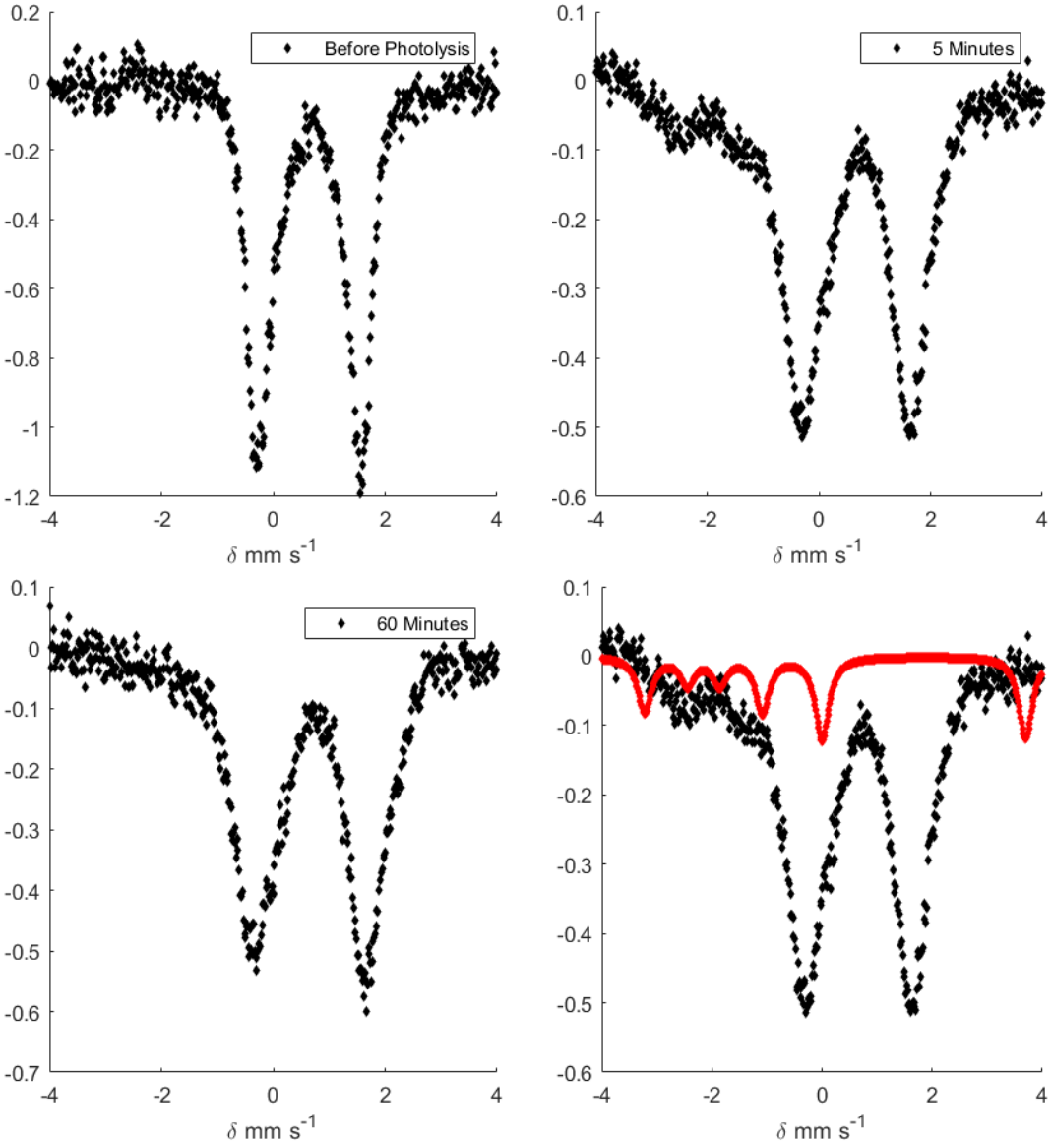

Figure 3.4 Mössbauer spectrum of **2** before photolysis, (b) after 5 minutes of photolysis and (c) 60 minutes of photolysis with a 40 W 390 nm LED. (d) Simulation of a fast relaxing S = ½ complex with hyperfine coupling parameters and g-values as determined by EPR spectroscopy overlaid on top of the spectrum collected after 5 minutes of photolysis.

Mössbauer spectra collected after photolysis of 2 mM **2-^{57}Fe** 2-MeTHF solutions show a decrease in signal intensity corresponding to **2**, with the formation of a broad feature (See Figure 3.4). The broad feature disappears upon prolonged photolysis in line with the time dependent EPR spectra (Figure 2). Compound **4** displays remarkably slow electronic spin relaxation (τ = 265 ns at 85 K) as determined through T_1 and T_2 measurements by respectively an inversion recovery or a two pulse ESEEM (See SI). These relaxation times are on the same order of magnitude as the lifetime of the excited ^{57}Fe nucleus (τ_M ~ 140 ns). For relaxation times $\tau >> \tau_M$ a Mössbauer spectrum consist of sextets with narrow lines, while a quadrupole doublet is observed for $\tau << \tau_M$.[15] The slow electronic relaxation, low conversion, signal intensity, and presence of **2** prevents the achievement of a reliable fit of the signal. However, simulating a spectrum using the *g*-values and ^{57}Fe hyperfine, as determined by EPR spectroscopy, in combination with a quadrupole splitting of around ~ 4 mm s^{-1}, gives a reasonable idea of what such a Mössbauer spectrum would look like (Figure 3.4) The thermal instability prevents the collection of spectra at higher temperatures where a quadrupole doublet with a characteristic large quadrupole splitting is expected (calculated quadrupole splitting ~ 4 mm/s).

The large boron hyperfine coupling constants indicates significant contribution of boron-based orbitals to the SOMO of **4**. Decomposition of ^{11}B hyperfine tensors into its isotropic (a_{iso} = 1/3 (A_x + A_y + A_z) = ±41.6) and anisotropic components (**T**=[((A_x – a_{iso}) + (A_y – a_{iso}) +(A_z – a_{iso})]) can be used to estimate the spin density residing in boron 2s and 2p$_z$ orbitals.[16] This analysis reveals an axial anisotropic boron hyperfine interaction with **T** = [-19.7 -19.7 39.33] MHz. Defining the anisotropic tensor for an electron fully localized in a B 2p$_z$ orbital as $\mathbf{T^0}$ = ±[-63.6 -63. 127.2], yields a spin density in the B 2p$_z$ orbital of $\rho \approx$

0.30 (or ca. 30 % of an electron). Using a_{iso}^{0} = 2547 MHz, the 2s character in the SOMO is found to be 1.7 %. Spin densities for ^{11}B and ^{14}N determined through this method are summarized in Table 2 and are close Löwdin spin populations calculated by DFT. The experimental and Löwdin spin populations show that the spin densities of **4** are significantly delocalized onto the nitrogen and boron atom, with the B p_z orbital accommodating most of the spin. The DFT computed SOMO of **4** has a_1 symmetry and nicely illustrates the proposed ground state based on EPR spectroscopy (Figure 3.5).

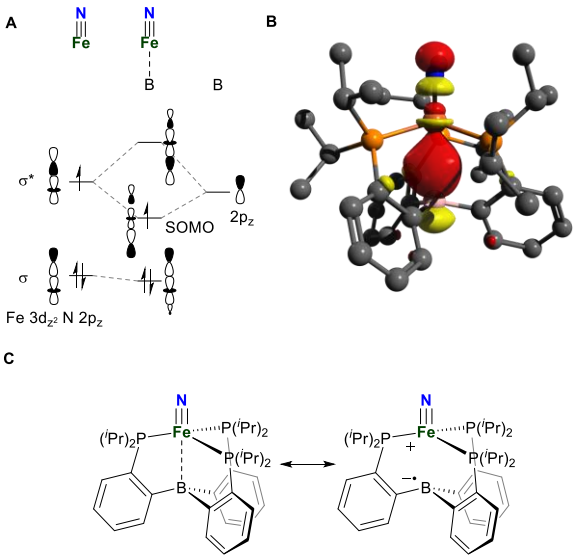

Figure 3.5 (A) Qualitative MO diagram describing the 3-center σ bonding of (P_3^B)Fe≡N and (B) its SOMO and (C) resonance structure description of compound.

Table 3.2 Calculated Löwdin spin populations and experimental spin density estimations.[a]

	^{14}N		^{11}B	
	EPR[b]	DFT	EPR[b]	DFT
s	0.3	0.2	1.7	2.0
p_z	15.9	20.8	30.4	30.1

[a] Spin densities are given as percentages. [b]Total spin density estimated from experimental EPR hyperfine coupling is calculated assuming all spin is located in the orbitals included in the Table.

3.3 Conclusions

In summary, photolysis of $(P_3^B)Fe(N_3)$ at low temperatures generates the transient low-spin Fe(III) nitrido complex $(P_3^B)Fe{\equiv}N$. The series of X-band and Q-band spectra in combination with ENDOR and HYSCORE spectroscopy, supported by DFT calculations, provide compelling data for the assignment of this highly reactive complex. Analysis of the ^{11}B and ^{15}N hyperfine coupling constants reveals significant delocalization of the unpaired electron (~ 50 %) onto these axial ligands. The degree of boron and nitrogen character in the SOMO shows the importance of these ligands in the stabilization of this unusually electron-rich iron-nitride complex.

3.4 References

[1] Chalkley, M. J.; Drover, M. W.; Peters, J. C. Catalytic N_2-to-NH_3 (or -N_2H_4) Conversion by Well-Defined Molecular Coordination Complexes. *Chem. Rev.* **2020**, *120* (12), 5582–5636

[2] a) Yandulov, D. V.; Schrock, R. R. Catalytic Reduction of Dinitrogen to Ammonia at a Single Molybdenum Center. *Science* **2003**, *301* (5629), 76–78. b) Anderson, J. S.; Rittle, J.; Peters, J. C. Catalytic Conversion of Nitrogen to Ammonia by an Iron Model Complex. *Nature* **2013**, *501* (7465), 84–87. c) Ashida, Y.; Arashiba, K.; Nakajima, K.; Nishibayashi, Y. Molybdenum-Catalysed Ammonia Production with Samarium Diiodide and Alcohols or Water. *Nature* **2019**, *568* (7753), 536–540. d) Hill, P. J.; Doyle, L. R.; Crawford, A. D.; Myers, W. K.; Ashley, A. E. Selective Catalytic Reduction of N_2 to N_2H_4 by a Simple Fe Complex. *J. Am. Chem. Soc.* **2016**, *138* (41), 13521–13524 e) Doyle, L. R.; Wooles, A. J.; Jenkins, L. C.; Tuna, F.; McInnes, E. J. L.; Liddle, S. T. Catalytic Dinitrogen Reduction to Ammonia at a Triamidoamine–Titanium Complex. *Angew. Chem. Int. Ed.* **2018**, *57* (21), 6314–6318 f) Chalkley, M. J.; Del Castillo, T. J.; Matson, B. D.; Peters, J. C. Fe-Mediated Nitrogen Fixation with a Metallocene Mediator: Exploring pK_a Effects and Demonstrating Electrocatalysis. *J. Am. Chem. Soc.* **2018**

[3] Seefeldt, L. C.; Hoffman, B. M.; Dean, D. R. Mechanism of Mo-Dependent Nitrogenase. *Annu. Rev. Biochem.* **2009**, *78*, 701–722

[4] Thompson, N. B.; Green, M. T.; Peters, J. C. Nitrogen Fixation via a Terminal Fe(IV) Nitride. *J. Am. Chem. Soc.* **2017**, *139* (43), 15312–15315

[5] Zolnhofer, E. M.; Käß, M.; Khusniyarov, M. M.; Heinemann, F. W.; Maron, L.; van Gastel, M.; Bill, E.; Meyer, K. An Intermediate Cobalt(IV) Nitrido Complex and Its N-Migratory Insertion Product. *J. Am. Chem. Soc.* **2014**, *136* (42), 15072–15078

[6] Mehn, M. P.; Peters, J. C. Mid- to High-Valent Imido and Nitrido Complexes of Iron. *J. Inorg. Biochem.* **2006**, *100* (4), 634–643

[7]a) Meyer, K.; Bill, E.; Mienert, B.; Weyhermüller, T.;Wieghardt, K. Photolysis of Cis- and Trans-$[Fe^{III}(Cyclam)(N_3)_2]^+$ Complexes: Spectroscopic Characterization of a Nitridoiron(V) Species. *J. Am. Chem. Soc.* **1999**, *121* (20), 4859–4876. b) Grapperhaus, C. A.; Mienert, B.; Bill, E.; Weyhermüller, T.; Wieghardt, K. Mononuclear (Nitrido)Iron(V) and (Oxo)Iron(IV) Complexes via Photolysis of $[(Cyclam\text{-}Acetato)Fe^{III}(N_3)]+$ and Ozonolysis of $[(Cyclam\text{-}Acetato)FeIII(O_3SCF_3)]+$ in Water/Acetone Mixtures. *Inorg. Chem.* **2000**, *39* (23), 5306–5317. c) Aliaga-Alcalde, M.; George, S. D.; Mienert, B.; Bill, E.; Wieghardt, K.; Neese, F. The Geometric and Electronic Structure of $[(Cyclam\text{-}Acetato)Fe(N)^+]$: A Genuine

Iron(V) Species with a Ground-State Spin S=1/2. *Angew. Chem., Int. Ed.* **2005**, *44* (19), 2908–2912. d) Berry, J. F.; Bill, E.; Bothe, E.; George, S. D.; Mienert, B.; Neese, F.; Wieghardt, K. An Octahedral Coordination Complex of Iron(VI). *Science* **2006**, *312* (5782), 1937–1941. e) Wagner, W. D.; Nakamoto, K. Formation Of Nitridoiron(V) Porphyrins Detected By Resonance Raman-Spectroscopy. *J. Am. Chem. Soc.* **1988**, *110* (12), 4044–4045

[8] Betley, T. A.; Peters, J. C. A Tetrahedrally Coordinated $L_3Fe–N_x$ Platform That Accommodates Terminal Nitride ($Fe^{IV}≡N$) and Dinitrogen ($Fe^{I}–N_2–Fe^{I}$) Ligands. *J. Am. Chem. Soc.* **2004**, *126* (20), 6252–6254. b) Hendrich, M. P.; Gunderson, W.; Behan, R. K.; Green, M. T.; Mehn, M. P.; Betley, T. A.; Lu, C. C.; Peters, J. C. On the Feasibility of N_2 Fixation via a Single-Site Fe^{I}/Fe^{IV} Cycle: Spectroscopic Studies of $Fe^{I}(N_2)Fe^{I}$, $Fe^{IV}≡N$, and Related Species. *Proc. Nat. Acad. Sci. U.S.A.* **2006**, *103* (46), 17107–17112 c) Rohde, J.-U.; Betley, T. A.; Jackson, T. A.; Saouma, C. T.; Peters, J. C.; Que, L. XAS Characterization of a Nitridoiron(IV) Complex with a Very Short Fe-N Bond. *Inorg. Chem.* **2007**, *46* (14), 5720–5726. d) Vogel, C.; Heinemann, F. W.; Sutter, J.; Anthon, C.; Meyer, K. An Iron Nitride Complex. *Angew. Chem., Int. Ed.* **2008**, *47* (14), 2681–2684. e (20) Scepaniak, J. J.; Fulton, M. D.; Bontchev, R. P.; Duesler, E. N.; Kirk, M. L.; Smith, J. M. Structural and Spectroscopic

Characterization of an Electrophilic Iron Nitrido Complex. *J. Am. Chem. Soc.* **2008**, *130* (32), 10515–10517

[9] a) Scepaniak, J. J.; Vogel, C. A.; Khusniyarov, M. M.; Heinemann, F. W.; Meyer, K.; Smith, J. M. Synthesis, Structure, and Reactivity of an Iron(V) Nitride. *Science* **2011**, *331*, 1049–1052. b) Keilwerth, M.; Grunwald, L.; Mao, W.; Heinemann, F. W.; Sutter, J.; Bill, E.; Meyer, K. Ligand Tailoring Toward an Air-Stable Iron(V) Nitrido Complex. *J. Am. Chem. Soc.* **2021**, *143* (3), 1458–1465

[10] Moret, M.-E.; Peters, J. C. Terminal Iron Dinitrogen and Iron Imide Complexes Supported by a Tris(Phosphino)Borane Ligand. Angew. Chem. Int. Ed. 2011, 50, 2063–2067

[11] Ayscough, P. B.; Thomson, C. Electron Spin Resonance Spectra of Alkyl Radicals in γ-Irradiated Alkyl Halides. *Trans. Faraday Soc.* **1962**, *58*, 1477–1494

[12] Nance, P. J.; Thompson, N. B.; Oyala, P. H.; Peters, J. C. Zerovalent Rhodium and Iridium Silatranes Featuring Two-Center, Three-Electron Polar σ Bonds. Angewandte Chemie International Edition 2019, 58 (19), 6220–6224

[13] Cutsail, G. E.; Stein, B. W.; Subedi, D.; Smith, J. M.; Kirk, M. L.; Hoffman, B. M. EPR, ENDOR, and Electronic Structure Studies of the Jahn-Teller Distortion in an Fe-V Nitride. J. Am. Chem. Soc. 2014, 136 (35), 12323–12336

[14] Cutsail, G. E.; Stein, B. W.; Subedi, D.; Smith, J. M.; Kirk, M. L.; Hoffman, B. M. EPR, ENDOR, and Electronic Structure Studies of the Jahn-Teller Distortion in an Fe-V Nitride. J. Am. Chem. Soc. 2014, 136 (35), 12323–12336

[15] See Mørup, S. Magnetic Relaxation Phenomena. In *Mössbauer Spectroscopy and Transition Metal Chemistry: Fundamentals and Applications*; Gütlich, P., Bill, E., Trautwein, A. X., Eds.; Springer Berlin Heidelberg: Berlin, Heidelberg, 2011; pp 201–234 for an in-depth discussion of lifetimes and the effect on Mössbauer line shapes.

[16] Morton, J. R.; Preston, K. F. Atomic Parameters for Paramagnetic Resonance Data. *Journal of Magnetic Resonance* (1969) 1978, 30 (3), 577–582

Chapter 4 : Snapshots of a Migrating H-atom: Characterization of a Reactive Fe(III) Indenide Hydride and its Nearly Isoenergetic Ring-Protonated Fe(I) Isomer

Reproduced in part with permission from:

Drover, M. W.; Schild, D. J.; Oyala, P. H.; Peters, J. C. Snapshots of a Migrating H-Atom: Characterization of a Reactive Iron(III) Indenide Hydride and its Nearly Isoenergetic Ring-Protonated Iron(I) Isomer

Angew. Chem. Int. Ed., **2019**, 58, 15504-15511

4.1. Introduction

For decades, cyclopentadienyl (Cp, $C_5H_5^-$) and derivatives thereof have been used as ligands to stabilize transition metal,[1] *f*-block,[2] and main-group[3] elements alike. This ligand class is ubiquitous among the synthetic community, no doubt a consequence of several alluring features, including variable hapticity,[4] whereby multiple coordination modes can be accommodated, ranging from η^1-to- η^5. There has been a surge of renewed interest in cooperative transformations with Cp-type ligands,[5] with protonation at such "non-innocent" rings being implicated in the context of hydride or proton-coupled-electron-transfer (PCET) pathways, for instance in H_2-evolving or dinitrogen reduction reactions (Chart 4.1A).[5,6] Metallocene (Cp_2'M) and half-sandwich complexes have been probed for decades in the context of ring protonation (or hydride attack) chemistry.[7] For species that are comparatively stable, characterization data for complexes wherein a ring is "protonated" can be distinguished from those wherein the "proton" instead resides on the metal as a hydride ligand. In certain cases, the H-atom may shuttle between these two positions. For example, the $[Fe^{III}\text{-H}]^+$ cation, $[Fe^{III}(\eta^5\text{-Cp*})(dppe)H]^+$ (Cp* = $C_5Me_5^-$, dppe = 1,2-*bis*(diphenylphosphino)ethane) is resistant to ring protonation (C-H elimination), but undergoes CO binding/reduction by $CoCp_2$ to give the diamagnetic complex $Fe^0(\eta^4\text{-Cp*H})(dppe)(CO)$ where H-migration has occurred onto the Cp*-ring.[8] More recently, crystallography has been used to show that protonation of ferrocene (Cp_2Fe) using a mixture of HF/PF_5 occurs at Fe, in spite of DFT calculations that favor (by 2 kcal mol^{-1}) a ring-protonated isomer, $CpFe(\eta^4\text{-CpH})^+$ (Chart 4.1B).[7e] Distinguishing such species when the respective M-H or C-H bonded isomers feature weak and hence reactive bonds (low homolytic bond dissociation free energies: $BDFE_{M\text{-}H}$ and $BDFE_{C\text{-}H}$) is particularly

challenging, especially for species that are open-shell. A recent study from our lab underscores this point, where protonation of Cp^*_2Co is thermodynamically favored at the ring (and not at Co); multi-frequency continuous-wave (CW) and pulse-EPR spectroscopies were performed at very low temperature to assign the site(s) of protonation.[6]

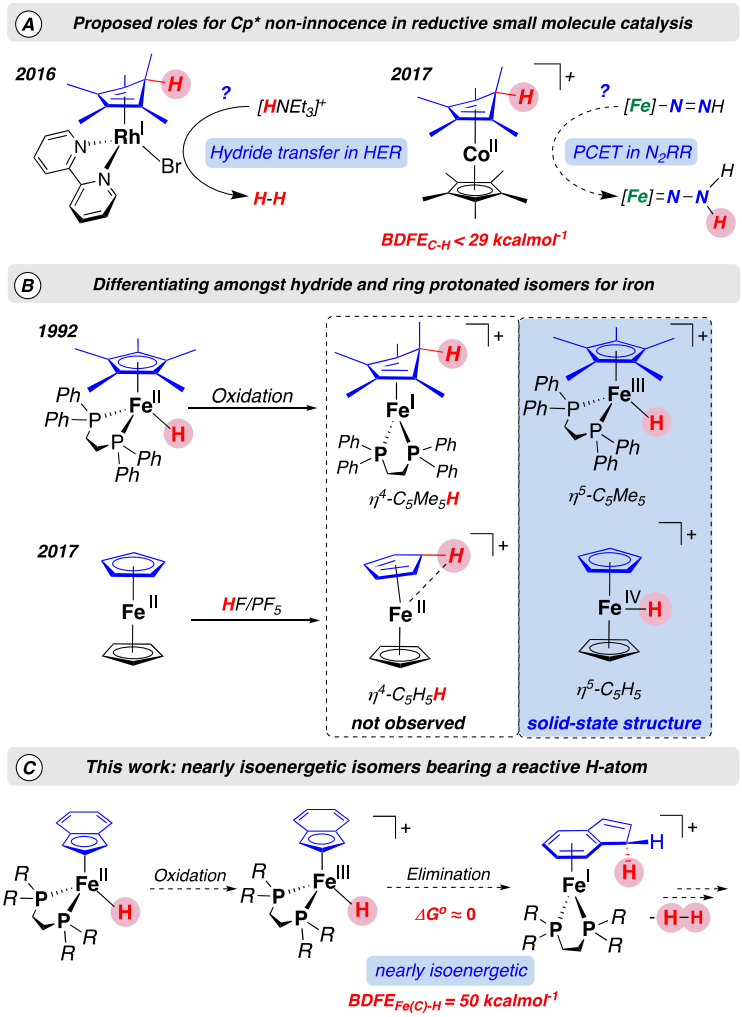

Chart 4.1. Previous work highlighting **A**) Cp* non-innocence for small-molecule fixation, **B**) interest in assigning H-atom location by XRD analysis, and **C**) the present study, featuring indene as a supporting ligand.

As part of an effort to extend such studies to other systems, our attention turned to iron hydride precursors of the type $Fe^{II}(\eta^3:\eta^2\text{-Ind})(P_2)H$ (Ind = indenide, $C_9H_7^-$, P_2 = diphosphine ligand), wherein an indenyl ligand was selected in an effort to stabilize reactive, ring-protonated complexes through [Fe]- η^6-IndH coordination, providing $6e^-$ through the η -system (Chart 4.1C). To our surprise, for the system described herein, the isomer of the metal-bound hydride (formally Fe(III)) is nearly isoenergetic to the isomer in which the ring is instead protonated (formally Fe(I)). This represents, what is to our knowledge, an exceptional case. In general, only one of the isomers is experimentally observed.

Herein, we present the characterization of this pair of S = ½ Fe isomers, wherein H-atom migration has been validated in the solution state by CW- and pulse-EPR spectroscopy. For the Fe(I) indene complex, an X-ray crystal structure has been obtained. The data presented provide a means for facile differentiation between isomers of these types. Finally, a combination of experiment and theory provides access to relevant thermochemistry, including respective homolytic bond dissociation free energies: $BDFE_{C\text{-}H}$ and $BDFE_{Fe\text{-}H}$. Facile PCET from either an Fe-H or C-H bond is predicted to be feasible, and is exemplified by the propensity of the system to liberate H_2 in solution.

4.2 Results and Discussion

Synthetic entry into the system of present interest is as follows: *trans*-$[Fe(Br)_2(depe)_2]$[9] (depe = 1,2-*bis*(diethylphosphino)ethane) was reacted with lithium indenide at −78 °C with warming to room-temperature over 2 h, providing $Fe(\eta^3:\eta^2\text{-Ind})(depe)Br$ (**1**) as a purple powder following work-up (δ_P = 92.98) (Figure 4.1A). Single crystals of **1** were grown from a saturated pentane-layered THF solution and analyzed by

X-ray diffraction (XRD) at 100 K (Figure 4.1B). Consistent with η^3: η^2 binding, the structure features short Fe(1)-C(1)/C(2)/C(3) bond lengths (avg. = 2.078(2) Å) and long Fe(1)-C(4)/C(5) (avg. = 2.206(4) Å) contacts, with $\Delta(\text{M-C})^{10}$ = 0.134 Å [Δ(M-C) = difference between these two averages] – this is true for all complexes discussed herein.

Complex **1** serves as a versatile starting material from which the Fe^{II}-hydride, Fe(η^3: η^2-Ind)(depe)H (**2**) can be accessed (Figure 4.1A).[11] Reaction of **1** with Li[BEt_3H] gives **2** in near-quantitative yield. Most characteristically, the ^{31}P NMR spectrum provides a doublet at δ_P = 92.98 ppm ($^2J_{P,H}$ = 70.8 Hz, $^1J_{Fe,P}$ = 60.3 Hz: for **2**-^{57}Fe) that directly couples with the Fe^{II}-H group at δ_H = -20.64 ppm ($^1J_{Fe,H}$ = 10.7 Hz).

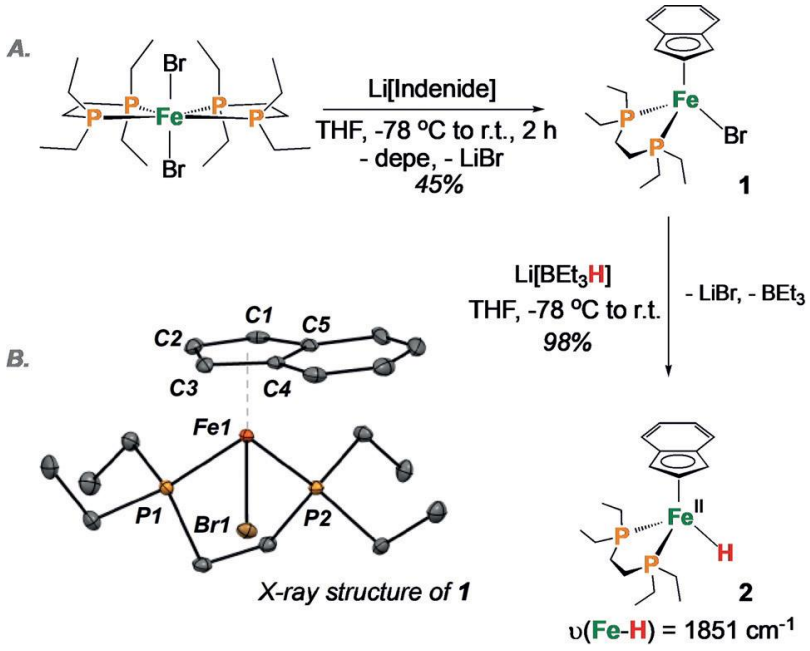

Figure 4.1 A) Synthesis of **2** by addition of Li[BEt_3H]. B) Solid-state structure of 1 with ellipsoids shown at 50% probability.

Complex **2** was also studied by cyclic voltammetry (CV), which reveals an irreversible feature centered at $E_{1/2}$ = - 0.81 V *vs.* Fc/Fc^+ (Fc = ferrocene) associated with

the Fe^{II}/Fe^{III} couple; only ~75% of the signal current is maintained on the return reductive wave (*SR* = 50 mV/s), suggesting reactivity of the *in-situ* generated Fe(III) cation.[12] Given our desire to generate a reactive open-shell $[Fe(III)\text{-}H]^+$ species, we next probed the oxidative chemistry of complex **2** using $[Fc]BAr^F{}_4$ ($E_{1/2}$ = 0 V *vs.* Fc/Fc^+; $Ar^F{}_4$ = 3,5-$(CF_3)_2(C_6H_3)$),[13] at −78 °C (Figure 4.2).

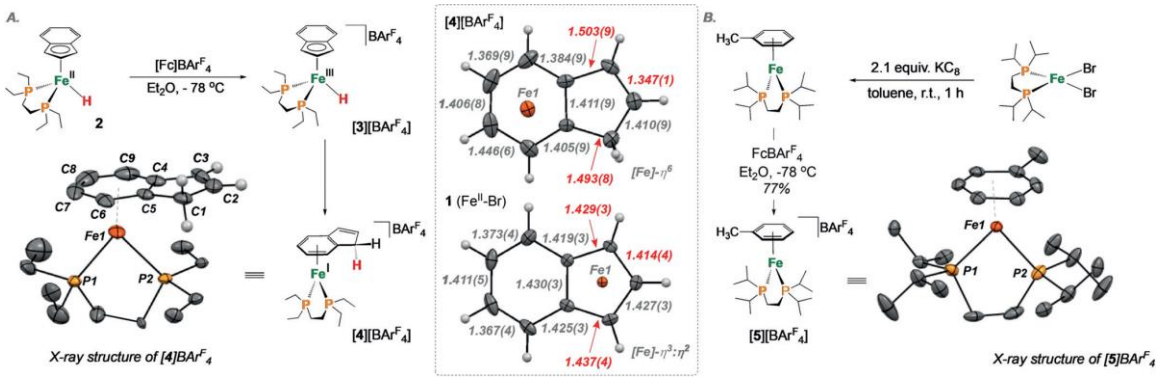

Figure 4.2 A) Synthesis of $[4][BAr^F{}_4]$ by oxidation using $[Fc]BAr^F{}_4$ and solid-state depiction of the solid-state molecular structure of $[4][BAr^F{}_4]$ with ellipsoids shown at 50% probability). Selected bond lengths [Å] and angles (°): Fe(1)-P(1) 2.222(3), Fe(1)-P(2) 2.298(3), Fe(1)-C(centroid), 1.589,φC(1)-C(5)]-[P(1)-Fe(1)-P(2)]), 90. B) Synthesis of $[5][BAr^F{}_4]$ and solid-state depiction of the solid-state molecular structure of $[5][BAr^F{}_4]$.

Monitoring this reaction mixture for both ^1H and ^2H isotopologues by freeze-quenched X-band CW-EPR spectroscopy (77 K) shows the formation of a single S = ½ species exhibiting roughly axial symmetry (g = [2.377, 2.039, 1.993]) with couplings of similar magnitude to two distinct ^{31}P (I = 1/2) nuclei. Significant additional couplings to ^1H are resolved in the ^1H isotopologue, consistent with the presence of a strongly coupled hydride ^1H nucleus (Figure 4.3A): thus we assign this spectrum to $[Fe^{III}(\eta^3\text{: }\eta^2\text{-Ind})(depe)H][BAr^F{}_4]$ $[\mathbf{3}]^+$. Collection of a series of X-band Davies ENDOR spectra across the EPR envelope of $[\mathbf{3}\text{-D}]^+$ (*see SI*) provide additional data showing large coupling to two

non-equivalent phosphines ($A(^{31}P\alpha)$ = ± [100, 88, 88] MHz and $A(^{31}P\beta)$ = ± [82, 85, 72] MHz).

To determine more accurate hyperfine parameters for the hydride ligand, than can be resolved from CW-EPR, we turned to X-band ^{2}H-HYSCORE of this same [**3**-D]$^{+}$ isotopologue. Simulation of field-dependent HYSCORE spectra of [**3**-D]$^{+}$ reveal a highly anisotropic deuterium hyperfine tensor $A(^{2}H)$ = ± [1.84, 12.6, 10.0] MHz, with a small Euler rotation of the hyperfine tensor relative to the g-tensor of (α,β,γ) = (40, 15, 0)◦. Scaling of the ^{2}H hyperfine tensor determined by ^{2}H HYSCORE by the proportion of ^{1}H/^{2}H gyromagnetic ratios ($\gamma^{1}H/\gamma^{2}H$ = 6. 514) provides a ^{1}H hyperfine tensor $A(^{1}H)$ = ± [12, 82, 65] MHz which is in agreement with simulation of the X-band CW-EPR spectrum. This hyperfine coupling tensor consists of both large isotropic ($a_{iso}(^{1}H)$ = ± 53 MHz) and anisotropic ($T(^{1}H)$ = ± [-41, 29, 12] MHz) components, consistent with those expected for a terminal metal hydride.[14]

For comparison, we have also undertaken study of Lapinte's *bonafide S* = ½ Fe^{III}-H species (for which an X-ray structure is available),[11a] Fe^{III}(η^{5}-Cp*)(dppe)H^{+}. Analogous EPR characterization reveals spectroscopic features consistent with those discussed above, namely, a large and very anisotropic ^{1}H coupling of $A(^{1}H)$ = ± [4, 68, 50] MHz ($a_{iso}(^{1}H)$ = ± 40.7 MHz, $T(^{1}H)$ = ± [-36.7, 27.3, 9.3] MHz) (Figure 4.6).

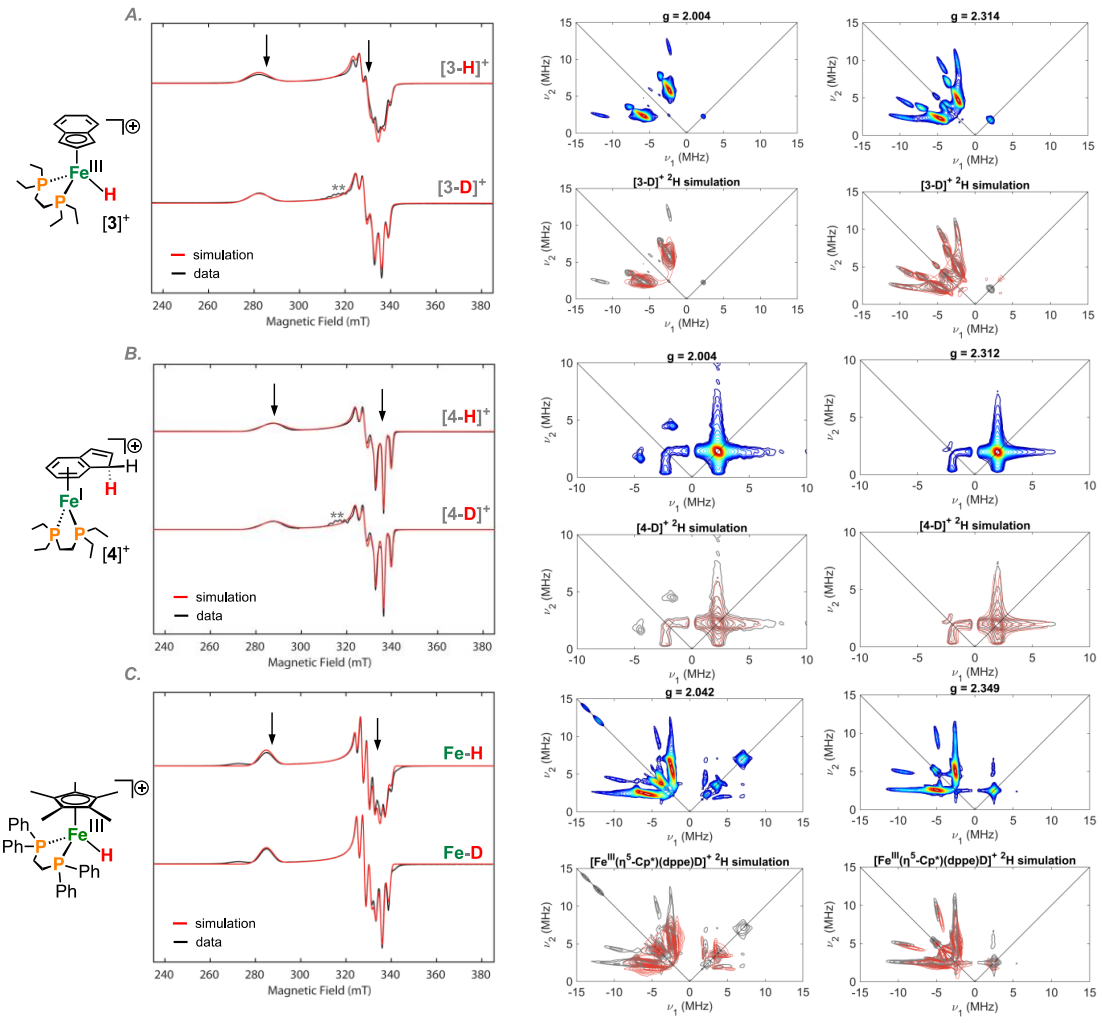

Figure 4.3. Freeze-quenched X-Band EPR spectrum (9.371 GHz) and corresponding X-band HYSCORE data recorded in 2-MeTHF glass at 77 K. **A**) [**3-H**][BAr^F_4] and [**3-D**]BAr^F_4; **B**) [**4-H**]BAr^F_4 and [**4-D**]BAr^F_4 and **C**) $[Fe^{III}(\eta^5\text{-Cp*})(dppe)H]^+$ and $[Fe^{III}(\eta^5\text{-Cp*})(dppe)D]^+$ HYSCORE simulations of the ^2H hyperfine couplings are overlaid in red over the data, which is plotted in grey. Downward pointed arrows represent *g*-values at which HYSCORE has been acquired. ** = $[Fe(depe)_2(N_2)][BAr^F_4]$[18] impurity.

Although at early reaction periods an Fe^{III}-H species is observed, timed freeze-quench experiments show that this complex is consumed at −78 °C ($t_{1/2}$ = 15 min) to provide a new roughly axial S = ½ species with g = [2.332, 2.042, 1.992].[15] X-band ENDOR spectroscopy provides data (*see ESI*) that is consistent with large coupling to two non-equivalent phosphines ($A(^{31}P\alpha)$ = ± [86, 104, 100] MHz and $A(^{31}P\beta)$ = ± [93, 88, 94] MHz). Unlike in the case of the terminal hydride species, Fe^{III}-H/D [**3**]$^+$ and [**3-D**]$^+$, no difference in the CW X-band EPR spectrum between [**4**]$^+$ and [**4-D**]$^+$ (associated with a large anisotropic ^{1}H coupling) is noted. Further analysis by ^{1}H/^{2}D difference HYSCORE spectroscopy reveals a very small anisotropic coupling to a single ^{1}H nucleus, $A(^1H)$ = ± [1, -4, -4] MHz, which we assign to an indene ring proton, formed by C-H elimination to give [$Fe^I(\eta^6$-IndH)(depe)]$^+$ ([**4**]$^+$). Consistent with the DFT-calculated spin-density plot for [**4**]$^+$, the Fe-bound indene fragment is observed to bear minimal spin *c.f.* the terminal hydide [**3**]$^+$ (Figure 4.4). Calculated and experimental EPR parameters are summarized in Figure 4.6.

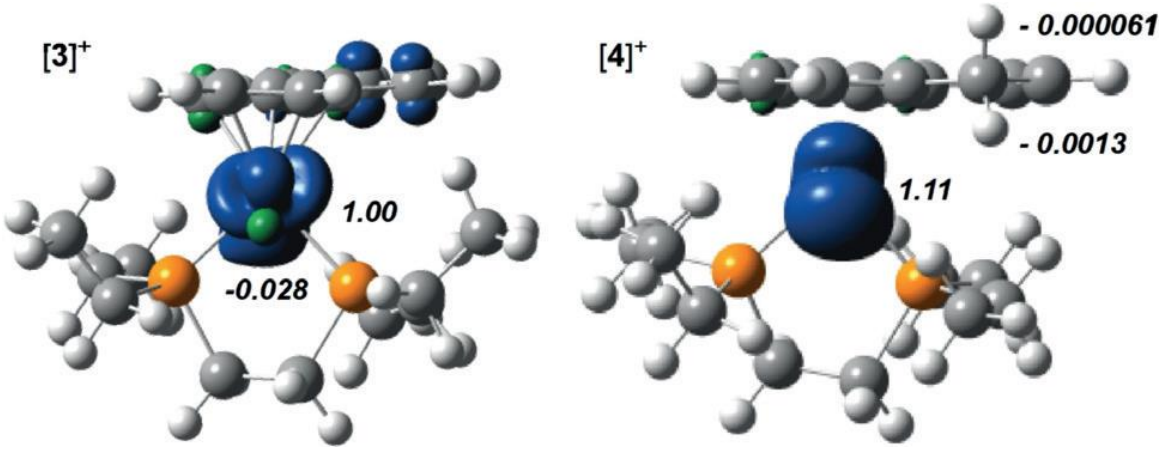

Figure 4.4. DFT-calculated spin-density plot for [3]$^+$ and [4]$^+$ (isovalue: 0.004 *e*-/Å^3; TPSS; def2tzvp (Fe), def2svp (all other atoms).

To ensure appropriate assignment of complex [**4**]$^+$ by EPR spectroscopy, the S = ½ model compound, [Fe(η^6-toluene)(dippe)][BAr$^F{}_4$] ([**5**]$^+$) (dippe = 1,2-*bis*(diisopropylphosphino)ethane) was prepared by oxidation of Fe(η^6-toluene)(dippe)[16] with [Fc]BAr$^F{}_4$ at -78 ^{o}C (Figure 4.2). By EPR spectroscopy, a similar spectrum to that of [**4**]$^+$ was acquired, with simulation parameters appropriate for a rhombic species with g = [2.371, 2.032, 1.990 (Figure 4.5).

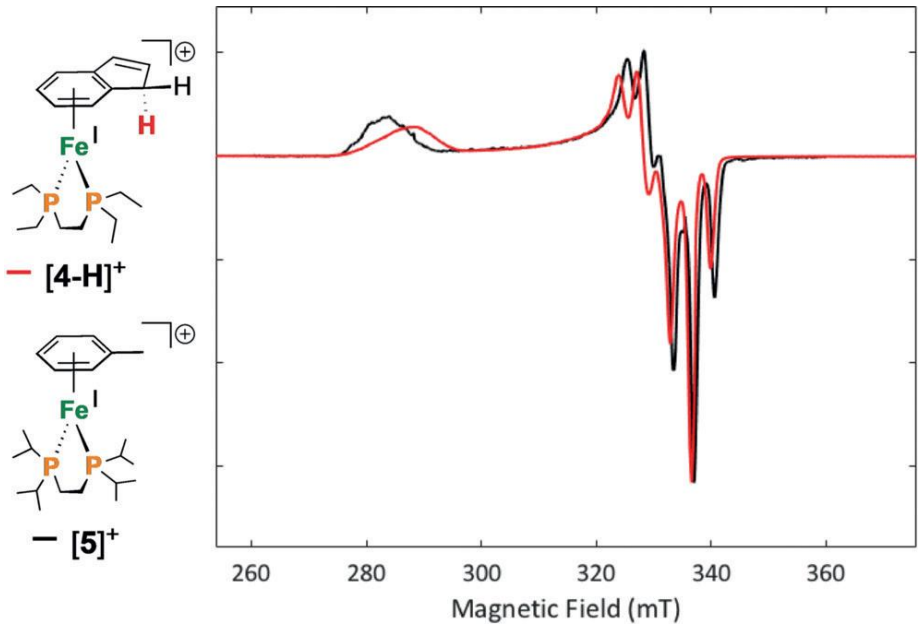

Figure 4.5. Freeze-quenched X-Band EPR spectrum (9.386 GHz) recorded in 2-MeTHF glass at 77 K for [**4-H**]BAr$^F{}_4$ (red) and [**5**]BAr$^F{}_4$ (black).

Despite its propensity to lose H_2 (vide infra), the assignment of [**4**]$^+$ could be further cemented by storing one such oxidation mixture cold, providing orange blocks suitable for XRD analysis (Figure 4.2A). On first inspection, the Fe-P contacts for this open-shell d^7 system were noted to be longer than those for the S = 0 variant (complex **1**, for example) with values of 2.222(3)/2.298(3) Å compared to 2.1792(6)/2.2217(6) Å. Furthermore, metrics associated with the dearomatized five-membered indene ring are markedly

different, with elongation along the C(1)-C(5) and C(3)-C(4) vectors [1.437(4)/1.429(3) Å to 1.493(8)/1.503(9) Å] and contraction along the C(2)-C(3) vector [1.414(4) to 1.347(1) Å], signifying new single and double bonds, respectively.[17] The presence of a "two-legged piano stool" complex is further corroborated by φ, where the plane created by P(1)-Fe(1)-P(2) is perfectly perpendicular (90°) to the iron-bound indene ring. For complex [**5**]$^+$, similar data were also obtained providing Fe-P contacts [2.2272(2)/2.254(2) Å] and a φ value [96.7°] close to that of [**4**]$^+$ [2.222(3)/2.298(3) Å and φ = 90°] (Figure 4.2B).

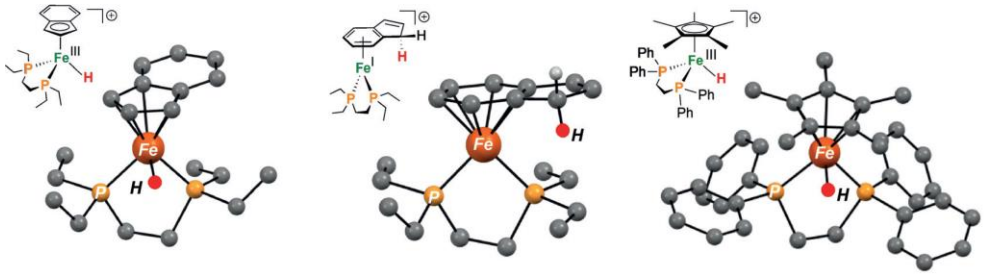

	[Fe^{III}(η^5-Ind)(depe)(H)]$^+$ ([**3**]$^+$)	[Fe^{I}(η^6-IndH)(depe)]$^+$ ([**4**]$^+$)	[Fe^{III}(η^5-Cp*)(dppe)(H)]$^+$
	G = 0 kcal mol^{-1} $BDFE_{Fe\text{-}H}$ = 50 kcal mol^{-1}	G_{rel} = 0 kcal mol^{-1} $BDFE_{C\text{-}H}$ = 50 kcal mol^{-1}	— $BDFE_{Fe\text{-}H}$ = 56 kcal mol^{-1}
	g = [2.377, 2.039, 1.993]	g = [2.332, 2.042, 1.992]	g = [2.352, 2.041, 1.992]
	$A(^{31}P_\alpha)$ = ± [100, 88, 88] MHz $A(^{31}P_\beta)$ = ± [82, 85, 72] MHz	$A(^{31}P_\alpha)$ = ± [86, 104, 100] MHz $A(^{31}P_\beta)$ = ± [93, 88, 94] MHz	$A(^{31}P_\alpha)$ = ± [88, 82, 79] MHz $A(^{31}P_\beta)$ = ± [82, 71, 76] MHz
	$A(^1H)$ = ± [12, 82, 65] MHz $a_{iso}(^1H)$ = ± 53 MHz $T(^1H)$ = ± [-41, 29, 12] MHz	$A(^1H)$ = ± [-1, -4, -4] MHz $a_{iso}(^1H)$ = ± 2.3 MHz $T(^1H)$ = ± [3.3, -1.7, -1.7] MHz	$A(^1H)$ = ± [4, 68, 50] MHz $a_{iso}(^1H)$ = ± 40.7 MHz $T(^1H)$ = ± [-36.7, 27.3, 9,3] MHz
DFT	$A(^1H)$ = [-15.4, -74.8, -73.2] MHz $a_{iso}(^1H)$ = -54.5 MHz $T(^1H)$ = [39.1, -20.3, -18.7] MHz	$A(^1H)$ = [1.1, -4.2, -4.6] MHz $a_{iso}(^1H)$ = -2.6 MHz $T(^1H)$ = [3.6, -1.7, -2] MHz	$A(^1H)$ = [-1.2, -59.9, -58.0] MHz $a_{iso}(^1H)$ = -39.7 MHz $T(^1H)$ = [38.5, -20.2, -18.3] MHz

Figure 4.6 DFT optimized structures of [**3**]$^+$, [**4**]$^+$, and [Fe^{III}(□^{5}-Cp*)(dppe)H]$^+$. Experimental and theoretical A(^{1}H) values are shown for the proton coded with a red circle. Equations: $a_{iso} = [A_x + A_y + A_z]/3$, T(^{1}H) = [$A_x$ - a_{iso}, A_y - a_{iso}, A_z - a_{iso}]. DFT: Structures were optimized using TPSS; def2tzvp (Fe), def2svp (all other atoms), and EPR calculations: CP(PPP) (Fe), TPSS/IGLO-III (all other atoms).

Complexes [**3**]$^{+}$ and [**4**]$^{+}$ undergo bimolecular degradation in solution, resulting in H_2 loss (Figure 4.7). For example, reaction of **2** with [Fc]BAr^F_4 in Et_2O at −78 ^oC and warming to room-temperature results in a visible precipitation of a maroon solid and formation of H_2 (~60% H_2 as quantified by GC). Analysis of the crude ^{31}P NMR spectrum (THF-d_8) evidences two major by-products that are assignable to [Fe(η^3: η ^{2}-Ind)(depe)N_2][BAr^F_4] ([**6**]$^{+}$;ν_{NN} = 2151 cm^{-1}, *ca.* 20%) and [Fe_2(η^3:η^2-Ind)$_2$(depe)$_2$(μ-depe)][BAr^F_4]$_2$ ([**7**]$^{2+}$; *ca.* 20%), respectively.[18] Consistent with formation of these two species, cooling of the reaction mixture produces yellow and violet crystals suitable for analysis by XRD (Figure 4.7B). Presumably these compounds are formed from bimolecular H_2 release from one (or more) of the following pairs: {[Fe^{III}]−H···H−[Fe^{III}]}‡, {[Ind]C−H···H−[Fe^{III}]}‡, or {[Ind]C−H···H−C[Ind]}‡.[19] To confirm bimolecular H_2 release, a 1:1 ratio of **2-H** and **2-D** was mixed, followed by oxidation with [Fc]BAr^F at −78 ^oC, and allowing the solution to warm. The release of HD, as detected by NMR spectroscopy, substantiates a bimolecular H-H coupling process.

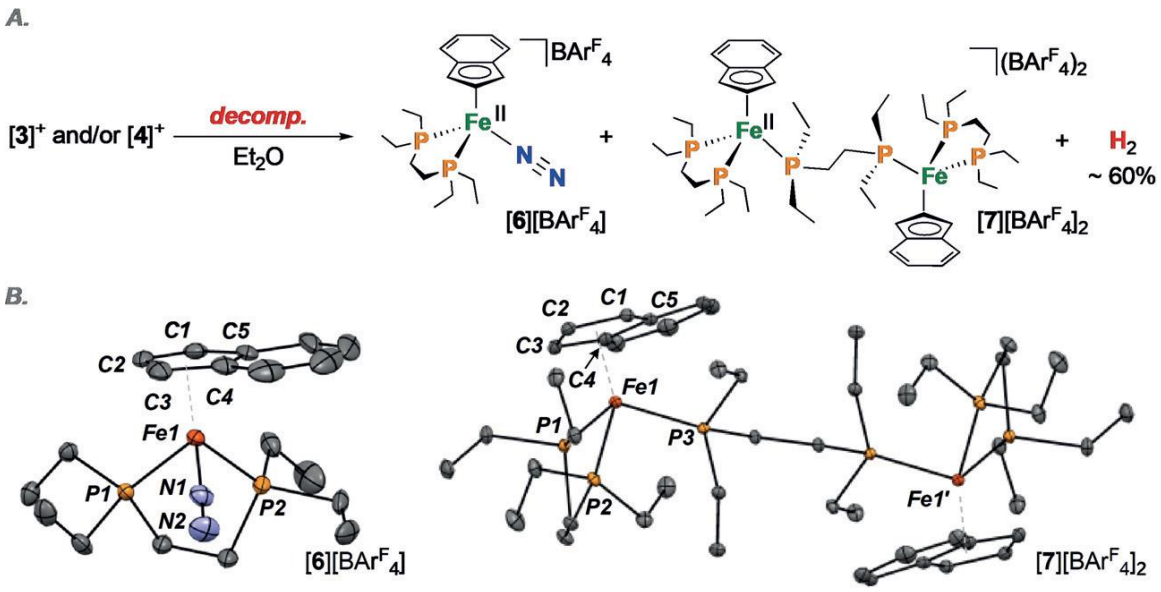

Figure 4.7. A) Decomposition of [**3**]$^{+}$ and [**4**]$^{+}$. **B**) Solid-state depiction of [**6**][BAr$^{F}_{4}$] and [**7**][BAr$^{F}_{4}$]$_2$. (Displacement ellipsoids are shown at the 50% probability). Selected bond length for [**6**][BAr$^{F}_{4}$]: N(1)-N(2)) = 1.108(6) Å.

To experimentally benchmark the H$^{\bullet}$ transfer propensity of [**4**]$^{+}$, we aimed to determine an upper limit for BDFE$_{Fe\text{-}H}$ which, based on the small energy difference between [**3**]$^{+}$ and [**4**]$^{+}$ (*vide infra*), should be similar to BDFE$_{C\text{-}H}$. Figures 4.8A-C summarize our findings via experiment and theory. Reaction of an MeCN solution of **2** with 1-benzyl-3-acetylpyridinium [BNAP]OTf[20] results in hydride transfer and clean formation of [Fe(η^3:η^2-Ind)(depe)(NCCH$_3$)]$^{+}$ [**8**]$^{+}$ (δ_P = 92.8 ppm) (Figure 4.8). Transfer also proceeds in THF, providing the N$_2$-adduct, [**6**]$^{+}$ and μ-depe complex, [**7**]$^{2+}$. The hydricity (defined as the heterolytic dissociation energy of M–H to give M^{+} and H^{-} ($\Delta G(\mathbf{2})_{H-}$) of **2** in MeCN must therefore be less than the hydricity of 1,4-BNAPH ($\Delta G_{H-} \approx 60$ kcal mol^{-1}), *i.e.* more hydridic.[21] In theory, loss of H^{-} from **2** should give [Fe(η^3: η^2-Ind)(depe)]$^{+}$, though this cation is not observed experimentally due to facile MeCN binding to give the adduct (ΔG^{o}(DFT) = - 17 kcal mol^{-1}; Fig. 8C). For comparison, hydricities of 54 kcal mol^{-1} and an

upper bound of < 44 kcal mol^{-1} have been established for the six-coordinate terminal iron hydrides, $(SiP_3)Fe(H)(H_2)$[22] and $(SiP_2S)Fe(H)(H_2)$[14b], respectively. Utilizing thermodynamic relationships that relate $H^{\bullet}$ and H^- in MeCN,[23] the upper bound for the free energy of H^- transfer from **2** and $H^{\bullet}$ transfer from $[\mathbf{3}]^+$ can be related (Eq. 4 and 5, Figure 4.8C). The [Fe]−H bond of $[\mathbf{3}]^+$ is thus conservatively estimated to have an upper bound BDFE ($\Delta G([\mathbf{3}]^+)_{H\bullet}$) of < 52 kcal mol^{-1} giving $[Fe(\eta^3\text{: }\eta^2\text{-Ind})(depe)(NCCH_3)]^+$ and $H^{\bullet}$; the DFT-predicted value is 33 kcal mol^{-1} (TPSS; def2tzvp (Fe), def2svp (all other atoms)) – these values suggest that, on the basis of thermodynamics alone, loss of H_2 should be facile ($BDFE_{H\text{-}H}$ = 102.3 kcal mol^{-1} in CH_3CN).[24]

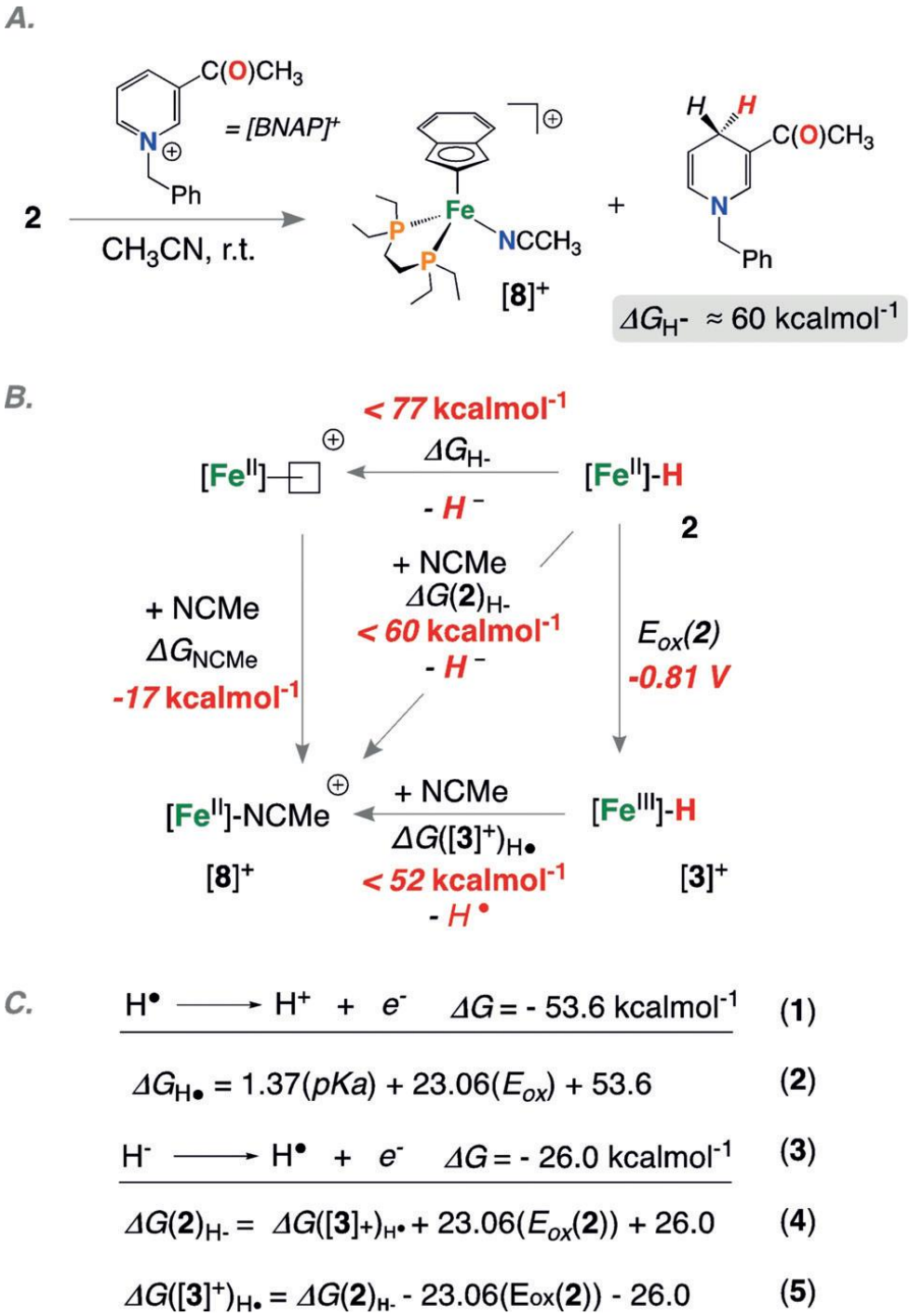

Figure 4.8. Reaction of **2** with 1-benzyl-3-acetylpyridinium triflate $(BNAP)^+$; **B**) Square scheme for experimentally calculated thermodynamic quantities. **C)** Thermodynamic relationships that relate $H^{\bullet}$ and H^- transfer in MeCN.

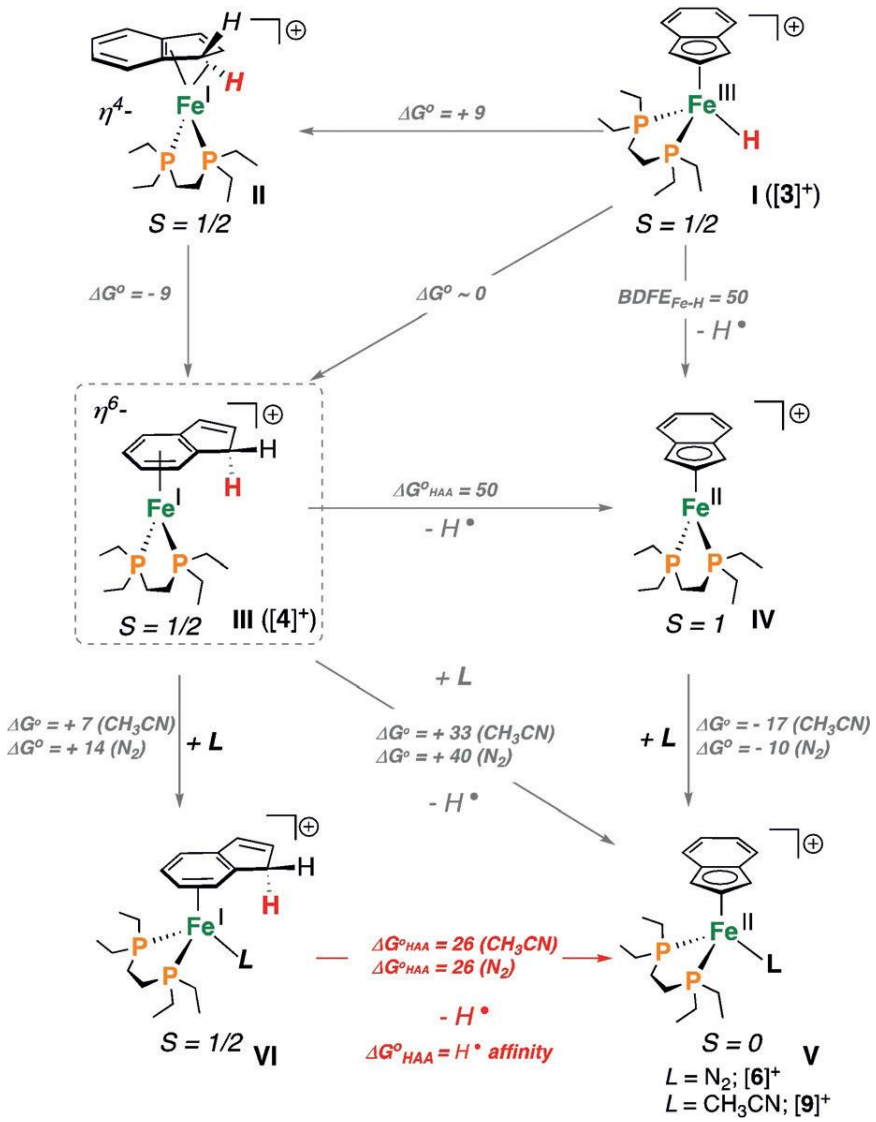

Figure 4.9. Free energy change (kcal mol^{-1}) for PCET involving $BDFE_{C\text{-}H}$ (TPSS; def2tzvp (Fe), def2svp (all other atoms)).

To gain insight into the elementary steps associated with the reactivity of these species, we turned to DFT (Figure 4.9). First, a negligible energy difference is calculated between [**3**]$^+$ (**I**) and [**4**]$^+$ (**II**) ($\Delta G^o \approx 0$ kcal mol^{-1}), which we attribute to stabilization of [**4**]$^+$ by η^6-indene coordination. For a related family of compounds, $Fe^{III}(\eta^5\text{-}C_5R_5)(P_2)H^+$ (R = H, P_2 = dippe (1,2-bis(diisopropylphosphino)ethane or R = CH_3, P_2 = dppe),[11] hydride-to-ring

migration is not observed. In this regard, a difference of + 13 kcal mol^{-1} is calculated between the theoretical compounds, $[Fe^{I}(\eta^{4}\text{-CpH})(depe)]^{+}$ and $[Fe^{III}(\eta^{5}\text{-Cp})(depe)H]^{+}$, and an even larger value of + 16 kcal mol^{-1} is calculated between $[Fe^{I}(\eta^{4}\text{-Cp*H})(depe)]^{+}$ and $[Fe^{III}(\eta^{5}\text{-Cp*})(depe)H]^{+}$ (Figure 4.10). These values do not correlate with the higher basicity of Cp*H (*pKa* = 26.1) versus IndH (*pKa* = 20.1) versus CpH (*pKa* = 18.0), and are instead likely ascribable to ligand steric effects.[25] Nonetheless, for this family of complexes, only the indene system manifests ring functionalization by H-migration due to a 9 kcal mol^{-1} stabilization resulting from ring slippage.

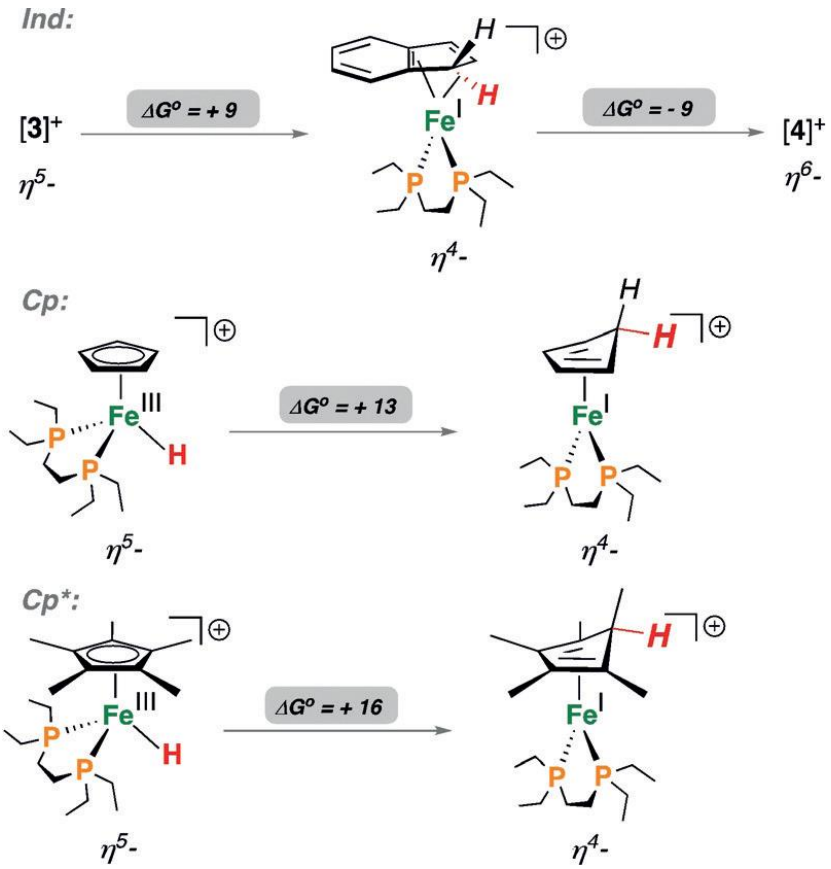

Figure 4.10. DFT-predicted free energy change (kcal mol^{-1}) for metal-to-ring H-migrations.

In terms of $BDFE_{C-H}$, the 17-electron complex **III** is calculated to have a $BDFE_{C-H}$ of 50 kcal mol^{-1}, and the terminal hydride **I** is calculated to possess an equivalent energy ($BDFE_{Fe-H}$ = 50 kcal mol^{-1}); both pathways provide the vacant S = 1 cation, $[Fe(\eta^3\text{: }\eta^2\text{-Ind})(depe)]^+$ (**IV**) and $H^{\bullet}$, indicating that both species should be competent for H_2 loss.[22] By contrast, we calculate $[Fe^{III}(\eta^5\text{-Cp*})(dppe)H]^+$ to possess a stronger Fe-H bond: $BDFE_{Fe-H}$ = 56 kcal mol^{-1}. We find experimentally this Fe^{III}-H cation is stable in ethereal solvent (by UV-VIS and ^1H NMR spectroscopy) and does not release H_2 under ambient conditions (< 5% decomposition after 1 week).

Alternatively, from the 17-electron cation **III**, 19-electron complexes **VI** can be optimized upon associative substitution of a two-electron donor (*L*) with the hydrogen atom affinity ΔG^{o}_{HAA} being 26 kcal mol^{-1} for both *L* = $NCCH_3$ and N_2. In this transformation, the driving force for **III** → **V** is proposed to be a dual consequence of i) indene rearomization and ii) formation of a stable 18-electron product.

Figure 4.11 Free energy change (kcalmol^{-1}) for PCET using $[Fe^{III}(\eta^5\text{-Cp*})(dppe)H]^+$ (TPSS; def2tzvp (Fe), def2svp (all other atoms)).

4.3 Conclusions

We have described the synthesis, electronic characterization, and thermochemistry associated with a pair of isomeric open-shell *S* = ½ complexes, $[Fe^{III}(\eta^2\text{:}\,\eta^3\text{-Ind})(depe)H]^+$ and $[Fe^{I}(\eta^6\text{-IndH})(depe)]^+$. By calculation and experiment, we have shown that these species are highly reactive, having C-H and Fe-H bonds that are close in energy ($BDFE_{C\text{-}H} \approx BDFE_{Fe\text{-}H} \approx 50$ kcal mol^{-1}) manifesting in PCET to provide H$^{\bullet}$ (identified as H_2), presumably through bimolecular combination of one (or more) of the following pairs: $\{[Fe^{III}]\text{–}H\cdots H\text{–}[Fe^{III}]\}^{\ddagger}$, $\{[Ind]C\text{–}H\cdots H\text{–}[Fe^{III}]\}^{\ddagger}$, or $\{[Ind]C\text{–}H\cdots H\text{–}C[Ind]\}^{\ddagger}$. With a unique opportunity to observe both species, detailed X-band (CW) and pulse EPR spectroscopic experiments were undertaken, that together, provide a reliable means to differentiate a ring- versus a metal- bound H-atom, an approach that should prove useful in other systems for which ligands might play a non-innocent role in hydride, proton, or

hydrogen atom transfer. Ongoing studies in our laboratory are currently focused on exploiting the PCET reactivity of weak C-H bonds in this and related systems.

4.4 References

[1] a) Collman, J. P.; Hegedus, L. S.; Norton, J. R.; Finke, R. G. Principles and Applications of Organotransition Metal Chemistry. University Science Books, CA, **1987**; b) Crabtree, R. H. The Organometallic Chemistry of the Transition Metals, 2nd ed., John Wiley & Sons, NY, **1994**.

[2] Poli, R. *Chem. Rev.* **1991**, *91*, 509; b) Evans, W. J. *Organometallics* **2016**, *35*, 3088.

[3] a) Jutzi, P.; Reumann, G. *J. Chem. Soc. Dalton Trans.* **2000**, *14*, 2237; b) Budzelaar, P. H.; Engelberts, J. J.; van Lenthe, J. H. *Organometallics* **2003**, *22*, 1562.

[4] a) Gridnev, I. D. *Coord. Chem. Rev.* **2008**, *252*, 1798; b) Veiros, L. F. *Organometallics* **2000**, *19*, 5549; c) O'Connor, J. M.; Casey, C. P. *Chem. Rev.* **1987**, *87*, 307.

[5] a) Quintana, L. M. A.; Johnson, S. I.; Corona, S. L.; Villatoro, W.; Goddard, W. A.; Takase, M. K.; VanderVelde, D. G.; Winkler, J. R.; Gray, H. B.; Blakemore, J. D. *PNAS* **2016**, *113*, 6409; b) Zamorano, A.; Rendón, N.; Valpuesta, J. E. V.; Álvarez, E.; Carmona, E. *Inorg. Chem.* **2015**, *54*, 6573; c) Pal, S.; Kusumoto, S.; Nozaki, K. *Organometallics* **2018**, *37*, 906; d) Moreno, J. J.; Espada, M. F.; Campos, J.; Lopez-Serrao, J.; Macgregor, S. A.; Carmona, E. *J. Am. Chem. Soc.* **2019**, *141*, 2205; e) Sapsford, J. S.; Gates, S. J.; Doyle, L. R.; Taylor, R. A.; Diez-Gonzalez, S.; Ashley, A. E. *Inorg. Chim. Acta.* **2019**, *488*, 201; f) Pitman, C. L.; Finster, O. N. L.; Miller, A. J. M. *Chem. Commun.* **2016**, *52*, 9105.

[6] Chalkley, M.; Del Castillo, T.; Matson, B.; Roddy, J.; Peters, J. C. *ACS Cent. Sci.* **2017**, *3*, 217; b) Chalkley, M. J.; Del Castillo, T. J.; Matson, B.; Peters, J. C. *J. Am. Chem. Soc.*

2018, *140*, 6122; c) Chalkley, M. J.; Oyala, P. H.; Peters, J. C. *J. Am. Chem. Soc.* **2019**, *141*, 4721-4729.

[7] a) Curphey, T. J.; Santer, J. O.; Rosenblum, M.; Richards, J. H. *J. Am. Chem. Soc.* **1960**, *82*, 5249−5250; b) Liles, D. C.; Shaver, A.; Singleton, E.; Wiege, M. B. *J. Organomet. Chem.* **1985**, *288*, c33−c36; c) Court, T. L.; Werner, H. *J. Organomet. Chem.* **1974**, *65*, 245−251; d) Koelle, U.; Khouzami, F. *Angew. Chem., Int. Ed. Engl.* **1980**, *19*, 640−641; e) Malischewski, M.; Seppelt, K.; Sutter, J.; Heinemann, F. W.; Birger, D.; Meyer, K. *Angew. Chem. Int. Ed.* **2017**, *56*, 13372.

[8] Hamon, P.; Hamon, J. R.; Lapinte, C. *J. Chem. Soc. Chem. Commun.* **1992**, 1602.

[9] Mays, M. J.; Prater, B. E. *Inorg. Synth.* **1974**, *15*, 21.

[10] Faller, J. W.; Crabtree, R. H.; Habib, A. *Organometallics* **1985**, *4*, 929.

[11] For related Fe(□^{5}-Cp)(P_2)H-derivatives, see: a) Hamon, P.; Toupet, L.; Hamon, J.R.; Lapinte, C. *Organometallics* **1992**, *11*, 1429; b) de la Jara Leal, A.; Tenorio, M. J.; Puerta, M. C.; Valerga, P. *Organometallics* **1995**, *14*, 3839.

[12] At greater scan rate (SR), reversibility increases.

[13] Connelly, N. G.; Geiger, W. E. *Chem. Rev.* **1996**, 96, 877-910.

[14] For example: a) Chiang, K. P.; Scarborough, C. C.; Horitani, M.; Lees, N. S.; Ding, K.; Dugan, T. R.; Brennessel, W. W.; Bill, E.; Hoffman, B. M.; Holland, P. L. *Angew. Chem., Int. Ed.* **2012**, *51*, 3658; b) Gu, N. X.; Oyala, P. H.; Peters, J. C. *J. Am. Chem. Soc.* **2018**, *140*, 6374.

[15] Monitoring the decay of [**3**]$^+$ at – 60 °C by UV/vis spectroscopy shows clean, first order kinetics (see ESI).

[16] Hermes, A. R.; Warren. T. H.; Girolami, G. S. *J. Chem. Soc. Dalton Trans.* **1995**, 301.

[17] Similar metrics are observed for other □^{6}-IndH (C_9H_8) complexes, see: a) Bercaw, J. E.; Hazari, N.; Labinger, J. A. *Organometallics* **2009**, 28, 5489; b) Fessenbecker, A.; Stephan, M.; Grimes, R. N.; Pritzkow, H.; Zenneck, U.; Siebert, W. *J. Am. Chem. Soc.* **1991**, *113*, 3061; c) Hung, M. Y.; Ng, M. S.; Zhou, Z.; Lau, C. P. *Organometallics* **2000**, *19*, 3692.

[18] Other side products were also identified including $Fe(depe)_2N_2^+$. This compound was analyzed by HYSCORE spectroscopy (see *ESI*), showing identical ^{14}N couplings to those determined by: Doyle, L. R.; Scott, D. J.; Hill, P. J.; Fraser, D. A. X.; Myers, W. K.; White, A. J. P.; Green, J. C.; Ashley, A. E. *Chem. Sci.* **2018**, *9*, 7362.

[19] See: a) Wayland, B. B.; Ba, S.; Sherry, A. E. *J. Am. Chem. Soc.* **1991**, *113*, 5305; b) Nocton, G.; Booth, C. H.; Maron, L.; Andersen, R. A. *Organometallics* **2013**, *32*, 1150; c) Halpern, J.; Pribanic, M. *Inorg. Chem.* **1970**, *9*, 2616.

[20] a) Zhang, F.; Jia, J.; Dong, S.; Wang, W.; Tung, C. -H. *Organometallics* **2016**, *35*, 1151; b) Zhang, F.; Xu, X.; Zhao, Y.; Jia, J.; Tung, C.- H. Wang, W. *Organometallics* **2017**, *36*, 1238.

[21] a) Ilic, S.; Kadel, U. P.; Basdogan, Y.; Keith, J. A.; Glusac, K. D. *J. Am. Chem. Soc.* **2018**, *140*, 4569; b) Ellis, W. W.; Raebiger, J. W.; Calvin, C. J.; Bruno, J. W.; DuBois, D. L. *J. Am. Chem. Soc.* **2004**, 126, 2738.

[22] Fong, H.; Peters, J. C. *Inorg. Chem.* **2015**, 54, 5124.

[23] a) Wiedner, E. S.; Chambers, M. B.; Pitman, C. L.; Bullock, R.M.; Miller, A. J. M.; Appel, A. M. *Chem. Rev.* **2016**, 116, 8655; b) Pearson, R. G. *Chem. Rev.* **1985**, *85*, 41.

[24] Warren, J. J.; Tronic, T. A.; Mayer, J. M. *Chem. Rev.* **2010**, *110*, 6961.

[25] Bordwell, F. G.; Bausch, M. J. *J. Am. Chem. Soc.* **1983**, *105*, 6188.

Chapter 5 : Generating potent C-H PCET donors: Ligand-induced Fe-to-ring proton migration from a Cp*Fe^{III}-H complex demonstrates a promising strategy

Reproduced in part with permission from:

Schild, D. J.; Drover, M. W; Oyala, P.; Peters,

Generating Potent C–H PCET Donors: Ligand-Induced Fe-to-Ring Proton Migration from a Cp*Fe^{III}–H Complex Demonstrates a Promising Strategy

J. C. *J. Am. Chem. Soc*., **2020**, 142, 44, 18963–18970.

5.1. Introduction

Proton-coupled electron transfer (PCET) reactions have emerged as powerful strategies for mediating sundry reductive transformations in organic synthesis, with clever new approaches being discovered to generate *in situ* highly reactive H-atom surrogates as intermediates.[1,2,3] Reactive fragments with weak element-hydrogen (*E*-*H*) bonds have thus been targeted to facilitate hydrogen atom delivery, revealing desirable substrate reductions that are fascinating in scope.[1,2,4] For example, dissolution of SmI_2 in H_2O/THF mixtures confers coordination-induced bond-weakening in the resulting $[Sm(H_2O)_n]^{2+}$ complex to provide weak and hence highly reactive O-H bonds ($BDFE_{O\text{-}H}$ ~ 26 kcal mol^{-1});[1h] such species can be employed towards substrate reductions such as ketones to alcohols and anthracene to dihydroanthracene,[5] and also towards catalytic N_2 fixation to NH_3 in the presence of a Mo catalyst.[6]

As an outgrowth of our own mechanistic studies of Fe-mediated N_2 fixation, we recently reported the rigorous characterization of a highly reactive [Cp*(*endo/exo*-η^4-Cp*H)Co]$^+$ (Cp* = $C_5Me_5^-$) species ($BDFE_{C\text{-}H}$ < 29 kcal mol^{-1} for the *exo*-analogue), generated *in situ via* ring protonation of decamethylcobaltocene, Cp^*_2Co.[7,8] Relatedly, we have examined an Fe(III) indenide hydride $[Fe^{III}(\eta^5\text{-Ind})(depe)H]^+$ (Ind = C_8H_7-, depe = 1,2-*bis*(diethylphosphino)ethane) and its low temperature isomerism to give a η^6-indene complex [Fe(η^6-IndH)(depe)]$^+$, ($BDFE_{X\text{-}H}$ = 50 kcal mol^{-1}; X = Fe or C).[9]

The highly reactive nature of these ring-protonated species has frustrated independent studies of their reactivity profiles towards exogenous substrates. We hence targeted a related system wherein a reactive ring-C-H PCET donor might be generated in solution, *via* association of a ligand to the metal to cause concomitant isomerization of a

metal-bound hydride to a Cp*-ring position. Such a strategy would, in principle, enable two unreactive partners to reside in solution, with a net PCET reaction being triggered by addition of a donor ligand L (see Chart 5.1).

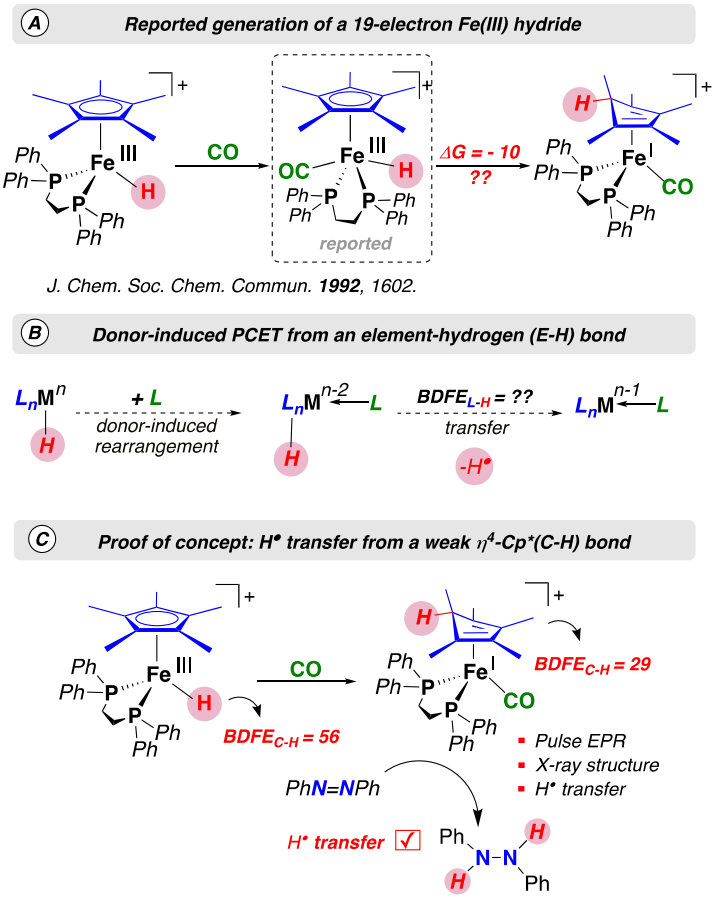

Chart 5.1. A) Reported generation of a 19-electron Fe^{III}-H[11]; B) Introducing the concept of donor-induced PCET and C) Tunable PCET. BDFE values (calculated by DFT) are in kcal mol^{-1}.

With this goal in mind, we turned to a known iron(III) hydride half-sandwich complex, $[Fe^{III}(\eta^5\text{-Cp*})(dppe)H]^+$ $[\mathbf{1}]^+$, (Cp* = $C_5Me_5^-$, dppe = 1,2-*bis*(diphenylphosphino)ethane), first prepared by Lapinte and co-workers in 1992.[10] Complex $[\mathbf{1}]^+$ was reported to undergo associative binding of CO to provide the 19-electron

hydride $[Fe^{III}(\eta^5\text{-Cp*})(dppe)(CO)H]^+$ ([**2**]$^+$), the latter having been characterized by X-band EPR spectroscopy. The reaction was deemed reversible with warming, returning [**1**]$^+$.[11]

Based on our findings with [Cp*(*endo*- η^4-Cp*H)Co]$^+$ and [Fe(η^6-IndH)(depe)]$^+$, we wondered whether [**2**]$^+$ would be best described as $[Fe^I(\eta^4\text{-Cp*H})(dppe)(CO)]^+$, which would occur *via* proton migration to the ring upon CO binding. Herein, we use a range of methods, including crystallography and various EPR techniques, with corresponding DFT analysis, to establish that this is indeed the case. We then demonstrate that an intermolecular PCET reaction is possible, with azobenzene as a model substrate, *via* this ligand-induced trigger.

5.2. Results and Discussion

We began our study with (re)examining the solution spectroscopy of $[Fe^{III}(\eta^5\text{-Cp*})(dppe)H]^+$ [**1**]$^+$ in the presence of CO. Addition of CO to the ^{1}H and ^{2}H isotopologues (Fe-H/D) of [**1**]$^+$ results in a change in the EPR spectrum, indicating the formation of a single S = ½ species exhibiting rhombic symmetry (g = [2.085, 2.039, 2.004]), parameters that are similar to those previously reported by Lapinte (g = [2.0777, 2.0367, 2.0019], $A(^{31}P)$ = ± [48, 50, 50] MHz, and $A(^1H)$ = ± [14, 17, 34] MHz ($a_{iso}(^1H)$= ± 22 MHz)).[11] Based on preliminary DFT calculations (*vide infra*) and the similarity of the proton hyperfine coupling to ring protonated cobaltocenes,[4] we posited its structure to be $[Fe^I$(*endo*- η^4-Cp*H/D)(dppe)(CO)]$^+$ (*endo*-isomer confirmed by XRD *vide infra*), *endo*-[**3-H/D**]$^+$, rather than the terminal hydride [**2**]$^+$ (Scheme 5.1).

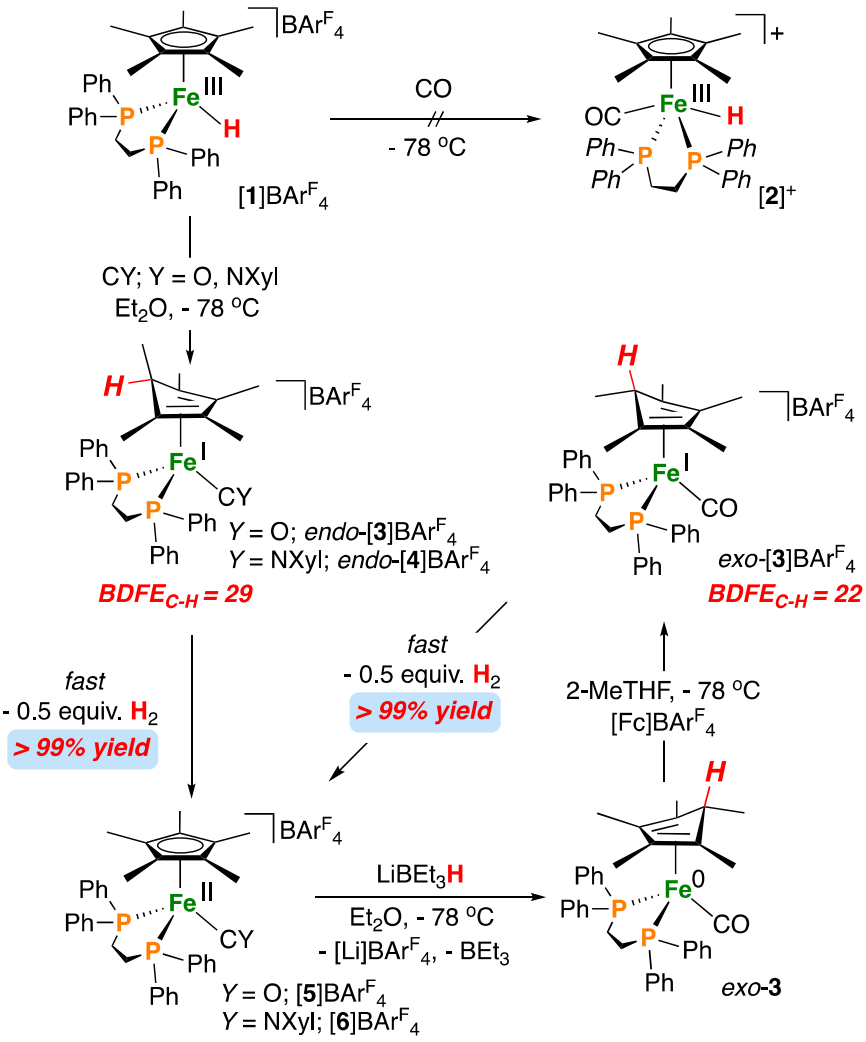

Scheme 5.1. Reported preparation of a 19-electron Fe(III)-H complex[11] and synthesis of *endo*-[**3**]$^+$/[**4**]$^+$ by addition of CO or CNXyl with accompanying H_2 release to give [**5**]$^+$ and [**6**]$^+$. BDFE values (calculated by DFT) are in kcal mol^{-1}.

Consumption of [**1**]$^+$ is easily identified by EPR spectroscopy based on the significant shift in the value of g_{max} (Figure 5.1). Besides coupling to two distinct ^{31}P (I = 1/2) nuclei with similar magnitude, significant additional coupling to ^{1}H is evident when the ^{1}H and ^{2}H isotopologues are compared, consistent with the presence of a relatively strongly coupled ^{1}H nucleus (Figure 5.2). Collection of a series of X-band Davies ENDOR

spectra acquired across the EPR envelope of *endo*-[**3-D**]$^+$ (see the Supporting Information) provides additional data consistent with large couplings to two non-equivalent phosphines ($A(^{31}P_1)$ = ± [72, 59, 58] MHz and $A(^{31}P_2)$ = ± [49, 42, 51] MHz).

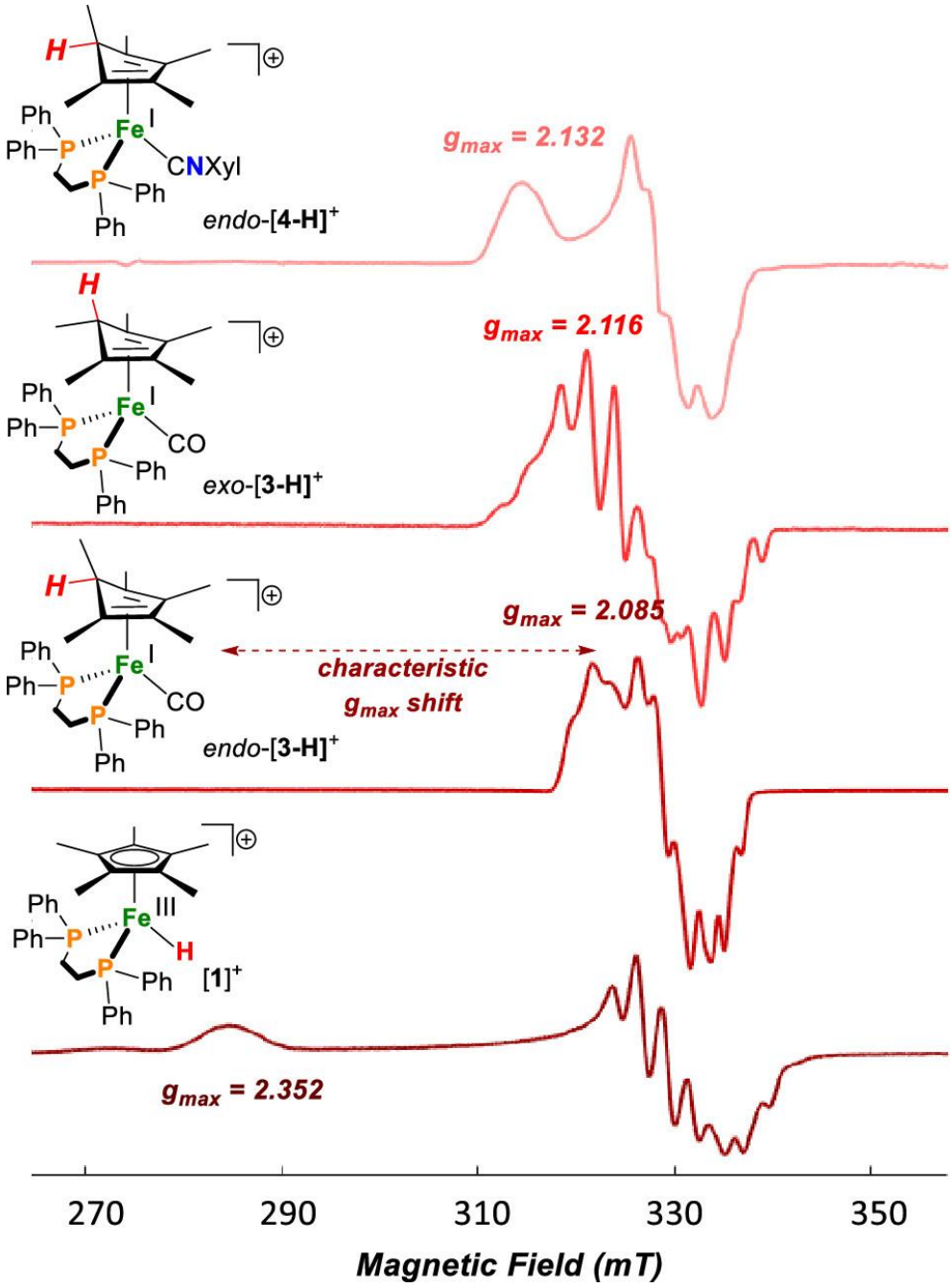

Figure 5.1. X-Band CW-EPR spectra of [1]$^+$, *endo*-[3-H]$^+$, *exo*-[3-H]$^+$, and *endo*-[4-H]$^+$ in 2-MeTHF at 77 K.

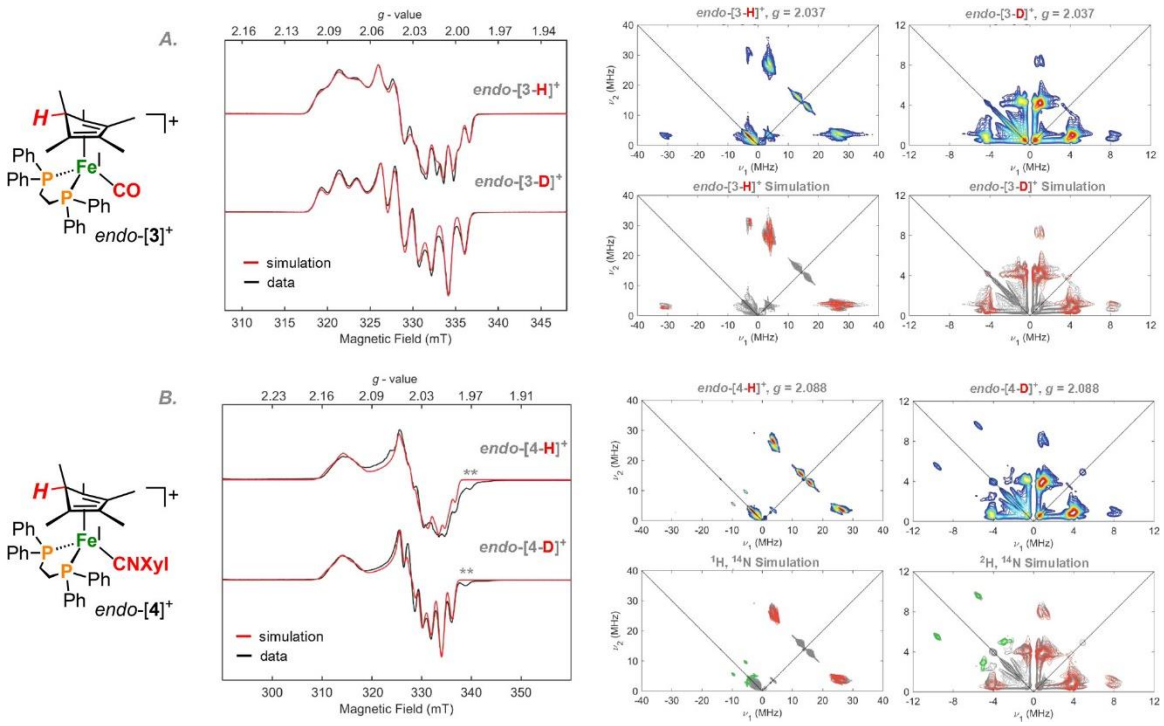

Figure 5.2. X-Band CW-EPR spectra and corresponding X-band HYSCORE spectra of freeze-quenched samples in 2-MeTHF. A) *endo*-[**3-H**]BAr^F_4 and *endo*-[**3-D**]BAr^F_4; B) *endo*-[**4-H**]BAr^F_4 and *endo*-[**4-D**]BAr^F_4. HYSCORE simulations of features from ^{1}H, ^{2}H (red), and ^{14}N (green, CNXyl only) hyperfine couplings are overlaid over the data, which is plotted in grey. ** = traces of [**1**]$^+$.

X-band HYSCORE spectroscopy of the ^{1}H and ^{2}H isotopologues was used to determine the hyperfine parameters for the hydride-derived hydrogen nucleus (Figure 5.2). Simulation of field-dependent HYSCORE spectra of *endo*-[**3-H**]$^+$ reveals a relatively isotropic proton hyperfine tensor, $A(^1H) = \pm$ [24, 20, 34.5] MHz ($a_{iso}(^1H) = \pm$ 26.2 MHz), with a small Euler rotation of the hyperfine tensor relative to the g-tensor of (α,β,γ) = (0, 30, 0)◦. HYSCORE spectra of *endo*-[**3-D**]$^+$ exhibit intense features arising from deuterium which are well simulated by scaling the ^{1}H hyperfine tensor determined from ^{1}H HYSCORE by the proportion of ^{1}H/^{2}H gyromagnetic ratios (γ^1H/γ^2H = 6.514), with $A(^2H)$

= ± [3.7, 3.1, 5.3] MHz. These parameters provide excellent agreement with simulations of the X-band CW-EPR spectra of these two isotopologues.

In contrast to terminal metal-hydrides,[12] the anisotropic component (T) of the ^{1}H hyperfine of *endo*-[**3**]$^{+}$, $T(^{1}H)$= ± [-2.2, -6.2, 8.3] MHz), is considerably smaller, indicating greater distance between the nucleus and Fe-centered spin density. Similarly, low anisotropy is also observed for the *endo*-Cp*(H) protonation product of Cp*$_2$Co. The low anisotropy suggests ring-protonation (*endo*-[**3**]$^{+}$), and not a terminal hydride (i.e., [**2**]$^{+}$) species. Hyperfine coupling constants and the predicted anisotropy as calculated by DFT further support the assignment and are independent of the method used (see see the Supporting Information).

We also explored the addition of an isocyanide donor, CNXyl (Xyl = 2,6-dimethylphenyl). Treatment of [**1**]$^{+}$ with CNXyl at − 78 ˚C provides [Fe^{I}(*endo*-$\square^{4}$-Cp*H)(dppe)(CNXyl)]$^{+}$ (*endo*-[**4**]$^{+}$) as evidenced by CW X-band EPR spectroscopy at 77 K; g = [2.132, 2.042, 2.004], $A(^{31}P_1)$ = ± [75, 35, 54] MHz, and $A(^{31}P\square)$ = ± [76, 64, 64] MHz. Simulations of HYSCORE spectra of *endo*-[**4-H/D**]$^{+}$ give $A(^{1}H)$ = ± [17, 22, 32.5] MHz, $a_{iso}(^{1}H)$ = ± 23.8 MHz, and $T(^{1}H)$ = ± [-6.8, -1.8, 8.7], which are nearly identical to those discussed above for the *endo*-Cp*(C-H) Fe(CO) adduct *endo*-[**3**]$^{+}$. Additional features present in the (-,+) quadrant of HYSCORE of both *endo*-[**4-H**]$^{+}$ and *endo*-[**4-D**]$^{+}$ can be assigned to hyperfine coupling to ^{14}N in the CNXyl ligand, with $A(^{14}N)$ = [7.4, 7.4, 9] MHz, a relatively small ^{14}N nuclear quadrupole coupling constant $e^2qQ/h(^{14}N)$ = 1.0 MHz, and a negligible electric field gradient rhombicity $\eta(^{14}N) \approx 0$, as expected for a triply bonded CN moiety with axial symmetry.[13]

The more stable, neutral *endo*/*exo*-species (*endo*/*exo*-**3**) were also prepared. Treatment of [Fe^{II}(η^5-Cp*)(dppe)(CO)][BAr^F_4] ([**5**]BAr^F_4) with $LiBEt_3H$ provides *exo*-[Fe^0(η^4-Cp*H)(dppe)(CO)] (*exo*-**3**) in good yield (Scheme 5.1). The alternative isomer, *endo*-**3**, was prepared *via* reduction of *endo*-[**3**]$^+$ with Cp_2Co at -78 ^oC.[11] The room temperature stability allowed for isolation and growth of crystalline material suitable for single crystal X-ray diffraction. The structures of *exo*/*endo*-**3** are presented in Figure 5.3. *Exo*- and *endo*-**3** feature an η^4-diene unit bound to a zerovalent iron center. Notably, the C(1)-C(6) bond distance in *endo*-**3** (1.538(3) Å) is slightly longer than that in *exo*-**3** (1.514(2) Å), possibly suggestive of Fe → C-C (σ*) donation in the former. Such an interaction is predicted based on the singularly occupied molecular orbitals (SOMOs) of *endo*/*exo*-[**3**]$^+$ (Figure 5.4). Two distinct C-H stretches are observed for *exo*-**3-H** at 2711 and 2612 cm^{-1} that shift to 2009 and 1955 cm^{-1} for *exo*-**3-D**; C-H stretches for *endo*-**3-H** are not discernable from the bulk C-H stretching region *i.e.,* > 2711 cm^{-1} (see the Supporting Information).[14] Similar observations have been made for the pairs [Cp*(*exo*-η^4-Cp*H)Co^{II}]/[Cp*(*exo*- η^4-Cp*D)Co^{II}][8] and [Cp(η^4-C_5H_6)Co]/[Cp(*exo*-η^4-C_5H_5D)Co].[15]

Despite its exceptionally weak C-H bond, the assignment of *endo*-[**3**]$^+$ could be corroborated by X-ray crystallography (Figure 5.3) *via* growth of suitable crystals at low temperature. Gratifyingly, the solid-state structure, which was unobtainable for [Cp*(*endo*-η^4-Cp*H)Co]$^+$, confirms the formation of an *endo*-Cp*(C-H) bond, with metrics associated with a dearomatized five-membered Cp*H ring that differs from that of a Cp* anion with elongation along the C(1)-C(5) and C(1)-C(2) vectors [1.51(1)/1.53(1) Å] from *ca.* 1.42 Å (average C-C bond distances in [**7**]$^+$, *vide infra*), signifying new C-C single bonds. The low

temperature stability of *endo*-[**3**]$^+$ likely derives from a high degree of steric shrouding of the reactive ring-bound H-atom *via* phenyl rings from the dppe ligand.

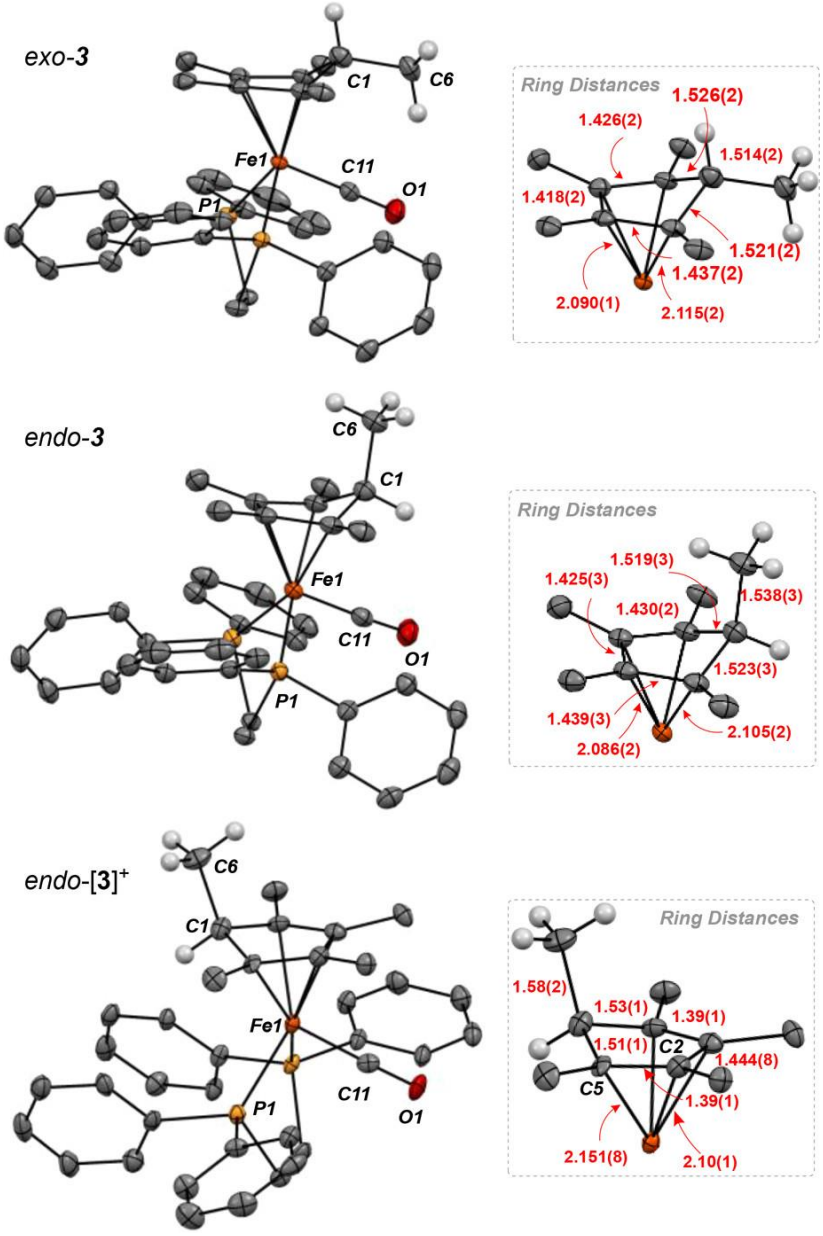

Figure 5.3. Solid-state structure of *exo*-**3**, *endo*-**3**, and *endo*-[**3**]$^+$ with ellipsoids shown at 50% probability. Counteranion omitted for *endo*-[**3**]$^+$.

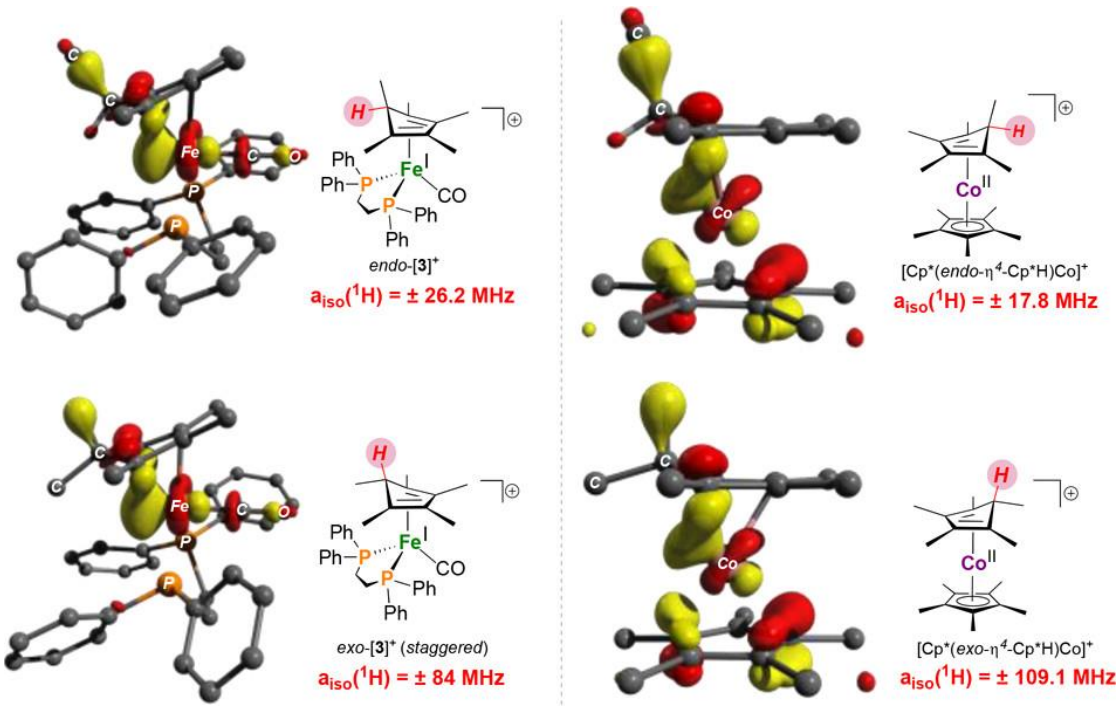

Figure 5.4. Frontier molecular orbitals (SOMOs) of *endo*/*exo*-[**3**]$^{+}$ (staggered conformers) and [Cp*(*endo*/*exo*-η^4-Cp*H)Co^{II}]$^{+}$ [7,8] optimized using TPSS; def2tzvp (Fe), def2svp (all other atoms). Inset shows a_{iso}(^{1}H) as obtained by ^{1,2}H HYSCORE and/or ENDOR.

Next, we sought to generate the alternative, and presumably more reactive, *exo*-isomer wherein steric shrouding by dppe is far less prominent. Oxidation of neutral *exo*-**3** with [Fc]BAr$^{F}_{4}$ at – 78 ^{o}C provides green solutions of reactive *exo*-[**3**]$^{+}$ that can be analyzed by EPR spectroscopy. From the CW data, we assign two conformational isomers of *exo*-[**3**]$^{+}$ (**A** and **B**), that presumably differ by rotation of the Cp*H ligand. both with rhombic symmetry (Figure 5.5): **A** with g = [2.116, 2.073, 1.997] and another, **B** with g = [2.093, 2.045, 2.013] The potential presence of multiple conformers is supported by DFT, as four distinct minima are found within 2 kcal mol^{-1} upon Cp*H rotation. The exact nature of the conformers present in solution could not be determined, due to the small differences in energies and predicted ^{1}H hyperfine tensors (see the Supporting Information). Least-

squares optimization of simulations of the X-band CW spectra converged at relative populations of 0.6:0.4 for conformers **A**:**B**, indicating that the two conformations are indeed of similar relative energies. Simulations of ^{2}H-^{1}H difference ENDOR spectra of this mixture of *exo*-[**3**]$^{+}$ products provided constraints on the ^{2}H (and by proxy ^{1}H) hyperfine couplings, with higher frequency ENDOR providing the same for ^{31}P hyperfine couplings for the two conformers in the above CW simulations, with $A(^{1}H)$ = ± [85, 84, 83] MHz, $a_{iso}(^{1}H)$ = ± 84 MHz, $T(^{1}H)$ = ± [1, 0, -1], $A(^{31}P_1)$ = ± [96, 88, 47] MHz, and $A(^{31}P_2)$ = ± [78, 75, 63] MHz for conformer **A** and $A(^{1}H)$ = ± [76, 74, 70] MHz, $a_{iso}(^{1}H)$ = ± 73 MHz, $T(^{1}H)$ = ± [3, 1, -3], $A(^{31}P_1)$ = ± [46, 44, 15] MHz, and $A(^{31}P_{\square})$ = ± [70, 64, 64] MHz for conformer **B**. The $a_{iso}(^{1}H)$ values for these isomers are much larger than that observed for the *endo* adduct, *endo*-[**3**]$^{+}$ ($a_{iso}(^{1}H)$ = ± 26.2 MHz), while the magnitude of $T(^{1}H)$ tensors are similar to that observed for *endo*-[**3**]$^{+}$ and are consistent with a ligand C-H, rather than M-H unit. This trend, $a_{iso}(^{1}H)$ (exo) > $a_{iso}(^{1}H)$ (endo) is also been observed for the protonated [Cp*(*endo*/*exo*-$\square^{4}$-Cp*H)Co^{II}]$^{+}$ derivative (Figure 5.4) and correlates with greater predicted spin density on the *exo* (versus the *endo*) hydrogen atom for the staggered[16] isomers (0.06 versus 0.02 e^{-}).

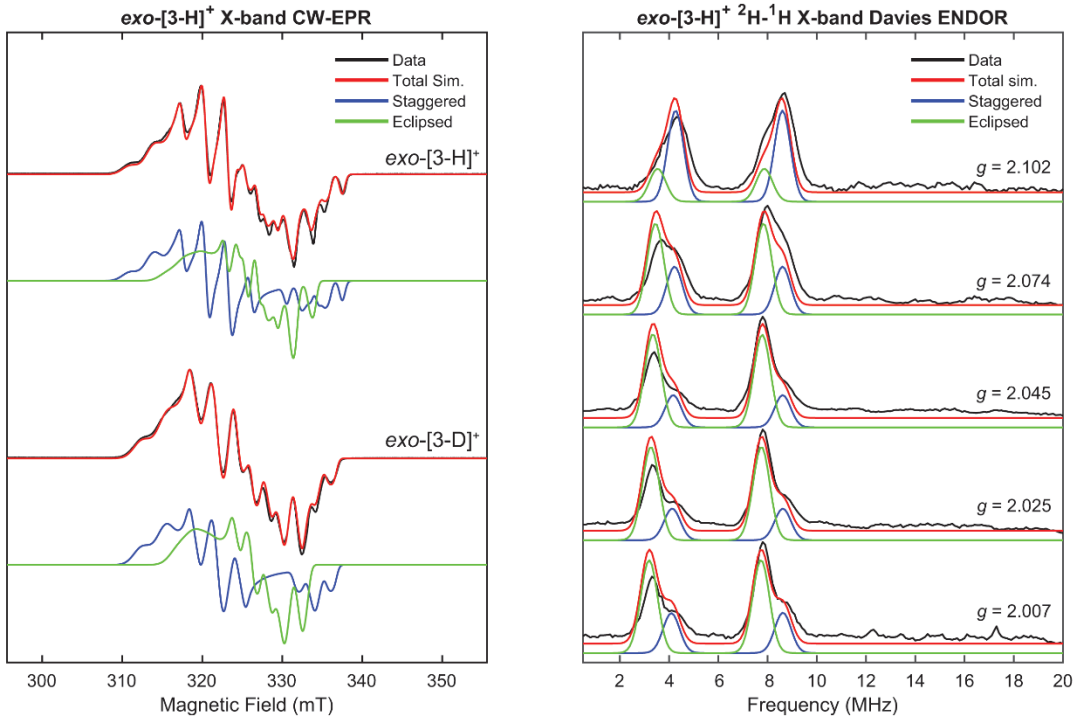

Figure 5.5. Left) X-Band CW-EPR spectra of freeze-quenched samples of *exo*-[3-H/D]$^{+}$ in 2-MeTHF at 77 K for with simulations of conformers A and B. Right) X-band ^{2}H-^{1}H Difference Davies ENDOR of *exo*-[3-H]$^{+}$ with data (black), total ^{2}H simulation (red), conformer A (blue) ,and conformer B (green).

Annealing frozen solutions of the 17-electron η^4-Cp*H complexes *endo*-[**3**]$^{+}$, *exo*-[**3**]$^{+}$, or *endo*-[**4**]$^{+}$ (Scheme 5.1) provides *ca.* 0.5 equiv H_2 and their corresponding 18-electron S = 0 stable adducts, [Fe^{II}(η^5-Cp*)(dppe)(CY)][BAr$^{F}_4$] ([**5**]BAr$^{F}_4$ (Y = O), [**6**]BAr$^{F}_4$ (Y = NXyl)). The Fe^{II}-CO adduct [**5**]$^{+}$ has been described previously;[17] full characterization data for [**6**]BAr$^{F}_4$ is in the Supporting Information. By contrast to *endo*-[**3**]$^{+}$, which can be isolated and characterized at temperatures below −70 ^{o}C, H_2 evolution and formation of [**5**]$^{+}$ from *exo*-[**3**]$^{+}$ is observed at temperatures as low as −100 $^{\circ}$C. As

previously noted, the difference in stability between *endo*-[**3**]$^+$ and *exo*-[**3**]$^+$ is likely due to a dramatic difference in steric hindrance between the *endo*- and *exo*-H positions.

To gauge the relative energies of the species discussed herein, we turned to DFT calculations to estimate relevant BDFEs (Scheme 5.2). The starting hydride complex [**1**]$^+$ was calculated to have a $BDFE_{Fe\text{-}H}$ of 56 kcal mol^{-1}, providing the vacant S = 1 cation, [Fe(η^5-Cp*)(dppe)]$^+$ (**III**).

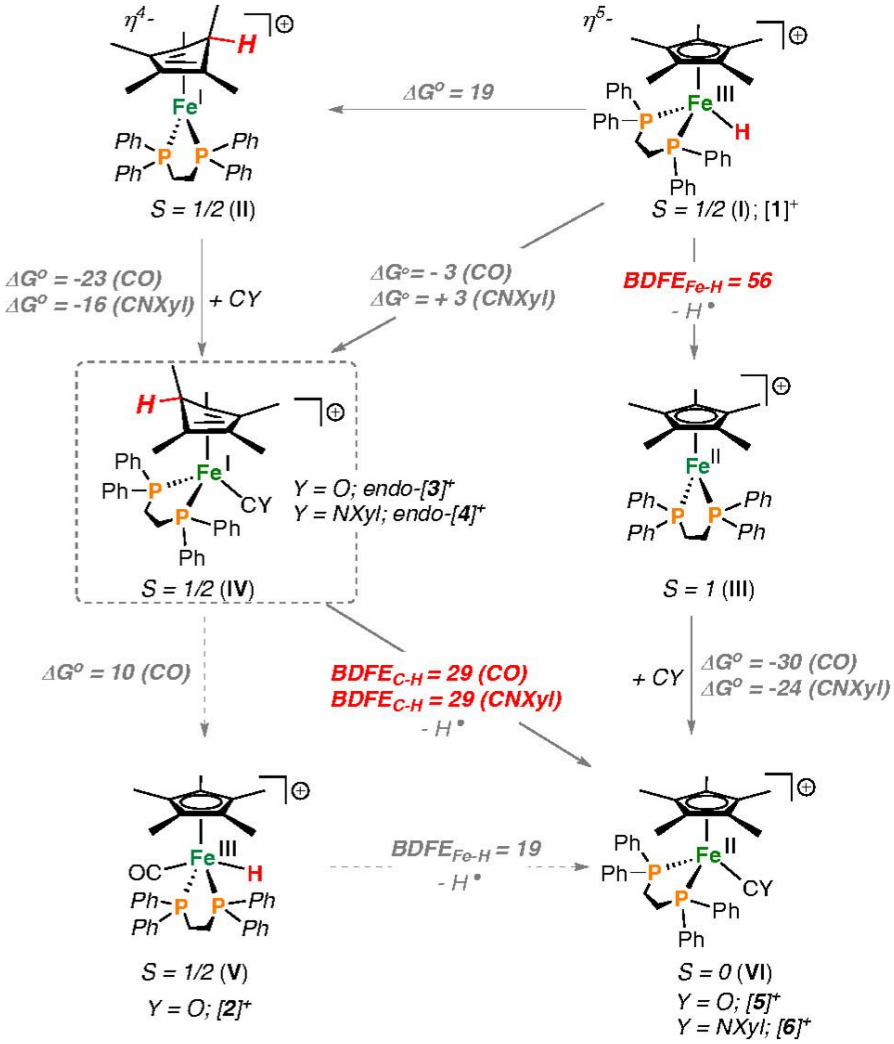

Scheme 5.2. Free energy change (kcal mol^{-1}) for PCET involving *endo*-[**3**]$^+$/[**4**]$^+$ (TPSS; def2tzvp (Fe), def2svp (all other atoms)).

Associative binding of an L-type donor (prior to H$^{\bullet}$ loss) was then considered. In this way, the CO (*endo*-[**3**]$^{+}$) and CNXyl (*endo*-[**4**]$^{+}$) adducts, **IV** were calculated to be - 3 and + 3 kcal mol^{-1} in energy relative to [**1**]$^{+}$. The process involves adduct formation and then reductive C-H elimination (or *vice-versa*). H_2 formation from **IV** to give complexes **VI** ([**5**]$^{+}$ and [**6**]$^{+}$) is calculated to be highly favorable (CO and CNXyl: $BDFE_{C\text{-}H}$ = 29 kcal mol^{-1} *vs.* $BDFE_{H\text{-}H}$ = 102.3 kcal mol^{-1} in CH_3CN)[1], correlating with a decrease in $BDFE_{X\text{-}H}$ of almost 30 kcal mol^{-1} (*c.f.* 56 kcal mol^{-1} for [**1**]$^{+}$). The $BDFE_{C\text{-}H}$ of *exo*-[**3**]$^{+}$ is calculated to be weaker (25 kcal mol^{-1}), which in combination with the reduced steric crowding, manifests experimentally *via* facile H_2 evolution at temperatures for which *endo*-[**3**]$^{+}$ is stable enough to isolate.

To experimentally benchmark the H$^{\bullet}$ transfer propensity of [**1**]$^{+}$, we aimed to determine an upper limit for its $BDFE_{Fe\text{-}H}$. Given the reduced Fe^{II}-H congener undergoes hydride transfer to 1-benzyl-3-acetamidopyridinium [BNAP]OTf ($\Delta G_{H^-} \approx$ 59 kcal mol^{-1})[18] and its known Fe^{II}/Fe^{III} oxidation potential ($E_{1/2}$ = - 0.71 V vs. Fc/Fc^{+}),[19] the Fe^{III}–H bond of [**1**]$^{+}$ is estimated to have an upper bound of $BDFE_{Fe\text{-}H}$ < 50 kcal mol^{-1};[20] this can be compared with a DFT-predicted value of 56 kcal mol^{-1}. In spite of its weak $BDFE_{Fe\text{-}H}$, complex [**1**]$^{+}$ is stable at room temperature in ethereal solvents (THF, Et_2O; <5 % yield of H_2 and [Fe(η^5-Cp*)(dppe)(N_2)]$^{+}$ [**7**]$^{+}$ at + 80 $^{\circ}$C, 1 week; Scheme 5.3); details pertaining to the characterization of [**7**]$^{+}$ are presented in the Supporting Information. Although [**7**]$^{+}$ is thermodynamically poised to release H_2, presumably a substantial kinetic barrier attenuates the rate of H_2 loss ($BDFE_{H\text{-}H}$ = 102.3 kcal mol^{-1}).

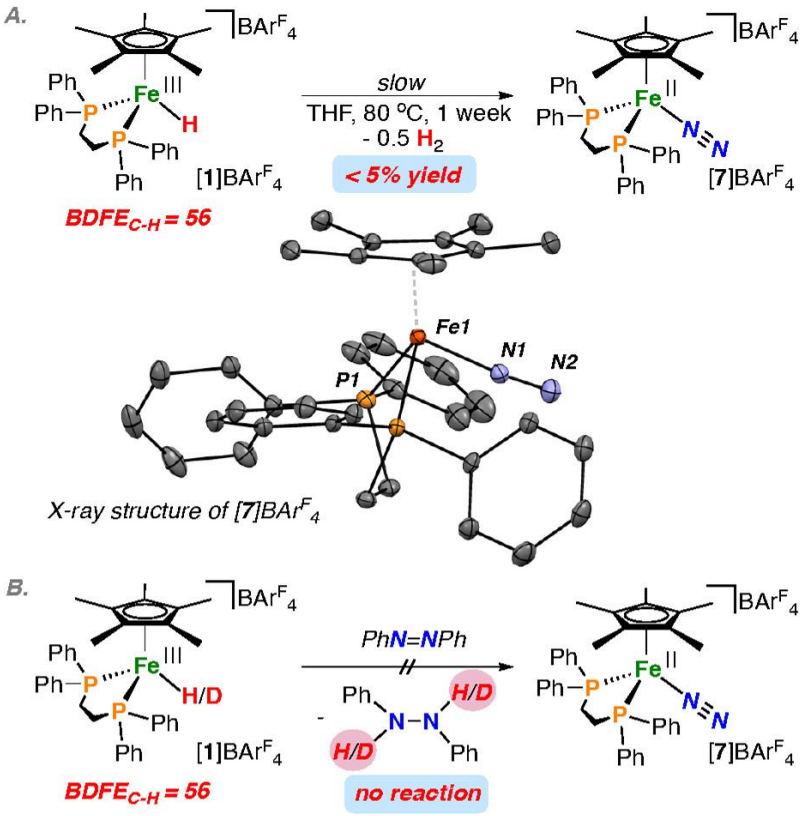

Scheme 5.3. A) Synthesis of [**7**]$^+$ by H_2 evolution (< 5%). Inset shows solid-state structure of [**7**]$^+$ with ellipsoids shown at 50% probability; B) Non-productive H$^\bullet$ transfer to azobenzene using [**1**]$^+$. BDFE values (kcal mol^{-1}) calculated by DFT using TPSS; def2tzvp (Fe), def2svp (all other atoms).

Subsequently, we aimed to determine an upper limit for the BDFE$_{C-H}$ of *endo*-[**3**]$^+$ (Scheme 5.4). Reaction of an MeCN solution of *endo*-**3** with CO_2 results in hydride transfer and formation of [Fe(η^5-Cp*)(dppe)(CO)]$^+$ [**5**]$^+$. The hydricity of *endo*-**3** in MeCN must therefore be less than the hydricity of HCO_2^- ($\Delta G_{H-} \approx 43$ kcal mol^{-1}). In other words, *endo*-**3** is more hydridic that HCO_2^-.[21] Utilizing thermodynamic relationships that relate H$^\bullet$ and H$^-$ transfer in MeCN,[22] the upper bound for the free energy of H$^-$ transfer from *endo*-**3** and H$^\bullet$ transfer from *endo*-[**3**]$^+$ can then be related. The *endo*-Cp*(C-H) bond of *endo*-[**3**]$^+$ (Fe$^{0/I}$, $E_{1/2}$ = - 0.81 V vs. Fc/Fc$^+$) is thus conservatively estimated to have an upper bound

BDFE ($\Delta G([\mathbf{3}]^{+})_{H\bullet}$) of < 36 kcal mol^{-1} (DFT prediction: 29 kcal mol^{-1}), generating [**5**]$^{+}$ and H$^{\bullet}$ as products. On the basis of thermodynamics alone, H_2 elimination from *endo*-[**3**]$^{+}$ should be facile. The experimentally determined upper bound for the hydricity results in a *p*Ka of 23 in acetonitrile as upper bound for *endo*-[**3**]$^{+}$ (summarizing square scheme presented in the Supporting Information).

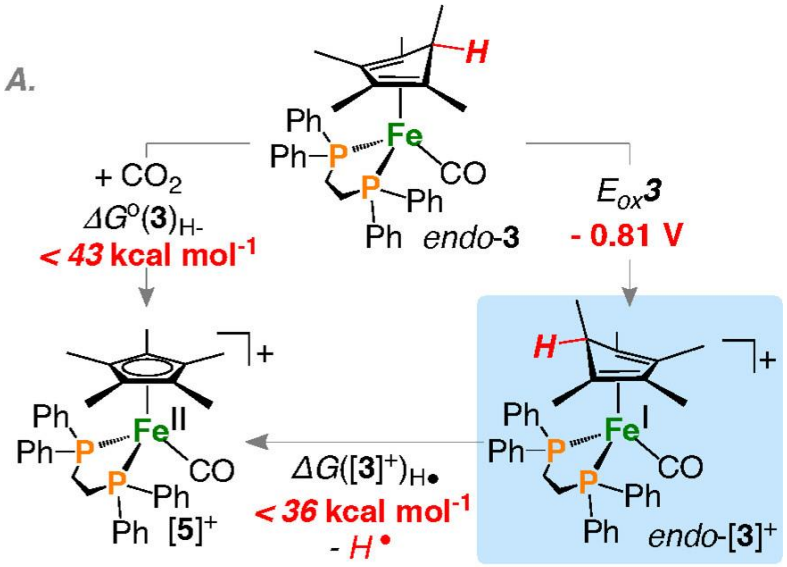

B.

$$H^{-} \longrightarrow H^{\bullet} + e^{-} \quad \Delta G = -26.0 \text{ kcal mol}^{-1} \qquad (1)$$

$$\Delta G(\mathbf{3})_{H^-} = \Delta G([\mathbf{3}]^{+})_{H\bullet} + 23.06(E_{ox}(\mathbf{3})) + 26.0 \qquad (2)$$

$$\Delta G([\mathbf{3}]^{+})_{H\bullet} = \Delta G(\mathbf{3})_{H^-} - 23.06(E_{ox}(\mathbf{3})) - 26.0 \qquad (3)$$

Scheme 5.4. A) Experimental determination of $BDFE_{C\text{-}H}$ for *endo*-[**3**]$^{+}$; B) Relevant thermodynamic equations relating H^{-} and H$^{\bullet}$ transfer for the *endo*-variant only.

In line with the predicted lower BDFE of *exo*-[**3**]$^{+}$, the $Fe^{0/I}$ redox potential is more positive ($E_{1/2}$ = - 0.70 V vs. Fc/Fc^{+}) with respect to *endo*-[**3**]+. The 110 mV difference between the *endo* and *exo* isomers corresponds to a 2.5 kcal mol^{-1} difference in BDFE,

suggesting that an additional difference in the BDFE is due to the different acidities of the isomers.

We next turned our focus to exploring whether a productive H• transfer to an exogenous substrate from either *endo*-[**3**]$^+$ or *exo*-[**3**]$^+$ could be accomplished, as opposed to undesired H_2 evolution. Azobenzene proved an interesting choice of substrate for this purpose as its conversion to diphenylhydrazine and *vice versa* has been studied over the years with various PCET donors and acceptors,[23] with some donors in a similar BDFE range.[3]

Complex [**1**]$^+$ does not react with a 20-fold excess of azobenzene (PhN=NPh) over a period of days (for an average $BDFE_{N\text{-}H}$ = 65 kcal mol^{-1} over two transfers), but upon addition of CO, which generates *endo*-[**3**]$^+$ *in-situ* at −78 °C, a reaction is triggered to generate 1,2-diphenylhydrazine (25% yield, Scheme 5.5), H_2 and [**5**]$^+$. Isotopic labeling studies using the deuterated analogue, *endo*-[**3**-**D**]$^+$, results in formation of the labeled isotopologue, PhDN-NDPh. *In situ* generation of *exo*-[**3**]$^+$ through oxidation of *exo*-**3** and reaction with PhN=NPh produces 1,2-diphenylhydrazine in 78% yield (Scheme 5.5). In line with *endo*-[**3**]$^+$**,** only H_2 and [**5**]$^+$ are observed as byproducts and labeling with deuterium results in the formation of PhDN-NDPh. No other organic or iron containing products can be detected by NMR spectroscopy. A proton transfer followed by electron transfer or *vice versa* is unlikely as *endo* and *exo*-[**3**]$^+$ are weak acids (*vide supra*), and the protonation step is calculated to be 27 kcal mol^{-1} uphill. Furthermore, *endo* and *exo*-[**3**]$^+$ are weak reductants ($E_{1/2}$ > −0.81 V vs Fc/Fc$^+$)[24] and not capable of reducing azobenzene to the radical anion ($E_{1/2}$ −1.73 V vs Fc/Fc$^+$).[25] Worth emphasizing is that the increase in reaction rate upon addition of CO to [**1**]$^+$ is orders of magnitude, as no H_2 formation or reduction of azobenzene is observed at room temperature in the absence of

added CO, while instantaneous formation of [**5**]$^+$, the terminal product of H• transfer, can be observed even at −78 °C . This remarkable difference in reactivity *via* addition of a simple L-type ligand highlights the potential for *in situ* generation of a powerful PCET reagent.

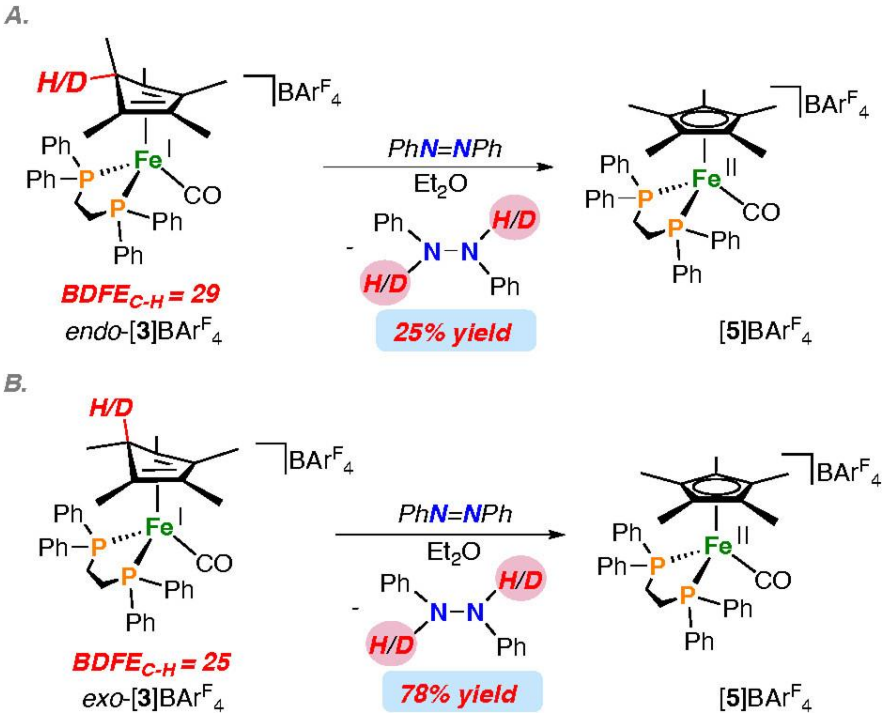

Scheme 5.5. Transfers to azobenzene using A) *endo*-[**3**]$^+$ gives 25% PhNHNHPh and B) *exo*-[**3**]$^+$ gives 78% PhNHNHPh. BDFE values (kcal mol^{-1}) calculated by DFT using TPSS; def2tzvp (Fe), def2svp (all other atoms).

5.3 Conclusions

In closing, building on recent work describing protonated metallocene and related species with very weak and hence reactive C-H bonds, we have herein described the characterization of *endo*-[Fe^I(η^4-Cp*H)(dppe)(L)]$^+$ (L = CO, CNXyl) and *exo*-[Fe^I(η^4-Cp*H)(dppe)(L)]$^+$ (L = CO). Notably, one of these systems, *endo*-[Fe^I(η^4-Cp*H)(dppe)(CO)] was previously studied, but had been instead assigned as the 19-

electron hydride species $[Fe^{III}(\eta^5\text{-Cp*})(dppe)(CO)(H)]^+$. Use of pulse EPR techniques (^{1,2}H HYSCORE, ENDOR) as well as the solid-state crystal structure of *endo*-$[Fe^{I}(\eta^4\text{-Cp*H})(dppe)(CO)]^+$, obtained at low temperature, cements this reassignment.

Our interest in these particular *endo*-$[Fe^{I}(\eta^4\text{-Cp*H})(dppe)(L)]^+$ systems is that they can be generated *in situ via* L addition to a far more stable iron hydride precursor, $[Fe^{III}(\eta^5\text{-Cp*})(dppe)H]^+$. This affords the opportunity to transfer $H^\bullet$ to a substrate, demonstrated for L = CO using the reduction of azobenzene to diphenylhydrazine as a model, where the $H^\bullet$ transfer reaction is triggered at low temperature *via* the addition of CO to a mixture of $[Fe^{III}(\eta^5\text{-Cp*})(dppe)H]^+$ and PhN=NPh. The latter two partners do not otherwise react under the same conditions; CO triggers the isomerization that leads to the weak and hence reactive C-H bond. This approach demonstrates an attractive strategy for designing a powerful, in situ generated PCET reagent ($BDFE_{C\text{-}H} \approx 29$ kcal mol^{-1} for *endo*-$[Fe^{I}(\eta^4\text{-Cp*H})(dppe)(CO)]^+$), with tunability of the *BDFE via* the choice of L donor.

5.4. References

[1] a) Warren, J. J.; Tronic, T. A.; Mayer, J. M. Thermochemistry of Proton-Coupled Electron Transfer Reagents and its Implications. *Chem. Rev.* **2010**, *110*, 6961; b) Weinberg, D. R.; Gagliardi, C. J.; Hull, J. F.; Murphy, C. F.; Kent, C. A.; Westlake, B. C.; Paul, A.; Ess, D. H.; McCafferty, D. G.; Meyer, T. J. Proton-Coupled Electron Transfer. *Chem. Rev.* **2012**, *112*, 4016; c) Hammes-Schiffer, S. Theory of Proton-Coupled Electron Transfer in Energy Conversion Processes. *Acc. Chem. Res.* **2009**, *42*, 1881; d) Gentry, E. C.; Knowles, R. R. Synthetic Applications of Proton-Coupled Electron Transfer. *Acc. Chem. Res.* **2016**, *49*, 1546. e) Matos, J. L. M.; Green, S. A.; Shenvi, R. A. Markovnikov Functionalization by Hydrogen Atom Transfer. *Organic Reactions* **2019**, *100*, 383 f) Tsui, E.; Metrano, A. J.; Tsuchiya Y.; Knowles, R. R. Catalytic Hydroetherification of Unactivated Alkenes Enabled by Proton-Coupled Electron Transfer *Angew. Chem., Int. Ed.* **2020**, *59*, 11845; g) Roos, C. B.; Demaerel, J.; Graff D. E.; Knowles, R. R. Enantioselective Hydroamination of Alkenes with Sulfonamides Enabled by Proton-Coupled Electron Transfer. *J. Am. Chem. Soc.* **2020**, *142*, 5974; h) Kolmar, S. S.; Mayer, J. M. $SmI_2(H_2O)_n$ Reduction of Electron Rich Enamines by Proton-Coupled Electron Transfer. *J. Am. Chem. Soc.* **2017**, *139*, 10687.

[2] Crossley, S. W. M.; Obradors, C.; Martinez, R. M.; Shenvi, R. A. Mn-, Fe-, and Co-Catalyzed Radical Hydrofunctionalizations of Olefins. *Chem. Rev.*, **2016**, *116*, 8912.

[3] Bezdek, M. J.; Guo, S.; Chirik, P. J. Coordination-induced weakening of ammonia, water, and hydrazine X–H bonds in a molybdenum complex. *Science* **2016**, *354*, 730.

[4] Chalkley, M.J.; Garrido-Barros, P.; Peters, J. C.; A molecular mediator for reductive concerted proton-electron transfers via electrocatalysis, *Science* **2020**, 369, 850.

[5] a) Chciuk, T. V.; Anderson, W. R.; Flowers, R. A. II. High-Affinity Proton Donors Promote Proton-Coupled Electron Transfer by Samarium Diiodide. *Angew. Chem. Int. Ed.* **2016**, *55*, 6033; b) Chciuk, T. V.; Anderson, W. R.; Flowers, R. A. II. Proton-Coupled Electron Transfer in the Reduction of Carbonyls by Samarium Diiodide-Water Complexes. *J. Am. Chem. Soc.* **2016**, *138*, 8738; c) Chciuk, T. V.; Anderson, W. R. Jr.; Flowers, R. A. II. Interplay between Substrate and Proton Donor Coordination in Reductions of Carbonyls by SmI_2-Water Through proton-Coupled-Electron Transfer. *J. Am. Chem. Soc.* **2018**, *140*, 15342

[6] Ashida, Y.; Arashiba, K.; Nakajima, K.; Nishibayashi, Y. Molybdenum-catalyzed ammonia production with samarium diiodide and alcohols or water. *Nature* **2019**, *568*, 536.

[7] a) Chalkley, M.; Del Castillo, T.; Matson, B.; Roddy, J.; Peters, J. C. Catalytic N_2-to-NH_3 Conversion by Fe at Lower Driving Force: A proposed Role for Metallocene-Mediated PCET. *ACS Cent. Sci.* **2017**, *3*, 217; b) Chalkley, M. J.; Del Castillo, T. J.; Matson, B.; Peters, J. C. Fe-Mediated Nitrogen Fixation with a Metallocene Mediator: Exploring p*K*a Effects and Demonstrating Electrocatalysis. *J. Am. Chem. Soc.* **2018**, *140*, 6122.

[8] Chalkley, M. J.; Oyala, P. H.; Peters, J. C. Cp* noninnocence Leads to a Remarkably Weak C-H bond via Metallocene protonation. *J. Am. Chem. Soc.* **2019**, *141*, 4721.

[9] Drover, M. W.; Schild, D. J.; Oyala, P. H. Peters, J. C. Snapshots of a Migrating H-Atom: Characterization of a reactive Iron(III) Indenide Hydride and its Nearly Isoenergetic Ring-Protonated Iron(I) Isomer. *Angew. Chem., Int. Ed.* **2019**, *58*, 15504.

[10] Hamon, P.; Toupet, L.; Hamon, J. R.; Lapinte, C. Novel diamagnetic and paramagnetic iron(II), iron(III), and iron(IV) classical and nonclassical hydrides. X-ray crystal structure of $[Fe(C_5Me_5)(dppe)D]PF_6$. *Organometallics* **1992**, *11*, 1429.

[11] Hamon, P.; Hamon, J. R.; Lapinte, C. Isolation and characterization of a cationic 19-electron iron(III) hydride complex; electron transfer induced hydride migration by carbon monoxide at an iron(III) center. *J. Chem. Soc. Chem. Commun.* **1992**, 1602.

[12] For example: a) Chiang, K. P.; Scarborough, C. C.; Horitani, M.; Lees, N. S.; Ding, K.; Dugan, T. R.; Brennessel, W. W.; Bill, E.; Hoffman, B. M.; Holland, P. L. Characterization of the Fe-H Bond in a Three-Coordinate Terminal Hydride Complex of Iron(I). *Angew. Chem., Int. Ed.* **2012**, *51*, 3658; b) Gu, N. X.; Oyala, P. H.; Peters, J. C. An S = ½ Iron Complex Featuring N_2, Thiolate, and Hydride Ligands: Reductive Elimination of H_2 and Relevant Thermochemical Fe-H Parameters. *J. Am. Chem. Soc.* **2018**, *140*, 6374.

[13] Lucken, E. A. C. *Nuclear Quadrupole Coupling Constants*; Academic Press: London, 1969. pp 227-131.

[14] For the IR spectrum of free Cp*H, see: Threlkel, R. S.; Bercaw, J. E.; Seidler, P. F.; Stryker, J. M.; Bergman, R. G. 1,2,3,4,5-pentamethylcyclopentadiene. *Org. Synth.*, **1987**, *65*, 42

[15] Green, M. L. H.; Pratt, L.; Wilkinson, G. 760. A new type of transition metal–cyclopentadiene compound. *J. Chem. Soc.* **1959**, 3753-3767

[16] Here, staggered refers to the puckered $CH(CH_3)$ group as being on the opposite side of the [Fe]-coordinated CO ligand.

[17] a) Paul, F.; Toupet, L.; Roisnel, T.; Hamon, P.; Lapinte, C. Solid-state characterisation of the $[(\eta^2\text{-dppe})(\eta^5\text{-}C_5Me_5)FeCO]^+$ cation: an unexpected 'oxidation' product of the $[(\eta^2\text{-dppe})(\eta^5\text{-}C_5Me_5)FeC{=}C(C_6H_4)NMe_2]^+$ radical cation. *C. R. Chim.* 2005, 1174; b) Catheline, D.; Astruc, D. Synthesis and characterization of $C_5(CH_3)_5Fe(CO)_3{}^+PF_6{}^-$ and $C_5(CH_3)_5Fe(CO)^{2-}K^+$. *J. Organomet. Chem.* **1982**, *226*, c52.

[18] "In the reaction between $[Fe(\eta^5\text{-Cp*})(dppe)(H)]$ and $[BNAP]^+$, the solvent adduct, $[Fe(\eta^5\text{-Cp*})(dppe)(NCMe)]^+$ and BNAPH are produced – in this case, acetonitrile binding will cause the experimentally determined BDFE (50 kcal mol-1) to be lower by as much as the binding strength of MeCN to the vacant Fe(II) complex, $[Fe(\eta^5\text{-Cp*})(dppe)]+$. By DFT, we estimate this value to be 12 kcal mol^{-1}, bringing the BDFE to 62 kcal mol^{-1}. See: Zhang, F.; Jia, J.; Dong, S.; Wang, W.; Tung, C. -H. Hydride Transfer from Iron(II) Hydride Compounds to $NAD(P)^+$ Analogues. *Organometallics* **2016**, *35*, 1151.

[19] Tilset, M.; Fjeldah, I.; Hamon, J.R.; Haon, P.; Toupet, L.; Saillard, J.Y.; Costuas, K.; Haynes, A. Theoretical, Thermodynamic, Spectroscopic, and Structural Studies of the Consequences of One-Electron Oxidation on the Fe−X Bonds in 17- and 18-Electron Cp*Fe(dppe)X Complexes (X = F, Cl, Br, I, H, CH_3). *J. Am. Chem. Soc.* **2001**, *123*, 9984.

[20] This value does not take into account the free energy associated with acetonitrile binding.

[21] a) Ilic, S.; Kadel, U. P.; Basdogan, Y.; Keith, J. A.; Glusac, K. D. Thermodynamic Hydricities of Biomimetic Organic Hydride Donors. *J. Am. Chem. Soc.* **2018**, *140*, 4569; b) Ellis, W. W.; Raebiger, J. W.; Calvin, C. J.; Bruno, J. W.; DuBois, D. L. Hydricities of BzNADH, $C_5H_5Mo(PMe_3)(CO)_2H$, and $C_5H_5Mo(PMe_3)(CO)_2H$ in Acetonitrile. *J. Am. Chem. Soc.* **2004**, *126*, 2738.

[22] a) Wiedner, E. S.; Chambers, M. B.; Pitman, C. L.; Bullock, R.M.; Miller, A. J. M.; Appel, A. M. Thermodynamic hydricity of Transition Metal Hydrides. *Chem. Rev.* **2016**, *116*, 8655; b) Pearson, R. G. The Transition-Metal-Hydrogen Bond. *Chem. Rev.* **1985**, *85*, 41.

[23] a) Savéant, J.-M.; Tard, C. Proton-Coupled Electron Transfer in Azobenzene/Hydrazobenzene Couples with pendant Acid-Base Functions. Hydrogen-Bonding and Structural Effects. *J. Am. Chem. Soc.* **2014**, *136*, 8907; b) Cattaneo, M.; Ryken S.A.; Mayer, J.M. Outer-Sphere $2e^-/2H^+$ Transfer Reactions of Ruthenium(II)-Amine and Ruthenium(IV)-Amido Complexes. *Angew. Chem., Int. Ed.* **2017** 56, 3675.

[24] Th $Fe^{I/II}$ redox potential of *endo* and *exo*-[3]+ could not be determined experimentally but the $Fe^{0/I}$ couples give conservative lower limits of, respectively, −0.81 and 0.70 V vs Fc/Fc.

[25] Goulet-Hanssens, A.; Utecht, M.; Mutruc, D.; Titov, E.; Schwarz, J.; Grubert, L.; Bleger, D.; Saalfrank, P.; Hecht, S. Electrocatalytic Z –> E Isomerization of Azobenzenes. *J. Am. Chem. Soc.* **2017**, *139*, 335−341

Appendix A : Supporting Information for Chapter 2

Experimental Section

General considerations. All manipulations were carried out using standard Schlenk or glovebox techniques under an N_2 atmosphere. Unless otherwise noted, solvents were deoxygenated and dried by thoroughly sparging with argon gas followed by passage through an activated alumina column in the solvent purification system by SG Water, USA LLC. 2-MeTHF was degassed by three freeze-pump-thaw cycles, followed by drying over NaK to remove traces of water. Deuterated solvents were purchased from Cambridge Isotope Laboratories, Inc., degassed, filtered through an alumina plug, and dried over 3Å molecular sieves prior to use. All reagents were purchased from commercial vendors and used without further purification unless stated otherwise. $P_2P^{Ph}FeBr_2$ (**3**) and $P_2P^{Ph57}FeCl_2$,[1] $[H(OEt_2)_2][BAr^F{}_4]$ ($BAr^F{}_4$ = tetrakis(3,5-bis(trifluoromethyl)phenyl)borate),[2] $Cp^*{}_2Co$,[3] and KC_8[4] were synthesized following literature procedures.

Physical Methods.

NMR spectra were recorded at room temperature unless otherwise noted. ^1H, ^{13}C and ^{29}Si chemical shifts are reported in ppm relative to tetramethylsilane, using residual solvent proton and ^{13}C resonances as internal standards. ^{29}Si NMR chemical shifts were determined from 29Si-HMBC two-dimensional spectra ^{15}N and ^{31}P chemical shifts are reported relative to CH_3NO_2 and 85 % aqueous H_3PO_4, respectively. Solution phase magnetic measurements were performed by the method of Evans.[5]

IR spectra were obtained using a Bruker Alpha Platinum ATR spectrometer with OPUS software in a glovebox under an N_2 atmosphere.

UV-Vis measurements were collected using a Cary 50 instrument with Cary WinUV software.

X-band EPR spectra were obtained on a Bruker EMX spectrometer on 2-5 mM solutions prepared as frozen glasses in 2-MeTHF. Samples were collected at powers ranging from 20 μW to 2 mW and modulation amplitudes of 1 – 5 Gauss. Spectra were simulated using the Easyspin suite of programs with Matlab 2018.

Mössbauer spectra were recorded on a spectrometer from SEE Co. operating in the constant acceleration mode in a transmission geometry. Spectra were recorded with the temperature of the sample maintained at 80 K. The sample was kept in an SVT-400 Dewar from Janis. The quoted isomer shifts are relative to the centroid of the spectrum of a metallic foil of α-Fe at room temperature. Data analysis was performed using the program WMOSS (www.wmoss.org) and quadrupole doublets were fit to Lorentzian lineshapes.

Cyclic voltammetry measurements were carried out in a glovebox under an N_2 atmosphere in a one-compartment cell using a CH Instruments 600B electrochemical analyzer. A glassy carbon electrode was used as the working electrode and a carbon rod was used as the auxiliary electrode. The reference electrode was AgOTf/Ag in THF isolated by a CoralPor™ frit (obtained from BASi). The ferrocenium/ferrocene couple (Fc^+/Fc) was used as an external reference. THF solutions of electrolyte (0.1 M $[NBu_4][PF_6]$) and analyte were also prepared under an inert atmosphere.

Hydrogen Analysis. The headspace of reaction flasks was analyzed by gas chromatography to quantify H_2 evolution with an Agilent 7890A gas chromatograph (HPPLOT U, 30 m,

0.32 mm i.d., 30 °C isothermal, 1 mL/min flow rate, N_2 carrier gas) using a thermal conductivity detector.

X-Ray Crystallography. X-ray diffraction studies were carried out at the Caltech Division of Chemistry and Chemical Engineering X-ray Crystallography Facility on a Bruker three-circle SMART diffractometer with a SMART 1K CCD detector, APEX CCD detector, or Bruker D8 VENTURE Kappa Duo PHOTON 100 CMOS detector. Data were collected at 100 K using Mo Kα radiation (λ = 0.71073 Å) or Cu Kα radiation (λ = 1.54178 Å). Structures were solved by direct or Patterson methods using SHELXS and refined against F2 on all data by full-matrix least squares with SHELXL-97.68 All non-hydrogen atoms were refined anisotropically. All hydrogen atoms were placed at geometrically calculated positions and refined using a riding model. The isotropic displacement parameters of all hydrogen atoms were fixed at 1.2 (1.5 for methyl groups) times the Ueq of the atoms to which they are bonded. See below for any special refinement details for individual data sets.

Combustion analysis measurements were collected using a PerkinElmer 2400 Series II CHN Elemental Analyzer.

Computational methods Geometry optimizations were performed using the Gaussian09 package all optimizations.[6] The TPSS functional[7] was employed in combination with def2-TZVP[8] basis set on transition metals and a def2-SVP[8] basis set for all remaining atoms in frequency calculations and geometry optimizations.

Experimental Section

P_2P^{Ph}: A 1.6 M *n*-BuLi solution (6.5 mL, 10.4 mmol) was added dropwise to a stirring solution of (2-bromophenyl)diisopropylphosphine (2.83 g, 10.3 mmol) in 40 mL diethyl ether at -78 °C. Following the addition,the light-yellow reaction mixture was stirred for 90 minutes at -78 °C. *P,P*-dichlorophenylphosphine (0.924 g, 5.1 mmol) in 6 mL diethyl ether was added over 30 minutes, resulting in a color change to red. The yellow suspension obtained after warming to room temperature overnight, was brought into the glovebox and filtered over celite. The flask was rinsed four times with 8 mL diethyl ether and the resulting solutionswere subsequently passed over celite and combined with the filtrate. The solvent of the combined filtrates was removed *in vacuo*, yielding a pale yellow powder. The powder was washed with pentane (3 x 5 mL) and dried under vacuum to give P_2P^{Ph} (**1**) as a white solid (1.23 g, 2.5 mmol, 47 %) evident by comparing spectroscopic properties with previously reported spectra.[1] ^{1}H NMR (Benzene-d_6, 400 MHz) δ ppm 7.49 – 7.40 (m, 2H), 7.39 – 7.31 (m, 2H), 7.08 (t, J = 6.7 Hz, 7H), 6.97 (t, J = 7.5 Hz, 2H), 2.11 (td, J = 7.0, 2.6 Hz, 2H), 1.98 (hept, J = 7.1 Hz, 2H), 1.18 (td, J = 13.8, 7.0 Hz, 12H), 0.92 (ddd, J = 32.8, 11.5, 7.0 Hz, 12H). ^{13}C NMR (C_6D_6, 101 MHz) δ ppm 148.42 (m), 142.42 (m), 139.73 (dt), 135.64 (d), 134.88 (m), 132.44 (m), 128.91 (s), 128.45 (d), 24.94 (m), 20.56 (m), 19.88 (m). ^{31}P{1H} (C_6D_6, 162 MHz) δ ppm -2.17 (dd, $^3J_{PP}$ = 158.7, $^3J_{PP}$ = 147.0 Hz, 2P, P-Ar), -14.26 (dt, $^3J_{PP}$ = 158.7, $^3J_{PP}$ = 147.0 Hz, 1P, P-Ph).

(P_2P^{Ph})FeBr (**4**): A dark purple solution of **3** (173.0 mg, 243 μmol) dissolved in 8 mL THF was stirred over sodium amalgam (5.8 mg, 252 μmol) for 2 h at room temperature during which the color changed to dark red. The red solution was filtered over celite and dried *in vacuo*. The resulting red solid was extracted with 4 mL Et_2O and filtered over celite.

Washing the red solid 4 times with 1.5 mL pentane yielded $P_2P^{Ph}FeBr$ as a red solid (99.8 mg, 158 μmol 65%). Crystals suitable for XRD were obtained by vapor diffusion of pentane into a benzene solution of $P_2P^{Ph}FeBr$. ^{1}H NMR (400 MHz, Benzene-d_6) δ 124.74 (2H), 104.79 (2H), 17.85 (2H), 7.96 (6H), 6.46,4.89, 3.84 (2H), 2.41 (2H), 1.02 (2H), -2.64 (6H), -7.19 (6H), -17.74 (2H), -20.57 (1H). UV-Vis (Benzene, nm {cm^{-1} M^{-1}}): 320 {6950}, 375 {5225}, 433 {4785}, 830 {1315}. μ_{eff} (C_6D_6, Evans Method, 25 °C): 4.11 μ_B. Anal: calculated for $C_{30}H_{41}BrFeP_3$: C 57.17, H 6.56 found: C 56.83, H 6.58

$[(P_2P^{Ph})Fe(H)]_2(\mu–N_2)$ (**1**): A 20 mL vial containing **4** (97.4 mg, 154.5 μmol) in 10 mL toluene was cooled down to −78 °C. 6.1 mL of an 0.25 M $NaHBEt_3$ solution in toluene was added after which the mixture was stirred at -78 °C for 30 minutes followed by 2 h at room temperature. Upon warming to room temperaturethe color changed from dark red to forest green. The solvent was removed *in vacuo,* after which the residue was extracted with 6 mL pentane. Reducing the solvent to 3 mL and storing at −35 °C yielded **1** as green crystals (50.1 μmol, 61 %), as was evident by comparing the spectroscopic properties with previously reported spectra.[1] 1H NMR (THF-d_8, 500 MHz) δ ppm 8.15 (d, J = 7.5 Hz, 2H), 7.52 (d, J = 7.5 Hz, 2H), 7.43 (t, J = 7.3 Hz, 2H), 7.26 (t, J = 7.3 Hz, 2H), 7.14 (t, J = 7.3 Hz, 2H), 6.63 (d, J = 7.4 Hz, 2H), 6.12 (t, J = 7.5 Hz, 1H), 2.99 (broad s, 2H), 2.59 (broad s, 2H), 0.72 (m, 6H), 0.42 (m, 6H).

$(P_2P^{Ph})Fe(N_2)_2$ (5) from 3: 50 mL of a THF solution of **3** (555.8 mg, 782 μmol) was stirred over sodium mercury amalgam (36.7 mg, 1.596 μmol, 9.6 g Hg) for 16 h at room temperature during which the color changed to wine red. The THF solution was filtered over celite, and the solvent was subsequently removed *in vacuo*. The material was extracted with pentane 40 mL and filtered over celite. Cooling down the filtrate down to −35 °C

yields crystalline $P_2P^{Ph}Fe(N_2)_2$ (205.2 mg, 339 µmol 43%). Additional product can be obtained by cooling down the concentrated mother liquor. No satisfactory elemental analysis could be obtained, with C and H percentages slightly higher than expected. The nitrogen content was consistently low, which is likely due to the loss of an N_2 ligand. The equilibrium discussed in the main text also hampers obtaining quantitative integrals in certain regions. ^{1}H NMR (400 MHz, Benzene-d_6) δ 7.63 (t, J = 6.3 Hz, 2H), 7.50 (dd, J = 6.0, 3.9 Hz, 2H), 7.12 – 6.75 (m, 9H), 2.86 – 2.53 (m, 4H), 1.57 – 1.40 (m, 6H), 1.35 – 0.96 (m, 18H), ^{13}C NMR (101 MHz, THF) δ 147.69, 131.47, 130.21, 129.07, 128.66, 127.29, 32.49, 27.99, 19.29, 18.84, ^{31}P NMR (162 MHz, Benzene-d_6) δ 122.76 (t, J = 63.0 Hz, 1H), 100.26 (d, J = 63.0 Hz 2P). IR (ATR, THF C_6D_6 film): νN_2 = 2065 cm^{-1}, 2005 cm^{-1}. UV-Vis (Et_2O, nm {cm^{-1} M^{-1}}): 251 {25000}, 322 {8816}, 405 {5480}, 490 {3820}, 830

$(P_2P^{Ph})Fe(N_2)_2$ (5) from 4: A 7 mL THF solution of **4** (81.0 mg, 128 µmol) was stirred over sodium mercury amalgam (3.6 mg, 156 µmol) for 1 hour and subsequently filtered over celite. THF was remove *in vacuo* and the residue was extracted with 6 mL pentane and filtered over celite. Cooling the solution to −35 °C yields $P_2P^{Ph}Fe(N_2)_2$ as a crystalline solid (37.8 mg, 62 µmol, 48%). Additional product can be obtained by cooling down the concentrated mother liquor.

$(P_2P^{Ph})^{57}Fe(N_2)_2$ (^{57}5): Complex **^{57}5** was prepared using the synthetic procedure for **5** with $P_2P^{Ph57}FeCl_2$ instead. The ^{1}H NMR spectrum matched that of **5**, while additional coupling with ^{57}Fe was present in the ^{31}P NMR spectrum. ^{31}P NMR (162 MHz, Benzene-d_6) δ 122.76 (dt, $^2J_{PP}$ = 64.5 Hz, $^1J_{FeP}$ = 46.2 Hz, 1P), 100.26 (t, J = 63.0 Hz, 2P).

[(P_2P^{Ph})Fe]$_2$μ–N_2 (6): An NMR tube containing **5** (20.5 mg, 33.8 μmol) in 0.6 mL toluene-d_8 was freeze-pump thawed three times, stored for 4 hours and freeze-pump thawed three additional times. A ^{31}P NMR spectrum was recorded to ensure full conversion to **6**. During the cycles, the color changes from maroon to a dark purple. If **5** was still present, additional freeze-pump thaw cycles were performed until the signal corresponding to **5** was negligible. Attempts to isolate the product as a crystalline solid were unsuccessful. ^{1}H NMR (500 MHz, Toluene-d_8) δ 7.97 (d, J = 7.4 Hz, 2H), 7.44 (d, J = 7.3 Hz, 2H), 7.31 (dd, J = 7.3 Hz, J = 7.3 Hz, 2H), 6.94 (dd, J = 7.4 Hz, J = 7.3 Hz, 2H), 6.87 (dd, J = 7.3 Hz, J = 7.3 Hz, 2H), 6.46 (s, 2H), 5.79 (s, 1H), 5.35 (s, 2H), 5.07 (s, 2H), 1.61 (s, 6H), 1.05 (s, 6H), 1.01 (s, 6H) 0.43 (s, 6H).^{31}P NMR (202 MHz, Toluene-d_8, 298 K) δ 184.84. ^{31}P NMR (202 MHz, Toluene-d_8, 203 K) δ 130.42, 123.63 Small amounts of an unknown species are present at 98.05 and 92.51 ppm, but they account for less than 5%

(P_2P^{Ph})Fe(N_2)(H_2) (2): A Schlenk tube containing **5** (60.9 mg, 100 μmol) in THF (6 mL) was freeze-pump-thawed 3 times and exposed to 1 atmosphere of H_2. The reaction was stirred vigorously at room temperature for 24 hours before it was freeze-pump-thawed 2 times, re-exposed to 1 atmosphere of N_2, and stirred for another 24 hours, during which thesolution turned yellow. The solvent was removed *in vacuo*, yielding **2** quantitatively (58.0 mg, 100 μmol, 100%). The nature of the solid was determined by comparing its NMR and IR features with those reported.[1] ^{1}H NMR (THF-d_8, 500 MHz) δ ppm 8.09 (t, J = 6.4 Hz, 2H), 7.77 (d, J = 7.2 Hz, 2H), 7.40 (p, J = 7.2 Hz, 4H), 7.22–7.15 (m, 5H), 2.67 (h, J = 6.8 Hz, 2H), 2.56–2.50 (m, 2H), 1.43 (q, J = 7.0 Hz, 6H), 1.15–1.19 (m, 12H), 0.46 (q, J = 6.9, 6H), -9.43 (td, J = 38.2 , 15.7 Hz, 1H), -20.71 (td, J = 43.2 , 15.6 Hz, 1H), ^{31}P NMR

(162 MHz, Benzene-d_6) δ ppm 119.2 (2P), 110.2 (1P). IR (ATR, THF C_6D_6 film): 2071 cm^{-1} (νN_2), 1796 cm^{-1} (νFe–H).

[(P_2P^{Ph})Fe(N_2)$_2$(H)][BAr^F_4] (7): A 20 mL vial containing **1** (16.4 mg, 14.5 µmol) in 1.5 mL diethyl ether was cooled down to −78 °C. A cooled solution of $FcBAr^F_4$ (32.8 mg, 31.2 µmol) in 1.5 mL diethyl ether was added dropwise during which the color changes from green to orange. The solution was stirred at −78 °C for 1 hour and warmed to room temperature. The mixture was subsequently filtered over celite. The filtrate was layered with 10 mL pentane and stored at −35 °C overnight, which resulted in the formation of orange crystals (41.0 mg, 27.8 µmol 96 %). The obtained crystalline material was suitable for X-ray diffraction. ^{1}H NMR (THF-d_8, 400 MHz) δ ppm 8.22–8.10 (m), 7.85–7.69 (m), 7.59–7.50 (m), 7.36 (t, J = 7.9, 1H), 7.30–7.27 (m), 7.27–7.21 (m), 6.60 (t, J = 9.3 Hz, 2H), 3.14–2.92 (m, 4H), 1.56–1.41 (m), 1.35–1.14 (m), -16.85 (dt (q), J = 54.9, 1H). ^{11}B NMR (THF-d_8, 128 MHz) δ ppm -4.68 (s). ^{19}F NMR (THF-d_8, 376 MHz) δ ppm -61.51 (s). ^{31}P{^{1}H} (THF-d_8, 162 MHz) δ ppm 113.41 (overlapping dt, J = 34.6, 25.0 Hz, 103 1P, PPh), 95.75 (dd, J = 29.5, 7.5 Hz, 2P, P*i*Pr$_2$). IR (thin film from evaporation of THF-d_8; cm^{-1}): 2193 (νN–N), 2162 (νN–N), 2069 (νFe–H). UV-Vis (Et_2O, nm {cm^{-1} M^{-1}}): 367{2200} Anal: calculated for $C_{62}H_{54}BF_{24}FeN_4P_3$: C 50.64, H 3.70 N 3.81, found: C 50.23, H 4.00, N 3.17

[(P_2P^{Ph})Fe(N_2)(H)][K(18-crown-6] (8): A 4 mL vial containing **1** (28.4 mg, 25 µmol) in THF was cooled down to −78 °C. Simultaneously, a 20 mL vial containing KC_8 (7.0 mg (51 µmol) and a stir bar was cooled down. After 20 minutes, the THF solution containing

1 was rapidly added to the vial containing KC_8. The mixture is stirred for 45 minutes at −78, after which 18-crown-6 (20.4 mg, 77 µmol) was added. The solution was stirred an additional 45 minutes at room temperature, layered with 6 mL pentane and stored at −35 °C. Over four days black crystals formed suitable for XRD, (35.4 mg, 40 µmol, 90%). ^{1}H NMR (400 MHz, THF-d_8) δ 7.75 (q, *J* = 4.2 Hz, 2H), 7.43 (t, *J* = 4.2 Hz, 2H), 7.24 (t, *J* = 7.6 Hz, 2H), 7.04 – 6.88 (m, 6H), 6.83 (t, *J* = 7.2 Hz, 1H), 2.53 (d, *J* = 9.2 Hz, 2H), 2.42 – 2.26 (m, 2H), 1.24 (ddt, *J* = 21.2, 13.8, 6.6 Hz, 6H), 0.88 (q, *J* = 6.8 Hz, 12H), 0.29 (q, *J* = 6.6 Hz, 6H), -9.69 (td, *J* = 68.8, 67.9, 27.3 Hz, 1H).^{31}P NMR (162 MHz, THF-d_8) δ ppm 120.62 (m, 1P) 119.89 – 118.98 (m. 2P). IR (thin film from evaporation of THF-d_8; cm^{-1}): 1924 (*ν*N–N), 1733 (*ν*Fe–H) Anal: calculated for $C_{62}H_{54}BF_{24}FeN_4P_3$: C 57.86, H 7.81 N 2.93, found: C 57.23, H 7.34, N 1.89

[(P_2P^{Ph})Fe(N_2)][K(18-crown-6] (9): A 20 mL vial containing **5** (20.6 mg, 34 µmol) in 1.5 Ml THF was cooled down to −78 °C and 340 µL of a 100 µM potassium naphthalide solution (34 µmol) was added after which the species was stirred. After one hour of stirring, an excess 18-crown-6 was added (18 mg, 68 µmol). The solution was stirred for an hour at room temperature and subsequently layered with 6 mL pentane. Storing the solution in the freezer for 24 h resulted in the formation of dark crystals suitable for XRD (20.9 mg, 23.8 µmol 70%). ^{1}H NMR (400 MHz, THF-d_8) δ 63.91 26.76, 20.51, 18.28, 13.61. 9.85, 6.27, 5.22, 1.04, -2.15, -7.78, -27.16 ppm. IR (ATR, THF C_6D_6 film): 1872 cm^{-1} (*ν*N_2), Anal: calculated for $C_{62}H_{53}BF_{24}FeN_4P_3$: C 57.64, H 7.61 N 2.93, found: C 57.23, H 7.34, N 1.89

[(P_2P^{Ph})Fe(N_2)][K_2(THF)$_3$] (10): A 20 mL vial containing **5** (120.1 mg, 198 µmol) dissolved in 5 mL NaK dried THF was cooled down to −78 °C. Simultaneously, a 20 mL vial containing KC_8 (80.2 mg, 600 µmol) and a stir bar was cooled down to −78 °C. The cooled solution containing **5** was added to the vial containing KC_8 after which the vial was rinsed with 0.5 mL THF which was subsequently added. The solution was stirred for 15 minutes. and filtered over celite. To assure the frit and celite are sufficiently dry, 3 mL NaK dried THF was passed through the frit four times before the reaction mixture was passed over celite. The reaction vial was rinsed with 1 mL THF, and the wash was passed over celite. The filtrate was divided into two 20 mL vials and each vial was layered with 15 mL pentane. Crystals of **10** suitable for XRD formed over a period of a week. (110.1 mg, 126 µmol, 63%). ^{1}H NMR (400 MHz, THF-d_8) δ 7.87 (m, 2H), 7.51 – 7.34 (m, 2H), 6.89 (m, 8H), 6.71 (t, J = 7.2 Hz, 1H), 2.90 – 2.58 (m, 2H), 2.58 – 2.38 (m, 2H), 1.29 (m, J = 12H), 0.81 (q, J = 5.8 Hz, 6H), 0.23 (q, J = 5.9 Hz, 6H). ^{13}C NMR (101 MHz, THF-d_8) δ 157.27, 154.67, 153.04, 131.46, 129.79, 128.62, 128.05 – 122.99 (m), 35.82, 29.23, 24.12 – 19.34 (m). ^{15}N NMR (41 MHz, THF-d_8) δ 2.36, -25.91. ^{31}P NMR (162 MHz, THF-d_8) δ 113.13 (d, J = 33.8 Hz), 95.15 (t, J = 33.8 Hz). No satisfactory combustion analysis could be obtained.

[(P_2P^{Ph})Fe(NNSiMe$_3$)]K (11- NNSiMe$_3$)K: A 20 mL vial containing **5** (55.9 mg, 92 µmol, in 5 mL NaK dried THF was cooled down to -78 °C in a glovebox Coldwell after which it was added to a vial containing KC_8 (37.4mg, 276 µmol 3 equiv.) at -78 °C, Stirring the solution for 30 minutes resulted in a color change to dark purple. The cold suspension was filtered over celite, and subsequently cooled down to -78 °C followed by the addition of

TMSCl (11.6 µL, 92 µmol) which resulted in an immediate color change to brown. The mixture was subsequently stirred at −78 °C for 30 minutes, followed by 30 minutes at room temperature. Volatiles were removed *in vacuo* and the residue was dissolved in benzene and filtered over celite. Benzene was removed *in vacuo*, and the solid washed with pentane (3 x 2 mL) and filtered over a celite plug. The remaining solids were dissolved in diethyl ether and passed over the same celite plug. Removal of diethyl ether *in vacuo* yields [P_2P^{Ph}Fe(NNTMS)]K (35 mg, 54 µmol, 58%). Crystals suitable for XRD could be grown by layering a concentrated benzene solution with pentane. ^{1}H NMR (C_6D_6, 400 MHz): δ 7.84 (m, 2H), 7.68 (d, $^3J_{HH}$ = 6.69 Hz, 2H), 7.10-6.96 (m, 6H), 6.66-6.42 (m, 3H), 2.99-2.76 (m, 2H), 2.31-2.17 (m, 2H), 1.59-1.40 (m, 6H), 1.33-0.89 (m, 18H), 0.38 (s, 9H, $Si(CH_3)_3$); ^{29}Si NMR (79 MHz, C_6D_6, HMBC) δ: 4.72 (s, N-SiCH3). ^{13}C NMR (101 MHz, C_6D_6) δ 130.65 (d, *J* = 10.4 Hz), 127.98, 127.54 (d, *J* = 6.0 Hz), 126.48 – 125.86 (m), 125.54 (d, *J* = 11.5 Hz), 32.72 (t, *J* = 9.4 Hz), 28.26 (d, *J* = 8.4 Hz), 21.36 – 19.79 (m), 0.98, -1.11. ^{31}P NMR (162 MHz, C_6D_6) δ 117.48 (d, *J* = 16.7 Hz, 2P, PAr), 109.12 (t, *J* = 16.6 Hz, 1P, PPh). Anal: calculated for $C_{33}H_{56}FeKN_2P_3Si$: C 57.38, H 7.81 N 4.06, found: C 57.17, H 7.07, N 3.61

[(P_2P^{Ph})Fe(NNSi^{i}Pr$_3$)]K (11-NNSi^{i}Pr$_3$): $P_2P^{Ph}Fe(N_2)_2$ (50.1 mg, 83 µmol) in 2.5 mL NaK dried THF was cooled down to −78 °C in a glovebox coldwell and passed over a pipette with a thin layer of KC_8 (4 mm). The mixture was passed over the pipette three times during which the color changed to dark purple. TiPSOTf (20 µL, 74 µmol was added upon which an immediate color change to orange brown was observed. The mixture was subsequently stirred at −78 °C for 30 minutes, after which it was taken out of the coldwell and stirred at room temperature for 30 minutes. Volatiles were removed *in vacuo* and the residue was

dissolved in benzene and filtered over celite. Benzene was removed *in vacuo* and the remaining residue washed with HMDSO (5 x 1.5 mL) and filtered over celite. The remaining brown residue in the vial and on the celite was dissolved in diethyl ether. Removal of diethyl ether *in vacuo* yields [P_2P^{Ph}Fe(NNT*i*PS)]K in 75 % yield (43.0 mg, 55 µmol). ^{1}H NMR (300 MHz, Benzene-d_6) δ 7.89 (s, 3H), 7.69 (d, *J* = 6.7 Hz, 2H), 7.09, (s, 6H), 6.62 (s, 3H), 3.55 (s, 3H) 2.88 (s, 2H), 2.62 (s, 2H), 1.50 (td, *J* = 14.5, 13.7, 6.4 Hz, 12H), 1.38 – 1.14 (m, 35H), 0.97 – 0.81 (m, 12H). ^{31}P NMR (121 MHz, Benzene-d_6) δ 118.22 (d, *J* = 17.9 Hz), 111.69 (t, *J* = 17.9 Hz). IR (ATR, C_6D_6 film): 1469 cm^{-1} (νN_2),

Stochiometric reactivity

Addition of H_2 to 5 at -78 °C. The headspace of a J-Young NMR tube containing **5** (5.9 mg, 9.7µmol) was degassed once by a freeze-pump-thaw cycle. The tube was warmed transferred into a dry ice acetone bath and one atmosphere of H_2 was added. The cold tube was rapidly shaken for 5 seconds and inserted into the precooled NMR spectrometer.

Addition of H_2 to 6 at -78 °C. To a J-Young NRM tube containing **6**, generated *in situ* according to the preparation described above, was added one atmosphere of H_2. The cold tube was rapidly shaken for 5 seconds and inserted into the precooled NMR spectrometer.

General procedure for the synthesis of [(P_2P^{Ph})Fe(N_2)$_2$(H)][BAr^F_4] (7) from 1, 2 or 5 with $HBAr^F_4$: A 20 mL vial containing **1**, **2**, or **5** (9.4 µmol for **1**, 18.8 µmol for **2** and **5**) in diethyl ether (1 mL) was chilled to −78 °C in the glovebox coldwell. In a separate 4 mL vial, a diethyl ether solution of $HBAr^F_4$ (0.019 g, 18.4 µmol, 250 µL diethyl ether) was chilled to −78 °C. Both solutions were allowed to cool for 20 min before the $HBAr^F_4$ solution was added to the vial containing **1**, **2** or **5** at -78 °C in one shot. The vial containing

$HBAr^{F}_{4}$ was subsequently rinsed with 250 µL of pre-chilled diethyl ether and the rinsing was added to the vial containing. The reaction mixture was stirred at −78 °C for 1 hour and 15 minutes before it was warmed to warm to room temperature. Analysis by NMR and IR spectroscopy confirms the nature of the product as **7**.

NMR analysis of addition of $HBAr^{F}_{4}$ to 5 at -78 °C: **5** (5.9 mg, 9.7µmol) was dissolved in 0.4 mL THF-d_8 and added to a J-Young NMR tube at −78 °C. $HBAr^{F}_{4}$ (10.3 mg, 10.7 µmol) was cooled to −78 °C and added to the NMR tube. The cold tube was rapidly shaken for 5 seconds, taken out of the glovebox and inserted into the precooled NMR spectrometer at −78 °C.

Oxidation of [(P_2P^{Ph})Fe(NNSiMe$_3$)]K at room temperature. To a stirring solution of [P_2P^{Ph}Fe(NNTMS)]K (13.0 mg, 17 µmol) in 3 mL THF was added [Cp*$_2$Co][PF_6] (8.2 mg, 17 17 µmol) suspended in 1 mL THF. The mixture was stirred for 24 hours, followed by removal of the solvent *in vacuo*. Extracting the solid twice with 5 mL pentane results in an off-white residue. The pentane extracts were combined and removal of the solvents *in vacuo* gives a brow solid (10 mg). Analysis of the solid by NMR spectroscopy reveals the presence of **5** and cobaltocene.

Oxidation of [(P_2P^{Ph})Fe(NNSiMe$_3$)]K (11-NNSiMe$_3$) at −78 °C. To a cooled stirring solution of [(P_2P^{Ph}) Fe(NNTMS)]K (4 µmol) in 1 mL 2-MeTHF at −78 °C was added [Cp*$_2$Co][PF_6] (8.2 mg, 17 µmol) suspended in 0.5 mL 2-MeTHF. The solution was stirred for 5 minutes at −78 °C after which the sample was frozen. The frozen solution was briefly thawed and a 300 µL aliquot was transferred to a precooled EPR tube which was

subsequently frozen. Additional EPR spectra were recorded for the frozen samples stored at −78 °C for 24 hours.

(P_2P^{Ph})Fe(NN^iPr_3) (12-NN^iPr_3): A cooled stirring solution of [(P_2P^{Ph}) Fe(NNTiPS)]K (15.0 mg, 19 μmol) in 1 mL was added to [Cp*$_2$Co][PF_6] (9.1 mg, 19 μmol) at −78 °C. The solution was stirred at −78 for 10 minutes followed by 10 minutes at room temperature. The solvent was removed *in vacuo* and the residue extracted with pentane. Filtering over celite and removal of the solvent in vacuo gives a product characterized as **12**–**TiPS**. ^{1}H NMR (300 MHz, Benzene-d_6) δ ^{1}H NMR (400 MHz, THF-d_8) δ 12.22 9.31 7.24 5.90, 4.92, 3.39, 2.36 1.63 – 0.48. IR (ATR, THF film): 1659 cm^{-1} (νN_2),

NMR Spectra

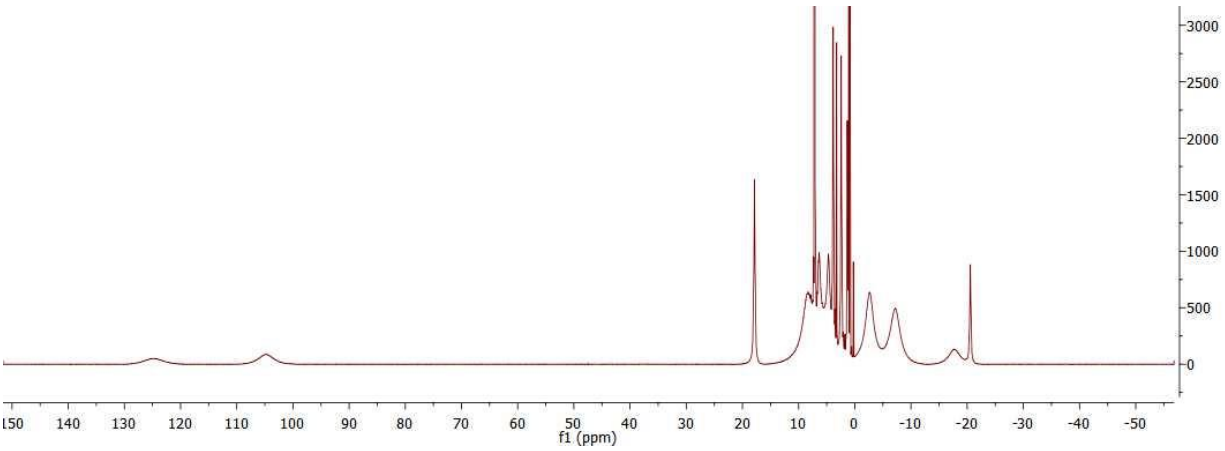

Figure A.1. ^{1}H NMR spectrum of (P_2P^{Ph})FeBr (**4**) in C_6D_6 at room temperature

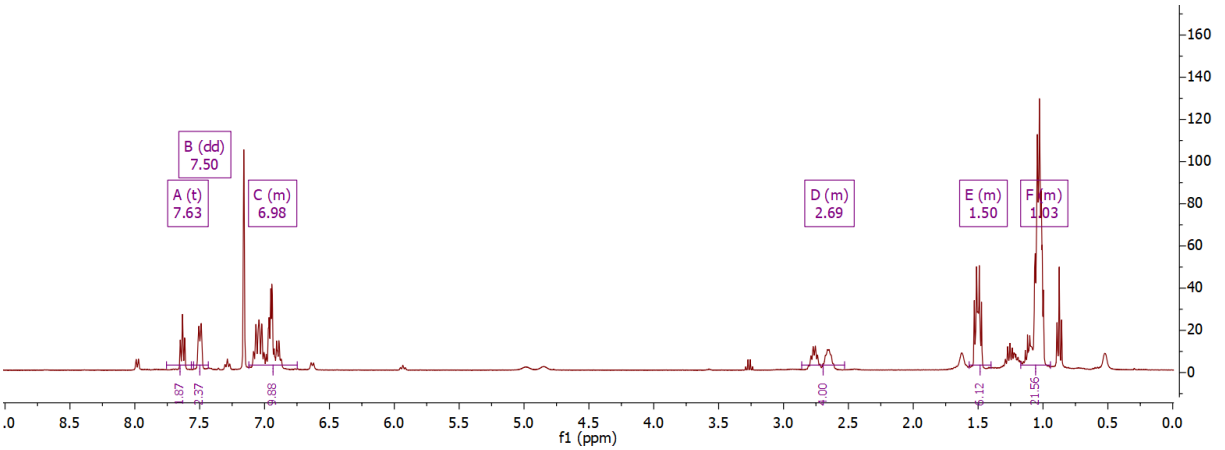

Figure A.2. ^{1}H NMR spectrum of (P_2P^{Ph})Fe(N_2)$_2$ (**5**) in C_6D_6 at room temperature. Additional broad peaks corresponding to **6** are present due to the equilibrium as described in the main text.

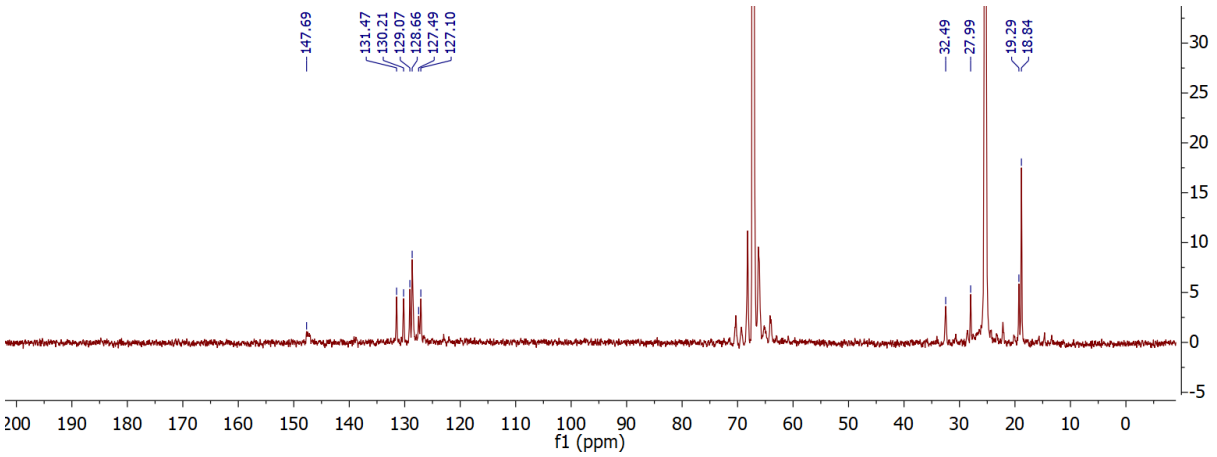

Figure A.3. ^{13}C NMR spectrum of $(P_2P^{Ph})Fe(N_2)_2$ (**5**) in THF at room temperature

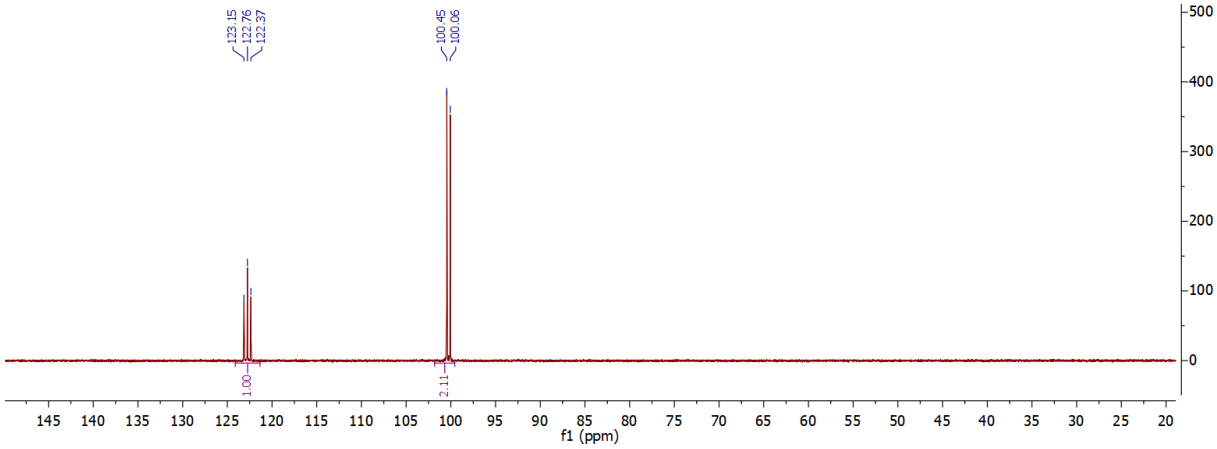

Figure A.4. ^{31}P NMR spectrum of $(P_2P^{Ph})Fe(N_2)_2$ (**5**) in C_6D_6 at room temperature

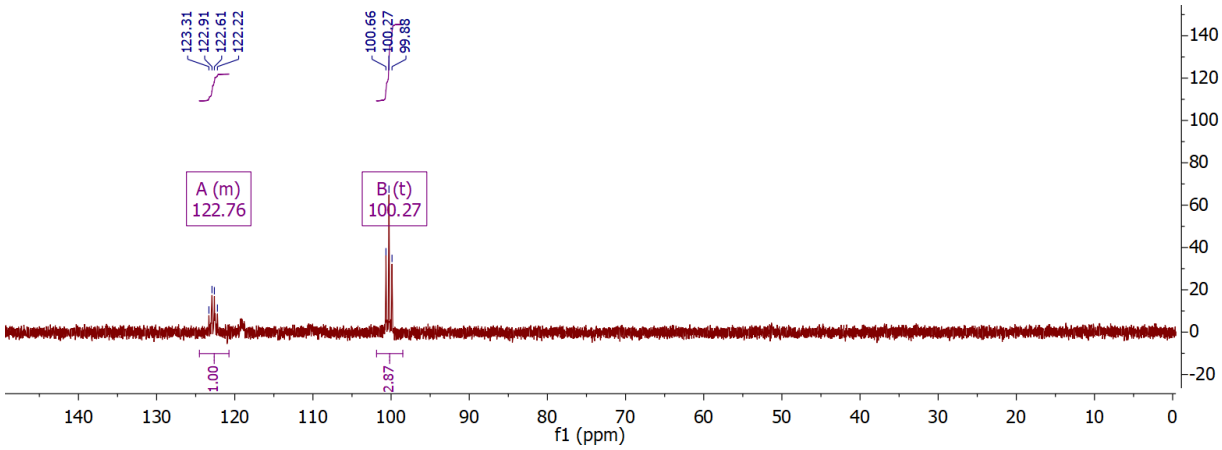

Figure A.5. ^{31}P NMR spectrum of $(P_2P^{Ph})^{57}Fe(N_2)_2$ (^{57}**5**) in C_6D_6 at room temperature

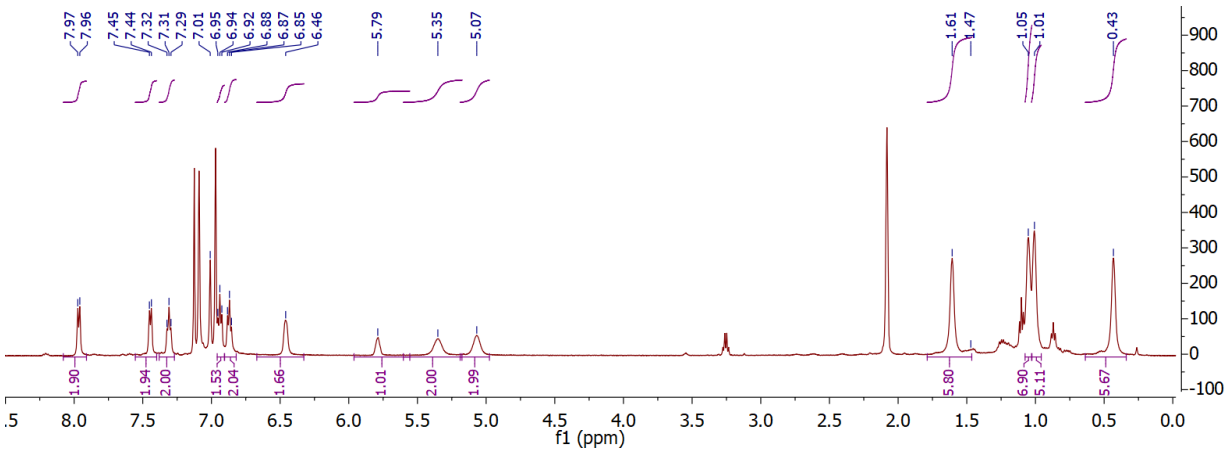

Figure A.6. ^{1}H NMR spectrum of $[(P_2P^{Ph})Fe]_2(\mu-N_2)$ (**6**) in Toluene-d_8 at room temperature

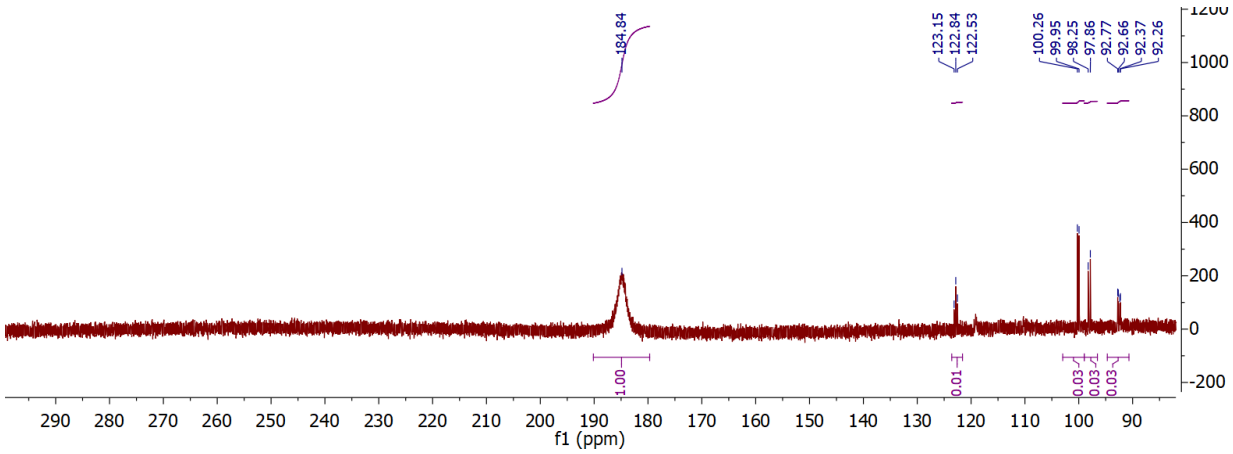

Figure A.7. ^{31}P NMR spectrum of $[(P_2P^{Ph})e]_2(\mu-N_2)$ (**6**) in Toluene-d_8 at room temperature

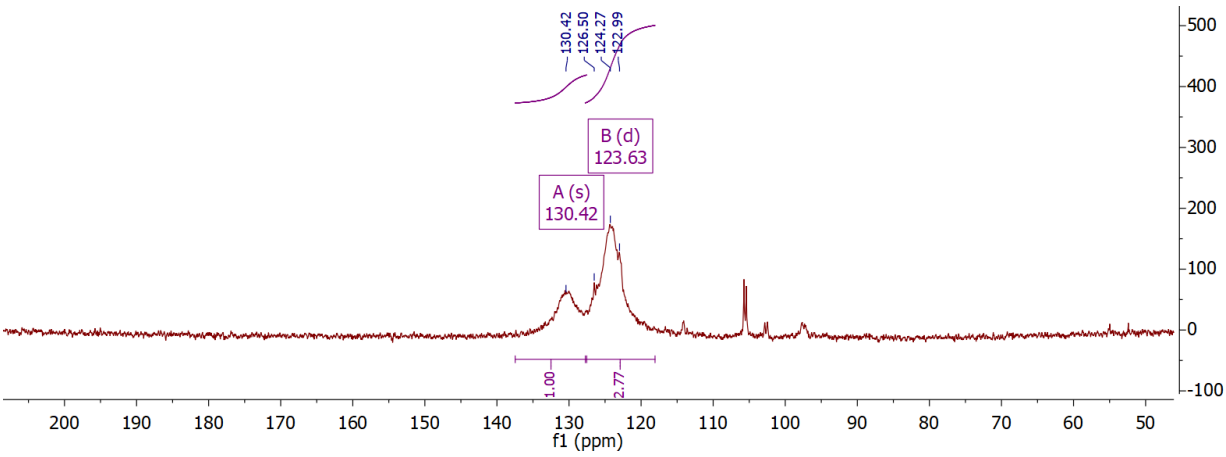

Figure A.8. ^{31}P NMR spectrum of $[(P_2P^{Ph})Fe]_2(\mu\text{–}N_2)$ (**6**) in Toluene-d_8 at 203 K

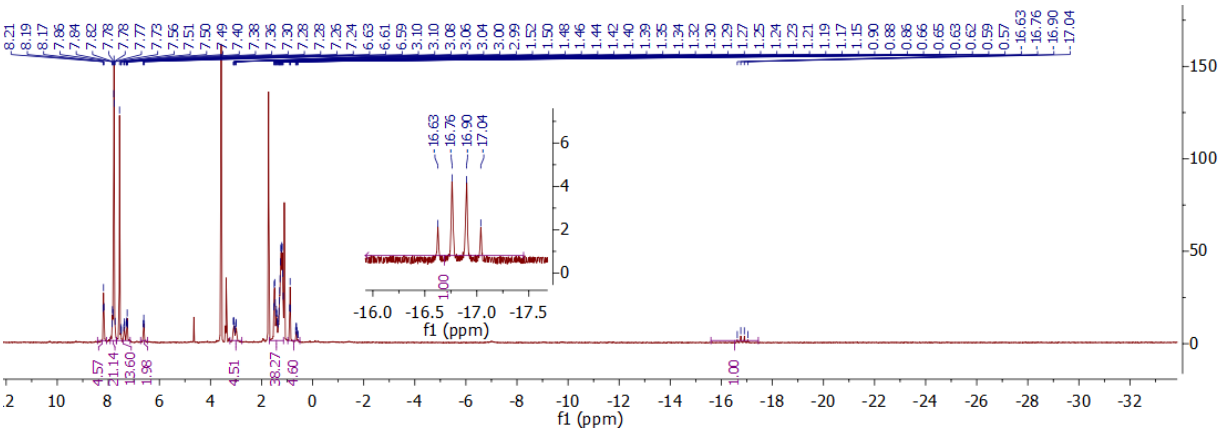

Figure A.9. ^{1}H NMR spectrum of $[(P_2P^{Ph})Fe(N_2)_2(H)][BAr^F{}_4]$ (**7**) in THF-d_8 at room temperature

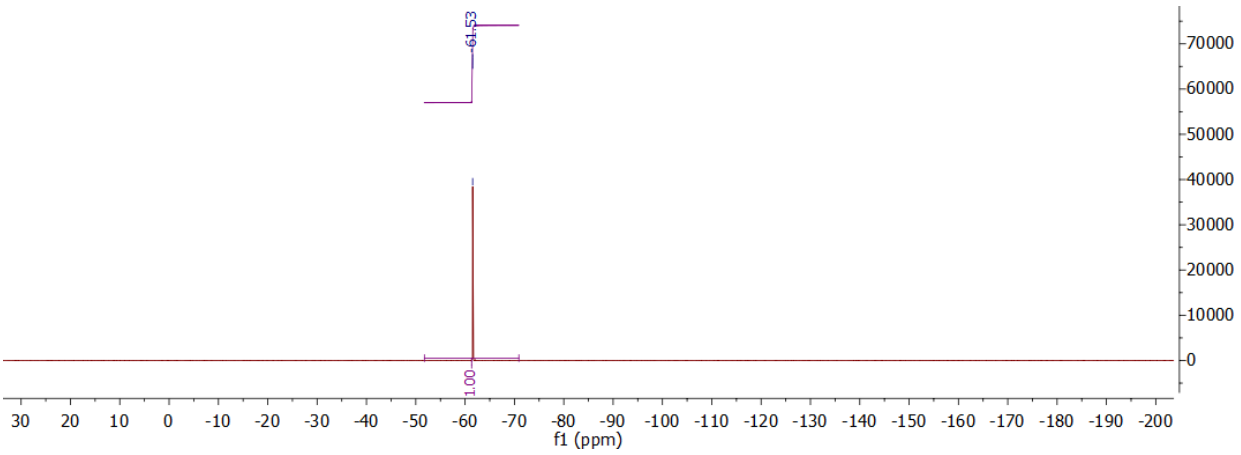

Figure A.10. ^{19}F NMR spectrum of $[(P_2P^{Ph})Fe(N_2)_2(H)][BAr^F{}_4]$ (**7**) in THF-d_8 at room temperature

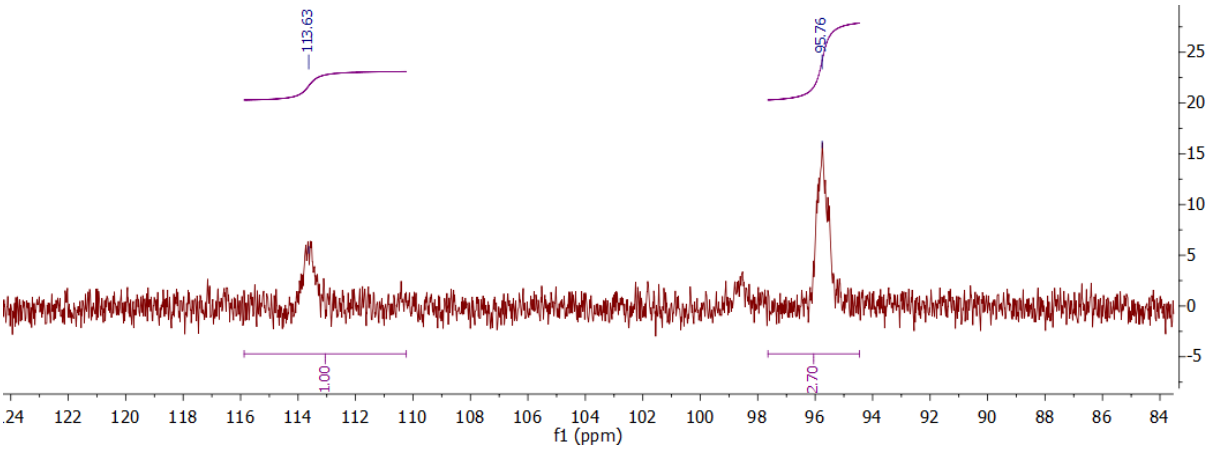

Figure A.11. ^{31}P NMR spectrum of $[(P_2P^{Ph})Fe(N_2)_2(H)][BAr^F{}_4]$ (**7**) in THF-d_8 at room temperature

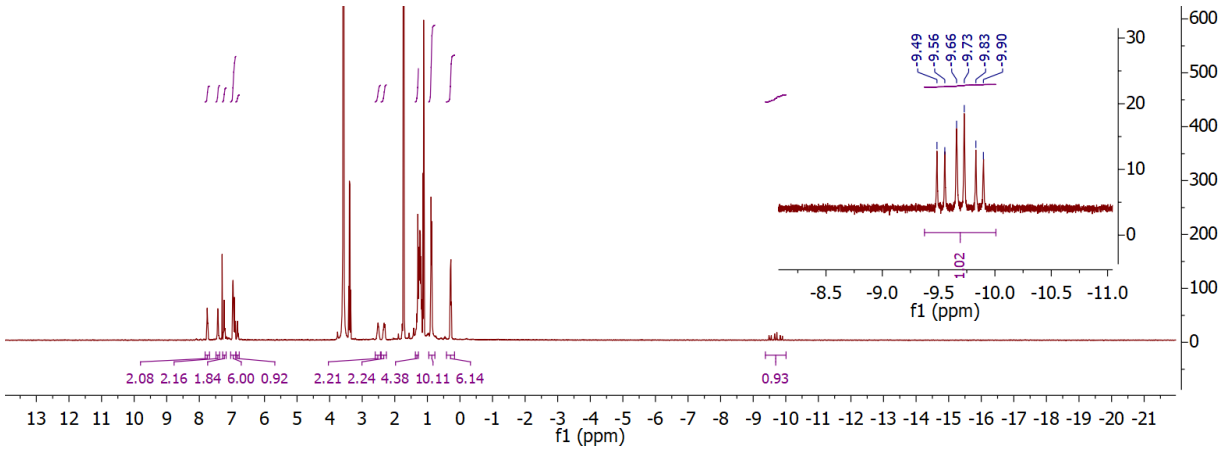

Figure A.12. ^{1}H NMR spectrum of [(P_2P^{Ph})Fe(N_2)(H)][K(18-crown-6)] (**8**) in THF-d_8 at room temperature

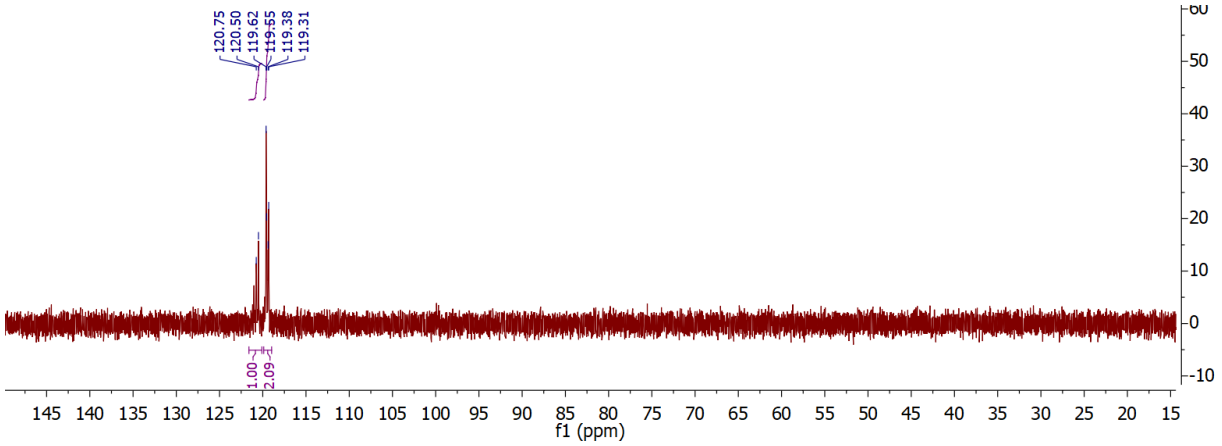

Figure A.13. ^{31}P NMR spectrum of [(P_2P^{Ph})Fe(N_2)(H)][K(18-crown-6)] (**8**) in THF-d_8 at room temperature

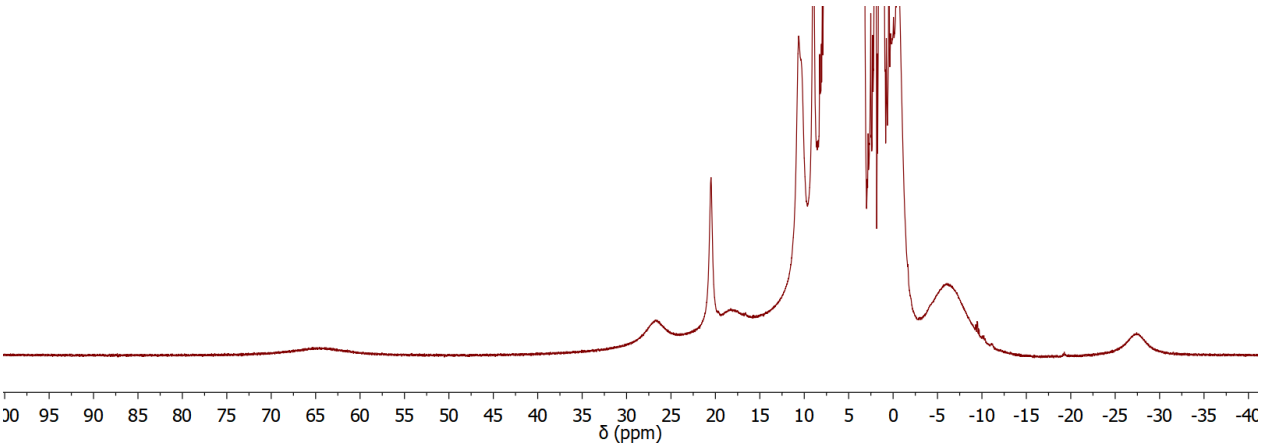

Figure A.14. ^{1}H NMR spectrum of [(P_2P^{Ph})Fe(N_2)][K(18-crown-6)] (**9**) in d_8-THF at room temperature

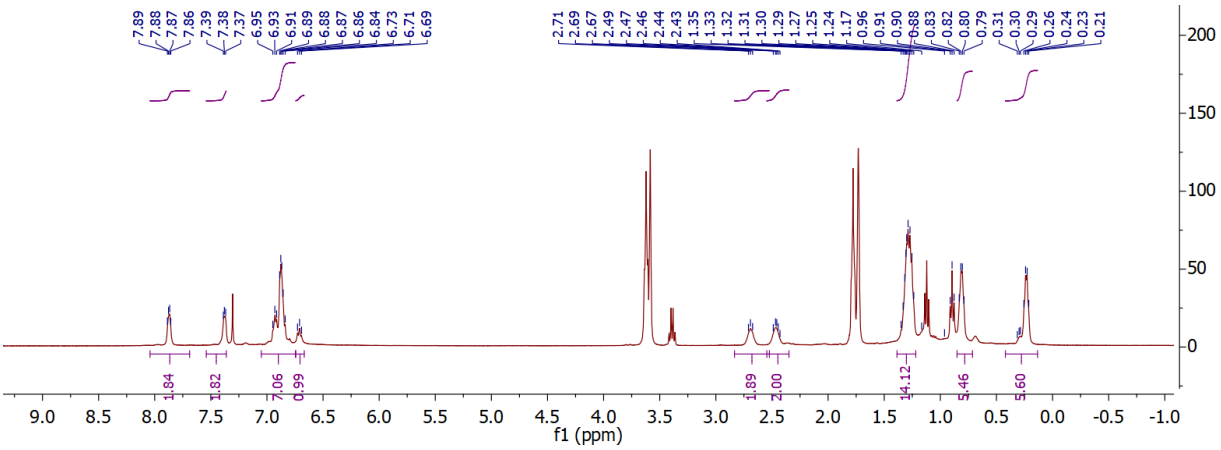

Figure A.15. ^{1}H NMR spectrum of [(P_2P^{Ph})Fe(N_2)][K_2(THF)$_3$] (**10**) in d_8-THF at room temperature

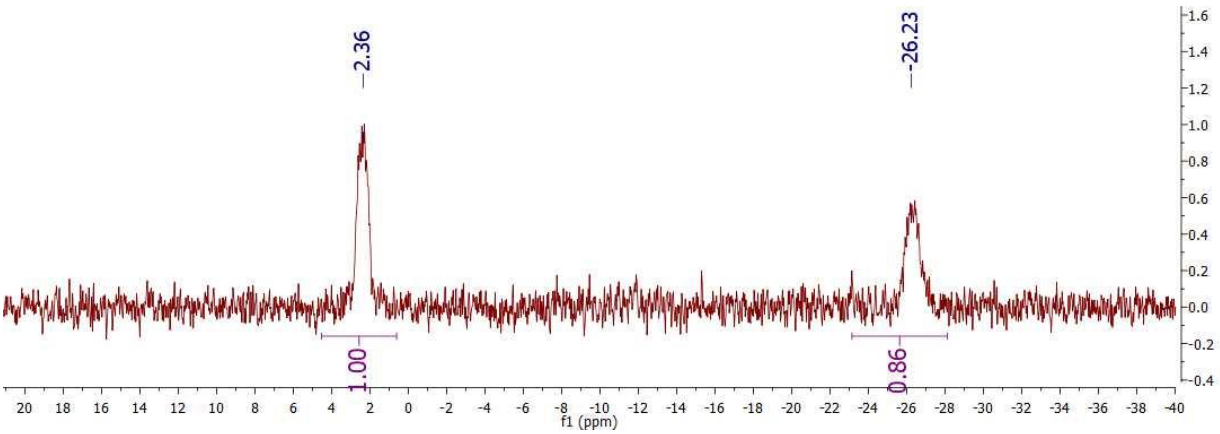

Figure A.16. ^{15}N NMR spectrum of $[(P_2P^{Ph})Fe(N_2)][K_2(THF)_3]$ in d_8-THF at room temperature

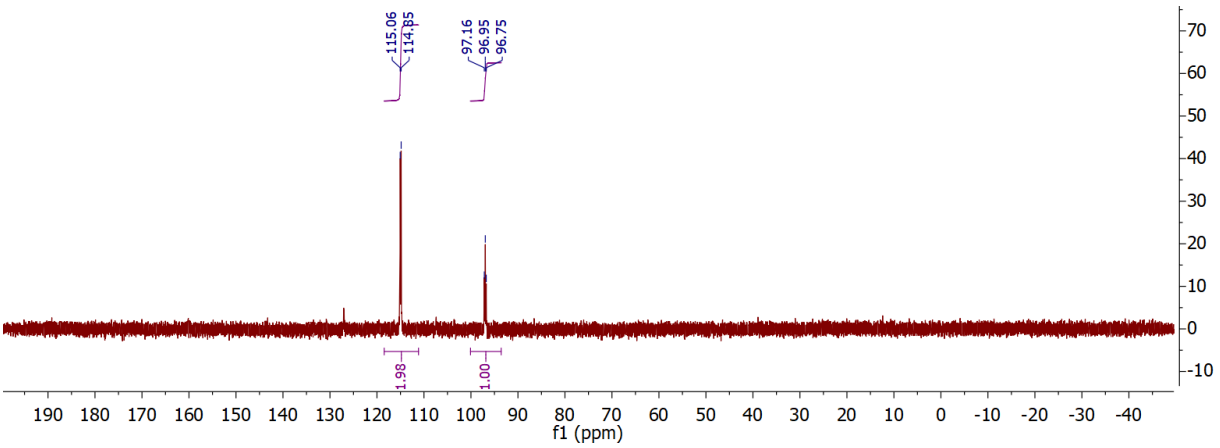

Figure A.17. ^{31}P NMR spectrum of $[(P_2P^{Ph})Fe(N_2)][K_2(THF)_3]$ in d_8-THF at room temperature

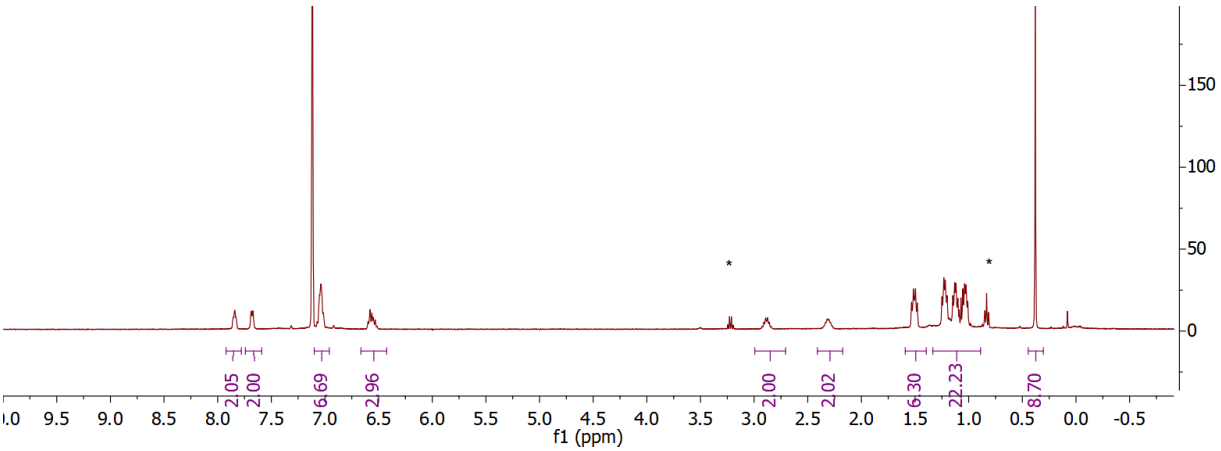

Figure A.18. ^{1}H NMR spectrum of [(P_2P^{Ph})Fe(NNTMS)]K in C_6D_6 at room temperature. The peaks labeled with a star correspond to residual diethyl ether.

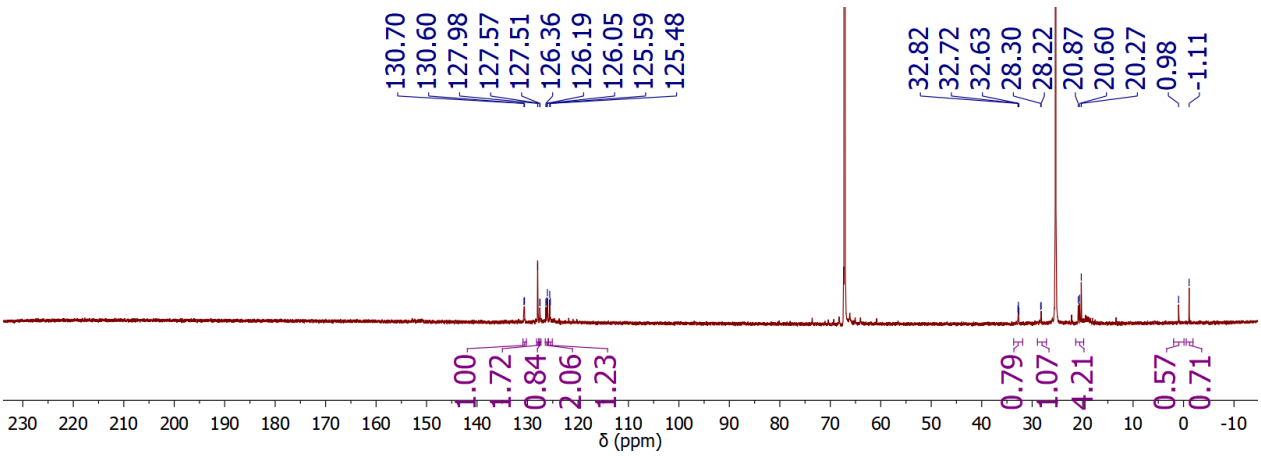

Figure A.19. ^{13}C NMR spectrum of [(P_2P^{Ph})Fe($NNSiMe_3$)]K (**11**-$NNSiMe_3$) in THF at room temperature. The peaks labeled with a star correspond to residual diethyl ether.

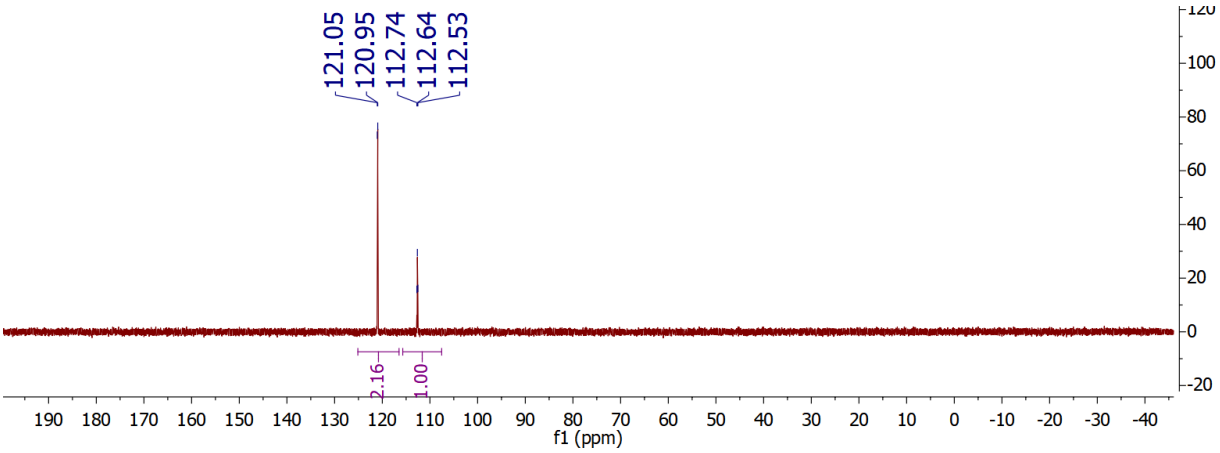

Figure A.20. ^{31}P NMR spectrum of [(P_2P^{Ph})Fe(NNSiMe_3)]K (**11**-NNSiMe_3) in C_6D_6 at room temperature. The peaks labeled with a star correspond to residual diethyl ether.

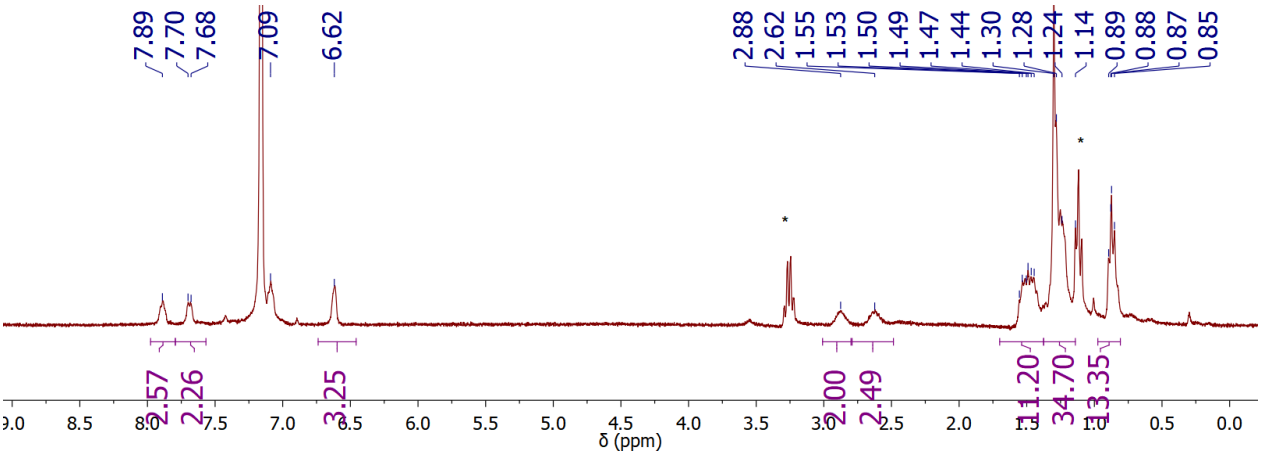

Figure A.21. ^{1}H NMR spectrum of [(P_2P^{Ph})Fe(NNSi$^{i}Pr_3$)]K (**11**-NNSi$^{i}Pr_3$) in C_6D_6 at room temperature. The peaks labeled with a star correspond to residual diethyl ether.

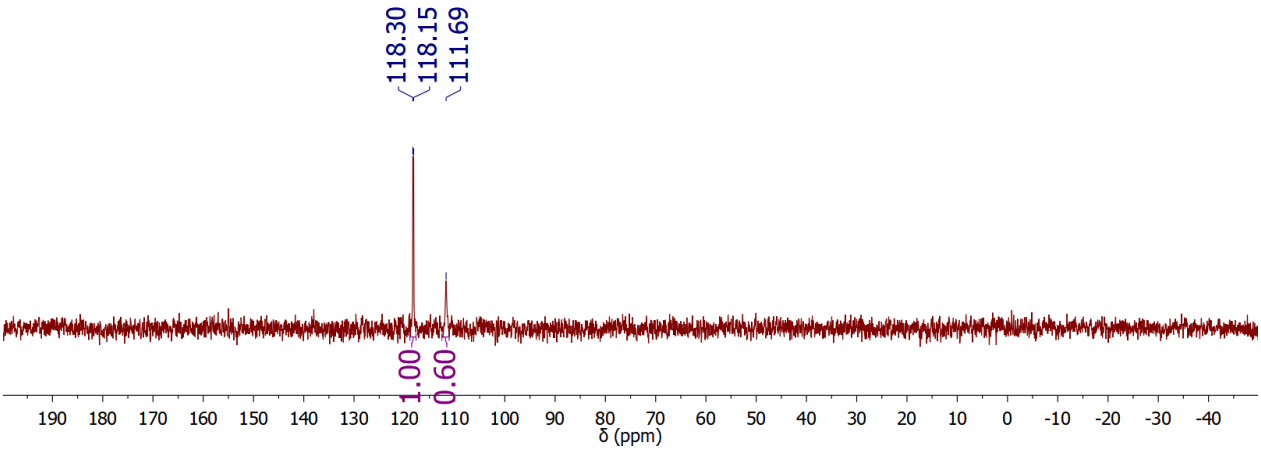

Figure A.22. ^{31}P NMR spectrum of [(P_2P^{Ph})Fe(NNSi^{i}Pr$_3$)]K (**11**-NNSi^{i}Pr$_3$) in C_6D_6 at room temperature. The peaks labeled with a star correspond to residual diethyl ether.

NMR spectra of stoichiometric reactivity

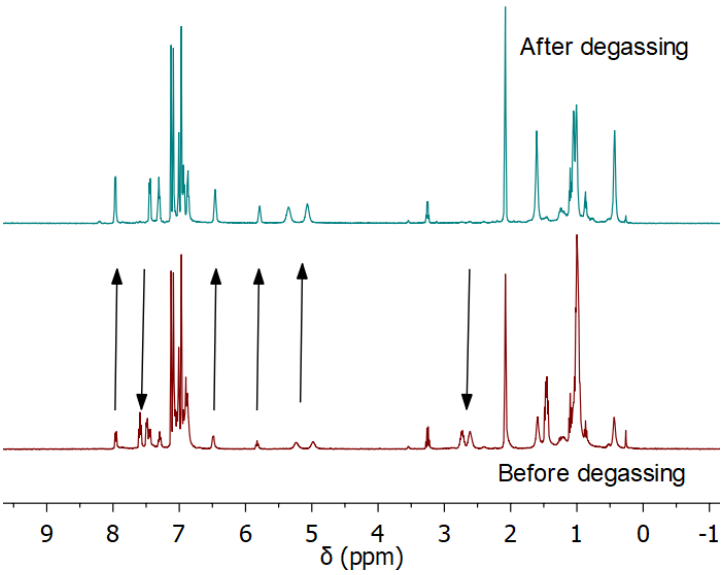

Figure A.23. ^{1}H NMR spectra of **5** before and after evacuation displaying the disappearance of **5** and the increased intensity of **6**.

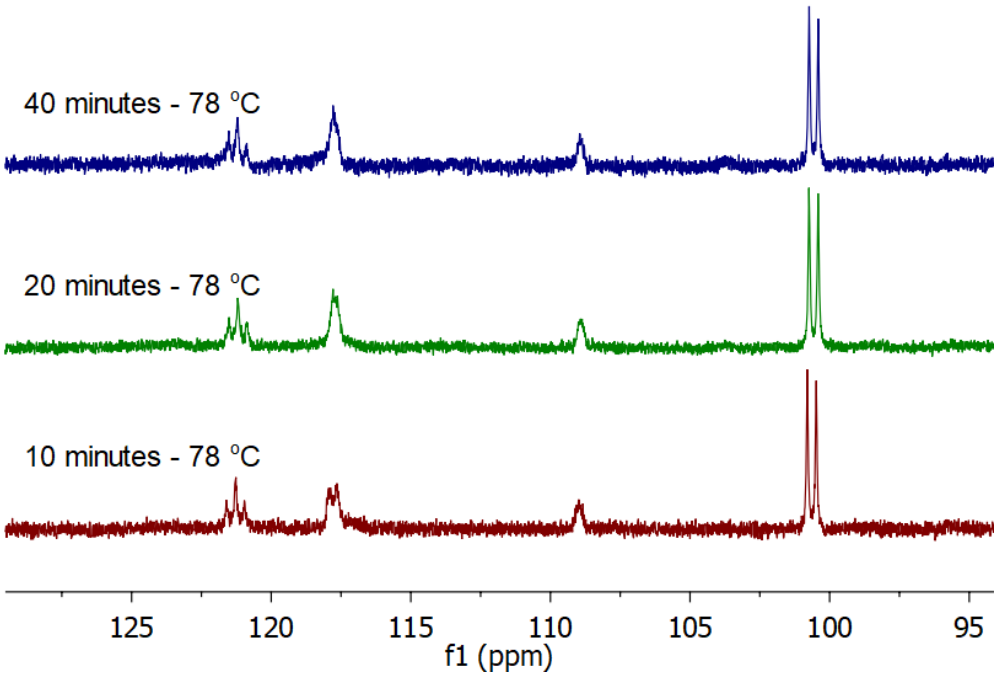

Figure A.24. ^{31}P NMR spectra of the addition of H_2 to **5** before at −78 °C. The ratios between **5** and **2 (**indicated by a star) remain virtually the same upon storing the sample at −78 °C

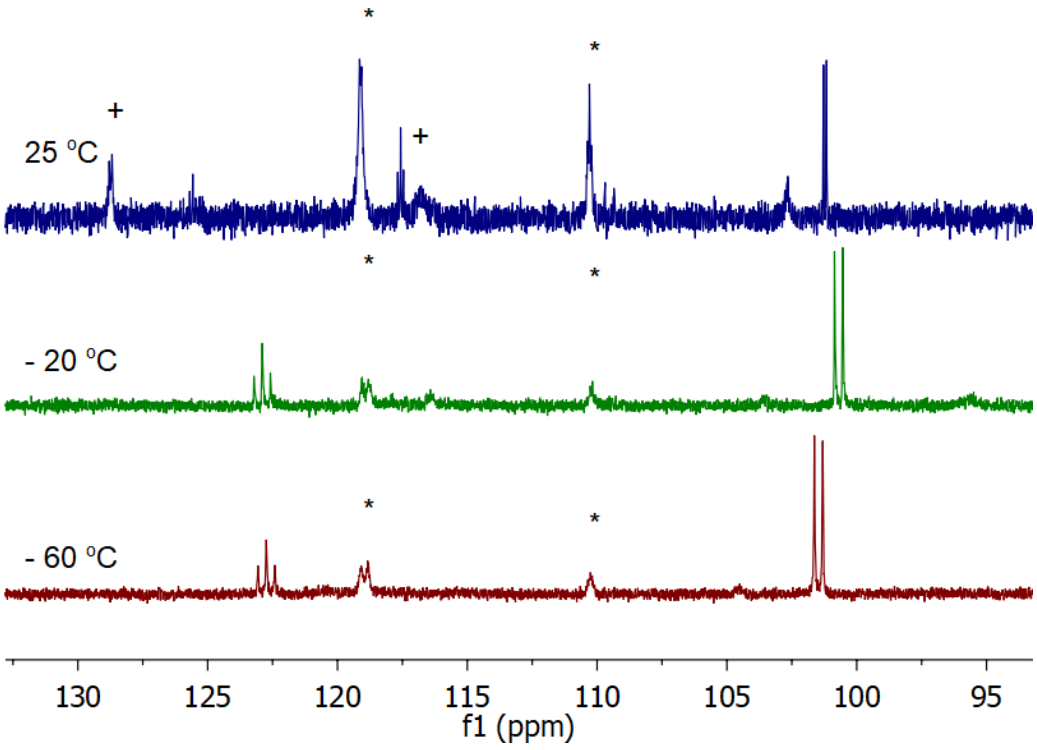

Figure A.25. ^{31}P NMR spectra of the addition of H_2 to **5** before at various temperatures. After the initial formation of **2** (indicated by a star), no appreciable reactivity was observed until the sample was warmed above −20 °C and a rapid change was observed at room temperature. The peaks labeled with (+) are likely due to the formation of "(P-$_2$P^{Ph})Fe(H_2)$(H)_2$ as they disappear after addition of N_2.

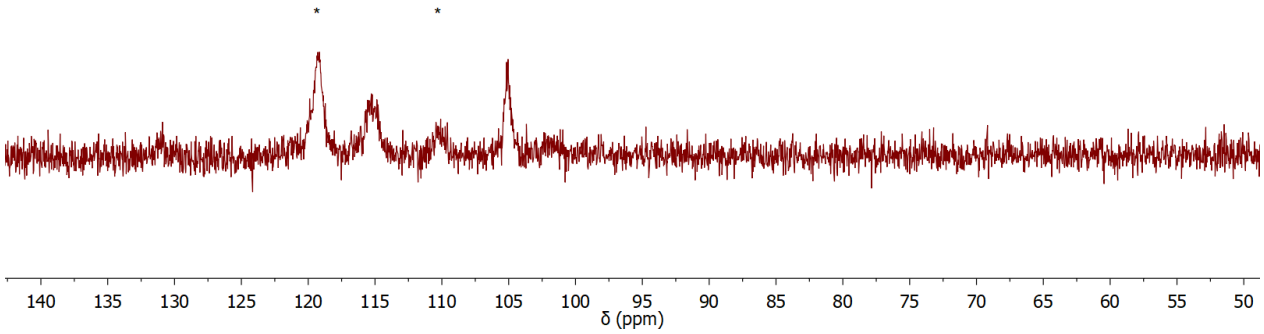

Figure A.26. ^{31}P NMR spectrum of the addition of H_2 to **6** before at various temperature. Addition of H_2 results in the rapid formation of **2** (indicated by a star) and an unidentified species.

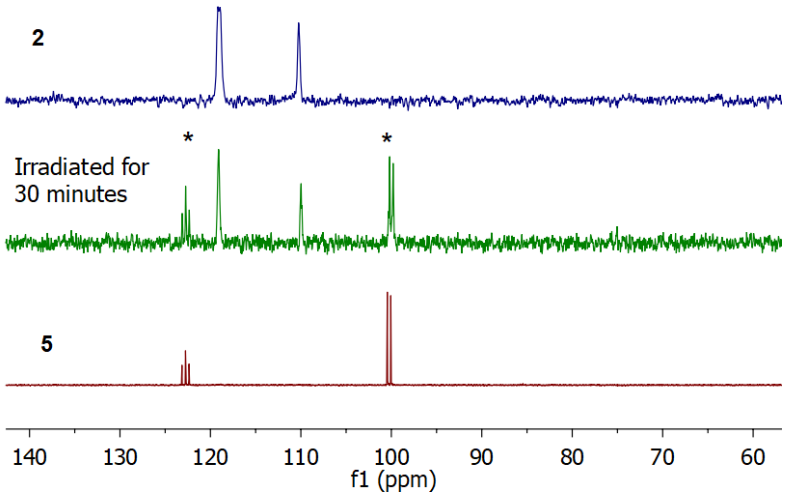

Figure A.27. ^{31}P NMR spectrum of the irradiation of **2** which results in the formation of **5**.

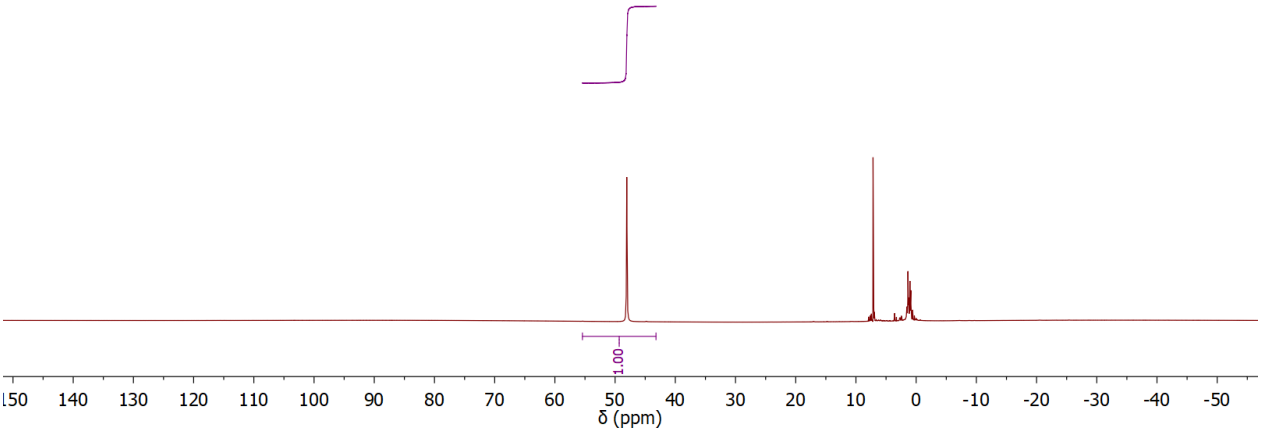

Figure A.28. ^{1}H NMR spectrum of the oxidation of [(P_2P^{Ph})Fe(NNTMS)]K with [Cp^*_2Co][PF_6] at room temperature.

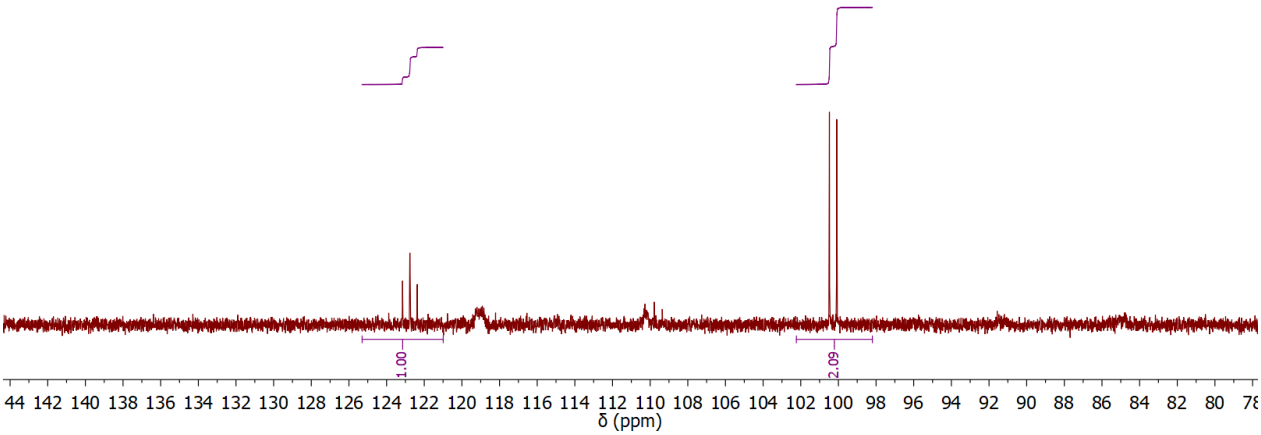

Figure A.29. ^{31}P NMR spectrum of the oxidation of [(P_2P^{Ph})Fe(NNTMS)]K with [Cp^*_2Co][PF_6] at room temperature with the characteristic features of **5**.

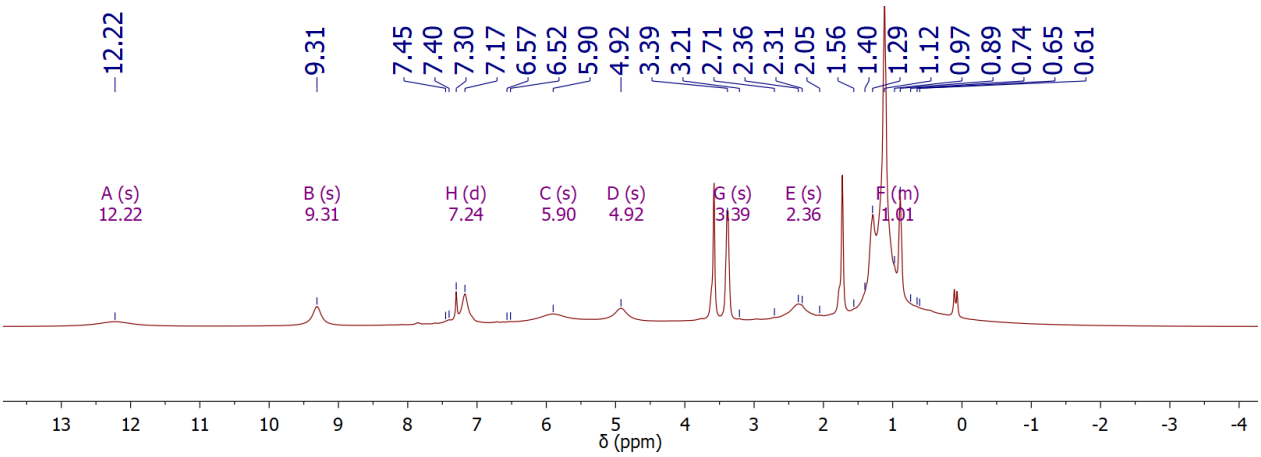

Figure A.30. ^{1}H NMR spectrum of the oxidation of [(P_2P^{Ph})Fe(NNTiPS)]K with [Cp^*_2Co][PF_6]

Fitting VT NMR data

The chemical shifts of the NMR active nuclei in **6** can be fit to a general equation accounting for the population of an excited state with equation S1:

$$\delta = \delta_o + \frac{B * (e^{\frac{2J}{kT}} + 5e^{\frac{6J}{kT}})}{(1 + 3e^{\frac{2J}{kT}} + 5e^{\frac{6J}{kT}}) * T} \qquad \textbf{S1}$$

Herein, δ is the observed chemical shift for a nucleus at a given temperature, δ_o is the chemical shift of that atom in the ground state, B is a fitting constant, and 2J and 6J (as obtained for a Heisenberg–Dirac–VanVleck Hamiltonian in the notation $H = -2JS_1 \cdot S_2$) correspond to the energy difference between the singlet and triplet, or the singlet and quintet states respectively. The theoretical framework for the use of this equation is described by Pfirrman *et al*.[9] Similar estimations of singlet–triplet gaps have been estimated for various systems.[9–13] One should note that such a large singlet triplet splitting (corresponding to a thermal energy of E/*k* = 2717 K) can be hardly detected by usual static magnetic susceptibility measurements as the thermal population of the triplet at 298 K is only about 0.034 % and the quintet is $6.7 \cdot 10^{-10}$ %.[9]

Overlap of three aromatic signals with toluene-d_8 hampered their analysis and therefore only ten out of the thirteen signals, expected in C_s symmetry, could be tracked reliably over the measured temperature range. The temperature-dependent shift of these ten signals were simultaneously fit to equation S1 to give one value for J (−940 ± 9.4 cm^{-1}), ten chemical shifts corresponding to the ground state and ten fitting constants. The obtained fitting parameters are summarized in Table A1. As expected, the chemical shifts observed at 201 K are close to those determined for the ground state.

Table A.1. Fit parameters for the chemicals shift of 6

δ (ppm) at 201 K	δ_o (ppm)	B (10^5)
7.73	7.76 ± 0.02	5.4 ± 0.7
7.53	7.54 ± 0.02	-2.3 ± 0.6
7.46	7.51 ± 0.02	-26.9 ± 2.3
6.95	7.84 ± 0.02	-32.5 ± 2.7
2.49	2.41 ± 0.02	68.1 ± 5.7
1.83	1.73 ± 0.03	93.3 ± 7.7
1.38	1.35 ± 0.02	7.2 ± 0.8
1.31	1.24 ± 0.02	-3.9 ± 0.6
0.95	0.92 ± 0.02	2.8 ± 0.6
0.68	0.71 ± 0.02	-7.1 ± 0.8

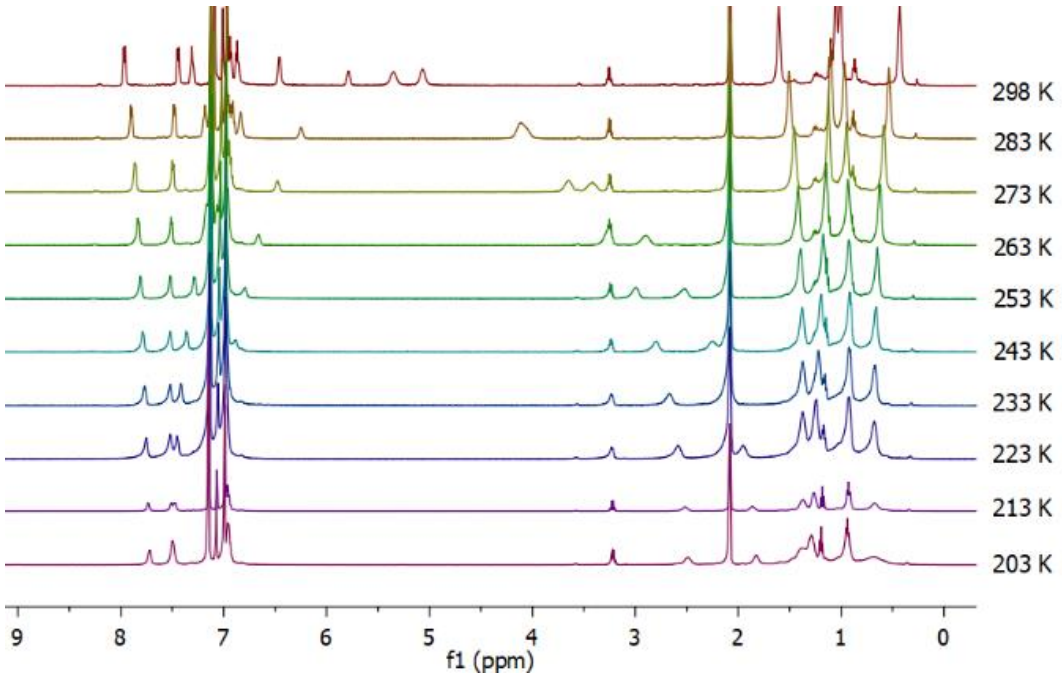

Figure A.31. Selected ^{1}H NMR spectra of **6** in d8-toluene plotted at various temperatures.

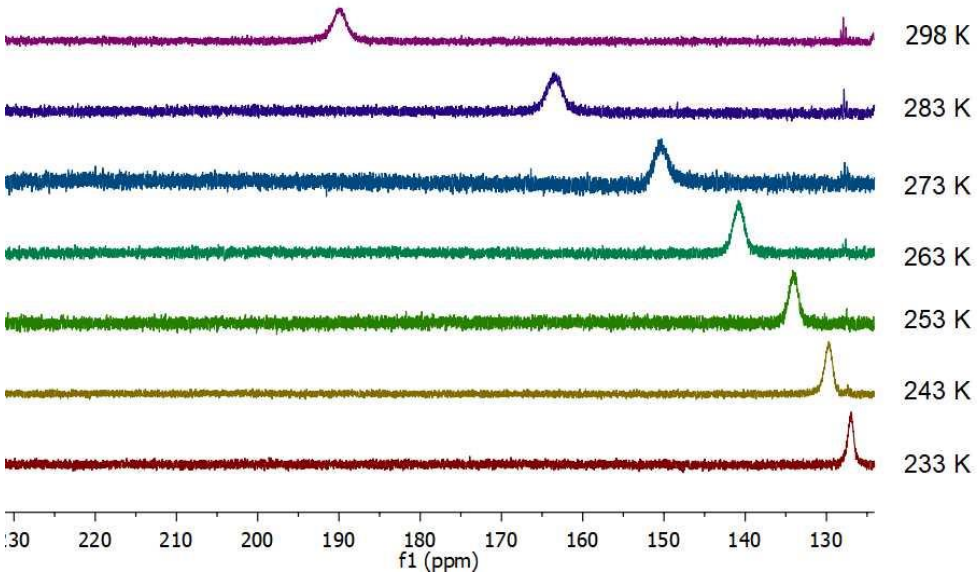

Figure A.32. Selected ^{31}P NMR spectra of **6** d8-toluene plotted at various temperatures.

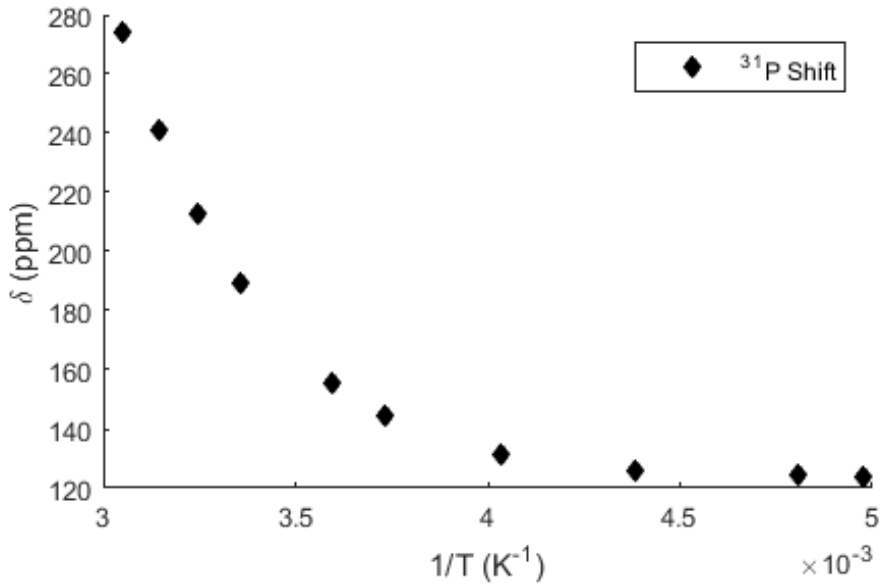

Figure A.33. ^{31}P NMR chemical shifts of **6** plotted as a function of 1/T.

IR Spectra

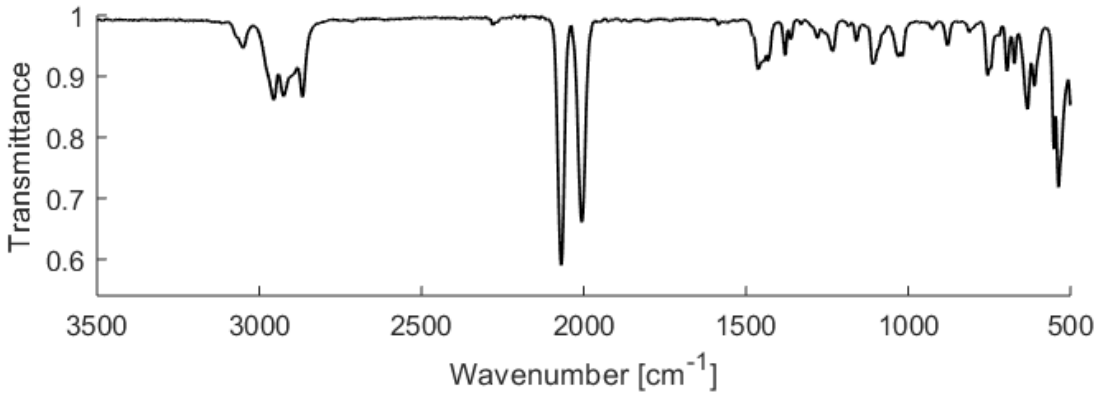

Figure A.34. IR spectrum of $(P_2P^{Ph})Fe(N_2)_2$ (**5**) (thin-film from C_6D_6 solution).

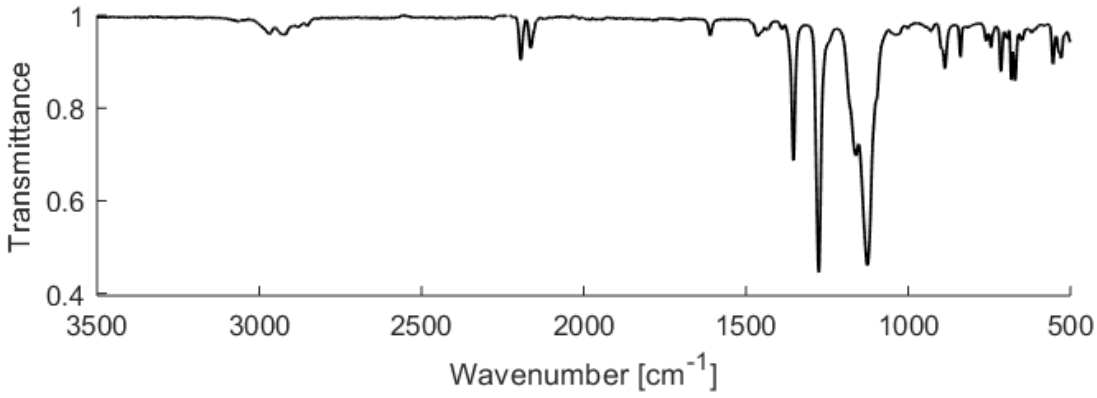

Figure A.35. IR spectrum of $[(P_2P^{Ph})Fe(N_2)_2(H)][BAr^F]$ (**7**) (thin-film from d8-THF solution).

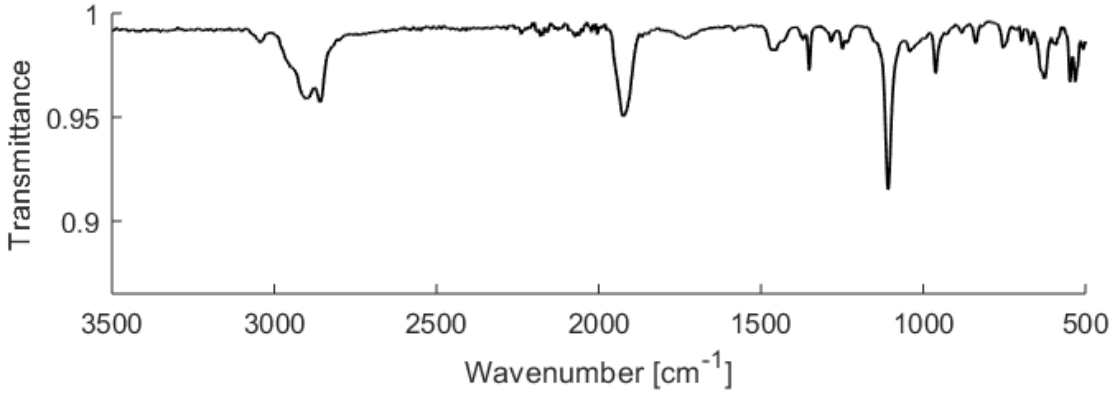

Figure A.36. IR spectrum of [(P_2P^{Ph})Fe(N_2)(H)][K(18-crown-6)] (**8**) (thin-film from d8-THF solution).

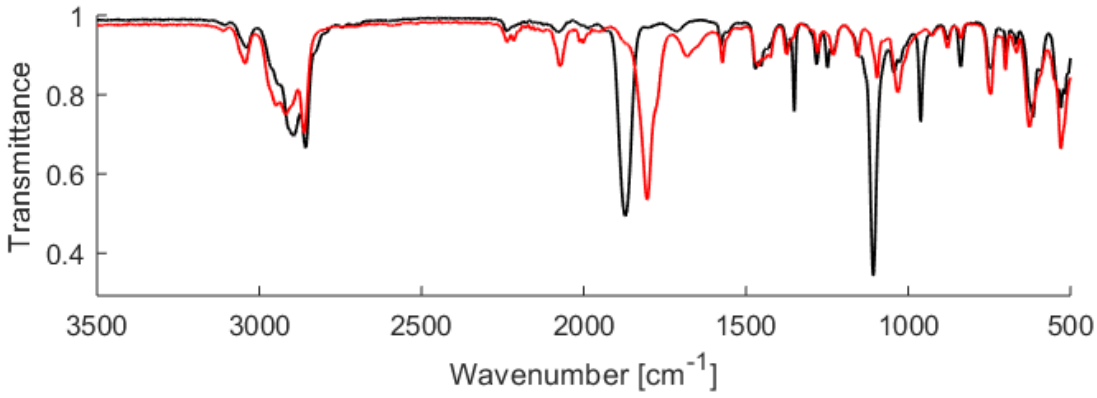

Figure A.37. IR spectrum of [(P_2P^{Ph})Fe(N_2)][K(18-crown-6)] (**9**) in black (thin-film from d8-THF solution) and the spectrum of [(P_2P^{Ph})Fe(N_2)][K$(THF)_x$] recorded of a crude mixture before the addition of 18-crown-6.

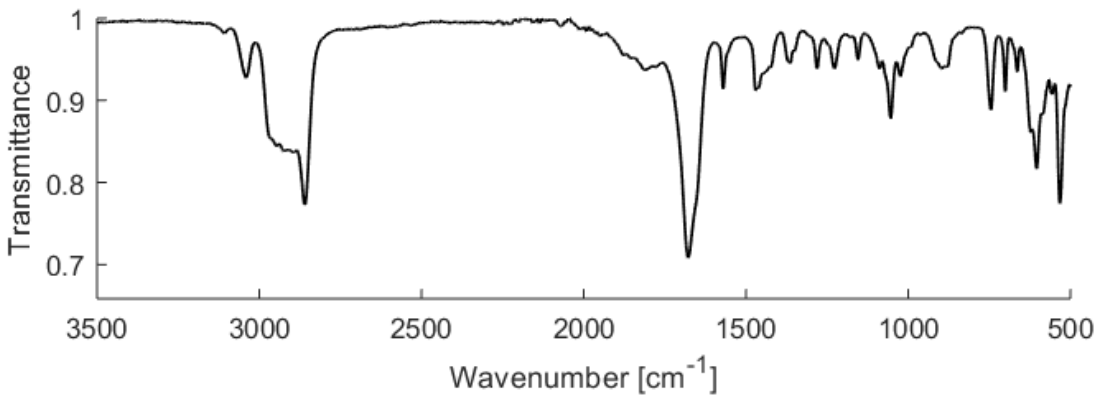

Figure A.38. IR spectrum of $[(P_2P^{Ph})Fe(N_2)][K_2(THF)_3]$ (**10**) (thin-film from THF solution).

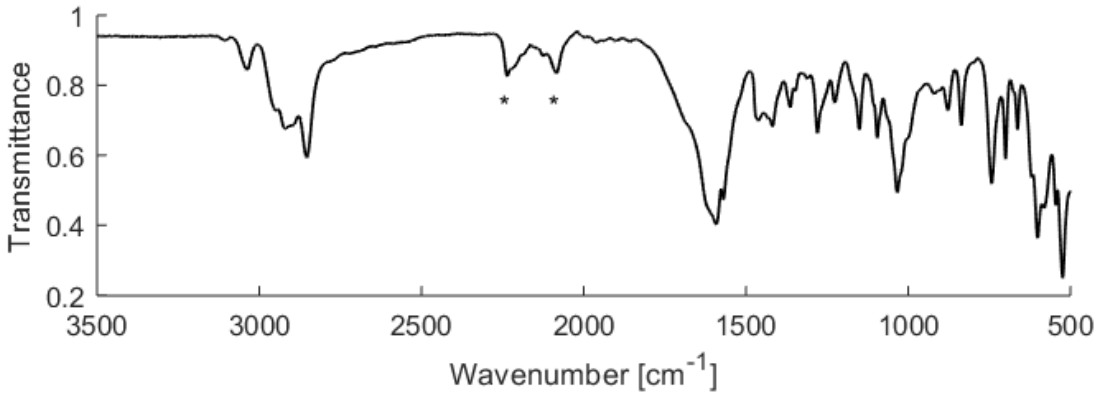

Figure A.39. IR spectrum of $[(P_2P^{Ph})Fe(^{15}N_2)][K_2(THF)_3]$ (**10**) (thin-film from d8-THF solution). Bands marked with a star correspond to d8-THF.

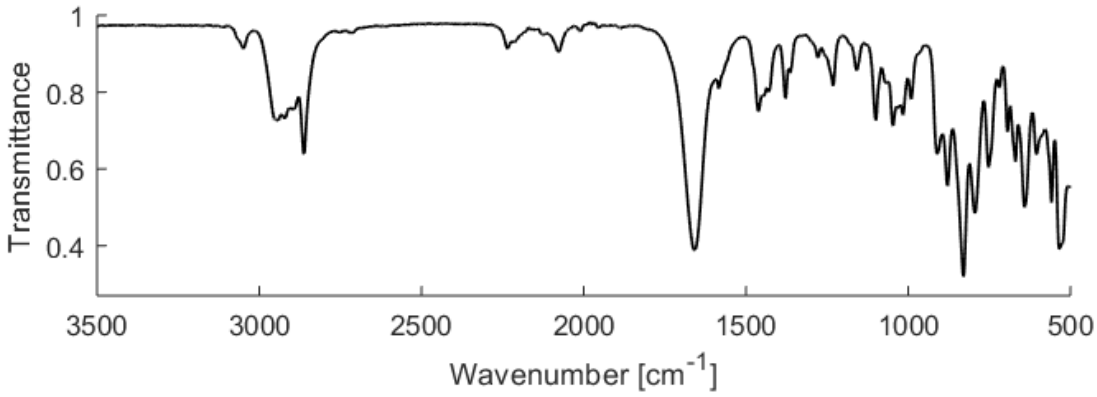

Figure A.40. IR spectrum recorded after the irradiation of $(P_2P^{Ph})Fe(NNSi^iPr_3)$ (**12-NNSi^{i}Pr$_3$**) (thin-film from d8-THF solution).

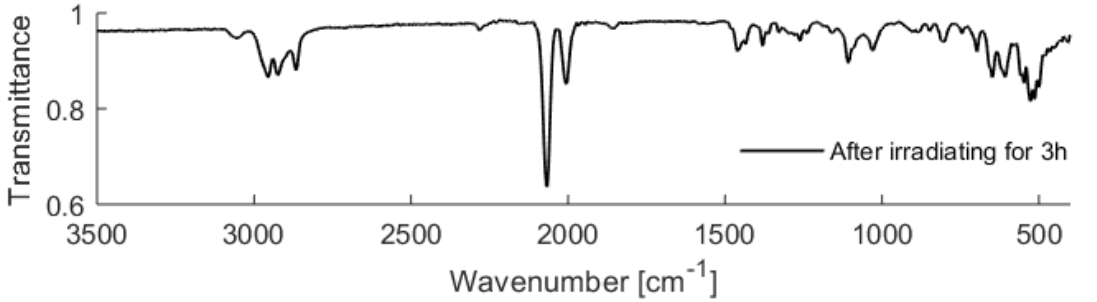

Figure A.41. IR spectrum recorded after the irradiation of $(P_2P^{Ph})Fe(N_2)(H_2)$ (**2**) (thin-film from C_6D_6 solution).

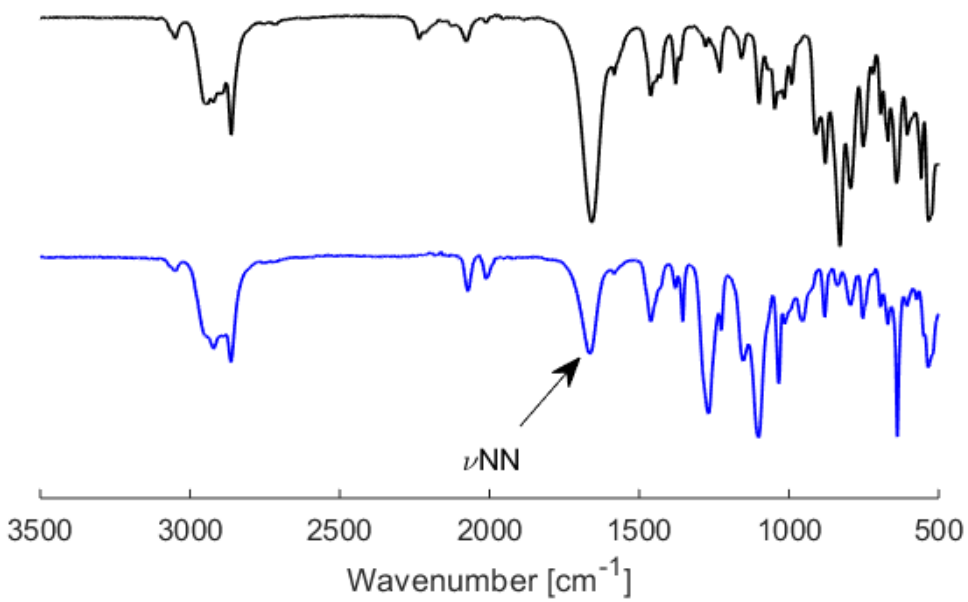

Figure A.42. Thin-film IR spectra of **12**-NNSi^{i}Pr$_3$ with νNN in black and the addition of ^{i}Pr$_3$SiOTf to **9** in blue.

Cyclic Voltammograms

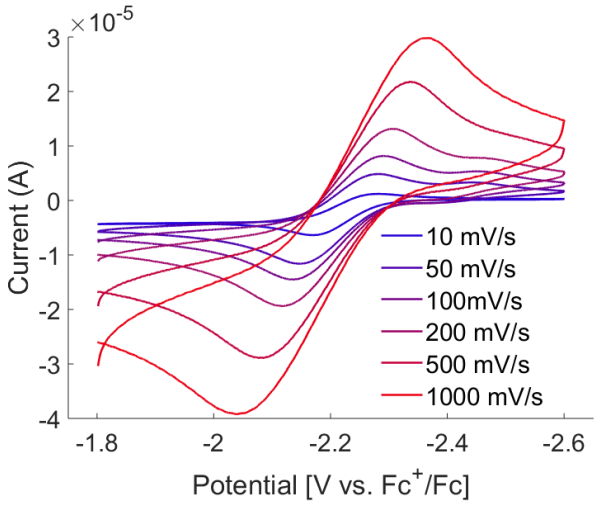

Figure A.43. Scan rate dependence of the wave observed at −2.4 V in the cyclic voltammogram of [(P_2P^{Ph})Fe(N_2)(H)][K(18-crown-6)] (**8**) scanning in the anodic direction.

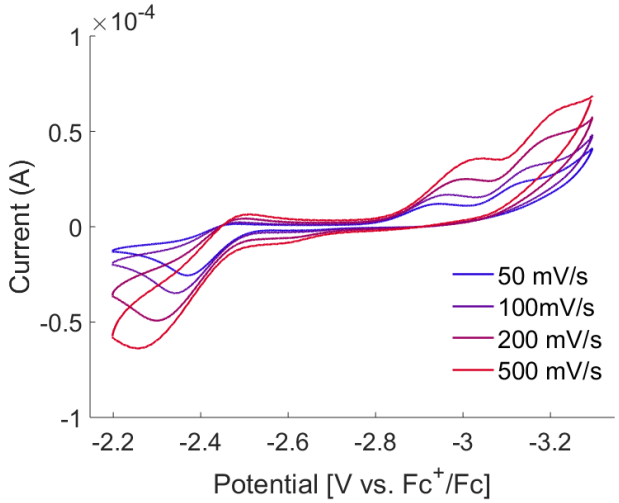

Figure A.44. Cyclic voltammogram of [(P_2P^{Ph})Fe(N_2)][K(18-crown-6)] (**9**) scanning in the cathodic direction.

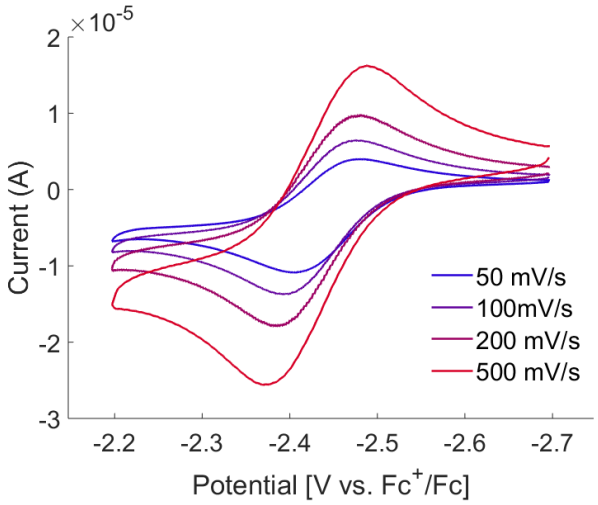

Figure A.45. Scan rate dependence of the r4 observed at −2.4 V in the voltammogram of $[(P_2P^{Ph})Fe(N_2)][K(18\text{-crown-6})]$ (**9**).

EPR Spectra

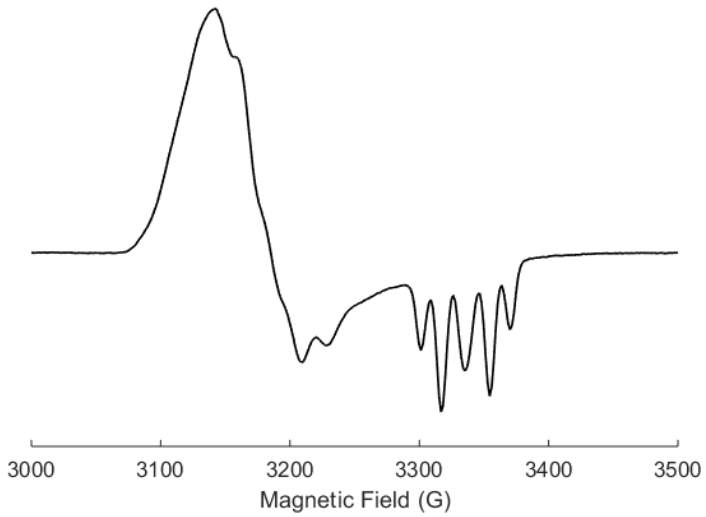

Figure A.46. EPR spectrum of [(P_2P^{Ph})Fe(N_2)][K(18-crown-6)] in 2-MeTHF, at 77 K, microwave frequency 9.39 GHz, microwave power 6.47 mW.

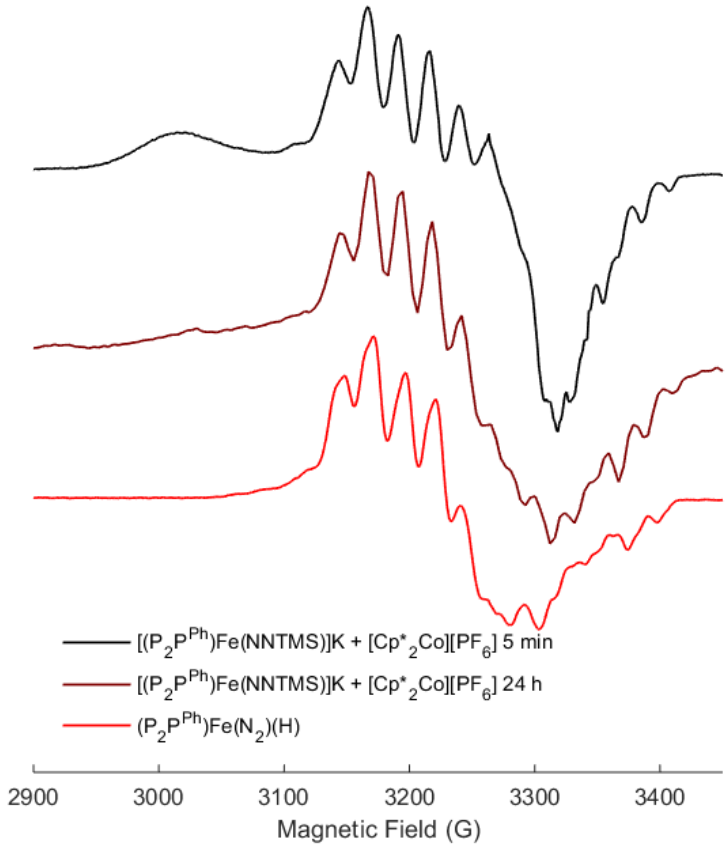

Figure A.47. EPR spectra of the oxidation of $[(P_2P^{Ph})Fe(NNSiMe_3)]K$ with $[Cp^*_2Co][PF_6]$ in THF at different time points and the EPR spectrum of $(P_2P^{Ph})Fe(N_2)(H)$.

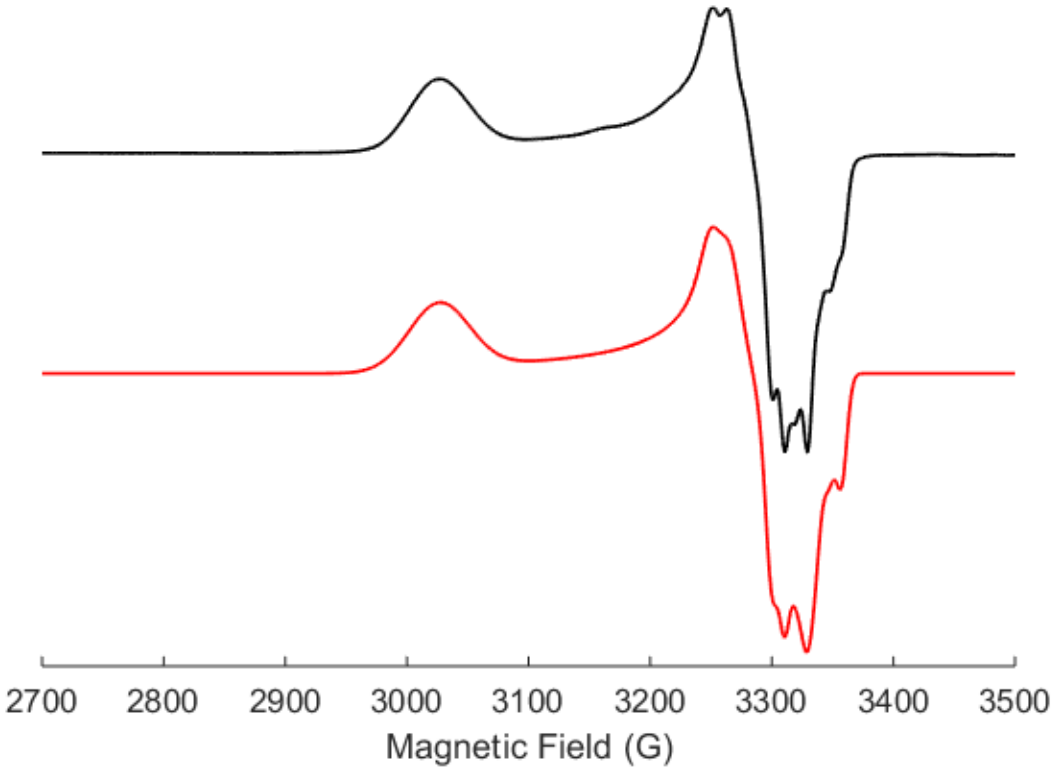

Figure A.48. EPR spectrum of the oxidation of [(P_2P^{Ph})Fe(NNSi^{i}Pr$_3$)]K (**11-**NNSi^{i}Pr$_3$) and [Cp*$_2$Co][PF_6] resulting in the formation of (P_2P^{Ph})Fe(NNSi^{i}Pr$_3$) (**12-**NNSi^{i}Pr$_3$) andd fit of the spectrum in respectively black and red. Simulation parameters: g = [2.213 2.041 2.012], P = [0 40.3 57.1] P = [0 40.3 75.0] P = [0 69.4 29.0] Hstrain = [1180 50 30].

Mössbauer Spectra

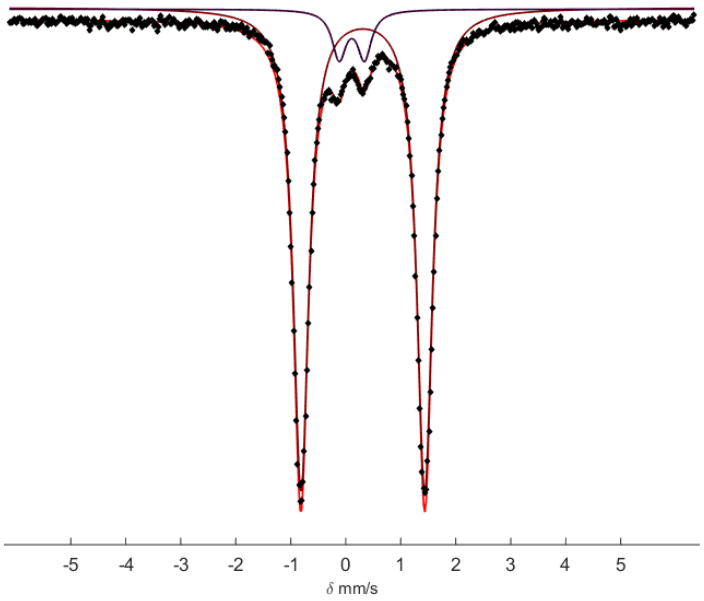

Figure A.49. Mössbauer spectrum collected of $(P_2P^{Ph})Fe(N_2)_2$ (**5**) at 80 K Raw data shown as black points, overall simulation as a red line. The major species, **5**, in purple is fit as a doublet ($\delta = 0.31$ mm s^{-1}, $\Delta E_Q = 2.16$ mm s^{-1}). The minor species (~ 5%) in blue was fit as a doublet ($\delta = 0.10$ mm s^{-1}, $\Delta E_Q = 0.45$ mm s^{-1}).

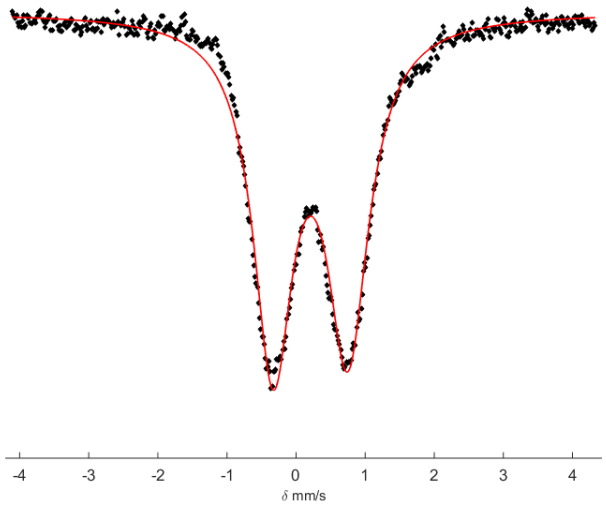

Figure A.50. Mössbauer spectrum collected of $[(P_2P^{Ph})Fe(N_2)_2(H)][BAr^F{}_4]$ (**7**) at 80 K Raw data shown as black points, overall simulation as a red line. $\delta = 0.21$ mm s^{-1}, $\Delta E_Q =$ 1.08 mm s^{-1}.

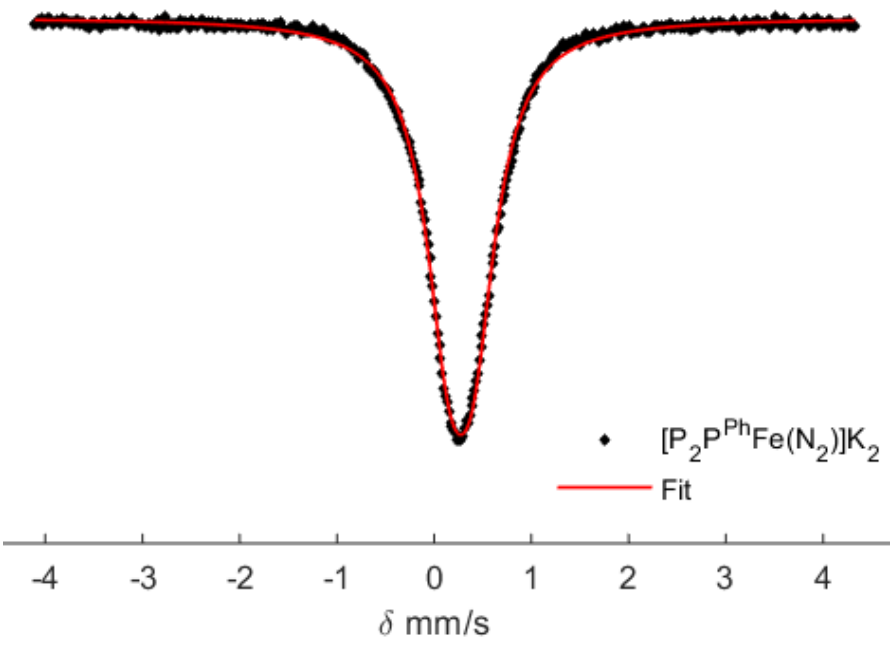

Figure A.51. Mössbauer spectrum collected of $[(P_2P^{Ph})Fe(N_2)]K_2(THF)_3]$ (**10**) at 80 K Raw data shown as black points and simulated spectrum in red (δ = 0.27 mm s^{-1}, ΔE_Q = 0.26 mm s^{-1}).

UV-vis Spectra

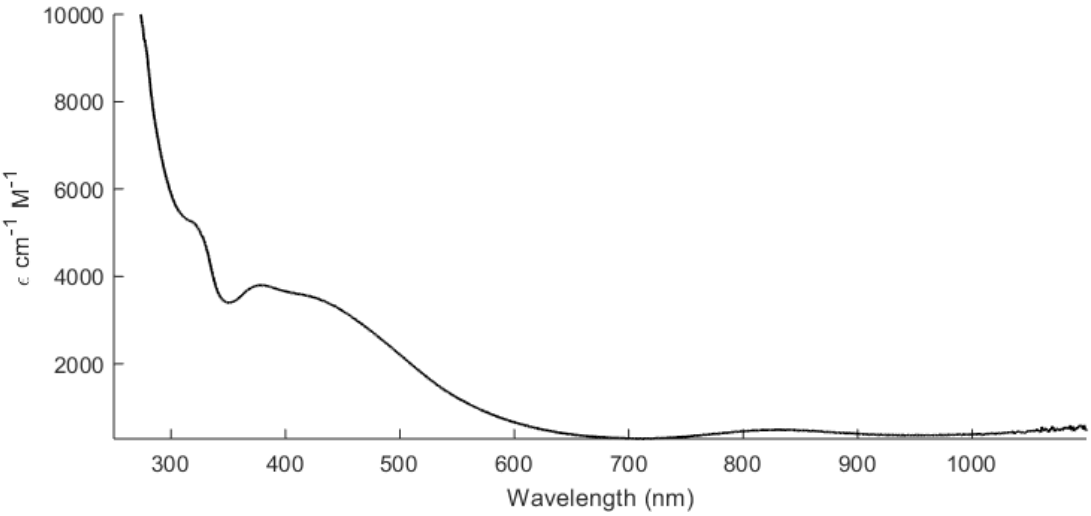

Figure A.52. UV-visible spectrum of (P_2P^{Ph})FeBr (**4**) THF, 293 K).

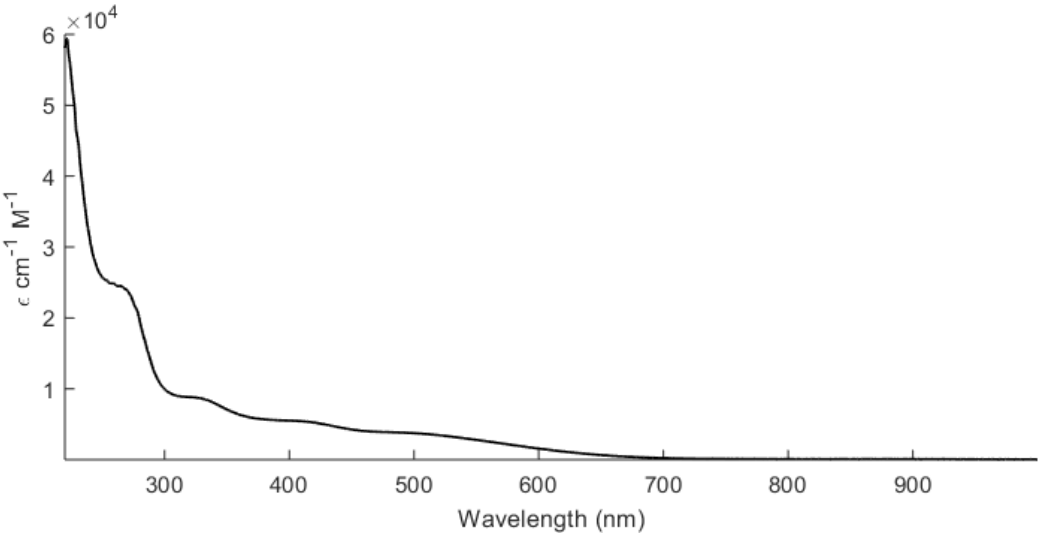

Figure A.53. UV-visible spectrum of (P_2P^{Ph})Fe(N_2)$_2$ (**5**) (Et_2O, 293 K).

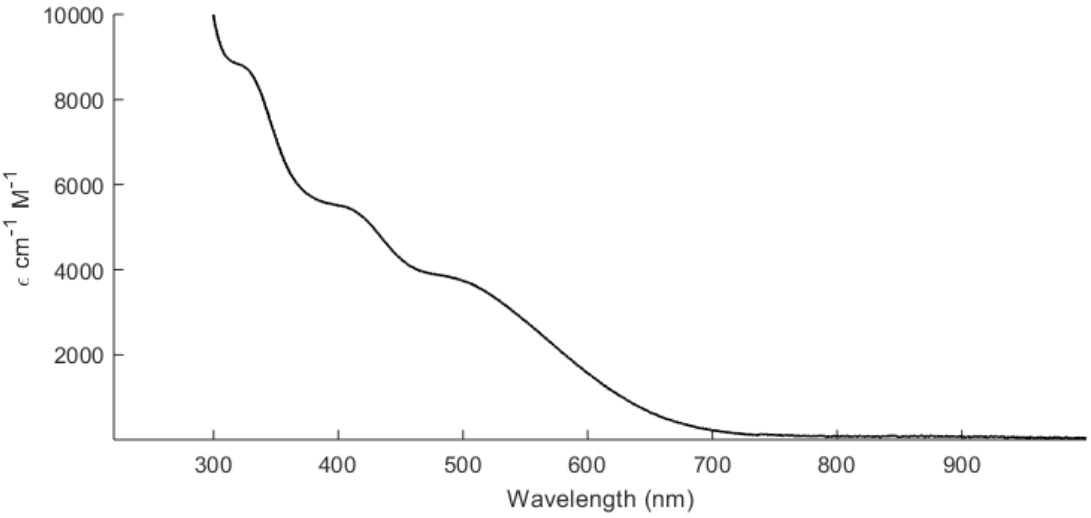

Figure A.54. UV-visible spectrum of $(P_2P^{Ph})Fe(N_2)_2$ (**5**) (Et_2O, 293 K).

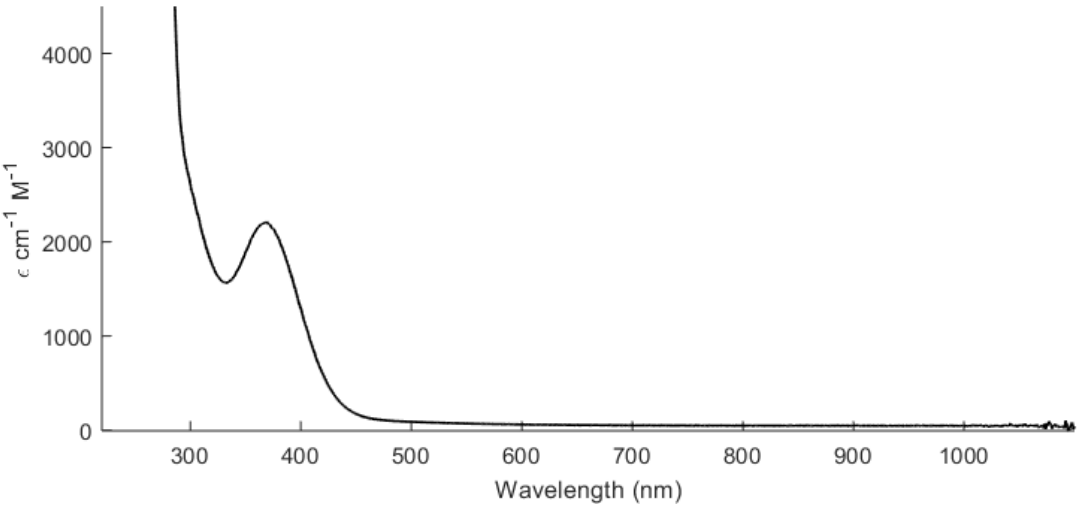

Figure A.55. UV-visible spectrum of $[(P_2P^{Ph})Fe(N_2)_2(H)][BAr^F{}_4]$ (**7**) (Et_2O, 293 K).

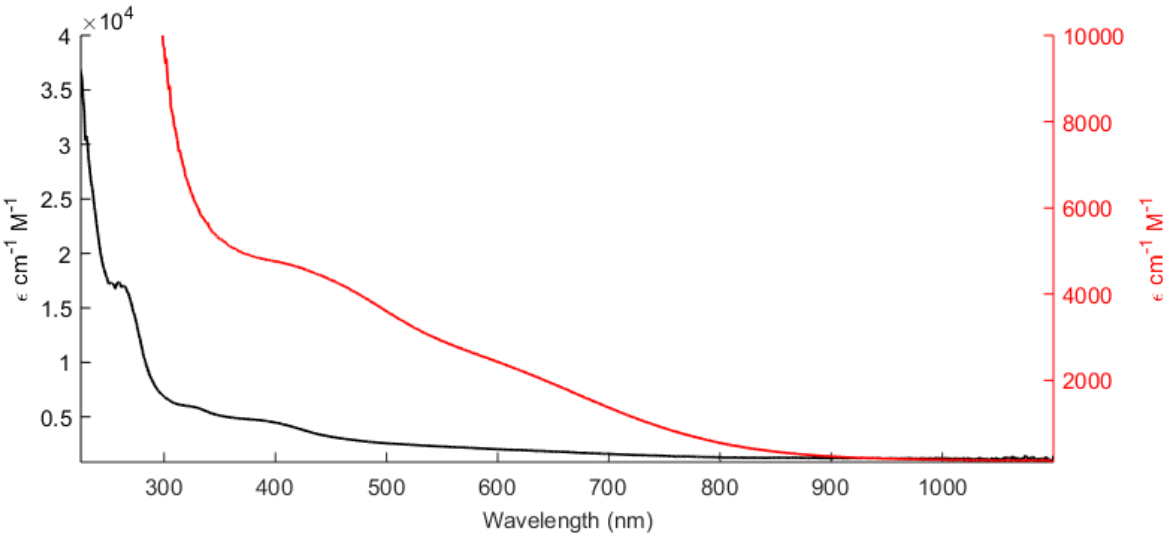

Figure A.56. UV-visible spectrum of [(P_2P^{Ph})Fe(N_2)(H)][K(18-crown-6)] (**8**) (2-MeTHF, 293 K). Black trace corresponds to the left axis scale, while the red trace corresponds to the right axis scale.

Catalytic experiments

Standard NH3 Generation Reaction Procedure. All solvents were stirred with Na/K for ≥1 hour and filtered through alumina prior to use. In a nitrogen-filled glovebox, a stock solution of the catalyst in THF (6.8 mM) was prepared. (Note: a fresh stock solution was prepared for each experiment and used immediately.) An aliquot of this stock solution (90 or 270 μL, 0.6 or 1.82 μmol) was added to a Schlenk tube and evaporated to dryness under vacuum to give a thin film of the precatalyst. The tube was allowed to cool to 77 K in the glovebox cold well. To the cold tube was added a solution of $[H(OEt_2)_2][BAr^F{}_4]$ (93 mg, 0.092 mmol) in Et_2O (0.5 mL). This solution was allowed to freeze before the vial which contained the $HBAr^F{}_4$ was rinsed with an additional 0.5 mL of Et_2O and added to the tube. After the acid layer froze, a suspension of KC_8 (15 mg, 0.111 mmol) in 0.5 mL of Et_2O (1.2 equiv. relative to $[H(OEt_2)_2][BAr^F{}_4]$) was added to the cold tube. A stir bar was added to the tube and the tube sealed with a Teflon screw-valve. The temperature of the system was allowed to equilibrate for 5 minutes. The Schlenk tube was passed out of the box into a liquid N_2 bath and transported to a fume hood. The reaction vessel was subsequently transferred to a dry ice/acetone bath where it thawed to -78 °C and was allowed to stir for at least 1 hour. The tube was then warmed to room temperature while stirring and subsequently stirred at room temperature for 5 minutes.

Standard NH3 Generation Reaction with Hg Lamp Photolysis Procedure. Preparation of the Schlenk tube containing reactants was performed as described for runs without light. The cold reaction vessel was transferred to a dry ice/isopropanol bath which was positioned

under a Hg lamp and turned on 1 minute prior to transfer of the Schlenk tube to the bath. The entire reaction apparatus was surrounded by aluminum foil and the reaction vessel was stirred for at least 1 hour before the Hg lamp was turned off and the Schlenk tube was allowed to warm to room temperature with stirring and stirred at room temperature for 5 minutes.

Ammonia Quantification. The catalytic reaction mixture was cooled to 77 K and allowed to freeze. The reaction vessel was opened to the atmosphere and to the frozen solution was slowly added a fourfold excess (with respect to acid) solution of a NaO*t*Bu in MeOH (0.25 M) over 1–2 minutes. The solution was allowed to freeze, then the tube was sealed, evacuated and allowed to warm to room temperature and stirred at room temperature for 10 minutes. An additional Schlenk tube was charged with HCl (3 mL of a 2.0 M solution in Et_2O, 6 mmol) to serve as a collection flask. The volatiles of the reaction mixture were vacuum transferred into the collection flask. After completion of the vacuum transfer, the collection flask was sealed and warmed to room temperature. Solvent was removed *in vacuo*, and the remaining residue dissolved in H_2O (1 mL) to make a stock solution that was used for ammonia quantification. An aliquot of this solution (20 μL) was then analyzed for the presence of NH_3 (present as NH_4Cl) by the indophenol method. Quantification was performed with UV−Vis spectroscopy by analyzing the absorbance at 635 nm.

Yields of Independent Catalytic Runs

Table A.2. Results of individual runs using 4 at 150 equiv. acid loading with no Hg lamp irradiation.

Run	Absorbance	Equiv. NH_3/Fe	% Yield (Based of H^+)
A	0.017	0.86	1.7
B	0.022	0.63	1.3

Table A.3. Results of individual runs using **5** at 50 equiv. acid loading with no Hg lamp irradiation.

Run	Absorbance	Equiv. NH_3/Fe	% Yield (Based of H^+)
A	0.401	5.09	30.6
B	0.399	5.06	30.4

Table A.4. Results of individual runs using **5** at 150 equiv. acid loading with no Hg lamp irradiation.

Run	Absorbance	Equiv. NH_3/Fe	% Yield (Based of H^+)
A	0.171	6.40	12.8
B	0.152	5.66	11.3

Table A.5. Results of individual runs using **5** at 150 equiv. acid loading with Hg lamp irradiation.

Run	Absorbance	Equiv. NH_3/Fe	% Yield (Based of H^+)
A	0.240	8.83	17.7
B	0.315	12.01	24.0
C	0.207	7.78	15.6

Table A.6. Results of individual runs using **5** at 150 equiv. acid loading with one equiv. TBABr added.

Run	Absorbance	Equiv. NH_3/Fe	% Yield (Based of H^+)
A	0.055	1.88	3.8
B	0.072	2.55	5.1

Table A.7. Results of individual runs using **5** with 150 equiv. Ph_2NH_2OTf with no Hg lamp irradiation.

Run	Absorbance	Equiv. NH_3/Fe	% Yield (Based of H^+)
A	0.019	0.51	1.0
B	0.018	0.46	0.9

General Procedure for Time-resolved H_2 Quantification: Inside of a nitrogen filled glovebox, the Fe precursor (**2** or **5**, 1.5 μmol) was added to a 300 mL Schlenk flask as a solution in THF, and subsequently deposited as a thin film in a Schlenk flask by removing the solvent in vacuo. To this flask was added solid $HBAr^F_4$ (0.23 mmol), KC_8 (0.28 mmol), and a stir bar. The flask was sealed with a septum at room temperature and subsequently chilled to -196 °C in the cold well of a nitrogen filled glovebox. Et_2O (3 mL) was added via syringe into the flask and completely frozen. The flask was passed out of the glovebox into a liquid N_2 bath, and subsequently thawed in a dry ice/acetone bath. The timer was set to zero as soon as the flask was transferred to the dry ice/acetone bath. The headspace of the reaction vessel was periodically sampled with a sealable gas sampling syringe (10 mL), which was immediately loaded into the GC, and analyzed for the presence of H_2(g). From these data, the percent H_2 evolved (relative to $HBAr^F_4$) was calculated, correcting for the vapor pressure of Et_2O and the removed H_2 from previous samplings. Each time course was measured from a single reaction maintained at −78 °C.

Table A.8. HER Yields

Entry	Fe precursor	Time	% Yield (Based of H^+)
A	**2**	0	0
B		5	25.9
C		25	70.7
.7D		60	74.4
E		120	72.6
F		1040	72.8
G	**5**	0	0
H		5	22.0
I		25	71.6
J		60	78.4
K		120	78.9
L		1040	79.5

General Procedure for the Preperation of Rapid-freeze-quenched Mössbauer Samples. The precatalyst was weighed into a vial (3 μmol) and dissolved in 0.5 mL Et_2O. The solvent was evaporated in a Schlenk tube to form a thin film of the precatalyst to which a stir bar was added. $HBAr^F_4$ (150 mg, 0.148 mmol) and KC_8 (24 mg, 0.178 mmol) are added as solids. The Schlenk tube was cooled to 77 K. To the cooled tube, 1 mL of Et_2O was added. The tube was then sealed with a Teflon screw tap and transferred to a prechilled cold well at − 78°C. The timer was set to zero as soon as the stir bar was freed from the thawing solvent. At the desired time, the tube was opened and the suspension was transferred to a Delrin cup pre-chilled to −78 °C using a pre-chilled pipette. The sample in the Delrin Cup was then rapidly frozen in liquid nitrogen. At this point, the frozen sample was taken outside the glovebox and mounted in the cryostat.

General Procedure for Fitting of Rapid-freeze-quench Mössbauer Samples. Simulations were constructed from the minimum number of quadrupole doublets required to attain a quality fit to the data (convergence of χ_R^2). Quadrupole doublets were constrained to be symmetric. It is known that the exact linewidths are sensitive to the particular sample, but the relative line breadth should be fairly constant. Using the non-linear error analysis algorithm provided by WMOSS, the errors in the computed parameters are estimated to be 0.02 mm s-1 for δ and 2% for ΔEq. We additionally note that in these spectra the exact percentage contributions given do not represent exact percentages. Particularly for components that represent less than 10% of the overall spectrum, these values are subject to a high degree of uncertainty; however, all the included components

are necessary to generate satisfactory fits of the data and therefore are believed to be present in the reaction mixtures.

Details of Individual of Rapid-freeze-quench Mössbauer Spectra

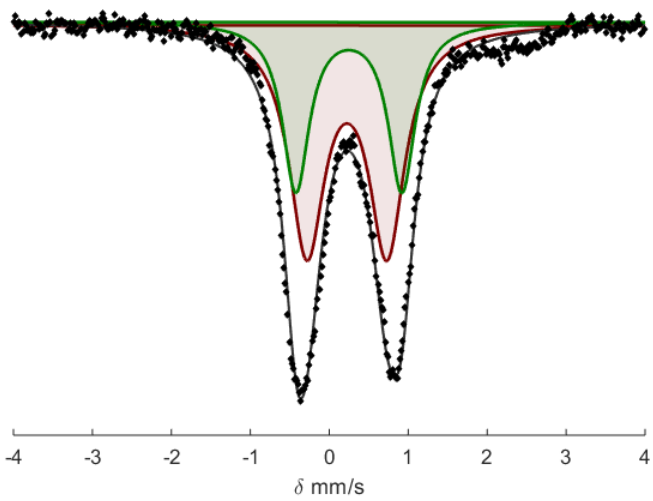

Figure A.57. Mössbauer spectrum collected after rapid-freeze-quenching a catalytic reaction after 5 minutes using $(P_2P^{Ph})Fe(N_2)(H)_2$ (**2**) as precatalyst. Raw data shown as black points, overall simulation as a grey line, with components in green and red (see Table for parameters). The spectrum was collected at 80 K with a parallel applied magnetic field of 50 mT.

Fitting details for Figure A.**57**: Various fits were attempted for the Mössbauer spectrum. The species could be fit with one quadruple doublet with a large linewidth. A better fit was obtained by fitting the spectrum with two quadrupole doublets with slightly different parameters. One of the species has parameters similar to $[(P_2P^{Ph})Fe(N_2)_2(H)][BAr^F{}_4]$ (**7**) The broad feature at 2 mm/s, present in various freeze quenched spectra, probably due to a magnetically split species, could not be fit.

Component	δ (mm s^{-1})	ΔE_Q (mm s^{-1})	Linewidths, Γ (mm s^{-1})	Relative area
A	0.22	1.01	0.54	0.63
B	0.24	1.34	0.41	0.37

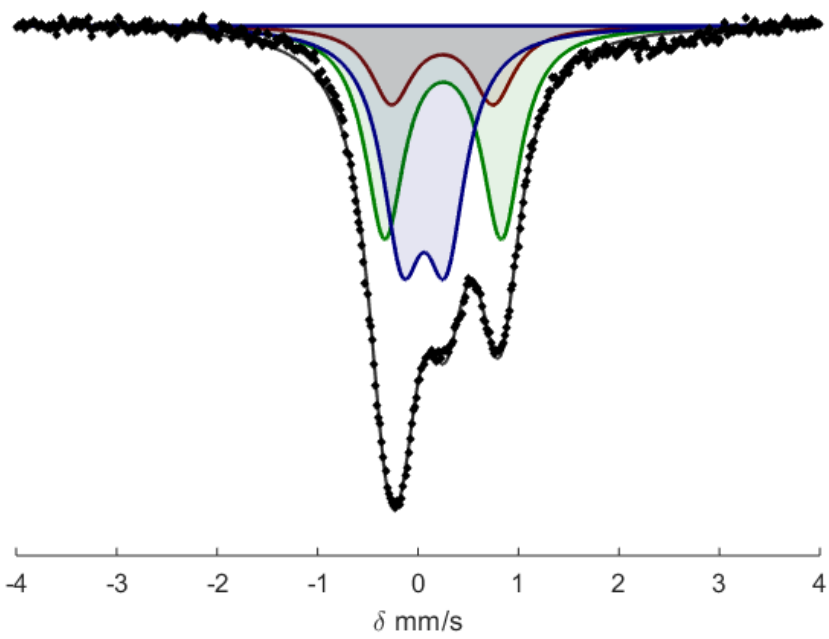

Figure A.58. Mössbauer spectrum collected after rapid-freeze-quenching a catalytic reaction after 30 minutes using $(P_2P^{Ph})Fe(N_2)(H)_2$ (**2**) as precatalyst. Raw data shown as black points, overall simulation as a grey line, with components in green, blue and red (see Table for parameters). The spectrum was collected at 80 K with a parallel applied magnetic field of 50 mT.

Fitting details for Figure A.**58**: Three quadrupole doublet were found to be necessary to obtain an adequate simulation. Two of the species could be fit with the same parameters as

required for the freeze-quenched sample measured after 5 minutes. The remaining quadrupole doublet can be well simulated as $(P_2P^{Ph})Fe(N_2)(H_2)$.

Component	δ (mm s^{-1})	ΔE_Q (mm s^{-1})	Linewidths, Γ (mm s^{-1})	Relative area
A	0.22	1.01	0.50	0.15
B	0.25	1.16	0.46	0.42
C	0.06	0.43	0.48	0.43

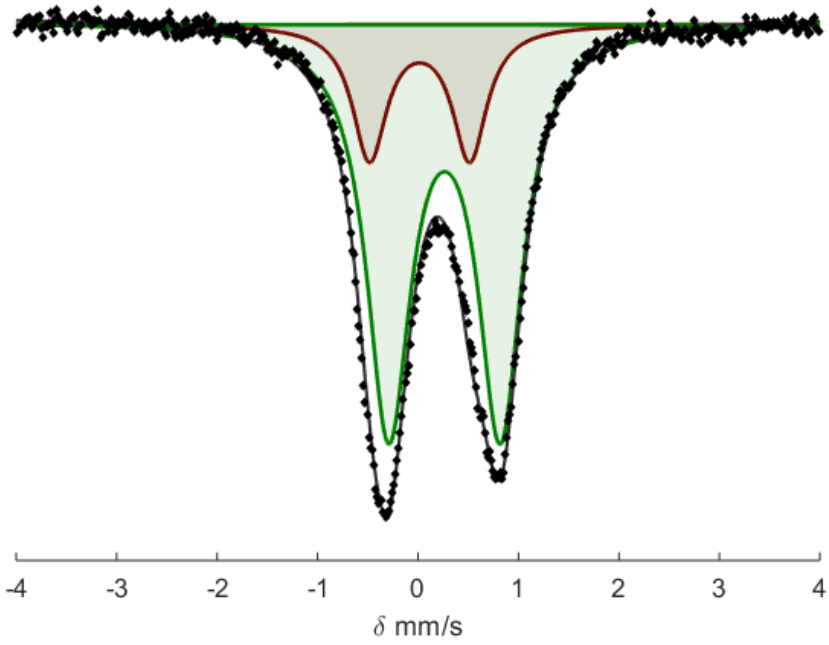

Figure A.59. Mössbauer spectrum collected after rapid-freeze-quenching a catalytic reaction after 30 minutes using $(P_2P^{Ph})Fe(N_2)_2$ (**5**) as precatalyst. Raw data shown as black points, overall simulation as a grey line, with components in green, blue and red (see Table for parameters). The spectrum was collected at 80 K with a parallel applied magnetic field of 50 mT.

Fitting details for Figure A.59. Mössbauer spectrum collected after rapid-freeze-quenching a catalytic reaction after 30 minutes using (P2PPh)Fe($_{N2}$)2 (5) as precatalyst. Raw data shown as black points, overall simulation as a grey line, with components in green, blue and red (see Table for parameters). The spectrum was collected at 80 K with a parallel applied magnetic field of 50 mT. Various fits were attempted for the Mössbauer spectrum. The species could be fit with one quadruple doublet with a large linewidth. A better fit was obtained by fitting the spectrum with two quadrupole doublets with slightly different parameters. Of the several options, one gave a species with a similar isomer shift (0.26 mm/s) and quadrupole splitting (1.12 mm/s) as observed in the reactions with **2**.

Component	δ (mm s^{-1})	ΔE_Q (mm s^{-1})	Linewidths, Γ (mm s^{-1})	Relative area
A	0.16	1.00	0.41	0.20
B	0.26	1.12	0.52	0.80

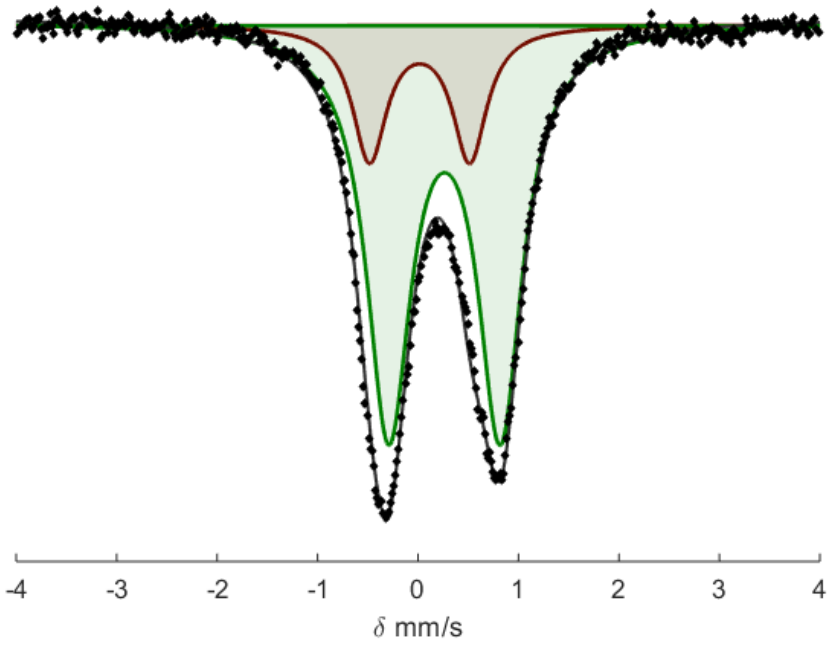

Figure A.60. Mössbauer spectrum collected after rapid-freeze-quenching a catalytic reaction after 30 minutes using (P_2P^{Ph})Fe(N_2)$_2$ (**5**) as precatalyst. Raw data shown as black points, overall simulation as a grey line, with components in green, blue and red (see Table for parameters). The spectrum was collected at 80 K with a parallel applied magnetic field of 50 mT.

Fitting details for Figure A.59. Mössbauer spectrum collected after rapid-freeze-quenching a catalytic reaction after 30 minutes using (P2PPh)Fe($_{N2}$)2 (5) as precatalyst. Raw data shown as black points, overall simulation as a grey line, with components in green, blue and red (see Table for parameters). The spectrum was collected at 80 K with a parallel applied magnetic field of 50 mT. Various fits were attempted for the Mössbauer spectrum. The species could be fit with one quadruple doublet with a large linewidth. A better fit was obtained by fitting the spectrum with two quadrupole doublets with slightly different

parameters. Of the several options, one gave a species with a similar isomer shift (0.26 mm/s) and quadrupole splitting (1.12 mm/s) as observed in the reactions with **2**.

Component	δ (mm s^{-1})	ΔE_Q (mm s^{-1})	Linewidths, Γ (mm s^{-1})	Relative area
A	0.16	1.00	0.41	0.20
B	0.26	1.12	0.52	0.80

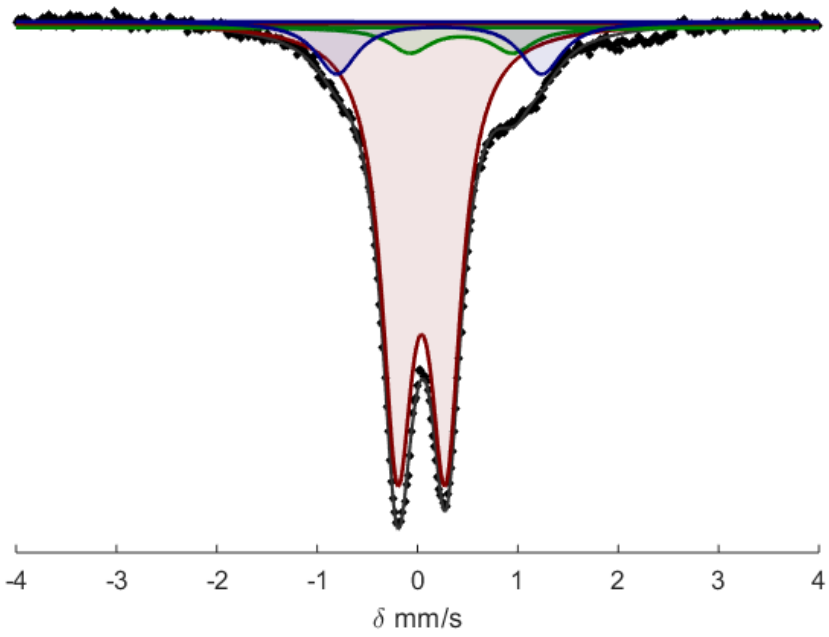

Figure A.61. Mössbauer spectrum collected from a catalytic reaction warmed to room temperature using $(P_2P^{Ph})Fe(N_2)_2$ (**5**) as precatalyst. Raw data shown as black points, overall simulation as a grey line, with components in green, blue and red (see Table for parameters). The spectrum was collected at 80 K with a parallel applied magnetic field of 50 mT.

Fitting details for Figure A.**61**: Three quadrupole doublet were found to be necessary to obtain an adequate simulation. The major species in the spectrum can be well simulated as $(P_2P^{Ph})Fe(N_2)(H_2)$. The residual signal exhibits two quadrupole doublets and a broad feature. The broad feature, potentially due to a magnetically split species, could not be fit. The remaining quadrupole doublets could be fit as two species with respective areas of 0.05 and 0.13.

Component	δ (mm s^{-1})	ΔE_Q (mm s^{-1})	Linewidths, Γ (mm s^{-1})	Relative area
A	0.04	0.48	0.37	0.82
B	0.20	2.08	0.50	0.05
C	0.45	1.02	0.50	0.13

Crystallographic Details and Tables

[(P_2P^{Ph})Fe(N_2)$_2$(H)][BAr^F_4] (**7**) This structure contains disorder in the CF_3 moieties of the BAr^F_4 anion which could only be poorly modeled. B level alerts persist due to this disorder.

[(P_2P^{Ph})Fe(N_2)(H)][K(18-crown-6)] (**9**) This structure contains residual electron density assignable to disordered solvent molecules. OLEX2 was used to identify voids and a solvent mask was applied. This application gave a good improvement of data statistics. In addition, A level alerts persist [PLAT360, PLAT 410] in the checkcif file related to treated disorder about an 18-crown-6 molecule that is positioned on a mirror plane

CCDC 1824471-1824478 contains the supplementary crystallographic data for this paper. These data can be obtained free of charge from The Cambridge Crystallographic Data Centre via www.ccdc.cam.ac.uk/data_request/cif

Compound	**3**	**5**
Identification code	p17260	p17278
Empirical formula	$C_{30}H_{41}Br_{1.03}FeP_3$	$C_{30}H_{41}FeN_4P_3$
Formula weight	632.69	606.43
Temperature/K	99.97	99.99
Crystal system	triclinic	monoclinic
Space group	P-1	$P2_1/c$
a/Å	9.4966(10)	17.626(2)
b/Å	9.5930(8)	10.7764(8)
c/Å	17.630(3)	16.1774(19)
α/°	101.894(6)	90
β/°	96.481(6)	98.630(3)
γ/°	102.236(4)	90
Volume/Å3	1515.2(3)	3038.0(5)
Z	2	4
ρcalcg/cm3	1.387	1.326
μ/mm-1	2.032	0.681
F(000)	656	1280
Crystal size/mm3	0.187 × 0.163 × 0.02	0.16 × 0.15 × 0.076
Radiation	MoKα (λ = 0.71073)	MoKα (λ = 0.71073)
2Θ range for data collection/°	4.448 to 55.118	4.444 to 64.162

Index ranges	$-12 \leq h \leq 12$, $-12 \leq k \leq 12$, $-22 \leq l \leq 22$	$-26 \leq h \leq 26$, $-16 \leq k \leq 16$, $-24 \leq l \leq 24$
Reflections collected	87122	112007
Independent reflections	7004 [R_{int} = 0.0784, R_{sigma} = 0.0244]	10593 [R_{int} = 0.0944, R_{sigma} = 0.0420]
Data/restraints/parameters	7004/0/345	10593/3/381
Goodness-of-fit on F2	1.061	1.114
Final R indexes [I>=2σ (I)]	R_1 = 0.0232, wR_2 = 0.0557	R_1 = 0.0385, wR_2 = 0.1013
Final R indexes [all data]	R_1 = 0.0272, wR_2 = 0.0573	R_1 = 0.0583, wR_2 = 0.1167
Largest diff. peak/hole / e Å-3	0.53/-0.37	1.39/-0.95

Compound	**7**	**8**
Identification code	p17303	p17651
Empirical formula	$C_{129}H_{106}B_2F_{48}Fe_2N_8P_6$	$C_{42}H_{65}FeKN_2O_6P_3$
Formula weight	2999.35	877.47
Temperature/K	100	100
Crystal system	monoclinic	monoclinic
Space group	$P2_1/n$	$P2_1/n$
a/Å	22.4451(18)	10.4864(6)
b/Å	12.1053(6)	23.9154(17)
c/Å	25.482(2)	17.8619(10)
α/°	90	90
β/°	101.904(4)	93.645(3)
γ/°	90	90
Volume/Å3	6774.6(9)	4470.5(5)
Z	2	4
ρcalcg/cm3	1.47	1.304
μ/mm-1	3.434	0.584
F(000)	3040	1859
Crystal size/mm3	0.284 × 0.142 × 0.06	0.26 × 0.26 × 0.23
Radiation	CuKα (λ = 1.54178)	MoKα (λ = 0.71073)
2Θ range for data collection/°	5.886 to 159.312	4.248 to 79.494

Index ranges	$-28 \leq h \leq 28$, $-14 \leq k \leq 15$, $-32 \leq l \leq 31$	$-18 \leq h \leq 18$, $-42 \leq k \leq 42$, $-31 \leq l \leq 32$
Reflections collected	86754	220099
Independent reflections	14524 [R_{int} = 0.0840, R_{sigma} = 0.0509]	26751 [R_{int} = 0.0480, R_{sigma} = 0.0334]
Data/restraints/parameters	14524/800/907	26751/0/544
Goodness-of-fit on F2	1.022	1.061
Final R indexes [I>=2σ (I)]	R_1 = 0.0967, wR_2 = 0.2547	R_1 = 0.0460, wR_2 = 0.0998
Final R indexes [all data]	R_1 = 0.1178, wR_2 = 0.2737	R_1 = 0.0682, wR_2 = 0.1080
Largest diff. peak/hole / e Å-3	2.19/-0.84	2.07/-0.65

Compound	**9**	**10**
Identification code	p17634Pnma	p17581
Empirical formula	$C_{40}H_{61}FeKN_2O_4P_3$	$C_{42}H_{65}FeK_2N_2O_3P_3$
Formula weight	816.72	872.92
Temperature/K	100(2)	100
Crystal system	orthorhombic	monoclinic
Space group	Pnma	P21/n
a/Å	25.9569(13)	14.6713(13)
b/Å	17.0296(9)	16.6256(9)
c/Å	12.1851(6)	18.7129(12)
α/°	90	90
β/°	90	102.506(3)
γ/°	90	90
Volume/Å3	5386.2(5)	4456.1(5)
Z	4	4
ρcalcg/cm3	1.007	1.301
μ/mm-1	0.478	0.671
F(000)	1728	1856
Crystal size/mm3	0.22 × 0.16 × 0.12	0.22 × 0.199 × 0.055
Radiation	MoKα (λ = 0.71073)	MoKα (λ = 0.71073)
2Θ range for data collection/°	4.586 to 55.012	5.088 to 66.06

Index ranges	$-33 \leq h \leq 33$, $-20 \leq k \leq 22$, $-15 \leq l \leq 15$	$-22 \leq h \leq 22$, $-24 \leq k \leq 25$, $-28 \leq l \leq 25$
Reflections collected	73356	64947
Independent reflections	6368 [R_{int} = 0.0545, R_{sigma} = 0.0235]	15164 [Rint = 0.0574, Rsigma = 0.0787]
Data/restraints/parameters	6368/303/287	15164/0/486
Goodness-of-fit on F2	1.123	1.014
Final R indexes [I>=2σ (I)]	R_1 = 0.1026, wR_2 = 0.3059	R1 = 0.0569, wR2 = 0.1094
Final R indexes [all data]	R_1 = 0.1162, wR_2 = 0.3201	R1 = 0.1074, wR2 = 0.1263
Largest diff. peak/hole / e Å-3	3.98/-1.50	1.56/-0.61

Compound	**11**
Identification code	p17555
Empirical formula	$C_{33}H_{50}FeKN_2P_3Si$
Formula weight	690.7
Temperature/K	124.99
Crystal system	orthorhombic
Space group	$P2_12_12_1$
a/Å	10.5863(9)
b/Å	16.3326(12)
c/Å	20.8095(17)
α/°	90
β/°	90
γ/°	90
Volume/Å3	3598.0(5)
Z	4
ρcalcg/cm3	1.275
μ/mm-1	6.154
F(000)	1464
Crystal size/mm3	0.164 × 0.077 × 0.059
Radiation	CuKα (λ = 1.54178)
2Θ range for data collection/°	6.88 to 158.208

Index ranges	$-12 \leq h \leq 13$, $-19 \leq k \leq 20$, $-26 \leq l \leq 24$
Reflections collected	38615
Independent reflections	7481 [R_{int} = 0.0728, R_{sigma} = 0.0653]
Data/restraints/parameters	7481/0/382
Goodness-of-fit on F2	1.062
Final R indexes [I>=2σ (I)]	R_1 = 0.0670, wR_2 = 0.1490
Final R indexes [all data]	R_1 = 0.0873, wR_2 = 0.1606
Largest diff. peak/hole / e Å-3	1.31/-0.81

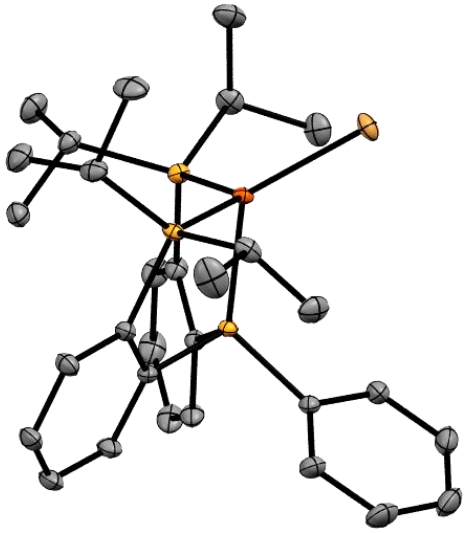

Figure A.62. ORTEP depiction of the solid-state molecular structure of **4** (displacement ellipsoids are shown at the 50% probability; hydrogens atoms and disorder from cocrystalized **3** are omitted for clarity).

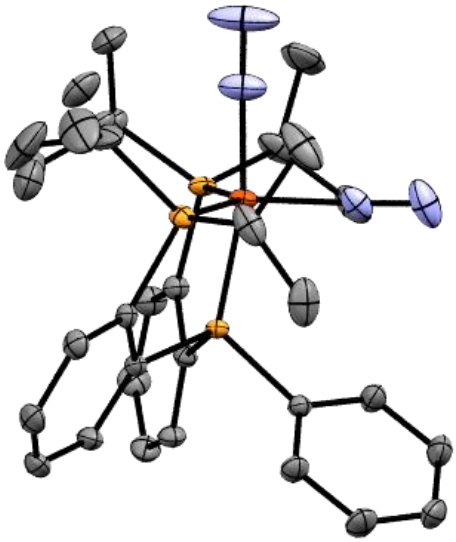

Figure A.63. ORTEP depiction of the solid-state molecular structure of **5** (displacement ellipsoids are shown at the 50% probability; hydrogens atoms are omitted for clarity).

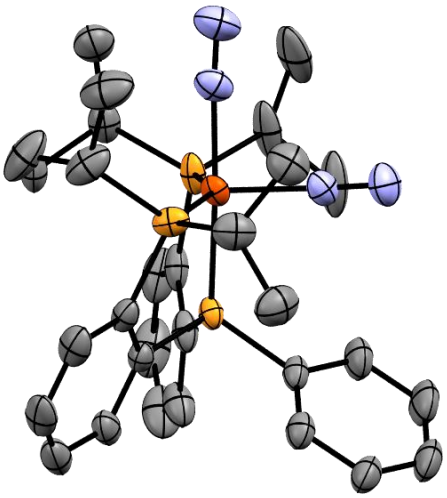

Figure A.64. ORTEP depiction of the solid-state molecular structure of **7** (displacement ellipsoids are shown at the 50% probability; hydrogens atoms, BAr^{F}_{4} and disordered solvent molecules are omitted for clarity).

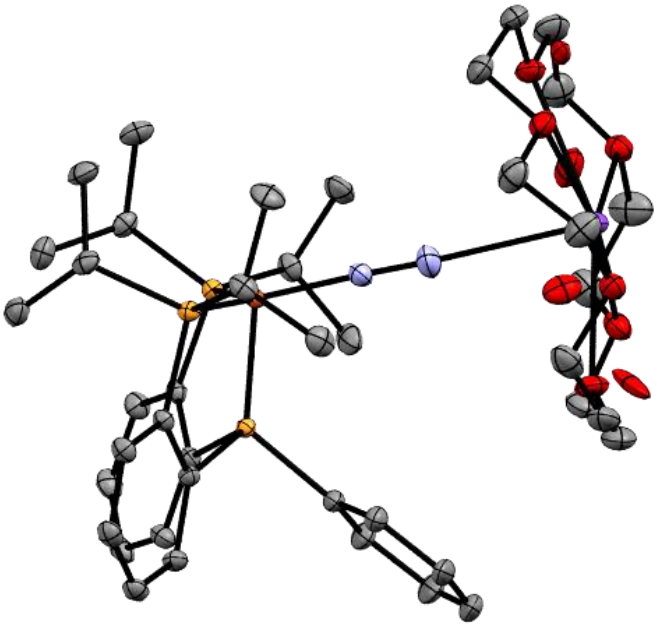

Figure A.65. ORTEP depiction of the solid-state molecular structure of **8** (displacement ellipsoids are shown at the 50% probability; hydrogens atoms are omitted for clarity).

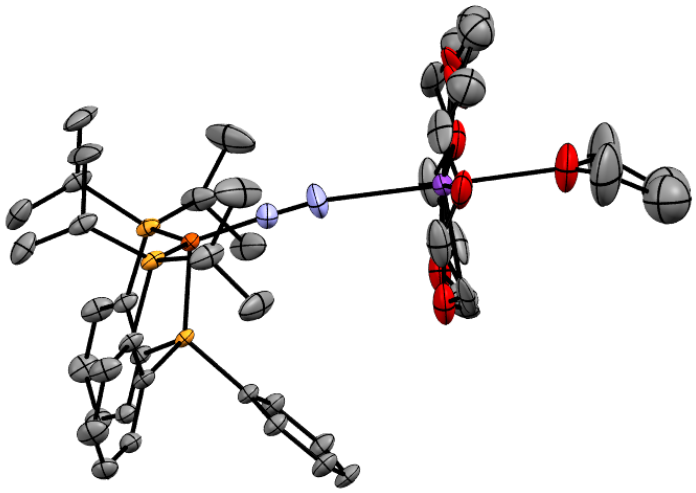

Figure A.66. ORTEP depiction of the solid-state molecular structure of **9** (displacement ellipsoids are shown at the 50% probability; hydrogens atoms are omitted for clarity).

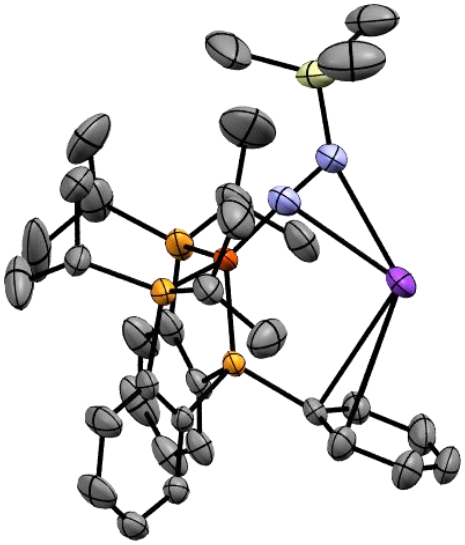

Figure A.67. ORTEP depiction of the solid-state molecular structure of **11** (displacement ellipsoids are shown at the 50% probability; hydrogens atoms are omitted for clarity).

DFT Calculations

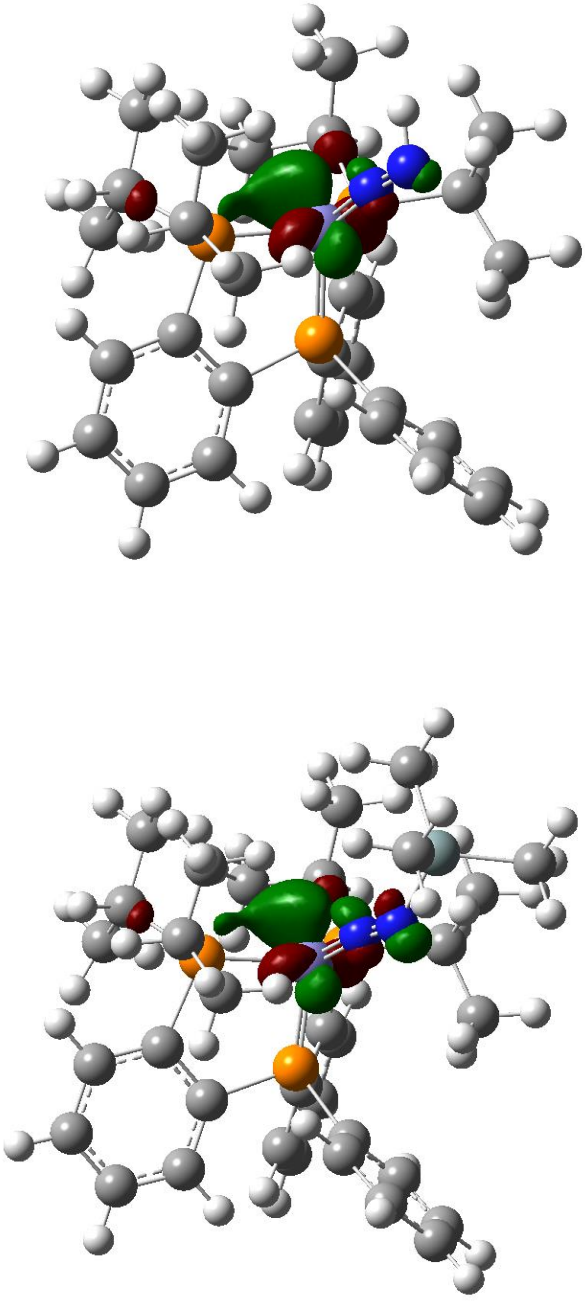

Figure A.68. Density function theory calculated molecular orbitals. (Left) HOMO of $[(P_2P^{Ph})Fe(NNH)]^-$ and (Right) HOMO of $[(P_2P^{Ph})Fe(NNTMS)]^-$ (isovalue = 0.06).

Table A.9. A comparison of gas phase optimized and experimental bond parameters demonstrating the good agreement between optimized gas-phase structures of $[(P_2P^{Ph})Fe(NNTMS)]^-$, $[(P_2P^{Ph})Fe(NNH)]^-$ and experimental values from X-ray data of $[(P_2P^{Ph})Fe(NNTMS)]K$.

Species	**Fe-N (Å)**	**Fe-P^{Ph} (Å)**	**N-N (Å)**
$[(P_2P^{Ph})Fe(NNTMS)]K$ (XRD)	1.664(7)	2.115(2)	1.270(9)
$[(P_2P^{Ph})Fe(NNTMS)]^-$	1.662	2.112	1.244
$[(P_2P^{Ph})Fe(NNH)]^-$	1.669	2.111	1.250

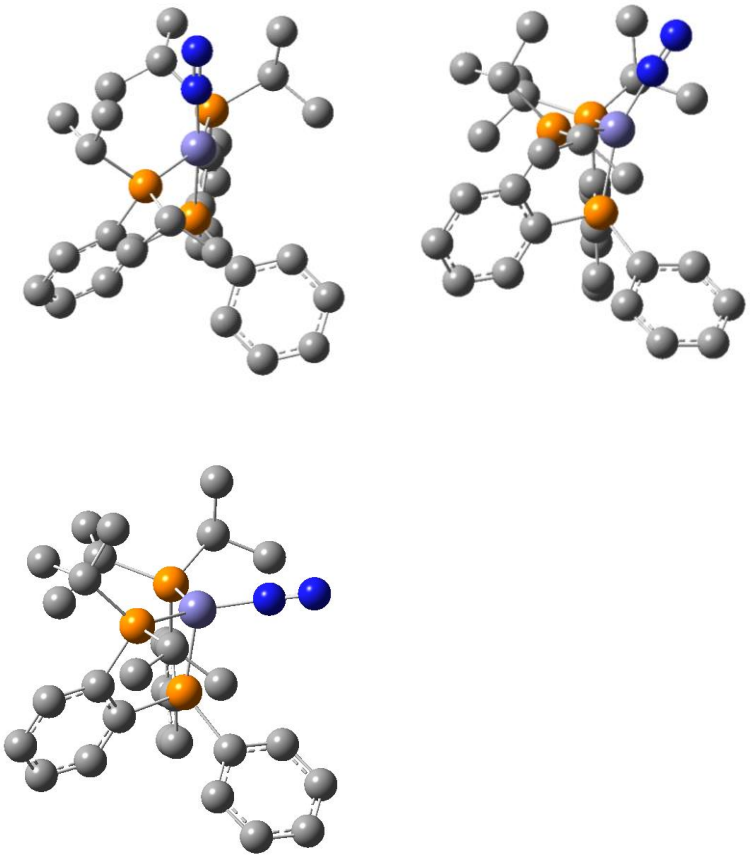

Figure A.69. The gas-phase optimized geometry of $(P_2P^{Ph})Fe(N_2)$ with different spin states and geometries. (Left) S = 0, (Middle) S = 1 and (Right) S = 1.

Table A.10. Energies of gas-phased optimized geometries of $(P_2P^{Ph})Fe(N_2)$. The energies are given relative to the lowest energy triplet state

Species	Spin	Energy	N–N	P^{Ph}–Fe–N	νN_2
$(P_2P^{Ph})Fe(N_2)$	S = 0	7.4	1.145	173.8	2076.7
$(P_2P^{Ph})Fe(N_2)$	S = 1	1.3	1.141	159.1	2093.4
$(P_2P^{Ph})Fe(N_2)$	S = 1	0	1.142	106.5	2093.2

DFT Coordinates

77

P2PPhFeN2_singlet

N	0.356700	-2.595000	-1.420600
Fe	0.127600	-0.946000	-0.809200
P	2.229500	-0.844000	-0.184700
P	-1.996900	-1.247100	-0.269500
P	-0.087800	0.996300	0.152500
C	3.827000	1.059300	1.334400
H	4.696900	0.409900	1.193200
C	4.219400	-2.517400	1.235600
H	4.798900	-2.668100	0.309500
H	4.342100	-3.428800	1.851300
H	4.674800	-1.684900	1.800300
C	2.722100	-2.278600	0.977200
H	2.317200	-3.153800	0.433300
C	3.983000	2.272600	2.024400
H	4.963400	2.545300	2.430700
C	3.668500	-0.797300	-1.435600
H	4.607400	-0.754400	-0.850600
C	2.894800	3.144800	2.170400
H	3.022800	4.102600	2.686700
C	2.571800	0.692800	0.808500
C	1.948700	-2.137100	2.300000
H	2.354800	-1.307800	2.907300
H	2.032700	-3.066200	2.894100
H	0.881600	-1.932800	2.109300
C	1.645100	2.800300	1.633100
H	0.812900	3.509600	1.700400
C	-3.086900	0.451800	-2.264000
H	-3.188400	1.315700	-1.584200
H	-3.798100	0.596100	-3.098900
H	-2.062200	0.469000	-2.674400
C	-3.378100	-0.870700	-1.539700
H	-3.234700	-1.691300	-2.269800
C	3.576600	0.467000	-2.306200
H	2.642600	0.466200	-2.897900
H	4.424800	0.503800	-3.015400
H	3.600500	1.389100	-1.700200
C	1.474800	1.566400	0.975900
C	-1.916500	4.514600	-1.230400
H	-2.763400	5.153200	-0.954700
C	0.243600	2.871300	-1.923600
H	1.088200	2.229400	-2.198100
C	-1.622900	3.379600	-0.457500
H	-2.247200	3.141600	0.409700
C	-2.366300	-0.137900	1.189800
C	-4.822700	-0.922300	-1.017900
H	-5.066500	-1.885100	-0.535600
H	-5.532000	-0.785300	-1.856500
H	-5.012600	-0.114100	-0.289500
C	3.681600	-2.063700	-2.309600
H	3.751200	-2.990900	-1.715800
H	4.548100	-2.038500	-2.996900
H	2.766100	-2.129800	-2.922300
C	-1.634900	-3.449200	1.481800

H	-0.641000	-3.680100	1.063500
H	-2.044800	-4.373800	1.930700
H	-1.502600	-2.708500	2.289200
C	-0.051300	4.004000	-2.693800
H	0.565000	4.241800	-3.568100
C	-1.133300	4.830100	-2.349300
H	-1.364500	5.714800	-2.952700
C	-2.596100	1.508000	3.479200
H	-2.672100	2.133800	4.375200
C	-1.537800	1.704100	2.575600
H	-0.798300	2.485200	2.773900
C	-3.437800	-0.301800	2.089700
H	-4.186300	-1.082700	1.922200
C	-0.537000	2.546800	-0.792700
C	-1.417900	0.887200	1.437100
C	-3.548100	0.512100	3.231400
H	-4.376600	0.355900	3.931200
C	-2.582600	-2.934900	0.387000
H	-3.569700	-2.739200	0.848000
C	-2.782700	-3.982600	-0.723700
H	-3.545500	-3.675600	-1.459300
H	-3.126900	-4.931600	-0.271300
H	-1.844600	-4.192000	-1.263000
N	0.524900	-3.640300	-1.857500

77

P2PPhFeN2_triplet_acute

N	0.587800	0.092700	-2.853300
Fe	0.188300	-0.648800	-1.244300
P	2.180500	-0.815200	-0.202600
P	-1.674200	-1.669700	-0.419200
P	-0.252000	1.011700	0.115700
C	3.663300	1.113200	1.397600
H	4.556600	0.496900	1.249600
C	3.909800	-2.497300	1.527100
H	4.549100	-2.803400	0.682100
H	3.910100	-3.329300	2.257100
H	4.380600	-1.631200	2.025100
C	2.464100	-2.191300	1.103200
H	2.060300	-3.082200	0.584100
C	3.768100	2.298200	2.142000
H	4.732800	2.587100	2.574100
C	3.771100	-0.900400	-1.235100
H	4.618400	-1.001500	-0.530600
C	2.644000	3.118800	2.316300
H	2.726100	4.051800	2.885000
C	2.434700	0.729800	0.821800
C	1.585300	-1.909500	2.333800
H	2.009700	-1.088200	2.938000
H	1.522400	-2.807100	2.976600
H	0.560700	-1.620800	2.044700
C	1.417500	2.753000	1.743300
H	0.551400	3.416100	1.847900
C	-3.161300	0.146600	-2.041100
H	-3.277000	0.881500	-1.225500
H	-3.991300	0.305200	-2.754900
H	-2.211500	0.362800	-2.557900

C	-3.202400	-1.292700	-1.507100
H	-3.049500	-1.976600	-2.363900
C	3.983200	0.375500	-2.067500
H	3.170100	0.521600	-2.796400
H	4.932500	0.298100	-2.630600
H	4.040500	1.275300	-1.431600
C	1.302200	1.559800	1.003100
C	-2.700100	4.396800	-0.346000
H	-3.658100	4.774200	0.029700
C	-0.259600	3.414200	-1.304700
H	0.686100	3.023700	-1.698300
C	-2.204200	3.171100	0.128100
H	-2.782700	2.607300	0.867100
C	-2.058300	-0.831900	1.206300
C	-4.560700	-1.606300	-0.860000
H	-4.643200	-2.652900	-0.518700
H	-5.369200	-1.437100	-1.595900
H	-4.754600	-0.945000	0.002900
C	3.719400	-2.152600	-2.129600
H	3.620600	-3.083300	-1.542700
H	4.643000	-2.232300	-2.732700
H	2.861500	-2.098200	-2.823700
C	-0.990000	-4.051600	1.005800
H	0.059100	-3.958400	0.676000
H	-1.192300	-5.123100	1.190900
H	-1.096300	-3.515700	1.963300
C	-0.751900	4.639600	-1.769300
H	-0.182300	5.205900	-2.514700
C	-1.975800	5.136400	-1.290900
H	-2.364300	6.092600	-1.658300
C	-2.444600	0.494400	3.671300
H	-2.581100	1.003900	4.631600
C	-1.594400	1.045400	2.700400
H	-1.074000	1.985200	2.912600
C	-2.923700	-1.364600	2.183600
H	-3.449300	-2.306800	1.995900
C	-0.973100	2.666800	-0.339400
C	-1.394100	0.396800	1.466900
C	-3.113200	-0.709900	3.410100
H	-3.779600	-1.145000	4.163300
C	-1.948900	-3.519200	-0.069500
H	-2.987600	-3.643300	0.292100
C	-1.789900	-4.312300	-1.380600
H	-2.554400	-4.047500	-2.130700
H	-1.882800	-5.395600	-1.179600
H	-0.795900	-4.132200	-1.830000
N	0.708800	0.540900	-3.896600

77

P2PPhFeN2_triplet

N	0.966900	-1.482800	-2.669000
Fe	0.388700	-0.566600	-1.210800
P	2.271400	0.036900	-0.109800
P	-0.920300	-2.072700	-0.183200
P	-0.645300	0.974800	-0.026000
C	2.961100	2.611300	1.078900
H	4.016500	2.335500	0.985200

C	4.417900	-0.494700	1.863000	H	3.036000	2.257300	-1.983100
H	5.170900	-0.580600	1.061900	C	0.602800	2.138500	0.720400
H	4.733000	-1.166100	2.684700	C	-4.139200	3.161700	-0.856400
H	4.446000	0.535500	2.259300	H	-5.177200	3.210600	-0.508200
C	3.003300	-0.882800	1.402000	C	-1.489100	3.013000	-1.744700
H	3.027600	-1.927400	1.036700	H	-0.456700	2.942500	-2.108800
C	2.630700	3.856300	1.637000	C	-3.244100	2.269700	-0.242600
H	3.425900	4.527500	1.980500	H	-3.596200	1.635100	0.576800
C	3.800500	0.355700	-1.185400	C	-1.659200	-1.252800	1.326000
H	4.555600	0.857400	-0.550300	C	-3.608800	-3.210300	-0.552400
C	1.287400	4.244400	1.742400	H	-3.289100	-4.174500	-0.120400
H	1.026800	5.219100	2.169700	H	-4.413000	-3.429200	-1.280200
C	1.956900	1.733300	0.623100	H	-4.050300	-2.600100	0.255600
C	2.009500	-0.797500	2.571600	C	4.391600	-0.970900	-1.697200
H	2.019500	0.211800	3.020300	H	4.699000	-1.639100	-0.873800
H	2.279800	-1.522800	3.361200	H	5.287800	-0.771000	-2.314200
H	0.979500	-1.012400	2.242700	H	3.666500	-1.515800	-2.324200
C	0.276800	3.390600	1.277600	C	0.543000	-3.858800	1.532300
H	-0.769600	3.713300	1.320000	H	1.504000	-3.437200	1.192000
C	-2.971000	-1.184800	-1.938100	H	0.726800	-4.902500	1.849700
H	-3.370700	-0.464700	-1.202400	H	0.212500	-3.289500	2.416800
H	-3.785600	-1.428200	-2.645700	C	-2.379100	3.909500	-2.347300
H	-2.165100	-0.679000	-2.499400	H	-2.035800	4.545000	-3.171300
C	-2.463300	-2.463300	-1.253900	C	-3.710800	3.986200	-1.905400
H	-2.041800	-3.118300	-2.040900	H	-4.410500	4.681400	-2.382000
C	3.436700	1.295500	-2.347700	C	-2.589900	0.147700	3.601300
H	2.676600	0.835200	-3.003300	H	-2.935700	0.690200	4.488100
H	4.332400	1.508300	-2.960900	C	-1.983100	0.845100	2.545100

H	-1.862400	1.931400	2.615500
C	-2.290500	-1.935600	2.385500
H	-2.418800	-3.022300	2.339300
C	-1.904800	2.188100	-0.674600
C	-1.517800	0.157500	1.408500
C	-2.746300	-1.242800	3.518400
H	-3.219300	-1.793000	4.339600
C	-0.496300	-3.836300	0.402700
H	-1.433300	-4.286700	0.783000
C	-0.008900	-4.666800	-0.800100
H	-0.781500	-4.774700	-1.580000
H	0.270600	-5.683400	-0.466400
H	0.878900	-4.204200	-1.266500
N	1.297800	-2.032700	-3.612800

90

P2PPhFeNNTMS_anion_singlet

Fe	-0.575400	0.101100	-0.281700
P	1.279600	-0.219700	0.674600
P	0.148500	2.094500	-0.800500
P	-0.168700	-1.634100	-1.508400
C	3.928400	1.073100	0.546400
H	4.357200	0.213000	1.072000
C	1.914100	-3.707200	-1.405300
H	1.389200	-4.229600	-2.215300
C	1.999600	2.217000	-0.423300
C	2.551500	1.104300	0.253800
C	0.132600	3.125400	-2.446300
H	0.549300	4.121000	-2.191100
C	4.215200	3.258500	-0.470800
H	4.858200	4.101100	-0.754600
C	1.516400	-0.381400	2.530800
C	1.418200	-2.481200	-0.919300
C	2.839900	3.297500	-0.759600
H	2.426200	4.182200	-1.258400
C	4.762900	2.141600	0.175700
H	5.836700	2.103100	0.397400
C	-1.302800	3.324500	-2.960400
H	-1.826900	2.353800	-3.041100
H	-1.294900	3.795900	-3.963600
H	-1.896900	3.972400	-2.294500
C	2.104000	-1.826300	0.126400
C	-5.309500	0.663000	-0.579300
H	-4.778600	1.593200	-0.852700
H	-6.397600	0.869900	-0.593000
H	-5.092500	-0.081700	-1.366800
C	1.569200	-0.655600	5.359400
C	3.073900	-4.280800	-0.857200
H	3.447400	-5.238300	-1.241800
C	-1.360400	-3.125600	-1.261800
H	-0.959700	-3.970300	-1.859500
C	2.096100	0.613500	3.347500
H	2.533700	1.505500	2.887400
C	-5.629600	-1.591000	1.533100
H	-5.434000	-2.358800	0.761700
H	-6.725900	-1.450600	1.607800
H	-5.270500	-1.992600	2.499100

C	2.121500	0.478100	4.745200
C	3.257800	-2.411800	0.683600
H	3.768300	-1.925800	1.523700
C	-2.784900	-2.801300	-1.741700
H	-3.133200	-1.861400	-1.279200
H	-3.482500	-3.611800	-1.449800
H	-2.847600	-2.691200	-2.837600
C	-0.513100	3.509500	0.352000
H	-0.254900	4.472500	-0.135400
C	-1.385500	-3.527700	0.222400
H	-0.381800	-3.810700	0.584600
H	-2.058200	-4.396400	0.370400
H	-1.755800	-2.690600	0.839500
C	1.006700	2.494600	-3.538700
H	2.038200	2.309500	-3.193200
H	1.056200	3.161400	-4.423100
H	0.586200	1.531800	-3.871100
Si	-4.734800	0.036300	1.123200
N	-2.038400	-0.033100	0.496400
N	-3.022200	-0.258100	1.224100
C	0.950300	-1.510600	3.166700
H	0.472600	-2.282800	2.553700
C	0.981300	-1.650500	4.559600
H	0.538200	-2.539200	5.025600
C	3.744400	-3.634200	0.192100
H	4.642300	-4.085400	0.632700
C	-2.038000	3.406100	0.515900
H	-2.577900	3.500100	-0.440800
H	-2.405800	4.202700	1.193700
H	-2.296900	2.425000	0.948800
C	1.533800	-1.271700	-3.778300
H	1.736400	-0.308300	-3.276600
H	1.630500	-1.114500	-4.871200
H	2.318400	-1.979000	-3.463300
C	0.151800	3.457000	1.736400
H	0.002300	2.463000	2.196000
H	-0.301500	4.213700	2.407400
H	1.236400	3.652600	1.685400
C	-5.227500	1.306000	2.452800
H	-6.326100	1.438300	2.509200
H	-4.774000	2.293100	2.246300
H	-4.871100	0.979100	3.447400
C	0.125800	-1.778700	-3.420900
H	0.043000	-2.849900	-3.697300
C	-0.949600	-0.981800	-4.177500
H	-1.953300	-1.424500	-4.069300
H	-0.714900	-0.933300	-5.259700
H	-1.007300	0.047400	-3.780400
H	1.590400	-0.761500	6.450600
H	2.579400	1.265800	5.356500

78

P2PPhFeNNH_anion_singlet

Fe	-0.083400	-0.757600	-0.968900
P	0.045200	1.025000	0.154600
P	1.871000	-1.284600	-0.176100
P	-1.987300	-1.128200	-0.020400

C	1.670100	1.901400	2.460700	C	1.610100	4.686400	-1.237000
H	0.984400	2.741900	2.613900	C	-1.802200	2.536800	1.890200
C	-3.705500	0.485900	1.732900	H	-1.076200	3.357900	1.922400
H	-4.463000	-0.305700	1.667900	C	-3.536800	-2.323700	-2.133400
C	2.335200	-0.093500	1.216700	H	-2.592000	-2.350200	-2.704000
C	1.445200	0.989300	1.411700	H	-4.371700	-2.230500	-2.856900
C	2.515900	-2.930500	0.629300	H	-3.657100	-3.289300	-1.613400
H	3.599100	-2.789700	0.821600	C	3.376800	-0.995200	-1.363800
C	3.675900	0.694600	3.107600	H	4.264400	-1.471800	-0.897400
H	4.546500	0.575500	3.764900	C	-3.587600	0.186200	-1.960300
C	0.281000	2.724100	-0.616000	H	-3.617700	1.064400	-1.291900
C	-2.472000	0.337600	1.068500	H	-4.494100	0.212600	-2.598300
C	3.460500	-0.214200	2.055900	H	-2.699500	0.273500	-2.610300
H	4.177700	-1.029100	1.899200	C	1.814500	-3.226200	1.962700
C	2.775300	1.748000	3.316700	H	1.894900	-2.385500	2.672800
H	2.934300	2.455100	4.140400	H	2.260200	-4.122300	2.440100
C	2.343700	-4.117400	-0.333500	H	0.743100	-3.430700	1.803800
H	1.308500	-4.152400	-0.722400	H	-0.449000	-1.852100	-4.253000
H	2.549600	-5.074500	0.186500	N	-0.228400	-0.920700	-2.623300
H	3.025700	-4.056800	-1.198100	N	-0.377900	-0.884000	-3.863400
C	-1.512000	1.368500	1.158600	C	-0.755300	3.208900	-1.446600
C	0.567000	5.162100	-2.044800	H	-1.672800	2.618800	-1.550900
C	-3.985700	1.646300	2.475600	C	-0.618500	4.414000	-2.146500
H	-4.952000	1.752000	2.985000	H	-1.439100	4.769000	-2.781900
C	-3.536800	-1.128800	-1.165400	C	-3.034500	2.674600	2.551500
H	-4.431500	-1.194200	-0.512200	H	-3.255200	3.588400	3.117400
C	1.468400	3.481200	-0.529500	C	3.116900	-1.628500	-2.742000
H	2.293600	3.125600	0.096300	H	2.945000	-2.716300	-2.687800

H	3.986700	-1.457000	-3.408400
H	2.225400	-1.175300	-3.207700
C	-1.937700	-2.318600	2.588100
H	-0.870100	-2.038000	2.534800
H	-2.019800	-3.230600	3.212900
H	-2.469000	-1.501200	3.102800
C	3.648900	0.506800	-1.541500
H	2.732900	1.019900	-1.887100
H	4.438100	0.667200	-2.303000
H	3.978100	0.985500	-0.603600
C	-2.495200	-2.572700	1.177100
H	-3.603200	-2.609500	1.222400
C	-1.965400	-3.906400	0.624800
H	-2.464600	-4.203800	-0.312100
H	-2.108700	-4.723200	1.360500
H	-0.887100	-3.814000	0.401000
H	0.677700	6.103300	-2.596700
H	2.544000	5.256500	-1.153600

Supplementary References

(1) Buscagan, T. M.; Oyala, P. H.; Peters, J. C. N_2-to-NH_3 Conversion by a triphos–iron catalyst and enhanced turnover under photolysis. *Angew. Chem. Int. Ed.* **2017**, *56*, 6921–6926.

(2) Del Castillo, T. J.; Thompson, N. B.; Peters, J. C. A synthetic single-site Fe nitrogenase: high turnover, freeze-quench ^{57}Fe Mössbauer data, and a hydride resting state. *J. Am. Chem. Soc.* **2016**, *138*, 5341–5350.

(3) Robbins, J. L.; Edelstein, N.; Spencer, B.; Smart, J. C. Syntheses and Electronic Structures of Decamethylmetallocenes. *J. Am. Chem. Soc.* **1982**, *104* (7), 1882–1893.

(4) Weitz, I. S.; Rabinovitz, M. The application of C_8K for organic synthesis: reduction of substituted naphthalenes. *J. Chem. Soc. Perkin Trans.* **1993**, *1*, 117.

(5) Evans, D. F. The determination of the pararnagnetic susceptibility of substances in solution by nuclear magnetic resonance. *J. Chem. Soc.* **1959**, 2003–2005.

(6) Gaussian 09, Revision **A.02**, Frisch, M. J.; Trucks, G. W.; Schlegel, H. B.; Scuseria, G. E.; Robb, M. A.; Cheeseman, J. R.; Scalmani, G.; Barone, V.; Petersson, G. A.; Nakatsuji, H.; Li, X.; Caricato, M.; Marenich, A.; Bloino, J.; Janesko, B. G.; Gomperts, R. ; Mennucci, B.; Hratchian, H. P.; Ortiz, J. V.; Izmaylov, A. F.; Sonnenberg, J. L.; Williams-Young, D.; Ding, F.; Lipparini, F.; Egidi, F.; Goings, J.; Peng, B.; Petrone, A.; Henderson, T.; Ranasinghe, D.; Zakrzewski, V. G.; Gao, J.; Rega, N.; Zheng, G.; Liang, W.; Hada, M.; Ehara, M.; Toyota, K.; Fukuda, R.; Hasegawa, J.; Ishida, M.; Nakajima, T.; Honda, Y.; Kitao, O.; Nakai, H.; Vreven,

T.; Throssell, K.; Montgomery, Jr., J. A.; Peralta, J. E.; Ogliaro, F.; Bearpark, M.; Heyd, J. J.; Brothers, E.; Kudin, K. N.; Staroverov, V. N.; Keith, T.; Kobayashi, R.; Normand, J.; Raghavachari, K.; Rendell, A.; Burant, J. C.; Iyengar, S. S.; Tomasi, J.; Cossi, M.; Millam, J. M.; Klene, M. ; Adamo, C.; Cammi, R.; Ochterski, J. W.; Martin, R. L.; Morokuma, K.; Farkas, O.; Foresman, J. B.; Fox, D. J. Gaussian, Inc., Wallingford CT, 2016

(7) Tao, J.; Perdew, J. P.; Staroverov, V. N.; Scuseria, G. E. Climbing the Density Functional Ladder: Nonempirical Meta–generalized Gradient Approximation Designed for Molecules and Solids. *Phys. Rev. Lett.* **2003**, *91* (14), 3–6.

(8) Weigend, F.; Ahlrichs, R. Balanced basis sets of split valence, triple zeta valence and quadruple zeta valence quality for H to Rn: design and assessment of accuracy. *Phys. Chem. Chem. Phys.* **2005**, *7*, 3297–3305.

(9) Pfirrmann, S.; Limberg, C.; Herwig, C.; Knispel, C.; Braun, B.; Bill, E.; Stösser, R. A reduced β-diketiminato-ligated Ni_3H_4 unit catalyzing H/D Exchange. *J. Am. Chem. Soc.* **2010**, *132*, 13684–13691.

(10) Creutz, S. E.; Peters, J. C. Spin-state tuning at pseudo-tetrahedral d^6 ions: spin crossover in $[BP_3]Fe^{II}–X$ complexes. *Inorg. Chem.* **2016**, *55*, 3894–3906.

(11) Rittle, J.; Mccrory, C. C. L.; Peters, J. C. A 10^6 fold enhancement in N_2 binding affinity of an $Fe_2(\mu\text{-}H)_2$ core upon reduction to a mixed-valence $Fe^{II}Fe^{I}$ state. *J. Am. Chem. Soc.* **2014**, *136*, 13853–13862.

(12) Tepper, A. W. J. W.; Bubacco, L.; Canters, G. W. Paramagnetic properties of the halide-bound derivatives of oxidised tyrosinase investigated by ^1H NMR spectroscopy. *Chem. - A Eur. J.* **2006**, *12*, 7668–7675.

(13) Zaballa, M. E.; Ziegler, L.; Kosman, D. J.; Vila, A. J. NMR study of the exchange coupling in the trinuclear cluster of the multicopperoxidase Fet3p. *J. Am. Chem. Soc.* **2010**, *132*, 11191–11196.

Appendix B : Supporting Information for Chapter 3

Experimental Section

General considerations. All manipulations were carried out using standard Schlenk or glovebox techniques under an N_2 atmosphere, except for the synthesis of trimethyltin azide. Unless otherwise noted, solvents were deoxygenated and dried by thoroughly sparging with Ar gas followed by passage through an activated alumina column in the solvent purification system by SG Water, USA LLC. 2-MeTHF was degassed by three freeze-pump-thaw cycles, followed by drying over NaK to remove traces of water. All reagents were purchased from commercial vendors and used without further purification unless stated otherwise. P_3^B,[1] $[(P_3^B)Fe(N_2)]$,[2] $[(P_3^B)Fe][BAr^F]$,[3] and were synthesized following literature procedures. Deuterated solvents were purchased from Cambridge Isotope Laboratories, Inc., degassed, and dried over activated 3-Å molecular sieves prior to use.

^1H and ^{13}C chemical shifts are reported in ppm relative to tetramethylsilane, using residual solvent proton and ^{13}C resonances as internal standards. ^{31}P chemical shifts are reported relative to 85 % aqueous H_3PO_4. Solution phase magnetic measurement were performed by the method of Evans.

IR measurements were performed on a Bruker Alpha Platinum ATR spectrometer. X-band EPR spectra were obtained on a Bruker EMX spectrometer and simulated using Easyspin. ESEEM and inversion recovery experiments were aquired using a Bruker (Billerica, MA) ELEXSYS E580 pulse EPR spectrometer equipped with a Bruker D2 resonator. Temperature control was achieved using an ER 4118HV-CF5-L Flexline Cryogen-Free VT cryostat manufactured by ColdEdge (Allentown, PA) equipped with an Oxford Instruments Mercury ITC.

Mössbauer spectra were recorded on a spectrometer from SEE Co. operating in the constant acceleration mode in a transmission geometry. Spectra were recorded with the temperature of the sample maintained at 80 K. The sample was kept in an SVT-400 Dewar from Janis. The quoted isomer shifts are relative to the centroid of the spectrum of a metallic foil of α-Fe at room temperature. Data analysis was performed using the program WMOSS (www.wmoss.org) and quadrupole doublets were fit to Lorentzian lineshapes.

X-Ray Crystallography. X-ray diffraction studies were carried out at the Caltech Division of Chemistry and Chemical Engineering X-ray Crystallography Facility on a Bruker three-circle SMART diffractometer with a SMART 1K CCD detector, APEX CCD detector, or Bruker D8 VENTURE Kappa Duo PHOTON 100 CMOS detector. Data were collected at 100 K using Mo Kα radiation (λ = 0.71073 Å) or Cu Kα radiation (λ = 1.54178 Å). Structures were solved by direct or Patterson methods using SHELXS and refined against F2 on all data by full-matrix least squares with SHELXL-97.68. All non-hydrogen atoms were refined anisotropically. All hydrogen atoms were placed at geometrically calculated positions and refined using a riding model. The isotropic displacement parameters of all hydrogen atoms were fixed at 1.2 (1.5 for methyl groups) times the Ueq of the atoms to which they are bonded.

[(P_3^B))Fe(Cl)] (1). A mixture of $FeCl_2$ (87 mg, 0.69 mmol), P_3^B (400 mg, 0.69 μmol), iron powder (415 mg, 7.4 mmol), and THF (20mL) was heated to 90 °C in a sealed bomb under vigorous stirring for 62 h, during which time the color of the liquid phase turned from pale yellow to brown. The remaining iron powder was removed by filtration, and the solvent was removed in vacuo. The brown residue was taken in toluene (10 mL) and dried *in vacuo*. The brown residue was extracted with pentane (200 mL) to give a brown solution. Solvent

evaporation in vacuo afforded the product as a greenish-brown powder (422 mg, 90%). An analytically pure sample was obtained by slow concentration of a saturated pentane solution. Crystals suitable for XRD were obtained upon cooling a saturated solution of (**P$_3^B$**)FeCl in pentane to −35 °C . ^{1}H NMR (C_6D_6, 300 MHz): δ 96.9 (1H), 35.0 (1H), 23.6 (1H), 9.8(1H), 5.8 (1H), 1.9 (3H), -0.3 (3H), -2.3 (3H), −22.4 (1H). UV-vis (THF, nm {cm^{-1} M^{-1}}): 280 {$2.0\cdot10^4$}, 320 {sh}, 560 {sh}, 790 {150}, 960 {190}. μ_{eff} (C_6D_6, Evans method, 20 °C): 4.0 μ_B. Anal: calcd for $C_{36}H_{54}BClFeP_3$: C 63.41, H 7.98; found: C 63.16, H 7.72.

[(P$_3^B$)Fe(N$_3$)] (2. A mixture of **1** (100 mg, 0.15 mmol) and sodium azide (15 mg, 0.23 mmol) in THF (3 mL) was stirred for 10 days at room temperature. The solvent was removed *in vacuo* and the solid residue was extracted with benzene. Lyophilization afforded the product as a brown powder (100 mg, 99%). ^{1}H NMR (C_6D_6, 300 MHz): δ 72.5 (3H), 34.3 (3H), 23.0 (3H), 12.3 (3H), 5.9 (3H), 1.7 (9H), 1.1 (9H), 0.5 (9H), −1.8 (9H), −21.5 (3H). UV-vis (DEE, nm {cm–1 M–1}): 280 {sh}, 340 {sh}, 370 {$1.1\cdot10^4$}, 600 {sh}, 820 {160}, 1000{190}. μ_{eff} (C_6D_6, Evans method, 20 °C): 3.8 μ_B. IR (ATR, THF film): ν_{NNN} = 2070 cm^{-1}. Anal: calcd for $C_{36}H_{54}BFeN_3P_3$: C 62.81, H 7.91, N 6.10; found: C 63.26, H 7.65, N 6.09.

[(P$_3^B$)Fe(N*NN*) (N*: 50% ^{15}N (2-^{15}N)] was prepared as **2** using Na^{15}NNN. ν_{NNN} = 2058 cm^{-1}.

[(P$_3^B$)^{57}Fe(N$_3$)] (2-^{57}Fe) was prepared as **2** using (P_3^B)^{57}FeCl.

[(P$_3^B$)]$_2$(μ-1,3-N$_3$) (3) A brown solution of (TPB*i*Pr)Fe(N2) (20 mg, 30 μmol) in benzene (1 mL) was layered on top of a brown solution of **2** (20 mg, 29 μmol) in benzene (1 mL)

and left standing for 2 days. Filtration, washing with benzene (2 × 1 mL) and pentane (2 × 1 mL) followed by drying *in vacuo* afforded the product as a dark brown powder (29 mg, 76%). IR (ATR): νNN= 2073 cm-1. NIR (KBr): 5400 cm-1 (IVCT). Anal: calcd for C72H108B2Fe2N3P6: C 64.79, H 8.16, N 3.15; found: C 64.39, H 7.81, N 3.18. Additional characterization was obtained on **3** generated in solution from equimolar amounts of **2** and (TPB*i*Pr)Fe(N2). 1H NMR (C6D6, 300 MHz): δ 47.0, 46.0 (sh), 39.3, 19.6, 12.0, 11.0 (sh), 4.3, 3.3, 2.1, 0.2, −1.8, −3.4, −7.2, −8.0. UV-vis (THF, nm {$cm^{-1}M^{-1}$}): 640 {sh}, 750 {sh}, 1000{sh}. NIR (THF, cm^{-1}{$cm^{-1}M^{-1}$}): 5250 {2.2 •103} (IVCT). IR (ATR, THF film): νNNN = 2090 cm^{-1}.

[(P_3^B)Fe(NCO)] (6). A mixture of [(P_3^B)Fe][BAr^F_4] (15 mg, 0.01 mmol) and KNCO (8.1 mg, 0.1 mmol) in THF (3 mL) was stirred for 48 hours at room temperature. The solvent was removed *in vacuo* and the solid residue extracted with pentane (2 x 5 mL). Removal of the solid *in vacuo* afforded the product as a yellow powder. ^{1}H NMR (400 MHz, Benzene-d_6) δ 84.42 (3H), 33.96 (3H), 23.31 (3H), 10.17 (3H), 1.97 (9H), 1.89 (3H), 1.40 (9H), 0.60 (9H), -1.35 (s, 9H), -22.29 (s, 3H).

2. NMR Spectra

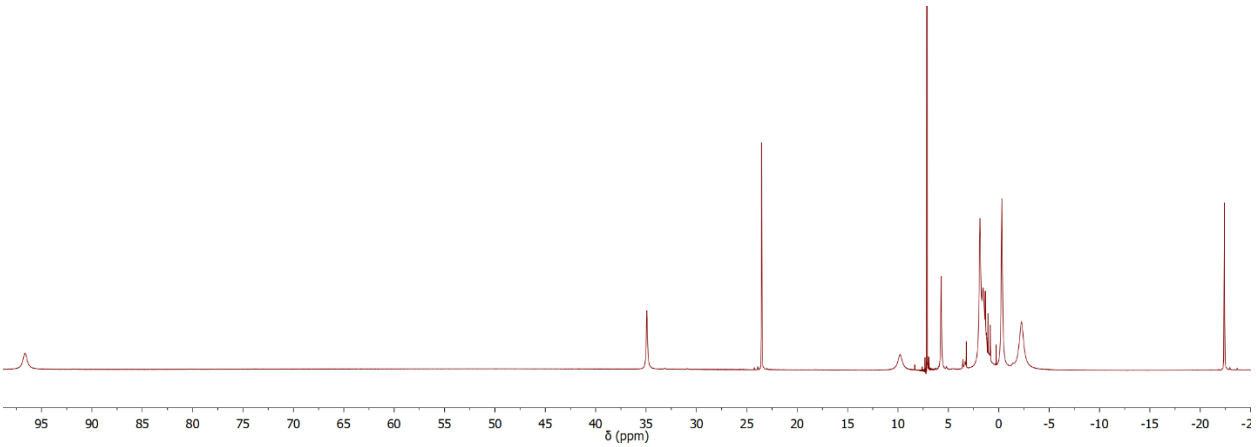

Figure B..1. 70 ^{1}H NMR spectrum of (P_3^B)FeCl 1 in C_6D_6.

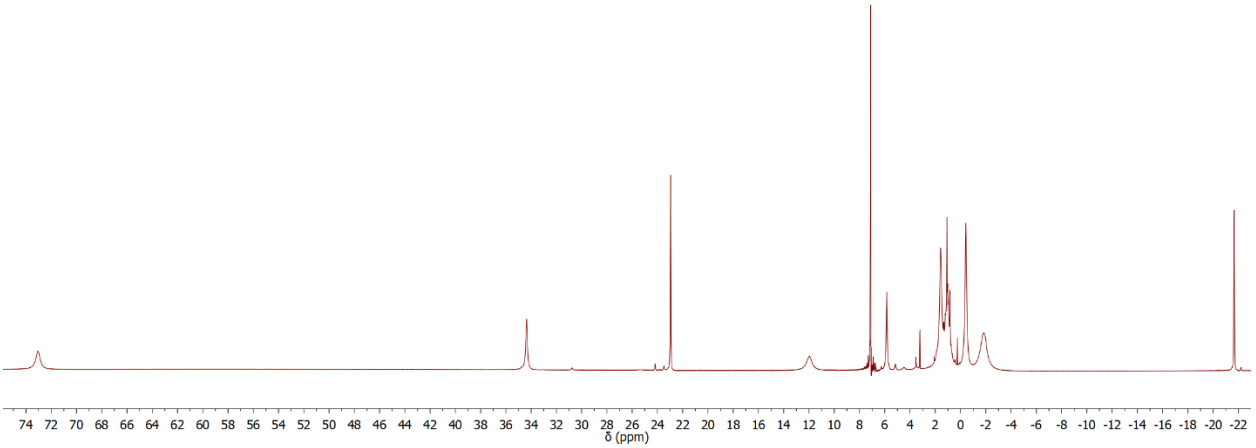

Figure B..2 ^{1}H NMR spectrum of (P_3^B)Fe(N_3) **2** in C_6D_6.

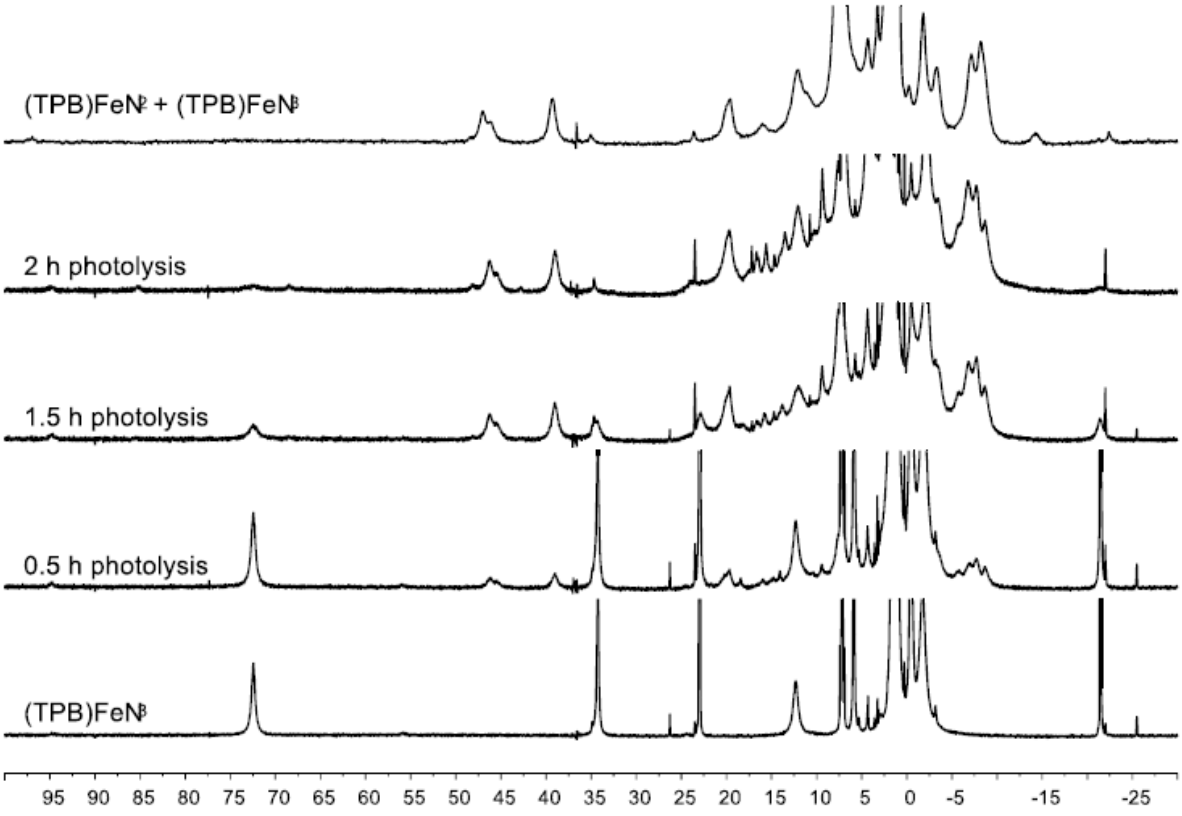

Figure B..3 ^{1}H NMR spectra monitoring the photolysis of $(P_3^B)Fe(N_3)$ (**2**) in C_6D_6 at room temperature and ^{1}H NMR spectrum of $[(P_3^B)]_2(\mu\text{-}1,3\text{-}N_3)$ (**3**) generated in situ by reaction of **2** and $(P_3^B)Fe(N_2)$ recorded before complete precipitation of insoluble **3**.

3. IR Spectra

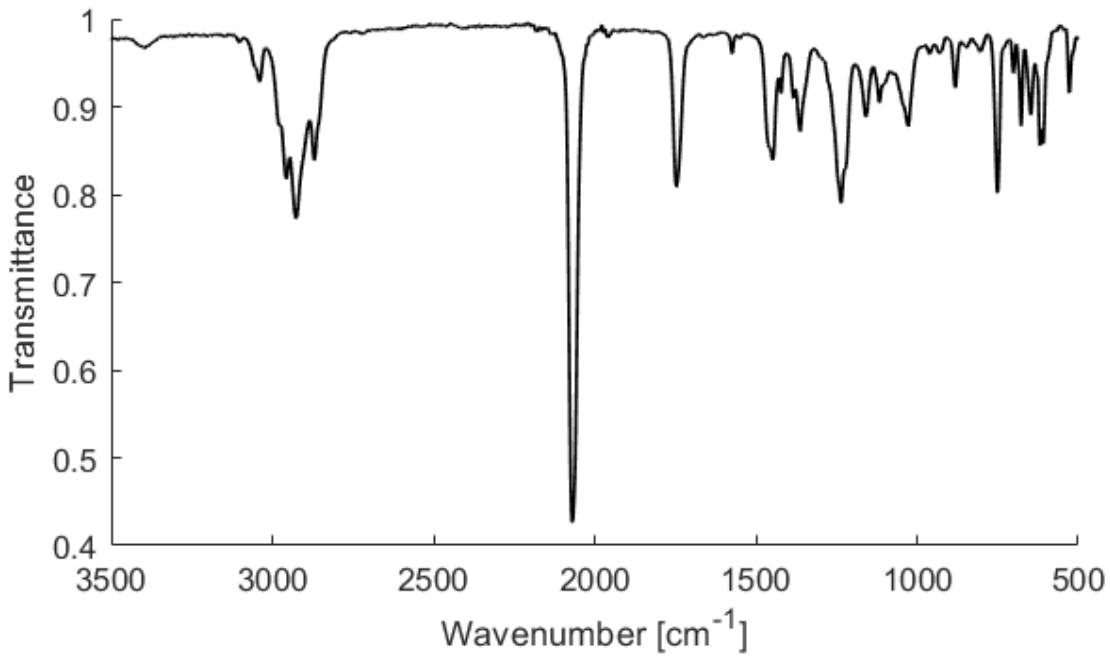

Figure B..4 IR spectrum of $(P_3^B)Fe(N_3)$ (**2**) (thin-film from C_6D_6 solution).

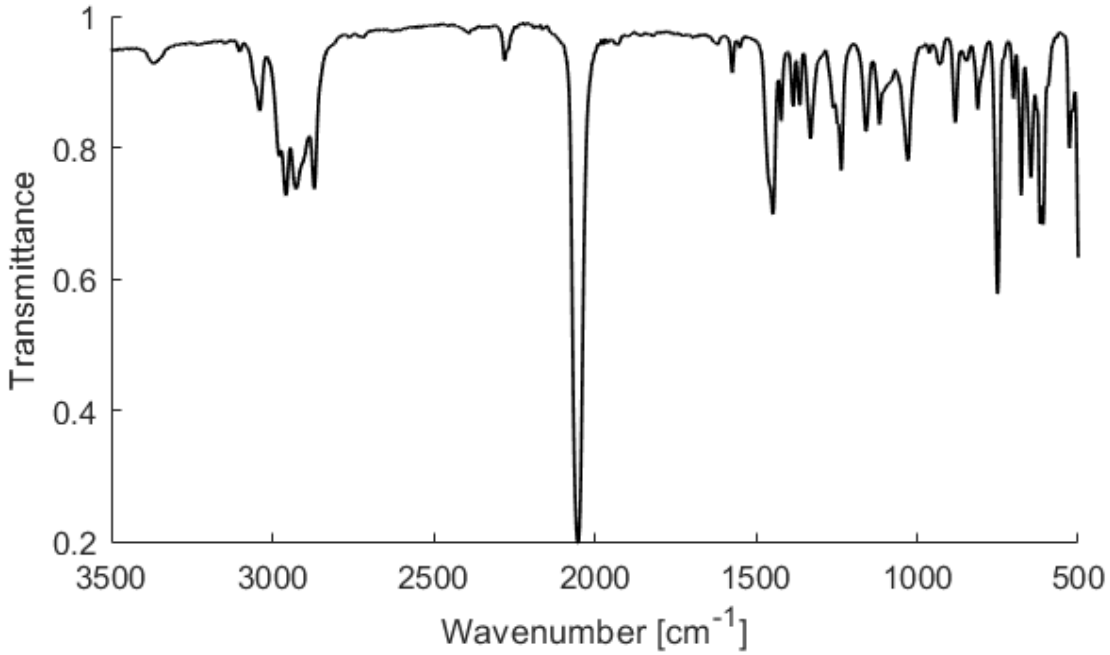

Figure B.5 IR spectrum of (P_3^B)Fe(^{15}NNN) (**2-^{15}N**) (thin-film from C_6D_6 solution).

4. EPR Spectra

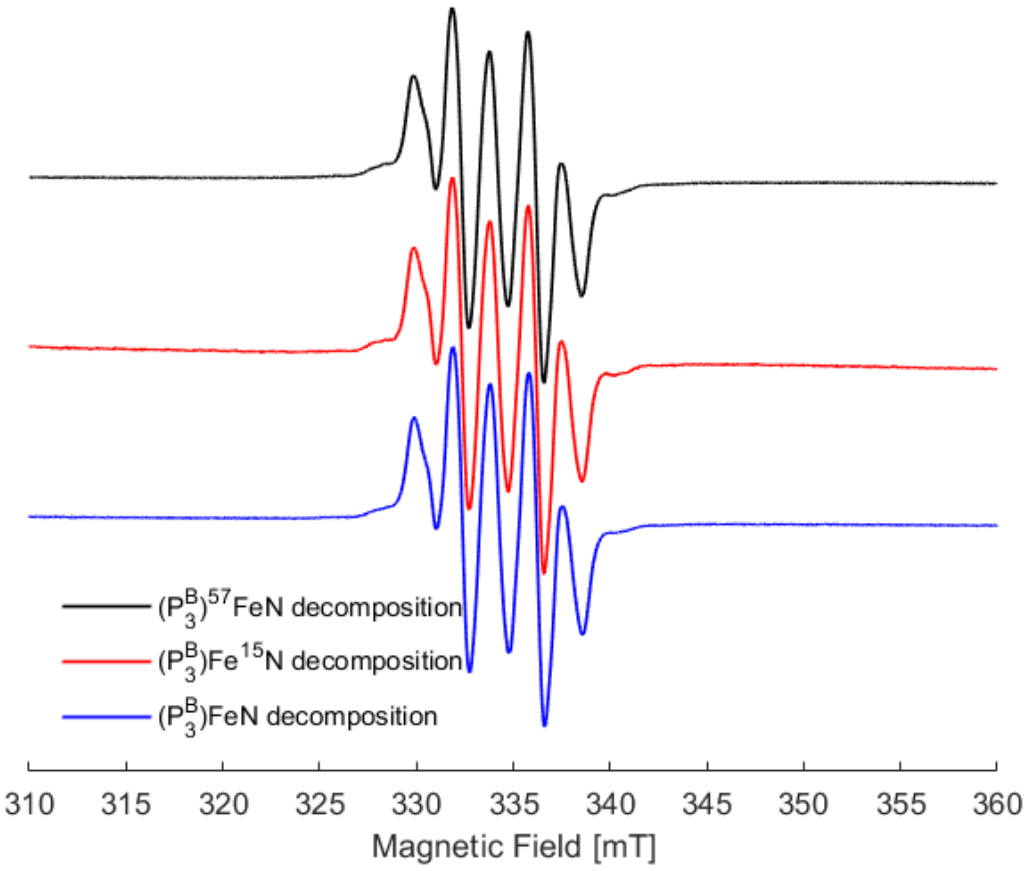

Figure B.6. EPR spectra recorded after irradiating a frozen 1 mM solution of **2**, **2-^{15}N**, and **2-^{57}Fe**, showcasing the absence of isotope effects on the signal and the absence of a signal corresponding to (P_3^B)Fe≡N (**4**). The observed signal is identical to i-Pr radical.[4]

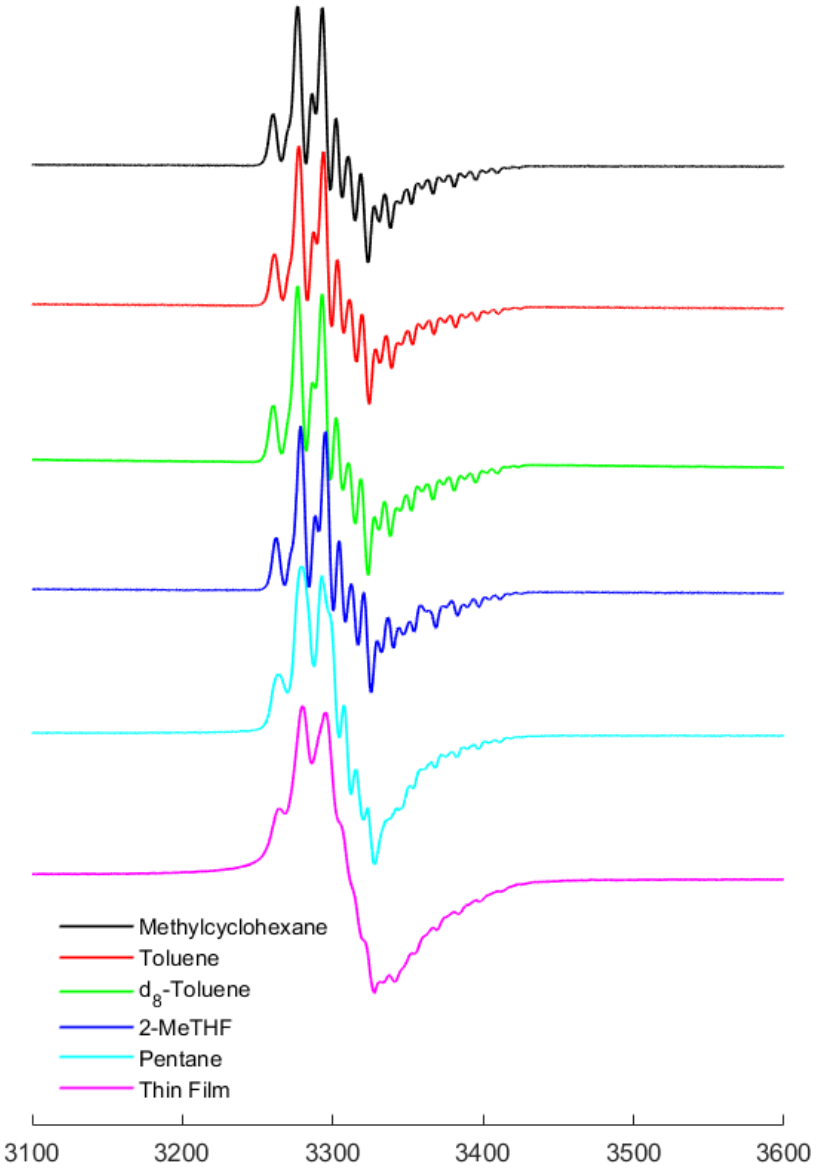

Figure B.6. EPR spectra recorded after irradiating a frozen 1 mM solution of **2** in methylcyclohexane, toluene, d_8-toluene, 2-MeTHF, pentane, and as thin films deposited from pentane solutions.

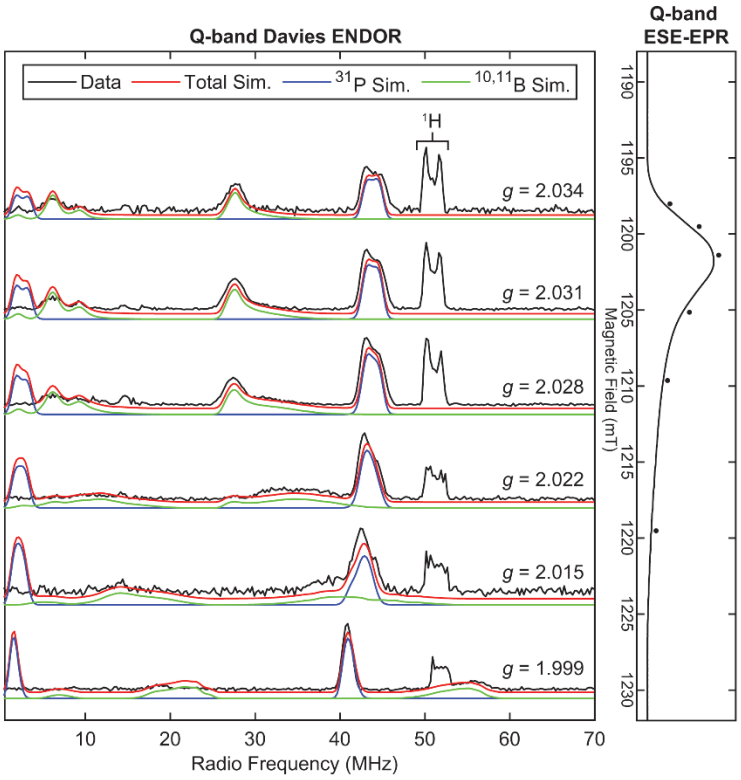

Figure B.7. Field-Dependent Q-band Davies ENDOR spectra (black) of natural abundance TPB-FeN with spectral simulations of contributions from the three ^{31}P nuclei (blue), $^{10/11}$B (green) overlaid using parameters in main text.

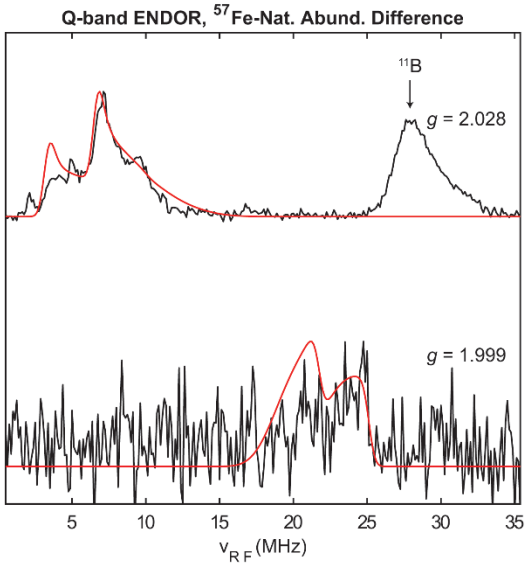

Figure B.8. Field-Dependent Q-band Davies ENDOR ^{57}Fe-minus-Natural abundance difference spectra (black) of TPB-FeN with spectral simulations of contributions from the ^{57}Fe overlaid using parameters in main text.

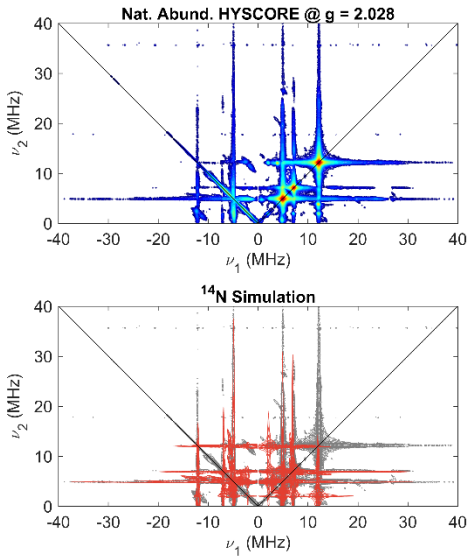

Figure B.9. (Top) Q-band HYSCORE spectrum of natural abundance TPB-FeN at acquired at 1201.5 mT (g = 2.028). (Bottom) Simulation of ^{14}N HYSCORE spectrum (red) overlaid over experimental data (grey) using parameters in main text.

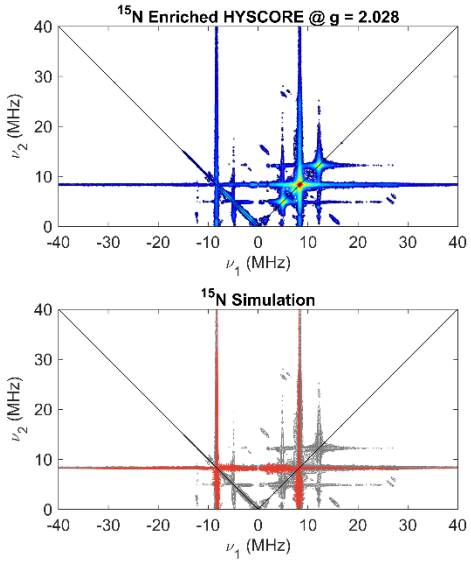

Figure B.10. (Top) Q-band HYSCORE spectrum of ^{15}N enriched (~ 50%) TPB-FeN at acquired at 1201.5 mT (g = 2.028). (Bottom) Simulation of ^{15}N HYSCORE spectrum (red) overlaid over experimental data (grey) using parameters in main text.

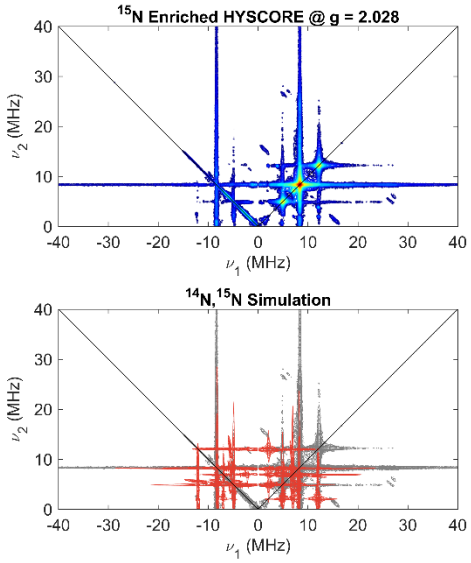

Figure B.11 (Top) Q-band HYSCORE spectrum of ^{15}N enriched (~ 50%) TPB-FeN at acquired at 1201.5 mT (g = 2.028). (Bottom) Simulation of both ^{14}N and ^{15}N contributions to HYSCORE spectrum (red) overlaid over experimental data (grey) using parameters in main text.

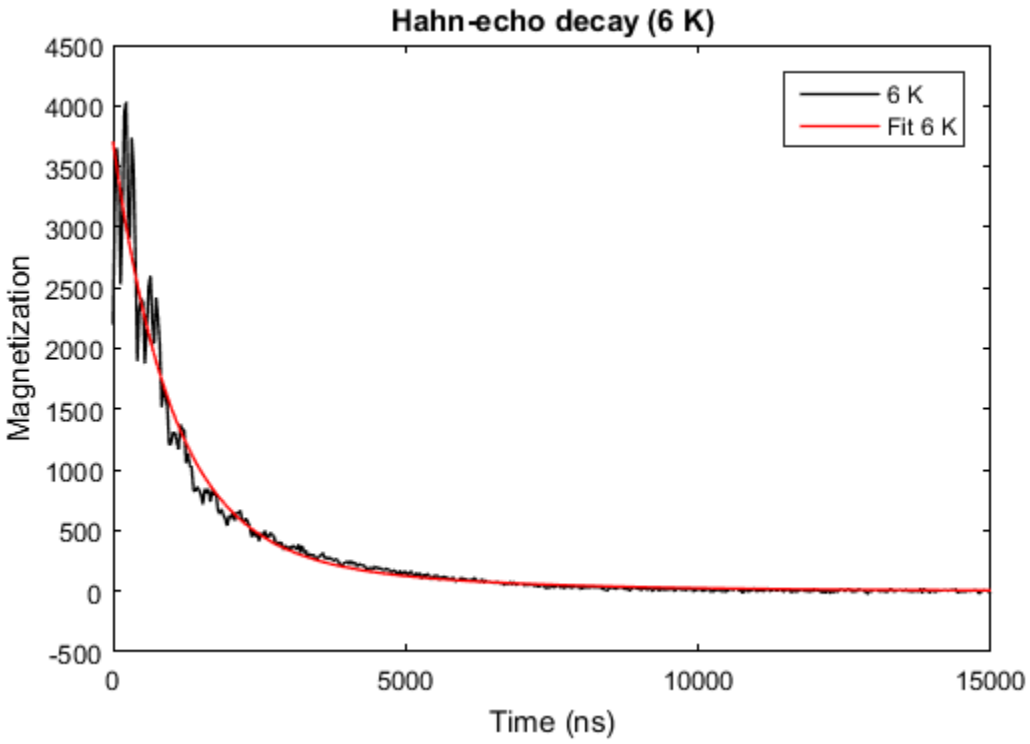

Figure B.12

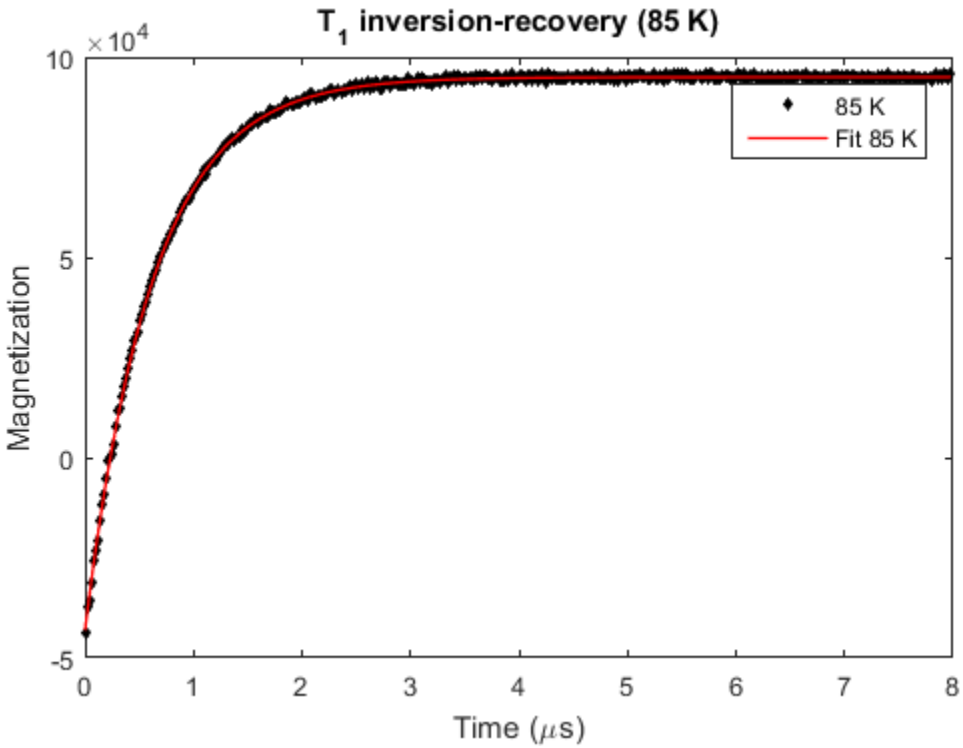

Figure B.13

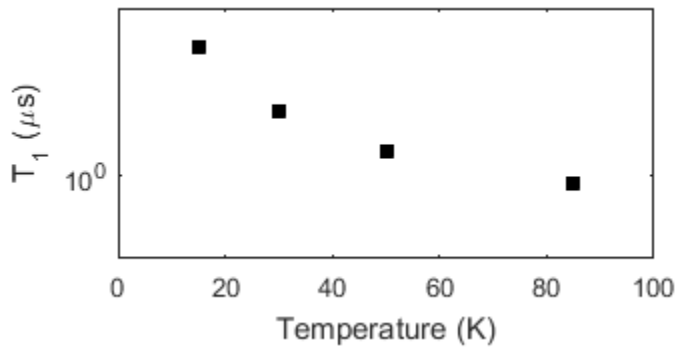

Figure B.14. T_1 relaxation times of **4**.

Temperature (K)	**T_1 (μs)**	**T_2 (ns)**	**τ (ns)**
15	1128	993.3	992.4
30	33.25	980.3	952.2
50	3.879	909	736.4
85	0.623	450.4	261.5

5. UV-Vis Spectra

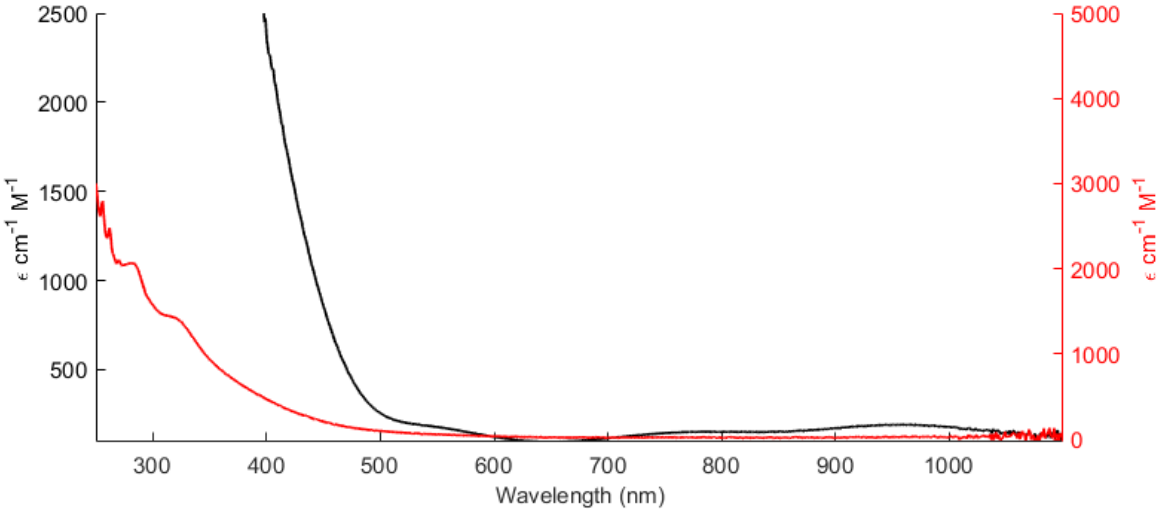

Figure B.15. UV-visible spectrum of (P_3^B)Fe(Cl) (**1**) (THF, 293 K). Black trace corresponds to the left axis scale, while the red trace corresponds to the right axis scale.

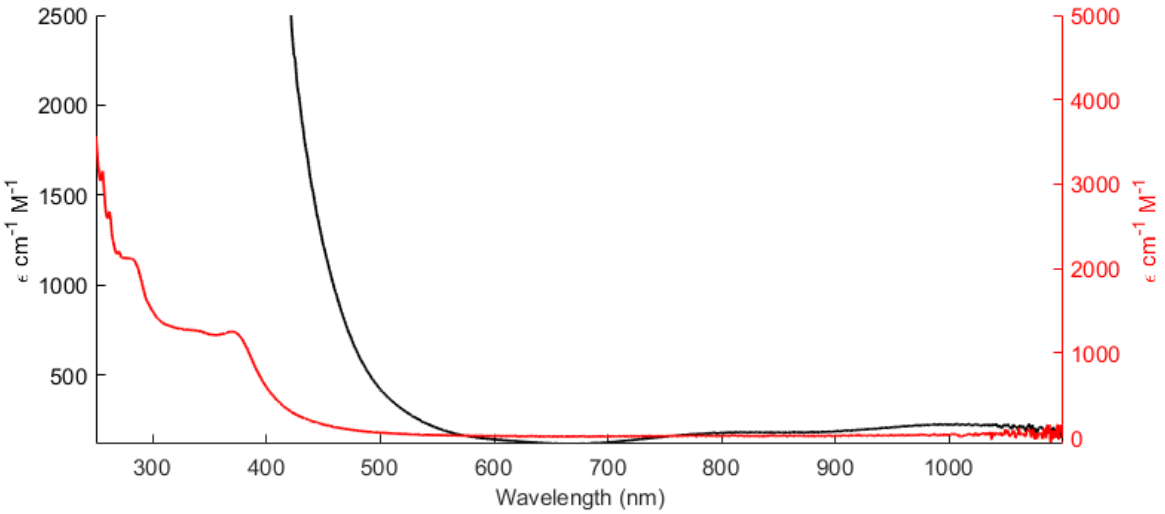

Figure B.16. UV-visible spectrum of (P_3^B)Fe(N_3) (**2**) (THF, 293 K). Black trace corresponds to the left axis scale, while the red trace corresponds to the right axis scale.

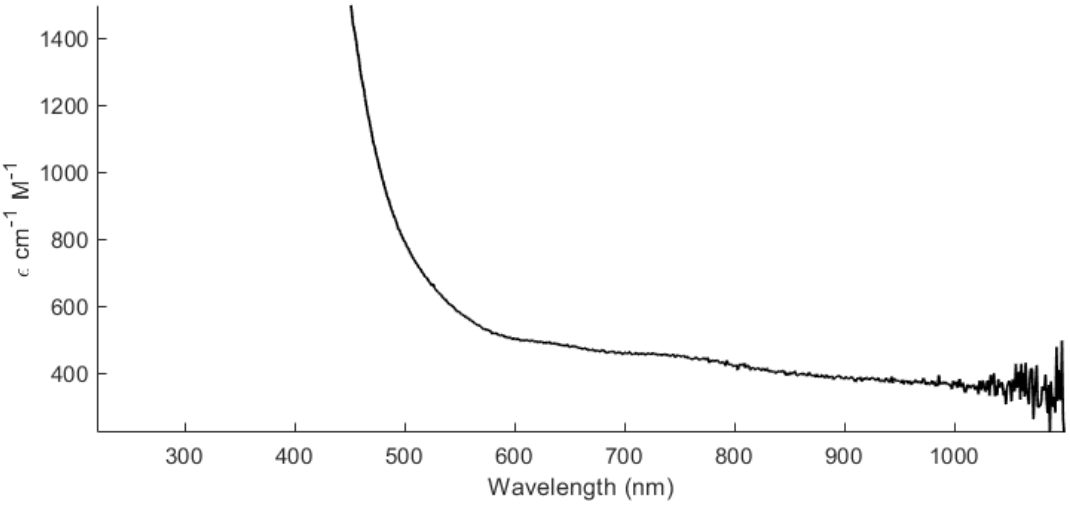

Figure B.17. UV-visible spectrum $[(P_3^B)]_2(\mu\text{-}1,3\text{-}N_3)$ (**3**) generated in-situ by mixing equimolar solution of **2** and $(P_3^B)Fe(N_2)$ (THF, 293 K).

6. Crystallographic Details and Tables

Table B.1. Crystallographic Data for Compounds **1-3**

	1	**2**	**3**
chem formula	$C_{35}H_{54}BClFeP_3$	$C_{38.5}H_{60}BFeN_3P_3$	$C_{84}H_{120}B_2Fe_2N_3P_6$
fw	681.81	724.46	1490.97
cryst syst	Triclinic	Cubic	Monoclinic
space group	P-1	Pa-3	P21/c
a [Å]	10.8929(7)	19.953(3)	11.0614(7)
b [Å]	11.5482(7)	19.953(3)	17.7504(11)
c [Å]	15.8266(9)	19.953(3)	20.8069(12)
α [°]	91.335(2)	90	90
β [°]	97.048(2)	90	102.344(3)
γ [°]	117.325(2)	90	90
V [$Å^3$]	1748.20(19)	7944(4)	3990.9(4)
Z	2	8	2
Dcalcd [g cm^{-3}]	1.295	1.213	1.241
F(000)	726	3107.4	1594
μ [mm^{-1}]	0.67	0.53	0.529
temp. [K]	100	100	100
wavelength [Å]	0.71073	0.71073	0.71073
measd rflns	104461	156002	41848
unique rflns	21944	8697	8148
data/restraints/param	21944/6/417	8697/68/182	8148/0/451
R(F) ($I>2\sigma(I)$)	0.0363	0.0379	0.0537
wR(F^2) (all)	0.0942	0.1101	0.113
GOF	1.021	1.085	1.018

DFT Calculations

General

All calculations were performed using the ORCA 4.0[5,6] program. In cases where crystal structures were available these coordinates were used as the input. The calculations were performed using the TPSS (meta-GGA)[7] functional with the def2-SVP basis set on C and H and the def2-TZVP basis set on Fe. To assure that optimized structures represented true stationary points was checked by doing a single-point frequency calculations on the optimized structure.

EPR parameters were calculated using TPPSh, TPSS, B3LYP, M06L, and BP86. The TPSS-optimized structures were calculated by doing a single point calculation on the optimized structures using CP(PPP)[8] on Fe and IGLO-III[9] on everything else grid 7. These basis sets and functionals have previously shown to be good predictors of phosphine and hydrogen hyperfine coupling constants in iron phosphine complexes.[10,11] See below for a summary of the results.

7.2 EPR predictions

Table B.2. Experimental and DFT-calculated EPR parameters. Experimental g = [2.0293, 2.0293, 1.9975].

Functional	Basis set	^{14}N (a_{iso}) (MHz)	$A(^{14}N)$ (MHz)	e^2Qq/h (^{14}N)	η (^{14}N)	^{11}B (a_{iso}) (MHz)	$A(^{11}B)$ (MHz)	e^2Qq/h (^{11}B)	η (^{11}B)	^{31}P (a_{iso}) (MHz)	$A(^{31}P)$ (MHz)	^{57}Fe (a_{iso}) (MHz)	$A(^{57}Fe)$ (MHz)
experimental		± 3.9	± [-4.3, -4.3, 20.3]	≈ ± 3.1	≈ 0	± 41.3	±[21.5, 21.5, 81]	≈ ± 2.8	≈ 0	± 44.3	± [49, 45, 39]	± 22	± [10, 10, 46]
TPSSh	IGLO-III	1.9	[-7.7 -7.8 21.2]			40.1	[20.3 20.3 79.65]			-40.4	[-35.5 -39.8 -45.8]	21.8	[11.3 11.3 42.7]
TPSS	IGLO-III	1.62	[-8.0 -8.0 20.87]			40.1	[20.3 20.3 79.7]			-33.5	[-28.7 -33.5 -38.3]	19.4	[9.2 9.3 39.7]
B3LYP	IGLO-III	3.6	[-4.8 -4.8 20.5]			39.0	[18.0 18.0 81.0]			-38.5	[-33.6 38.2 43.6]	21.9	[10.5 10.6 44.6]
BP86	IGLO-III	-0.26	[-9.0 -9.0 17.3]			34.23	[13.8 13.80 75.1]			-35.4	[-30.2 -35.56 -40.51]	16.75	[6.5 6.5 37.23]
M06l	IGLO-III	3.52	[-11.6 -11.7 33.9]			25.0	[2.3 2.8 69.8]			-59.0	[-52.4 -59.4 65.1]	20.5	[10.1 10.2 41.1]

References:

(1) Bontemps, S.; Bouhadir, G.; Dyer, P. W.; Miqueu, K.; Bourissou, D. Quasi-Thermoneutral P -> B Interactions within Di- and Tri-Phosphine Boranes. *Inorg. Chem.* **2007**, *46* (13), 5149–5151.

(2) Moret, M.-E.; Peters, J. C. Terminal Iron Dinitrogen and Iron Imide Complexes Supported by a Tris(Phosphino)Borane Ligand. *Angew. Chem. Int. Ed.* **2011**, *50*, 2063–2067.

(3) Anderson, J. S.; Moret, M. E.; Peters, J. C. Conversion of Fe–NH_2 to Fe–N_2 with Release of NH_3. *J. Am. Chem. Soc.* **2013**, *135* (2), 534–537..

(4) Ayscough, P. B.; Thomson, C. Electron Spin Resonance Spectra of Alkyl Radicals in γ-Irradiated Alkyl Halides. *Trans. Faraday Soc.* **1962**, *58* (0), 1477–1494.

(5) Neese, F. The ORCA Program System. *WIREs Computational Molecular Science* **2012**, *2* (1), 73–78.

(6) Neese, F. Software Update: The ORCA Program System, Version 4.0. *WIREs Computational Molecular Science* **2018**, *8* (1), e1327.

(7) Tao, J.; Perdew, J. P.; Staroverov, V. N.; Scuseria, G. E. Climbing the Density Functional Ladder: Nonempirical Meta-Generalized Gradient Approximation Designed for Molecules and Solids. *Phys. Rev. Lett.* **2003**, *91* (14), 146401–146404.

(8) Neese, F. Prediction and Interpretation of the 57Fe Isomer Shift in Mössbauer Spectra by Density Functional Theory. *Inorganica Chimica Acta* **2002**, *337*, 181–192.

(9) Kutzelnigg, W.; Fleischer, U.; Schindler, M. The IGLO-Method: Ab-Initio Calculation and Interpretation of NMR Chemical Shifts and Magnetic Susceptibilities. In *Deuterium and Shift Calculation*; Fleischer, U., Kutzelnigg, W., Limbach, H.-H., Martin, G. J., Martin, M. L., Schindler, M., Eds.; Springer Berlin Heidelberg: Berlin, Heidelberg, 1991; pp 165–262.

(10) Drover, M. W.; Schild, D. J.; Oyala, P. H.; Peters, J. C. Snapshots of a Migrating H-Atom: Characterization of a Reactive Iron(III) Indenide Hydride and Its Nearly Isoenergetic Ring-Protonated Iron(I) Isomer. *Angewandte Chemie International Edition* **2019**, *58* (43), 15504–15511.

(11) Schild, D. J.; Drover, M. W.; Oyala, P. H.; Peters, J. C. Generating Potent C–H PCET Donors: Ligand-Induced Fe-to-Ring Proton Migration from a Cp^*Fe^{III}–H Complex Demonstrates a Promising Strategy. *J. Am. Chem. Soc.* **2020**, *142* (44), 18963–18970.

Appendix C : Supporting Information for Chapter 4

General Considerations

All experiments were carried out employing standard Schlenk techniques under an atmosphere of dry nitrogen employing degassed, dried solvents in a solvent purification system supplied by SG Water, LLC. Non-halogenated solvents were tested with a standard purple solution of sodium benzophenone ketyl in tetrahydrofuran in order to confirm effective moisture removal. *trans*-$FeBr_2(depe)_2$cvi, $FeBr_2$(dippe)cvii, Fe(η^6-toluene)(dippe), Fe(Cp*)(dppe)H were prepared according to a literature procedure. All other reagents were purchased from commercial vendors and used without further purification unless otherwise stated.

***Hydrogen Analysis*:** The headspace of reaction flasks was analyzed by gas chromatography to quantify H_2 evolution with an Agilent 7890A gas chromatograph (HPPLOT U, 30 m, 0.32 mm i.d., 30 °C isothermal, 1 mL/min flow rate, N_2 carrier gas) using a thermal conductivity detector.

Nuclear Magnetic Resonance Spectroscopy

^1H and ^{13}C chemical shifts are reported in ppm relative to tetramethylsilane, using residual solvent resonances as internal standards. ^{31}P chemical shifts are reported in ppm and referenced externally to 85% aqueous H_3PO_4 at 0 ppm.

III. ^{57}Fe Mössbauer Spectroscopy

Mössbauer spectra were recorded on a spectrometer from SEE Co. (Edina, MN) operating in the constant acceleration mode in transmission geometry. The sample was kept in an SVT-400 cryostat form Janis (Wilmington, MA), using liquid N_2 as a cryogen for 80 K measurements. The quoted isomer shifts are relative to the centroid of the spectrum of a metallic foil of α-Fe at room temperature. Solid samples were prepared by grinding solid material into a fine powder and then mounted in to a Delrin cup fitted with a screw cap as a boron nitride pellet. Solution samples were transferred to a sample cup and chilled to 77 K inside of the glovebox, and quickly removed from the glovebox and immersed in liquid N_2 until mounted in the cryostat. Data analysis was performed using WMOSS version 4 (www.wmoss.org) and quadrupole doublets were fit to Lorentzian lineshapes.[cviii]

IV. Infrared Spectroscopy:

Solid and thin film IR measurements were obtained on a Bruker Alpha spectrometer equipped with a diamond ATR probe.

UV-VIS Spectroscopy

UV-Visible spectroscopy measurements were collected with a Cary 50 UV-Vis spectrophotometer using a 1 cm two-window quartz cell.

EPR Spectroscopy:

Continuous wave X-band EPR spectra were obtained on a Bruker EMX spectrometer using solutions prepared as frozen glasses in 2-MeTHF. Pulse EPR spectroscopy: All pulse X-band (9.4-9.7) EPR, electron nuclear double resonance (ENDOR), and hyperfine sublevel correlation spectroscopy (HYSCORE) experiments were acquired using a Bruker ELEXSYS E580 pulse EPR spectrometer. X-band ENDOR and HYSCORE experiments were performed using a Bruker MD-4 X-band ENDOR resonator. Temperature control was achieved using an ER 4118HV-CF5-L Flexline Cryogen-Free VT cryostat manufactured by ColdEdge equipped with an Oxford Instruments Mercury ITC temperature controller.

All pulse X-band ($\nu \approx 9.4$-9.7 GHz) EPR and electron nuclear double resonance (ENDOR) experiments were aquired using a Bruker (Billerica, MA) ELEXSYS E580 pulse EPR spectrometer equipped with a Bruker MD-4 resonator. Temperature control was achieved using an ER 4118HV-CF5-L Flexline Cryogen-Free VT cryostat manufactured by ColdEdge (Allentown, PA) equipped with an Oxford Instruments Mercury ITC.

Pulse X-band ENDOR was acquired using the Davies pulse sequence ($\pi - T_{RF} - \pi_{RF} - T_{RF} - \pi/2 - \tau - \pi -$ echo), where T_{RF} is the delay between mw pulses and RF pulses, π_{RF} is the length of the RF pulse and the RF frequency is randomly sampled during each pulse sequence.

X-band HYSCORE spectra were acquired using the 4-pulse sequence ($\pi/2 - \tau - \pi/2 - t_1 - \pi - t_2 - \pi/2$ – echo), where τ is a fixed delay, while t_1 and t_2 are independently incremented by Δt_1 and Δt_2, respectively. The time domain data was baseline-corrected (third-order polynomial) to eliminate the exponential decay in the echo intensity, apodized with a Hamming window function, zero-filled to eight-fold points, and fast Fourier-transformed to yield the 2-dimensional frequency domain. For ^{2}H-^{1}H difference spectra, the time domain of the HYSCORE spectrum of the ^{1}H sample was subtracted from that of the ^{2}H sample, and the same data processing procedure detailed above was used to generate the frequency spectrum.

In general, the ENDOR spectrum for a given nucleus with spin I= ½ (^{1}H, ^{31}P) coupled to the S = ½ electron spin exhibits a doublet at frequencies

$$\nu_{\pm} = \left|\frac{A}{2} \pm \nu_N\right| \quad (1)$$

Where ν_N is the nuclear Larmor frequency and A is the hyperfine coupling. For nuclei with $I \geq 1$ (^{2}H), an additonal splitting of the $\nu_{\pm}$ manifolds is produced by the nuclear quadrupole interaction (P)

$$\nu_{\pm,m_I} = \left|\nu_N \pm \frac{3P(2m_I - 1)}{2}\right| \quad (2)$$

In HYSCORE spectra, these signals manifest as cross-peaks or ridges in the 2-D frequency spectrum which are generally symmetric about the diagonal of a given quadrant. This technique allows hyperfine levels corresponding to the same electron-nuclear submanifold to be differentiated, as well as separating features from hyperfine couplings in the weak-coupling regime ($|A| < 2|\nu_I|$) in the (+,+) quadrant from those in the strong coupling

regime ($|A| > 2|\nu_I|$) in the (−,+) quadrant. The (−,−) and (+,−) quadrants of these frequency spectra are symmetric to the (+,+) and (−,+) quadrants, thus typically only two of the quadrants are typically displayed in literature.

For systems with appreciable hyperfine anisotropy in frozen solutions or solids, HYSCORE spectra typically do not exhibit sharp cross peaks, but show ridges that represent the sum of cross peaks from selected orientations within the excitation bandwidth of the MW pulses at the magnetic field position at which the spectrum is collected. The length and curvature of these correlation ridges can allow for the separation and estimation of the magnitude of the isotropic and dipolar components of the hyperfine tensor, as shown in Fig. C1.

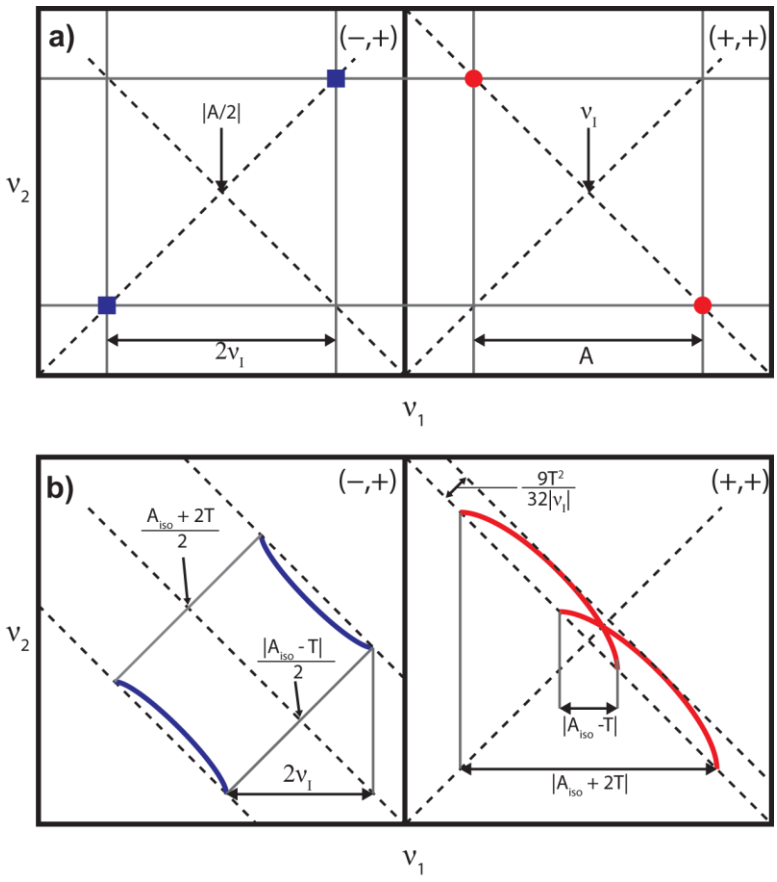

Figure C.1 a) HYSCORE powder patterns for an S = 1/2, I = 1/2 spin system with an isotropic hyperfine tensor A. b) HYSCORE powder patterns for an S = 1/2, I = 1/2 spin system with an isotropic hyperfine tensor which contains isotropic (a_{iso}) and dipolar (T) contributions. Blue correlation ridges represent the strong coupling case; red correlation ridges represent the weak coupling case.

EPR Simulations. Simulations of all CW and pulse EPR data were achieved using the EasySpincix simulation toolbox (release 5.2.21) with Matlab 2018b using the following Hamiltonian:

$$\hat{H} = \mu_B \vec{B}_0 g \hat{S} + \mu_N g_N \vec{B}_0 \hat{I} + h\hat{S} \cdot \mathbf{A} \cdot \hat{I} + h\hat{I} \cdot \mathbf{P} \cdot \hat{I} \qquad (3)$$

In this expression, the first term corresponds to the electron Zeeman interaction term where μ_B is the Bohr magneton, g is the electron spin g-value matrix with principle components g = [g_{xx} g_{yy} g_{zz}], and $\hat{S}$ is the electron spin operator; the second term corresponds to the nuclear Zeeman interaction term where μ_N is the nuclear magneton, g_N is the characteristic nuclear g-value for each nucleus (e.g. ^{1}H, ^{2}H ,^{31}P) and $\hat{I}$ is the nuclear spin operator; the third term corresponds to the electron-nuclear hyperfine term, where **A** is the hyperfine coupling tensor with principle components **A** = [A_{xx}, A_{yy}, A_{zz}]; and for nuclei with $I \geq 1$, the final term corresponds to the nuclear quadrupole (NQI) term which arises from the interaction of the nuclear quadrupole moment with the local electric field gradient (efg) at the nucleus, where **P** is the quadrupole coupling tensor. In the principal axis system (PAS), **P** is traceless and parametrized by the quadrupole coupling constant e^2Qq/h and the asymmetry parameter η such that:

$$\mathbf{P} = \begin{pmatrix} P_{xx} & 0 & 0 \\ 0 & P_{yy} & 0 \\ 0 & 0 & P_{zz} \end{pmatrix} = \frac{e^2Qq/h}{4I(2I-1)} \begin{pmatrix} -(1-\eta) & 0 & 0 \\ 0 & -(1+\eta) & 0 \\ 0 & 0 & 2 \end{pmatrix} \qquad (4)$$

where $\frac{e^2Qq}{h} = 2I(2I-1)P_{zz}$ and $\eta = \frac{P_{xx}-P_{yy}}{P_{zz}}$. The asymmetry parameter may have values between 0 and 1, with 0 corresponding to an electric field gradient with axial symmetry and 1 corresponding to a fully rhombic efg.

The orientations between the hyperfine and NQI tensor principal axis systems and the g-matrix reference frame are defined by the Euler angles (α, β, γ), with rotations performed within the zyz convention where α rotates xyz counterclockwise about z-axis to give x'y'z', β rotates x'y'z counterclockwise about y'-axis to give x",y",z", γ rotates xyz counterclockwise about z"-axis to give final frame orientation.

Electrochemistry

Electrochemical measurements were carried out using a CD instruments 600B electrochemical analyzer. A freshly polished glassy carbon electrode was used as the working electrode and a graphite rod was used as the auxiliary electrode. Solutions (THF) of electrolyte (0.4 M tetra-n-butylammonium hexafluorophosphate) contained ferrocene (0.1 mM), to serve as an internal reference, and analyte (0.2 mM). All reported potentials are referenced to the ferrocene/ferrocenium couple, $[Cp_2Fe]^+$ /Cp_2Fe.

Synthetic Procedures

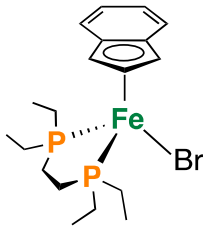

Fe(η^3:η^2-Ind)(depe)(Br) (**1**): To a solution of *trans*-$FeBr_2(depe)_2$ (402 mg, 0.64 mmol, 1 equiv.) in THF at -78 °C was added drop-wise a chilled (-78 °C) solution of lithium indenide (78 mg, 0.64 mmol, 1 equiv.). Following addition, the resulting mixture was stirred for an additional 2 h at room temperature, giving a clear purple solution. Subsequently, all volatiles were removed *in-vacuo* and the residue was washed with pentane (2 x 20 mL) and Et_2O (2 x 20 mL). The resulting purple solid was dissolved in THF and filtered through a pad of Celite®. Cooling a pentane-layered THF solution at –35 ºC afforded **1** as dark purple crystals (132

mg, 45%). ***N.B.*** Allowing this reaction mixture to stir for longer than 2 h results in appreciable formation of $Fe(Ind)_2$ and free ligand.

^{1}H NMR (C_6D_6, 400 MHz, 298 K): δ = 7.54 (m, 2H), 7.10 (m, 2H), 4.56 (br s, 1H), 4.01 (br s, 2H), 2.13 (m, 2H), 1.79 (m, 2H), 1.64 (m, 2H), 1.28 (m, 2H), 1.12 (m, 4H), 1.01 (m, 6H), 0.77 (m, 6H). **^{31}P{^{1}H} NMR (C_6D_6, 162 MHz, 298 K)**: δ = 92.98. **^{13}C NMR (THF-d_8, 100 MHz, 298 K)**: δ = 127.99, 125.39, 83.13 (η^3:η^2-C_9H_7), 58.07 (η^3:η^2-C_9H_7), 23.60, 21.92, 20.40, 10.13, 8.99. **CV data (1 mM, vs. Fc/Fc$^+$)**: - 0.53 V (Fe^{II}/Fe^{III}). **UV-VIS (THF, 1 cm cell, 298 K)**: ε = 529 {313 $M^{-1}cm^{-1}$}, 687 {208 $M^{-1}cm^{-1}$}. **Anal. Calcd.** for $C_{19}H_{31}BrFeP_2$ (456.04): C, 49.92; H, 6.84. Found: C, 50.40; H, 6.96.

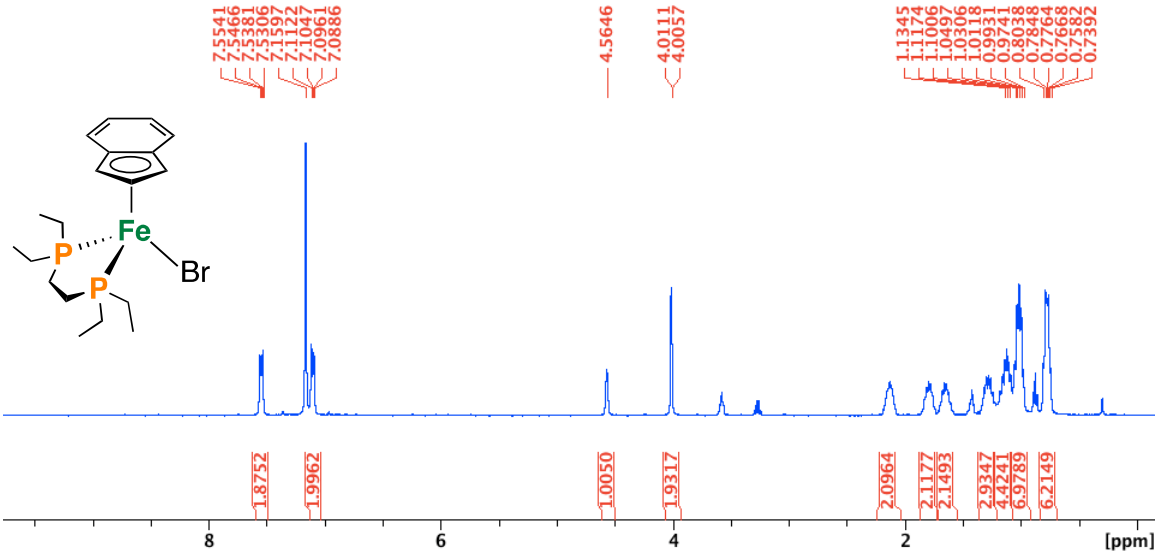

Figure C.2 ^{1}H NMR, C_6D_6, 400 MHz, 298 K

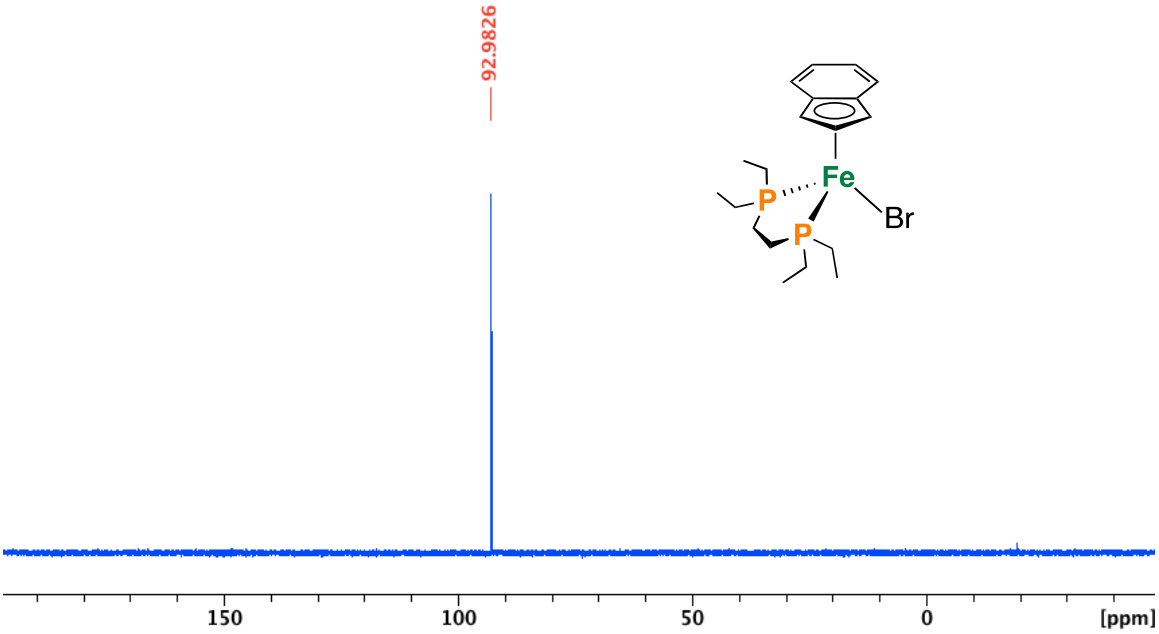

Figure C.3. $^{31}P\{^{1}H\}$ NMR, C_6D_6, 162 MHz, 298 K

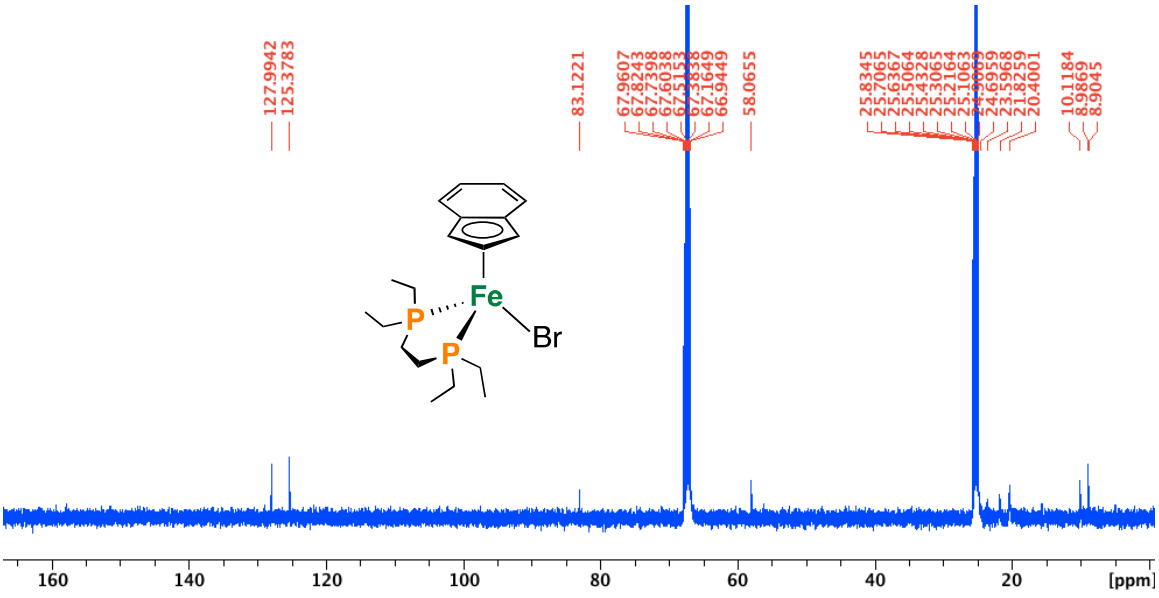

Figure C.4. $^{31}C\{^{1}H\}$ NMR, THF-d_8, 100 MHz, 298 K

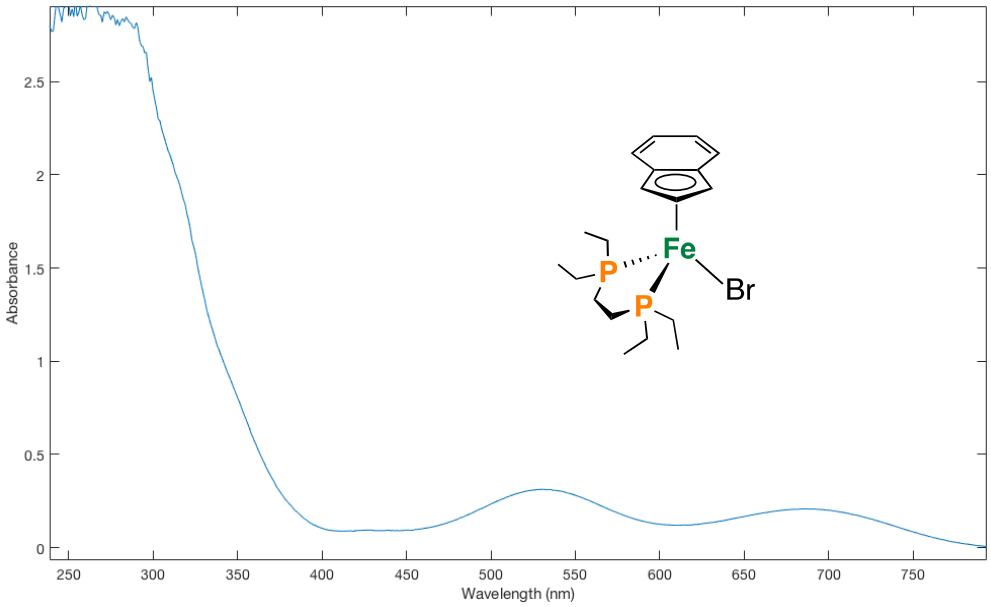

Figure C.5. UV-Visible spectrum, THF, 298 K (= 529, 687 nm)

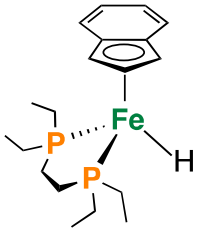

Fe(η^3:η^2-Ind)(depe)(H) (**2**): To a solution of **1** (21.5 mg, 0.047 mmol, 1 equiv.) in THF at -78 °C was added drop-wise a chilled (-78 °C) 1.0 M solution of Li[BEt_3H] (47.1 L, 0.047 mmol, 1 equiv.). Following addition, the resulting mixture was stirred for an additional 10 min at -78 °C and then at room temperature for 2 h, giving a clear red solution. Subsequently, all volatiles were removed *in-vacuo* and the residue was dissolved in pentane (5 mL) and filtered through a pad of Celite®. This was repeated three times to give **2** as a red oil (17.5 mg, 98%). Efforts to recrystallize **2** were unsuccessful.

^{1}H NMR (C_6D_6, 400 MHz, 298 K): δ = 7.39 (m, 2H), 6.81 (m, 2H), 4.73 (br s, 2H), 4.71 (m, 1H), 1.57-1.34 (m, 8H), 1.25 (m, 4H), 0.99 (m, 6H), 0.75 (m, 6H), -20.64 (t, $^2J_{H,P}$ = 70.8 Hz, $^1J_{Fe,H}$ = 10.3 Hz). **^{31}P{^{1}H} NMR (C_6D_6, 162 MHz, 298 K)** δ = 106.38 ($^2J_{H,P}$ = 70.8 Hz, $^1J_{Fe,P}$ = 60.3 Hz). **^{13}C NMR (C_6D_6, 100 MHz, 298 K)**: δ = 126.69, 121.00, 97.73, 80.09

(η^3:η^2-C_9H_7), 62.22 (η^3:η^2-C_9H_7), 27.01 (m), 25.89 (dd, $J_{C,P}$ = 21.4 Hz, $J_{C,P}$ = 19.5 Hz), 25.24 (dd, $J_{C,P}$ = 6.9 Hz, $J_{C,P}$ = 4.89 Hz), 9.27, 9.14. **IR (thin film, 298 K, cm^{-1})**: 1851 cm^{-1} (ν_{FeH}). **^{57}Fe Mössbauer (80 K, Et$_2$O solution, mm/s)**: δ = 0.28, ΔE_Q = 1.61. **CV data (1 mM, vs. Fc/Fc$^+$)**: - 0.81 V (Fe^{II}/Fe^{III}). **UV-VIS (THF, 1 cm cell, 298 K)**: ε = 396 {498 $M^{-1}cm^{-1}$}, 506 {912 $M^{-1}cm^{-1}$}. *N.B.* Given the physical nature of **2**, elemental analysis was not acquired.

Probing bimolecular H_2 loss:

To a *J. Young* NMR tube cooled to -78 °C containing a THF-d_8 solution (300 μL) of 4.5 mg (12 μmol) **2-H** and 4.5 mg (12 μmol) **2-D** (500 μL) was added 25.6 mg (25 μmol)

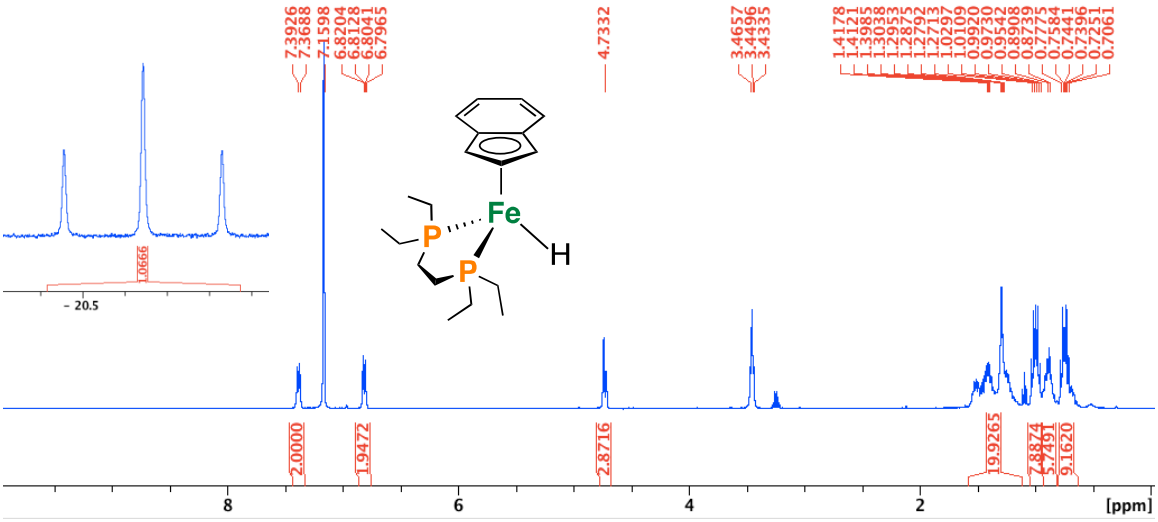

Figure C.6. ^{1}H NMR, C_6D_6, 400 MHz, 298 K

[Fc]$BAr^F{}_4$ in 200 μL THF-d_8. The tube was shaken and warmed to room temperature. NMR spectroscopy confirms the presence of both H_2 and HD. **^{1}H NMR (THF-d_8, 400 MHz, 298 K)**:δ= 4.50 ppm (t, $^1J_{H,D}$ = 42 Hz; HD), 4.55 (s, H_2).

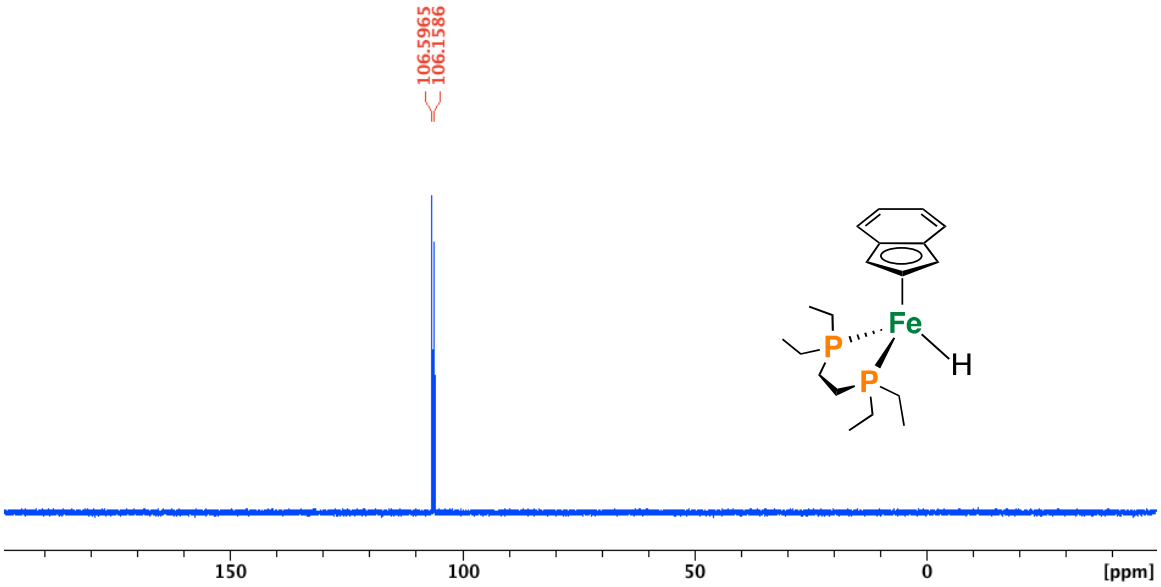

Figure C.7. $^{31}P\{^{1}H\}$ NMR, C_6D_6, 162 MHz, 298 K

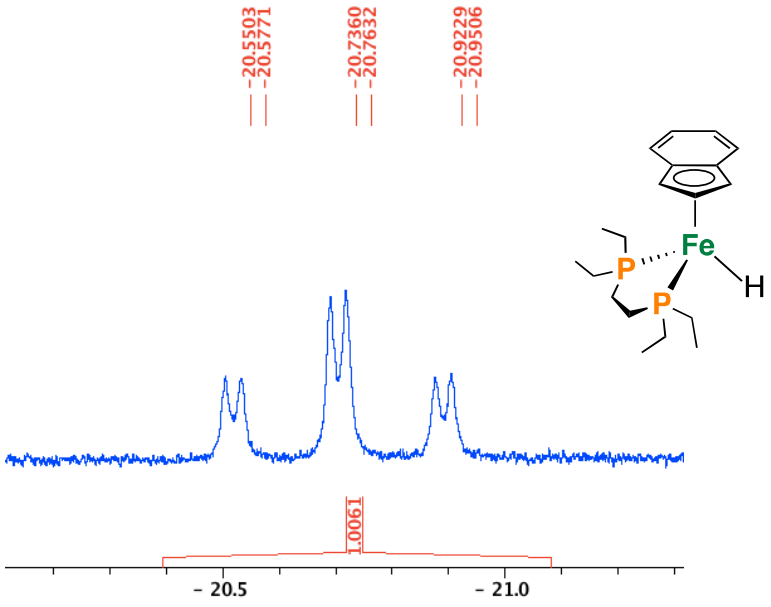

Figure C.8. ^{1}H NMR, C_6D_6, 400 MHz, 298 K

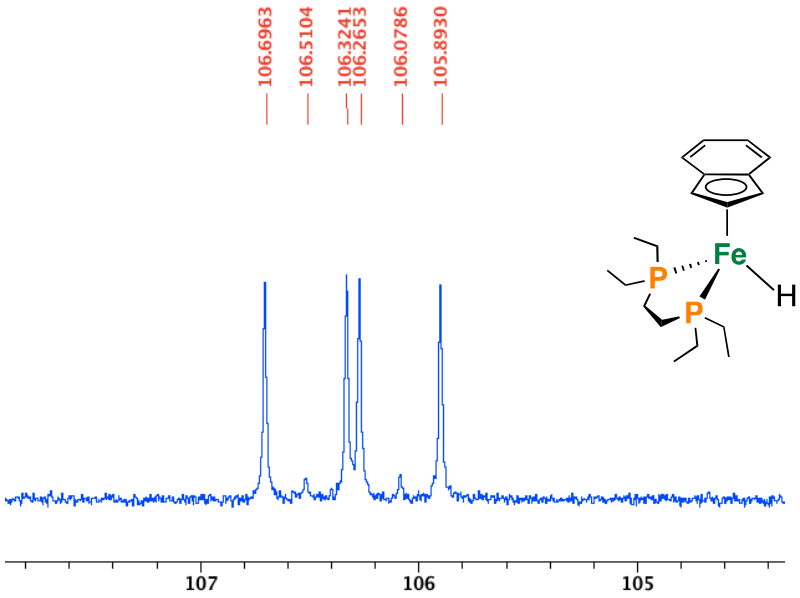

Figure C.9. 2-^{57}Fe, ^{31}P{^{1}H} NMR, C_6D_6, 162 MHz, 298 K

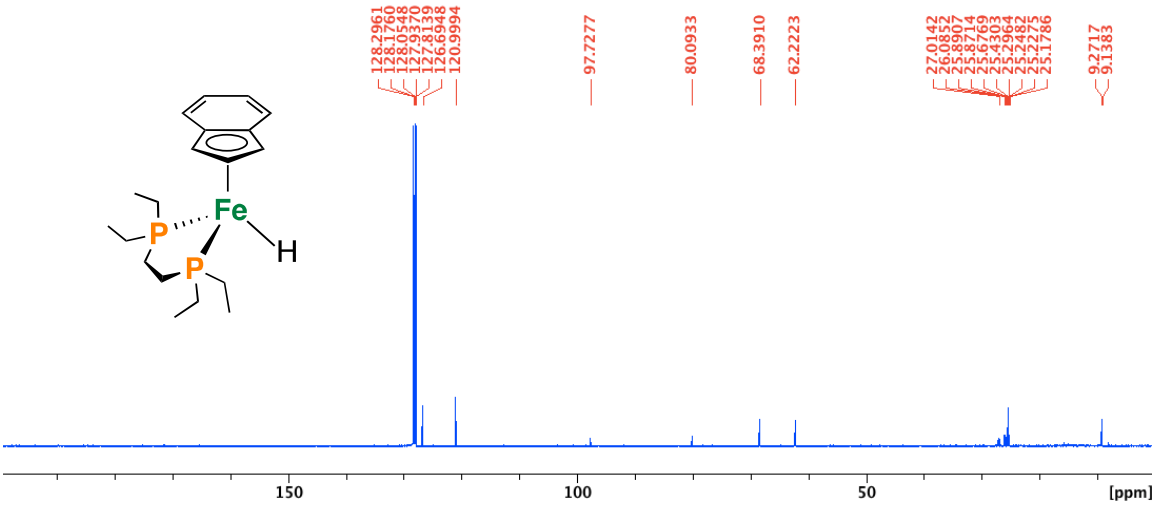

Figure C.10. $^{13}C\{^{1}H\}$ NMR, C_6D_6, 100 MHz, 298 K

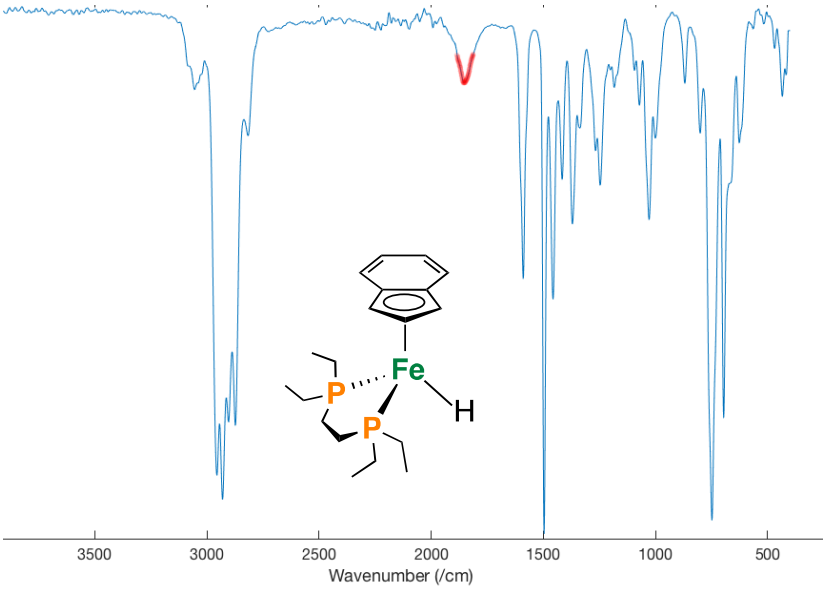

Figure C.11. 2, FT-IR ATR, thin film, 298 K (μ_{FeH} = 1851 cm^{-1})

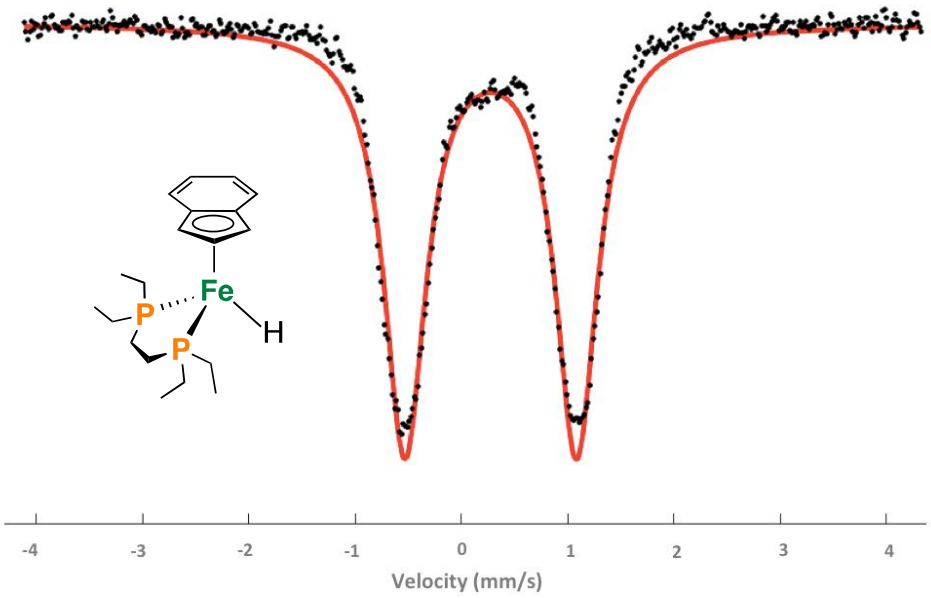

Figure C.12. 80 K ^{57}Fe Mössbauer spectrum collected in the presence of a 50 mT magnetic field oriented parallel to the propagation of the γ-beam (frozen solution in Et_2O).δ= 0.28 mm/s, ΔE_Q = 1.61 mm/s.$\Gamma_L = \Gamma_R$ = 0.50 mm/s.

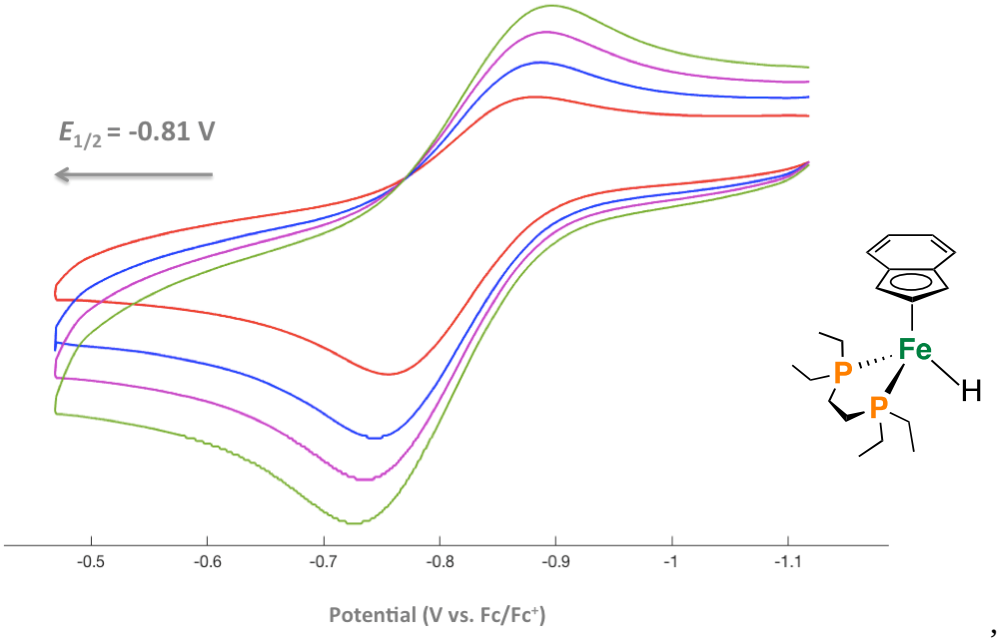

,

Figure C.13. Cylic Voltammogram, THF, 298 K showing a reversible feature at - 0.81 V for the Fe(II)/Fe(III) couple (vs. Fc/Fc^+) in 4 mL THF, 0.4 M $[NBu_4][PF_6]$ and analyte (1 mM). Data was collected at x mV/s with Pt counter, glassy carbon working, and Ag/AgOTf reference electrodes (■ 100 mV/s, ■ 200 mV/s, ■ 300 mV/s, and ■ 400 mV/s).

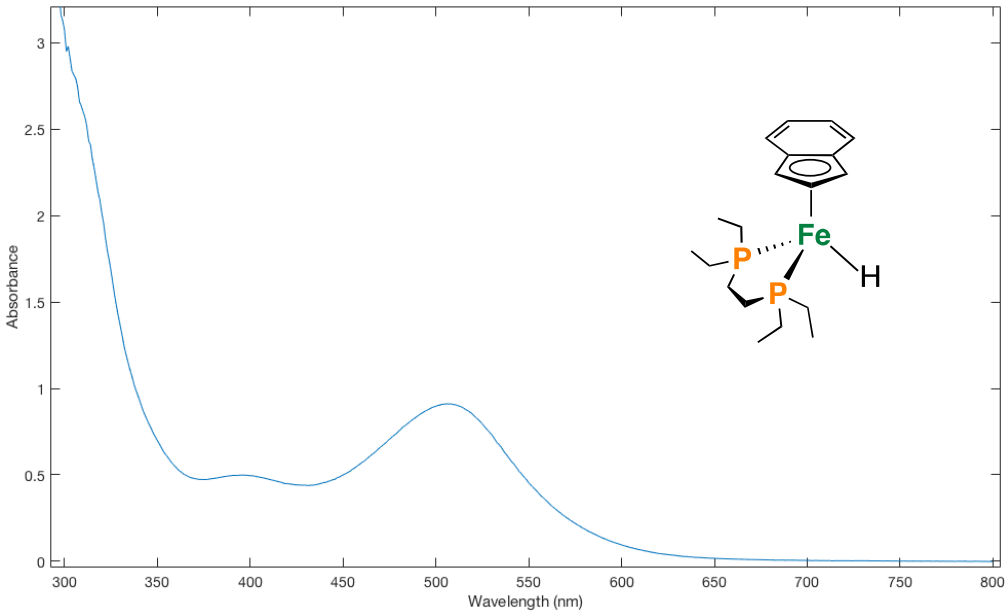

Figure C.14. UV-Visible spectrum, THF, 298 K

[Fe(η^6-IndH)(depe)][BAr$^F_4$] [**4**][BAr$^F_4$]: To a solution of **2** (12.9 mg, 0.034 mmol, 1 equiv.) in Et_2O at -78 ˚C was added drop-wise a chilled (-78 ˚C) solution of Fc[BAr$^F_4$] (35.9 mg, 0.034 mmol, 1 equiv.). Following addition, the resulting dark orange mixture was stirred for an additional 20 min at -78 ˚C and then all volatiles were removed *in-vacuo* at -78 ˚C. Next, the residue was washed with 20 mL cold (-78 ˚C) pentane, dissolved in cold (-78 ˚C) Et_2O, layered with pentane and placed in the freezer at -35 ˚C causing deposition of yellow ([**4**][BAr$^F_4$]) and purple ([**7**][BAr$^F_4$]$_2$) crystals. *N.B.* Considerably fewer (~ 1:10) orange crystals were observed.

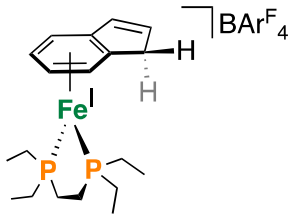

Yield: According to a ^{57}Fe Mössbauer experiment, oxidation of **2**-^{57}Fe at -78 ºC produces *ca.* 30% of [**4**]$^+$ after 5 min.

^{57}Fe Mössbauer (80 K, Et$_2$O solution, mm/s): δ= 0.59 mm/s, ΔE_Q = 1.80 mm/s. **X-Band EPR (77 K, 2-MeTHF):** Sys.g = [2.332, 2.042, 1.992], Sys.lw = 1.2, Sys.Nucs = '^{31}P, ^{31}P', Sys.A = [86, 104, 100; 93, 88, 94], Sys.HStrain = [319 67 11], Exp.mwFreq = 9.389.

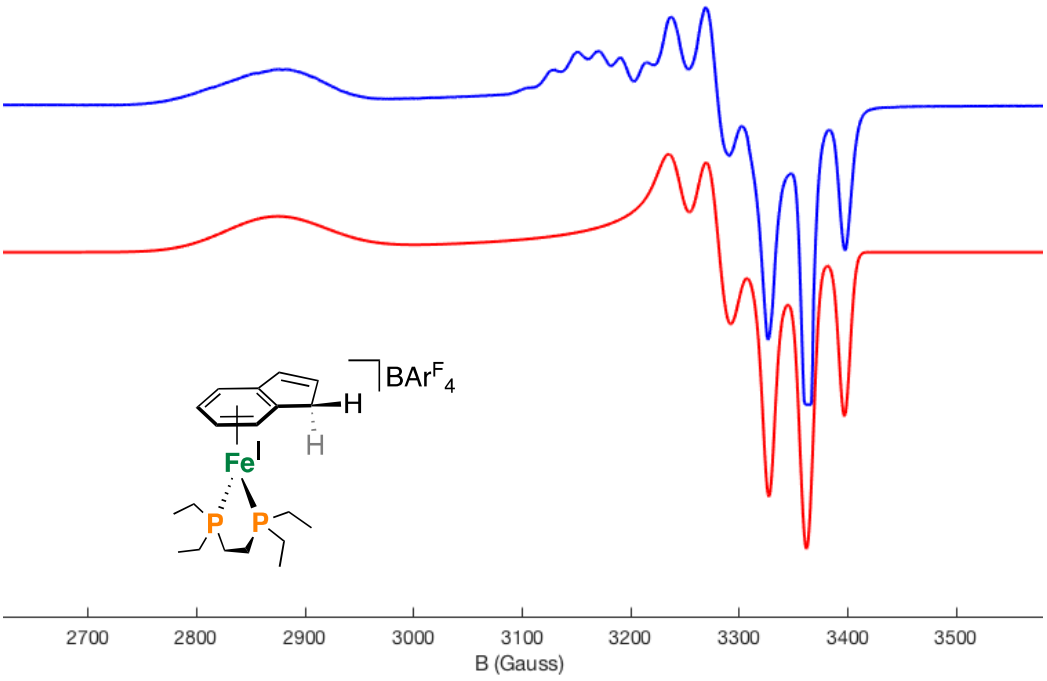

Figure C.15. [**4**][BAr$^F_4$], 77 K X-band EPR spectrum in 2-MeTHF with simulations; blue trace: experiment; red trace: simulation (Sys.g = [2.332, 2.042, 1.992], Sys.lw = 1.2, Sys.Nucs = '^{31}P, ^{31}P', Sys.A = [86, 104, 100; 93, 88, 94], Sys.HStrain = [319 67 11], Exp.mwFreq = 9.389].

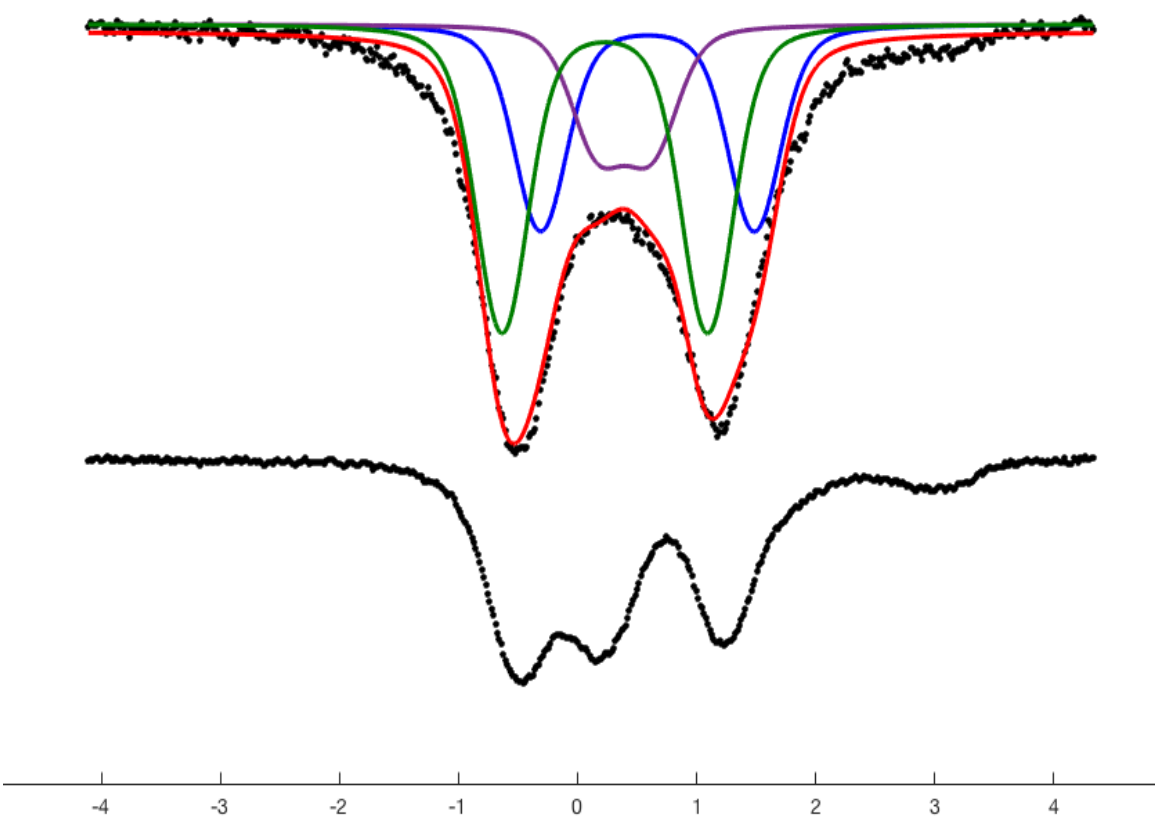

Figure C.16. 80 K ^{57}Fe Mössbauer spectrum collected in the presence of a 50 mT magnetic field oriented parallel to the propagation of the γ-beam (frozen solution in 2-MeTHF).

Addition of [Fc]BAr$^{F}_{4}$ to **2-^{57}Fe** at -78 ^{o}C. Top spectrum shows freeze-quenched sample after 5 min. Bottom spectrum shows freeze-quench after stirring at room temperature for 15 min. Parameters: δ = 0.23 mm/s, ΔE_Q = 1.73 mm/s (**green, 42%**); δ = 0.59 mm/s, ΔE_Q = 1.80 mm/s (**blue, 28%**), δ = 0.40 mm/s, ΔE_Q = 0.46 mm/s (**violet, 16%**); $\Gamma_L = \Gamma_R$ = -0.50 mm/s. *N.B.* These fits are not strictly required by the data.

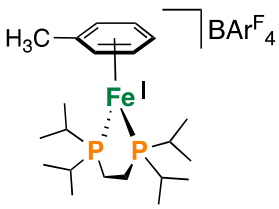

[Fe(η^6-toluene)(dippe)][BAr$^F_4$] [**5**][BAr$^F_4$]: To a solution of Fe^0(η^6-toluene)(dippe) (16.7 mg, 0.041 mmol, 1 equiv.) in Et_2O at -78 ˚C was added drop-wise a chilled (-78 ˚C) solution of Fc[BAr$^F_4$] (38.4 mg, 0.037 mmol, 0.9 equiv.). Following addition, the resulting dark orange mixture was stirred for an additional 10 min at -78 ˚C and then at room temperature for 10 min. Next, all volatiles were removed *in-vacuo* and the orange residue was washed with 20 mL pentane. Cooling a pentane-layered THF solution at –35 ºC afforded [**7**][BAr$^F_4$] as orange crystals (40 mg, 77%).

^{1}H NMR (THF-d$_8$, 400 MHz, 298 K):δ = 35.37, 19.83, 7.78 (BAr$^F_4$), 7.56 (BAr$^F_4$), 6.60, 3.04, -0.17, -7.04. **X-Band EPR (77 K, 2-MeTHF)**: Sys.g = [2.371, 2.032, 1.990], Sys.lw = 1.2, Sys.Nucs = '^{31}P, ^{31}P', Sys.A = [--, 90, 105; --, 99, 89], Sys.HStrain = [256 71 10], Exp.mwFreq = 9.389 mT. **^{57}Fe Mössbauer (160 K, frozen THF solution, mm/s)**:δ= 0.50 ΔE_Q = 1.71. **CV data (1 mM, vs. Fc/Fc$^+$)**: - 1.51 V (Fe^I/Fe^0). **UV-VIS (THF, 1 cm cell, 298 K)**:ε = 267 {3231 M^{-1}cm^{-1}}, 280 {2615 M^{-1}cm^{-1}}, 352 {849 M^{-1}cm^{-1}}, 428 {282 M^{-1}cm^{-1}}. **Anal. Calcd.** for $C_{53}H_{52}BF_{24}FeP_2$ (1273.3): C, 49.98; H, 4.12. Found: C, 51.20; H, 4.66.

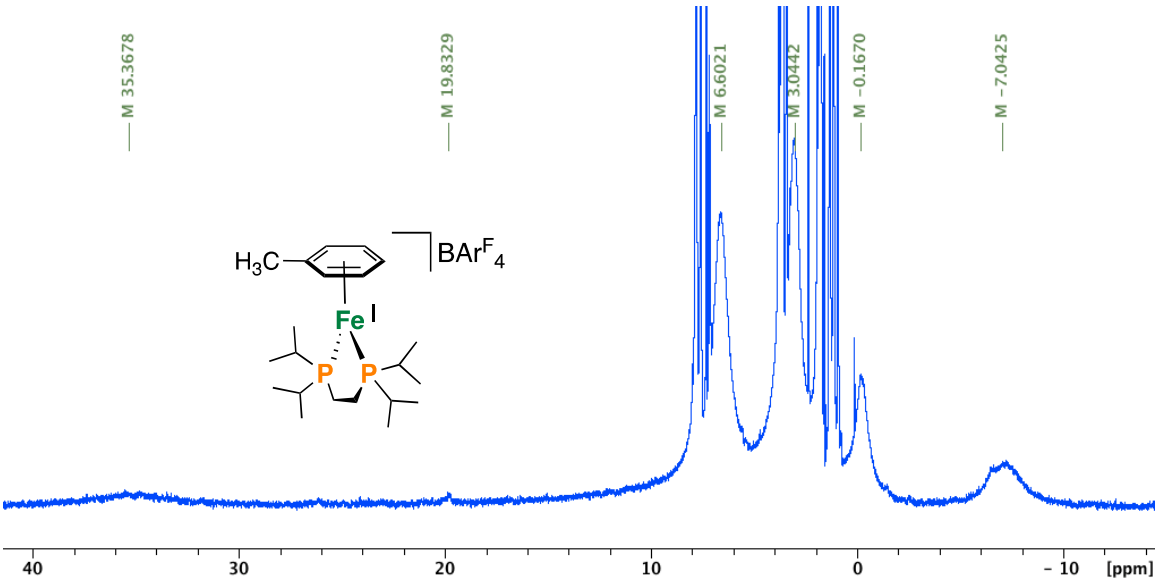

Figure C.17. [**5**][BAr^F_4], ^{1}H NMR, THF-d_8, 400 MHz, 298 K

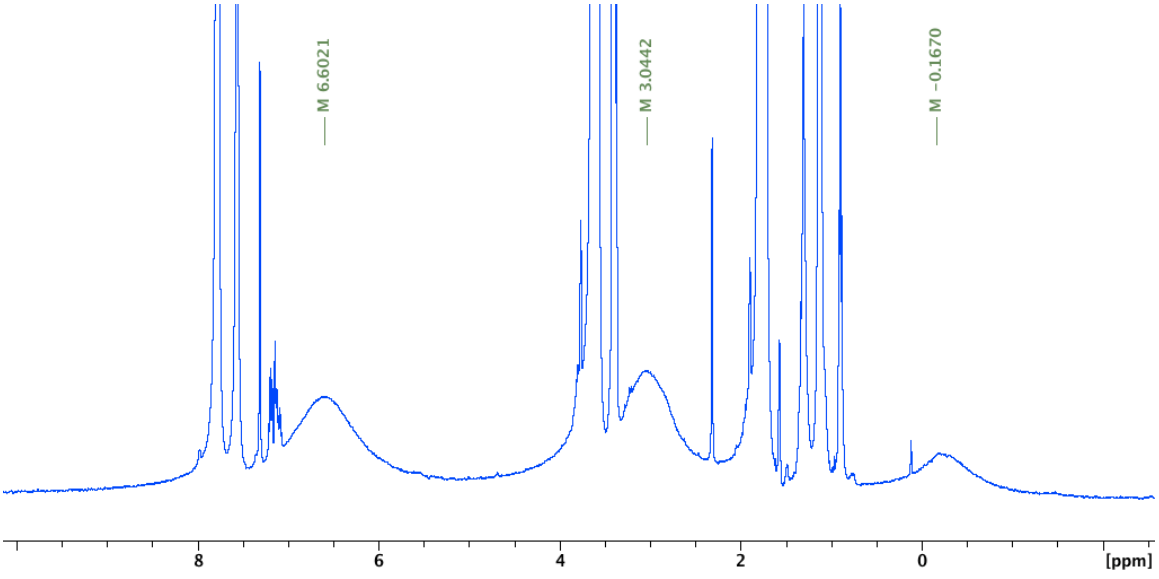

Figure C.18. [**5**][BAr^F_4], ^{1}H NMR (expanded view), THF-d_8, 400 MHz, 298 K

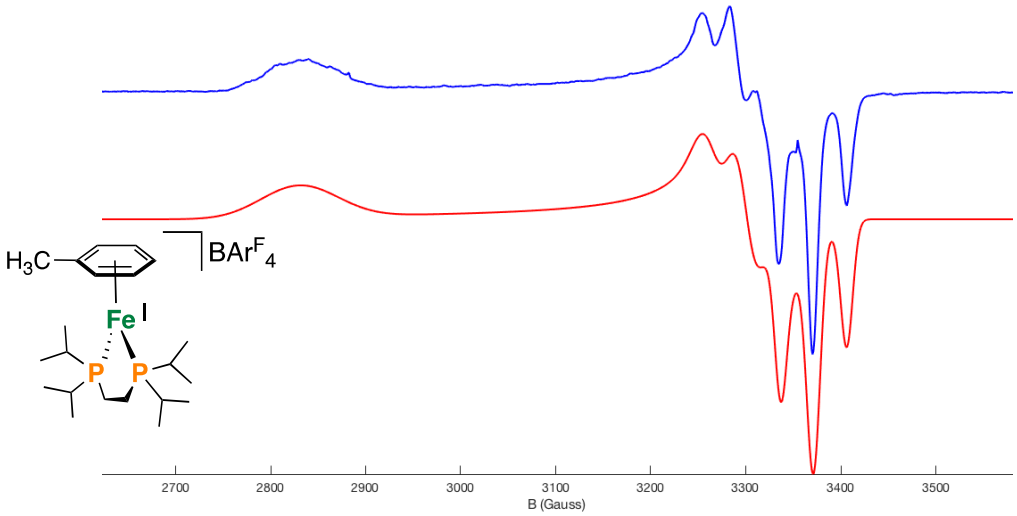

Figure C.19. [**5**][BAr^F_4], 77 K X-band EPR spectrum in 2-MeTHF with simulations; blue trace: experiment; red trace: simulation. Sys.g = [2.371, 2.032, 1.990], Sys.lw = 1.2, Sys.Nucs = '^{31}P, ^{31}P', Sys.A = [--, 90, 105; --, 99, 89], Sys.HStrain = [256 81 40], Exp.mwFreq = 9.389].

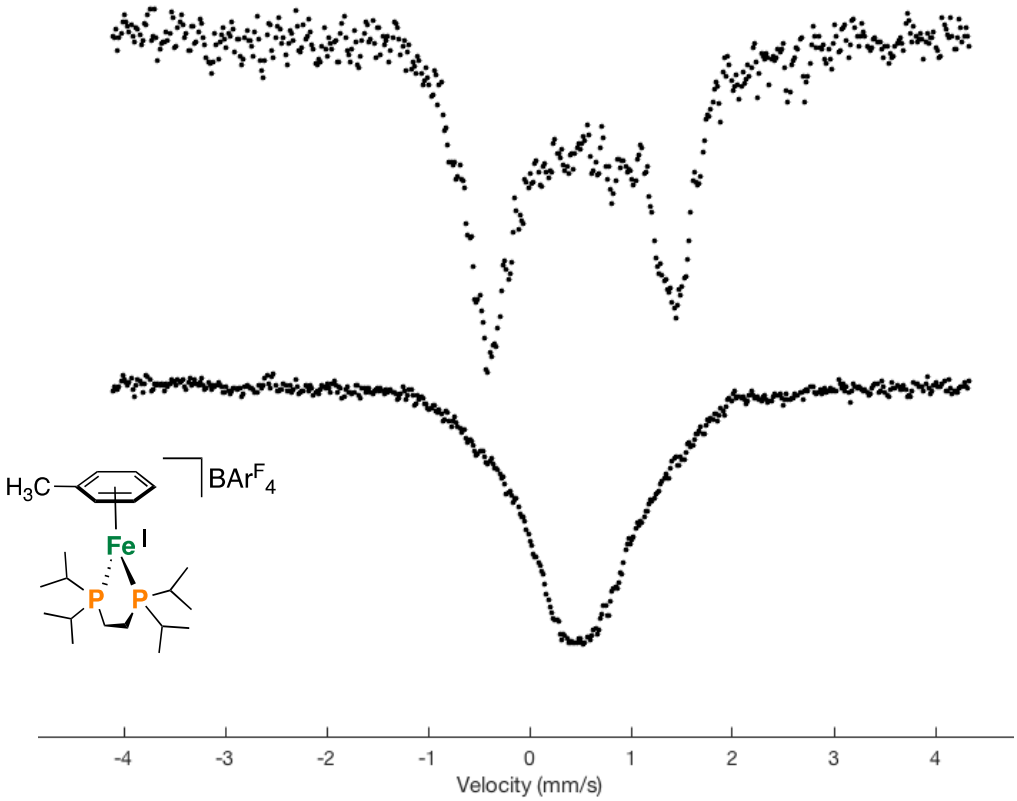

Figure C.20. [**5**][BAr^F_4], 80 K (bottom) and 160 K (top) ^{57}Fe Mössbauer spectrum collected in the presence of a 50 mT magnetic field oriented parallel to the propagation of the γ-beam (frozen solution in Et_2O). **)**:δ~ 0.50 mm/s, ΔE_Q ~ 1.71 mm/s.

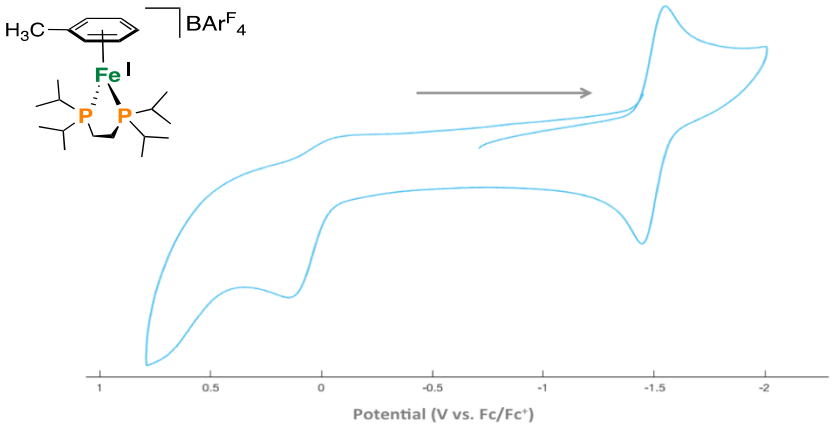

Figure C.21. [**5**][BAr^F_4], Cylic Voltammogram, THF, 298 K showing a reversible feature at - 1.51 V for the Fe(I)/Fe(0) couple (vs. Fc/Fc^+) in 4 mL THF, 0.4 M [NBu_4][PF_6] and analyte (1 mM). Data was collected at 100 mV/s with Pt counter, glassy carbon working, and Ag/AgOTf reference electrodes

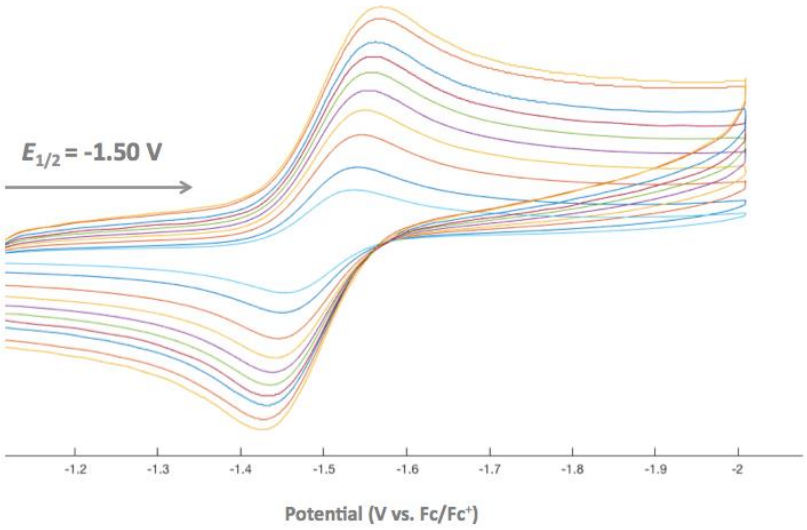

Figure C.22. [**5**][BAr^F_4], Cylic Voltammogram, THF, 298 K showing a reversible feature at - 1.51 V for the Fe(I)/Fe(0) couple (vs. Fc/Fc^+) as a function of scan rate (50 mV/s to 500 mV/s at 50 mV/s increments).

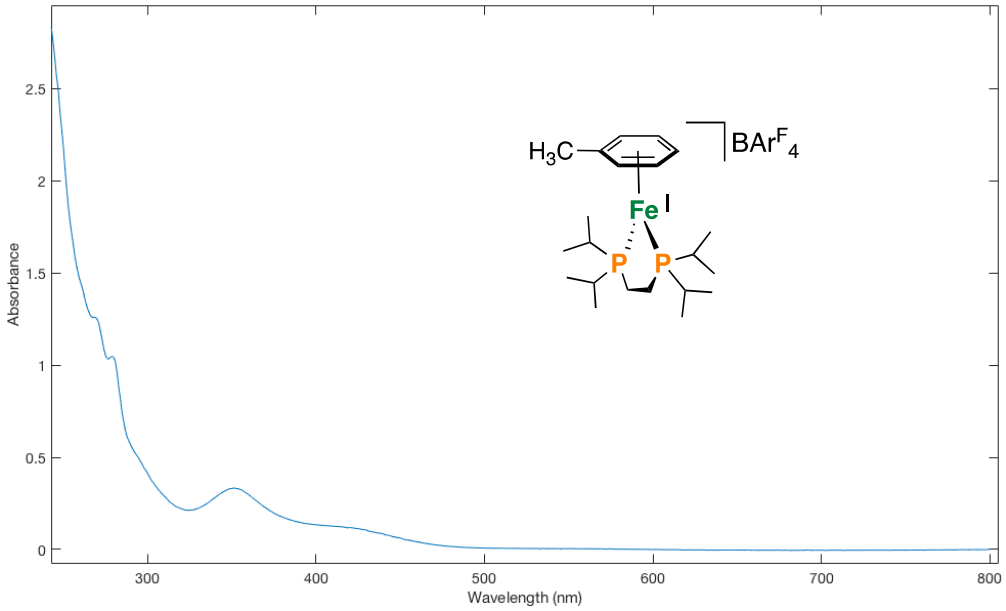

Figure C.23. [**5**][BAr^F_4], UV-Visible spectrum, THF, 298 K (= 267, 280, 352, 428 nm)

[Fe(η^3:η^2-Ind)(depe)N_2][BAr^F_4]$_2$ [**6**][BAr^F_4]: *N.B.* This compound can be prepared via treatment of **2** with Fc[BAr^F_4] or $H(OEt_2)_2$[BAr^F_4]. To a solution of **2** (22.1 mg, 0.058 mmol, 1 equiv.) in Et_2O (2 mL) at -78 ˚C was added drop-wise a chilled (-78 ˚C) solution of $H(OEt_2)_2$[BAr^F_4] (53.4 mg, 0.053 mmol, 0.9 equiv.) in Et_2O (2 mL). Following addition, the resulting mixture was stirred at -78 ˚C and warmed to 25 ˚C over 2 h. During this time, a purple solid ([**7**][BAr^F_4]$_2$) precipitated and was removed by filtration. The supernatant was dried *in-vacuo* and washed with pentane. Cooling a pentane-layered THF solution at –35 ºC afforded [**6**][BAr^F_4] as orange crystals that were mechanically separated from [**7**][BAr^F_4]$_2$ for analysis by X-ray diffraction. Complex [**6**][BAr^F_4] was not obtained in pure form, however, by $^{31}P\{^1H\}$ NMR spectroscopy, the yield is estimated to

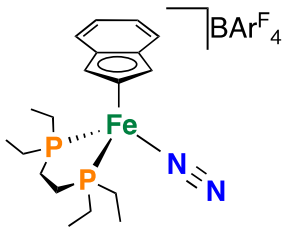

be ~30%. The N_2 ligand in [**6**][BAr^F_4] was also observed to be labile; exposure to vacuum caused a change in color from orange to maroon.

^{1}H NMR (THF-d_8, 400 MHz, 298 K, select signals):δ= 7.79 (s, 8H; BAr^F_4), 7.70 (m, 2H), 7.58 (br s, 4H, BAr^F_4), 7.47 (m, 2H), 5.23 (s, 1H), 5.01 (s, 2H). **^{31}P{^{1}H} NMR (THF-d_8, 162 MHz, 298 K)**:δ= 89.7. **IR (thin film, 298 K, cm^{-1})**: 2151 cm^{-1} (ν_{NN}).

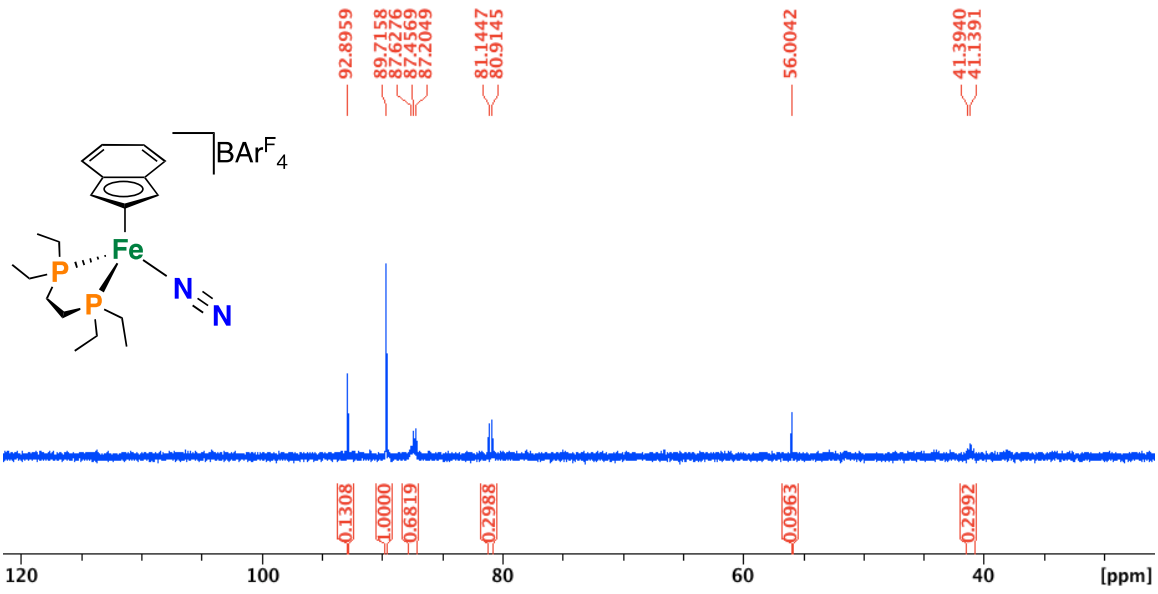

Figure C.24. [**6**][BAr^F_4], ^{31}P{^{1}H} NMR, THF-d_8, 162 MHz, 298 K [signals at □ = 87.51 and 41.16 are due to [**7**][BAr^F_4]$_2$, those at □ = 56.0, 81.1, 87.3, and 92.9 ppm are due to impurities].

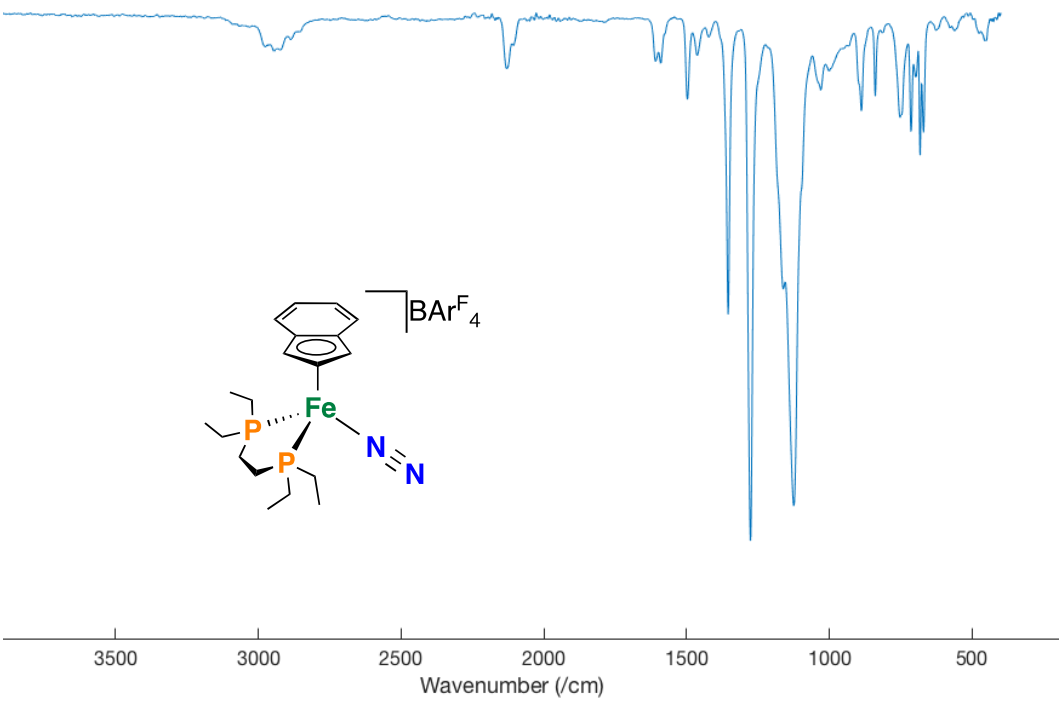

Figure C.25. [**6**][BAr$^F_4$], FT-IR ATR, thin film, 298 K ($\tilde{\nu}_{NN}$ = 2151 cm^{-1})

[Fe$_2$(η^3:η^2-Ind)$_2$(depe)$_2$(μ-depe)][BAr$^F_4$]$_2$ [**7**][BAr$^F_4$]$_2$: *N.B.* This compound can be prepared *via* treatment of **2** with Fc[BAr$^F_4$] or H(OEt)$_2$[BAr$^F_4$]. To a solution of **2** (22.1 mg, 0.058 mmol, 1 equiv.) in Et$_2$O (2 mL) at -78 ˚C was added drop-wise a chilled (-78 ˚C) solution of H(OEt$_2$)$_2$[BAr$^F_4$] (53.4 mg, 0.053 mmol, 0.9 equiv.) in Et$_2$O (2 mL). Following addition, the resulting mixture was stirred at -78 ˚C and warmed to 25 ˚C over 2 h. During this time, a purple solid precipitated that was isolated *via* filtration, washed with pentane, and dried *in-vacuo*. Cooling a pentane-layered THF solution at –35 ºC afforded [**7**][BAr$^F_4$]$_2$ as a dark purple crystals (11.4 mg, 22%).

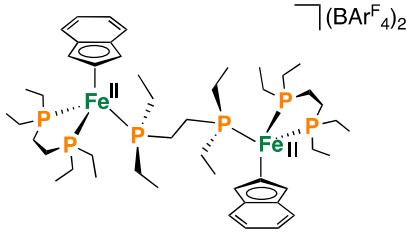

^{1}H NMR (THF-d$_8$, 400 MHz, 298 K):δ= 7.79 (s, 16H; BAr$^F_4$), 7.76 (m, 4H), 7.58 (br s, 8H, BAr$^F_4$), 7.41 (m, 2H), 5.39 (2H), 4.83 (m, 4H), 2.58 (m, 4H), 2.28-2.04 (m, 8H), 1.97 (m, 4H), 1.67 (m, 8H), 1.43 (m, 4H), 1.37-1.07 (m, 26H), 1.01 (m, 18H). **^{31}P{^{1}H} NMR**

(THF-d$_8$, 162 MHz, 298 K):δ= 87.51 (d, $^2J_{P,P}$ = 37.8 Hz), 41.16 (t, $^2J_{P,P}$ = 37.8 Hz). **^{13}C NMR (THF-d$_8$, 100 MHz, 298 K)**:δ= 162.63 (q, $^1J_{C,B}$ = 37 Hz, BAr$^F{}_4$, ipso quaternary C), 135.41 (BAr$^F{}_4$, ortho C), 129.81 (q, $^2J_{C,F}$ = 31 Hz, BAr$^F{}_4$, meta quaternary C), 128.76, 127.38, 124.93 (q, $^1J_{C,F}$ = 273 Hz, BAr$^F{}_4$, CF$_3$), 117.97 (m, BAr$^F{}_4$, para C), 104.28, 86.62 (η^3:η^2-C$_9$H$_7$), 64.62 (η^3:η^2-C$_9$H$_7$), 23.67 (br), 21.41 (br), 21.18 (br), 9.78 (br), 9.17 (br), 7.85 (br). **UV-VIS (THF, 1 cm cell, 298 K)**: ε = 329 {1657 M^{-1}cm^{-1}}, 491 {637 M^{-1}cm^{-1}}. **Anal. Calcd.** for C$_{112}$H$_{110}$B$_2$F$_{48}$Fe$_2$P$_6$ (2685.5): C, 50.06; H, 4.13. Found: C, 49.86; H, 4.21.

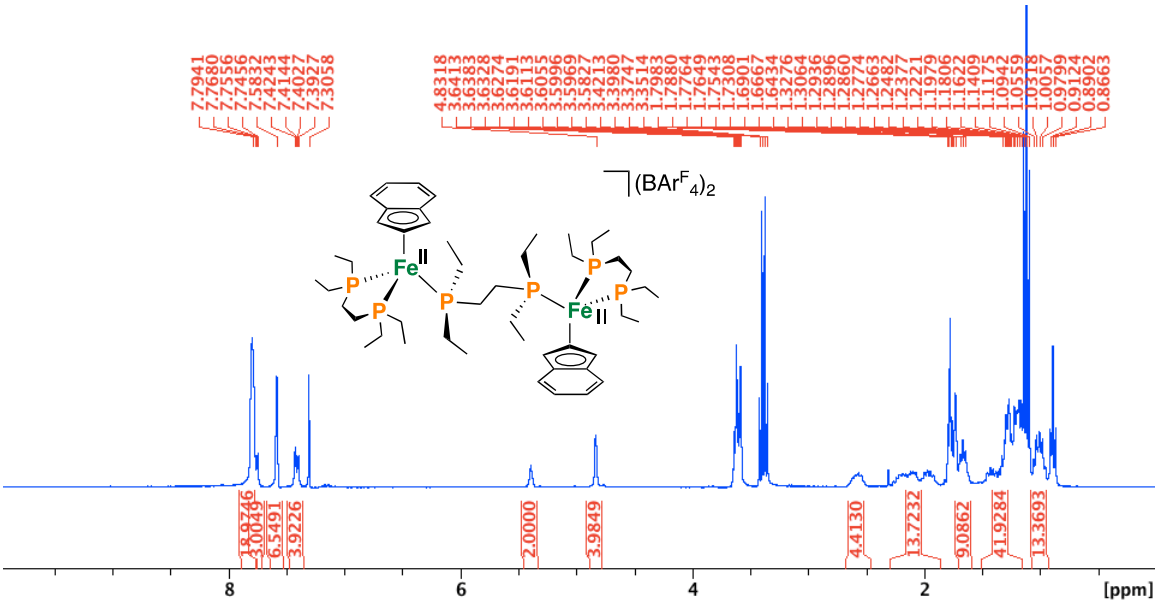

Figure C.26. [**7**][BAr$^F{}_4$]$_2$, ^{1}H NMR, THF-d$_8$, 162 MHz, 298 K

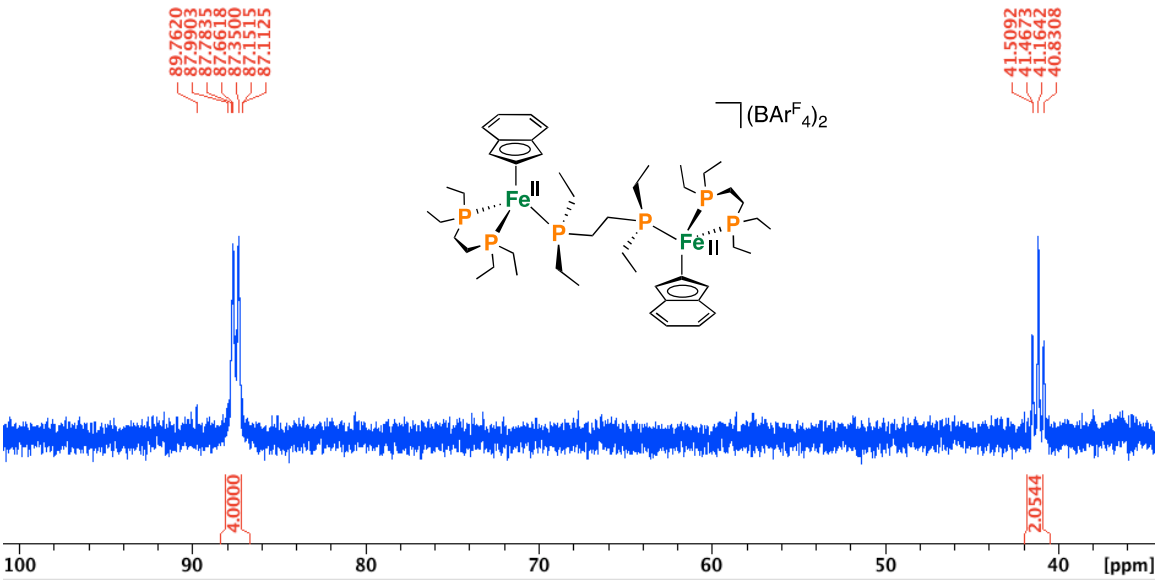

Figure C.27. [**7**][BAr^F_4]$_2$, $^{31}P\{^1H\}$ NMR, THF-d_8, 162 MHz, 298 K

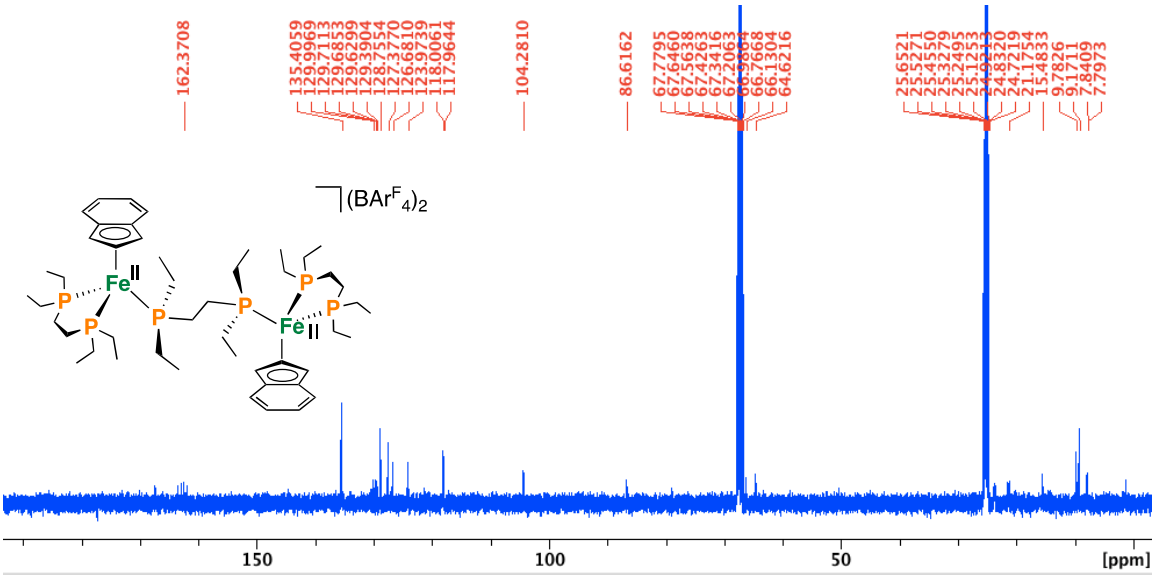

Figure C.28. [**7**][BAr^F_4]$_2$, $^{31}C\{^1H\}$ NMR, THF-d_8, 100 MHz, 298 K

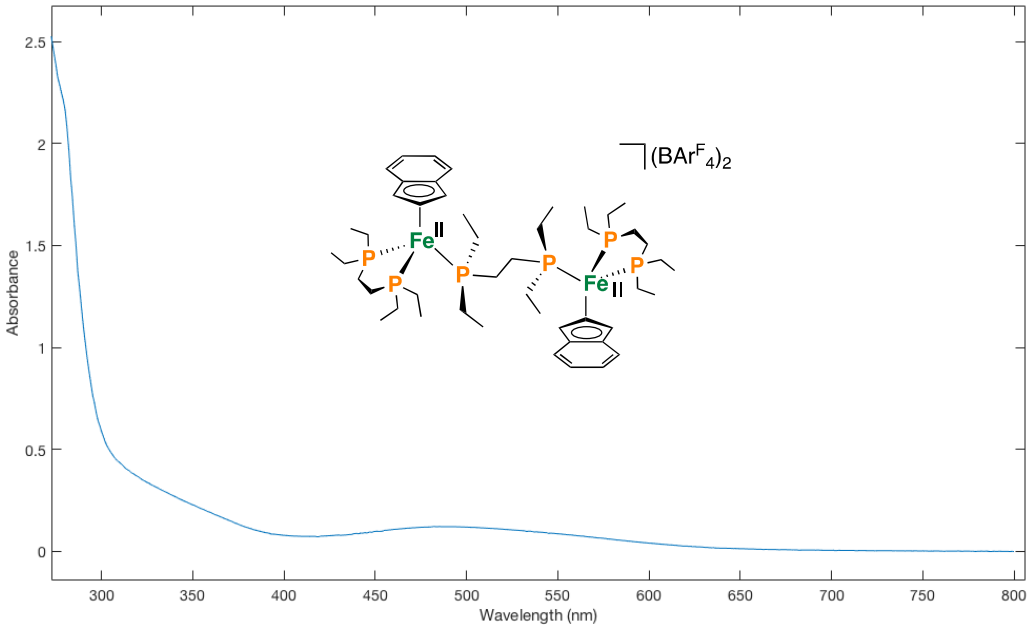

Figure C.29. [**7**][BAr$^F_4$]$_2$, UV-Visible spectrum, THF, 298 K

[Fe(η^3:η^2-Ind)(depe)NCCH$_3$][BAr$^F_4$] [**8**][BAr$^F_4$]: **Route A)**: To a *J. Young* tube containing CD_3CN (500 µL) and **2** was added 1-benzyl-3-acetylpyridinium triflate [BNAP]OTf as a solid; the color changed from red to orange. Analysis by NMR spectroscopy evidenced formation of [Fe(η^3:η^2-Ind)(depe)(NCCH$_3$)]OTf and 1,4-BNAPH (~65% by ^{31}P NMR). **Route B)**: To a solution of **2** (4.7 mg, 0.012 mmol, 1 equiv.) in CH_3CN (2 mL) at -35 °C was added drop-wise a chilled (-35 °C) solution of H(OEt$_2$)$_2$[BAr$^F_4$] (12.6 mg, 0.012 mmol, 1 equiv.) in CH_3CN (1 mL). Following addition, the resulting mixture was stirred at 25 °C over 10 min giving a clear purple solution. Removal of volatiles *in-vacuo* and washing with pentane gave [**8**][BAr$^F_4$] as a purple solid (15.1 mg, 95%).

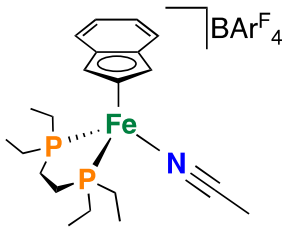

^{1}H NMR (CD$_3$CN, 400 MHz, 298 K, 1,4-BNAPH):δ= 5.82 (dq, *J* = 8.1 Hz, *J* = 1.5 Hz, 1H), 4.86 (dt, *J* = 8.1 Hz, *J* = 3.4 Hz, 1H), 4.38 (s, 2H), 2.94 (br s, 2H).

^{1}H NMR (CD$_3$CN, 400 MHz, 298 K):δ = 7.69 (s, 8H; BAr$^{F}_4$), 7.67 (s, 4H; BAr$^{F}_4$), 7.56 (dd, $^{3}J_{H,H}$ = 6.6 Hz, $^{3}J_{H,H}$ = 3.1 Hz), 7.27 (dd, $^{3}J_{H,H}$ = 6.6 Hz, $^{3}J_{H,H}$ = 3.1 Hz), 4.66 (m, 1H), 4.49 (2H), 2.27 (m, 2H), 1.88 (m, 2H), 1.73 (m, 2H), 1.44 (m, 2H), 1.24 (m, 2H), 1.14 (m, 6H), 0.90 (m, 6H). **^{31}P{^{1}H} NMR (CD$_3$CN, 162 MHz, 298 K)**:δ= 92.90. **^{13}C NMR (CD$_3$CN, 100 MHz, 298 K)**:δ = 162.52 (q, $^{1}J_{C,B}$ = 37 Hz, BAr$^{F}_4$, ipso quaternary C), 135.61 (BAr$^{F}_4$, ortho C), 129.86 (q, $^{2}J_{C,F}$ = 31 Hz, BAr$^{F}_4$, meta quaternary C), 127.74, 127.25, 125.42 (q, $^{1}J_{C,F}$ = 273 Hz, BAr$^{F}_4$, CF$_3$), 117.97 (m, BAr$^{F}_4$, para C), 84.98 (□^{3}:□^{2}-C$_9$H$_7$), 62.17 (η^3:η^2-C$_9$H$_7$) 23.29 (m), 21.24 (m), 18.63 (m). **Anal. Calcd.** for C$_{53}$H$_{46}$BF$_{24}$FeNP$_2$ (1281.2): C, 49.67; H, 3.62; N, 1.09. Found: C, 49.30; H, 3.54; N, 1.02.

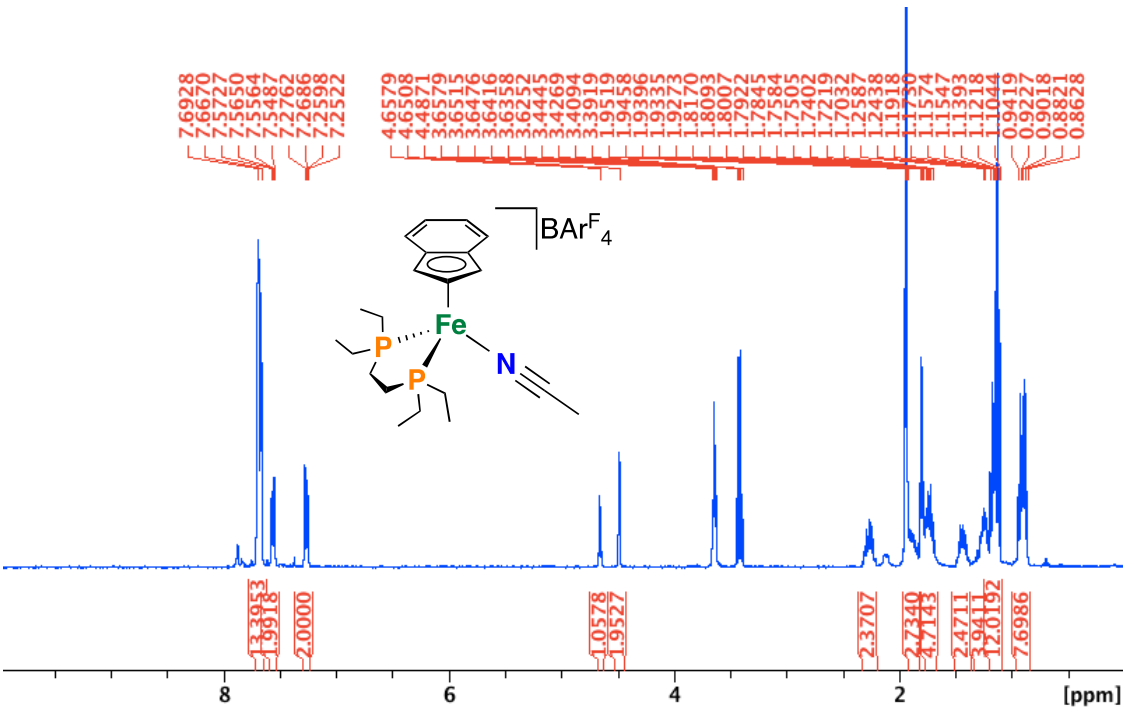

Figure C.30. [**8**][BAr$^{F}_4$], ^{1}H NMR, CD$_3$CN, 162 MHz, 298 K

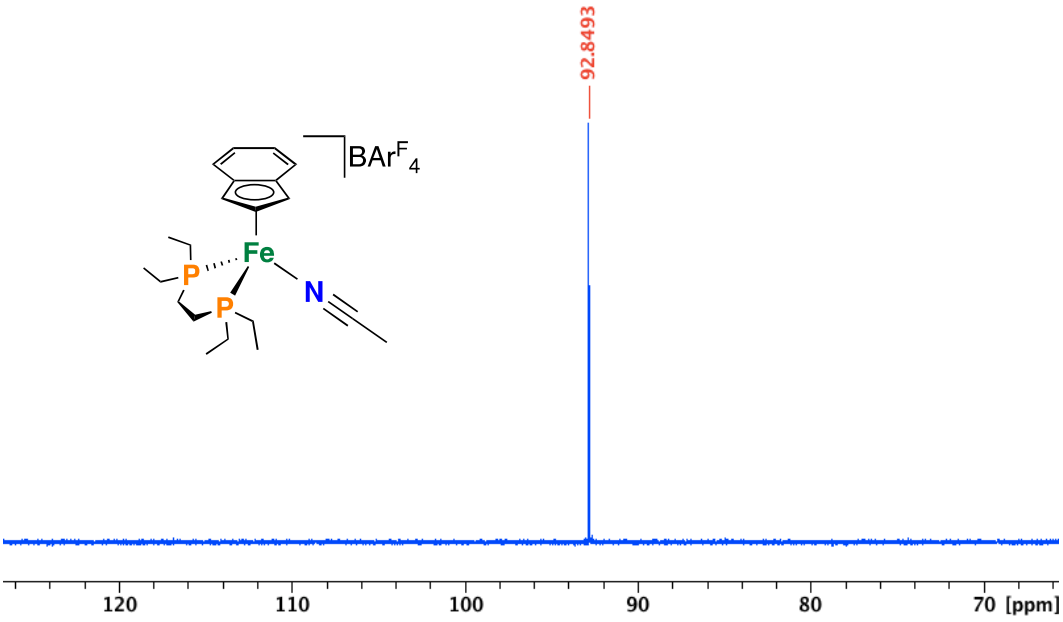

Figure C.31. [**8**][BAr$^F_4$], ^{31}P{^{1}H} NMR, CD_3CN, 162 MHz, 298 K

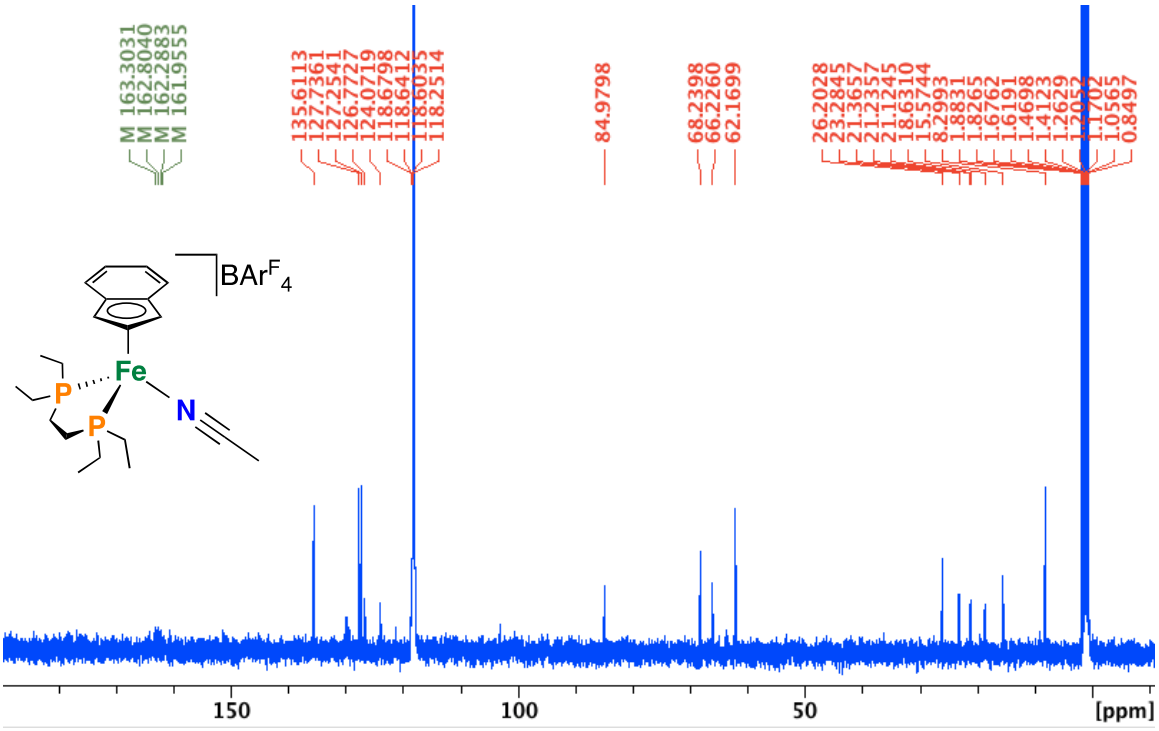

Figure C.32. [**8**][BAr$^F_4$], ^{31}C{^{1}H} NMR, CD_3CN, 100 MHz, 298 K

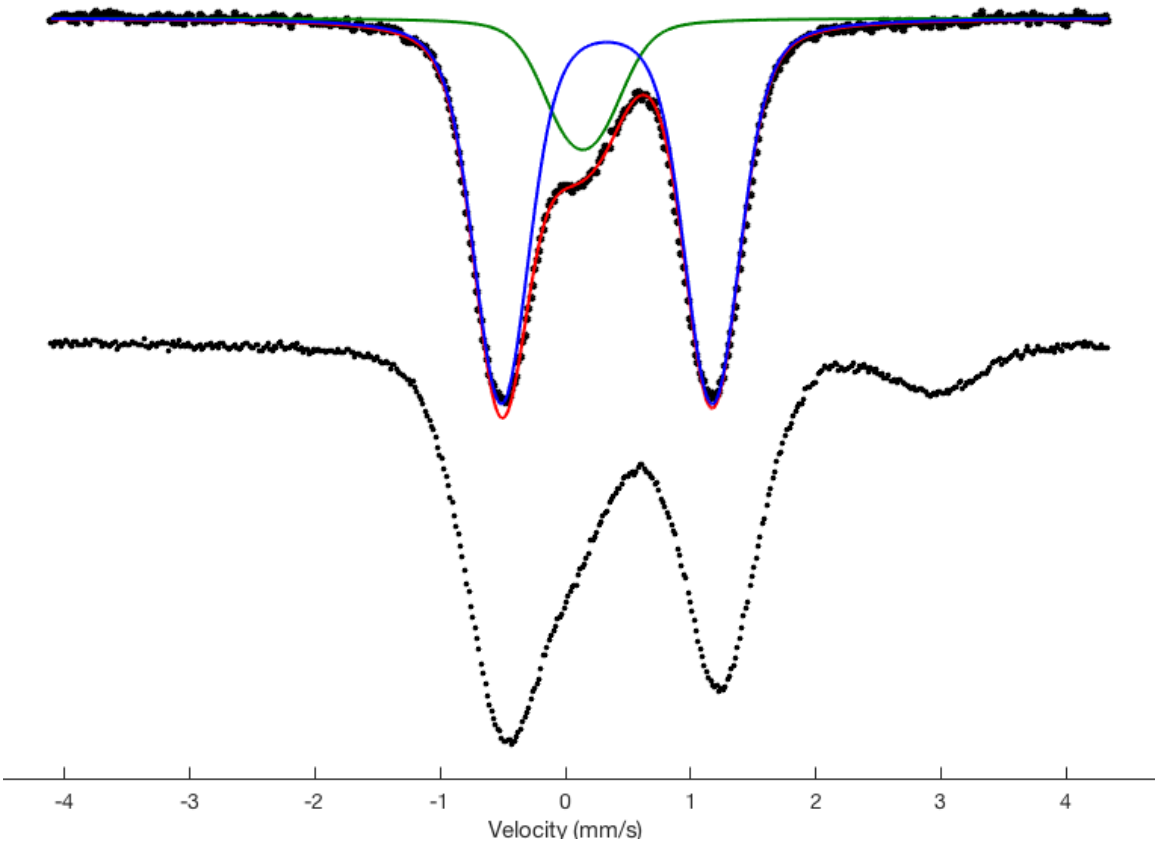

Figure C.33. 80 K ^{57}Fe Mössbauer spectrum collected in the presence of a 50 mT magnetic field oriented parallel to the propagation of the γ-beam (frozen solution in 2-MeTHF).

Addition of $[H(OEt_2)_2]BAr^F{}_4$ to **2-^{57}Fe** at -78 °C. Top spectrum shows freeze-quenched sample after 5 min. Bottom spectrum shows freeze-quench after stirring at room temperature for 15 min. Parameters: δ= 0.33 mm/s, ΔE_Q = 1.69 mm/s (**blue, 82%**), δ= 0.14 mm/s, ΔE_Q = 0.29 mm/s (**green, 18%**); $\Gamma_L = \Gamma_R$ = - 0.50 mm/s.

IX. EPR Spectroscopy data:

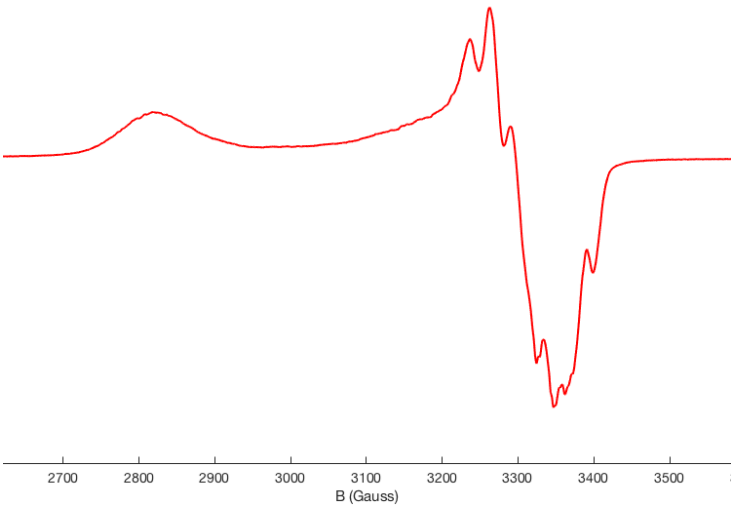

Figure C.34. 77 K X-band EPR spectrum in 2-MeTHF generated by oxidation of **2-H** using [Fc]$BAr^F{}_4$ at -78 ^oC (< 30 s).

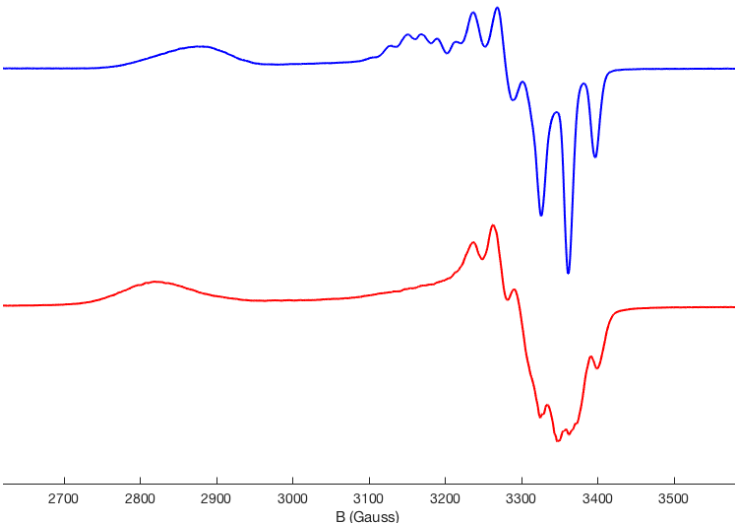

Figure C.35. 77 K X-band EPR spectrum in 2-MeTHF generated by oxidation of **2-H** using [Fc]$BAr^F{}_4$ at -78 ^oC, **red** (< 30 s), **blue** (20 min).

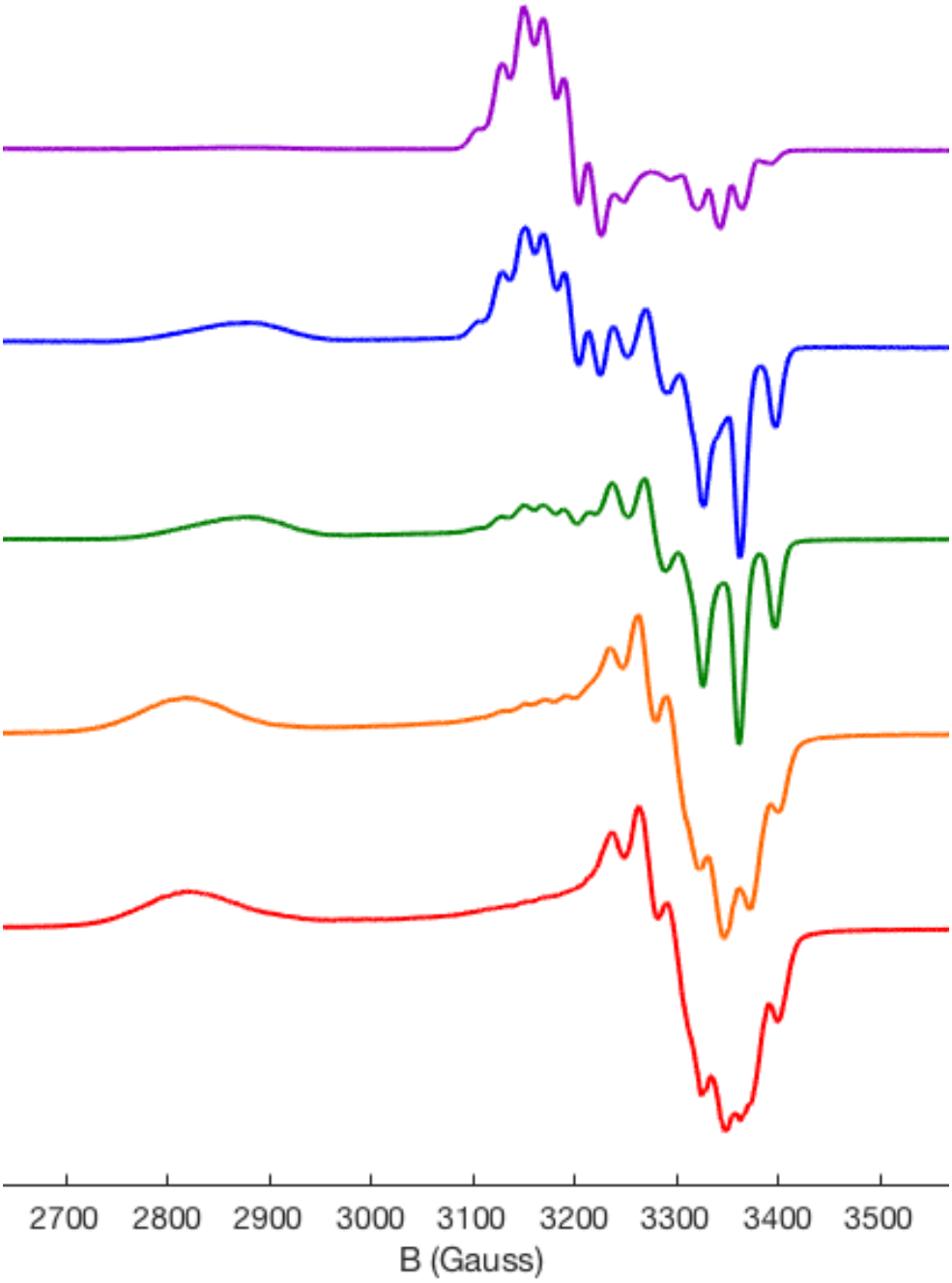

Figure C.36. A series of 77 K X-band EPR spectra in 2-MeTHF generated by oxidation of **2-H** using [Fc]BAr^F_4 at -78 ^oC showing **red** ([**3**]$^+$) giving **green** ([**4**]$^+$), which decomposes to give $[Fe^I(depe)N_2]^+$ (**purple**).

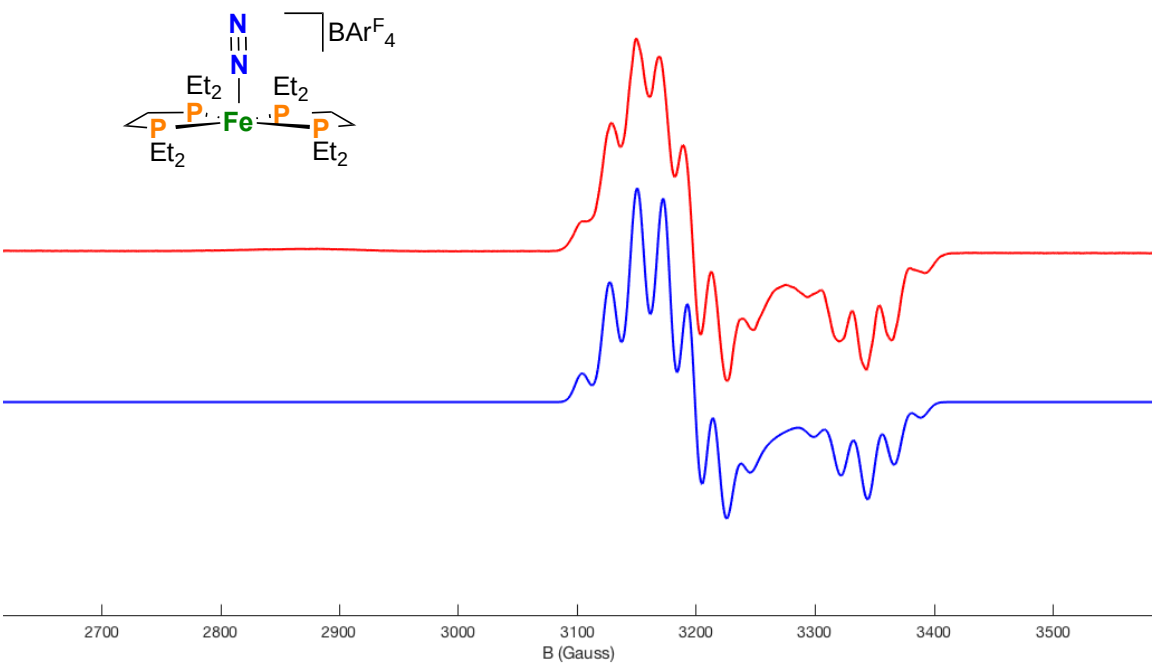

Figure C.37. 77 K X-band EPR spectrum of $[Fe^{I}(depe)N_2]^+$ in 2-MeTHF generated by oxidation of **2** using [Fc]BAr^F_4 at -78 °C (after 24 h). The fit is consistent with that provided by Ashley*cx* and co-workers. Microwave frequency 9.369 GHz; **red** trace: experiment; **blue** trace: simulation. Simulation parameters: Sys.g = [2.125 2.093 2.0016] with four ^{31}P hyperfine interactions, two of type 1, A(^{31}P) = [65.6 61.4 60.9] MHz and two of type 2, A(^{31}P) = [72 61.7 64.3] MHz.

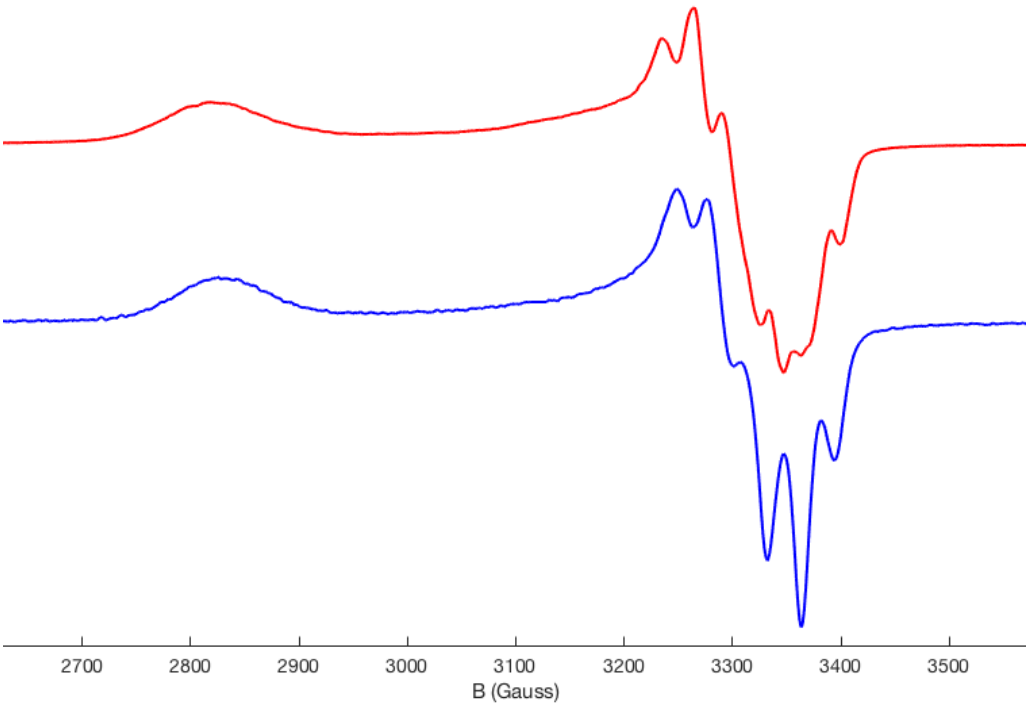

Figure C.38. 77 K X-band EPR spectrum in 2-MeTHF generated by oxidation of **2-H** (**red**) and **2-D** (**blue**) using [Fc]BAr^F_4 at -78 ^oC (< 30 s).

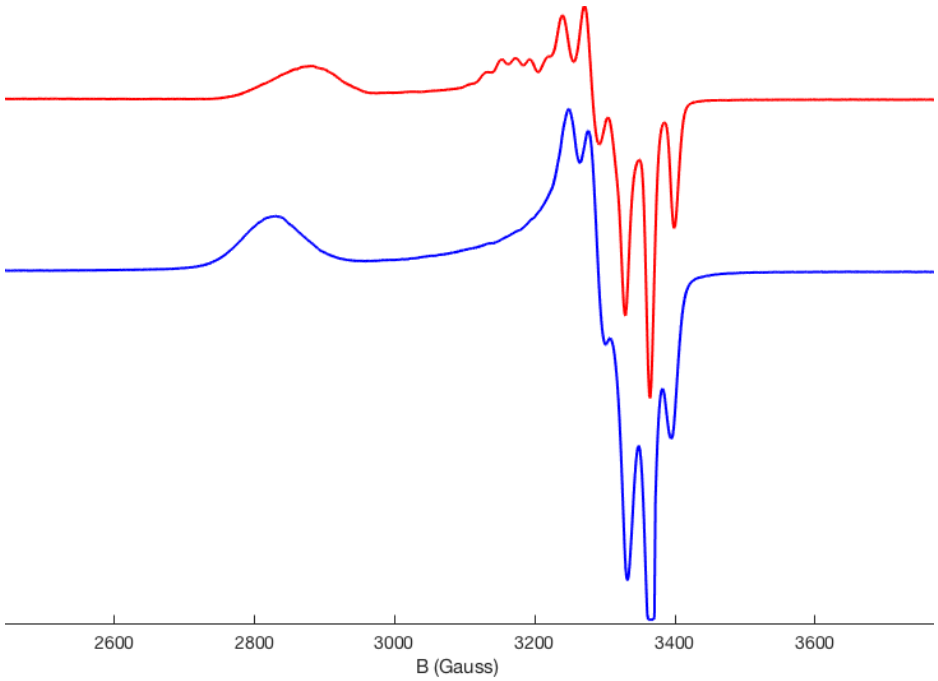

Figure C.39. 77 K X-band EPR spectrum in 2-MeTHF generated by oxidation of **2-D** using [Fc]BAr^{F}_{4} at -78 ^{o}C **blue** (< 30 s), **red** (20 min).

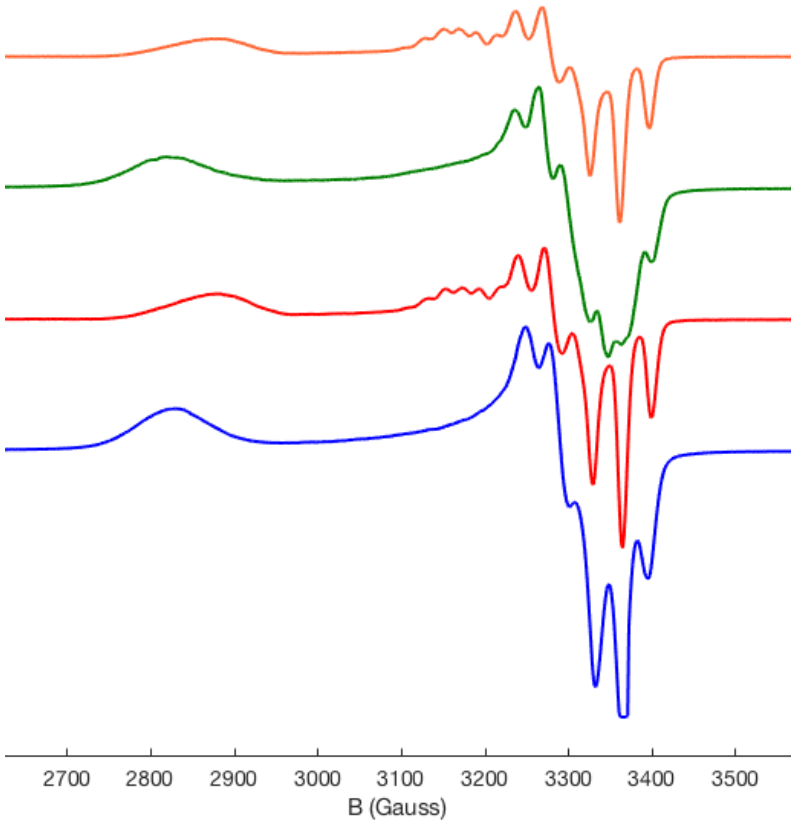

Figure C.40. 77 K X-band EPR spectrum in 2-MeTHF generated by oxidation using [Fc]$BAr^F{}_4$ at -78 °C of **2-D**: **blue** (< 30 s), **red** (20 min) or **2-H**: **green** (< 30 s), **orange** (20 min) or **2-D** at -78 °C.

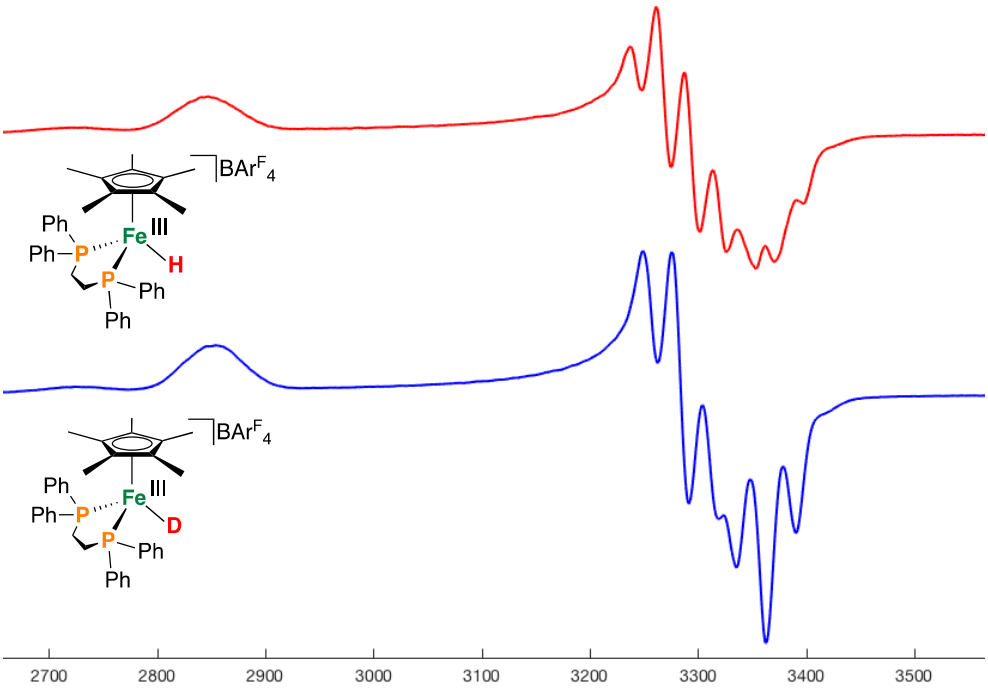

Figure C.41. 77 K X-band EPR spectrum of [Fe(η^5-Cp*)(dppe)X]$^+$ (X = H or D) in 2-MeTHF generated by oxidation of the corresponding Fe^{II}-X precursor using [Fc]BAr$^F_4$ at -78 ^{o}C. These spectra show changes at high field, due to coupling of the unpaired electron to a hydride nucleus. For X = D (**blue**), the following fit paramaters were obtained: Sys.g = [2.352, 2.041, 1.992], Sys.lw = 1.2, Sys.Nucs = '^{31}P, ^{31}P', Sys.A = [88, 82, 79; 82, 71, 76], Sys.HStrain = [180 32 31], Exp.mwFreq = 9.370].

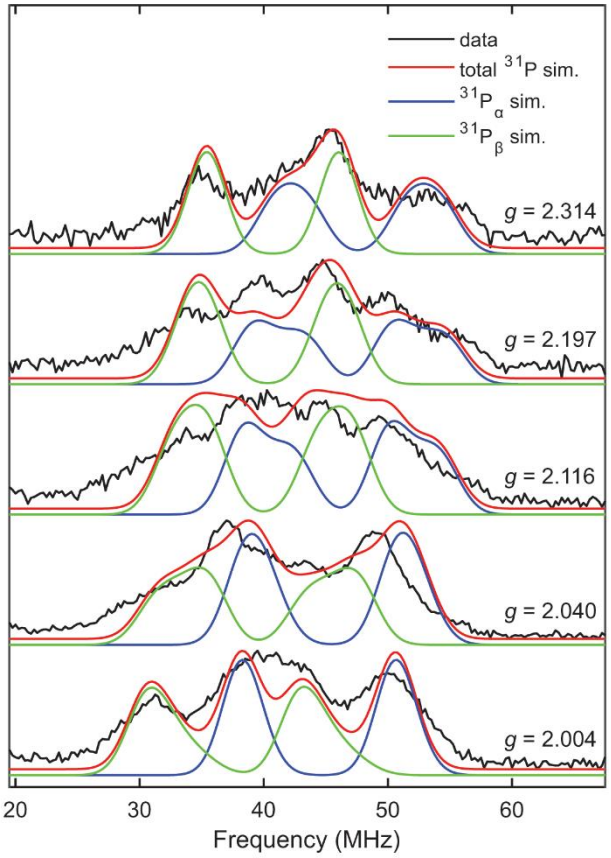

Figure C.42. Field-dependent X-band ^{31}P Davies ENDOR of [**3**-D]$^{+}$ (black), with simulations of ^{31}P hyperfine couplings overlaid (total ^{31}P simulation (red), $^{31}P_{\alpha}$, (blue), $^{31}P_{\beta}$ (green)). Simulation parameters: g = [2.377, 2.039, 1.993]; A($^{31}P_{\alpha}$) = [100, 88, 88] MHz, Euler rotation angles [α, β, γ] = [35, 0, 0]°; A($^{31}P_{\beta}$) = [82, 85, 72] MHz, Euler rotation angles [α,β,γ] = [10, 0, 0]°. Acquisition parameters: temperature = 10 K; MW frequency = 9.718 GHz; MW pulse length (π/2, π) = 40 ns, 80 ns; RF pulse length = 15 μs; shot repetition time = 2 ms.

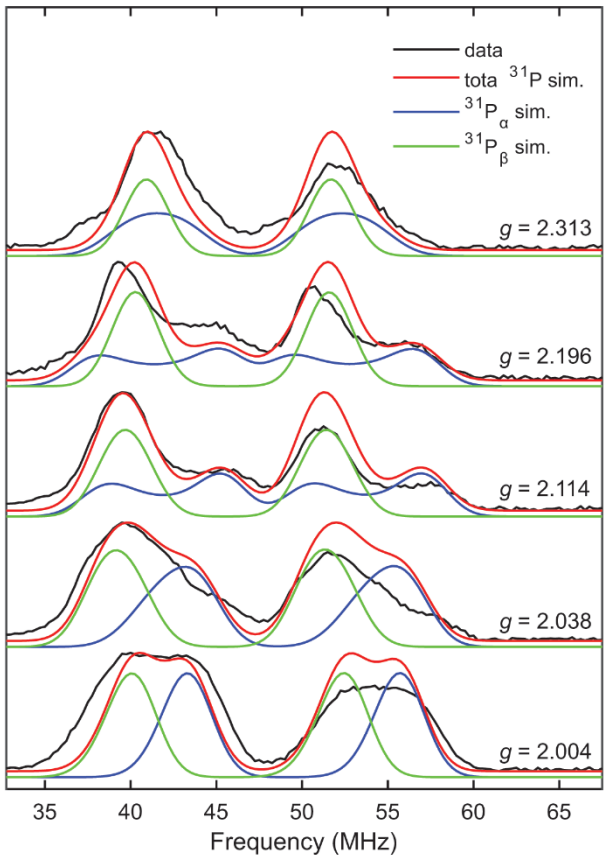

Figure C.43. Field-dependent X-band ^{31}P Davies ENDOR of [**4**-D]$^{+}$ (black), with simulations of ^{31}P hyperfine couplings overlaid (total ^{31}P simulation (red), $^{31}P_{\alpha}$, (blue), $^{31}P_{\beta}$ (green)). Simulation parameters: g = [2.332, 2.042, 1.992]; A($^{31}P_{\alpha}$) = [86, 104, 100] MHz, Euler rotation angles [α, β, γ] = [40, 0, 0]$^{\circ}$; A($^{31}P_{\beta}$) = [93, 88, 94] MHz, Euler rotation angles [α,β,γ] = (0, 0, 0)$^{\circ}$. Acquisition parameters: temperature = 10 K; MW frequency = 9.712 GHz; MW pulse length (π/2, π) = 40 ns, 80 ns; RF pulse length = 15 μs; shot repetition time = 2 ms.

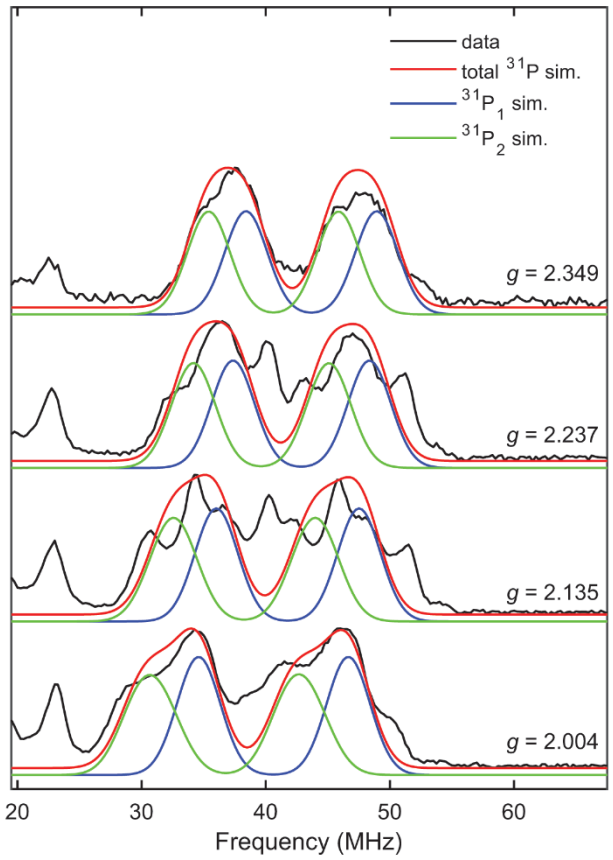

Figure C.44. Field-dependent X-band ^{31}P Davies ENDOR of [Fe(η^5-Cp*)(dppe)**D**]$^+$ (black), with simulations of ^{31}P hyperfine couplings overlaid (total ^{31}P simulation (red), $^{31}P_\alpha$, (blue), $^{31}P_\beta$ (green)). Simulation parameters: g = [2.352, 2.041, 1.992]; A($^{31}P_\alpha$) = [88, 82, 79] MHz, Euler rotation angles (α, β, γ) = [0, 0, 0]°; A($^{31}P_\beta$) = [82, 71, 76] MHz, Euler rotation angles (α,β,γ) = [0, 0, 0]°. Acquisition parameters: temperature = 10 K; MW frequency = 9.719 GHz; MW pulse length (π/2, π) = 40 ns, 80 ns; RF pulse length = 15 μs; shot repetition time = 2 ms.

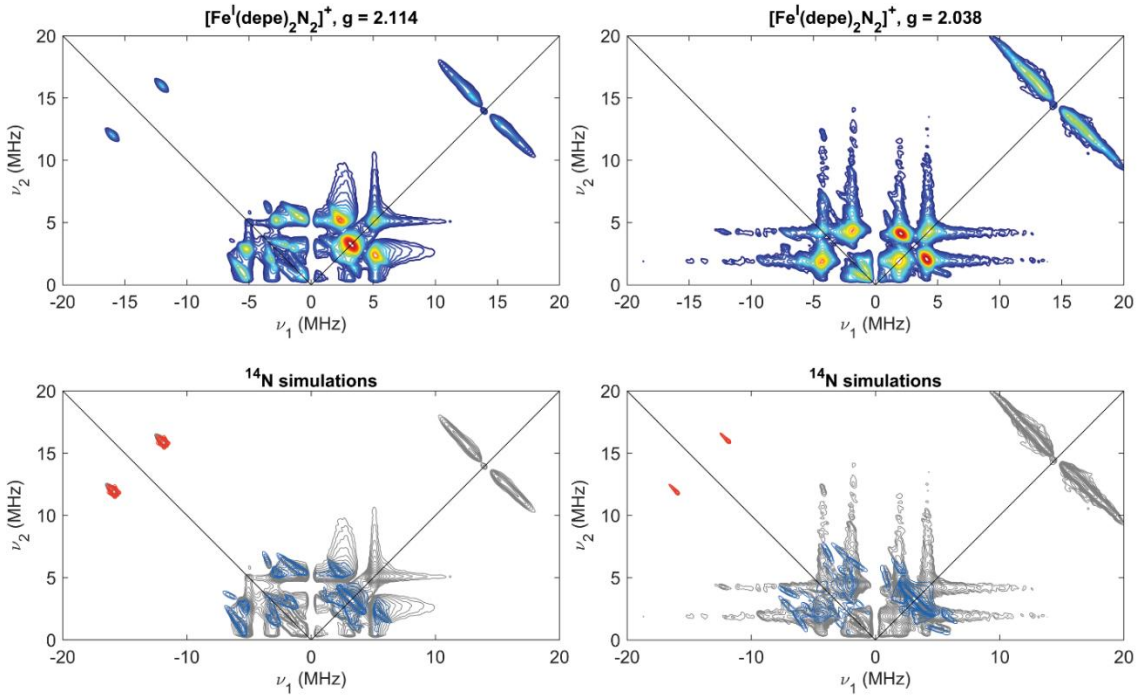

Figure C.45. X-band HYSCORE spectra of $[Fe^{I}(depe)N_2]^+$ in 2-MeTHF (top panels) with simulations of features arising from hyperfine couplings to proximal ^{14}N ($^{14}N_p$, red) and distal ^{14}N ($^{14}N_d$, blue) which are consistent with those previously reported by Ashley and co-workers.[7] Simulation parameters: g = [2.125 2.093 2.0016]; A($^{14}N_p$) = [13.6, 13.6, 15.4] MHz, $e^2qQ/h(^{14}N_p)$ = 3.2 MHz, $\eta(^{14}N_p) \approx 0$; A($^{14}N_d$) = [2.7, 2.7, 6.9] MHz, $e^2qQ/h(^{14}N_d)$ = 3.2 MHz, $\eta(^{14}N_d) \approx 0$. Acquisition parameters: temperature = 20 K; microwave frequency = 9.711 GHz; MW pulse length ($\pi/2$, π) = 8 ns, 16 ns; τ = 144 ns (g = 2.114), 138 ns (g = 2.038); $t_1 = t_2$ = 100 ns; $\Delta t_1 = \Delta t_2$ = 16 ns; shot repetition time (srt) = 2 ms.

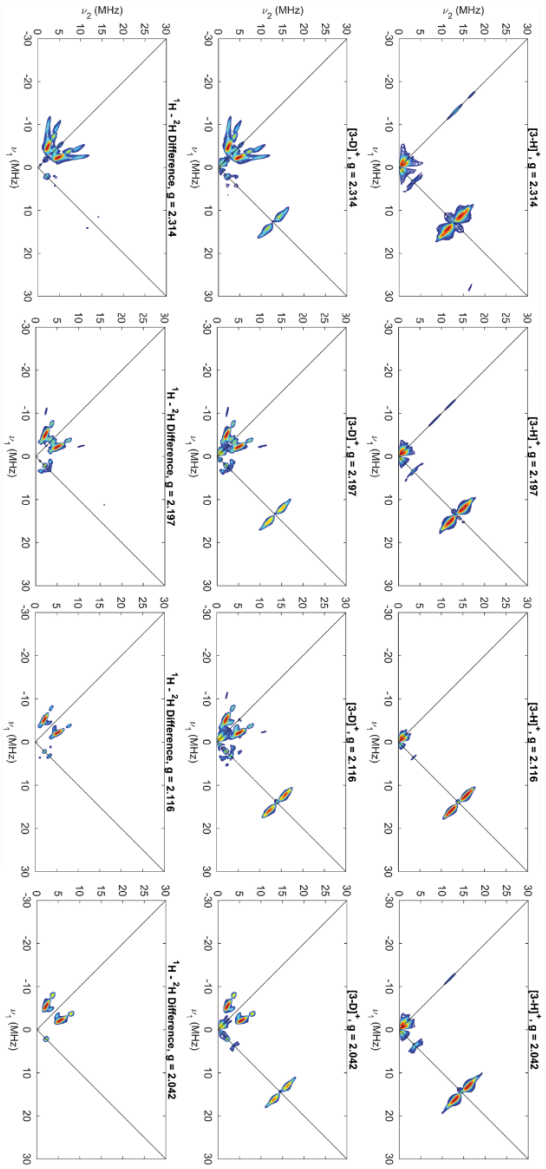

Figure C.46. Field-dependent X-band HYSCORE spectra of [**3-H**][BAr^F_4] (top panels) [**3-D**]BAr^F_4 (middle panels) and ^1H-^2H difference HYSCORE spectra (bottom panels). Acquisition parameters: temperature = 10 K; microwave frequency = 9.718 GHz; MW pulse length ($\pi/2$, π) = 8 ns, 16 ns; τ = 156 ns (g = 2.314), 148 ns (g = 2.197); 144 ns (g = 2.116); 138 ns (g = 2.042); $t_1 = t_2$ = 100 ns; $\Delta t_1 = \Delta t_2$ = 16 ns; shot repetition time (srt) = 2 ms.

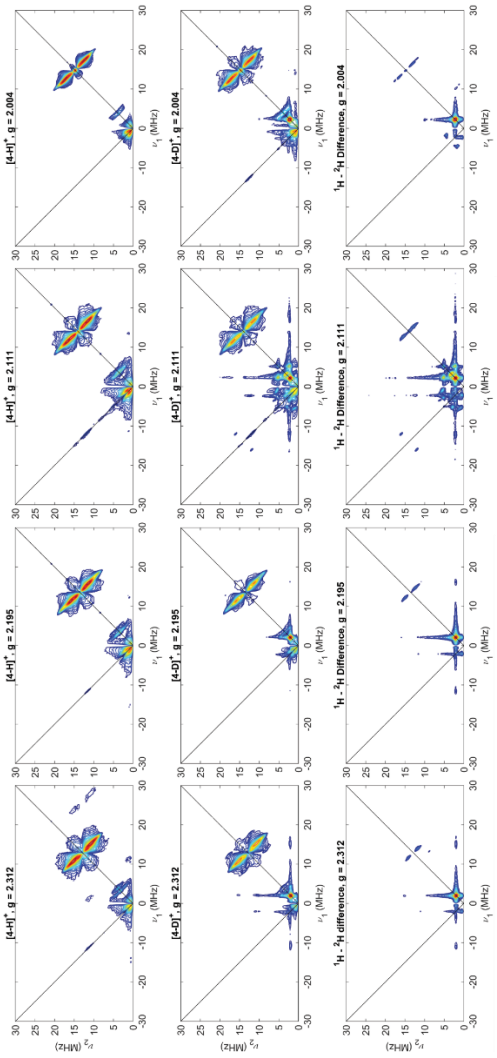

Figure C.47. Field-dependent X-band HYSCORE spectra of [**4-H**][BAr^F_4] (top panels) [**4-D**]BAr^F_4 (middle panels) and ^1H-^2H difference HYSCORE spectra (bottom panels). Acquisition parameters: temperature = 10 K; microwave frequency = 9.718 GHz; MW pulse length ($\pi/2$, π) = 8 ns, 16 ns; τ = 156 ns (g = 2.312), 148 ns (g = 2.195); 144 ns (g = 2.111); 138 ns (g = 2.002); $t_1 = t_2$ = 100 ns; $\Delta t_1 = \Delta t_2$ = 16 ns; shot repetition time (srt) = 2 ms.

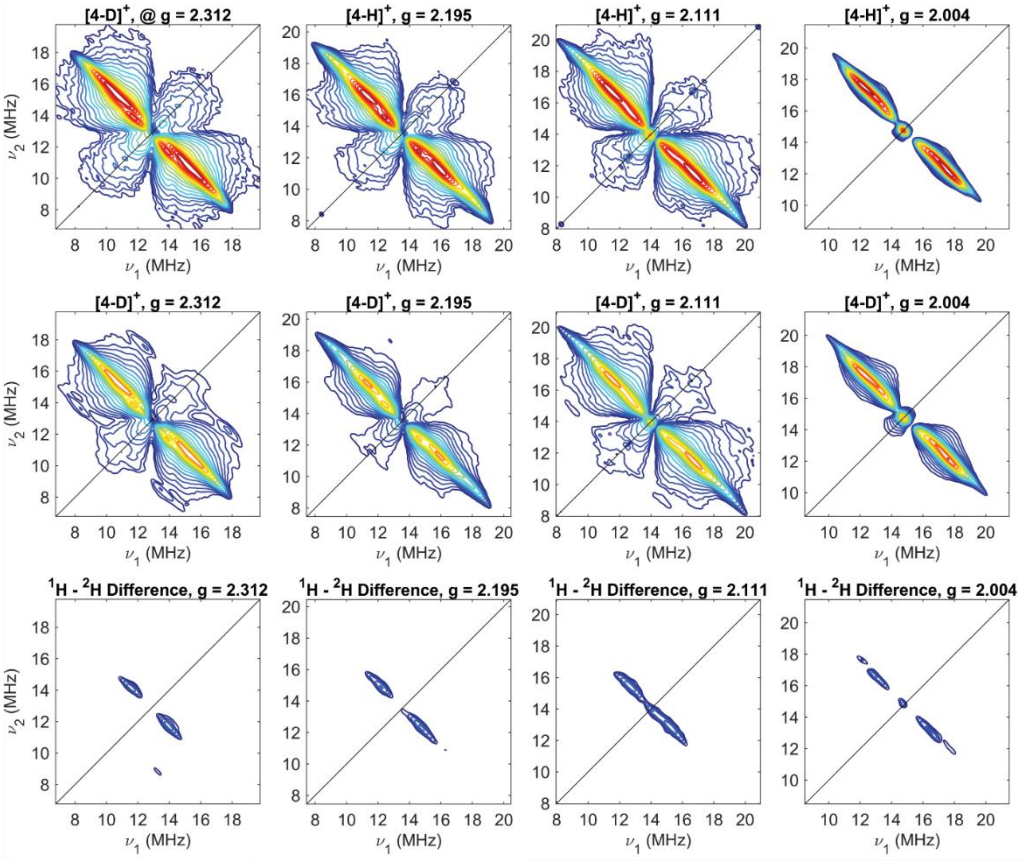

Figure C.48. Field-dependent X-band HYSCORE spectra of [**4-H**][BAr^F_4] (top panels) [**4-D**]BAr^F_4 (middle panels) and ^{1}H-^{2}H difference HYSCORE spectra (bottom panels) focused on the region in which ^{1}H features manifest. Acquisition parameters: temperature = 10 K; microwave frequency = 9.718 GHz; MW pulse length ($\pi/2$, π) = 8 ns, 16 ns; τ = 156 ns (g = 2.312), 148 ns (g = 2.195); 144 ns (g = 2.111); 138 ns (g = 2.002); $t_1 = t_2$ = 100 ns; $\Delta t_1 = \Delta t_2$ = 16 ns; shot repetition time (srt) = 2 ms.

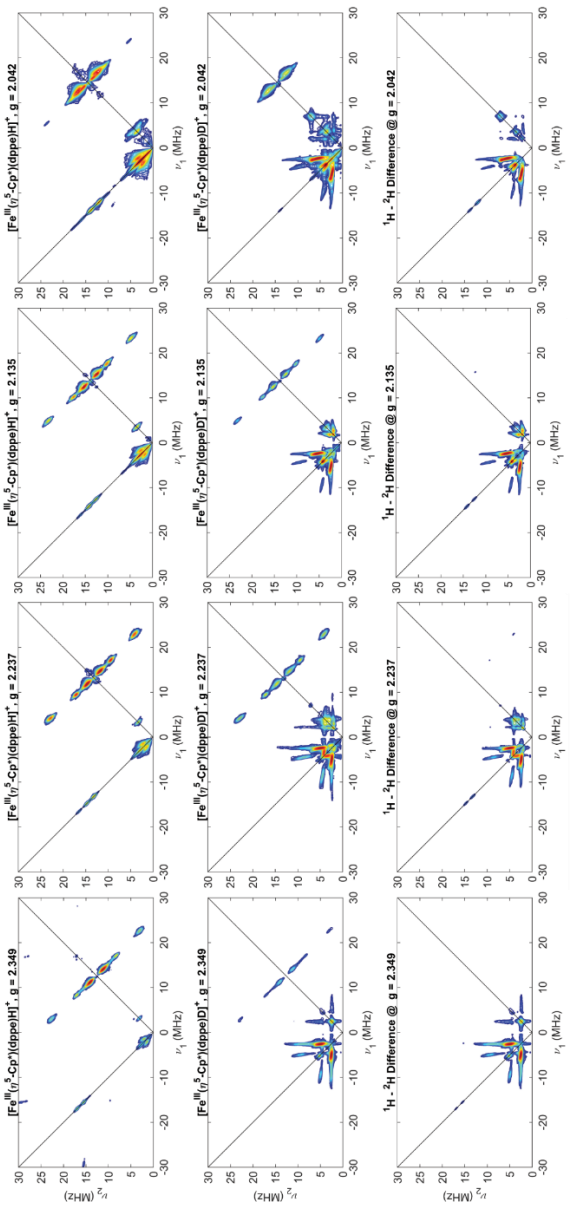

Figure C.49. Field-dependent X-band HYSCORE spectra of [Fe^{III}(η^5-Cp*)(dppe)**H**]$^+$ (top panels), [Fe^{III}(η^5-Cp*)(dppe)**D**]$^+$ (middle panels), and ^{1}H-^{2}H difference HYSCORE spectra (bottom panels). Acquisition parameters: temperature = 12 K; microwave frequency = 9.718 GHz; MW pulse length ($\pi/2$, π) = 8 ns, 16 ns; τ = 158 ns (g = 2.349), 152 ns (g = 2.237); 144 ns (g = 2.135); 138 ns (g = 2.042); $t_1 = t_2$ = 100 ns; $\Delta t_1 = \Delta t_2$ = 16 ns; shot repetition time (srt) = 2 ms.

cvi Mays, M. J.; Prater, B. E. *Inorg. Synth.* **1974**, *15*, 21.

cvii Hermes, A.R.; Girolami, G. S. *Organometallics* **1987**, *6*, 763.

cviii Prisecaru, I. *WMOSS4 Mössbauer Spectral Analysis Software, www.wmoss.org, 2009-2016.*

cix Stoll, S.; Schweiger, A. *J. Magn. Reson*. **2006**, *178*, 42.

cx Doyle, L. R.; Scott, D. J.; Hill, P. J.; Fraser, D. A. X.; Myers, W. K.; White, A. J. P.; Green, J. C.; Ashley, A. E. *Chem. Sci.* **2018**, *9*, 7362.

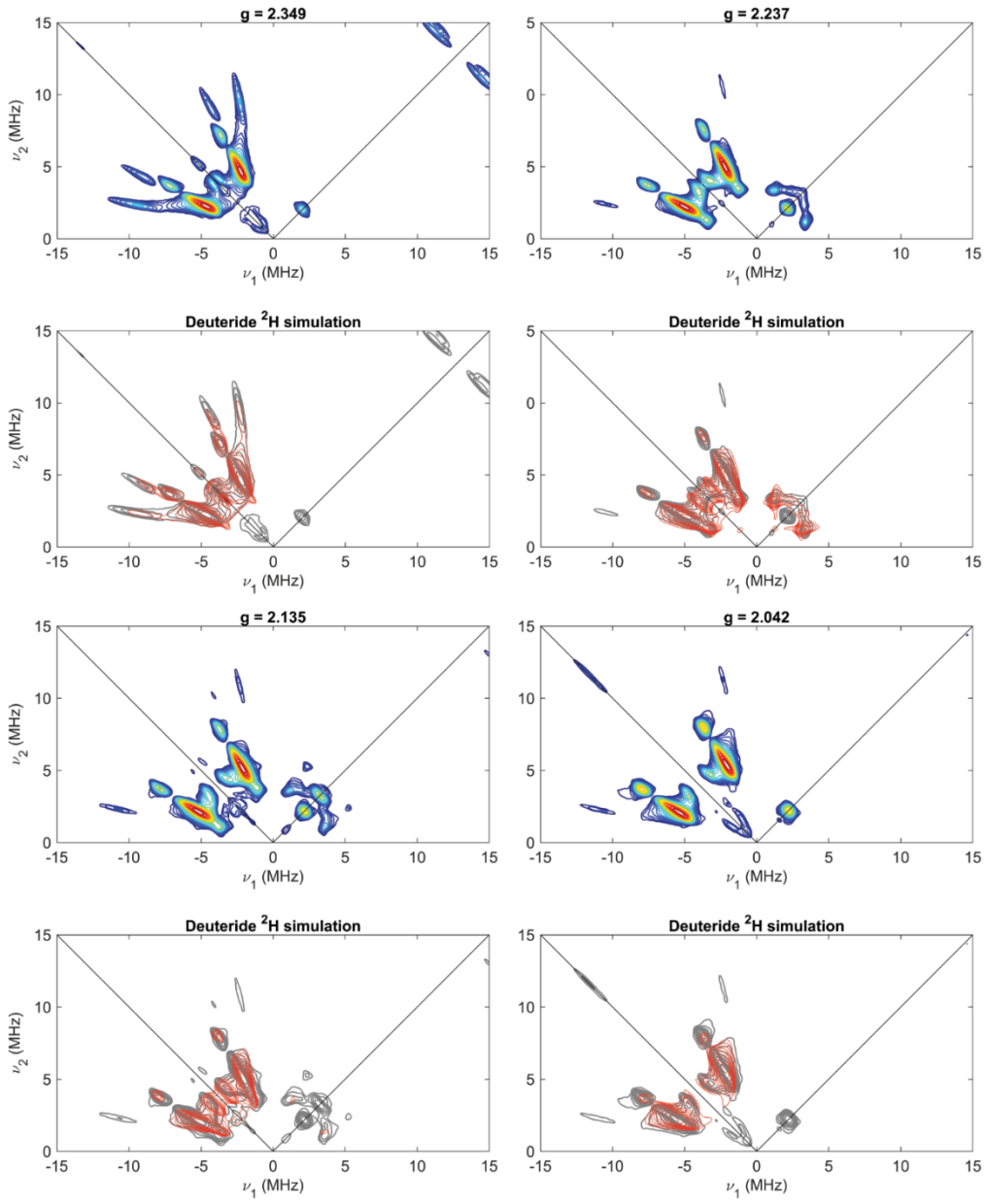

Figure C.50 Field-dependent X-band ^{1}H-^{2}H difference HYSCORE spectra of [**3-D**]BAr$^{F}_{4}$ (top panels) and simulations of deuteride ^{2}H features overlaid in red over experimental data displayed in grey (bottom panels). Acquisition parameters: temperature = 10 K; microwave frequency = 9.718 GHz; MW pulse length ($\pi/2$, π) = 8 ns, 16 ns; τ = 156 ns (g = 2.314), 148 ns (g = 2.197); 144 ns (g = 2.116); 138 ns (g = 2.042); $t_1 = t_2$ = 100 ns; $\Delta t_1 = \Delta t_2$ = 16 ns; shot repetition time (srt) = 2 ms.

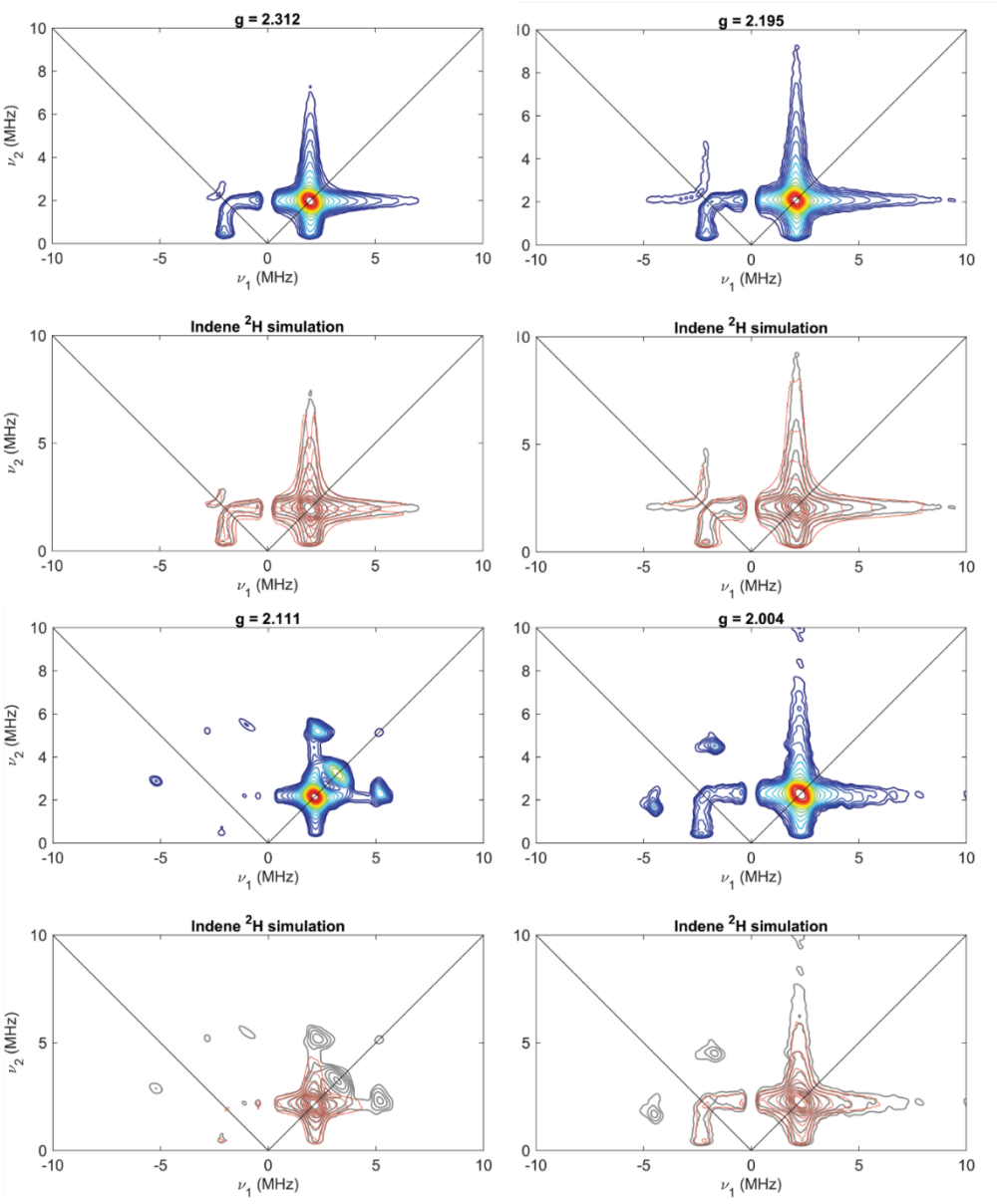

Figure C.51 Field-dependent X-band ^{1}H-^{2}H difference HYSCORE spectra of [**4-D**]BAr$^F{}_4$ (top panels) and simulations of Indene ^{2}H features overlaid in red over experimental data displayed in grey (bottom panels). Acquisition parameters: temperature = 10 K; microwave frequency = 9.718 GHz; MW pulse length ($\pi/2$, π) = 8 ns, 16 ns; τ = 156 ns (g = 2.312), 148 ns (g = 2.195); 144 ns (g = 2.111); 138 ns (g = 2.002); $t_1 = t_2$ = 100 ns; $\Delta t_1 = \Delta t_2$ = 16 ns; shot repetition time (srt) = 2 ms.

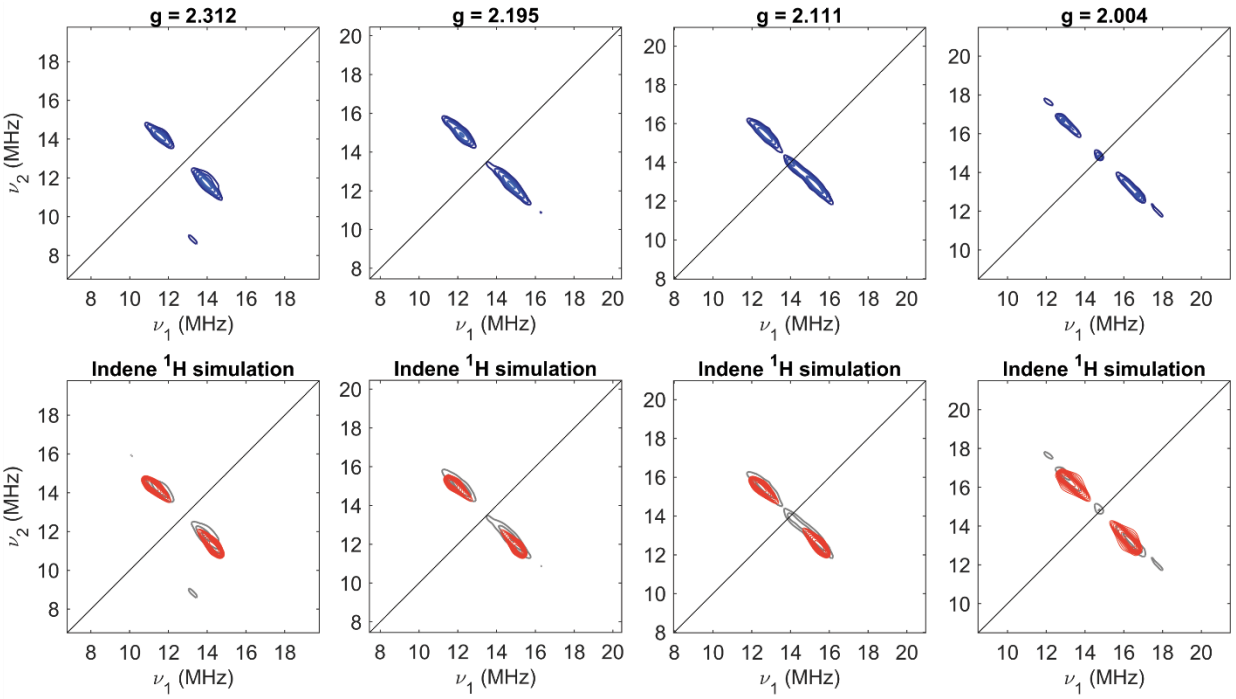

Figure C.52 Field-dependent X-band ^{1}H-^{2}H difference HYSCORE spectra of [**4-D**]BAr$^F{}_4$ (top panels) and simulations of Indene ^{1}H features overlaid in red over experimental data displayed in grey (bottom panels). Acquisition parameters: temperature = 10 K; microwave frequency = 9.718 GHz; MW pulse length ($\pi/2$, π) = 8 ns, 16 ns; τ = 156 ns (g = 2.312), 148 ns (g = 2.195); 144 ns (g = 2.111); 138 ns (g = 2.002); $t_1 = t_2$ = 100 ns; $\Delta t_1 = \Delta t_2$ = 16 ns; shot repetition time (srt) = 2 ms.

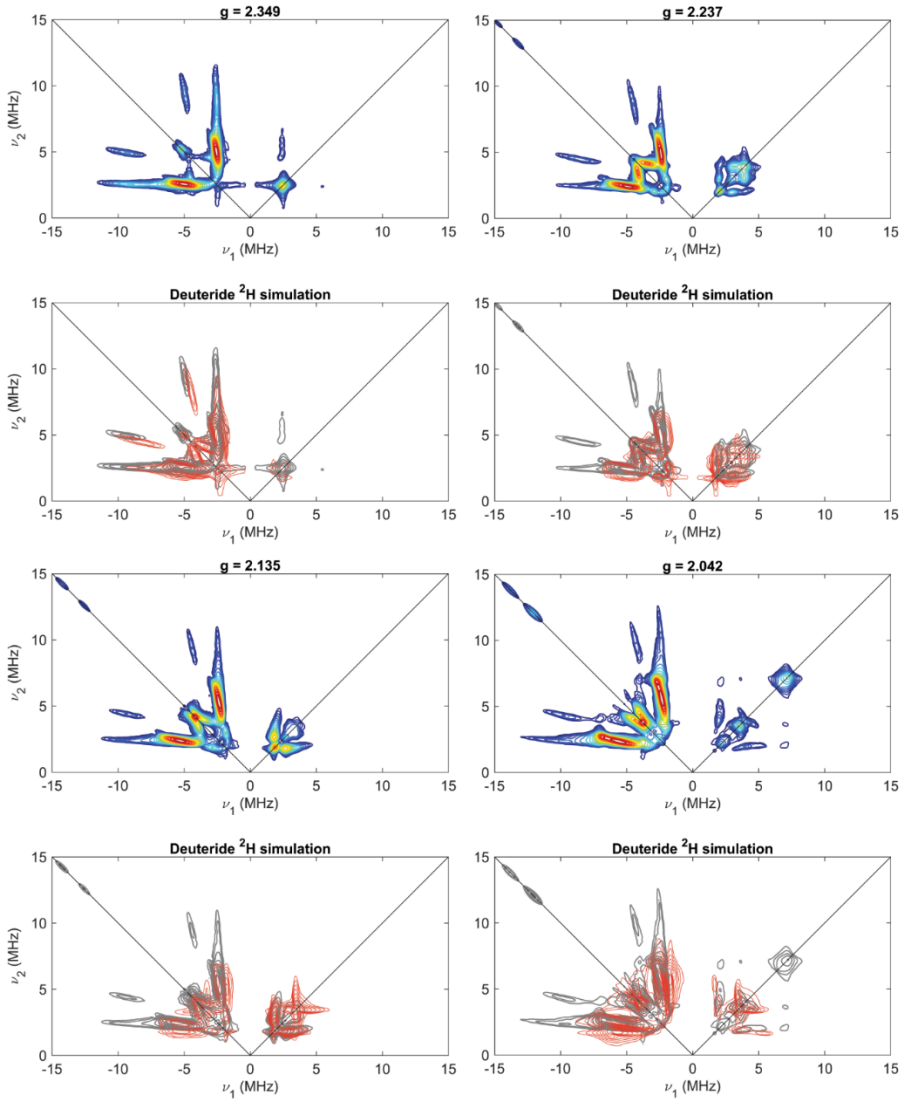

Figure C.53 Field-dependent X-band ^{1}H-^{2}H difference HYSCORE spectra of [Fe^{III}(η^5-Cp*)(dppe)**D**]$^{+}$ (top panels) and simulations of deuteride ^{2}H features overlaid in red over experimental data displayed in grey (bottom panels). Acquisition parameters: temperature = 12 K; microwave frequency = 9.718 GHz; MW pulse length ($\pi/2$, π) = 8 ns, 16 ns; τ = 158 ns (g = 2.349), 152 ns (g = 2.237); 144 ns (g = 2.135); 138 ns (g = 2.042); $t_1 = t_2$ = 100 ns; $\Delta t_1 = \Delta t_2$ = 16 ns; shot repetition time (srt) = 2 ms.

Rate Data

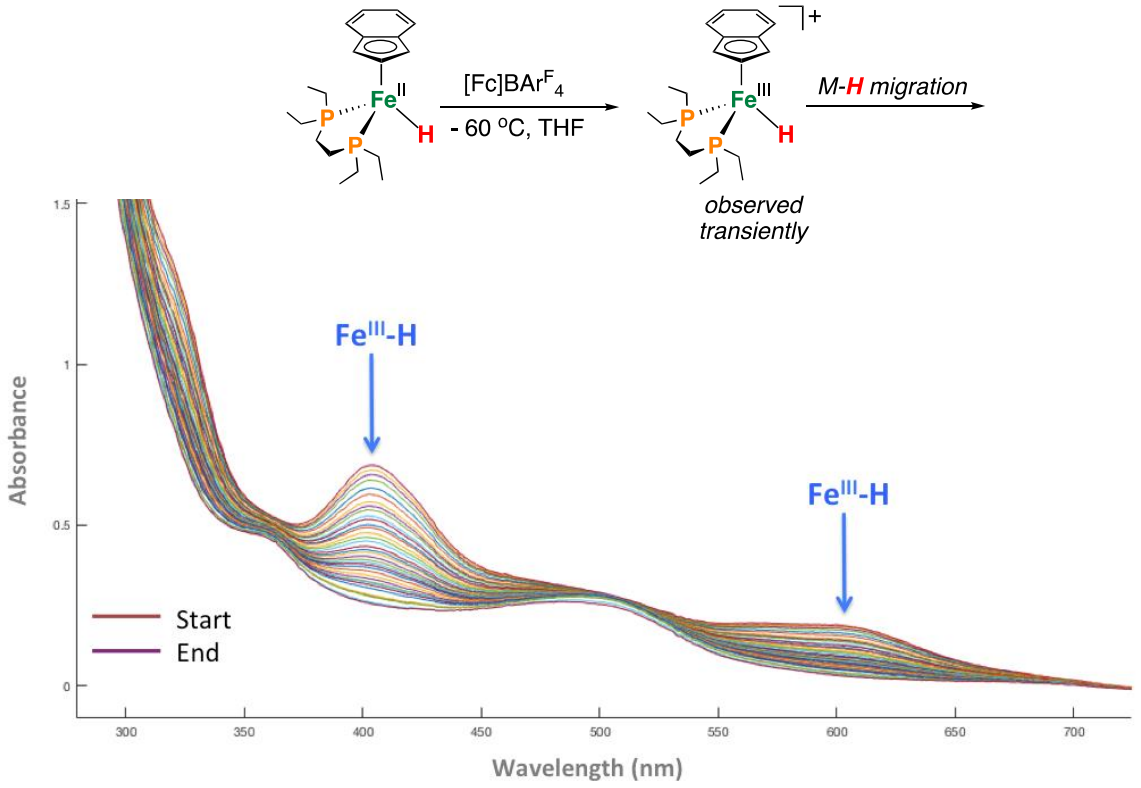

Figure C.54 UV-VIS spectrum showing decay of [**3**]$^+$ to give [**4**]$^+$ at -60 °C in 2-MeTHF.

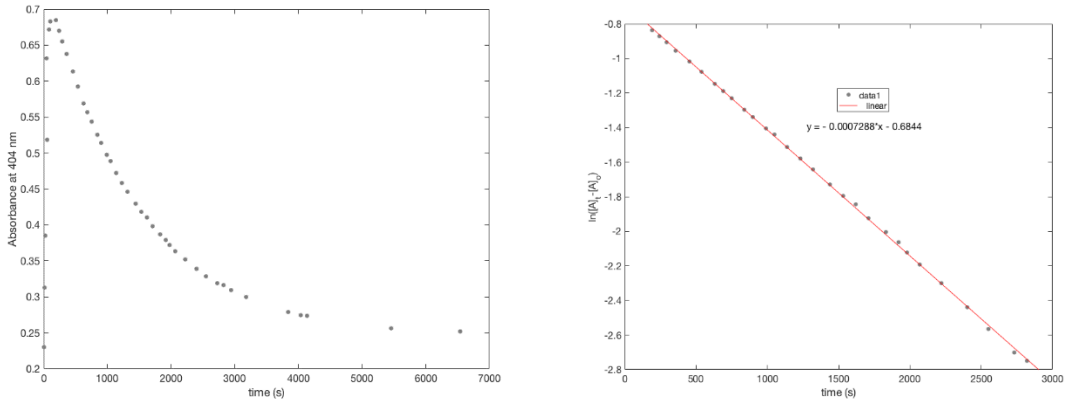

Figure C.55 Reaction monitoring at ε = 404 nm showing decay of [**3**]$^+$ at -60 °C in 2-MeTHF.

Crystallographic details

All crystals were mounted on a glass fiber loop. All measurements were made using graphite-monochromated Mo or Cu K_α radiation (λ = 0.71073 or 1.54178 Å) on a Bruker AXS D8 VENTURE KAPPA diffractometer coupled to a PHOTON 100 CMOS detector. The structures were solved by direct methods111 and refined by full-matrix least-squares procedures on F2 (SHELXL-2013)[6] using the OLEX2 interface.112 All hydrogen atoms were placed in calculated positions. Non-hydrogen atoms were refined anisotropically.

1: This crystal is a twin. The following twin law was obtained: **TWIN LAW** (-1.0, 0.0, 0.0, 0.0, 1.0, 0.0, 0.0, 0.0, -1.0, 2.0), **BASF** [0.562(6)] using OLEX2; this led to improved data statistics.

4: This crystal features disorder about an entire depe ligand that was modeled as a 41:59 split; this led to improved data statistics.

[**5**][BAr^F_4]: A q-peak near Fe was assigned as a partially occupied Fe site (PLAT307). Q-peaks for the remainder of the Fe-containing molecule were not observed, due to the degree of disorder being relatively small. PLAT971 suggested that there was residual electron density, however, this is not attributable to an atom. The electron density appears near a phenyl ring and Fe.

[**6**][BAr^F_4]: One side of the depe ligand was modeled in two orientations in a 38/62 split C16/C17/C20/C21 [38] and C18/C19/C22/C23 [62]; this led to improved data statistics. [**7**][BAr^F_4]$_2$: This crystal contains a disordered pentane molecule located on an inversion center (this was not modeled).

CCDC **1896047-1896051** contains the supplementary crystallographic data for this paper. These data can be obtained free of charge from The Cambridge Crystallographic Data Centre via www.ccdc.cam.ac.uk/data_request/cif

Table C.1. Crystallographic data for **1**, **4**, [**5**][BAr^F_4], and [**6**][BAr^F_4].

Compound	**1**	**4**	[**5**][BAr^F_4]
Empirical formula	$C_{19}H_{31}BrFeP_2$	$C_{51}H_{44}BF_{24}FeP_2$	$C_{53}H_{52}BF_{24}FeP_2$
Formula weight	457.14	1241.46	1273.54
Temperature/K	100(2)	100(2)	100(2)
Crystal system	Orthorhombic	Monoclinic	Monoclinic
Space group	$Pna2_1$	$P2_1/c$	$P2_1/c$
a/Å	15.4701(4)	11.9688(6)	17.9424(6)
b/Å	17.1275(5)	17.5103(11)	17.3777(5)
c/Å	7.5971(2)	24.9005(16)	19.0513(6)
α/°	90	90	90
β/°	90	95.858(2)	111.447(2)
γ/°	90	90	90
V/Å^3	2012.96(9)	5191.3(5)	5528.8(3)
Z	4	4	4
ρ/ g/cm^{-3}	1.508	1.588	1.530
μ/ mm^{-1}	2.891	0.475	3.802
F(000)	944.0	2508.0	2588.0
Crystal size/ mm^3	0.18 × 0.18 × 0.16	0.23 × 0.17 × 0.17	0.38 × 0.29 × 0.23
Radiation	MoKα (λ = 0.71073)	MoKα (λ = 0.71073)	CuKα (λ = 1.54178)
2θ range for data collection/°	4.756 to 54.994	4.498 to 52.878	5.292 to 147.104
Index ranges	$-20 \le h \le 20$, $-22 \le k \le 22$, $-9 \le l \le 9$	$-14 \le h \le 14$, $-21 \le k \le 21$, $-31 \le l \le 31$	$-21 \le h \le 22$, $-20 \le k \le 21$, $-23 \le l \le 23$
Independent reflections	4612 [R_{int} = 0.0752, R_{sigma} = 0.0242]	10453 [R_{int} = 0.1878, R_{sigma} = 0.1618]	11079 [R_{int} = 0.0572, R_{sigma} = 0.0199]
Data/restraints/parameters	4612/1/213	10453/912/866	11079/729/744
Goodness-of-fit on F^2	1.046	0.995	1.051
R [I>=2θ (I)] (R1, wR2)	R_1 = 0.0175, wR_2 = 0.0432	R_1 = 0.0828, wR_2 = 0.2121	R_1 = 0.0995, wR_2 = 0.2894
R (all data) (R1, wR2)	R_1 = 0.0189, wR_2 = 0.0439	R_1 = 0.1053, wR_2 = 0.2400	R_1 = 0.1122, wR_2 = 0.3046
Largest diff. peak/hole / (e Å^{-3})	0.27/-0.32	1.01/-0.48	4.25/-1.24

Table C2. Crystallographic data for [**7**][BAr^F_4]$_2$.

Compound	[**6**][BAr^F_4]	[**7**][BAr^F_4]$_2$
Empirical formula	$C_{56}H_{52}BF_{24}FeN_2P_2$	$C_{60}H_{55}BF_{24}FeP_3$
Formula weight	1337.59	1391.61
Temperature/K	100(2)	100(2)
Crystal system	Monoclinic	Triclinic
Space group	$P2_1/n$	P-1
a/Å	16.4173(6)	12.5836(7)
b/Å	16.3342(5)	13.0412(7)
c/Å	22.0278(8)	19.6731(11)
α/°	90	103.588(2)
β/°	91.9240(10)	106.523(2)
γ/°	90	90.595(2)
V/Å^3	5903.7(4)	2998.2(3)
Z	4	2
ρ/ g/cm^{-3}	1.505	1.541
μ/ mm^{-1}	0.425	0.446
F(000)	2716.0	1414.0
Crystal size/ mm^3	0.28 × 0.2 × 0.17	0.71 × 0.22 × 0.16
Radiation	MoKα (λ = 0.71073)	MoKα (λ = 0.71073)
2θ range for data collection/°	4.462 to 55.826	4.352 to 70.178
Index ranges	$-21 \le h \le 21$, $-21 \le k \le 21$, $-29 \le l \le 29$	$-20 \le h \le 20$, $-20 \le k \le 18$, $-30 \le l \le 28$
Independent reflections	14128 [R_{int} = 0.0849, R_{sigma} = 0.0379]	19818 [R_{int} = 0.0368, R_{sigma} = 0.0568]
Data/restraints/parameters	14128/786/821	19818/0/808
Goodness-of-fit on F^2	1.014	1.051
R [I>=2θ (I)] (R1, wR2)	R_1 = 0.0744, wR_2 = 0.1872	R_1 = 0.0546, wR_2 = 0.1311
R (all data) (R1, wR2)	R_1 = 0.1060, wR_2 = 0.2106	R_1 = 0.0853, wR_2 = 0.1533
Largest diff. peak/hole / (e Å^{-3})	1.26/-0.97	0.78/-0.77

$R1 = \Sigma ||F_o|-|F_c|| / \Sigma |F_o|$; $wR2 = [\Sigma(w(F_o^2 - F_c^2)^2) / \Sigma w(F_o^2)^2]^{1/2}$

Table C.3. Summary of data obtained from X-ray analyses

	1	[**4**][BAr^F_4]	[**5**][BAr^F_4]	[**6**][BAr^F_4]	[**7**][BAr^F_4]$_2$
Spin-state	*S* = 0	*S* = ½	*S* = ½	*S* = 0	*S* = 0
o.s.	2+	1+	1+	2+	2+
d(Fe-P1) (Å)	2.1792(6)	2.222(3)	2.254(2)	2.208(1)	2.1960(7)
d(Fe-P2) (Å)	2.2217(6)	2.298(3)	2.272(2)	2.206(1)	2.2413(7)
Ω	4.58	-	-	4.30	6.02
M-C)	0.134	-	-	0.089	0.134
127.5	90	96.7	127.5	135.1	

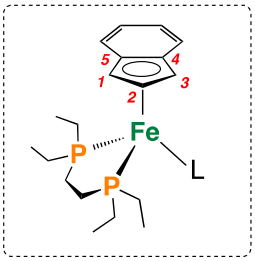

ϕ = angle between the two planes made by P1,Fe1,P2 and C1, C2, C3, C4, C5

Δ(M-C) = average of d(Fe-C1, Fe-C2, Fe-C3) minus average of d(Fe-C4, Fe-C5)

Ω = angle between the two planes made by C1, C2, C3 and C1, C5, C4, C3 [envelope angle]

DFT Calculations

General:

Geometry optimizations were performed using Gaussian 09 [Rev. A.02] at the following level of theory: TPSS functional, a def2-TZVP basis set on iron and a def2-SVP basis set on all other atoms. Frequency calculations were used to confirm true minima and to determine gas phase free energy values (G_{gas}).

$BDFE_{X\text{-}H}$ Calculations:

Consistent with a previous report, a calibration curve of ΔG vs. $BDFE_{lit}$ was employed. The free-energy difference between the H-atom donor/acceptor pair was calculated based on the thermochemical information provided by frequency calculations after structure optimizations using the procedure described in the general computational section.

^{57}Fe Mössbauer Calculations:

The ^{57}Fe Mössbauer isomer shifts in Table C4 have been calculated using the extended calibration parameters according to Neese. Isomer shifts were calculated according to the equation $\delta_{calc} = \alpha(\rho(0)-C+\beta$, with $\alpha = -0.17683$, $\beta = 0.35964$ and $C = 23600$.[9] Taking the systematic overestimation of this method into account, this provides a good indication of the isomer shifts. In contrast, the older set of calibration parameters (not included in Table C4) underestimate the observed isomer shifts.

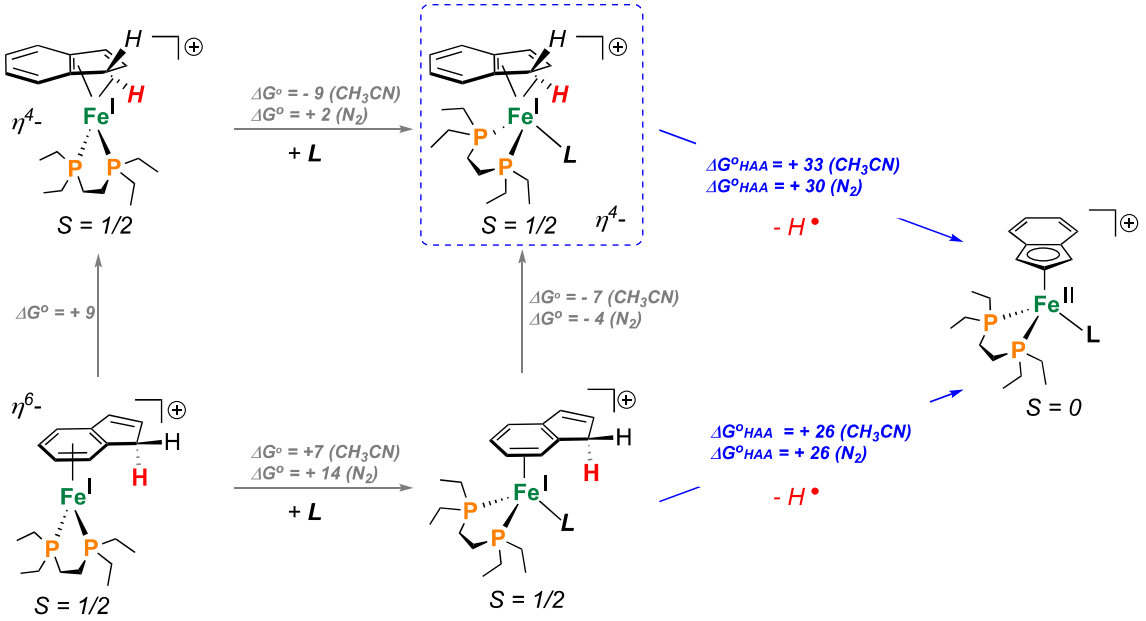

Figure C.56 Free energy change (kcal mol^{-1}) for PCET from the η-dienyl complex, involving $BDFE_{C\text{-}H}$ (TPSS; def2tzvp (Fe), def2svp (all other atoms)). ΔG^{o}_{HAA} = hydrogen atom affinity.

Functional	Basis set	^{1}H (a_{iso}) (MHz)	^{1}H A (MHz)	^{1}H T (MHz)
experimental		36.7	[-10, 60, 60]	[-46.7, 23.3 23.3]
TPSSh	EPR-III (C & H) IGLO-III (P)	-66.34	[-19.33 -83.31 -85.15]	[43.23, -22.55, -20.67]
TPSSh	IGLO-III	-62.59	[-23.11, -88.89, 87.01]	[43.26, -20.72, -22.54]
TPSS	EPR-III (C & H) IGLO-III (P)	-42.33	[-3.85, -62.55, -60.59]	[38.48, -20.22, -18.26]
TPSS	IGLO-III	-39.72	[-1.21, -59.92, -58.02]	[38.51, -20.20, -18.30]

Table C.0.4. Summary of DFT-calculated EPR parameters for $[Fe^{III}Cp^*(dppe)H]^+$

Table C.0.5. Summary of DFT-calculated ^{57}Fe Mössbauer parameters

Compound	δ_{exp} ($mm\,s^{-1}$)	δ_{calc} ($mm\,s^{-1}$)	$\rho(0)$ TPSSh+DKH	$\lvert\Delta E_{Qexp}\rvert$ ($mm\,s^{-1}$)	$\lvert\Delta E_{Qcalc}\rvert$ ($mm\,s^{-1}$)	*Ref.*
Ferrocene	0.51	0.54	23598.91995	2.5	2.6	[i]
Ferrocenium	0.57	0.59	23598.94994	0	0.47	**16**
Fe(η^5-Cp)(dppe)(H)	0.26	0.33	23600.32909	1.91	1.86	[ii]
[Fe(η^5-Cp*)(dppe)(H)]$^+$	0.26	0.33	23600.16782	0.84	1.10	[iii, iv]
Fe(η^3:η^2-Ind)(depe)(H) (**2**)	0.28	0.35	23600.02363	1.61	1.62	*this work*
[Fe(η^3:η^2-Ind)(depe)(H)]$^+$	--	0.33	23600.13298	--	0.90	*this work*
[Fe(η^6-IndH)(depe)]$^+$ ([**4**][BAr$^F_4$])	0.59	0.55	23598.90502	1.80	0.75	*this work*
[Fe(η^3:η^2-Ind)(depe)(PEt$_3$)]$^+$	--	0.36	23599.42829	--	1.72	*this work*
[Fe(η^3:η^2-Ind)(depe)(N$_2$)]$^+$	--	0.40	23599.72057	--	1.69	*this work*
[Fe(η^3:η^2-Ind)(depe)(H$_2$)]$^+$	--	0.40	23599.78043	--	1.65	*this work*
[Fe(η^3:η^2-Ind)(depe)(H)$_2$]$^+$	--	0.17	23601.04992	--	1.66	*this work*
[Fe(η^3:η^2-Ind)(depe)]$^+$ (S = 1)	--	0.55	23598.94974	--	1.35	*this work*
[Fe(η^6-C$_6$H$_5$CH$_3$)(dippe)]$^+$([**5**][BAr$^F_4$])	0.50	0.56	23598.82654	1.71	0.70	*this work*

[i] Malischewski, M.; Seppelt, K.; Sutter, J.; Munz, D.; Meyer, K. *Angew. Chem. Int. Ed.* **2018**, *57*, 14597.

[ii] Patel, D.; Wooles, A.; Cornish, A.D.; Steven, L.; Davies, S.E.; Evans, D.J.; McMaster, J.; Lewis, W.; Blake, A.J.; Liddle, S.T. *Dalton Trans.* **2015**, *44*, 14159.

[iii] Hamon, P.; Toupet, L.; Hamon, J.R.; Lapinte, C. *Organometallics* **1992**, *11*, 1429.

[iv] Hamon, P.; Hamon, J.R.; Lapinte, C. *J. Chem. Soc., Chem. Commun.* **1992**, 1602.

Table C.0.6. Mulliken atomic spin densities calculated for [Fe(η^3:η^2-Ind)(depe)(H)][BAr^F_4] ([**3**][BAr^F_4]). The red italicized atom corresponds to the hydride ligand with the value of $a_{iso}(^1H)$ provided to its right.

1	Fe	1.004222
2	P	-0.023195
3	P	-0.029529
4	C	0.049194
5	C	-0.041834
6	C	0.003854
7	C	0.075785
8	H	-0.003139
9	C	-0.047046
10	H	0.001708
11	C	0.002200
12	C	0.020057
13	H	-0.001148
14	C	0.004944
15	H	-0.000302
16	C	-0.037762
17	H	0.001462
18	C	0.003755
19	C	0.004541
20	H	0.002211
21	H	-0.000232
22	C	-0.042396
23	H	0.001438
24	C	0.000510
25	H	-0.000910
26	H	0.000278
27	C	0.002046
28	C	0.081118
29	H	-0.003645
30	C	0.000412
31	H	0.000098
32	H	0.000298
33	H	0.000009
34	C	0.000508
35	H	0.000364
36	H	-0.000094
37	H	0.000008
38	C	0.000560
39	H	-0.000002

40	H	-0.000152	
41	H	-0.000484	
42	C	-0.000034	
43	H	0.000031	
44	H	0.000339	
45	H	0.000035	
46	***H***	***-0.028443***	***$a_{iso}(^1H)$ = 40.4 MHz***
47	H	-0.001568	
48	H	0.000283	
49	H	0.000351	
50	H	-0.000554	
51	H	-0.000013	
52	H	-0.000248	
53	H	0.000445	
54	H	-0.000331	

Table C.0.7. Mulliken atomic spin densities calculated for [Fe(η^6-IndH)(depe)][$BAr^F{}_4$] ([**4**][$BAr^F{}_4$]). The red italicized atoms correspond to the CH_2 moiety of the indene ligand with the value of $a_{iso}(^1H)$ provided to its right.

1	Fe	1.107057
2	C	-0.020525
3	C	-0.007300
4	C	0.030112
5	H	0.002934
6	C	0.005009
7	C	-0.013393
8	H	0.000614
9	C	0.008598
10	H	-0.000140
11	C	-0.014147
12	H	0.002396
13	C	-0.034156
14	H	0.002322
15	C	-0.002793
16	H	0.001041
17	P	-0.045210
18	P	-0.043973
19	C	0.000078
20	H	-0.000075
21	H	0.000442
22	H	0.000062
23	C	0.000278

24	H	0.000043	
25	H	0.000802	
26	H	0.000188	
27	C	-0.002335	
28	H	0.000578	
29	H	0.000021	
30	C	-0.001156	
31	H	-0.000991	
32	H	-0.000082	
33	C	0.010649	
34	H	0.003180	
35	H	-0.000727	
36	C	0.001213	
37	H	-0.000028	
38	H	0.000390	
39	H	-0.000062	
40	C	0.000236	
41	H	0.000004	
42	H	0.000174	
43	H	-0.000123	
44	C	0.004419	
45	H	0.000103	
46	H	-0.001413	
47	C	0.008216	
48	H	0.000470	
49	H	-0.000183	
50	C	-0.000183	
51	H	-0.001390	
52	H	0.000085	
53	***H***	***-0.000061***	***$a_{iso}(^1H)$ = 0.087 MHz***
54	***H***	***-0.001270***	***$a_{iso}(^1H)$ = 1.80 MHz***

Table C.0.8. Mulliken atomic spin densities calculated for [Fe(η^6-$C_6H_5CH_3$)(dippe)][BAr^F_4] ([**5**][BAr^F_4]). The red italicized atoms correspond to the toluene hydrogen atoms with the value of $a_{iso}(^1H)$ provided to its right.

1	Fe	1.109224	
2	P	-0.051012	
3	P	-0.045018	
4	C	0.008734	
5	***H***	***0.003451***	***$a_{iso}(^1H)$ = 4.90 MHz***
6	C	-0.000236	
7	H	0.000277	

8	H	0.000530	
9	H	0.000063	
10	C	0.001060	
11	C	0.012531	
12	H	0.000427	
13	C	-0.027437	
14	***H***	***0.001502***	***$a_{iso}(^1H)$ = 2.13 MHz***
15	C	0.000183	
16	H	-0.000005	
17	H	0.000301	
18	H	0.000008	
19	C	0.009207	
20	H	-0.000350	
21	C	-0.003332	
22	***H***	***0.001605***	***$a_{iso}(^1H)$ = 2.28 MHz***
23	C	-0.022314	
24	***H***	***0.001202***	***$a_{iso}(^1H)$ = 1.71 MHz***
25	C	0.000830	
26	H	0.000004	
27	H	-0.000220	
28	H	-0.000595	
29	C	-0.009873	
30	***H***	***0.001819***	***$a_{iso}(^1H)$ = 2.58 MHz***
31	C	0.000214	
32	H	-0.000003	
33	H	-0.000140	
34	H	0.000312	
35	C	0.005435	
36	H	-0.001251	
37	C	-0.000346	
38	H	0.000101	
39	H	0.000873	
40	H	0.000020	
41	C	-0.001815	
42	H	0.000681	
43	H	-0.000093	
44	C	0.002110	
45	H	-0.000682	
46	H	-0.000168	
47	H	0.000017	
48	C	0.002660	
49	***H***	***-0.000541***	***$a_{iso}(^1H)$ = -0.77 MHz***
50	***H***	***0.001438***	***$a_{iso}(^1H)$ = 2.04 MHz***

51	***H***	***-0.000513***	***$a_{iso}(^1H)$ = 0.73 MHz***
52	C	0.002485	
53	H	0.000163	
54	C	-0.002381	
55	H	-0.000963	
56	H	0.000033	
57	C	0.000474	
58	H	0.000526	
59	H	-0.000122	
60	H	-0.000004	
61	C	-0.000895	
62	H	0.000069	
63	H	-0.000299	
64	H	0.000040	

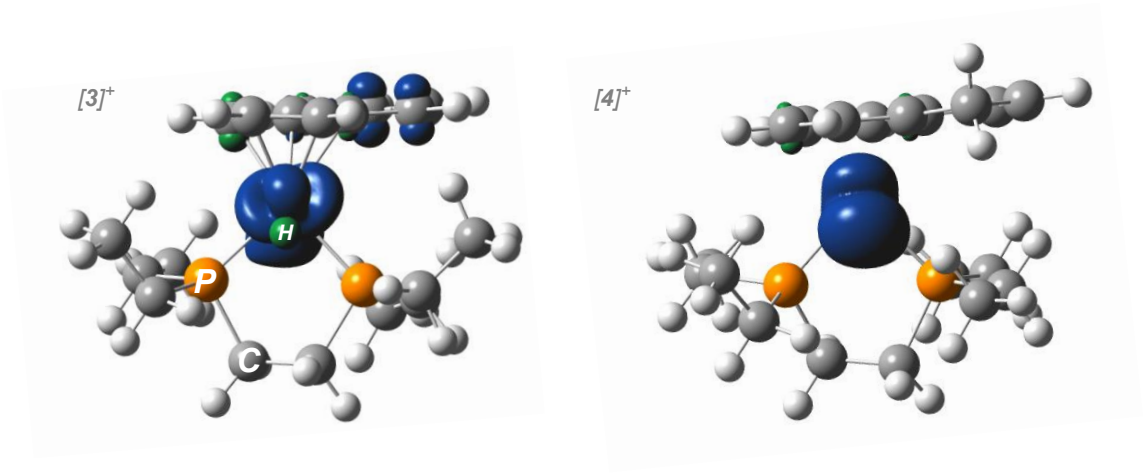

Figure C57 Spin density map of gas-phase optimized structures (isovalue: 0.004 e-/Å^3; TPSS functional: def2tzvp (Fe), def2svp (all other atoms).

Appendix D : Supporting Information for Chapter 5

Experimental Section

General Considerations

All experiments were carried out employing standard Schlenk techniques under an atmosphere of dry nitrogen or argon employing degassed, dried solvents in a solvent purification system supplied by SG Water, LLC. Non-halogenated solvents were tested with a standard purple solution of sodium benzophenone ketyl in tetrahydrofuran to confirm effective moisture removal. $Fe^{II}(\eta^5\text{-Cp*})(dppe)X$ (X = Cl, H, CH_3, OTf) were prepared according to a literature procedure. All other reagents were purchased from commercial vendors and used without further purification unless otherwise stated.

Nuclear Magnetic Resonance Spectroscopy

^{1}H and ^{13}C chemical shifts are reported in ppm relative to tetramethylsilane, using residual solvent resonances as internal standards. ^{31}P chemical shifts are reported in ppm and referenced externally to 85% aqueous H_3PO_4 at 0 ppm.

^{57}Fe Mössbauer Spectroscopy

Mössbauer spectra were recorded on a spectrometer from SEE Co. (Edina, MN) operating in the constant acceleration mode in transmission geometry. The sample was kept in an SVT-400 cryostat form Janis (Wilmington, MA), using liquid N_2 as a cryogen for 80 K measurements. The quoted isomer shifts are relative to the centroid of the spectrum of a metallic foil of α-Fe at room temperature. Solid samples were prepared by grinding solid material into a fine powder and then mounted in to a Delrin cup fitted with a screw cap as a boron nitride pellet. Solution samples were transferred to a sample cup and chilled to 77 K inside of the glovebox, and quickly removed from the glovebox and immersed in liquid N_2 until mounted in the cryostat. Data analysis was performed using WMOSS version 4 (www.wmoss.org) and quadrupole doublets were fit to Lorentzian lineshapes.1

Infrared Spectroscopy

Solid and thin film IR measurements were obtained on a Bruker Alpha spectrometer equipped with a diamond ATR probe.

UV-VIS Spectroscopy

UV-Visible spectroscopy measurements were collected with a Cary 50 UV-Vis spectrophotometer using a 1 cm two-window quartz cell.

EPR Spectroscopy

Continuous wave X-band EPR spectra were obtained on a Bruker EMX spectrometer on 2-9 mM solutions prepared as frozen glasses in 2-MeTHF. Pulse EPR spectroscopy: All pulse X-band (9.4-9.7 GHz) EPR, electron nuclear double resonance (ENDOR), and hyperfine sublevel correlation spectroscopy (HYSCORE) experiments were acquired using a Bruker ELEXSYS E580 pulse EPR spectrometer. X-band ENDOR experiments were performed using a Bruker MD-4 X-band ENDOR resonator, and X-band HYSCORE experiments were performed using a Bruker MS-5 resonator. Temperature control was achieved using an ER 4118HV-CF5-L Flexline Cryogen-Free VT cryostat manufactured by ColdEdge equipped with an Oxford Instruments Mercury ITC temperature controller.

All pulse X-band ($\nu \approx$ 9.4-9.7 GHz) EPR and electron nuclear double resonance (ENDOR) experiments were aquired using a Bruker (Billerica, MA) ELEXSYS E580 pulse EPR spectrometer equipped with a Bruker MD-4 resonator. Temperature control was achieved using an ER 4118HV-CF5-L Flexline Cryogen-Free VT cryostat manufactured by ColdEdge (Allentown, PA) equipped with an Oxford Instruments Mercury ITC.

Pulse X-band ENDOR was acquired using the Davies pulse sequence ($\pi - T_{RF} - \pi_{RF} - T_{RF} - \pi/2 - \tau - \pi -$ echo), where T_{RF} is the delay between mw pulses and RF pulses, π_{RF} is the length of the RF pulse and the RF frequency is randomly sampled during each pulse sequence.

X-band HYSCORE spectra were acquired using the 4-pulse sequence ($\pi/2 - \tau - \pi/2 - t_1 - \pi - t_2 - \pi/2 -$ echo), where τ is a fixed delay, while t_1 and t_2 are independently incremented by Δt_1 and Δt_2, respectively. The time domain data was baseline-corrected

(third-order polynomial) to eliminate the exponential decay in the echo intensity, apodized with a Hamming window function, zero-filled to eight-fold points, and fast Fourier-transformed to yield the 2-dimensional frequency domain. For ^{2}H-^{1}H difference spectra, the time domain of the HYSCORE spectrum of the ^{1}H sample was subtracted from that of the ^{2}H sample, and the same data processing procedure detailed above was used to generate the frequency spectrum.

In general, the ENDOR spectrum for a given nucleus with spin I= ½ (^{1}H, ^{31}P) coupled to the S = ½ electron spin exhibits a doublet at frequencies

$$\nu_{\pm} = \left|\frac{A}{2} \pm \nu_N\right| \quad (1)$$

Where ν_N is the nuclear Larmor frequency and A is the hyperfine coupling. For nuclei with $I \geq 1$ (^{2}H), an additonal splitting of the $\nu_{\pm}$ manifolds is produced by the nuclear quadrupole interaction (P)

$$\nu_{\pm,m_I} = \left|\nu_N \pm \frac{3P(2m_I - 1)}{2}\right| \quad (2)$$

In HYSCORE spectra, these signals manifest as cross-peaks or ridges in the 2-D frequency spectrum which are generally symmetric about the diagonal of a given quadrant. This technique allows hyperfine levels corresponding to the same electron-nuclear submanifold to be differentiated, as well as separating features from hyperfine couplings in the weak-coupling regime ($|A| < 2|\nu_I|$) in the (+,+) quadrant from those in the strong coupling regime ($|A| > 2|\nu_I|$) in the (−,+) quadrant. The (−,−) and (+,−) quadrants of these frequency spectra are symmetric to the (+,+) and (−,+) quadrants, thus typically only two of the quadrants are displayed in literature.

For systems with appreciable hyperfine anisotropy in frozen solutions or solids, HYSCORE spectra typically do not exhibit sharp cross peaks, but show ridges that represent the sum of cross peaks from selected orientations within the excitation bandwidth of the MW pulses at the magnetic field position at which the spectrum is collected. The length and curvature of these correlation ridges can allow for the separation and estimation of the magnitude of the isotropic and dipolar components of the hyperfine tensor, as shown in Fig. S1.

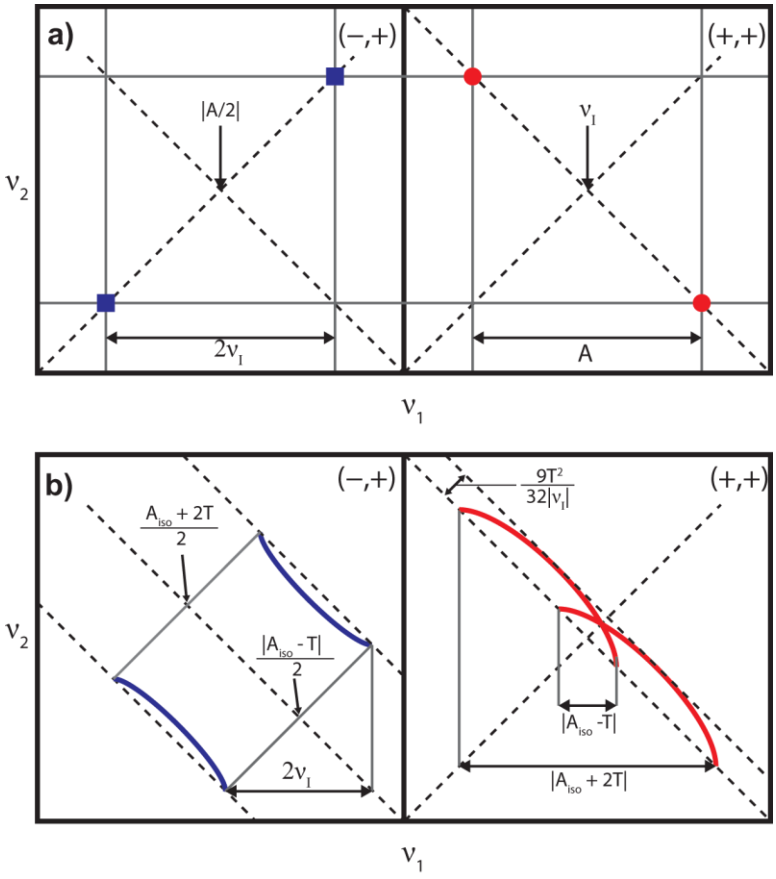

Figure D.1 a) HYSCORE powder patterns for an S = 1/2, I = 1/2 spin system with an isotropic hyperfine tensor A. b) HYSCORE powder patterns for an S = 1/2, I = 1/2 spin system with an isotropic hyperfine tensor which contains isotropic (a_{iso}) and dipolar (T) contributions. Blue correlation ridges represent the strong coupling case; red correlation ridges represent the weak coupling case.

EPR Simulations. Simulations of all CW and pulse EPR data were achieved using the EasySpin2 simulation toolbox (release 5.2.21) with Matlab 2018b using the following Hamiltonian:

$$\hat{H} = \mu_B \vec{B}_0 g \hat{S} + \mu_N g_N \vec{B}_0 \hat{I} + h\hat{S} \cdot \mathbf{A} \cdot \hat{I} + h\hat{I} \cdot \mathbf{P} \cdot \hat{I} \qquad (3)$$

In this expression, the first term corresponds to the electron Zeeman interaction term where μ_B is the Bohr magneton, g is the electron spin g-value matrix with principle components g = [g_{xx} g_{yy} g_{zz}], and $\hat{S}$ is the electron spin operator; the second term corresponds to the nuclear Zeeman interaction term where μ_N is the nuclear magneton, g_N is the characteristic nuclear g-value for each nucleus (e.g. ^{1}H, ^{2}H ,^{31}P) and $\hat{I}$ is the nuclear spin operator; the third term corresponds to the electron-nuclear hyperfine term, where **A** is the hyperfine coupling tensor with principle components **A** = [A_{xx}, A_{yy}, A_{zz}]; and for nuclei with $I \geq 1$, the final term corresponds to the nuclear quadrupole (NQI) term which arises from the interaction of the nuclear quadrupole moment with the local electric field gradient (efg) at the nucleus, where **P** is the quadrupole coupling tensor. In the principle axis system (PAS), **P** is traceless and parameterized by the quadrupole coupling constant e^2Qq/h and the asymmetry parameter η such that:

$$\mathbf{P} = \begin{pmatrix} P_{xx} & 0 & 0 \\ 0 & P_{yy} & 0 \\ 0 & 0 & P_{zz} \end{pmatrix} = \frac{e^2Qq/h}{4I(2I-1)} \begin{pmatrix} -(1-\eta) & 0 & 0 \\ 0 & -(1+\eta) & 0 \\ 0 & 0 & 2 \end{pmatrix} \qquad (4)$$

where $\frac{e^2Qq}{h} = 2I(2I-1)P_{zz}$ and $\eta = \frac{P_{xx}-P_{yy}}{P_{zz}}$. The asymmetry parameter may have values between 0 and 1, with 0 corresponding to an electric field gradient with axial symmetry and 1 corresponding to a fully rhombic efg.

The orientations between the hyperfine and NQI tensor principle axis systems and the g-matrix reference frame are defined by the Euler angles (α, β, γ).

Electrochemistry

Electrochemical measurements were carried out using a CD instruments 600B electrochemical analyzer. A freshly polished glassy carbon electrode was used as the working electrode and a graphite rod was used as the auxiliary electrode. Solutions (THF) of electrolyte (0.4 M tetra-n-butylammonium hexafluorophosphate) contained ferrocene (0.1 mM), to serve as an internal reference, and analyte (0.2 mM). All reported potentials are referenced to the ferrocene/ferrocenium couple, $[Cp_2Fe]^+$ /Cp_2Fe.

Synthetic Procedures

[Fe^{III}(η^5-Cp*)(dppe)H]BAr$^F_4$ ([**1**]BAr$^F_4$: $C_{68}H_{52}BF_{24}FeP_2$; 1453.3 gmol^{-1}): To a solution of **Fe^{II}(η^5-Cp*)(dppe)H** (40 mg, 0.07 mmol, 1 equiv.) in Et_2O (2 mL) at -78 °C was added an Et_2O (2 mL) solution of [Fc]BAr$^F_4$ (60 mg, 0.06 mmol, 0.85 equiv.). Following addition, the resulting dark orange mixture was stirred at 25 °C over 10 min giving a dark red-orange solution. Removal of volatiles *in-vacuo* and washing with pentane gave [**1**]BAr$^F_4$ as a red solid (72 mg, 74%). ***N.B.*** The PF_6^- salt has been prepared previously, though ^{1}H NMR data was not provided.3 **^{1}H NMR (THF-d$_8$, 400 MHz, 298 K)**:δ = 54.12 (br), 26.46 (br), 9.88 (br), 8.71 (br), 7.80 (BAr$^F_4$), 7.58 (BAr$^F_4$), 7.40 (br), 5.61 (br), -0.15 (br), -2.51 (br), -9.00 (br).

Fe(*endo* η^4-Cp*H)(dppe)(CO) (*endo*-**3**): Prepared as previously reported.4 The solid-state molecular structure was not reported and is shown in the crystallography section. **UV-VIS (THF, nm {cm^{-1} M^{-1})**: 450 {1130}. **IR (ATR, C$_6$D$_6$ film)**: 1864 cm^{-1} (νCO).

[Fe(*endo* η^4-Cp*H)(dppe)(CO)]BAr$^F_4$ (*endo*-[**3**]BAr$^F_4$): To a solution of [**1**]BAr$^F_4$ (10 mg, 0.007 mmol) in 2-MeTHF (2 mL) at -78 °C was added CO (~1 atm) in a J. Young EPR tube, giving a green solution. CW X-band EPR spectroscopy evidenced complete consumption of the Fe^{III}-H starting material. **UV-VIS (THF, nm {cm^{-1} M^{-1})**: 891 {252}, 712 {425}, 459 {870}, 383 {1530}. **EPR Parameters (30 K, 2-MeTHF, 9.717 GHz):** g = [2.085, 2.039, 2.004]; A(^{31}P$_1$) = [72, 59, 58] MHz; A(^{31}P$_2$) = [49, 42, 51] MHz; *A*(^{1}H) = ± [24, 20, 34.5] MHz.

Fe(*exo* η^4-Cp*H)(dppe)(CO) (*exo*-**3**): To a solution of [Fe(η^5-Cp*)(dppe)CO]OTf (229.9 mg, 0.3 mmol, 1 equiv.) in Et_2O (20 mL) at -78 °C was added drop-wise a solution of 1 M $LiBEt_3H$ in Et_2O (0.3 mL, 0.3 mmol, 1 equiv. Following addition, the resulting mixture

was stirred at 25 °C over 10 min giving a clear yellow solution. Volatiles were removed *in-vacuo* and the sample was extracted with 200 mL pentane, and filtered over celite. Removal of pentane *in-vacuo* yields *exo*-**3** as a yellow solid (158 mg, 85%). X-ray quality crystals are formed by cooling down a concentrated pentane solution of *exo*-**3** to -35 °C. **^{1}H NMR (400 MHz, C_6D_6)**: δ= 7.91 (t, $^{3}J_{H,H}$ = 8.2 Hz, 4H), 7.33 (h, $^{3}J_{H,H}$ = 3.8, 2.9 Hz, 4H), 7.27 – 7.18 (m, 4H), 7.14 – 7.03 (m, 8H), 3.04 (q, $^{3}J_{H,H}$ = 6.8 Hz, 1H), 2.23 – 2.01 (m, 2H), 1.83 (q, $^{3}J_{H,H}$ = 2.2 Hz, 9H), 1.65 (td, $^{3}J_{H,H}$ = 15.7, 12.7, 6.8 Hz, 2H), 0.97 (s, 6H), **^{13}C NMR (101 MHz, THF-d_8)**: δ = 139.7 – 138.8 (m), 138.3 (d, *J* = 16.8 Hz), 133.8 (t, *J* = 6.0 Hz), 133.1 (d, *J* = 5.3 Hz), 128.6 (d, *J* = 27.6 Hz), 127.3 (dt, *J* = 11.6, 4.1 Hz), 92.3, 60.8, 58.1, 31.0 – 29.9 (m), 13.1, 11.3. **^{31}P NMR (162 MHz, C_6D_6)**: δ= 85.3. **UV-VIS (THF, nm {cm^{-1} M^{-1})**: 441 {1850}. **IR (ATR, C_6D_6 film)**: 2711 cm^{-1} (νC–H), 2612 cm^{-1} (νC–H), 1854 cm^{-1} (νCO).

[Fe(*exo*-η^4-Cp*H)(dppe)(CO)]BAr$^{F}_4$ (*exo*-[**3**]BAr$^{F}_4$): In an 4 mm EPR tube, a frozen solution of *exo*-**3** (1.3 mg, 0.002 mmol) in 2-MeTHF (0.25 mL) was layered with a frozen solution of [Fc]BAr$^{F}_4$ (2.2 mg, 0.002 mmol, 1 equiv) in 0.25 mL 2-MeTHF. The two frozen solutions where slow thawed and stirred with a needle by taking the tube out of a cold well cooled with liquid nitrogen. Upon mixing, a color change to green can be observed. CW X-band EPR spectroscopy evidenced complete consumption of the Fe^{III}-H starting material. **UV-VIS (THF, nm {cm^{-1} M^{-1})**: 923 {130}, 767 {180}, 441 {1645}. **EPR Parameters (30 K, 2-MeTHF, 9.717 GHz):** g = [2.116, 2.073, 1.997]; A(^{31}P$_1$) = [96, 88, 47] MHz; A(^{31}P$_2$) = [78, 75, 63] MHz; *A*(^{1}H) = ± [85, 84, 83] MHz, HStrain = [70, 22, 22] MHz for conformer **A** (0.6 weight) and g = [2.093, 2.045, 2.013]; A(^{31}P$_1$) = [46, 44, 15]

MHz; A($^{31}P_2$) = [70, 64, 64] MHz; *A*(^{1}H) = ± [76, 74, 70] MHz, HStrain = [70, 22, 22] MHz for conformer **B** (0.4 weight).

[Fe(*endo*-η^4-Cp*H)(dppe)(CNXyl)]BAr$^F_4$ (*endo*-[**4**]BAr$^F_4$): To a solution of [**1**]BAr$^F_4$ (10 mg, 0.007 mmol) in 2-MeTHF (2 mL) at -78 °C was added CNXyl (~1 mg, 0.008 mmol, ~1.1 equiv.), giving a green solution. CW X-band EPR spectroscopy evidenced complete consumption of the Fe^{III}-H starting material. **UV-VIS (THF, nm):** 828. **EPR Parameters (20 K, 2-MeTHF, 9.716 GHz):** g = [2.132, 2.042, 2.004]; A($^{31}P_1$) = [75, 35, 54] MHz; A($^{31}P_2$) = [76, 64, 64] MHz; *A*(^{1}H) = ± [17.0, 22.0, 32.5] MHz; *A*(^{14}N) = [7.4, 7.4, 9] MHz.

[Fe(η^5-Cp*)(dppe)CO]BAr$^F_4$ ([**5**]BAr$^F_4$): This molecule and H_2 cleanly result (>99%) by annealing of solutions of *exo*- or *endo*-[**3**]$^+$ to room temperature. Characterization data is consistent with that reported in ref. 6.

[Fe(η^5-Cp*)(dppe)CNXyl]BAr$^F_4$ ([**6**]BAr$^F_4$): To a solution of **Fe^{II}(η^5-Cp*)(dppe)H** (9.5 mg, 0.016 mmol, 1 equiv.) and CNXyl (2.1 mg, 0.016 mmol, 1 equiv.) in Et_2O (2 mL) at -78 °C was added drop-wise a chilled (-78 °C) solution of [H(OEt)$_2$]BAr$^F_4$ (16.3 mg, 0.016 mmol, 1 equiv.) in Et_2O (1 mL). Following addition, the resulting mixture was stirred at 25 °C over 10 min giving a clear yellow solution. Removal of volatiles *in-vacuo* and washing with pentane gave [**6**]BAr$^F_4$ as a yellow solid (20 mg, 80%). **^{1}H NMR (THF-d$_8$, 400 MHz, 298 K)**:δ = 7.79 (s, 8H; BAr$^F_4$), 7.57 (s, 4H; BAr$^F_4$), 7.55 (m, 10H; Ph), 7.39 (m, 10H; Ph), 7.08 (t, $^3J_{H,H}$ = 7.2 Hz, 1H; CNXyl), 7.00 (d, $^3J_{H,H}$ = 7.2 Hz, 2H; CNXyl), 2.67 (m, 2H; CH_2), 2.45 (m, 2H; CH_2), 1.63 (s, 6H; CNXyl), 1.55 (s, 15H; Cp*). **^{31}P{^{1}H} NMR (THF-d$_8$, 162 MHz, 298 K)**:δ = 94.0. **^{13}C NMR (THF-d$_8$, 100 MHz, 298 K)**: δ = 162.5 (q, $^1J_{C,B}$ = 37 Hz, BAr$^F_4$, ipso quaternary C), 135.6 (BAr$^F_4$, ortho C), 135.0, 134.6, 133.7, 131.9, 129.9, 129.9 (q, $^2J_{C,F}$ = 31 Hz, BAr$^F_4$, meta quaternary C), 129.6, 129.4, 129.2,

129.1, 125.4 (q, $^{1}J_{C,F}$ = 273 Hz, BAr^{F}_{4}, CF_3), 117.9 (m, BAr^{F}_{4}, para C), 93.6 (Cp*), 30.5 (CH_2; dppe), 18.8, 10.1 (Cp*). **IR (THF film)**: 2050 cm^{-1} ($\nu_{C\equiv N}$). **^{57}Fe Mössbauer (80 K, Et_2O solution, mm/s)**: δ = 0.16, ΔE_Q = 1.75.

[Fe(η^5-Cp*)(dppe)N_2]BAr^{F}_{4} ([**7**]BAr^{F}_{4}): To a solution of Fe(η^5-Cp*)(dppe)CH_3**Error! Bookmark not defined.** (21.8 mg, 0.036 mmol, 1 equiv.) in Et_2O (2 mL) at -78 °C was added drop-wise a chilled (-78 °C) solution of [$H(OEt)_2$]BAr^{F}_{4} (36.5 mg, 0.036 mmol, 1 equiv.) in Et_2O (1 mL). Following addition, the resulting mixture was stirred at 25 °C over 10 min giving a clear yellow solution. Removal of volatiles *in-vacuo* and washing with pentane gave [**7**]BAr^{F}_{4} as a yellow solid (53 mg, 92%). [**7**]BAr^{F}_{4} is also the product of H_2 release by [**1**]BAr^{F}_{4} in THF (< 5% yield after 1 week, + 80 °C, THF-d_8). **^{1}H NMR (THF-d_8, 400 MHz, 298 K)**: δ= 7.79 (s, 8H; BAr^{F}_{4}), 7.57 (s, 4H; BAr^{F}_{4}), 7.75-7.54 (m, 16H; Ph), 7.44 (m, 4H; Ph), 2.54 (m, 2H; CH_2), 2.38 (m, 2H; CH_2), 1.43 (s, 15H; Cp*). **^{31}P{^{1}H} NMR (THF-d_8, 162 MHz, 298 K)**: δ= 86.6. **^{13}C NMR (THF-d_8, 100 MHz, 298 K)**: δ= 162.5 (q, $^{1}J_{C,B}$ = 37 Hz, BAr^{F}_{4}, ipso quaternary C), 135.6 (BAr^{F}_{4}, ortho C), 135.4, 134.3, 133.2, 132.4, 132.2, 129.9 (q, $^{2}J_{C,F}$ = 31 Hz, BAr^{F}_{4}, meta quaternary C), 125.4 (q, $^{1}J_{C,F}$ = 273 Hz, BAr^{F}_{4}, CF_3), 118.0 (m, BAr^{F}_{4}, para C), 117.0, 92.7 (Cp*), 28.8 (CH_2; dppe), 9.2 (Cp*). **IR (THF film)**: 2119 cm^{-1} (ν_{NN}).

Spectroscopic Data

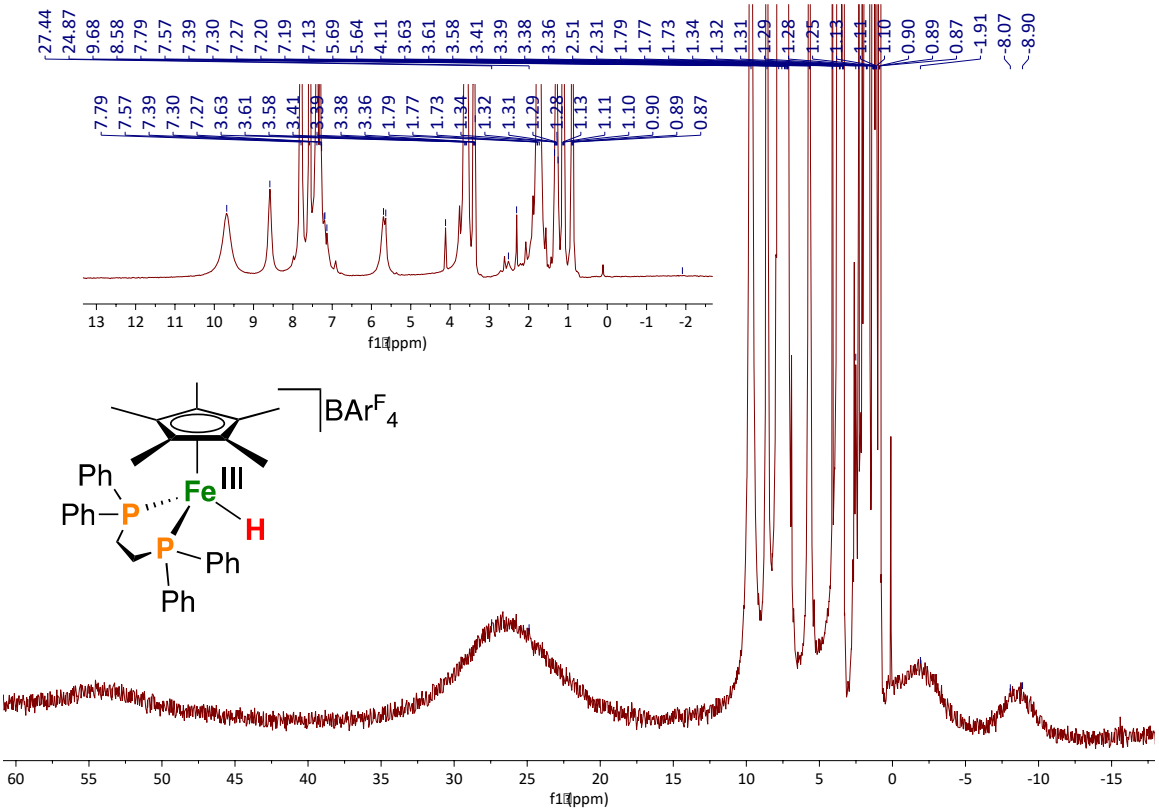

Figure D.2 [**1**]BAr$^F_4$, ^{1}H NMR, THF-d$_8$, 400 MHz, 298 K

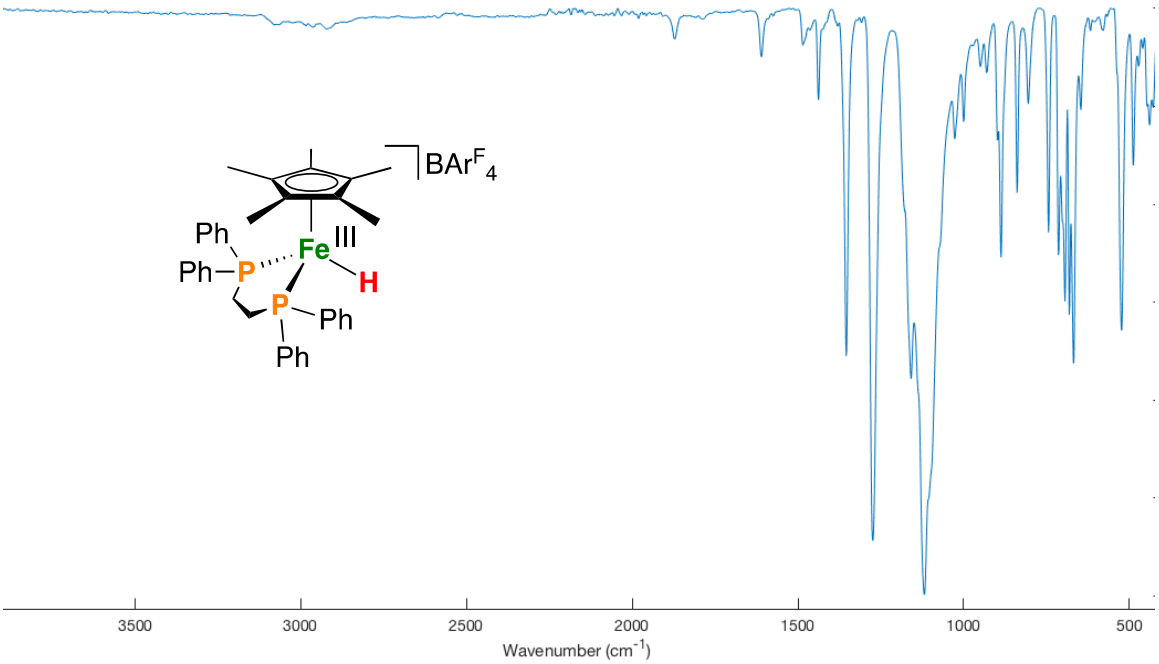

Figure D.3 [**1**]BAr$^F_4$, FT-IR ATR, thin film, 298 K (ν_{FeH} = 1874 cm^{-1})

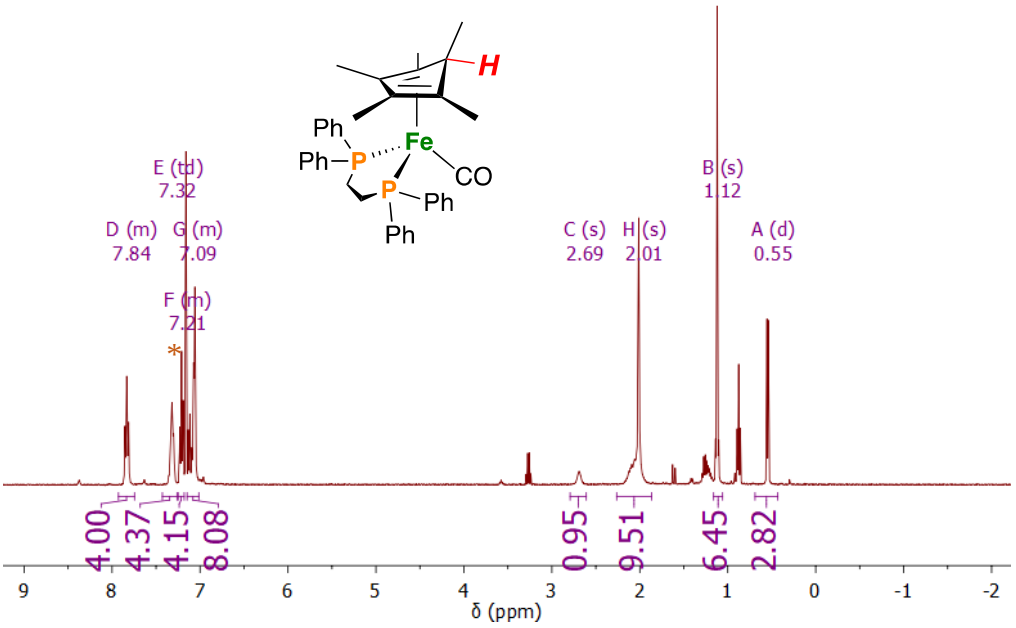

Figure D.4 *endo*-**3**, ^{1}H NMR, C_6D_6, 400 MHz, 298 K. The data match that previously reported.[5] (* = C_6D_6)

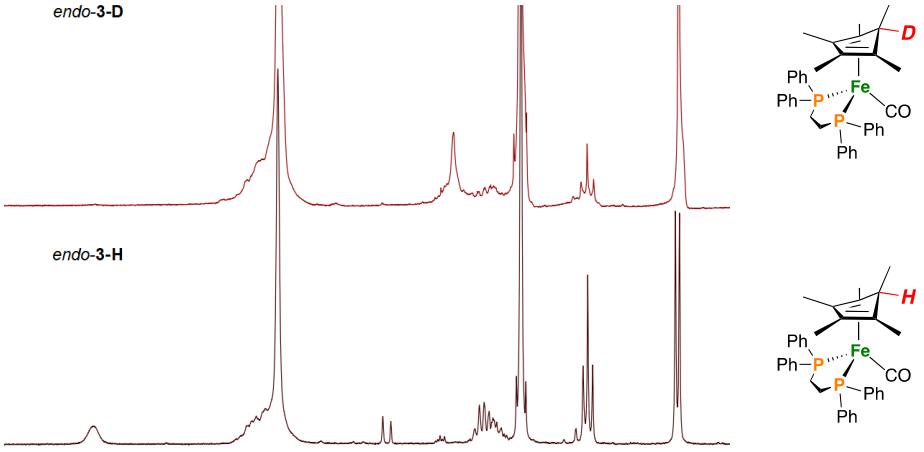

Figure D.5 *endo*-3-H/D stacked plot, ^{1}H NMR, C_6D_6, 400 MHz, 298 K showing disappearance of a signal at δ_H = 2.65.

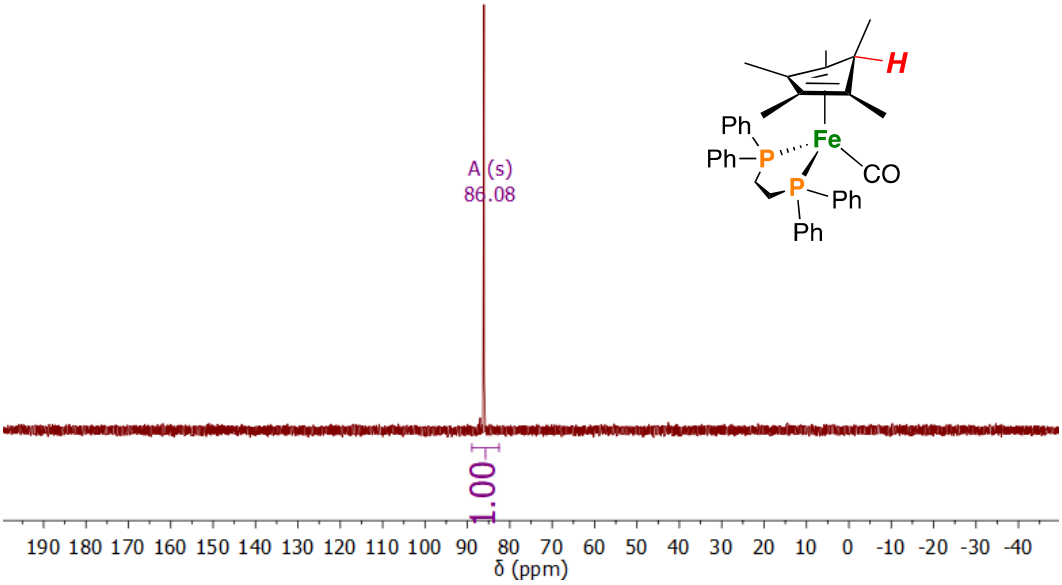

Figure D.6 *endo*-**3**, $^{31}P\{^{1}H\}$ NMR, C_6D_6, 162 MHz, 298 K. The data match that previously reported.[5]

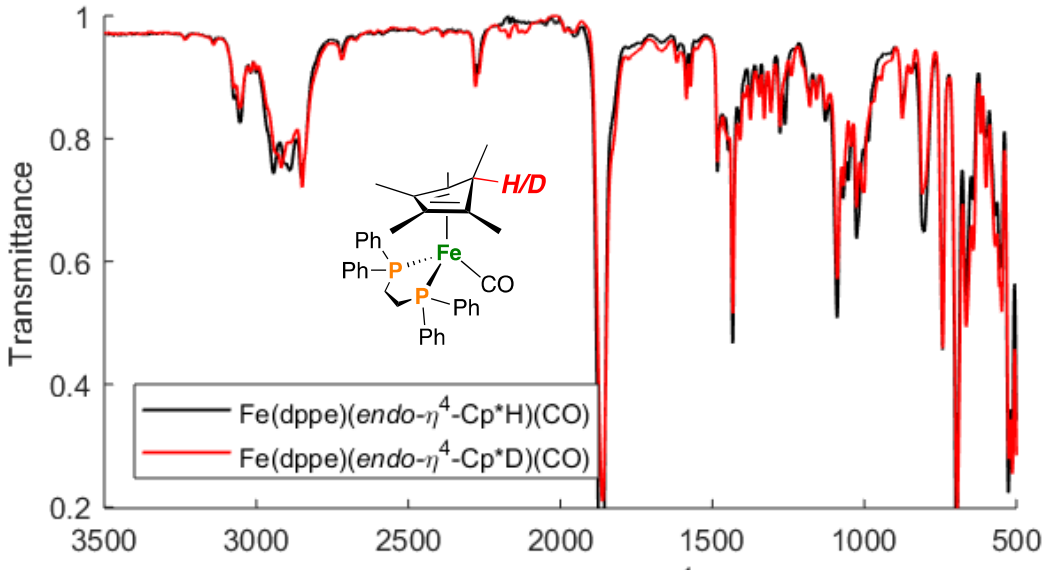

Figure D.7. *endo*-**3**-H/D, FT-IR ATR, thin film, 298 K

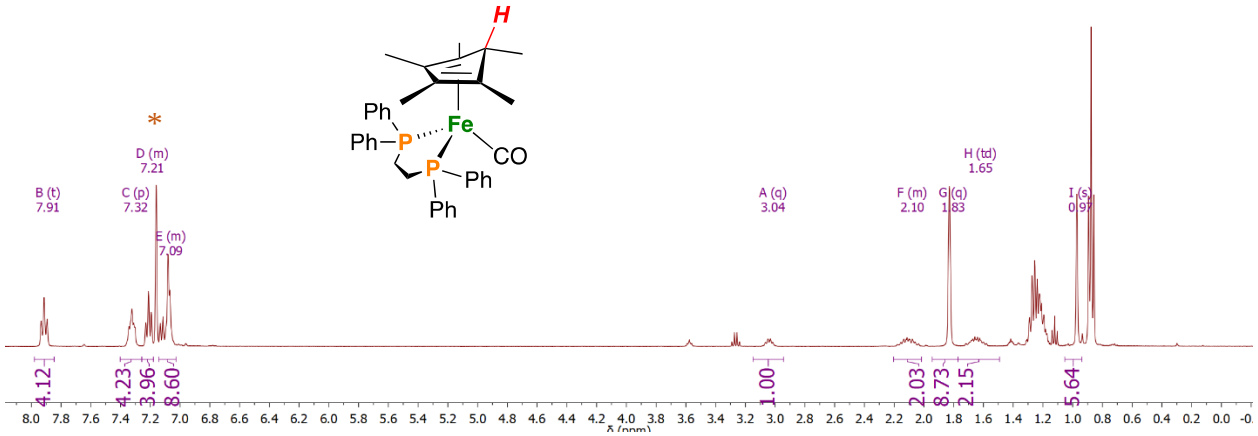

Figure D.8. *exo*-**3**, ^{1}H NMR, C_6D_6, 400 MHz, 298 K (* = C_6D_6)

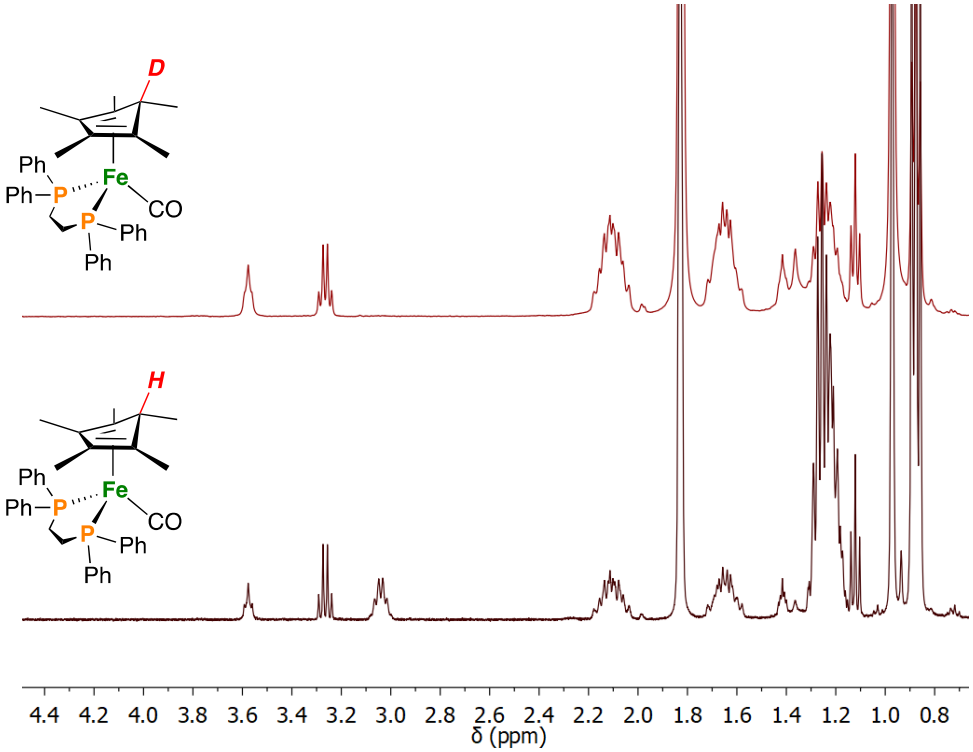

Figure D.9. *exo*-3-H/D stacked plot, ^{1}H NMR, C_6D_6, 400 MHz, 298 K showing disappearance of a signal at δ_H = 2.65.

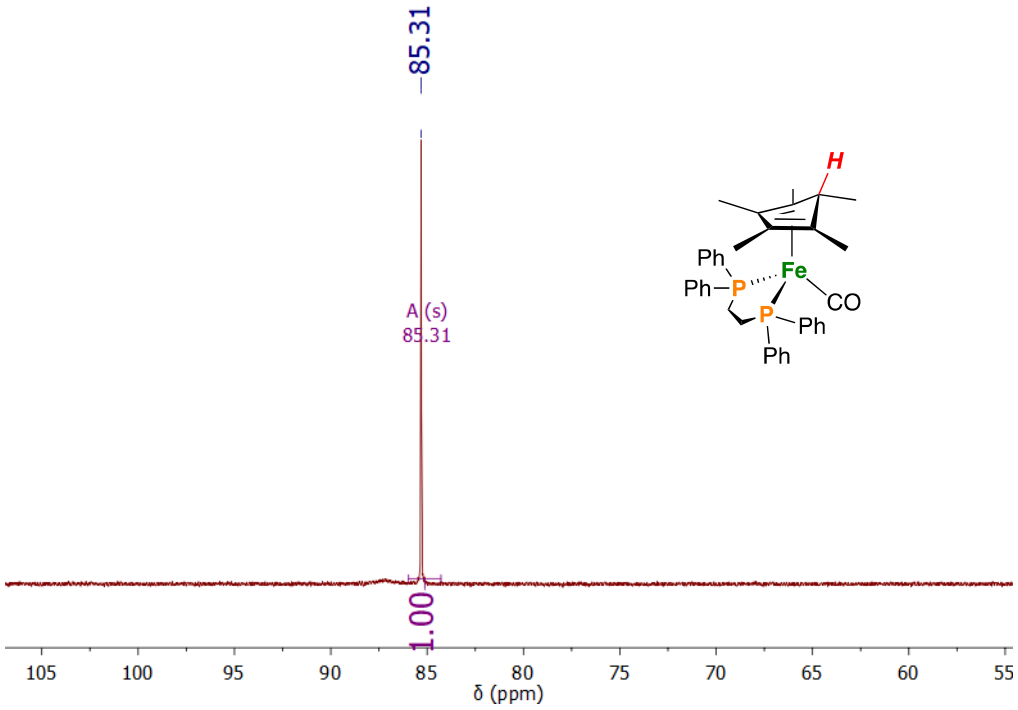

Figure D.10. *exo*-**3**, $^{31}P\{^{1}H\}$ NMR, C_6D_6, 162 MHz, 298 K

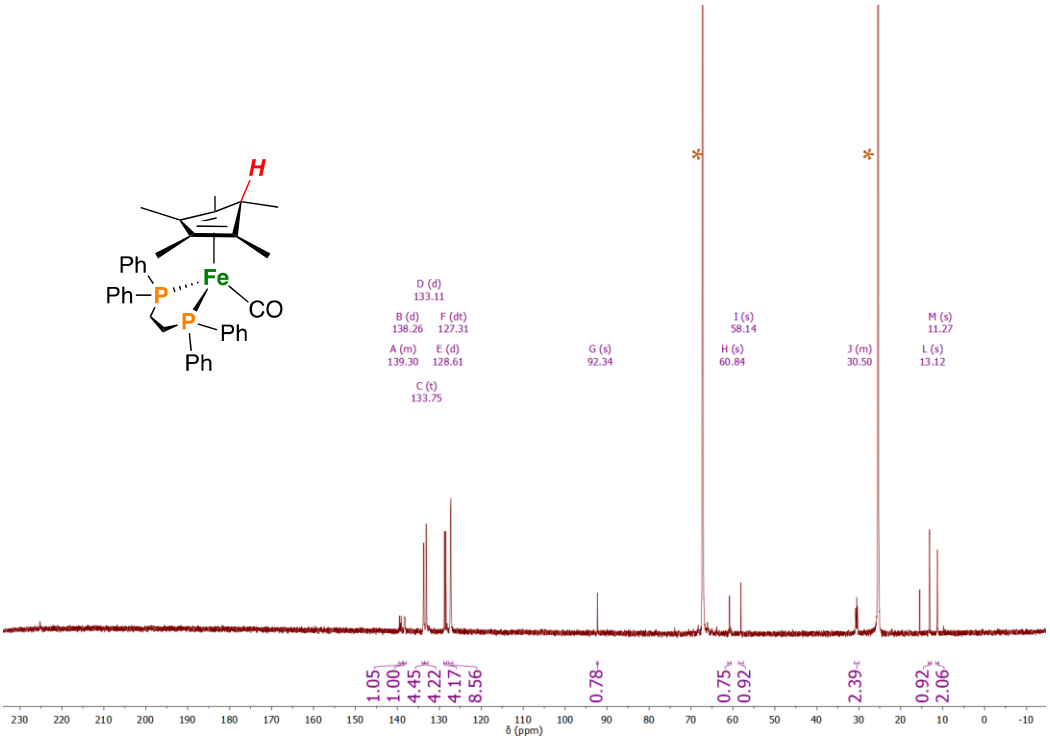

Figure D.11. *exo*-**3**, $^{13}C\{^{1}H\}$ NMR, THF-d_8, 100 MHz, 298 K (* = THF-d_8)

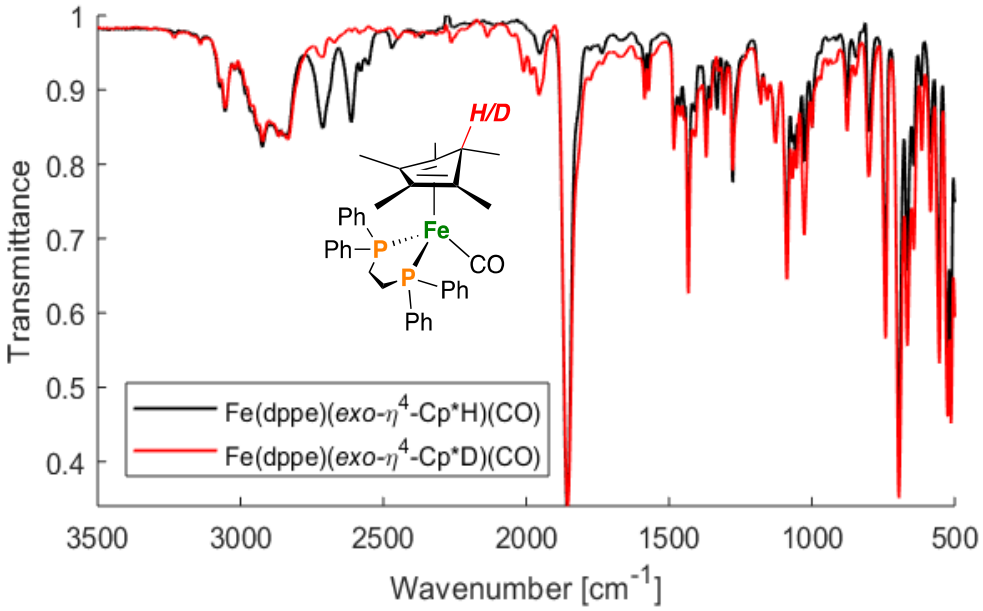

Figure D.13. *exo*-**3**-H/D, FT-IR ATR, thin film, 298 K (*exo*-3-H: 2711 and 2612 cm^{-1} and *exo*-3-D: 2009 and 1955 cm^{-1}).

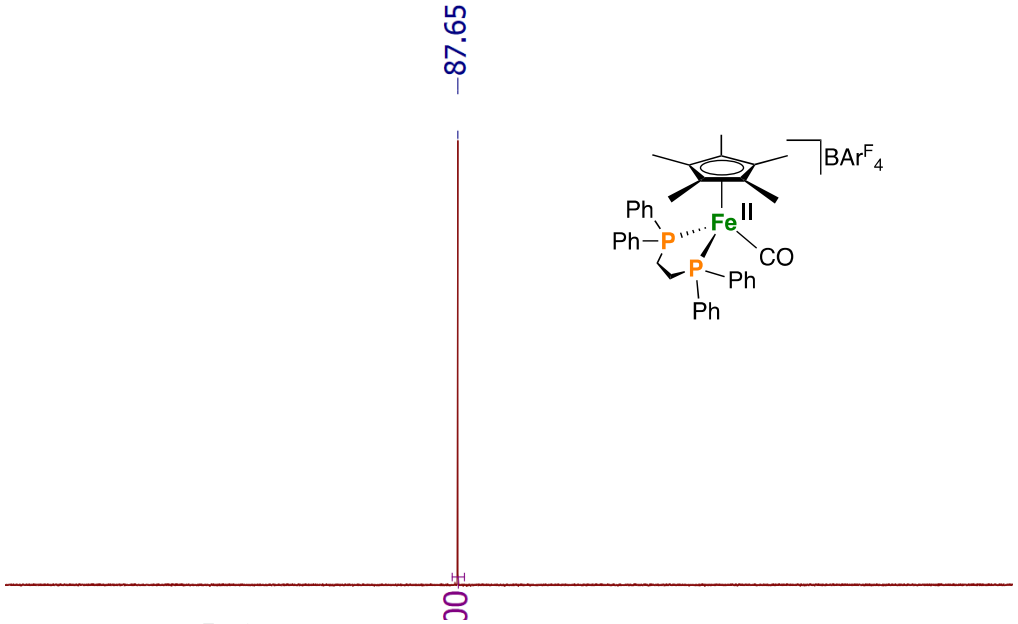

Figure D.12. [5]BAr^F_4, ^1H NMR, THF-d_8, 400 MHz, 298 K (this compound is formed from H_2 evolution from 0.5 equiv. *exo*-/*endo*-$[3]^+$ - signals match those previously provided in ref. **1**). (* = THF-d_8)

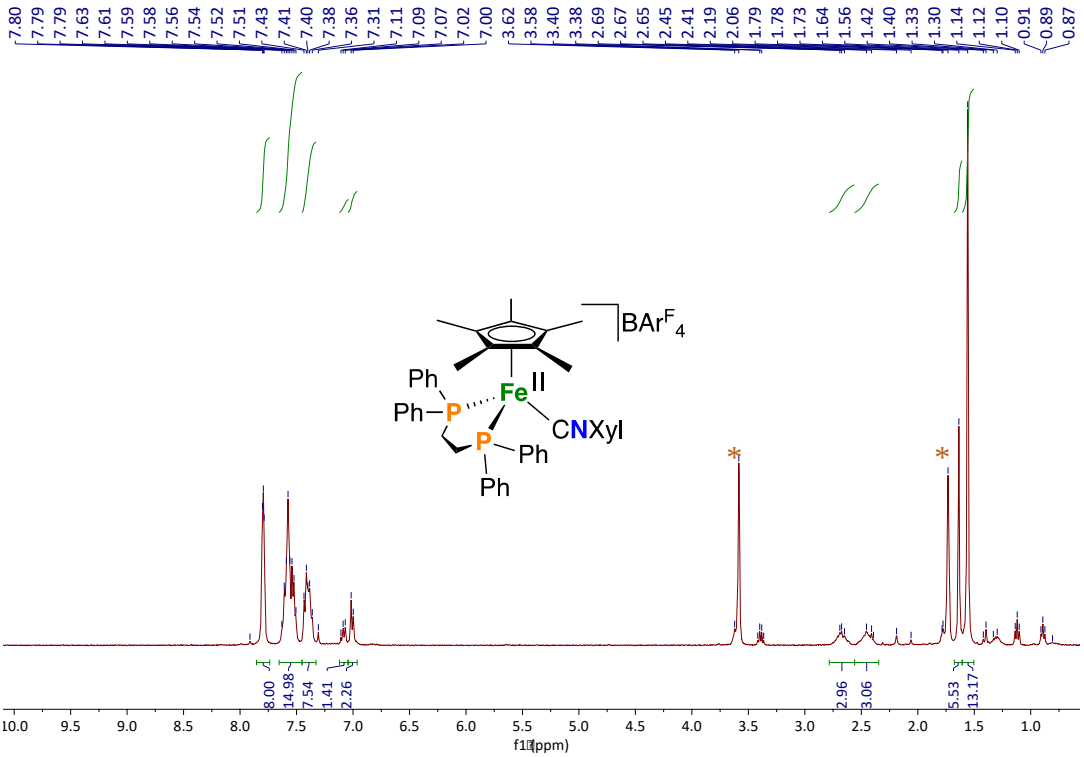

Figure D.14. [6]BAr$^F_4$, ^{1}H NMR, THF-d$_8$, 400 MHz, 298 K (* = THF-d$_8$)

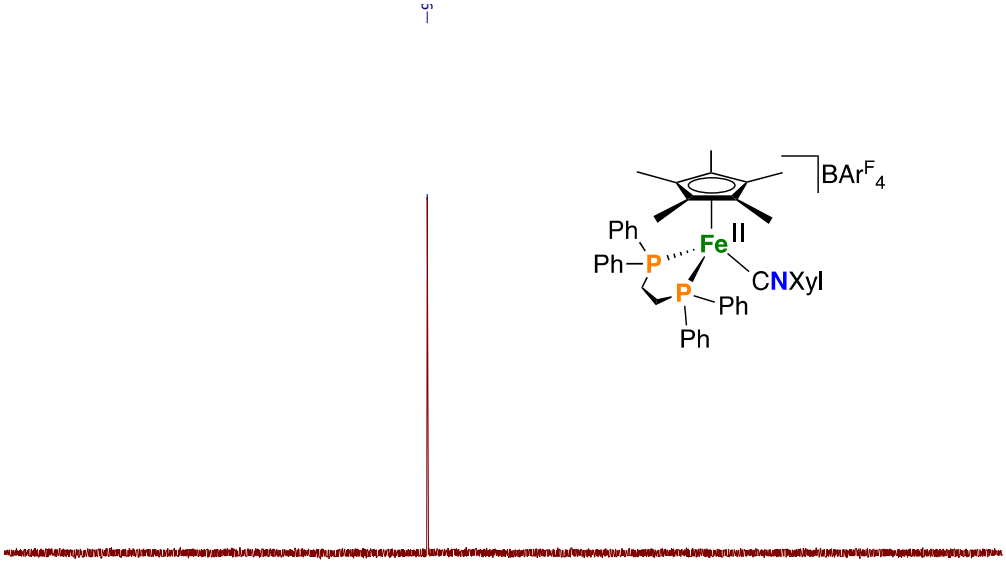

Figure D.15. [6]BAr$^F_4$, ^{31}P{^{1}H} NMR, THF-d$_8$, 162 MHz, 298 K

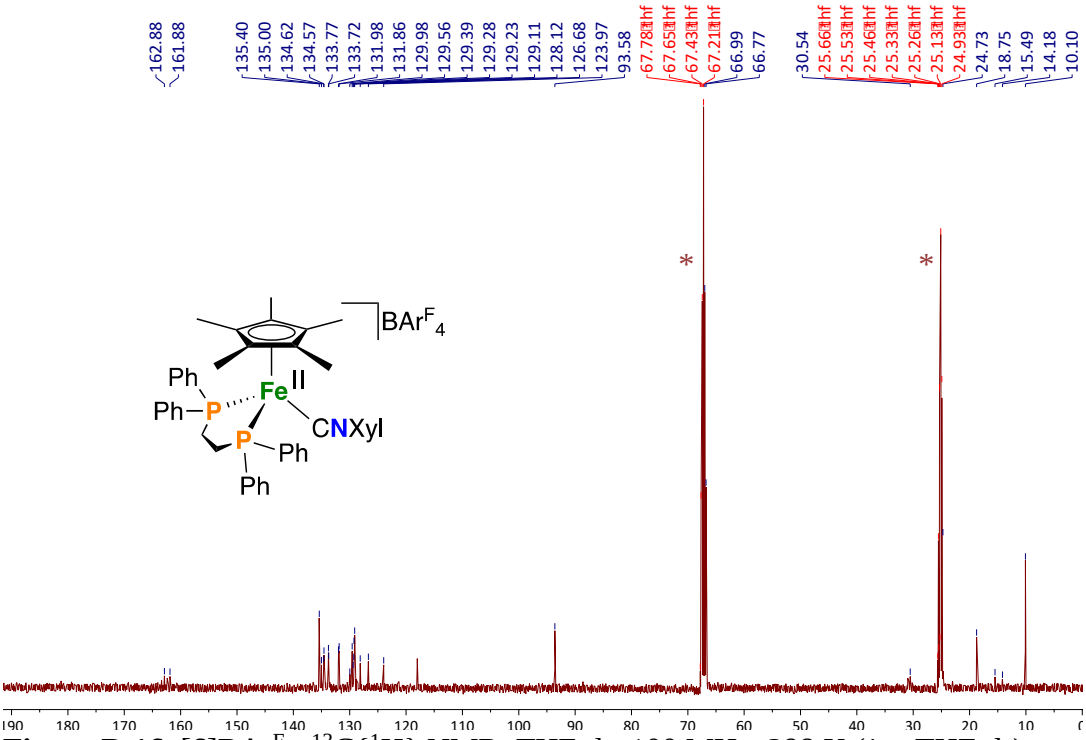

Figure D.16. [**6**]BAr$^F_4$, $^{13}C\{^1H\}$ NMR, THF-d_8, 100 MHz, 298 K (* = THF-d_8)

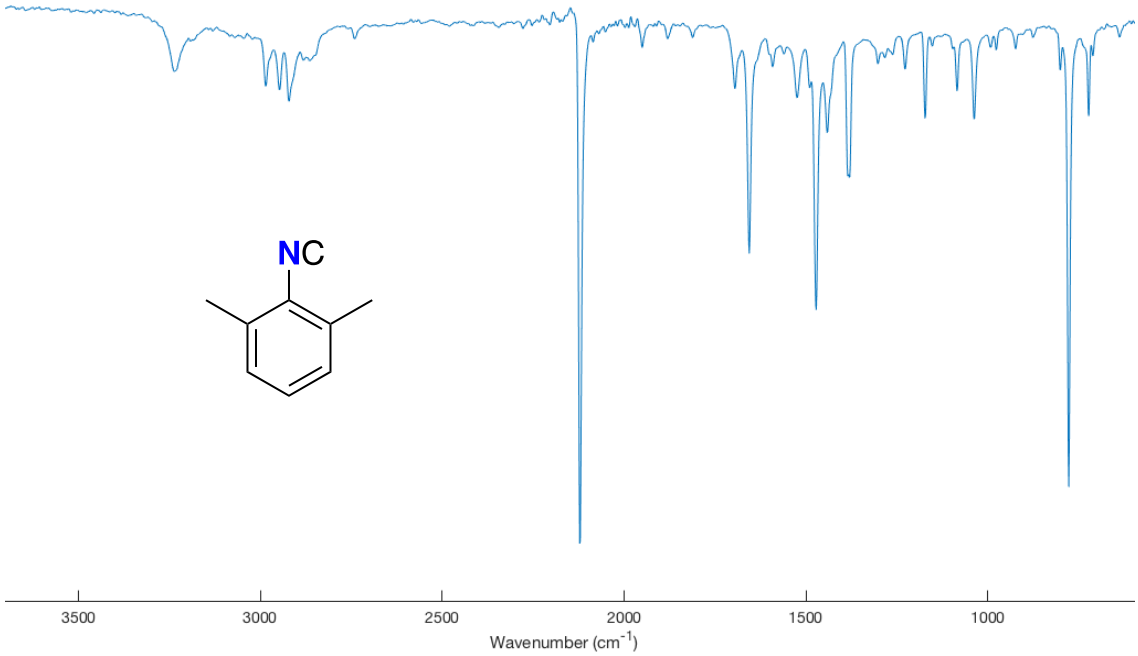

Figure D.17 [**6**]BAr^F_4, FT-IR ATR, thin film, 298 K (ν_{CN} = 2050 cm^{-1})

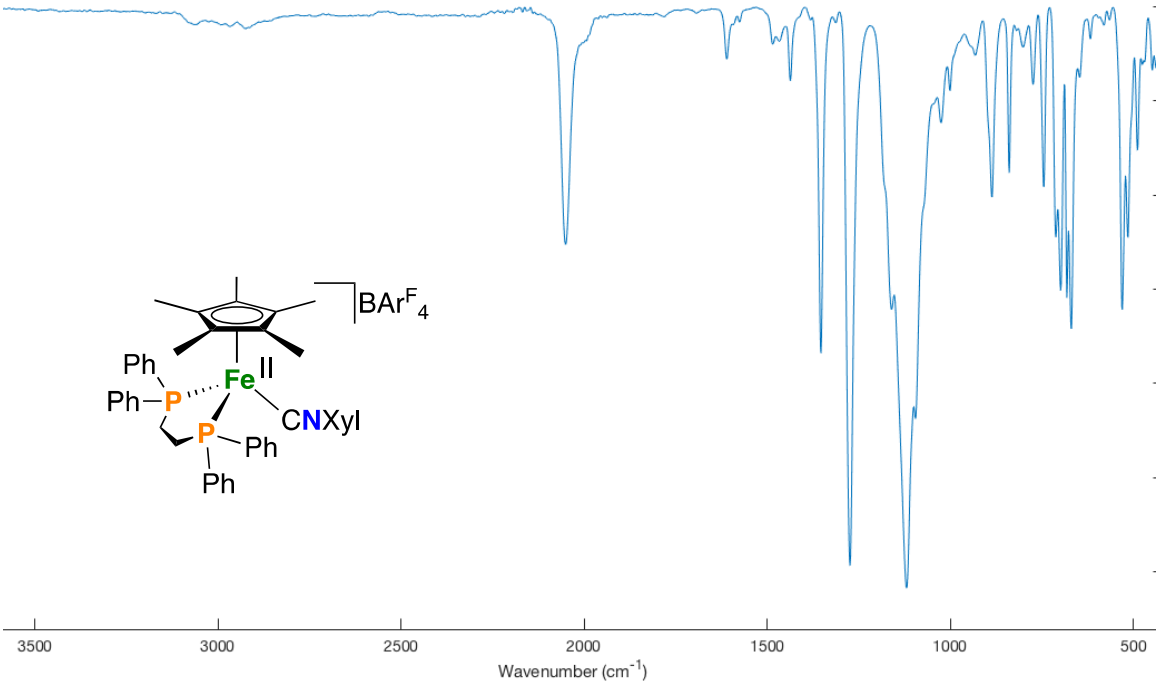

Figure D.18. CNXyl, FT-IR ATR, thin film, 298 K (ν_{CN} = 2151 cm^{-1})

H_2 Evolution by [1]BAr^F_4 in THF:

To a J-Young NMR tube containing THF-d_8 (606 mg) was added [**1**]BAr^F_4 (4.9 mg, 0.003 mmol). The reaction mixture was monitored by NMR spectroscopy, showing no observable reaction. However, heating the reaction mixture at 80 °C for 24 h results in minimal (<5 % deterioration) to give $[Fe^{II}(\eta^5\text{-Cp*})(dppe)(N_2)]BAr^F_4$ ([**7**]BAr^F_4) and H_2. [**2**]BAr^F_4 is cleanly accessible on preparative scale by protonation of $Fe^{II}(\eta^5\text{-Cp*})(dppe)CH_3$ using $[H(OEt)_2]BAr^F_4$ (*as outlined above*).

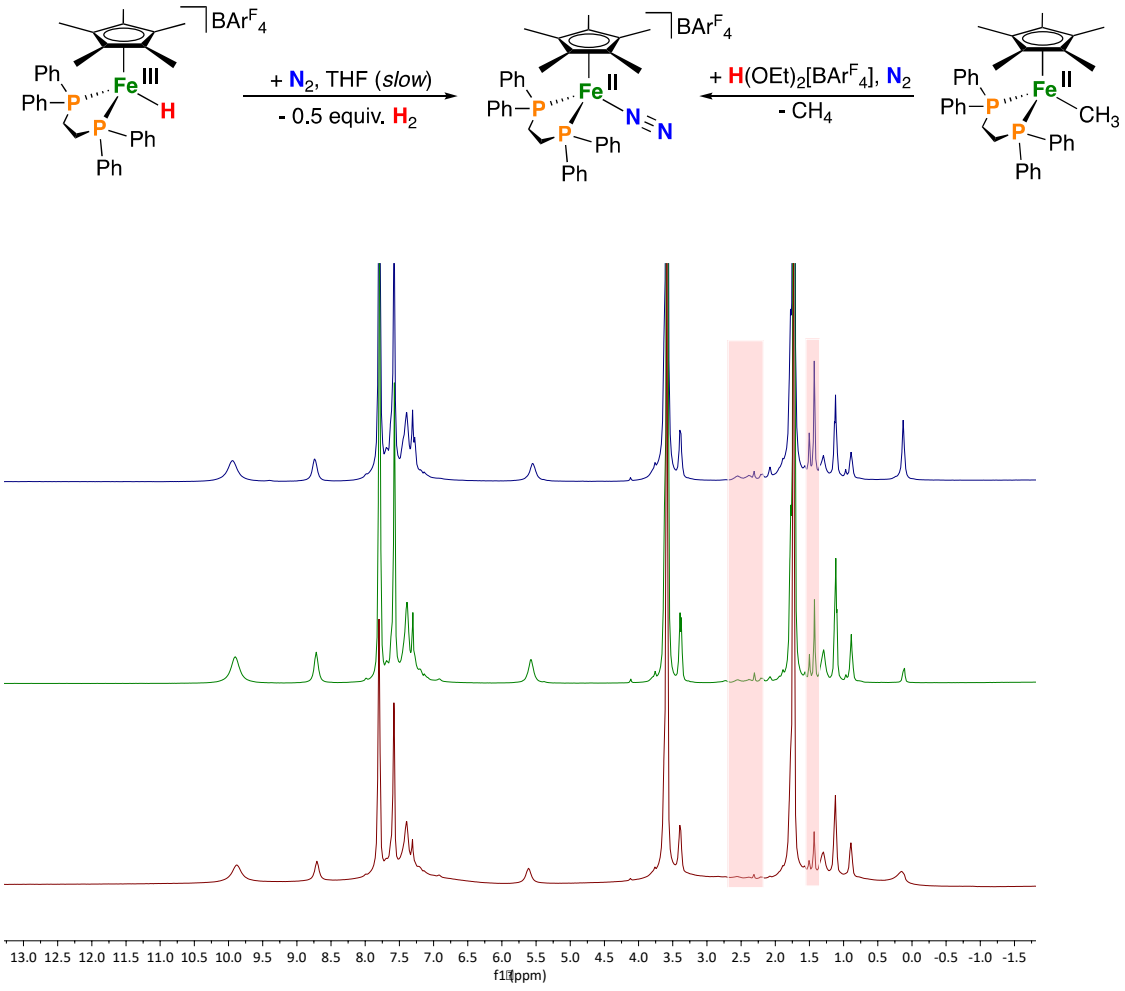

Figure D.19. Heating [**1**]BAr^F_4 at 80 °C, ^{1}H NMR, THF-d_8, 400 MHz, 298 K (Red; 1 h, green; 5 h, blue; 23 h); dppe(CH_2) and Cp*(CH_3) groups for [**7**]BAr^F_4 highlighted in pink.

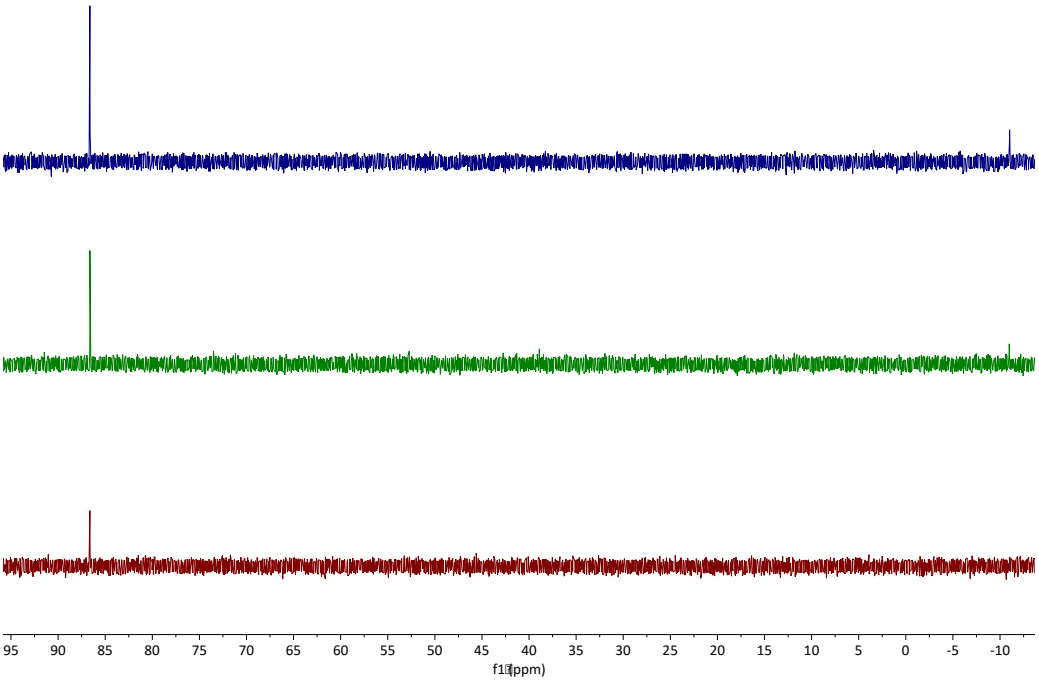

Figure D.20. Heating [**1**]BAr^F_4 at 80 °C, $^{31}P\{^1H\}$ NMR, THF-d_8, 162 MHz, 298 K (Red; 1 h, green; 5 h, blue; 23 h) (free ligand at □ = -12.8 ppm).

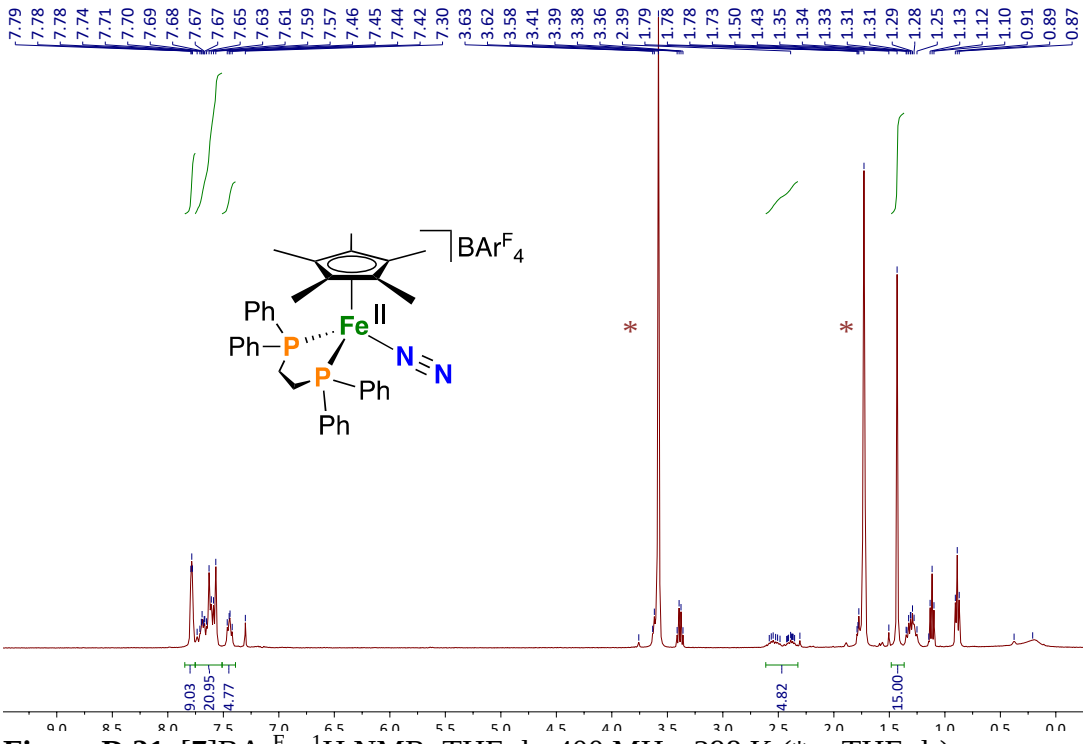

Figure D.21. [**7**]BAr^F_4, ^1H NMR, THF-d_8, 400 MHz, 298 K (* = THF-d_8)

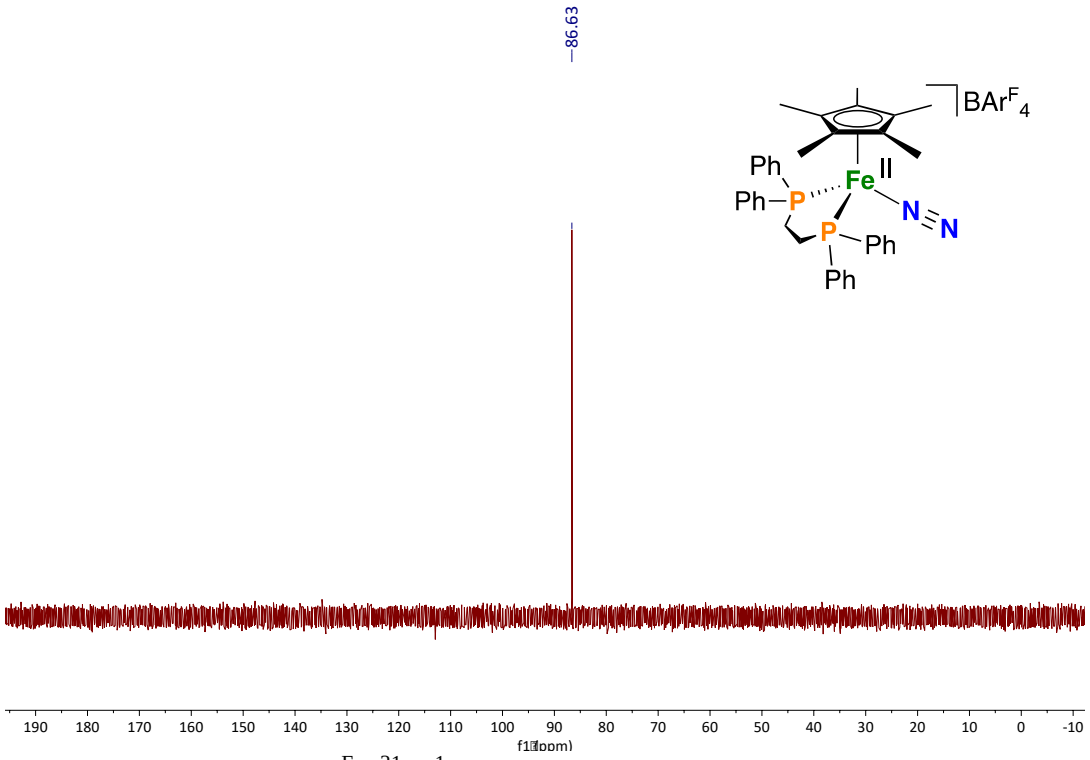

Figure D.22. [7]BAr$^F_4$, $^{31}P\{^1H\}$ NMR, THF-d_8, 162 MHz, 298 K

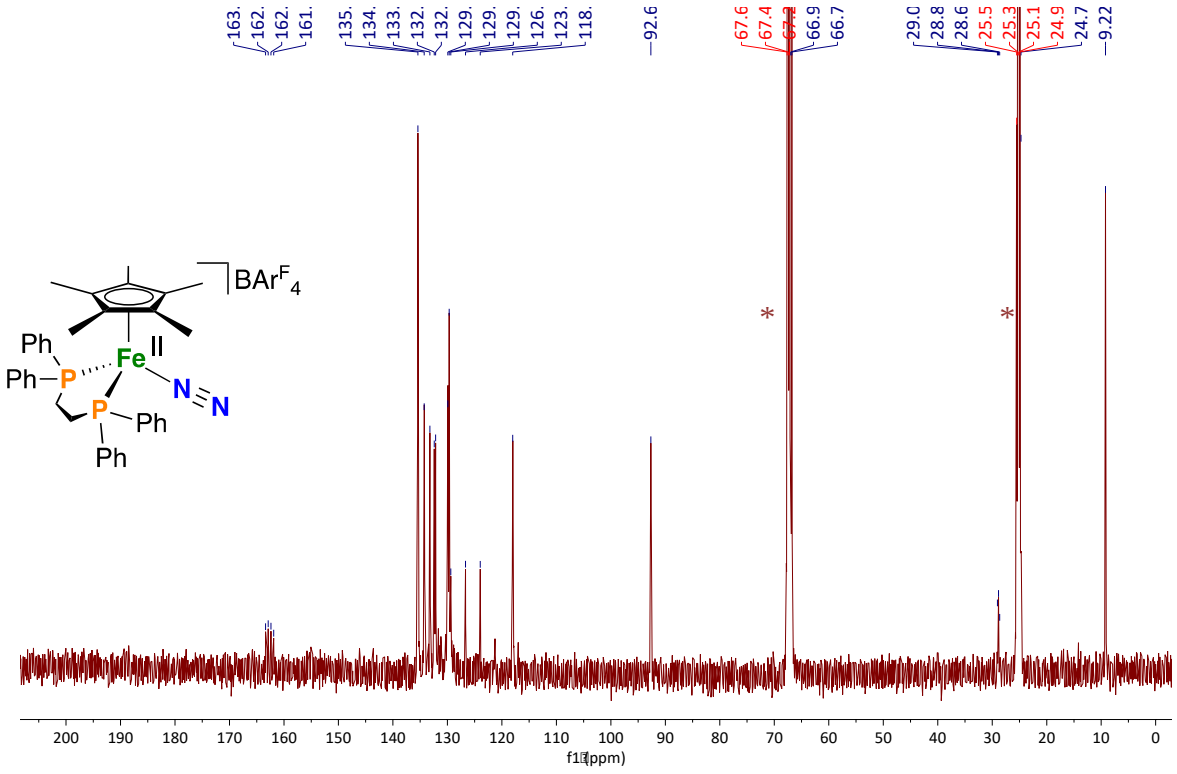

Figure D.23. [**7**]BAr$^F_4$, $^{13}C\{^1H\}$ NMR, THF-d_8, 100 MHz, 298 K (* = THF-d_8)

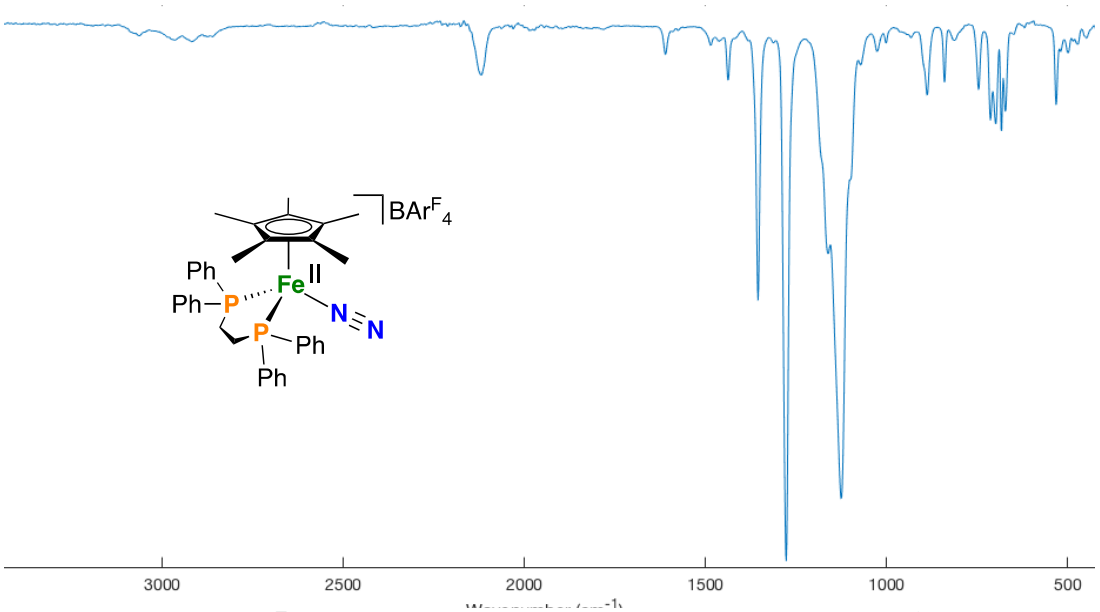

Figure D.24. [**7**]BAr$^F_4$, FT-IR ATR, thin film, 298 K ($\tilde{\nu}_{NN}$ = 2119 cm^{-1})

H_2 evolution by [1]BAr^F_4 in MeCN:

To a J-Young NMR tube containing MeCN-d_3 (646 mg) was added [**1**]BAr^F_4 (5.0 mg, 0.003 mmol). The reaction mixture was monitored by NMR spectroscopy, showing consumption of [**1**]BAr^F_4 to cleanly give [$Fe^{II}(\eta^5$-Cp*)(dppe)(NCMe)]BAr^F_4 ([**8**]BAr^F_4) and H_2.5

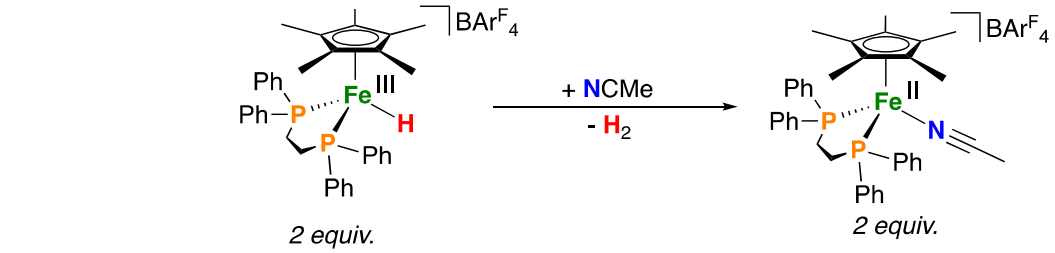

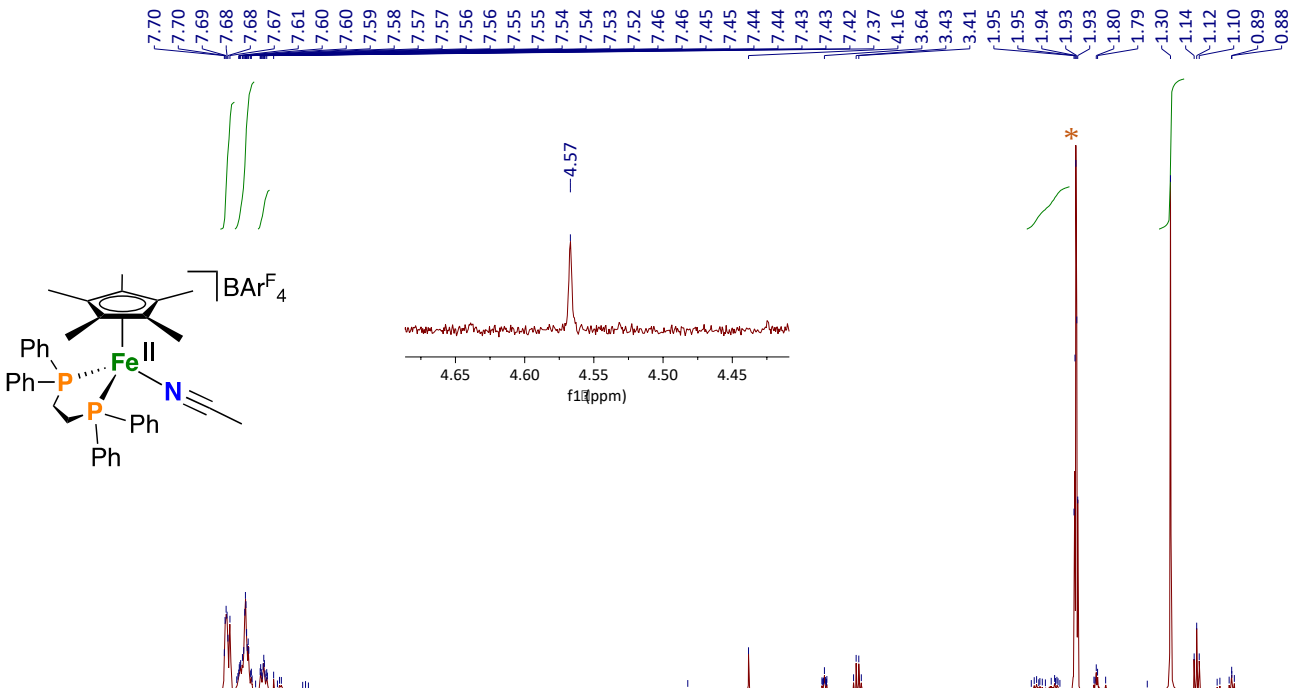

Figure D.25. [**8**]BAr^F_4, ^{1}H NMR, ACN-d_3, 400 MHz, 298 K (inset shows signal for generated H_2 at δ = 4.57 ppm). (* = ACD-d_3)

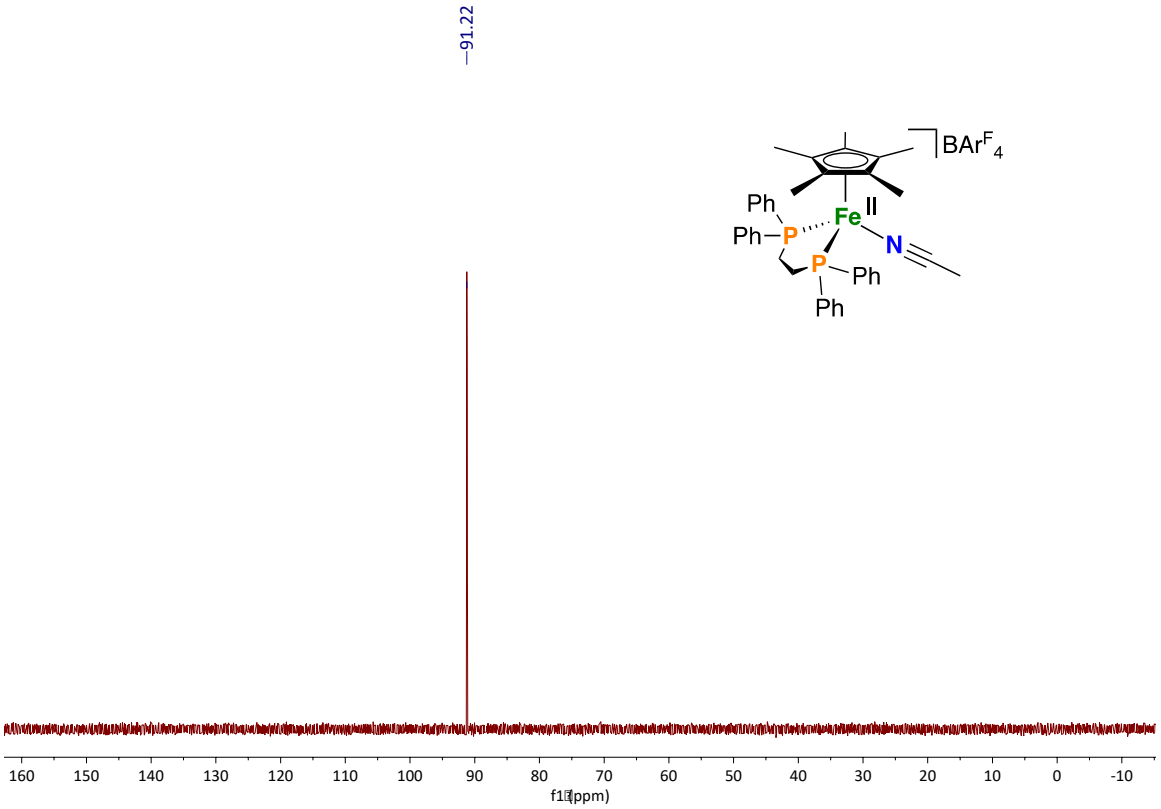

Figure D.26. [**8**]BAr$^F_4$, $^{31}P\{^1H\}$ NMR, ACN-d_3, 162 MHz, 298 K

3.3 Hydricity measurement: Hydride transfer to CO_2:

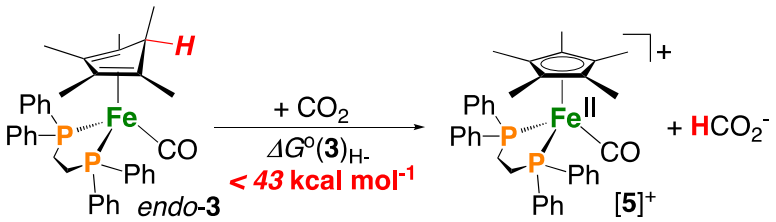

To an NMR J-Young tube containing a solution of *endo*-**3** (3.9 mg, 0.006 mmol, 1 equiv.) in d_3-acetonitrile (*ca.* 0.6 mL) was added CO_2. The reaction mixture was monitored by NMR spectroscopy, showing consumption of *endo*-**3** to give $[\mathbf{5}]^+$ and HCO_2^-.

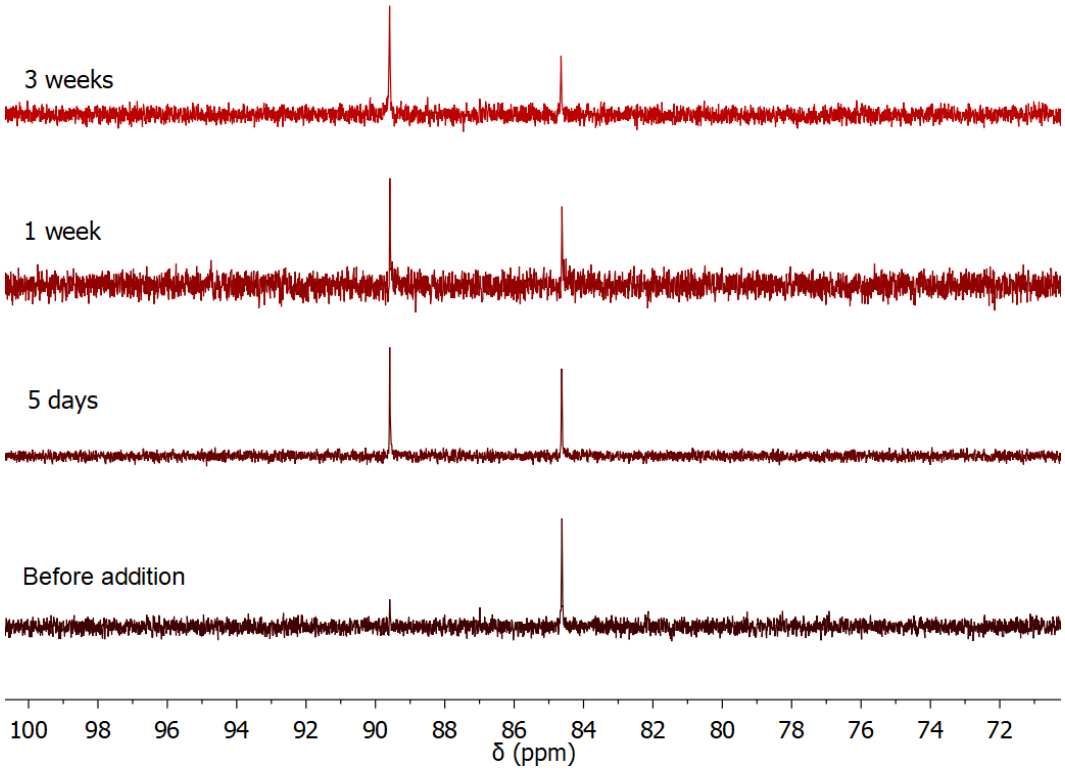

Figure D.27. $^{31}P\{^{1}H\}$ NMR, C_6D_6, 162 MHz, 298 K for the treatment of *endo*-**3** with CO_2 before addition, 5 days, 1 week, and 3 weeks post addition showing consumption of *endo*-**3** (δ_P = 84.5 ppm) and formation of [**5**]$^+$ (δ_P = 89.8 ppm)

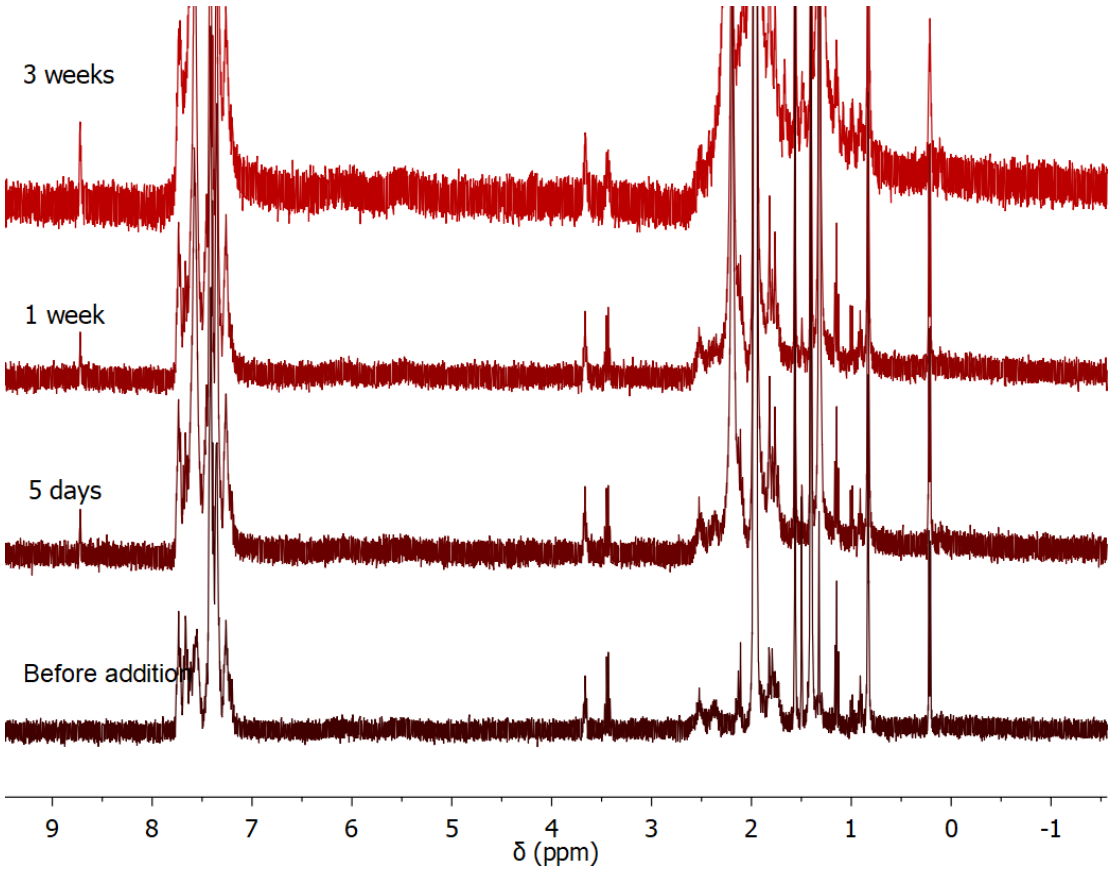

Figure D.28. ^{1}H NMR, C_6D_6, 162 MHz, 298 K for the treatment of *endo*-**3** with CO_2 before addition, 5 days, 1 week, and 3 weeks post addition showing formation of HCO_2^- at δ_H = 8.6 ppm)

3.4 Azobenzene reduction:

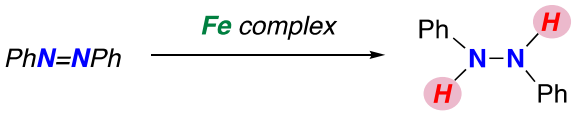

Using [**1**]$^+$: To a J-Young NMR tube containing a solution of [**1**]$^+$ (14.5 mg, 1 mmol) in d_8-THF (*ca.* 500 µL) was added PhNNPh (36 mg, 20 mmol). The reaction mixture was monitored by NMR spectroscopy, showing no reaction.

Azobenzene reduction by addition of CO: On top of a 0.5 mL of a frozen diethyl ether solution containing 2 µmol azobenzene and 0.1 µmol of *endo/exo*-[**3**]$^+$ was layered 0.25 mL of a 0.4 mM FcBArF solution in diethyl ether. The reaction mixture was stirred at −78 °C for 30 minutes followed by 10 minutes at room temperature. The solvent was removed *in vacuo* and the residue was dissolved in 0.6 mL C_6D_6 with trimethylbenzene as internal standard and analyzed by NMR.

General procedure for azobenzene reduction by oxidation: On top of a 0.5 mL of a frozen diethyl ether solution containing 2 µmol azobenzene and 0.1 µmol of *endo/exo*-[**3**]$^+$ was layered 0.25 mL of a 0.4 mM FcBArF solution in diethyl ether. The reaction mixture was stirred at −78 °C for 30 minutes followed by 10 minutes at room temperature. The solvent was removed *in vacuo* and the residue was dissolved in 0.6 mL C_6D_6 with trimethylbenzene as internal standard and analyzed by NMR.

Table D.1. Summary of azobenzene reduction yields based on transferred H-atom equivalents

Fe complex	**Yield**
[**1**]$^{+}$	no reaction
endo-[**3**]$^{+}$	25 %
exo-[**3**]$^{+}$	78 %

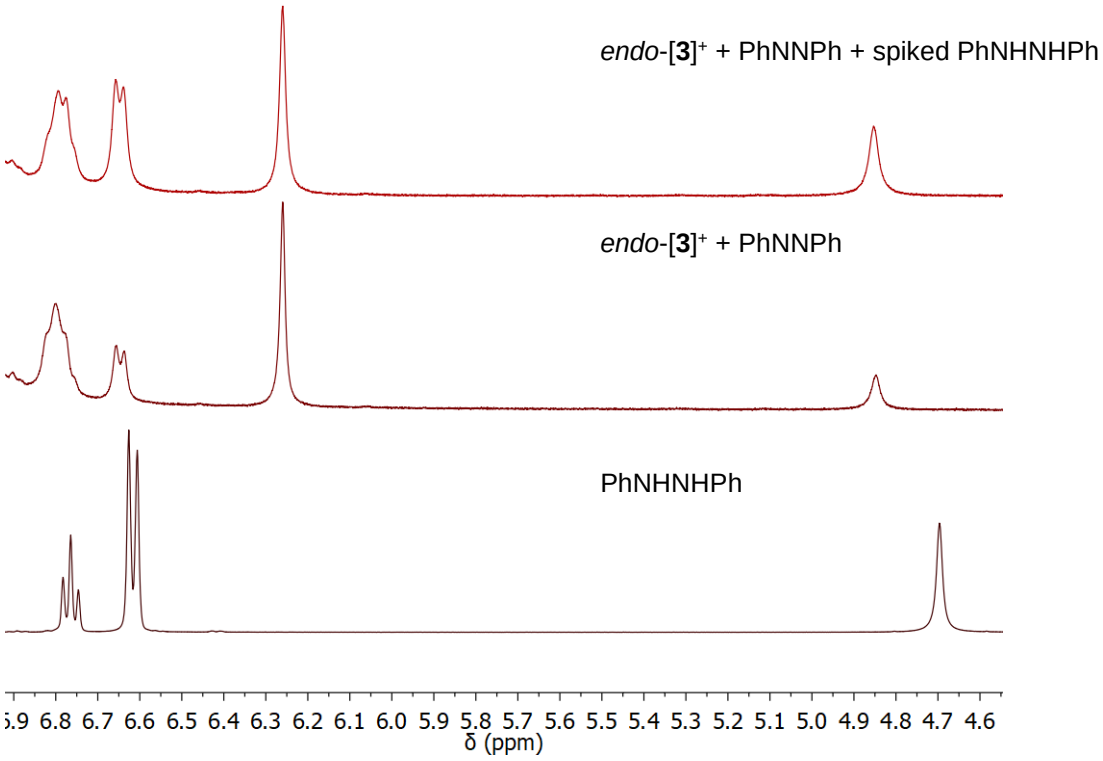

Figure D.29. ^{1}H NMR, C_6D_6, 400 MHz, 298 K showing the aromatic region following treatment of *endo*-[**3**]$^{+}$ with azobenzene to give [**5**]$^{+}$ and PhNHNHPh. **Bottom trace**: PhNNPh; **Middle trace**: oxidation of *endo*-**3** using [Fc]BAr^{F}_{4} to give *endo*-[**3**]$^{+}$ in the presence of azobenzene, giving PhNHNHPh, and **Top trace**, the reaction mixture spiked with authentic PhNHNHPh.

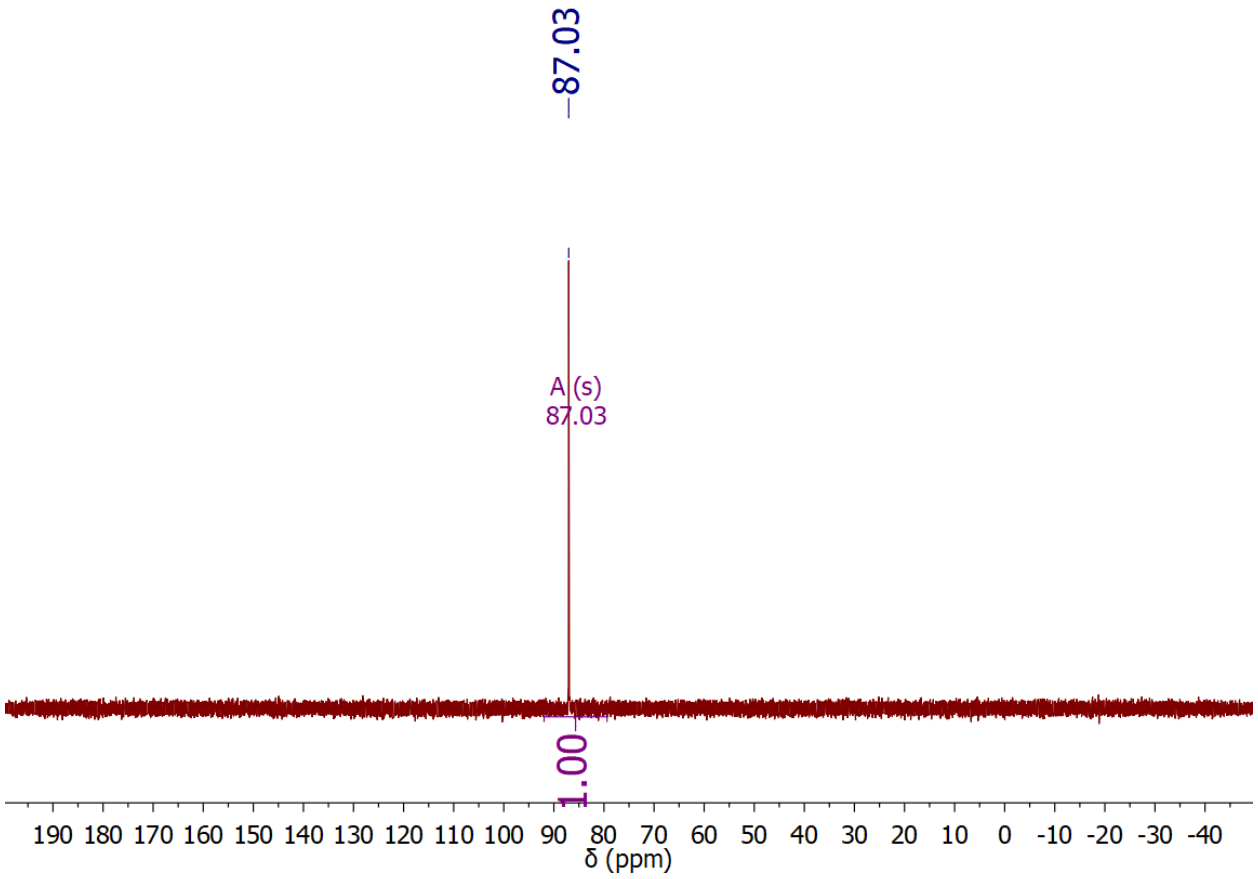

Figure D.30. $^{31}P\{^{1}H\}$ NMR, C_6D_6, 162 MHz, 298 K following treatment of *endo*-[**3**]$^{+}$ with azobenzene to give [**5**]$^{+}$.

3.5 ^{57}Fe Mössbauer Spectroscopy:

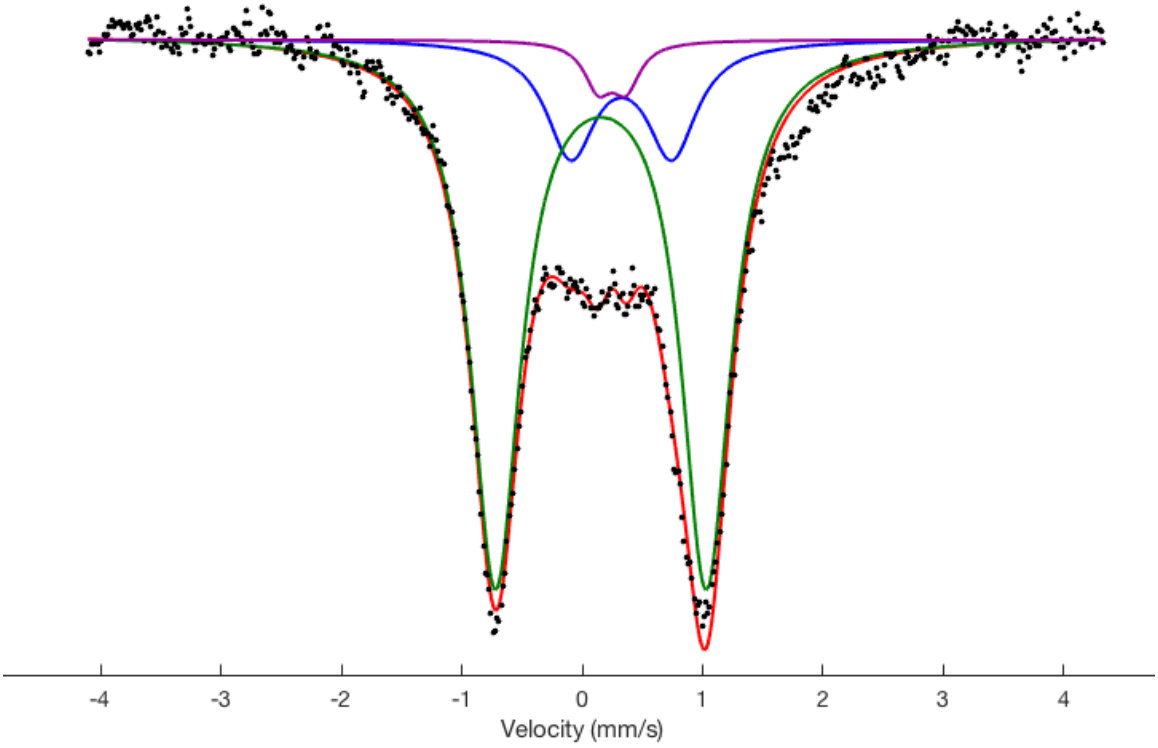

Figure D.31. [**6**]BAr^{F}_{4}, 80 K ^{57}Fe Mössbauer spectrum collected in the presence of a 50 mT magnetic field oriented parallel to the propagation of the γ-beam (frozen solution in Et_2O). δ = 0.16 mm/s, ΔE_Q = 1.75 mm/s for major species. $\Gamma_L = \Gamma_R$ = 0.50 mm/s.

δ= 0.16 and ΔE_Q = 1.75 (81%)

δ = 0.33 and ΔE_Q = 0.84 (17%)

δ = 0.24 and ΔE_Q = 0.23 (3%)

UV-Visible Spectroscopy:

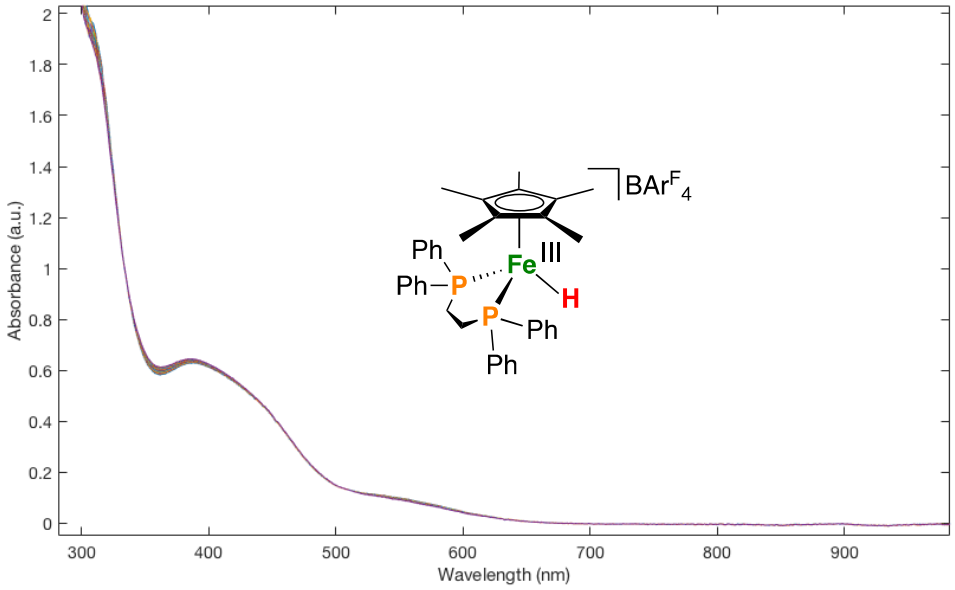

Figure D.32. [**1**]BAr$^F_4$, UV-Visible spectrum showing stability over 24 h, 2-MeTHF, 298 K

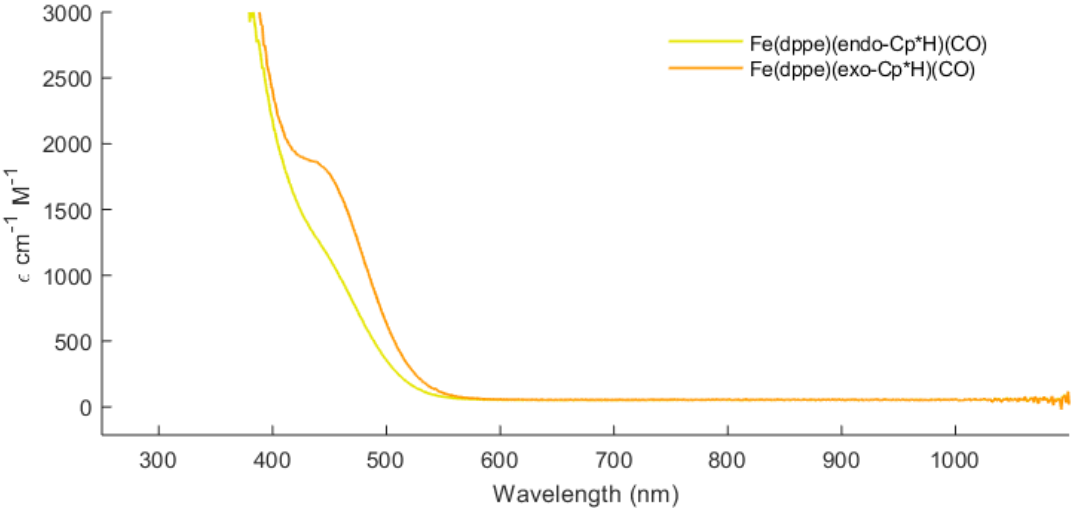

Figure D.33. *endo*-**3** and *exo*-**3**, UV-Visible spectrum (2-MeTHF, 298 K, 1 cm cell). *endo*-**3**:δ = 450 {1130}, *exo*-**3**: δ = 441 {1850}.

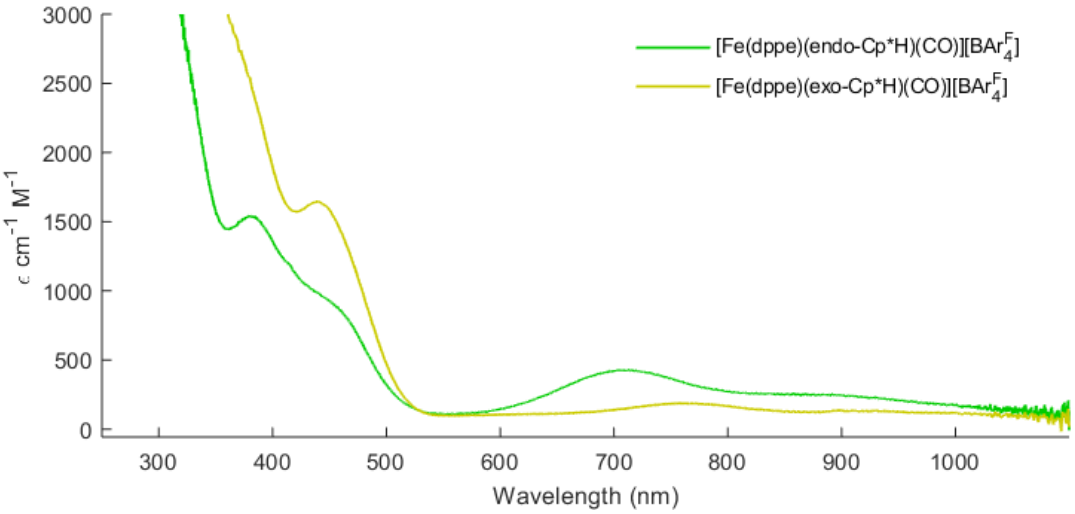

Figure D.34. *endo*-[**3**]$^+$ and *exo*-[**3**]$^+$, UV-Visible spectrum (2-MeTHF, 218 K, 1 cm cell). *endo*-[**3**]$^+$: ε = 891 {252}, 712 {425}, 459 {870}, 383 {1530}, *exo*-[**3**]$^+$: ε = 923 {130}, 767, {180}, 441 {1645}.

EPR Spectroscopy

CW-EPR

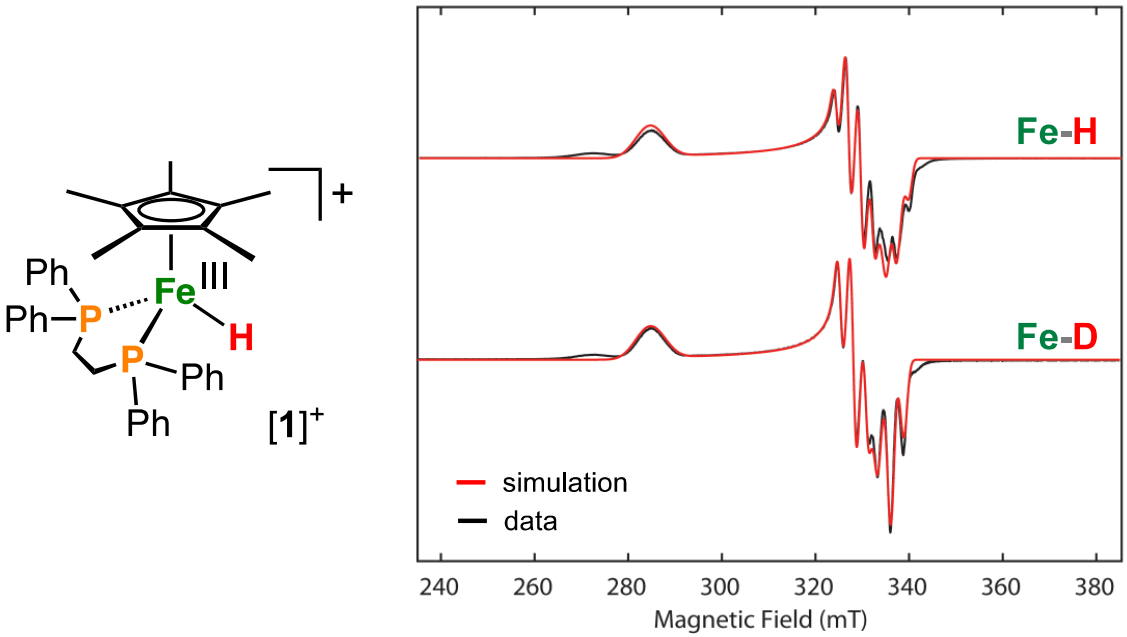

Figure D.35. CW X-band EPR data for **[1]**$^{+}$ (2-MeTHF, 77 K; MW frequency = 9.36 GHz; MW power = 20 μW; modulation amplitude = 10 mT; conversion time = 10.24 ms). Simulation parameters: g = [2.352, 2.041, 1.992]; A(^{31}P$_1$) = [88, 82, 79] MHz; A(^{31}P$_2$) = [82, 71, 76] MHz. For details, see: Drover, M. W.; Schild, D. J.; Oyala, P. H.; Peters, J. C. *Angew. Chem. Int. Ed.* **2019**, *58*, 15504.

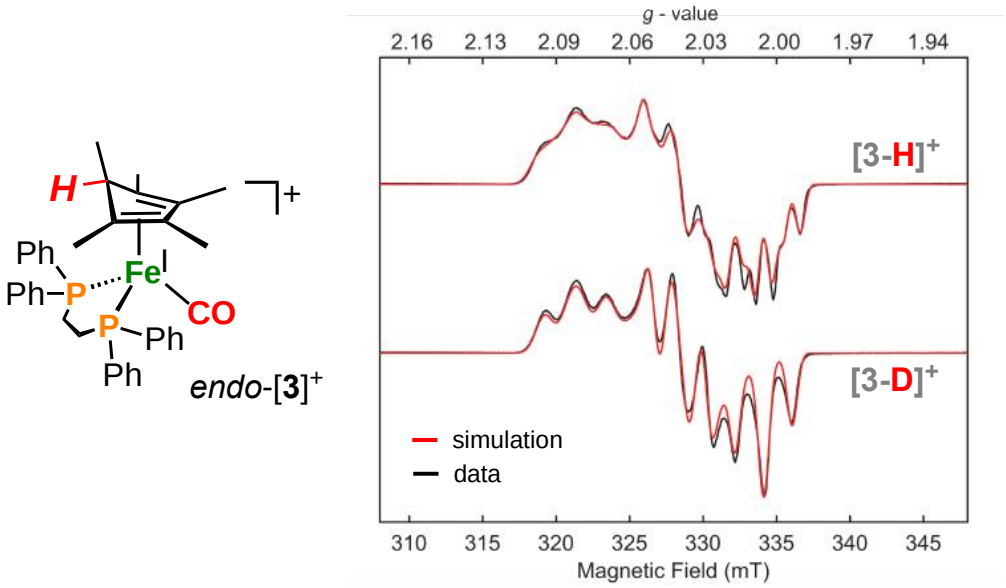

Figure D.36. CW X-band EPR data for *endo*-[**3-H/D**]$^{+}$ (2-MeTHF, 77 K; MW frequency = 9.37 GHz; MW power = 2 mW; modulation amplitude = 10.0 mT; conversion time = 5.12 ms). Parameters: g = [2.085, 2.039, 2.004]; A($^{31}P_1$) = [72, 59, 58] MHz, A($^{31}P_2$) = [49, 42, 51] MHz.

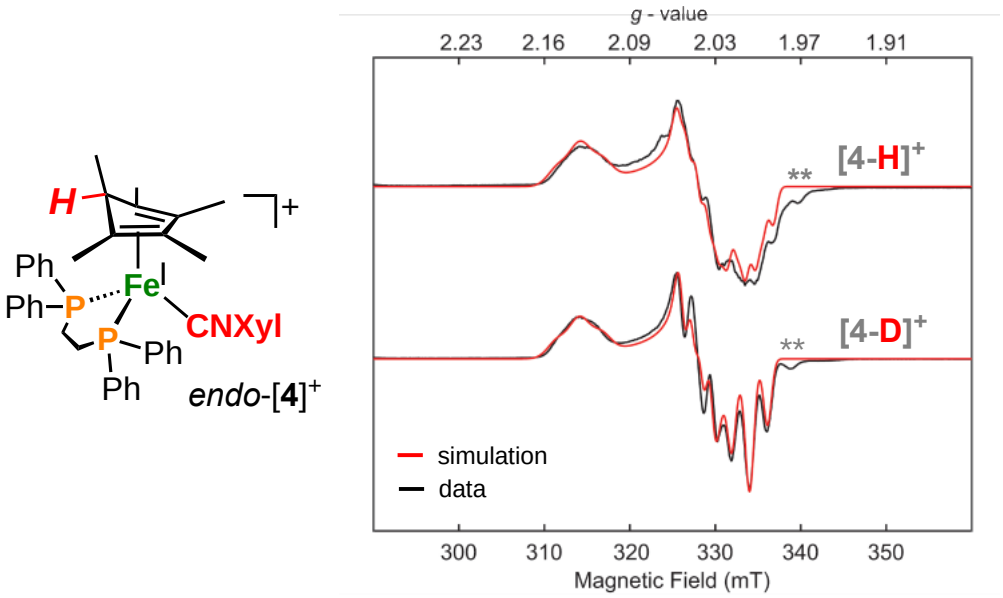

Figure D.37. CW X-band EPR data for *endo*-[**4-H/D**]$^{+}$ (2-MeTHF, 77 K; MW frequency = 9.37 GHz; MW power = 2 mW; modulation amplitude = 10 mT; conversion time = 10.24 ms). Parameters: g = [2.132, 2.042, 2.004]; A($^{31}P_1$) = [75, 35, 54] MHz, A($^{31}P_2$) = [76, 64, 64] MHz. ** = traces of [**1**]$^{+}$.

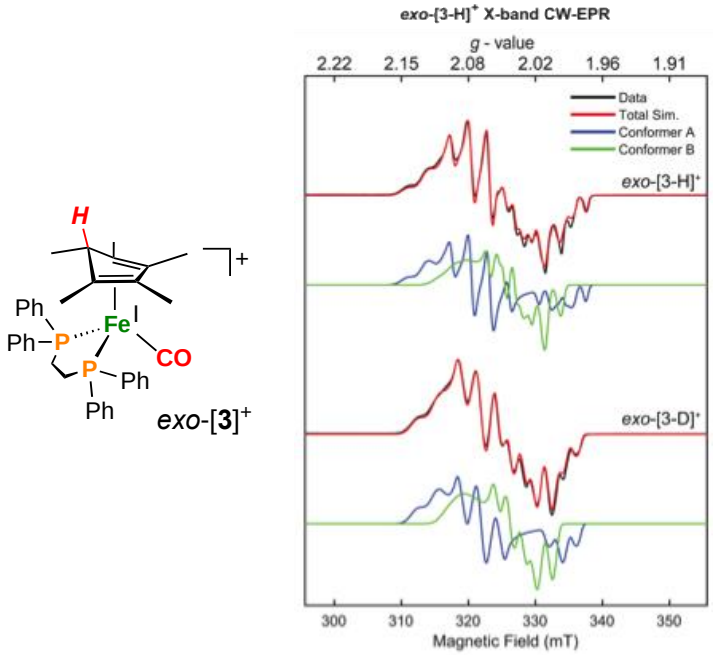

Figure D.38. CW X-band EPR data for *exo*-[**3-H**]$^{+}$ and *exo*-[**3-D**]$^{+}$ (2-MeTHF, 77 K, 9.33 GHz; MW power = 6.44 mW; modulation amplitude = 2.0 mT; conversion time = 20.48 ms). **Parameters:** g = [2.116, 2.073, 1.997]; A($^{31}P_1$) = [96, 88, 47] MHz; A($^{31}P_2$) = [78, 75, 63] MHz; *A*(^{1}H) = ± [85, 84, 83] MHz, HStrain = [70, 22, 22] MHz for conformer **A** (0.6 weight) and g = [2.093, 2.045, 2.013]; A($^{31}P_1$) = [46, 44, 15] MHz; A($^{31}P_2$) = [70, 64, 64] MHz; *A*(^{1}H) = ± [76, 74, 70] MHz, HStrain = [70, 22, 22] MHz for conformer **B** (0.4 weight).

Figure D.39. EPR sample of $[4\text{-H}]^+$ frozen at 77 K.

3.7.2 X-band Davies ENDOR:

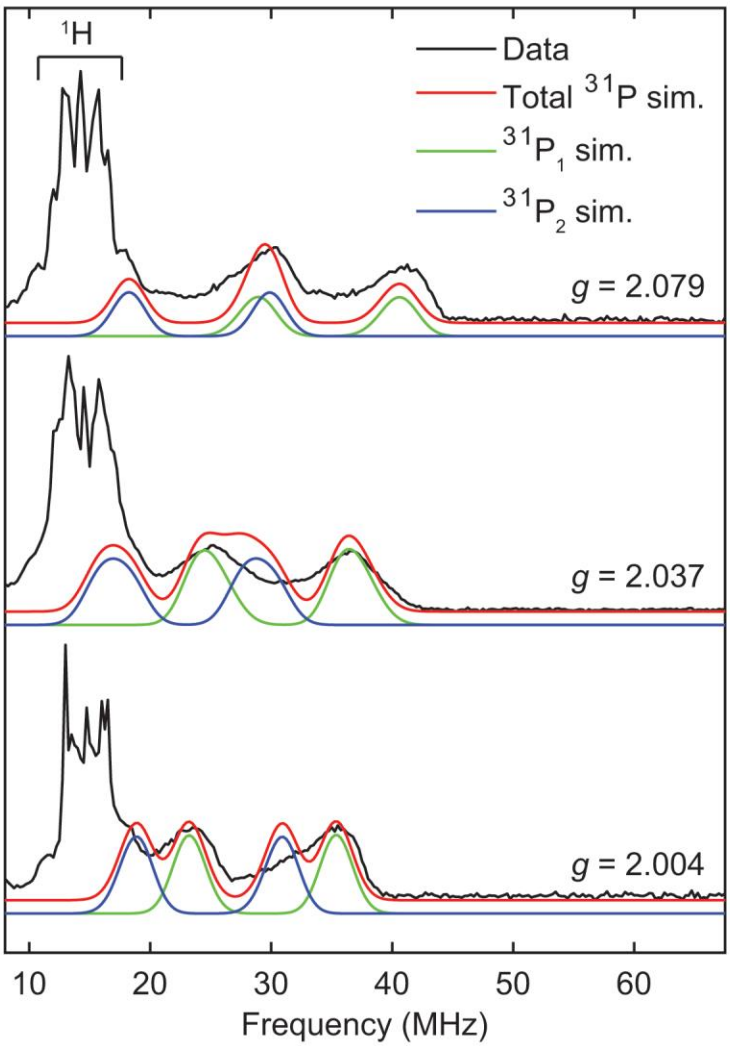

Figure D.40. Field-dependent X-band ^{31}P Davies ENDOR of *endo*-[**3-D**]$^{+}$ (black), with simulations of ^{31}P hyperfine couplings overlaid (total ^{31}P simulation (red), $^{31}P_1$, (green), $^{31}P_2$ (blue)). Simulation parameters: g = [2.085, 2.039, 2.004]; A($^{31}P_1$) = [72, 59, 58] MHz, A($^{31}P_2$) = [49, 42, 51] MHz. Acquisition parameters: temperature = 30 K; MW frequency = 9.717 GHz; MW pulse length ($\pi/2$, π) = 40 ns, 80 ns; tau = 200 ns; RF pulse length = 15 μs; shot repetition time = 4 ms.

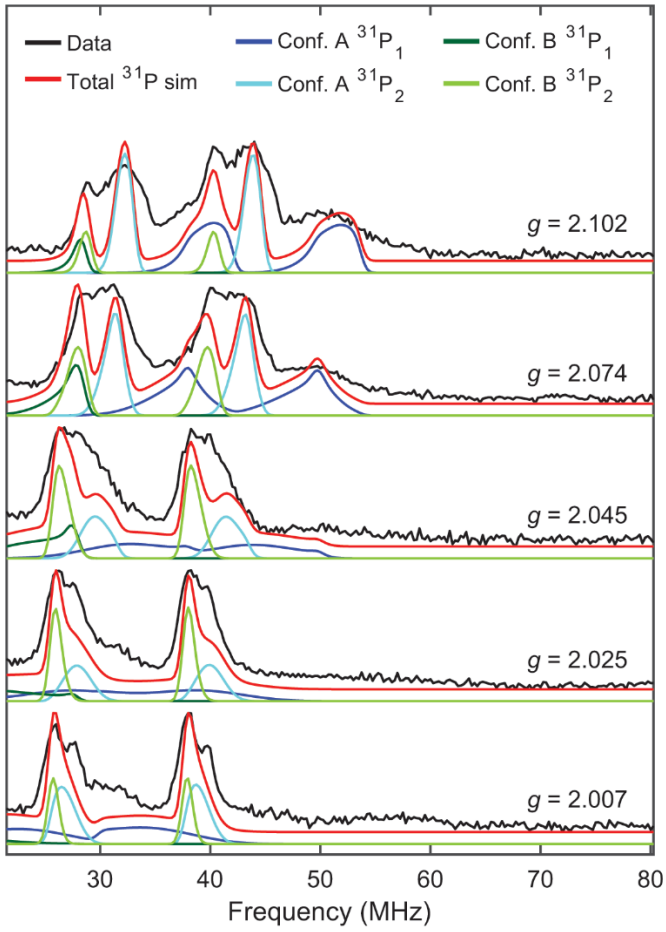

Figure D.41. Field-dependent X-band ^{31}P Davies ENDOR of *exo*-[**3-D**]$^{+}$ (black), with simulations of ^{31}P hyperfine couplings overlaid (total ^{31}P simulation (red), $^{31}P_1$ conformer **A**, (dark blue), $^{31}P_2$ conformer **A** (turquoise), $^{31}P_1$ conformer **B**, (forest green), $^{31}P_2$ conformer **B** (lime green). Simulation parameters for conformer **A**: g = [2.116, 2.073, 1.997]; A($^{31}P_1$) = [96, 88, 47] MHz, A($^{31}P_2$) = [78, 75, 63] MHz. Simulation parameters for conformer **B**: g = [2.093, 2.045, 2.013]; A($^{31}P_1$) = [46, 44, 15] MHz, A($^{31}P_2$) = [70, 64, 64] MHz. Acquisition parameters: temperature = 20 K; MW frequency = 9.734 GHz; MW pulse length (π/2, π) = 40 ns, 80 ns; tau = 200 ns; RF pulse length = 15 μs; shot repetition time = 4 ms.

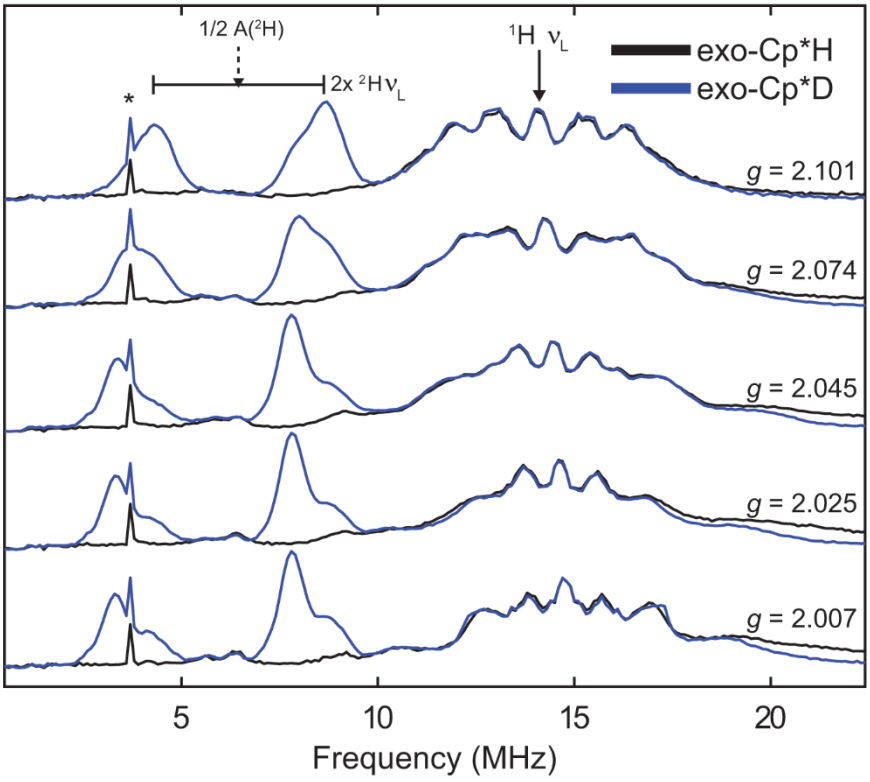

Figure D.42. Field-dependent X-band Davies ENDOR spectra of *exo*-[**3-H**]$^+$ (black) and *exo*-[**3-D**]$^+$ (black). Acquisition parameters: temperature = 20 K; microwave frequency = 9.734 GHz; MW pulse length ($\pi/2$, π) = 40 ns, 80 ns; τ = 200; RF pulse length π_{RF} = 15 µs; T_{RF} = 2 µs; shot repetition time (srt) = 4 ms. Asterisk at ~ 4 MHz indicates an RF artifact.

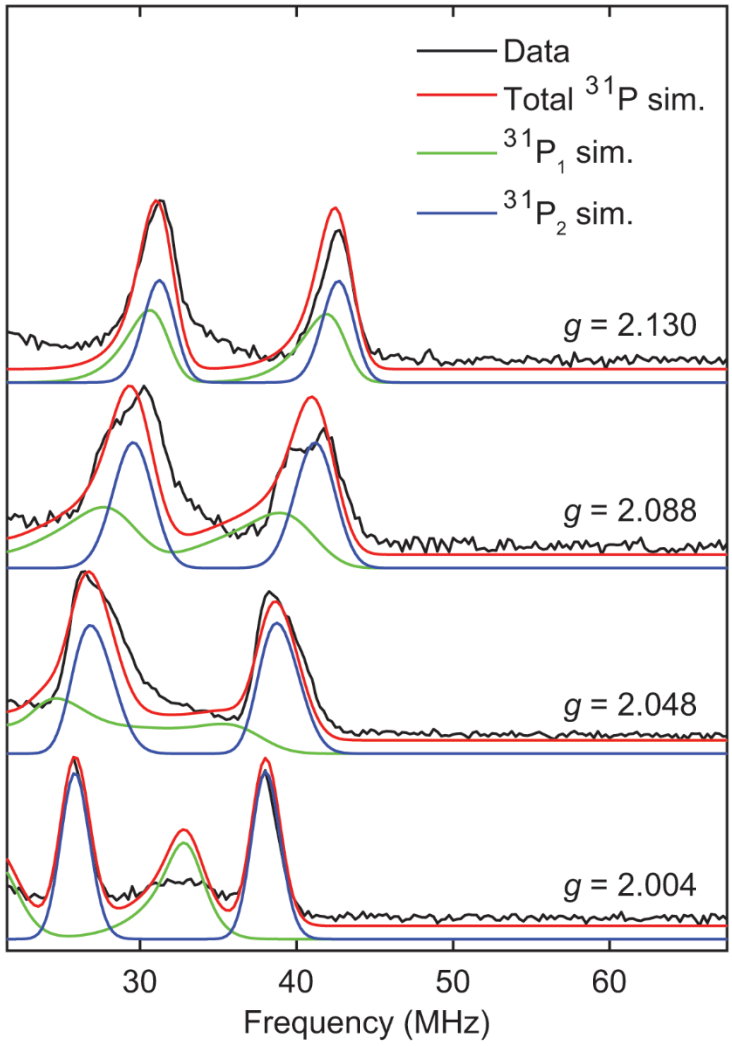

Figure D.43. Field-dependent X-band ^{31}P Davies ENDOR of *endo*-[**4-D**]$^{+}$ (black), with simulations of ^{31}P hyperfine couplings overlaid (total ^{31}P simulation (red), $^{31}P_1$, (green), $^{31}P_2$ (blue)). Simulation parameters: g = [2.132, 2.042, 2.004]; A($^{31}P_1$) = [75, 35, 54] MHz, A($^{31}P_2$) = [76, 64, 64] MHz. Acquisition parameters: temperature = 20 K; MW frequency = 9.716 GHz; MW pulse length ($\pi/2$, π) = 40 ns, 80 ns; tau = 200 ns; RF pulse length = 15 µs; shot repetition time = 4 ms.

X-band HYSCORE

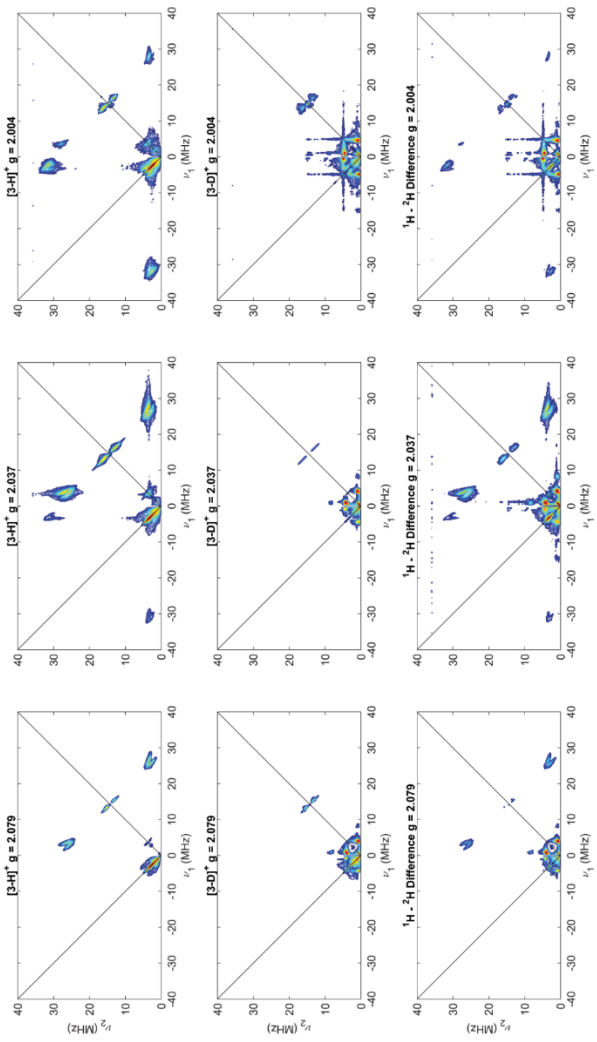

Figure D.44. Field-dependent X-band HYSCORE spectra of *endo*-[**3-H**]$^+$ (top panels) *endo*-[**3-D**]$^+$ (middle panels) and ^{1}H-^{2}H difference HYSCORE spectra (bottom panels). Acquisition parameters: temperature = 30 K; microwave frequency = 9.717 GHz; MW pulse length ($\pi/2$, π) = 8 ns, 16 ns; τ = 140 ns (g = 2.079), 138 ns (g = 2.037); 138 ns (g = 2.004); $t_1 = t_2$ = 100 ns; $\Delta t_1 = \Delta t_2$ = 12 ns; shot repetition time (srt) = 2 ms.

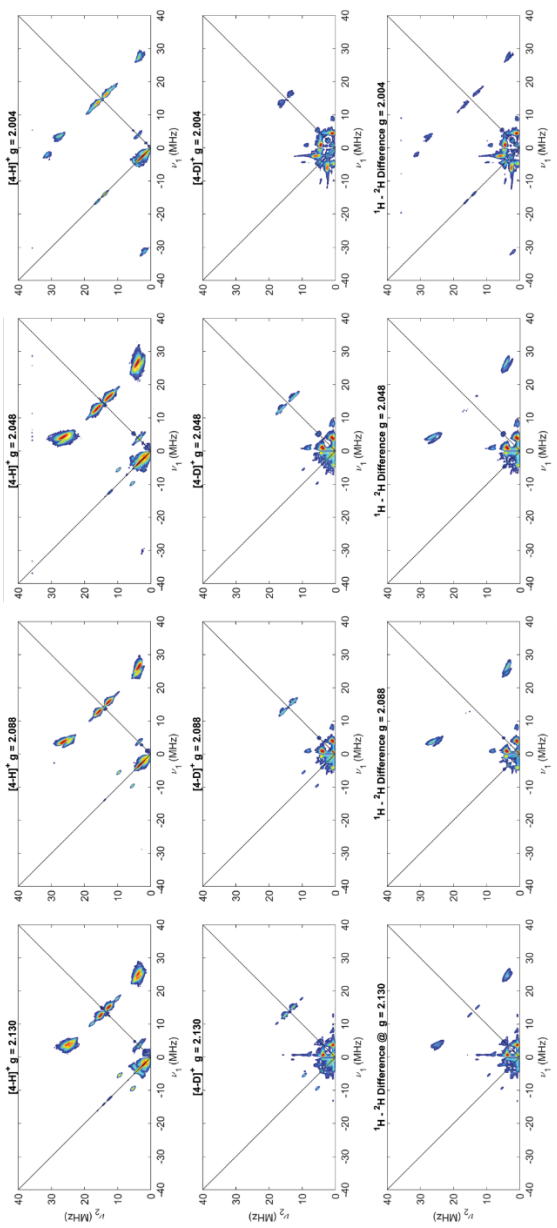

Figure D.45. Field-dependent X-band HYSCORE spectra of *endo*-[**4-H**]$^+$ (top panels) *endo*-[**4-D**]$^+$ (middle panels) and ^{1}H-^{2}H difference HYSCORE spectra (bottom panels). Acquisition parameters: temperature = 30 K; microwave frequency = 9.717 GHz; MW pulse length ($\pi/2$, π) = 8 ns, 16 ns; τ = 144 ns (g = 2.130), 142 ns (g = 2.088); 138 ns (g = 2.048); 138 ns (g = 2.004); $t_1 = t_2$ = 100 ns; $\Delta t_1 = \Delta t_2$ = 12 ns; shot repetition time (srt) = 2 ms.

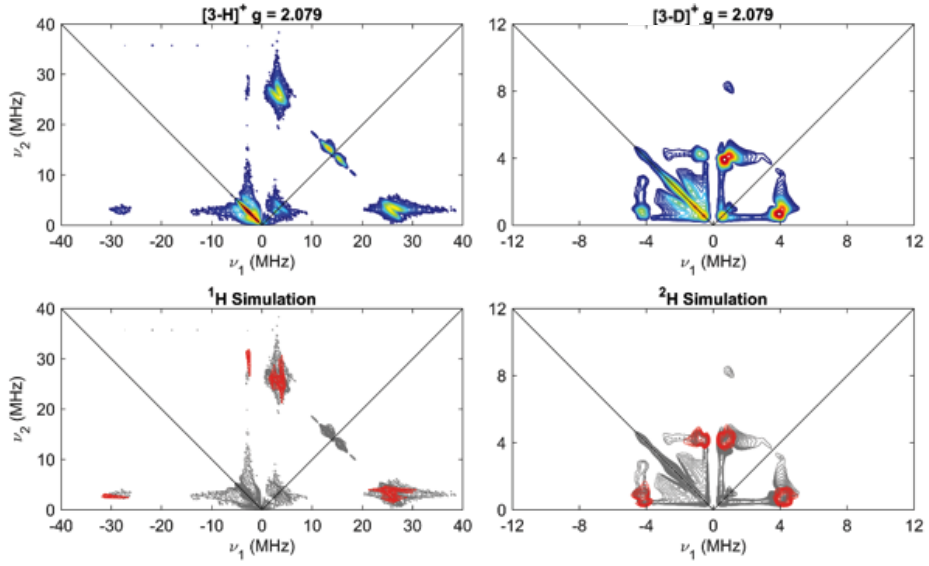

Figure D.46 Field-dependent X-band HYSCORE spectra of *endo*-[**3-H**]$^+$ and *endo*-[**3-D**]$^+$ (top panels) and ^{1}H/^{2}H HYSCORE simulation spectra (bottom panels). Acquisition parameters: temperature = 30 K; microwave frequency = 9.717 GHz; Magnetic field = 334 mT; MW pulse length ($\pi/2$, π) = 8 ns, 16 ns; τ = 140 ns, $t_1 = t_2$ = 100 ns; $\Delta t_1 = \Delta t_2$ = 12 ns; shot repetition time (srt) = 2 ms.

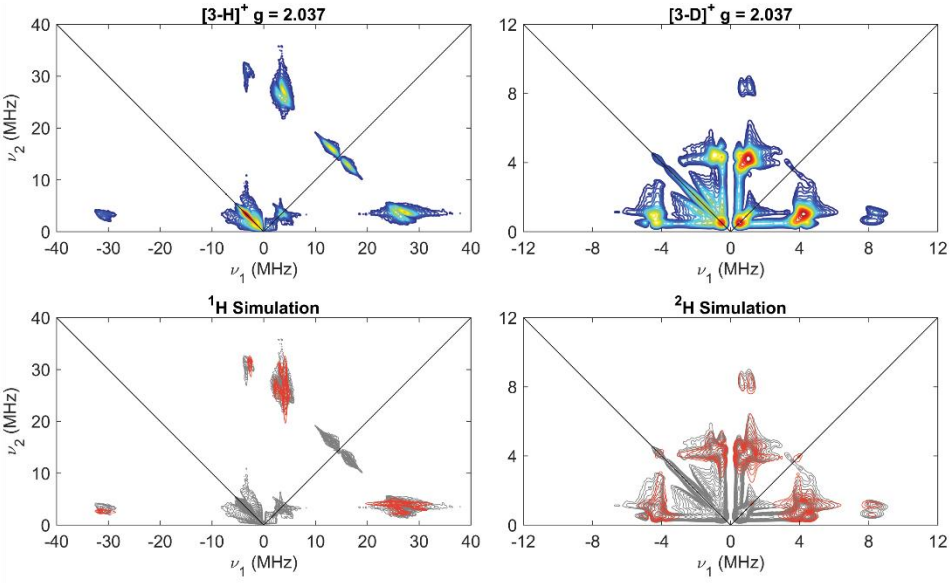

Figure D.47. Field-dependent X-band HYSCORE spectra of *endo*-[**3-H**]$^+$ and *endo*-[**3-D**]$^+$ (top panels) and ^{1}H/^{2}H HYSCORE simulation spectra (bottom panels). Acquisition parameters: temperature = 30 K; microwave frequency = 9.717 GHz; Magnetic field = 340.8 mT; MW pulse length ($\pi/2$, π) = 8 ns, 16 ns; τ = 138 ns, $t_1 = t_2$ = 100 ns; $\Delta t_1 = \Delta t_2$ = 12 ns; shot repetition time (srt) = 2 ms.

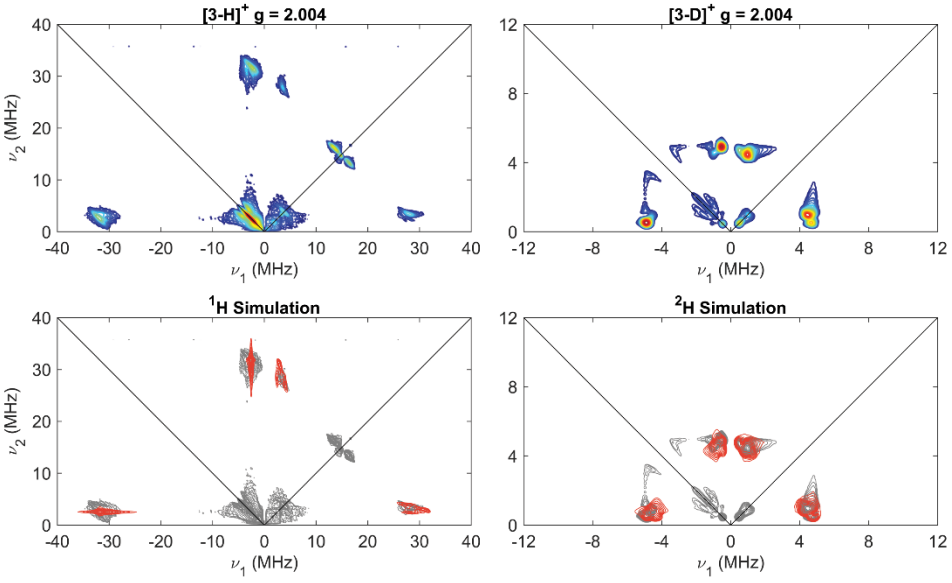

Figure D.48. Field-dependent X-band HYSCORE spectra of *endo*-[**3-H**]$^+$ and *endo*-[**3-D**]$^+$ (top panels) and ^{1}H/^{2}H HYSCORE simulation spectra (bottom panels). Acquisition parameters: temperature = 30 K; microwave frequency = 9.717 GHz; Magnetic field = 346.5 mT; MW pulse length ($\pi/2$, π) = 8 ns, 16 ns; τ = 138 ns, $t_1 = t_2$ = 100 ns; $\Delta t_1 = \Delta t_2$ = 12 ns; shot repetition time (srt) = 2 ms.

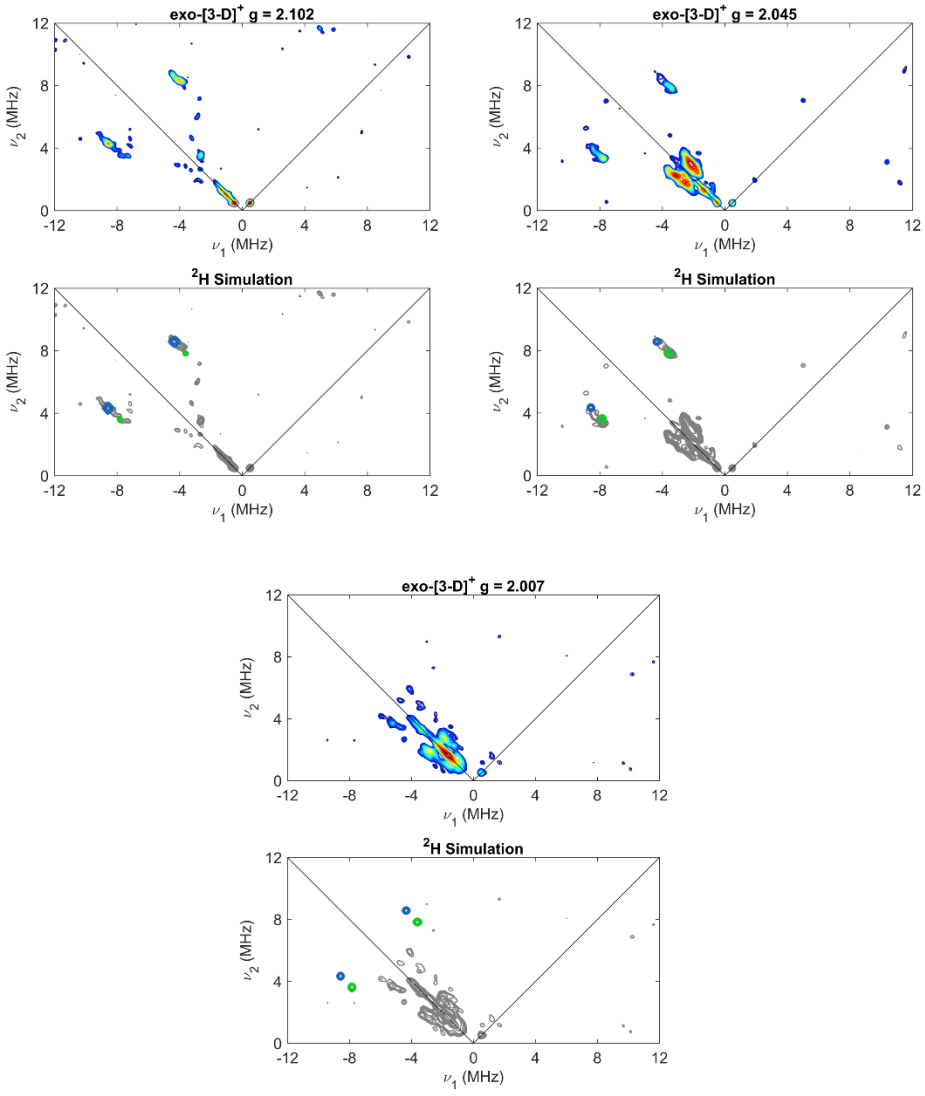

Figure D.49. Field-dependent X-band HYSCORE spectra of *exo*-[**3-D**]$^+$ (top panels) and ^{2}H HYSCORE simulations (bottom panels) of conformations A (blue) and B (green) (bottom panels). Acquisition parameters: temperature = 25 K; microwave frequency = 9.734 GHz; Magnetic field = 330.8 mT (g = 2.102), 340.0 mT (g = 2.045), 346.5 mT (g = 2.007); MW pulse length ($\pi/2$, π) = 8 ns, 16 ns; τ = 142 ns (g = 2.102), τ = 138 ns (g = 2.045), τ = 136 ns (g = 2.007); $t_1 = t_2$ = 100 ns; $\Delta t_1 = \Delta t_2$ = 12 ns; shot repetition time (srt) = 2 ms.

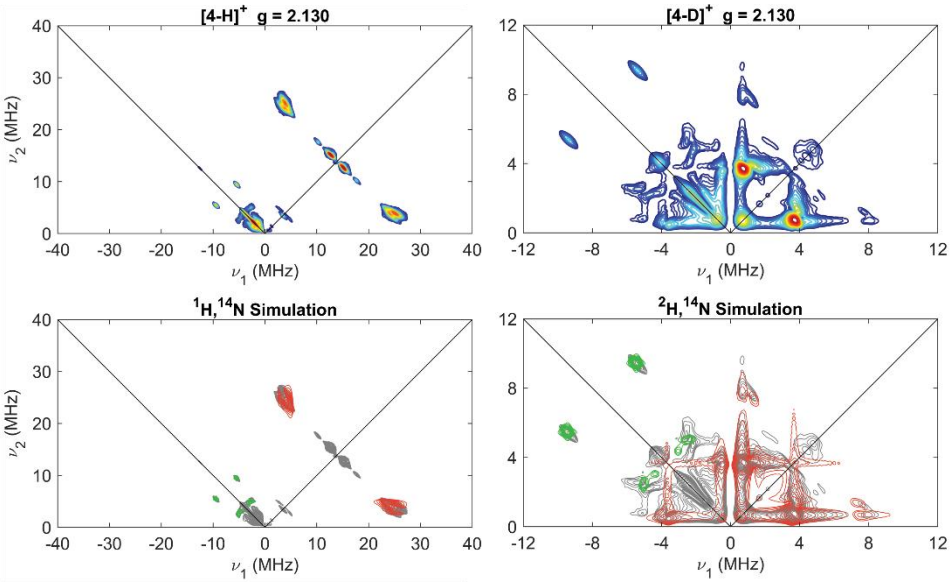

Figure D.50. Field-dependent X-band HYSCORE spectra of *endo*-[**4-H**]$^{+}$ and *endo*-[**4-D**]$^{+}$ (top panels) and ^{1}H,^{14}N/^{2}H,^{14}N HYSCORE simulation spectra (bottom panels). Acquisition parameters: temperature = 30 K; microwave frequency = 9.717 GHz; MW pulse length ($\pi/2$, π) = 8 ns, 16 ns; τ = 144 ns; Magnetic Field = 326.0 mT; $t_1 = t_2$ = 100 ns; $\Delta t_1 = \Delta t_2$ = 12 ns; shot repetition time (srt) = 2 ms.

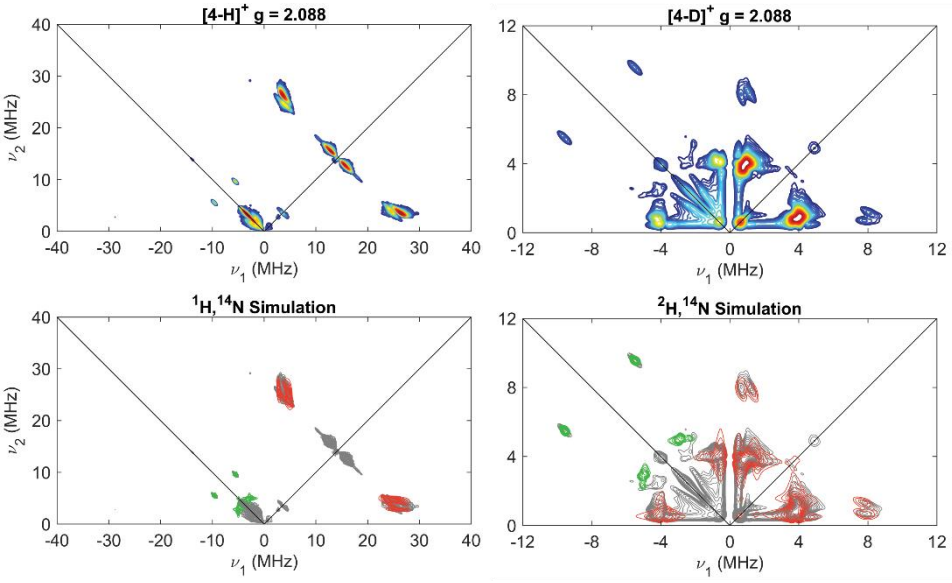

Figure D.51. Field-dependent X-band HYSCORE spectra of *endo*-[**4-H**]$^+$ and *endo*-[**4-D**]$^+$ (top panels) and ^{1}H,^{14}N/^{2}H,^{14}N HYSCORE simulation spectra (bottom panels). Acquisition parameters: temperature = 30 K; microwave frequency = 9.717 GHz; MW pulse length ($\pi/2$, π) = 8 ns, 16 ns; τ = 142 ns; Magnetic Field = 332.5 mT; $t_1 = t_2$ = 100 ns; $\Delta t_1 = \Delta t_2$ = 12 ns; shot repetition time (srt) = 2 ms.

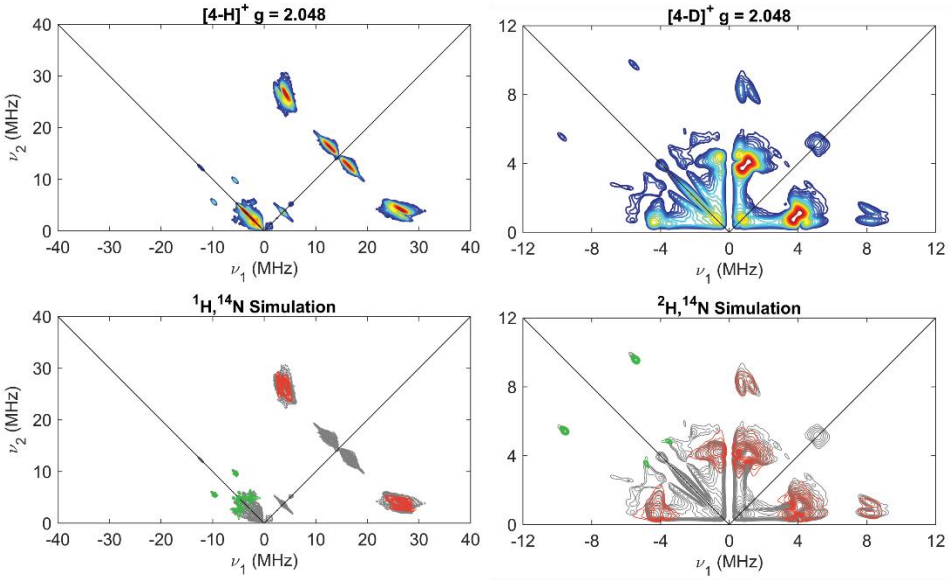

Figure D.52. Field-dependent X-band HYSCORE spectra of *endo*-[**4-H**]$^+$ and *endo*-[**4-D**]$^+$ (top panels) and ^{1}H,^{14}N/^{2}H,^{14}N HYSCORE simulation spectra (bottom panels). Acquisition parameters: temperature = 30 K; microwave frequency = 9.717 GHz; MW pulse length ($\pi/2$, π) = 8 ns, 16 ns; τ = 138 ns; Magnetic Field = 339.0 mT; $t_1 = t_2$ = 100 ns; $\Delta t_1 = \Delta t_2$ = 12 ns; shot repetition time (srt) = 2 ms.

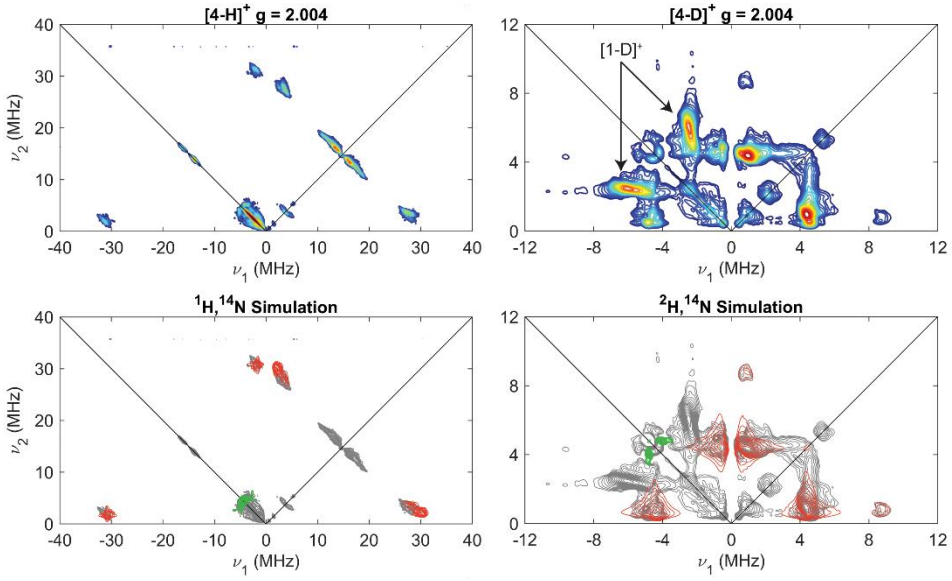

Figure D.53. Field-dependent X-band HYSCORE spectra of *endo*-[**4-H**]$^+$ and *endo*-[**4-D**]$^+$ (top panels) and ^{1}H,^{14}N/^{2}H,^{14}N HYSCORE simulation spectra (bottom panels). Intense features in the (+,-) quadrant of the HYSCORE spectrum of *endo*-[**4-D**]+ are due to contribution of a small amount of residual starting [**1-D**]$^+$. Acquisition parameters: temperature = 30 K; microwave frequency = 9.717 GHz; MW pulse length ($\pi/2$, π) = 8 ns, 16 ns; τ = 138 ns; Magnetic Field = 346.5 mT; $t_1 = t_2$ = 100 ns; $\Delta t_1 = \Delta t_2$ = 16 ns; shot repetition time (srt) = 2 ms.

3.8 Electrochemistry

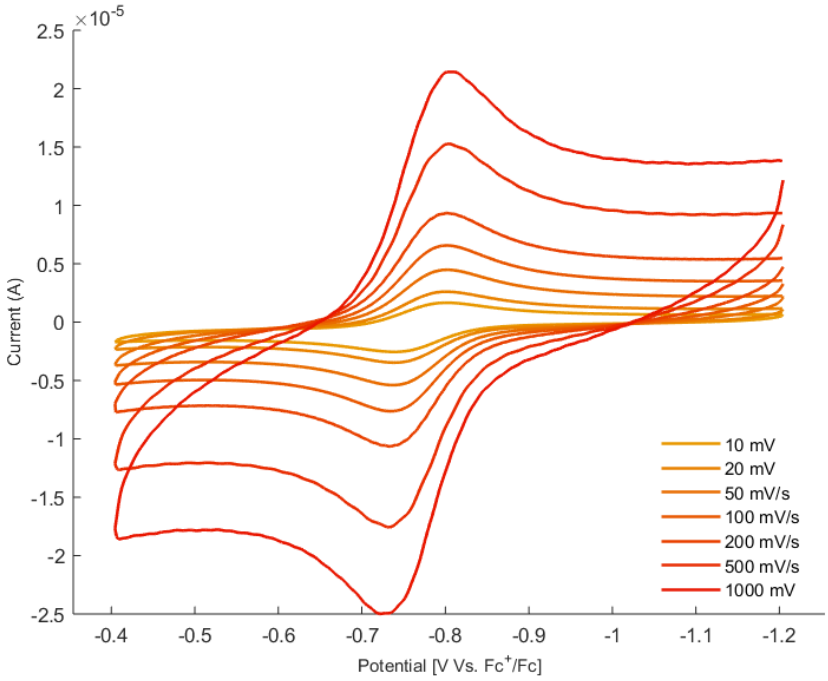

Figure. 0.54 Cyclic voltammogram of *endo*-**3**, showing a reversible Fe^0/Fe^{1+} feature at E_{ox} = -0.81 V (versus Fc/Fc^+).

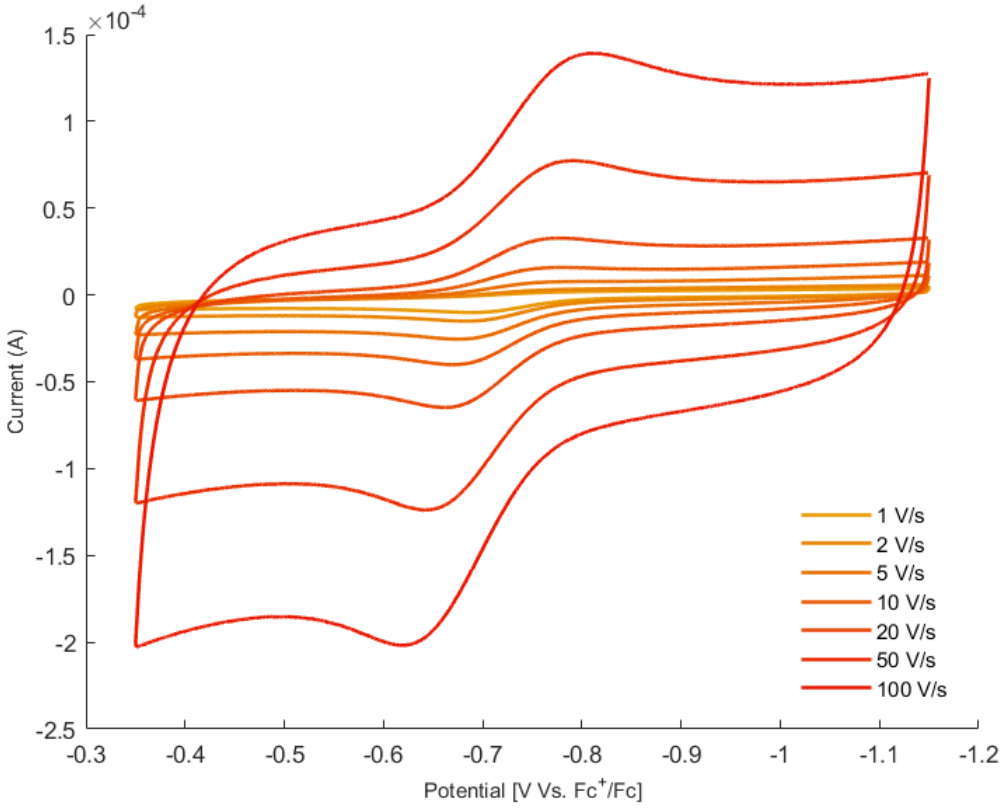

Figure D.55. Cyclic voltammogram of *exo*-**3**, showing the Fe^0/Fe^{1+} feature become more reversable upon increasing the scan rate from 1 V/s to 100 V/s at E_{ox} = -0.70 V (versus Fc/Fc^+).

Crystallographic details

All crystals were mounted on a glass fiber loop. All measurements were made using graphite-monochromated Mo or Cu K_α radiation (λ = 0.71073 or 1.54178 Å) radiation on a Bruker AXS D8 VENTURE KAPPA diffractometer coupled to a PHOTON 100 CMOS detector. The structures were solved by direct methods6 and refined by full-matrix least-squares procedures on F2 (SHELXL-2013)[6] using the OLEX2 interface.7 All hydrogen atoms were placed in calculated positions. Non-hydrogen atoms were refined anisotropically. *endo*-[**3**]$BAr^F{}_4$ (L = CO): ISOR (0.001 0.001) was applied to a 2-methylcyclohexane moiety (C70-C76). Applications of these constraints improved data statistics. An A-level alert also persists for this molecule:

PLAT029_ALERT_3_A _diffrn_measured_fraction_theta_full value Low . 0.938 Why? Author Response: This crystal has many weak reflections at higher values of 2theta (it is weakly diffracting and small). That said, it more than corroborates the connectivity for this species.

[**6**]$BAr^F{}_4$ (*L* = CNXyl): Rotational disorder about two of the -CF_3 groups of the $BAr^F{}_4^-$ counterion was modeled F1/F2/F3 [46/54] and F7/F8/F9 [51/49]. RIGU was applied to two pentane solvent molecules [C77-C87] and ISOR (0.01 0.01) was applied to F1/F2/F3 and F7/F8/F9. Applications of these constraints improved data statistics.

[**7**]$BAr^F{}_4$ (*L* = N_2): Rotational disorder about one of the -CF_3 groups of the $BAr^F{}_4^-$ counterion was modeled [50/50]. Application of these constraints improved data statistics.

CCDC **1943147-1943149** and **2021150-2021151** contains the supplementary

crystallographic data for this paper. These data can be obtained free of charge from The Cambridge Crystallographic Data Centre via www.ccdc.cam.ac.uk/data_request/cif

Table D.2. Crystallographic data for *endo*-**3** and *exo*-**3**.

Compound	*endo*-**3**	*exo*-**3**
Empirical formula	$C_{37}H_{40}FeOP_2$	$C_{37}H_{40}FeOP_2$
Formula weight	618.48	618.48
Temperature/K	100(2)	100(2)
Crystal system	Monoclinic	Monoclinic
Space group	$P2_1/n$	$P2_1/n$
a/Å	12.071(4)	12.161(5)
b/Å	19.165(3)	19.178(6)
c/Å	14.020(4)	13.920(5)
α/°	90	90
β/°	102.72(3)	104.70(2)
γ/°	90	90
V/Å^3	3164.0(16)	3140.2(19)
Z	4	4
ρ/ g/cm^{-3}	1.298	1.308
μ mm^{-1}	4.983	5.021
F(000)	1304.0	1304.0
Crystal size/ mm^3	0.12 × 0.11 × 0.09	0.32 × 0.19 × 0.14
Radiation	CuKα (λ = 1.54178)	CuKα (λ = 1.54178)
2θ range for data collection/°	7.942 to 163.416	8.024 to 149.76
Index ranges	-15 ≤ h ≤ 15, -24 ≤ k ≤ 23, -17 ≤ l ≤ 17	-13 ≤ h ≤ 15, -23 ≤ k ≤ 23, -17 ≤ l ≤ 17
Reflections collected	58389	102570
Independent reflections	6809 [R_{int} = 0.0727, R_{sigma} = 0.0358]	6420 [R_{int} = 0.0536, R_{sigma} = 0.0209]
Data/restraints/parameters	6809/0/375	6420/0/375
Goodness-of-fit on F^2	1.049	1.052
R [I>=2θ (I)] (R1, wR2)	R_1 = 0.0364, wR_2 = 0.0859	R_1 = 0.0272, wR_2 = 0.0754
R (all data) (R1, wR2)	R_1 = 0.0409, wR_2 = 0.0880	R_1 = 0.0276, wR_2 = 0.0757
Largest diff. peak/hole / (e Å^{-3})	0.55/-0.42	0.28/-0.39

$R1 = \Sigma ||F_o|-|F_c|| / \Sigma |F_o|$; $wR2 = [\Sigma(w(F_o^2 - F_c^2)^2) / \Sigma w(F_o^2)^2]^{1/2}$

Table D.3. Crystallographic data for *endo*-[**3**]BAr^F_4 and [**6**]BAr^F_4.

Compound	*endo*-[**3**]BAr^F_4	[**6**]BAr^F_4 (*L* = CNXyl)
Empirical formula	$C_{76}H_{66}BF_{24}FeOP_2$	$C_{87}H_{84}BF_{24}FeNP_2$
Formula weight	1579.88	1728.15
Temperature/K	100(2)	100(2)
Crystal system	Triclinic	Triclinic
Space group	*P-1*	*P-1*
a/Å	14.148(6)	13.7115(6)
b/Å	16.393(4)	16.4188(8)
c/Å	17.640(7)	19.4299(9)
α/°	113.13(2)	86.338(2)
β/°	106.52(2)	69.671(2)
γ/°	90.961(16)	88.504(2)
V/Å^3	3568(2)	4093.3(3)
Z	2	2
ρ/ g/cm^{-3}	1.470	1.402
μ mm^{-1}	3.079	2.727
F(000)	1614.0	1780.0
Crystal size/ mm^3	0.23 × 0.13 × 0.11	0.21 × 0.16 × 0.14
Radiation	CuKα (λ = 1.54178)	CuKα (λ = 1.54178)
2θ range for data collection/°	5.744 to 161.046	4.858 to 161.348
Index ranges	-18 ≤ h ≤ 16, -20 ≤ k ≤ 14, -20 ≤ l ≤ 21	-17 ≤ h ≤ 17, -19 ≤ k ≤ 20, -24 ≤ l ≤ 24
Reflections collected	20853	204590
Independent reflections	13512 [R_{int} = 0.1012, R_{sigma} = 0.1579]	17660 [R_{int} = 0.0836, R_{sigma} = 0.0278]
Data/restraints/parameters	13512/42/940	17660/114/1112
Goodness-of-fit on F^2	1.086	1.049
R [I>=2θ (I)] (R1, wR2)	R_1 = 0.1289, wR_2 = 0.2951	R_1 = 0.0693, wR_2 = 0.2042
R (all data) (R1, wR2)	R_1 = 0.1857, wR_2 = 0.3381	R_1 = 0.0710, wR_2 = 0.2061
Largest diff. peak/hole / (e Å^{-3})	2.13/-0.92	2.12/-0.94

$R1 = \Sigma ||F_o|-|F_c|| / \Sigma |F_o|$; $wR2 = [\Sigma(w(F_o^2 - F_c^2)^2) / \Sigma w(F_o^2)^2]^{1/2}$

Table D.4. Crystallographic data for [**7**]BAr^F_4.

Compound	[**7**]BAr^F_4 (L = N_2)
Empirical formula	$C_{68}H_{51}BF_{24}FeN_2P_2$
Formula weight	1480.70
Temperature/K	100(2)
Crystal system	Triclinic
Space group	*P-1*
a/Å	12.139(5)
b/Å	14.282(3)
c/Å	19.549(4)
α/°	91.970(16)
β/°	93.347(19)
γ/°	106.142(18)
V/Å^3	3245.4(15)
Z	2
ρ/ g/cm^{-3}	1.515
μ mm^{-1}	3.343
F(000)	1500.0
Crystal size/ mm^3	0.20 × 0.16 × 0.14
Radiation	CuKα (λ = 1.54178)
2θ range for data collection/°	6.452 to 162.704
Index ranges	-15 ≤ h ≤ 15, -18 ≤ k ≤ 18, -24 ≤ l ≤ 24
Reflections collected	175771
Independent reflections	14063 [R_{int} = 0.0447, R_{sigma} = 0.0204]
Data/restraints/parameters	14063/0/916
Goodness-of-fit on F^2	1.066
R [I>=2θ (I)] (R1, wR2)	R_1 = 0.0465, wR_2 = 0.1288
R (all data) (R1, wR2)	R_1 = 0.0510, wR_2 = 0.1331
Largest diff. peak/hole / (e Å^{-3})	1.12/-0.55

$R1 = \Sigma ||F_o|-|F_c|| / \Sigma |F_o|$; $wR2 = [\Sigma(w(F_o^2 - F_c^2)^2) / \Sigma w(F_o^2)^2]^{1/2}$

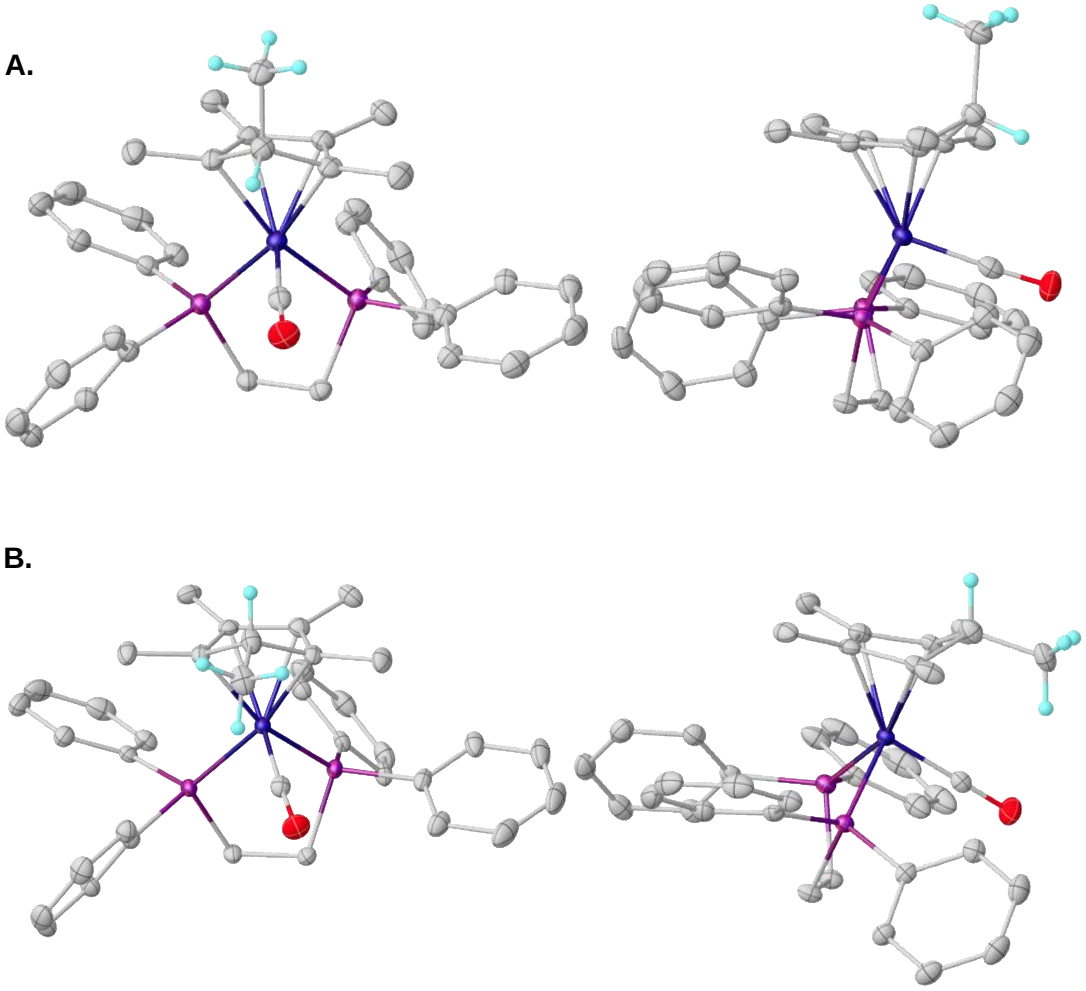

Figure D.56 . Thermal ellipsoid plot (50%) of **A**) *endo*-**3** and **B**) *exo*-**3** (*endo*-**3** had been reported previously[5], though the crystal structure was not obtained).

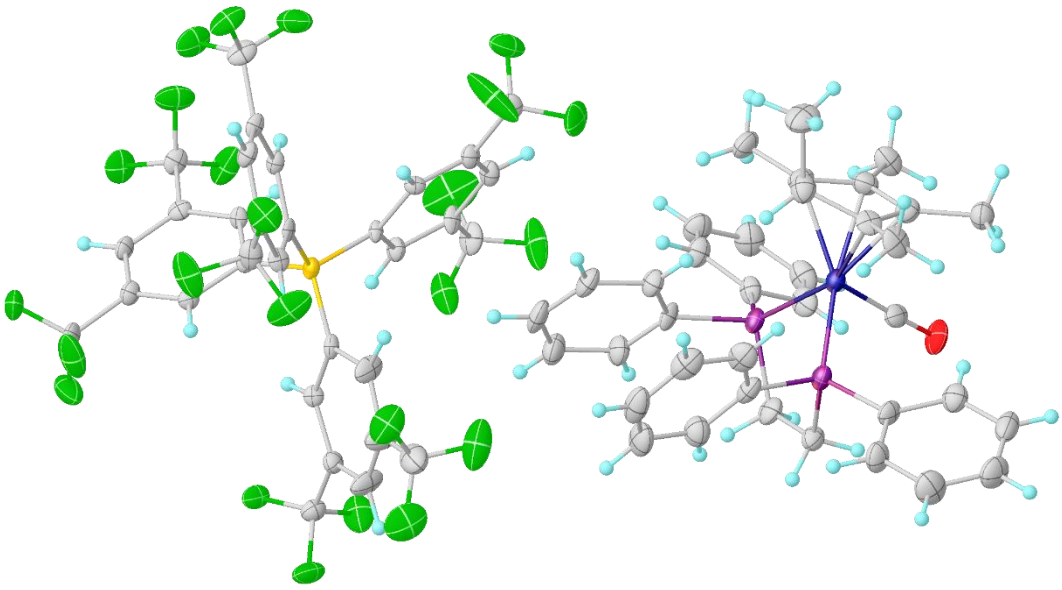

Figure D.57. *endo*-[**3**]BAr^F_4, Thermal ellipsoid plot (50%).

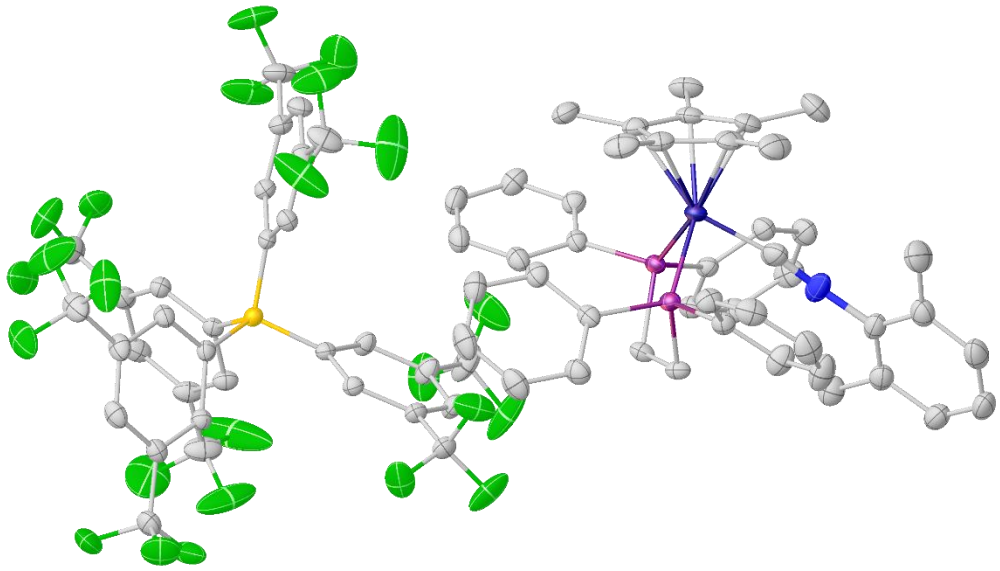

Figure D.58. [**6**]BAr^F_4, Thermal ellipsoid plot (50%, hydrogens omitted for clarity).

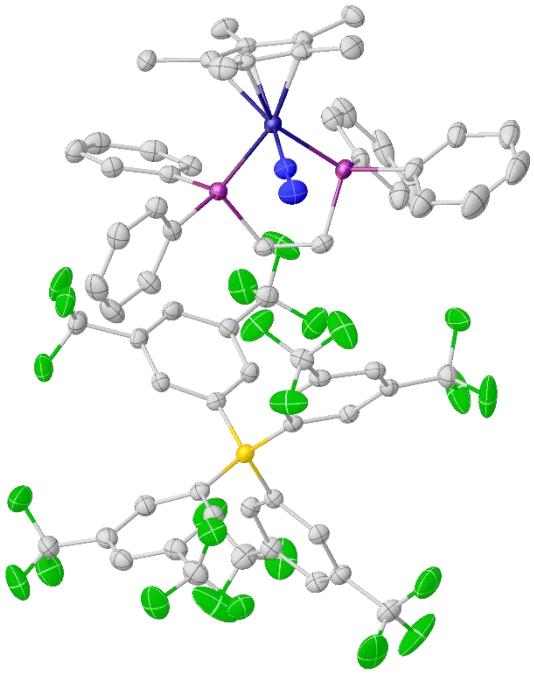

Figure D.59. [**7**]BAr^F_4, Thermal ellipsoid plot (50%, hydrogens omitted for clarity).

DFT Calculations

General

All calculations were performed using the ORCA 4.08,9 program. In cases where crystal structures were available these coordinates were used as the input. The calculations were performed using the TPSS (meta-GGA)10 functional with the def2-SVP basis set was on C and H and the def2-TZVP basis set on Fe.11 To assure that optimized structures represented true stationary points was checked by doing a single-point frequency calculations on the optimized structure.

EPR parameters were calculated using, TPPSh, TPSS, B3LYP, M06L and BP86 with for the TPSS-optimized structure were calculated by doing a single point calculation on the optimized structures using CP(PPP)12 on Fe and IGLO-III13 on everything else grid 7. The results were very similar. Thus the EPR parameters were also calculated using CP(PPP) on Co and def2-TZVP on C and H with TPSS, BP86, and B3LYP. Lastly, the EPR parameters for the structures optimized using TPSSh, BP86, and B3LYP were all calculated via a single point calculation using TPSSh with CP(PPP) on Co and Fe and def2-TZVP on C and H with Grid7. See below for a summary of the results.

$BDFE_{X\text{-}H}$ Calculations:

Consistent with a previous report, a calibration curve of ΔG vs. $BDFE_{lit}$ was employed.14 The free-energy difference between the H-atom donor/acceptor pair was calculated based on the thermochemical information provided by frequency calculations after structure optimizations using the procedure described in the general computational section.

EPR predictions

Table D.5. EPR parameters of [**1**]$^{+}$ with different functionals and basis sets. Although a_{iso} varies significantly between the methods, T(^{1}H) remains constant and is characteristic for iron hydrides.

Functional	**Basis set**	**^{1}H (a_{iso}) (MHz)**	**A(^{1}H) (MHz)**	**T(^{1}H) MHz)**
experimental		36.7	[-10, 60, 60]	[-46.7, 23.3 23.3]
TPSSh	EPR-III (C & H) IGLO-III (P)	-66.34	[-19.33 -83.31 -85.15]	[43.23, -22.55, -20.67]
TPSSh	IGLO-III	-62.59	[-23.11, -88.89, 87.01]	[43.26, -20.72, -22.54]
TPSS	EPR-III (C & H) IGLO-III (P)	-42.33	[-3.85, -62.55, -60.59]	[38.48, -20.22, -18.26]
TPSS	IGLO-III	-39.72	[-1.21, -59.92, -58.02]	[38.51, -20.20, -18.30]
B3LYP	IGLO-III	-81.68	[-36.01, -105.51, -103.51]	[45.67, -23.83, -21.83]
BP86	IGLO-III	-34.39	[2.68, -54.06, -51.78]	[37.07, -19.67, -17.39]
M06l	IGLO-III	-49.08	[-4.69, -72.89, -69.67]	[44.39, -23.81, -20.59]

Table D.6. EPR parameters of endo-[**3**]$^{+}$ with different functionals and basis sets. Although a_{iso} varies significantly between the methods, T(^{1}H) remains constant and the small anisotropy is characteristic for ring functionalized (and not metal-hydride) species.

Functional	**Basis set**	**^{1}H (a_{iso}) (MHz)**	**A(^{1}H) (MHz)**	**T(^{1}H) (MHz)**
experimental		23.33	[34, 16, 20]	[10.67, -7.33, -3.33]
TPSSh	IGLO-III	25.16	[33.11, 19.93, 22.43]	[7.95, -5.23, -2.73]
TPSS	IGLO-III	26.52	[34.11, 21.34, 24.1]	[7.59, -5.17, -2.42]
B3LYP	IGLO-III	24.24	[32.39, 18.89, 21.42]	[8.16, -5.34, -2.81]
BP86	IGLO-III	23.96	[33.6, 20.81, 23.96]	[7.48, -5.31, -2.16]
M06l	IGLO-III	20.85	[29.43, 15.27, 17.86]	[8.58, -5.58, -2.99]

Table D.7. Calculated energies and isotropic ^{1}H hyperfine coupling for rotational isomers of exo-[**3**]$^{+}$ around the Fe-Cp*H centroid axis.

C-Fe-Centroid-C Dihedral Angle (°)	**ΔG (kcal/mol)**	**^{1}H (a_{iso}) (MHz)**	**T(^{1}H) (MHz)**	**T(^{1}H) (MHz)**
-53.25	0	92.27	[95.44, 91.12, 90.25]	[3.17, -1.15, -2.02]
19	0.446322	43.24	[45.81, 41.67, 42.24]	[2.57, -1.57, -1.00]
89.36	1.098098	63.07	[66.46, 61.83, 60.92]	[3.39.-1.24, -2.15]
-170.03	2.108162	86.32	[81.02, 86.88, 91.05]	[-5,30, 0.56, 4.73]

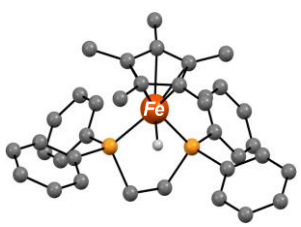

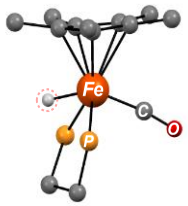

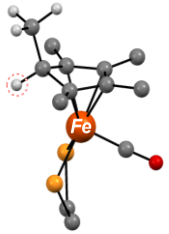

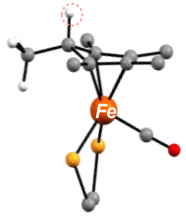

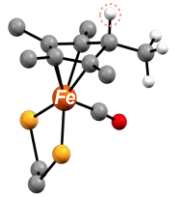

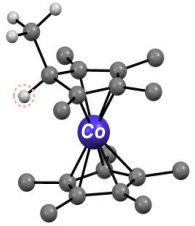

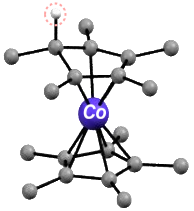

[Fe^{III}(η^5-Cp*)(dppe)(H)]$^+$	[Fe^{III}(η^5-Cp*)(dppe)(CO)(H)]$^+$	[Fe^{I}(*endo*-η^4-Cp*H)(dppe)]$^+$	[Fe^{I}(*exo*-η^4-Cp*H)(dppe)]$^+$ A	[Fe^{I}(*exo*-η^4-Cp*H)(dppe)]$^+$ B	[Cp*(*endo*-η^4-Cp*H)Co]$^+$	[Cp*(*exo*-η^4-Cp*H)Co]$^+$
g = [2.352, 2.041, 1.992]	-	*g* = [2.083, 2.037, 2.003]	*g* = [2.116 2.073 1.997]	*g* = [2.093 2.035, 2.0012]	*g* = [2.626, 2.349, 1.984]	*g* = [2.170, 2.085, 2.005]
$A(^{31}P_1)$ = ± [88, 82, 79] MHz $A(^{31}P_2)$ = ± [82, 71, 76] MHz	- -	$A(^{31}P_1)$ = ± [73, 60, 49] MHz $A(^{31}P_2)$ = ± [49, 51, 49] MHz	$A(^{31}P_1)$ = ± [86, 84, 87] MHz $A(^{31}P_2)$ = ± [78, 75, 63] MHz	$A(^{31}P_1)$ = ± [46, 44, 15] MHz $A(^{31}P_2)$ = ± [70, 54, 54] MHz	- -	- -
$A(^1H)$ = ± [4, 68, 50] MHz $a_{iso}(^1H)$ = ± 40.7 MHz $T(^1H)$ = ± [-36.7, 27.3, 9.3] MHz	- - -	$A(^1H)$ = ± [20, 16, 34] MHz $a_{iso}(^1H)$ = ± 23.3 MHz $T(^1H)$ = ± [-3.3, -7.3, 10.7] MHz	$A(^1H)$ = ± [85, 84, 83] MHz $a_{iso}(^1H)$ = ± 84.0 MHz $T(^1H)$ = ± [1, 0, -1] MHz	$A(^1H)$ = ± [76 74 70] MHz $a_{iso}(^1H)$ = ± 73 MHz $T(^1H)$ = ± [2 1 3] MHz	$A(^1H)$ = ± [19.0, 15.0, 19.5] MHz $a_{iso}(^1H)$ = ± 17.8 MHz $T(^1H)$ = ± [1.2, -2.8, 1.7] MHz	$A(^1H)$ = ± [106.5 112.5, 108.2] MHz $a_{iso}(^1H)$ = ± 109.1 MHz $T(^1H)$ = ± [-2.6, 3.4, -0.9] MHz
DFT $A(^1H)$ = [-1.2, 59.9, 58.0] MHz $a_{iso}(^1H)$ = - 39.7 MHz $T(^1H)$ = [38.5, -20.2, -18.3] MHz	$A(^1H)$ = [31.9, 29.2, 70.2] MHz $a_{iso}(^1H)$ = 43.8 MHz $T(^1H)$ = [-11.9, -14.9, 26.4] MHz	$A(^1H)$ = [24.1, 21.4, 34.1] MHz $a_{iso}(^1H)$ = 26.5 MHz $T(^1H)$ = [-2.4, -5.2, 7.6] MHz	$A(^1H)$ = [81.0, 86.9, 91.0] MHz $a_{iso}(^1H)$ = 86.3 MHz $T(^1H)$ = [4.7, 0.5, -5.3] MHz	$A(^1H)$ = [66.4, 61.8 60.9] MHz $a_{iso}(^1H)$ = 63.1 MHz $T(^1H)$ = [3.3, -1.3, -2.2] MHz	$A(^1H)$ = [30.8 27.9 41.4] MHz $a_{iso}(^1H)$ = 33.4 MHz $T(^1H)$ =[-2.6, -5.5, 8.0] MHz	$A(^1H)$ = [116.6, 122,5, 117.7] MHz $a_{iso}(^1H)$ = 118.9 MHz $T(^1H)$ = [-2.3, 3.6, -1.2] MHz

Figure D.60. DFT-optimized structures showing experimental and predicted A(^{1}H) values

DFT Coordinates

79
dppeFe Cp* hydride cation doublet

Fe	-0.056500	-0.514900	0.761900
P	1.568200	0.112700	-0.666800
P	-1.575600	0.278700	-0.684900
C	-1.221500	-0.778900	2.516800
C	-0.940300	-2.042600	1.869500
C	0.498000	-2.216400	1.843200
C	1.094700	-1.067300	2.484200
C	0.033700	-0.192400	2.908100
C	-2.586500	-0.258100	2.876500
C	-1.961300	-3.068100	1.464200
C	1.237000	-3.440000	1.376200
C	2.556000	-0.909400	2.802200
C	0.192500	1.054500	3.734700
C	0.703200	0.770300	-2.214800
C	-0.729900	0.246300	-2.357500
C	2.730400	1.505000	-0.317400
C	2.523300	2.319200	0.811800
C	3.333500	3.441900	1.040000
C	4.357600	3.760700	0.137300
C	4.569200	2.957000	-0.994400
C	3.761500	1.835700	-1.224600
C	2.665700	-1.243300	-1.269600
C	3.974300	-1.403900	-0.768200
C	4.775000	-2.470200	-1.204300
C	4.282800	-3.385200	-2.145300
C	2.982400	-3.232900	-2.649100
C	2.176900	-2.173900	-2.210300
C	-2.092100	2.045800	-0.532700
C	-2.933800	2.653300	-1.491400
C	-3.264100	4.009600	-1.379600
C	-2.759800	4.775200	-0.315700
C	-1.921700	4.181700	0.637900
C	-1.590800	2.822600	0.528900
C	-3.144800	-0.645000	-0.975200
C	-3.117900	-1.879500	-1.659900
C	-4.300000	-2.601100	-1.871500
C	-5.522300	-2.109200	-1.389800
C	-5.556900	-0.892600	-0.694000
C	-4.377600	-0.161700	-0.487400
H	-2.620200	0.843800	2.880700
H	-3.357100	-0.623300	2.179800
H	-2.864400	-0.604200	3.889800

H	-2.900100	-2.603700	1.126800
H	-1.590300	-3.714600	0.653100
H	-2.198800	-3.718000	2.327700
H	0.659700	-3.995800	0.620900
H	2.213700	-3.184700	0.935000
H	1.420500	-4.119300	2.230100
H	3.190800	-1.413800	2.056900
H	2.859500	0.147900	2.856700
H	2.773900	-1.370000	3.784500
H	1.185600	1.514600	3.610600
H	-0.577300	1.809800	3.506100
H	0.086300	0.800600	4.807600
H	1.316200	0.543300	-3.104400
H	0.693300	1.867100	-2.088100
H	-1.305500	0.846400	-3.082900
H	-0.743200	-0.801100	-2.704600
H	1.717500	2.072100	1.511000
H	3.164800	4.068000	1.922600
H	4.991100	4.636500	0.312100
H	5.366400	3.204600	-1.703400
H	3.936800	1.216300	-2.111200
H	4.380700	-0.685200	-0.048900
H	5.790900	-2.578800	-0.810900
H	4.912100	-4.212200	-2.489900
H	2.593600	-3.940000	-3.389700
H	1.162300	-2.075300	-2.610800
H	-3.343100	2.066500	-2.321600
H	-3.919100	4.471700	-2.126100
H	-3.022600	5.834700	-0.231800
H	-1.524500	4.776100	1.467300
H	-0.934000	2.354200	1.271300
H	-2.171800	-2.290300	-2.027900
H	-4.264700	-3.551900	-2.412800
H	-6.445400	-2.673200	-1.557400
H	-6.507200	-0.503100	-0.314900
H	-4.422700	0.794500	0.043000
H	-0.106300	-1.484400	-0.400800

81

dppeFe H Cp* CO cation doublet

Fe	2.143600	1.077600	1.582100
P	4.107000	0.498600	2.517100
P	2.727200	0.138600	-0.368600
C	1.635800	2.818000	2.900200
C	2.401600	3.409100	4.052000
H	3.376700	3.808100	3.737700
H	2.579400	2.674600	4.854100

H	1.822300	4.244300	4.490700
C	0.464700	1.967900	3.038800
C	-0.081700	1.406000	4.319900
H	-0.367800	0.344000	4.220200
H	-0.995500	1.956700	4.612300
H	0.634400	1.499600	5.151300
C	-0.142800	1.833700	1.763700
C	-1.429500	1.107900	1.495400
H	-1.406900	0.064400	1.858700
H	-1.684800	1.097600	0.424400
H	-2.260700	1.609100	2.025500
C	0.667300	2.563700	0.804600
C	0.279500	2.847900	-0.621400
H	-0.216200	1.986100	-1.097200
H	1.151500	3.119500	-1.235900
H	-0.429800	3.697700	-0.653300
C	1.689300	3.269300	1.536300
C	2.537100	4.388600	0.998700
H	3.452100	4.529100	1.593900
H	1.967100	5.336900	1.033400
H	2.828300	4.219100	-0.050600
C	5.131600	-0.199500	1.107600
C	4.254100	-0.876300	0.050800
H	3.857700	-1.834200	0.431400
H	4.833500	-1.088300	-0.863800
C	5.234700	1.799900	3.201100
C	5.705500	2.830600	2.359900
H	5.383300	2.878400	1.313500
C	6.582200	3.808100	2.847600
H	6.948100	4.593300	2.177600
C	6.988600	3.780600	4.190900
H	7.672500	4.545600	4.573500
C	6.517100	2.768900	5.037800
H	6.831400	2.739000	6.086100
C	5.647800	1.781600	4.548700
H	5.298800	0.992000	5.221100
C	4.135700	-0.789400	3.842900
C	5.230900	-1.662900	4.015400
H	6.090100	-1.629000	3.337200
C	5.246100	-2.580000	5.074600
H	6.100900	-3.254700	5.192800
C	4.177900	-2.629200	5.982400
H	4.194000	-3.345900	6.810400
C	3.091700	-1.756900	5.827400
H	2.254700	-1.788200	6.533300
C	3.069900	-0.845700	4.762600

H	2.216000	-0.172300	4.641800
C	3.233900	1.226000	-1.781100
C	2.532000	1.203900	-3.004700
H	1.669800	0.542500	-3.132100
C	2.933100	2.024500	-4.070000
H	2.375700	1.995300	-5.012000
C	4.041500	2.871000	-3.934500
H	4.357300	3.503200	-4.770700
C	4.744900	2.904300	-2.720500
H	5.614000	3.560500	-2.605400
C	4.337200	2.097400	-1.650100
H	4.889000	2.148600	-0.706300
C	1.659000	-1.119900	-1.194800
C	0.279200	-1.184200	-0.930200
H	-0.165900	-0.491100	-0.212000
C	-0.526600	-2.136200	-1.572000
H	-1.598500	-2.177400	-1.352300
C	0.041200	-3.035600	-2.484100
H	-0.585600	-3.782100	-2.982800
C	1.416700	-2.977600	-2.757900
H	1.865900	-3.676200	-3.471900
C	2.222500	-2.025100	-2.122400
H	3.289600	-1.984900	-2.363900
O	1.088000	-1.634000	2.293300
C	1.416700	-0.543700	2.058400
H	5.678000	0.657000	0.679200
H	5.891800	-0.898100	1.493500
H	3.329500	1.846300	0.982200

81

endo dppeFe Cp*H CO cation doublet

Fe	1.706100	0.849800	1.780200
P	3.772200	0.554300	2.668900
P	2.714500	0.147400	-0.141100
C	1.223800	2.679600	2.842800
C	1.974200	3.476200	3.873800
H	2.898100	3.917800	3.469500
H	2.233900	2.867200	4.753200
H	1.339000	4.310800	4.230600
C	0.289700	1.650800	3.141700
C	-0.035600	1.116300	4.509100
H	-0.407100	0.080300	4.469700
H	-0.821200	1.739100	4.977300
H	0.846600	1.138600	5.168500
C	-0.370700	1.265600	1.896800
C	-1.523900	0.307000	1.779900
H	-1.504300	-0.475000	2.555500

H	-1.544700	-0.182700	0.794200
H	-2.471500	0.867100	1.892800
C	0.178000	2.042900	0.839300
C	-0.365700	2.051500	-0.564700
H	-0.623000	1.039400	-0.914500
H	0.344500	2.487300	-1.286100
H	-1.287800	2.663300	-0.607700
C	0.912900	3.239100	1.450300
C	0.046700	4.534400	1.492500
H	0.600600	5.352000	1.983600
H	-0.890100	4.358600	2.048200
H	-0.204900	4.859600	0.469300
C	4.621000	-0.836400	1.692700
H	5.610000	-0.444700	1.406500
H	4.792300	-1.693000	2.365200
C	3.807700	-1.250400	0.453800
H	3.100000	-2.060700	0.696500
H	4.451000	-1.626500	-0.359800
C	5.059300	1.882600	2.591600
C	4.845000	3.041500	1.824100
H	3.887900	3.180800	1.313100
C	5.855200	4.005700	1.689900
H	5.674600	4.902200	1.087900
C	7.092600	3.817200	2.319700
H	7.882000	4.569500	2.216800
C	7.320600	2.659200	3.080000
H	8.287400	2.505500	3.570400
C	6.313700	1.694800	3.215500
H	6.505900	0.796200	3.811900
C	3.827600	-0.010400	4.428500
C	3.500400	-1.344300	4.755400
H	3.248800	-2.066500	3.972900
C	3.489200	-1.766300	6.091700
H	3.240500	-2.806200	6.327200
C	3.795400	-0.864300	7.121000
H	3.789000	-1.197300	8.163900
C	4.116900	0.463800	6.807500
H	4.366300	1.172900	7.603600
C	4.133100	0.890900	5.471800
H	4.408800	1.925000	5.243800
C	3.858600	1.286500	-1.046900
C	3.380500	2.540800	-1.485300
H	2.343300	2.827400	-1.289000
C	4.212900	3.422500	-2.186900
H	3.819900	4.385600	-2.528200
C	5.545200	3.070900	-2.452000

H 6.199100 3.760900 -2.995500
C 6.033300 1.830100 -2.020700
H 7.069600 1.544800 -2.227600
C 5.197300 0.941900 -1.327900
H 5.603400 -0.024600 -1.017300
C 1.729300 -0.651100 -1.484500
C 0.745300 -1.602400 -1.135900
H 0.551700 -1.840100 -0.084900
C 0.013300 -2.261800 -2.131600
H -0.739100 -3.005400 -1.847400
C 0.242300 -1.970500 -3.485300
H -0.333300 -2.483700 -4.262200
C 1.211900 -1.022200 -3.838200
H 1.398000 -0.791900 -4.892600
C 1.955600 -0.365900 -2.846400
H 2.716300 0.364900 -3.137900
O 0.952300 -1.900400 2.583200
C 1.283100 -0.825800 2.263400
H 1.835800 3.488900 0.889600
81
exo dppeFe Cp*H CO D 89 cation doublet
Fe 1.659500 1.152600 1.279000
P 3.165700 -0.005700 2.656400
P 3.288500 0.931300 -0.413900
C -0.326000 1.800300 1.582200
C -1.586900 0.981700 1.546200
H -1.601700 0.211800 2.336300
H -1.735000 0.482000 0.576600
H -2.458700 1.642300 1.721100
C 0.254300 2.469200 0.452400
C -0.279300 2.472900 -0.953100
H 0.517900 2.624300 -1.697500
H -1.015800 3.290700 -1.074400
H -0.791700 1.527800 -1.193200
C 1.351600 3.277900 0.947300
C 2.077400 4.294100 0.109000
H 2.319000 3.919300 -0.897600
H 3.003100 4.653100 0.579500
H 1.410400 5.168000 -0.019400
C 1.478300 3.070900 2.348300
C 2.398700 3.823400 3.268100
H 3.288700 4.213700 2.749700
H 2.741000 3.201200 4.110700
H 1.862400 4.692000 3.698800
C 0.147200 2.497700 2.859300
C 4.550500 -0.594600 1.519800

H	5.375800	0.133400	1.595000
H	4.924700	-1.562300	1.892900
C	4.081800	-0.700500	0.063100
H	3.336100	-1.504900	-0.056200
H	4.929200	-0.914800	-0.610800
C	4.067800	0.756700	4.086000
C	5.269300	1.478200	3.921300
H	5.729800	1.584000	2.934400
C	5.905800	2.066800	5.023600
H	6.846900	2.606400	4.877200
C	5.348600	1.956100	6.305000
H	5.849200	2.412400	7.164800
C	4.150400	1.248200	6.479600
H	3.711000	1.148500	7.477700
C	3.515200	0.651800	5.382300
H	2.592400	0.085700	5.541900
C	2.557600	-1.584700	3.415100
C	3.485300	-2.446600	4.043400
H	4.544800	-2.171700	4.101300
C	3.060700	-3.653300	4.611100
H	3.791000	-4.314600	5.088700
C	1.703600	-4.012200	4.571100
H	1.372900	-4.956900	5.014500
C	0.774300	-3.157100	3.965500
H	-0.286000	-3.428700	3.935000
C	1.199000	-1.949300	3.390200
H	0.464400	-1.289700	2.920100
C	4.806300	1.992100	-0.501900
C	5.102200	2.879000	0.550000
H	4.388100	2.991500	1.372500
C	6.302300	3.607300	0.558400
H	6.516600	4.295400	1.383300
C	7.221700	3.453400	-0.488300
H	8.157600	4.021500	-0.486300
C	6.940300	2.565300	-1.538800
H	7.658100	2.436900	-2.356300
C	5.743700	1.836300	-1.548100
H	5.539400	1.146700	-2.373900
C	2.797400	0.725800	-2.179100
C	2.273300	-0.497600	-2.649600
H	2.188800	-1.363600	-1.986600
C	1.850200	-0.623200	-3.980500
H	1.454100	-1.581800	-4.331100
C	1.936100	0.466800	-4.858100
H	1.606700	0.364000	-5.896900
C	2.451300	1.688200	-4.399500

H 2.530600 2.542900 -5.079500
C 2.877200 1.819400 -3.070900
H 3.297100 2.774100 -2.735900
O 0.520500 -1.296600 0.142800
C 1.020900 -0.351600 0.613000
C 0.151800 1.681600 4.158900
H 0.556800 2.283900 4.989400
H 0.757200 0.764500 4.072900
H -0.875200 1.388900 4.434200
H -0.531500 3.369200 3.037300
81
exo dppeFe Cp*H CO D -53 cation doublet Opt Freq
Fe 1.717900 1.116100 1.485500
P 3.594100 0.356900 2.688800
P 2.876000 0.493900 -0.376400
C 0.992900 3.094700 0.790000
C 1.287100 3.907400 -0.437800
H 1.108900 3.331000 -1.360100
H 2.317200 4.290300 -0.462200
H 0.602400 4.777700 -0.467100
C 1.624000 3.215700 2.052400
C 2.702600 4.191100 2.437200
H 3.490600 3.731500 3.054300
H 2.250400 5.007000 3.032900
H 3.170700 4.656300 1.556200
C 0.927600 2.351900 3.000800
C 1.158700 2.358600 4.486500
H 2.213600 2.546100 4.737800
H 0.848800 1.414700 4.960700
H 0.559300 3.168100 4.945900
C -0.150400 1.720200 2.310100
C -1.232700 0.902100 2.960200
H -0.871500 0.369300 3.854000
H -1.665100 0.160200 2.269600
H -2.053700 1.572000 3.282000
C -0.388800 2.453900 0.989000
C 4.705300 -0.500900 1.421100
H 5.476300 0.224800 1.112300
H 5.221300 -1.348200 1.902000
C 3.901900 -0.959400 0.199000
H 3.218300 -1.785300 0.459900
H 4.564200 -1.302200 -0.614800
C 4.807700 1.437500 3.596400
C 5.805700 2.165900 2.912000
H 5.906100 2.088900 1.824600
C 6.696100 2.993200 3.611700

H	7.473500	3.535300	3.062700
C	6.598800	3.119500	5.004900
H	7.297100	3.762700	5.550500
C	5.607800	2.407200	5.695500
H	5.529300	2.490400	6.785200
C	4.721600	1.572000	5.000600
H	3.973500	1.002400	5.561100
C	3.328800	-0.983200	3.946300
C	4.437900	-1.697700	4.454100
H	5.453600	-1.450900	4.124500
C	4.257600	-2.715300	5.398000
H	5.126300	-3.262500	5.778200
C	2.968800	-3.029200	5.858500
H	2.828500	-3.826000	6.596500
C	1.864400	-2.318100	5.373300
H	0.857200	-2.554900	5.730900
C	2.044300	-1.301700	4.422100
H	1.176100	-0.755600	4.044700
C	4.177600	1.560000	-1.144700
C	4.604000	2.737600	-0.504500
H	4.111400	3.052600	0.419300
C	5.656100	3.499200	-1.036700
H	5.975500	4.416400	-0.531200
C	6.293400	3.086200	-2.214200
H	7.113100	3.679400	-2.632400
C	5.879200	1.909200	-2.857400
H	6.375100	1.582300	-3.777000
C	4.829200	1.147400	-2.328700
H	4.513700	0.233600	-2.843400
C	1.905400	-0.120000	-1.819000
C	1.378500	-1.429800	-1.833500
H	1.566900	-2.118600	-1.005200
C	0.602800	-1.868300	-2.916200
H	0.209600	-2.889900	-2.918500
C	0.335000	-1.007300	-3.990300
H	-0.269500	-1.353900	-4.834900
C	0.848600	0.297800	-3.981200
H	0.648200	0.974400	-4.818600
C	1.628300	0.741000	-2.904500
H	2.040400	1.754900	-2.920900
O	0.508400	-1.560800	1.463300
C	1.025500	-0.513300	1.491000
C	-1.012000	1.669900	-0.177200
H	-2.009000	1.294500	0.107100
H	-0.393400	0.812600	-0.486900
H	-1.148700	2.328400	-1.051300

H -1.086000 3.301800 1.210500
81
exo dppeFe Cp*H CO D -170 cation doublet
Fe 1.766800 0.941300 1.709800
P 3.826100 0.583500 2.630400
P 2.707700 0.218500 -0.240400
C 1.304600 2.776900 2.810400
C 2.063400 3.584200 3.825400
H 3.003400 3.995000 3.427000
H 2.295200 3.000500 4.728900
H 1.438200 4.444400 4.138300
C 0.404900 1.722100 3.131300
C 0.131400 1.165300 4.500900
H -0.220400 0.122600 4.458500
H -0.653300 1.766500 4.998300
H 1.030300 1.196300 5.136000
C -0.312200 1.355500 1.913300
C -1.484400 0.414400 1.856300
H -1.379000 -0.443300 2.538700
H -1.655000 0.032700 0.838300
H -2.396000 0.966700 2.154000
C 0.172700 2.164800 0.849600
C -0.417000 2.221000 -0.532100
H -0.760300 1.237000 -0.886700
H 0.303400 2.618700 -1.264100
H -1.290100 2.903800 -0.533500
C 0.872500 3.381500 1.465600
C 4.714300 -0.726500 1.582800
H 5.706200 -0.304500 1.353300
H 4.890700 -1.618500 2.206400
C 3.947300 -1.088800 0.301000
H 3.316700 -1.979600 0.464900
H 4.629800 -1.322400 -0.533700
C 5.163400 1.863100 2.763800
C 5.084700 3.069200 2.045200
H 4.192600 3.288400 1.454800
C 6.147000 3.986600 2.069300
H 6.068400 4.922600 1.506600
C 7.302500 3.702800 2.808600
H 8.131400 4.418600 2.831600
C 7.397200 2.495300 3.518500
H 8.300400 2.264800 4.093000
C 6.338300 1.578400 3.497400
H 6.427800 0.641400 4.056900
C 3.781400 -0.129600 4.337800
C 3.522500 -1.501100 4.544500

H	3.378700	-2.178400	3.697500
C	3.440800	-2.021900	5.843500
H	3.245500	-3.090100	5.984700
C	3.608900	-1.183000	6.953800
H	3.547600	-1.593200	7.967100
C	3.863700	0.182200	6.760000
H	4.008100	0.843000	7.621000
C	3.948800	0.707400	5.463100
H	4.174700	1.770000	5.329500
C	3.662500	1.382800	-1.315900
C	3.007500	2.084000	-2.353900
H	1.948800	1.896200	-2.558700
C	3.710500	2.993400	-3.154500
H	3.189400	3.519000	-3.961600
C	5.077200	3.221200	-2.932300
H	5.626600	3.929400	-3.561200
C	5.738300	2.528600	-1.908600
H	6.807100	2.691600	-1.733800
C	5.037800	1.616900	-1.104800
H	5.579900	1.088800	-0.315600
C	1.722700	-0.756000	-1.465700
C	0.466600	-1.286600	-1.114300
H	0.040700	-1.066100	-0.132000
C	-0.236900	-2.105200	-2.009800
H	-1.213800	-2.507800	-1.724400
C	0.309600	-2.404900	-3.265100
H	-0.240500	-3.040900	-3.966400
C	1.564700	-1.889000	-3.620900
H	1.998800	-2.124600	-4.597900
C	2.270400	-1.070300	-2.729600
H	3.248300	-0.675000	-3.022600
O	1.037200	-1.837600	2.432000
C	1.352100	-0.748600	2.152100
C	1.895900	4.125200	0.599700
H	1.388000	4.620800	-0.244400
H	2.656300	3.448400	0.177800
H	2.399600	4.914900	1.182700
H	0.073700	4.126900	1.708500

81

exo dppeFe Cp*H CO D 19 cation doublet

Fe	1.930200	11.829200	2.651800
P	1.089800	12.865800	4.495200
P	3.287000	13.655100	2.407400
O	3.807200	10.589400	4.561400
C	2.646100	16.459700	-1.284000
H	2.494800	17.105800	-2.155200

C	2.098800	9.375100	1.435100
H	1.537700	8.681800	0.758200
C	2.199300	10.706200	0.687200
C	0.954900	11.376400	0.816200
C	1.490900	11.336400	6.855100
H	2.561400	11.512000	6.717400
C	3.045700	14.802000	0.970800
C	-0.826300	11.629100	6.173300
H	-1.577900	12.060900	5.504100
C	1.106900	9.798100	2.519400
C	-1.190800	11.034500	2.331800
H	-1.374800	10.836300	3.399100
H	-1.821700	10.333000	1.753900
H	-1.535800	12.054000	2.105100
C	-2.127000	16.222900	4.041300
H	-2.865700	17.024300	3.934100
C	3.683900	15.516700	-1.277200
H	4.349900	15.425900	-2.142200
C	2.519500	13.915600	5.104300
H	2.198300	14.556200	5.943400
H	3.311700	13.239800	5.471200
C	0.402400	12.394600	-0.144500
H	-0.405300	12.996200	0.301600
H	-0.024500	11.874500	-1.023400
H	1.181900	13.079800	-0.513700
C	7.063500	11.941600	2.120200
H	7.481100	10.943300	1.952900
C	7.914800	13.040500	2.292800
H	9.001100	12.903900	2.264100
C	7.372200	14.319200	2.497500
H	8.032200	15.183600	2.624400
C	3.177700	10.926700	-0.429300
H	3.172000	11.968400	-0.785700
H	2.913100	10.277100	-1.288100
H	4.207800	10.662800	-0.138300
C	-1.242400	10.841700	7.255600
H	-2.310600	10.656800	7.411000
C	-1.656100	15.867100	5.315200
H	-2.025200	16.391100	6.202700
C	3.019000	14.751800	3.919500
H	3.956500	15.278600	4.162700
H	2.268800	15.514800	3.650600
C	3.885700	14.694700	-0.159800
H	4.715900	13.980500	-0.161800
C	0.738800	8.896800	3.663800
H	1.632500	8.523900	4.190900

H	0.192900	8.012100	3.280100
H	0.092500	9.401700	4.399100
C	5.984000	14.496400	2.534900
H	5.578900	15.505300	2.672400
C	3.106500	11.040000	3.741000
C	-0.297300	10.301400	8.139900
H	-0.624700	9.691800	8.988500
C	-1.651400	15.549900	2.908100
H	-2.017000	15.822000	1.912500
C	0.546900	11.888000	5.961600
C	3.384000	8.636200	1.810700
H	3.923800	8.333000	0.897300
H	3.151400	7.714100	2.370000
H	4.065800	9.242900	2.426600
C	2.002300	15.752000	0.952300
H	1.333400	15.864900	1.811400
C	-0.705900	14.522000	3.049700
H	-0.326700	14.001800	2.164700
C	5.117700	13.390900	2.377900
C	-0.714500	14.839900	5.458200
H	-0.363200	14.566300	6.459100
C	1.809700	16.577200	-0.164800
H	1.003700	17.319200	-0.155300
C	1.067300	10.551800	7.937400
H	1.810700	10.138300	8.626500
C	0.254300	10.813100	1.970700
C	5.671800	12.115900	2.162200
H	5.010600	11.256300	2.023400
C	-0.230000	14.154400	4.321600

80

dppeFe Cp* CO cation singlet

Fe	1.819800	0.784200	1.741600
P	3.826000	0.582200	2.757600
P	2.927200	0.150100	-0.118400
C	1.253500	2.578600	2.805500
C	1.944800	3.445100	3.819900
H	2.860400	3.910700	3.427400
H	2.202400	2.882400	4.729600
H	1.256600	4.257600	4.120000
C	0.382600	1.476800	3.123500
C	0.072500	0.962100	4.501900
H	-0.249200	-0.091100	4.479300
H	-0.746400	1.553500	4.953100
H	0.946400	1.035600	5.168500
C	-0.276500	1.069900	1.894800
C	-1.417200	0.094600	1.797200

H	-1.314900	-0.746700	2.500700
H	-1.522500	-0.314300	0.780600
H	-2.361000	0.617800	2.040500
C	0.232600	1.882300	0.826200
C	-0.307800	1.931500	-0.576100
H	-0.572000	0.935100	-0.962500
H	0.409300	2.393000	-1.271600
H	-1.225000	2.550000	-0.591300
C	1.181600	2.821000	1.387500
C	1.735600	4.012200	0.649700
H	2.398800	4.614400	1.289000
H	0.902500	4.668500	0.335700
H	2.291500	3.729000	-0.259200
C	4.738100	-0.832500	1.892600
H	5.801900	-0.547500	1.851000
H	4.671300	-1.725500	2.535200
C	4.169100	-1.127100	0.489500
H	3.586000	-2.063200	0.502900
H	4.962700	-1.256600	-0.265500
C	5.118100	1.910500	2.730000
C	4.947500	3.068800	1.953500
H	4.021500	3.201900	1.390300
C	5.963000	4.035300	1.878000
H	5.814200	4.933200	1.269500
C	7.165600	3.844100	2.570300
H	7.959600	4.596700	2.512800
C	7.354400	2.680900	3.334400
H	8.295200	2.523000	3.871900
C	6.340300	1.718400	3.415700
H	6.500900	0.819200	4.020700
C	3.788900	0.075300	4.538700
C	3.410900	-1.237300	4.896800
H	3.173500	-1.981300	4.130600
C	3.330200	-1.613100	6.244400
H	3.044800	-2.638200	6.502000
C	3.613900	-0.684700	7.256500
H	3.552700	-0.981800	8.308500
C	3.982200	0.623500	6.913400
H	4.213100	1.354200	7.695500
C	4.069400	1.003000	5.566000
H	4.379900	2.022700	5.318600
C	3.920100	1.339100	-1.131200
C	3.288200	2.094000	-2.145200
H	2.222900	1.949100	-2.352100
C	4.021600	2.994900	-2.928800
H	3.517000	3.561500	-3.718500

C	5.398900	3.156700	-2.714300
H	5.973900	3.854300	-3.332300
C	6.037400	2.410500	-1.714400
H	7.113800	2.522800	-1.545800
C	5.305000	1.509600	-0.926700
H	5.831300	0.940500	-0.154500
C	2.059000	-0.837500	-1.424000
C	0.820800	-1.451200	-1.152300
H	0.331800	-1.286200	-0.188000
C	0.212600	-2.282300	-2.104200
H	-0.752000	-2.748900	-1.880200
C	0.837100	-2.512800	-3.337600
H	0.361600	-3.158900	-4.082800
C	2.074800	-1.914000	-3.614300
H	2.571500	-2.095400	-4.573100
C	2.684800	-1.081400	-2.666700
H	3.651200	-0.622700	-2.898400
C	1.520800	-0.901200	2.111100
O	1.243900	-2.003300	2.387700

78

dppeFe Cp* cation singlet

Fe	0.187400	-0.217000	0.934900
P	-1.398000	0.108800	-0.658300
P	1.645700	-0.165200	-0.768500
C	0.977200	-1.849400	1.952400
C	1.275000	-0.630700	2.658100
C	0.006300	-0.017700	3.013700
C	-1.060000	-0.834900	2.519200
C	-0.458000	-1.966800	1.830700
C	1.966100	-2.896600	1.527900
C	2.635100	-0.153200	3.090400
C	-0.149000	1.230300	3.840600
C	-2.522900	-0.666200	2.821700
C	-1.184700	-3.178200	1.321200
C	-0.554600	0.344200	-2.344800
C	0.788400	-0.392100	-2.416600
C	-2.659300	-1.192800	-1.043400
C	-2.306800	-2.315200	-1.822700
C	-3.254000	-3.303800	-2.121300
C	-4.566300	-3.192000	-1.637900
C	-4.926900	-2.082100	-0.860600
C	-3.982800	-1.086300	-0.567200
C	-2.436900	1.638900	-0.564200
C	-2.418700	2.435700	0.595200
C	-3.185200	3.609100	0.667400
C	-3.972600	3.999700	-0.424400

C	-3.997700	3.211600	-1.586500
C	-3.239300	2.036200	-1.657100
C	3.308600	-0.912900	-0.991000
C	3.461200	-2.138100	-1.675800
C	4.731000	-2.712500	-1.824300
C	5.860000	-2.075700	-1.289100
C	5.716800	-0.860600	-0.603300
C	4.449600	-0.280900	-0.451100
C	1.886400	1.652000	-0.701500
C	1.224200	2.241200	0.395000
C	1.181500	3.632600	0.554300
C	1.827600	4.443700	-0.391400
C	2.494700	3.868600	-1.486000
C	2.518400	2.475700	-1.651100
H	1.644900	-3.418300	0.611600
H	2.969100	-2.479200	1.352600
H	2.054600	-3.658700	2.326300
H	3.427800	-0.540500	2.431100
H	2.704500	0.947900	3.093700
H	2.857700	-0.500300	4.117300
H	0.675400	1.944600	3.677300
H	-1.103300	1.744900	3.641800
H	-0.139600	0.966300	4.915900
H	-2.804600	0.392100	2.939100
H	-3.157200	-1.106500	2.036900
H	-2.768700	-1.182600	3.769300
H	-2.219900	-2.950200	1.027000
H	-0.675200	-3.628800	0.454500
H	-1.224700	-3.945400	2.119600
H	-0.394300	1.431600	-2.444700
H	-1.237700	0.026200	-3.150100
H	0.650800	-1.476300	-2.575400
H	1.424000	-0.012700	-3.236500
H	-1.287600	-2.424600	-2.207200
H	-2.965900	-4.162900	-2.736400
H	-5.306800	-3.963200	-1.874100
H	-5.951800	-1.981000	-0.488800
H	-4.288400	-0.211100	0.015300
H	-1.796400	2.129000	1.441900
H	-3.165900	4.219400	1.576800
H	-4.567900	4.917100	-0.371900
H	-4.613000	3.512000	-2.441200
H	-3.281300	1.424200	-2.564900
H	2.592900	-2.652100	-2.101500
H	4.837400	-3.659800	-2.362200
H	6.851400	-2.524000	-1.410300

H 6.596100 -0.355600 -0.190500
H 4.351900 0.675400 0.073400
H 0.776400 1.604700 1.202300
H 0.662000 4.082700 1.406100
H 1.812200 5.532600 -0.273500
H 2.997200 4.511100 -2.216700
H 3.034200 2.034400 -2.511200
78
dppeFe Cp* cation triplet
Fe 0.056500 -0.478000 0.834500
P -1.539400 0.085200 -0.717600
P 1.617000 0.114700 -0.700000
C 0.882900 -2.009800 2.012600
C 1.176400 -0.718100 2.627500
C -0.067600 -0.115000 3.014000
C -1.130300 -0.981900 2.586100
C -0.544200 -2.167500 1.991200
C 1.902700 -3.056100 1.651700
C 2.549800 -0.209700 2.973200
C -0.223200 1.161800 3.796300
C -2.594600 -0.789300 2.867800
C -1.301500 -3.386700 1.537900
C -0.622200 0.495000 -2.320300
C 0.773800 -0.141100 -2.358700
C -2.719700 -1.250600 -1.202000
C -2.294400 -2.300900 -2.043500
C -3.168100 -3.345200 -2.375900
C -4.474700 -3.360700 -1.865700
C -4.904200 -2.325200 -1.023000
C -4.034400 -1.276000 -0.690400
C -2.602600 1.571100 -0.487000
C -2.426900 2.391200 0.643400
C -3.178000 3.567200 0.791000
C -4.108400 3.932000 -0.192200
C -4.290200 3.118700 -1.322800
C -3.543500 1.943300 -1.472800
C 3.249900 -0.716500 -0.904200
C 3.325300 -1.998200 -1.492300
C 4.560000 -2.647000 -1.625300
C 5.732800 -2.032800 -1.161500
C 5.666000 -0.766500 -0.563300
C 4.433900 -0.109200 -0.434000
C 2.006200 1.917000 -0.714100
C 1.533300 2.731600 0.332300
C 1.783200 4.111900 0.328600
C 2.510100 4.687500 -0.722600

C	2.988400	3.882400	-1.769400
C	2.740700	2.503900	-1.767900
H	1.530300	-3.738000	0.869600
H	2.843600	-2.610400	1.294100
H	2.142400	-3.673300	2.538900
H	3.308100	-0.561200	2.255200
H	2.586800	0.892100	3.000900
H	2.847900	-0.576300	3.973800
H	0.564100	1.896600	3.557700
H	-1.204100	1.635900	3.627900
H	-0.149700	0.951600	4.881200
H	-2.876800	0.275200	2.898600
H	-3.224200	-1.294300	2.118300
H	-2.845500	-1.226700	3.853200
H	-2.288300	-3.127700	1.121200
H	-0.745800	-3.947100	0.768400
H	-1.469900	-4.072600	2.390200
H	-0.536400	1.595700	-2.332700
H	-1.233100	0.195700	-3.189500
H	0.715200	-1.230100	-2.532500
H	1.391600	0.288700	-3.166600
H	-1.278300	-2.309800	-2.452300
H	-2.827200	-4.147300	-3.039200
H	-5.158000	-4.174500	-2.129400
H	-5.925100	-2.325900	-0.627600
H	-4.389900	-0.463700	-0.047800
H	-1.696100	2.103500	1.406700
H	-3.035700	4.198900	1.674300
H	-4.693700	4.850400	-0.080000
H	-5.016600	3.401200	-2.092100
H	-3.697900	1.313400	-2.356000
H	2.420800	-2.501900	-1.849800
H	4.604600	-3.635900	-2.092200
H	6.697000	-2.540100	-1.267700
H	6.577900	-0.281300	-0.200600
H	4.398900	0.885600	0.021300
H	0.968800	2.273500	1.153500
H	1.410100	4.736800	1.146600
H	2.708800	5.764400	-0.727000
H	3.559500	4.330500	-2.589600
H	3.132400	1.885200	-2.583300

97

dppeFe Cp* CNXyl cation singlet

Fe	1.850700	0.959100	1.750600
P	3.872200	0.572800	2.691100
P	2.740300	0.230300	-0.173300

C	1.532500	2.849700	2.757300
C	2.322500	3.685800	3.724900
H	3.255100	4.076900	3.294300
H	2.572100	3.131900	4.642700
H	1.703200	4.552000	4.026600
C	0.539800	1.883200	3.144300
C	0.169000	1.546500	4.561400
H	-0.499600	0.675700	4.607800
H	-0.361400	2.400400	5.024800
H	1.052800	1.327900	5.182000
C	-0.194200	1.506900	1.953500
C	-1.448500	0.677300	1.927200
H	-1.391700	-0.189900	2.604500
H	-1.675100	0.307100	0.915500
H	-2.307200	1.296000	2.248800
C	0.373600	2.211600	0.840400
C	-0.214600	2.312300	-0.540100
H	-0.682200	1.374600	-0.875700
H	0.541200	2.607100	-1.282800
H	-0.998900	3.093900	-0.540700
C	1.457100	3.038200	1.333900
C	2.143800	4.109900	0.529300
H	2.946200	4.598900	1.102200
H	1.412200	4.894400	0.258700
H	2.571900	3.724000	-0.410100
C	4.874300	-0.552300	1.537400
C	4.075300	-1.003100	0.311800
H	3.512100	-1.924600	0.529900
H	4.730500	-1.209300	-0.551300
C	5.164400	1.876500	2.986000
C	5.241000	2.962800	2.091700
H	4.481000	3.071500	1.312300
C	6.283000	3.896700	2.184800
H	6.324600	4.736500	1.482400
C	7.266100	3.755300	3.174900
H	8.079200	4.485100	3.252600
C	7.206500	2.670900	4.061800
H	7.976000	2.547300	4.831600
C	6.167200	1.733100	3.968400
H	6.147600	0.886000	4.661000
C	3.834600	-0.334100	4.307500
C	3.893000	-1.741300	4.369800
H	3.999900	-2.336900	3.457900
C	3.817300	-2.408600	5.601400
H	3.871900	-3.502200	5.626500
C	3.676500	-1.681700	6.791300

H	3.624400	-2.203300	7.752700
C	3.609900	-0.281300	6.743400
H	3.508000	0.296800	7.668000
C	3.685300	0.386100	5.513300
H	3.658900	1.480900	5.497700
C	3.586700	1.359100	-1.382900
C	2.897600	1.852200	-2.513500
H	1.869500	1.534400	-2.711700
C	3.529100	2.720700	-3.415200
H	2.978900	3.086000	-4.288700
C	4.860600	3.108600	-3.209500
H	5.354700	3.781200	-3.918400
C	5.559300	2.618300	-2.097500
H	6.603900	2.902700	-1.933300
C	4.927800	1.754200	-1.191300
H	5.499800	1.385800	-0.335000
C	1.723900	-0.817600	-1.318700
C	0.397400	-1.160800	-0.999200
H	-0.043900	-0.780200	-0.074100
C	-0.349300	-1.995700	-1.845200
H	-1.382100	-2.250100	-1.586100
C	0.228200	-2.505200	-3.015900
H	-0.352900	-3.156000	-3.678000
C	1.554800	-2.178200	-3.339300
H	2.011500	-2.575100	-4.251700
C	2.298100	-1.337800	-2.500600
H	3.326600	-1.079600	-2.774300
N	1.171700	-1.893000	2.474400
C	1.444800	-0.763400	2.179500
C	0.847400	-3.170600	2.914600
C	1.158900	-4.295800	2.100300
C	0.811700	-5.569900	2.578800
H	1.040700	-6.443600	1.959000
C	0.185200	-5.738700	3.818400
H	-0.078200	-6.741800	4.168200
C	-0.103900	-4.620500	4.609200
H	-0.589900	-4.749100	5.582000
C	0.216600	-3.322600	4.182300
C	1.865500	-4.152400	0.774700
H	1.478100	-3.303300	0.189500
H	1.751900	-5.068600	0.173800
H	2.951200	-3.993100	0.921600
C	-0.106700	-2.128300	5.042100
H	-0.907600	-1.517400	4.584500
H	0.773900	-1.476000	5.175200
H	-0.457500	-2.446700	6.035600

H 5.747100 0.052800 1.243000
H 5.271700 -1.410000 2.104400
98
dppeFe endo Cp*H CNXyl cation singlet
Fe 1.792800 0.952800 1.781300
P 3.860800 0.601200 2.672700
P 2.675000 0.223900 -0.180100
C 1.445100 2.806100 2.832100
C 2.169300 3.569000 3.908500
H 3.130900 3.980400 3.567500
H 2.352700 2.950500 4.800600
H 1.542300 4.422900 4.233600
C 0.410100 1.866900 3.100000
C -0.038700 1.427100 4.464500
H -0.658400 0.521400 4.417100
H -0.643100 2.227300 4.933900
H 0.815000 1.223100 5.130700
C -0.249200 1.545500 1.844600
C -1.497600 0.715000 1.720500
H -1.447400 -0.212800 2.312800
H -1.711300 0.448900 0.673900
H -2.361700 1.299300 2.090000
C 0.390200 2.279300 0.806600
C -0.111000 2.394100 -0.608200
H -0.469000 1.434200 -1.012400
H 0.670200 2.784700 -1.279000
H -0.960200 3.104800 -0.646100
C 1.233800 3.390800 1.431700
C 0.520700 4.776800 1.441000
H 1.152300 5.530800 1.940000
H -0.443500 4.714600 1.973700
H 0.334100 5.118200 0.409000
C 4.877100 -0.474200 1.484200
H 5.714200 0.165200 1.159600
H 5.327000 -1.312600 2.041600
C 4.058100 -0.964000 0.287000
H 3.523700 -1.895400 0.535800
H 4.698400 -1.168300 -0.588000
C 5.110200 1.943700 2.972200
C 5.064000 3.117700 2.193700
H 4.235500 3.272700 1.494400
C 6.069500 4.089800 2.302300
H 6.016500 4.997600 1.691900
C 7.135200 3.900600 3.193400
H 7.919000 4.660500 3.283800
C 7.194900 2.732700 3.967700

H	8.028100	2.575000	4.661100
C	6.193500	1.757400	3.857800
H	6.261600	0.848000	4.463500
C	3.869600	-0.332400	4.271400
C	3.923600	-1.740800	4.300400
H	4.001500	-2.315800	3.372300
C	3.878400	-2.434000	5.519000
H	3.928600	-3.528000	5.519500
C	3.771500	-1.731800	6.727300
H	3.741600	-2.273600	7.678400
C	3.711300	-0.330300	6.711300
H	3.637700	0.228200	7.650600
C	3.758200	0.363900	5.494700
H	3.739200	1.459000	5.502500
C	3.466200	1.407100	-1.375000
C	2.802600	1.805700	-2.556800
H	1.823700	1.386300	-2.806600
C	3.400200	2.716200	-3.439800
H	2.872200	3.005500	-4.354400
C	4.669600	3.242800	-3.164000
H	5.137100	3.947300	-3.859800
C	5.340300	2.853100	-1.996400
H	6.336600	3.248500	-1.773900
C	4.742400	1.948400	-1.108000
H	5.288400	1.665000	-0.204000
C	1.678800	-0.853800	-1.308300
C	0.356700	-1.209500	-0.983800
H	-0.089900	-0.821000	-0.064800
C	-0.377300	-2.067600	-1.817700
H	-1.406900	-2.332100	-1.555900
C	0.209200	-2.588000	-2.979200
H	-0.361900	-3.257400	-3.631300
C	1.532000	-2.249100	-3.305900
H	1.995400	-2.654900	-4.211000
C	2.263200	-1.386100	-2.479600
H	3.288700	-1.118700	-2.755500
N	1.085400	-1.923600	2.604700
C	1.345100	-0.798600	2.283100
C	0.789100	-3.212600	3.031800
C	1.125200	-4.320900	2.204600
C	0.800600	-5.607400	2.665500
H	1.047500	-6.468700	2.035500
C	0.174400	-5.803200	3.901400
H	-0.071800	-6.815300	4.237600
C	-0.135600	-4.701000	4.706700
H	-0.619600	-4.851600	5.677300

C	0.161000	-3.391800	4.296900
C	1.834000	-4.143500	0.884800
H	1.412400	-3.312300	0.297300
H	1.769000	-5.063400	0.282600
H	2.909100	-3.931100	1.041000
C	-0.183300	-2.214600	5.172600
H	-0.996200	-1.612800	4.724400
H	0.686100	-1.548300	5.312800
H	-0.526200	-2.552600	6.162400
H	2.188300	3.524700	0.882900

98

dppeFe hydride Cp* CNXyl cation doublet

Fe	1.634700	1.309700	1.476700
P	4.208700	0.554000	3.036900
P	2.609900	0.323200	-0.237000
C	1.323700	3.223000	2.300100
C	2.254400	4.035300	3.156800
H	3.101400	4.431600	2.576900
H	2.664500	3.442200	3.990200
H	1.714000	4.897600	3.590800
C	0.318300	2.327400	2.781700
C	0.001700	2.088100	4.230900
H	-0.618600	1.192500	4.372200
H	-0.561100	2.950000	4.637700
H	0.916900	1.977600	4.835000
C	-0.457300	1.862900	1.635600
C	-1.698800	1.019100	1.713900
H	-1.606200	0.213500	2.460000
H	-1.945500	0.560400	0.743600
H	-2.561300	1.646400	2.008000
C	0.067500	2.482900	0.460000
C	-0.512900	2.418300	-0.926300
H	-1.069400	1.484200	-1.102600
H	0.266800	2.505800	-1.700000
H	-1.219800	3.256900	-1.074800
C	1.186800	3.301900	0.857100
C	1.935000	4.245500	-0.041700
H	2.951000	4.449000	0.330400
H	1.396000	5.210800	-0.087800
H	2.018700	3.860000	-1.068800
C	5.013900	0.057900	1.411000
C	4.112800	-0.631600	0.371000
H	3.699100	-1.567500	0.781300
H	4.716700	-0.904400	-0.512600
C	5.553600	1.634700	3.716600
C	5.836500	2.847900	3.049100

H	5.278300	3.121500	2.145200
C	6.829300	3.712400	3.525900
H	7.042500	4.643100	2.989500
C	7.542200	3.391000	4.690500
H	8.315800	4.068700	5.066300
C	7.256900	2.199100	5.370200
H	7.809600	1.940500	6.279600
C	6.271500	1.324100	4.890000
H	6.071400	0.391700	5.427000
C	4.304000	-0.961000	4.088700
C	5.003000	-2.136900	3.745100
H	5.559000	-2.200500	2.804700
C	5.012700	-3.240000	4.612700
H	5.563200	-4.144300	4.332000
C	4.333200	-3.183200	5.837500
H	4.347800	-4.044000	6.514300
C	3.634700	-2.018800	6.192000
H	3.103700	-1.966100	7.148100
C	3.610100	-0.922900	5.319300
H	3.055400	-0.018800	5.599000
C	3.256400	1.381300	-1.615300
C	2.601000	1.415600	-2.865300
H	1.714300	0.797900	-3.037800
C	3.084500	2.225800	-3.903800
H	2.562900	2.237100	-4.866600
C	4.233700	3.006000	-3.716200
H	4.616500	3.627700	-4.532000
C	4.891700	2.983100	-2.477400
H	5.791700	3.586700	-2.321400
C	4.401000	2.187800	-1.432900
H	4.920600	2.202700	-0.470300
C	1.713300	-1.006300	-1.172200
C	0.352300	-1.253200	-0.914800
H	-0.163500	-0.652700	-0.159500
C	-0.332800	-2.266300	-1.603900
H	-1.392100	-2.448600	-1.394300
C	0.340500	-3.046400	-2.554200
H	-0.191400	-3.839000	-3.090800
C	1.698600	-2.807800	-2.819400
H	2.227700	-3.411800	-3.564200
C	2.381900	-1.792400	-2.137500
H	3.436100	-1.607800	-2.371100
N	1.108400	-1.485200	2.621500
C	1.346300	-0.398700	2.187300
C	0.805900	-2.730600	3.159500
C	1.276100	-3.907700	2.512500

C	0.932400	-5.146400	3.076800
H	1.282300	-6.060900	2.586500
C	0.160500	-5.230100	4.240700
H	-0.095200	-6.208100	4.660000
C	-0.281900	-4.060200	4.868400
H	-0.880100	-4.122600	5.783500
C	0.026300	-2.793700	4.349000
C	2.139800	-3.849200	1.278400
H	1.740700	-3.147800	0.528400
H	2.221100	-4.845200	0.816200
H	3.162600	-3.518500	1.537100
C	-0.460300	-1.544500	5.037100
H	-1.192400	-1.003300	4.409400
H	0.373100	-0.851700	5.245800
H	-0.953400	-1.792300	5.989400
H	5.431500	0.995300	1.008700
H	5.888500	-0.583800	1.621700
H	3.058000	1.784800	1.195900

52

Cp* endo Cp*H Co cation doublet

Co	0.057800	0.005100	-0.066800
C	1.739600	1.231500	-0.241100
C	-1.636200	-1.155500	-0.197500
C	-1.401300	-0.785700	1.161600
C	1.506200	-2.052800	-2.116500
H	2.515600	-2.260700	-2.518500
H	0.853500	-1.821600	-2.973800
H	1.145600	-2.981100	-1.647500
C	1.856100	-1.034100	0.285500
C	1.573300	-0.915400	-1.136500
C	2.097700	-2.321900	1.019200
H	3.157900	-2.619900	0.909000
H	1.484900	-3.146300	0.620200
H	1.895500	-2.227900	2.098000
C	1.854800	2.724400	-0.129100
H	2.913400	3.023200	-0.249700
H	1.522900	3.092100	0.854800
H	1.277700	3.244900	-0.909000
C	1.344900	1.072600	-2.835400
H	2.326900	1.190000	-3.331400
H	0.876100	2.068800	-2.798800
H	0.729800	0.423400	-3.480200
C	-1.389800	0.670500	1.245600
C	-1.616600	1.196400	-0.062700
C	1.967100	0.287600	0.834000
C	1.528800	0.488500	-1.463000

C	-1.248000	-1.721500	2.326000
H	-2.233700	-1.879300	2.802900
H	-0.570600	-1.318500	3.095900
H	-0.875700	-2.708200	2.011200
C	-1.228100	1.466300	2.509200
H	-2.218400	1.614700	2.979300
H	-0.808700	2.465500	2.311600
H	-0.587500	0.954400	3.244500
C	-2.137700	0.072400	-0.962300
C	2.349400	0.635700	2.244900
H	3.450400	0.706200	2.331800
H	2.014400	-0.129300	2.964900
H	1.935800	1.607700	2.556100
C	-3.692500	0.094200	-1.128800
H	-4.017200	-0.762300	-1.742000
H	-4.004400	1.020600	-1.638300
H	-4.185600	0.041000	-0.144600
C	-1.762700	2.644500	-0.427200
H	-2.821200	2.955900	-0.328600
H	-1.467700	2.829800	-1.473800
H	-1.167500	3.301100	0.226300
C	-1.803700	-2.550800	-0.723200
H	-2.859800	-2.871200	-0.625200
H	-1.189500	-3.278700	-0.169500
H	-1.543000	-2.614200	-1.792600
H	-1.705400	0.127300	-1.982800

52

Cp* exo Cp*H Co cation doublet

Co	0.012400	-0.001600	-0.037400
C	-1.714900	-1.164000	-0.249300
C	1.753300	1.118800	0.007900
C	1.397000	0.693500	1.323600
C	-1.308500	2.108700	-2.119500
H	-2.301300	2.375800	-2.527700
H	-0.662200	1.845700	-2.972200
H	-0.899100	3.012600	-1.642500
C	-1.754100	1.104400	0.269800
C	-1.444600	0.972700	-1.144400
C	-1.970700	2.402600	0.993000
H	-3.011700	2.744000	0.834900
H	-1.307500	3.200000	0.620800
H	-1.821900	2.302200	2.079700
C	-1.884400	-2.652200	-0.143100
H	-2.945700	-2.917100	-0.310900
H	-1.608800	-3.029800	0.854500
H	-1.290300	-3.191100	-0.897400

C	-1.323400	-1.038500	-2.837600
H	-2.329600	-1.255900	-3.242900
H	-0.766800	-1.989400	-2.820700
H	-0.827200	-0.357600	-3.546900
C	1.344500	-0.763400	1.337100
C	1.665100	-1.235700	0.027600
C	-1.932200	-0.211400	0.817700
C	-1.453600	-0.432900	-1.468100
C	1.186600	1.577100	2.519700
H	2.139500	1.671300	3.074600
H	0.440100	1.164900	3.217800
H	0.875100	2.592000	2.230200
C	1.077700	-1.611700	2.547400
H	2.034000	-1.823800	3.061900
H	0.632600	-2.581800	2.276800
H	0.418500	-1.109600	3.272500
C	2.340300	-0.087500	-0.743400
C	-2.376300	-0.540400	2.214700
H	-3.482000	-0.550200	2.263400
H	-2.025500	0.203300	2.949000
H	-2.028000	-1.534600	2.534200
H	3.422800	-0.128600	-0.464500
C	1.803400	-2.671100	-0.385400
H	2.854400	-3.000100	-0.260600
H	1.545400	-2.817300	-1.447600
H	1.173900	-3.339900	0.221600
C	1.993500	2.532900	-0.430400
H	3.061700	2.793500	-0.292800
H	1.399200	3.253800	0.152500
H	1.761700	2.674400	-1.498700
C	2.274300	-0.090600	-2.276600
H	2.727100	-1.011400	-2.680200
H	2.845200	0.759100	-2.685900
H	1.240400	-0.023600	-2.648300
2			
CO			
C	0.000000	0.000000	-0.651200
O	0.000000	0.000000	0.488400
19			
CNXyl			
N	1.118400	-1.963900	2.628900
C	1.404500	-0.868500	2.268400
C	0.800400	-3.246900	3.053500
C	1.127600	-4.340200	2.212400
C	0.794900	-5.626600	2.666800
H	1.035600	-6.490000	2.037000

C	0.164500	-5.815400	3.903800
H	-0.087700	-6.827200	4.238000
C	-0.146400	-4.715700	4.714500
H	-0.638300	-4.869300	5.680900
C	0.163000	-3.407200	4.309700
C	1.806700	-4.110800	0.884100
H	1.192400	-3.467300	0.228200
H	1.988800	-5.065900	0.367200
H	2.775200	-3.594900	1.016100
C	-0.162300	-2.206200	5.164100
H	-0.824500	-1.502600	4.627200
H	0.752400	-1.642900	5.424100
H	-0.659100	-2.511800	6.098200

81

dppeFeI exo CpstarH CO D 89 cation doublet

Fe	1.659500	1.152600	1.279000
P	3.165700	-0.005700	2.656400
P	3.288500	0.931300	-0.413900
C	-0.326000	1.800300	1.582200
C	-1.586900	0.981700	1.546200
H	-1.601700	0.211800	2.336300
H	-1.735000	0.482000	0.576600
H	-2.458700	1.642300	1.721100
C	0.254300	2.469200	0.452400
C	-0.279300	2.472900	-0.953100
H	0.517900	2.624300	-1.697500
H	-1.015800	3.290700	-1.074400
H	-0.791700	1.527800	-1.193200
C	1.351600	3.277900	0.947300
C	2.077400	4.294100	0.109000
H	2.319000	3.919300	-0.897600
H	3.003100	4.653100	0.579500
H	1.410400	5.168000	-0.019400
C	1.478300	3.070900	2.348300
C	2.398700	3.823400	3.268100
H	3.288700	4.213700	2.749700
H	2.741000	3.201200	4.110700
H	1.862400	4.692000	3.698800
C	0.147200	2.497700	2.859300
C	4.550500	-0.594600	1.519800
H	5.375800	0.133400	1.595000
H	4.924700	-1.562300	1.892900
C	4.081800	-0.700500	0.063100
H	3.336100	-1.504900	-0.056200
H	4.929200	-0.914800	-0.610800
C	4.067800	0.756700	4.086000

C	5.269300	1.478200	3.921300
H	5.729800	1.584000	2.934400
C	5.905800	2.066800	5.023600
H	6.846900	2.606400	4.877200
C	5.348600	1.956100	6.305000
H	5.849200	2.412400	7.164800
C	4.150400	1.248200	6.479600
H	3.711000	1.148500	7.477700
C	3.515200	0.651800	5.382300
H	2.592400	0.085700	5.541900
C	2.557600	-1.584700	3.415100
C	3.485300	-2.446600	4.043400
H	4.544800	-2.171700	4.101300
C	3.060700	-3.653300	4.611100
H	3.791000	-4.314600	5.088700
C	1.703600	-4.012200	4.571100
H	1.372900	-4.956900	5.014500
C	0.774300	-3.157100	3.965500
H	-0.286000	-3.428700	3.935000
C	1.199000	-1.949300	3.390200
H	0.464400	-1.289700	2.920100
C	4.806300	1.992100	-0.501900
C	5.102200	2.879000	0.550000
H	4.388100	2.991500	1.372500
C	6.302300	3.607300	0.558400
H	6.516600	4.295400	1.383300
C	7.221700	3.453400	-0.488300
H	8.157600	4.021500	-0.486300
C	6.940300	2.565300	-1.538800
H	7.658100	2.436900	-2.356300
C	5.743700	1.836300	-1.548100
H	5.539400	1.146700	-2.373900
C	2.797400	0.725800	-2.179100
C	2.273300	-0.497600	-2.649600
H	2.188800	-1.363600	-1.986600
C	1.850200	-0.623200	-3.980500
H	1.454100	-1.581800	-4.331100
C	1.936100	0.466800	-4.858100
H	1.606700	0.364000	-5.896900
C	2.451300	1.688200	-4.399500
H	2.530600	2.542900	-5.079500
C	2.877200	1.819400	-3.070900
H	3.297100	2.774100	-2.735900
O	0.520500	-1.296600	0.142800
C	1.020900	-0.351600	0.613000
C	0.151800	1.681600	4.158900

H 0.556800 2.283900 4.989400
H 0.757200 0.764500 4.072900
H -0.875200 1.388900 4.434200
H -0.531500 3.369200 3.037300
81
dppeFeI exo CpstarH CO D -53 cation doublet Opt Freq
Fe 1.717900 1.116100 1.485500
P 3.594100 0.356900 2.688800
P 2.876000 0.493900 -0.376400
C 0.992900 3.094700 0.790000
C 1.287100 3.907400 -0.437800
H 1.108900 3.331000 -1.360100
H 2.317200 4.290300 -0.462200
H 0.602400 4.777700 -0.467100
C 1.624000 3.215700 2.052400
C 2.702600 4.191100 2.437200
H 3.490600 3.731500 3.054300
H 2.250400 5.007000 3.032900
H 3.170700 4.656300 1.556200
C 0.927600 2.351900 3.000800
C 1.158700 2.358600 4.486500
H 2.213600 2.546100 4.737800
H 0.848800 1.414700 4.960700
H 0.559300 3.168100 4.945900
C -0.150400 1.720200 2.310100
C -1.232700 0.902100 2.960200
H -0.871500 0.369300 3.854000
H -1.665100 0.160200 2.269600
H -2.053700 1.572000 3.282000
C -0.388800 2.453900 0.989000
C 4.705300 -0.500900 1.421100
H 5.476300 0.224800 1.112300
H 5.221300 -1.348200 1.902000
C 3.901900 -0.959400 0.199000
H 3.218300 -1.785300 0.459900
H 4.564200 -1.302200 -0.614800
C 4.807700 1.437500 3.596400
C 5.805700 2.165900 2.912000
H 5.906100 2.088900 1.824600
C 6.696100 2.993200 3.611700
H 7.473500 3.535300 3.062700
C 6.598800 3.119500 5.004900
H 7.297100 3.762700 5.550500
C 5.607800 2.407200 5.695500
H 5.529300 2.490400 6.785200
C 4.721600 1.572000 5.000600

H	3.973500	1.002400	5.561100
C	3.328800	-0.983200	3.946300
C	4.437900	-1.697700	4.454100
H	5.453600	-1.450900	4.124500
C	4.257600	-2.715300	5.398000
H	5.126300	-3.262500	5.778200
C	2.968800	-3.029200	5.858500
H	2.828500	-3.826000	6.596500
C	1.864400	-2.318100	5.373300
H	0.857200	-2.554900	5.730900
C	2.044300	-1.301700	4.422100
H	1.176100	-0.755600	4.044700
C	4.177600	1.560000	-1.144700
C	4.604000	2.737600	-0.504500
H	4.111400	3.052600	0.419300
C	5.656100	3.499200	-1.036700
H	5.975500	4.416400	-0.531200
C	6.293400	3.086200	-2.214200
H	7.113100	3.679400	-2.632400
C	5.879200	1.909200	-2.857400
H	6.375100	1.582300	-3.777000
C	4.829200	1.147400	-2.328700
H	4.513700	0.233600	-2.843400
C	1.905400	-0.120000	-1.819000
C	1.378500	-1.429800	-1.833500
H	1.566900	-2.118600	-1.005200
C	0.602800	-1.868300	-2.916200
H	0.209600	-2.889900	-2.918500
C	0.335000	-1.007300	-3.990300
H	-0.269500	-1.353900	-4.834900
C	0.848600	0.297800	-3.981200
H	0.648200	0.974400	-4.818600
C	1.628300	0.741000	-2.904500
H	2.040400	1.754900	-2.920900
O	0.508400	-1.560800	1.463300
C	1.025500	-0.513300	1.491000
C	-1.012000	1.669900	-0.177200
H	-2.009000	1.294500	0.107100
H	-0.393400	0.812600	-0.486900
H	-1.148700	2.328400	-1.051300
H	-1.086000	3.301800	1.210500

Square Scheme:

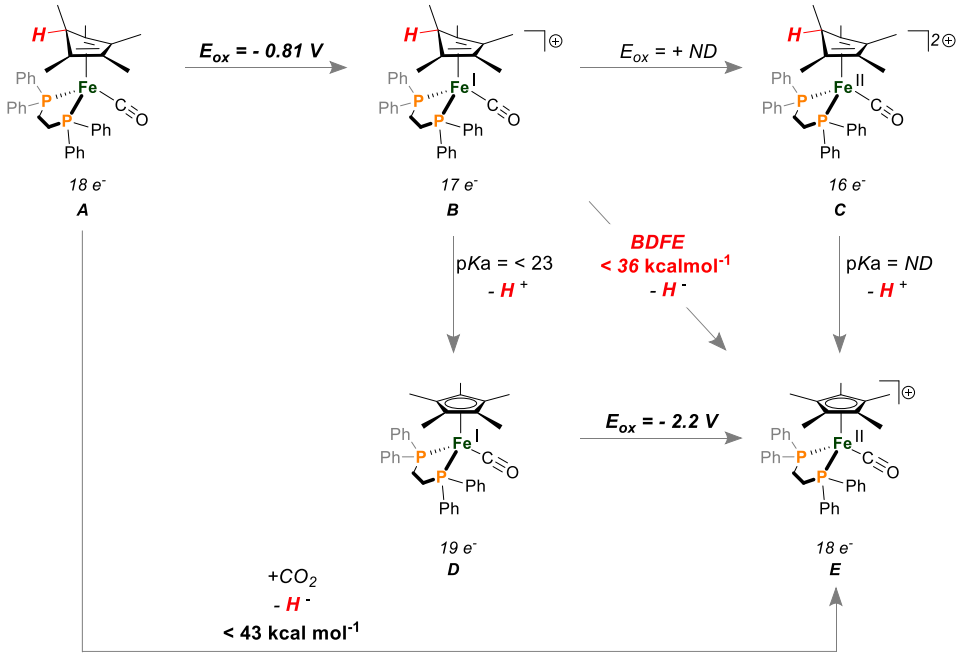

$$BDFE_{(C\text{-}H)} = 1.37pK_a(\mathbf{B}) + 23.06E_{ox}(\mathbf{D}) + 53.6$$

$$BDFE_{(C\text{-}H)} = 1.37pK_a(\mathbf{C}) + 23.06E_{ox}(\mathbf{B}) + 53.6$$

$$BDFE_{(C\text{-}H)} = \Delta G_{(H\text{-})}(\mathbf{A}) - 23.06E_{ox}(\mathbf{A}) - 26$$

Figure D.61. Thermochemical scheme relating H+, H•, and H− transfers for *endo*-[**3**]$^{+}$. The oxidation potential of **B** and the p*K*a of **C** could not be determined due to the low stability of the species involved. The upper limit for the p*Ka* of **B** was estimated using the experimentally determined upper limit of the BDFE of **B** and reduction potential of **E**

References:

1 Prisecaru, I. *WMOSS4 Mössbauer Spectral Analysis Software, www.wmoss.org, 2009-2016.*

2 Stoll, S.; Schweiger, A. EasySpin, a comprehensive software package for spectral simulation and analysis in EPR. *J. Magn. Reson*. **2006**, *178*, 42.

2 Hamon, P.; Toupet, L.; Hamon, J. R.; Lapinte, C. Novel diamagnetic and paramagnetic iron(II), iron(III), and iron(IV) classical and nonclassical hyrides. X-ray crystal structure of $[Fe(C_5Me_5)(dppe)D]PF_6$. *Organometallics* **1992**, *11*, 1429.

4 Hamon, P.; Hamon, J. R.; Lapinte, C. Isolation and characterization of a cationic 19-electron iron(III) hydride complex; electron transfer induced hydride migration by carbon monoxide at an iron(III) centre. *J. Chem. Soc. Chem. Commun.* 1992, **1602**.

4 Similar behavior has been noted: a) Zhang, F.; Xu, X.; Zhao, Y.; Jia, J.; Tung, C. –H.; Wang, W. Solvent Effects on Hydride Transfer from Cp*(P-P)FeH to BNA^+ Cation. *Organometallics* **2017**, *36*, 1238; b) Zhang, F.; Jia, J.; Dong, S.; Wang, W.; Tung, C. –H. Hydride Transfer from Iron(II) Hydride Compounds to $NAD(P)^+$ Analogues. *Organometallics* **2016**, *35* 1151.

6 Sheldrick, G. M.; A short history of *SHELX*. IUCr. *Acta Crystallogr., Sect. A: Found. Crystallogr*. **2008**, *64*, 112.

7 Dolomanov, O. V.; Bourhis, L. J.; Gildea, R. J.; Howard, J. A. K.; Puschmann, H. *OLEX2*: a complete structure solution, refinement and analysis program. *J. Appl. Crystallogr*. **2009**, *42*, 339.

8 Neese, F. The ORCA program system. *Wiley Interdiscip. Rev.: Comput. Mol. Sci*. **2012**, *2*, 73.

9 Neese, F. Software update: the ORCA program system, version 4.0. *Wiley Interdiscip. Rev.: Comput. Mol. Sci.* **2018**, *8*, 1327.

10 Tao, J.; Perdew, J. P.; Staroverov, V. N.; Scuseria, G. E. Climbing the density functional ladder: nonempirical meta-generalized gradient approximation designed for molecules and solids. *Phys. Rev. Lett.* **2003**, *91*, 146401.

11Weigend, F.; Ahlrichs, R. Balanced basis sets of split valence, triple zeta valence and quadruple zeta valence quality for H to Rn: design and assessment of accuracy. *Phys. Chem. Chem. Phys.* **2005**, *7*, 3297.

12 Neese, F. Prediction and interpretation of the ^{57}Fe isomer shift in Mössbauer spectra by density functional theory. *Inorg. Chim. Acta* **2002**, *337*, 181.

13 Kutzelnigg, Werner, Fleischer, Ulrich, Schindler, Michael. The IGLO-Method: Ab-initio Calculation and Interpretation of NMR Chemical Shifts and Magnetic Susceptibilities in 'Deuterium and Shift Calculation' ed. Maryvonne L. Martin, Gérard J. Martin, NMR Basic Principles and Progress, *16*, 165-262

14 Matson, B. D.; Peters, J. C. *ACS Catal.* **2018**, *8*, 1448.